Development of a Chipless RFID Based Aerospace Structural Health Monitoring Sensor System

By

Kevin McGee (M. Eng)

A thesis submitted to Dublin City University in fulfilment of the requirements for the degree of

Doctor of Philosophy

Principal Supervisor: Dr. David Collins

Secondary Supervisor: Dr. Prince Anandarajah

March 2023

School of Biotechnology

Dublin City University

Declaration:

I hereby certify that this material, which I now submit for assessment on the programme of study leading to the award of Doctor of Philosophy is entirely my own work, and that I have exercised reasonable care to ensure that the work is original, and does not to the best of my knowledge breach any law of copyright, and has not been taken from the work of others save and to the extent that such work has been cited and acknowledged within the text of my work

Signed: _(signature)_   ID No.: 12387171   Date: 06/03/2023

List of Publications and Presentations

Research Papers

1. Mc Gee, K.; Anandarajah, P.; Collins, D. Use of Chipless RFID as a Passive, Printable Sensor Technology for Aerospace Strain and Temperature Monitoring. Sensors 2022, 22, 8681. https://doi.org/10.3390/s22228681

2. Invited Paper - Mc Gee, K.; Anandarajah, P.; Collins, D. Proof of Concept Novel Configurable Chipless RFID Strain Sensor. Sensors 2021, 21, 6224. https://doi.org/10.3390/s21186224

3. Invited Paper - Mc Gee, K.; Anandarajah, P.; Collins, D. Current Progress towards the Integration of Thermocouple and Chipless RFID Technologies and the Sensing of a Dynamic Stimulus. Micromachines 2020, 11, 1019. https://doi.org/10.3390/mi11111019

Conference Proceedings

1. K. M. Gee, P. Anandarajah and D. Collins, "Zero-Power Wireless Strain and Permittivity Sensor," 2022 33rd Irish Signals and Systems Conference (ISSC), 2022, pp. 1-5, doi: 10.1109/ISSC55427.2022.9826209.

Review Papers

1. Mc Gee, K.; Anandarajah, P.; Collins, D. A Review of Chipless Remote Sensing Solutions Based on RFID Technology. Sensors 2019, 19, 4829. https://doi.org/10.3390/s19224829

Table of Contents

Contents

List of Abbreviations

RFID	-	Radio Frequency Identification
SHM	-	Structural Health Monitoring
ESA	-	European Space Agency
STC	-	Self-Temperature Compensating
TCR	-	Temperature-dependent Compensating Resistor
K	-	Gauge Factor
RTD	-	Resistance Temperature Detector
NTC	-	Negative Temperature Coefficient
NASA	-	National Aeronautics and Space Administration
FBG	-	Fiber Bragg Grating
UV	-	Ultraviolet
ZST	-	Zirconium Tin Titanate
SOI	-	Silicon-On-Insulator
SiC	-	Silicon Carbide
SiCN	-	Silicon Carbide Nitride
IGZO	-	Indium Gallium Zinc Oxide
LEO	-	Low Earth Orbit
AO	-	Atomic Oxygen
PTFE	-	Polytetrafluoroethylene
RCS	-	Radar Cross Section
LH	-	Left Handed
RH	-	Right Handed
CRLH	-	Composite Right-Left-Handed
SAW	-	Surface Acoustic Wave
IDT	-	Interdigital Transducer
CPW	-	Co-Planar Waveguide
SIR	-	Stepped Impedance Resonator
MLA	-	Meander Line Antenna
BST	-	Barium Strontium Titanate

FDM	-	Fused Deposition Modelling
CNT	-	Carbon Nanotubes
DPI	-	Dots Per Inch
PSA	-	Pressure-Sensitive Adhesive
AFM	-	Atomic Force Microscopy
GF	-	Gauge Factor
ε	-	Strain
PDMS	-	Polydimethylsiloxane
MWCNT	-	Multiwalled CNT
Ag	-	Silver
NP	-	Nanoparticle
Q	-	Quality
GFRP	-	Glass Fiber Reinforced Polymer
CFRP	-	Carbon Fiber Reinforced Polymer
UWB	-	Ultrawideband
FE	-	Finite Element
FEM	-	Finite Element Method
VNA	-	Vector Network Analyser
LPDA	-	Log-Periodic Dipole Array
PMMA	-	Poly (methyl Methacrylate)
EDM	-	Electro-Discharge Machining
ELC	-	Electric LC
TRL	-	Technology Readiness Level
PVD	-	Physical Vapor Deposition
CVD	-	Chemical Vapor Deposition
IPL	-	Intense Pulsed Light
IR	-	Infrared
CHE	-	Coefficient of Humidity Expansion
CTE	-	Coefficient of Thermal Expansion
PPM	-	Parts per Million
HD	-	High Definition

DUT	-	Device Under Test
UHF	-	Ultrahigh Frequency
MW	-	Microwave
PET	-	Polyethylene Terephthalate
LCP	-	Liquid Crystal Polymer
VOC	-	Volatile Organic Compound
PVA	-	Polyvinyl Alcohol
MEMS	-	Micro-Electromechanical Systems
ADC	-	Analog to Digital Converter
FRAM	-	Ferroelectric Random-Access Memory
PCB	-	Printed Circuit Board
VHF	-	Very High Frequency
BTO	-	Barium Titanate
FR4	-	Flame Resistant Grade-4
LDR	-	Light Dependent Resistor
EM	-	Electromagnetic
IR-UWB	-	Impulse Radio Ultrawideband
FMCW	-	Frequency Modulated Continuous Wave
SFCW	-	Stepped Frequency Continuous Wave
LOS	-	Line of Sight
FFT	-	Fast Fourier Transform
dB	-	Decibel
ϕ	-	Phase
ET	-	Equivalent Time
VCO	-	Voltage Controlled Oscillator
TF	-	Transfer Function
GD	-	Gradient Descent
LHS	-	Left Hand Side
RHS	-	Right Hand Side
DFT	-	Discrete Fourier Transform
LDPA	-	Log Periodic Dipole Array

PTP	-	Peak to Peak
CRR	-	Circular Ring Resonator
VSWR	-	Voltage Standing Wave Ratio
TEM	-	Transverse Electro-Magnetic
Q-Factor	-	Quality Factor
LDPA	-	Log Periodic Dipole Array
RTT	-	Round Trip Time
SRD	-	Step Recovery Diode
PSD	-	Power Spectral Density
FEA	-	Finite Element Analysis
GD	-	Gradient Descent
IF	-	Intermediate Frequency

List of Figures

List of Tables

XXIII

Acknowledgements

First and foremost, I want to thank my supervisors Dr. David Collins and Dr. Prince Anandarajah and the Irish Research Council (IRC) for the opportunity to perform this project. Both of my supervisors have been highly insightful and a constant source of reassurance and much-needed pragmatism. As well as that, they have provided ample assistance via technical support, advice on time management and general life advice. I must also thank the other members of staff in the schools of Biotechnology, Electronic and Mechanical engineering for their support and general willingness to help me along this path. My sole lab mate Brian and lunch mates were also of key importance to me reaching this point as their input into both technical and general challenges greatly helped me through the tough parts of the project. All of the aforementioned people have helped in an immeasurable way to stop me getting "bogged down" along this journey. Their tools included humour, kindness and useful technical advice but to name a few, and for them I am very grateful.

To my friends and family at home, thanks for putting up with me these past few years and my almost constant late arrivals, absent mindedness and general single-mindedness towards completing this project. I can assure you that these tendencies are not built into the hardware and will be removed soon (hopefully!)

Thesis Overview

Chapter 1: Thesis Introduction

This chapter outlines the motivation behind this project and the basic reasons as why chipless RFID has been used in this work. The general research questions that were considered during this project are also listed here.

Chapter 2: Literature Review on SHM and Chipless RFID Technologies

In this chapter, existing sensor technologies are discussed such as foil strain gauges, thermistors, thermocouples and other such devices. Optical sensors and other modern sensor technologies are also briefly described. This discussion includes discussions about design, performance and ease of fabrication.

An overview of the sensing requirements of generic aerospace applications is presented in this chapter, along with a thorough discussion on the environmental challenges posed by the aerospace setting.

Chipless RFID technology is also reviewed in this chapter, with a brief overview of the current state of the art in this field. Again, this discussion contains analysis related to the design and ease of fabrication. A more thorough discussion on in-situ fabrication methods for chipless RFID tags is also presented.

Chapter 3: Strain Sensor Development

This chapter explores the existing chipless RFID strain sensor designs and proposes an alternative design approach. It then presents several different sensor designs and performs the relevant performance analysis. Emphasis is placed on the fabrication avenues available to develop the final sensor and several rapid-fabrication sensor implementations were also tested and compared.

Chapter 4: Temperature Sensor Development

Chapter four depicts the temperature sensing research arising from this project. This includes a critical overview of the existing designs that can be found in the literature. Thermocouple integration into chipless RFID is conceptually demonstrated and a variety of other low-temperature (< 350°C) devices are also constructed and tested.

The novel designs put forward in this chapter have made use of both dielectric-based and mechanical-based sensing approaches and a significant emphasis has been placed on sensor response time and other important sensor performance metrics.

As found in the strain sensing chapter, a significant emphasis has also been placed on the need to fabricate the final sensor design in-situ.

Chapter 5: Sensor Response Analysis

The fifth chapter explores the challenges that have occurred during sensor testing that have made moderate/high resolution sensing extremely difficult. The main goals of this chapter are to highlight the limitations of the methods used in most work to detect the minimum of the response curve. Most other works assume that the minimum point in the dataset has to be the minimum of the curve and they use a visual inspection of the dataset to validate this claim. An automated system will need to check for the presence of the resonant curve in some way, which is why the use of a matched filter has been explored in this work. Secondly, making the resolution of the extracted stimulus value, dependent on the resolution of the dataset will lead to excessively long interrogation times. Finally, a potential method for dealing with a dynamic stimulus has been put forward as ignoring this possibility can have detrimental effects on the reader's ability to interpret the response dataset.

Chapter 6: Sensor System Deployment

Chapter six moves away from bespoke sensor design focussing on issues such as sensor addressing, read range, polarization and sensor orientation. Each of these issues have been explored in the context of aerospace strain and temperature monitoring and where possible, novel design solutions have been proposed and tested, so as to enhance system performance.

This final research chapter presented in this document is also focussed on the isolation and detection of individual sensors in a multi-sensor environment. This includes a review of the issues that can occur when multiple identical sensors are illuminated. Some novel reader/sensor enhancements are also implemented and tested to give a future reader system designer some additional design flexibility.

Chapter 7: Conclusions and Further Work

The final chapter discusses the overall outcomes of this research project and begins a more in-depth discussion on the next steps to potentially be taken in this project.

Abstract

Kevin McGee

Development of a Chipless RFID Based Aerospace Structural Health Monitoring Sensor System

Chipless Radio Frequency Identification (RFID) is modern wireless technology that has been earmarked as being suitable for low-cost item tagging/tracking. These devices do not require integrated circuitry or a battery and thus, are not only are cheap, but also easy to manufacture and potentially very robust. A great deal of attention is also being put on the possibility of giving these tags the ability to sense various environmental stimuli such as temperature and humidity.

This work focusses on the potential use of chipless RFID as a sensor technology for aerospace Structural Health Monitoring. The project is focussed on the sensing of mechanical strain and temperature, with an emphasis placed on fabrication simplicity, so that the final sensor designs could be potentially fabricated in-situ using existing printing technologies.

Within this project, a variety of novel chipless RFID strain and temperature sensors have been designed, fabricated and tested. A thorough discussion is also presented on the topic of strain sensor cross sensitivity, which places emphasis on issues like, transverse strain, dielectric constant variations and thermal swelling. Additionally, an exploration into other key technological challenges was also performed, with a focus on challenges such as: accurate and reliable stimulus detection, sensor polarization and multi-sensor support.

Several key areas of future research have also been identified and outlined, with aims related to: Enhancing strain sensor fabrication simplicity, enhancing temperature sensor sensitivity and simplicity and developing a fully functional interrogation system.

Chapter 1: Introduction

1.1   Project Introduction

This project is focussed on the development of passive wireless sensors for aerospace Structural Health Monitoring (SHM). The resulting devices are also designed to support their fabrication in-situ using conventional printing technologies.

Passive sensors, in the context of this project, are defined as those that do not require a dedicated power source in order to operate but instead rely on some external source of power to measure/communicate stimulus information. Wireless, as the name suggests, means that the resulting sensors can be communicated with via a non-wired method, such as radio/microwave propagation or ultrasonics. The topic of SHM is a vast one but for the sake of simplicity, it is limited to the sensing of only temperature and mechanical strain, although the explored sensor technology has been shown to be capable of sensing a wide variety of other stimuli [1]. As to the in-situ fabrication aspect of this project, conventional printing technologies such as inkjet deposition and aerosol deposition are of most interest to this work.

1.2   Project Motivation

This work was largely motivated by several recent works originating from the aerospace sector [2][3][4][5] which collectively state the need for a printable wireless sensor technology for performing SHM in aerospace settings. The challenges presented by this goal are discussed more thoroughly in Chapter 2, however it is important to initially state that such an environment will expose these sensors to extremes of temperature, pressure and radiation, amongst other things.

In-situ fabrication of these sensors is another aspect of the project, which has been emphasised as important in works such as [2], where technologies from the printed electronics industry are being considered as target fabrication methods for the resulting sensors. Printed electronics is widely becoming a vast area of both commercial and research interest and many conventional electronic components have been demonstrated to be capable of being fabricated using direct-write or similar printing technology. This has also extended into the printing of antennas and similarly, Radio Frequency Identification (RFID) tags [6][7]. Said tags may or may not require an Integrated Circuit (IC) and usually do not require a battery either. The resulting tag is interrogated wirelessly and can be easily turned into a sensing device [8][1]. Given the potential ease of fabrication and simplicity of the sensor

nodes, this technology appears to be an ideal candidate technology for aerospace SHM, over more conventional IC-based wireless technologies such as ZigBee [9] or WiFi [10].

Although a potentially suitable candidate technology has been selected, the resulting sensors must be able to support all of the requirements put forward by aerospace SHM applications. Therefore, this project has focussed on developing sensors that boast both the desired sensing performance and the other desired performance goals of aerospace SHM applications.

1.3   Objectives and Research Questions

The overall goal of this project is to develop a passive remote sensing technology that could be suitable for aerospace SHM applications. This project could have been pursued with slightly different overall goals in mind, e.g. focus exclusively on sensor design and performance, but that route was avoided because more pressing challenges presented themselves in demonstrating that this technology could indeed be capable of meeting aerospace SHM requirements. The chosen direction of the project therefore placed greater emphasis on issues related to; stimulus resolution, dynamic stimuli and multi-sensor support. Hence, emphasis was placed on answering the following research questions:

- Can the performance of existing chipless RFID strain sensor designs be enhanced (Chapter 3)?
- Can a working chipless RFID strain sensor be fabricated and deployed using straightforward in-situ fabrication/deployment methods (Chapter 3)?
- How can temperature sensing be incorporated into chipless RFID tags (Chapter 4)?
- Can thermocouple sensors be integrated into chipless RFID tags (Chapter 4)?
- How can the response information be accurately and reliably extracted (Chapter 5)?
- Is it possible to extract time domain information from rapidly changing sensor responses and what impact does it have on the measured response (Chapter 5)?
- What issues exist with polarization, sensor orientation and read range with this technology (Chapter 6)?
- What issues arise with multi-sensor environments (Chapter 6)?
- What sort of and how do cross sensitives affect the performance of chipless RFID sensors (Chapter 6)?

1.4 References

[1] K. Mc Gee, P. Anandarajah, and D. Collins, "A Review of Chipless Remote Sensing Solutions Based on RFID Technology," Sensors, vol. 19, no. 19, p. 4829, 2019.

[2] ESA, "ESA Open Invitation To Tender [FR] AO8922 - DIRECT PRINTING OF MECHANICAL AND THERMAL SENSORS ONTO SPACECRAFT HARDWARE," 2017. [Online]. Available: http://emits.sso.esa.int/emits/owa/emits_online.showao?typ1=7345&user=Anonymo us. [Accessed: 10-Oct-2017].

[3] W. C. Wilson and P. D. Juarez, "Emerging needs for pervasive passive wireless sensor networks on aerospace vehicles," in Procedia Computer Science, 2014, vol. 37, pp. 101–108.

[4] W. C. Wilson and G. M. Atkinson, "Rapid SAW Sensor Development Tools." 2007.

[5] W. C. Wilson, D. F. Perey, G. M. Atkinson, and R. O. Barclay, "Passive wireless SAW sensors for IVHM," in 2008 IEEE International Frequency Control Symposium, FCS, 2008, pp. 273–277.

[6] E. M. Amin, N. C. Karmakar, and B. W. Jensen, "Fully printable chipless RFID multi-parameter sensor," Sensors Actuators A Phys., vol. 248, pp. 223–232, Sep. 2016.

[7] A. Galehdar and D. V. Thiel, "Flexible, light-weight antenna at 2.4GHz for athlete clothing," in IEEE Antennas and Propagation Society, AP-S International Symposium (Digest), 2007, pp. 4160–4163.

[8] F. Requena et al., "Thermal Modeling of Resonant Scatterers and Reflectometry Approach for Remote Temperature Sensing," IEEE Trans. Microw. Theory Tech., vol. 69, no. 11, pp. 4720–4734, Nov. 2021.

[9] "What is Zigbee? | Zigbee Alliance." [Online]. Available: https://www.zigbee.org/what-is-zigbee/. [Accessed: 12-Dec-2018].

[10] A. Varghese, D. Tandur, and A. Ray, "Suitability of WiFi based communication devices in low power industrial applications," in 2017 IEEE International Conference on Industrial Technology (ICIT), 2017, pp. 1307–1312.

Chapter 2: Literature Review

2.1   Introduction

This chapter sets out to give a gentle introduction to the problem at hand, namely, the use of chipless RFID for Structural Health Monitoring (SHM) in aerospace settings. This is done through the following steps:

1. Overview of existing strain and temperature sensing systems, commonly found in aerospace SHM

2. Exploration of the challenges and requirements posed by the goal of aerospace SHM

3. Overview of chipless RFID and potential rapid fabrication methods

This chapter is by no means meant to be the most comprehensive overview of the above topics, but rather an introduction to the topics. More can be found in many other works such as those referenced here [1][2][3]. Much of the other relevant discussions are also presented in the subsequent chapters. This approach was taken so that this chapter would not discuss large numbers of largely unconnected topics.

2.2   Overview of Conventional Wired Strain Sensors

2.2.1   Basic Design

Conventional strain sensor systems utilise metal foil strain gauges, as depicted in Figure 2.1. The application of strain to these devices alters the resistance of these devices in accordance with Equation 2.1. Devices such as these are bonded to the surface of interest (superstrate) using epoxy-based adhesives or other methods besides [4]. More commonly, a bespoke "grid" material is used under the conductive foil and said "grid" part is adhered to the superstrate. Interest into in-situ deposition of these devices has also been hinted at by entities such as the European Space Agency (ESA) [5]. Commonly found foil gauges have a major dimension of below 13mm [4] and conductor thicknesses on the order of 5µm [6]. These are commonly made from commercial materials such as Constantan (Copper≈56%: Nickel≈44%) and Karma (Nickel≈74%: Chromium 20%: Iron & Aluminium≈6%) [4][7]. The resistance change is caused not only by the geometric change in the gauge but also by strain dependencies in the materials resistivity [4][7]. A more thorough discussion on the strain sensitivity of the resistivity of various conductors can be found in [4][7].
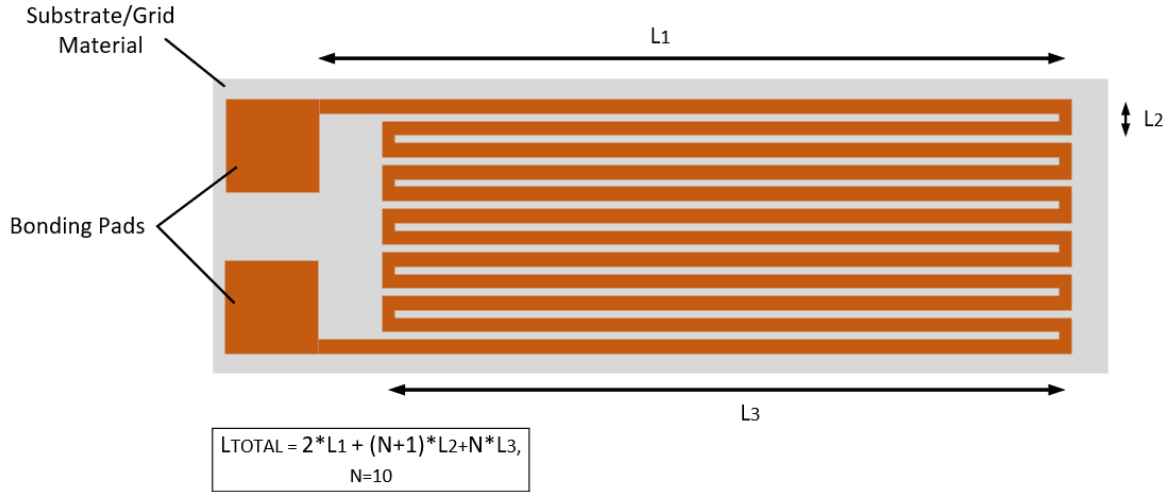
Figure 2.1: Diagram of Conventional Metal Foil Strain Gauge

$$R = \rho\left(A/L\right) \qquad (2.1)$$

A thorough discussion on the fabrication and deployment of foil gauges can be found in References [7] and [4]. Conventional implementations can support strain ranges of ±0.3% and have gauge factors (sensitivities) of approximately two [7]. This gauge factor measurement normalises the sensitivity based on the initial resistance of the gauge and can be calculated, as described in [7], using Equation 2.2 below. In terms of resolvable strain levels, works such as [8] have demonstrated resolutions and accuracies well below 10με.

$$K = \left(\frac{\Delta R}{R_0}\right) \Big/ \left(\frac{\Delta L}{L_0}\right) \qquad (2.2)$$

2.2.2 Cross Sensitivities in Foil Gauges

As one can imagine the resistance of a foil gauge will also change with temperature and this issue has long been explored. Self-Temperature Compensating (STC) strain gauges can be made out of materials like constantan which through highly controlled annealing can exhibit a near-zero temperature coefficient or resistivity over a reasonable temperature range (i.e. ±0.27/°C from 0-175°C) [4]. Alternative approaches are to add a Temperature-dependent (compensating) Resistor (TCR) of the opposite sensitivity to that of the gauge in series with the sensor [4].

Similar to the static resistance of the strain gauge, its gauge factor (K) can also be temperature sensitive. This arises due to temperature dependencies present in the mechanical properties of the both the gauge and structural materials (i.e. Young's Modulus and Poisson's Ratio) [4]. Compensation for this is performed using either TCRs or by selecting gauge materials which within the entire assembly result in a zero net change in gauge factor [4].

6

Another important variable that can affect axial strain measurement is that of transverse strain. Foil gauge geometries, such as that depicted in Figure 2.1 above, will exhibit changes in resistance under transverse strain. This occurs mostly due to deformation of the end loops in the transverse deformation [4]. This effect can be mitigated by enhancing the thickness of these regions and/or altering the length/width of the longitudinal (axial) tracks in the gauge so that their change in cross sectional area (A) exactly compensates for the change in length (L) so that Equation 2.1 above experiences no net change in resistance with increasing transverse strain [4].

Many if not all of these alternatives to this strain sensing technology are less well- established than foil gauges and thus have not been proven to the same extent as the latter. Other than the optical methods, the majority of the alternative approaches also make use of resistance changes as a means to encode strain information [6][7]. Piezoresistive designs also exist and exhibit large gauge factors, but also exhibit very large temperature dependencies [9], thus foil gauges have taken precedence.

2.2.3   Wheatstone Bridge Circuit

Changes in foil gauge resistance are usually very small and to allow for a computer system to measure this change accurately and precisely, a differential sensing method is employed. The most common method makes use of a Wheatstone Bridge circuit (as seen in Figure 2.2) which can incorporate one or more strain gauges and whose output can be characterised as that seen in Equation 2.3 [4]. Through the use of various assumptions [7], such as the change in resistance being small compared to the initial resistance, Equation 2.3 can be simplified down through Equation 2.4 to yield the expression seen in Equation 2.5, which gives the result in terms of strains and gauge factor [4].
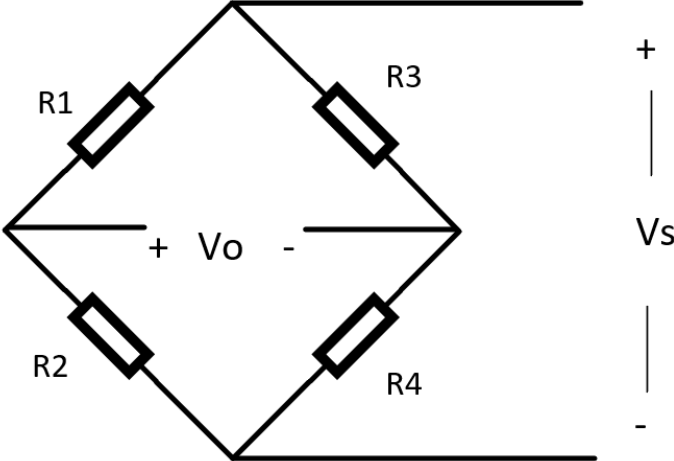
Figure 2.2: Conventional Wheatstone Bridge Circuit

7

$$V_o = V_s \left(\frac{R_1}{R_1 + R_2} - \frac{R_4}{R_3 + R_4} \right) \qquad (2.3)$$

$$= V_s \left(\frac{R_1 + \Delta R_1}{R_1 + \Delta R_1 + R_2 + \Delta R_2} - \frac{R_4 + \Delta R_4}{R_3 + \Delta R_3 + R_4 + \Delta R_4} \right) \qquad (2.4)$$

$$\frac{V_o}{V_s} = \frac{1}{4} \left(\frac{\Delta R_1}{R_1} - \frac{\Delta R_2}{R_2} + \frac{\Delta R_3}{R_3} - \frac{\Delta R_4}{R_4} \right) = \frac{K}{4} (\varepsilon_1 - \varepsilon_2 + \varepsilon_3 - \varepsilon_4) \qquad (2.5)$$

There are a variety of popular Wheatstone bridge implementations, some of which use all four positions to measure strain. More commonly, only one position is used for strain measurements and the other three positions have fixed resistances [4]. A popular variant of this "quarter" bridge implementation uses an additional wire to allow for lead wire resistance/temperature effects to be mitigated [4][7]. This design can be seen in Figure 2.3(a) below. Also of interest to this discussion is the use of the half bridge configuration which makes use of a dummy strain gauge alongside the sensing gauge. This approach is depicted graphically in Figure 2.3(b) below and this dummy gauge is positioned and connected so that it experiences the same temperature, humidity, etc. as the sensing gauge but without the influence of the strain variable. Said implementation allows for compensation of the static effects of virtually all of the environmental variables experienced by the sensing gauge. This last bridge implementation is brought up here in passing as although STC gauges are available, they have a limited temperature range in which their compensation performance is adequate [4][7].

(a)   (b)
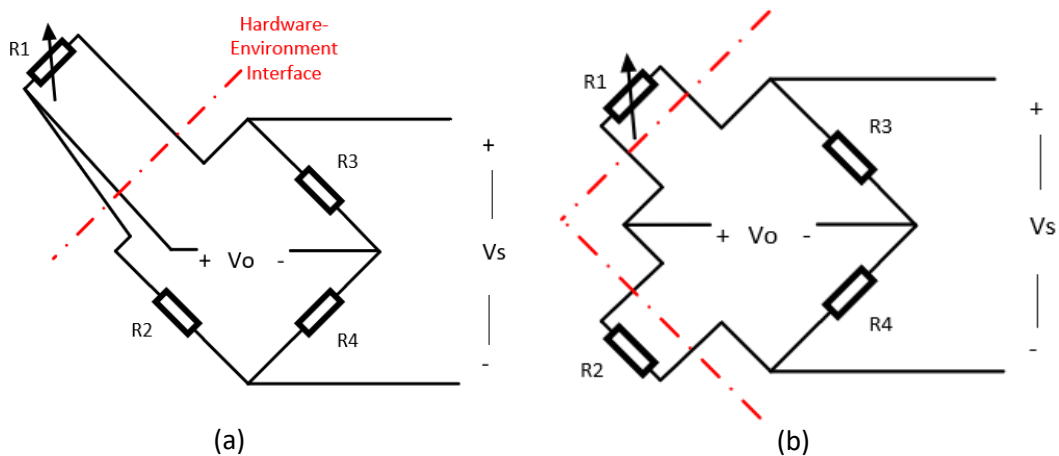
Figure 2.3: (a) - 3-Wire Quarter Bridge Design, (b) - Half Bridge with Dummy Sensor

2.2.4   Sensor Layout

If we assume that the superstrate is a 2D plane, then to fully characterise the stress experienced by that surface, the 2x2 tensor in Equation 2.6 [10] needs to be solved for. This is a symmetric matrix with components representing axial stress in the x-direction (σ_{xx}), y-

direction (σ_{yy}) and a shear stress component in the xy-direction ($\tau_{xy} = \tau_{yx}$). The measurements made by the sensors are strain measurements and the relationship between stress and strain under the plane strain assumption, described in [10], can be seen in Equation 2.7, where Young's Modulus is denoted as (E) and Poisson's ratio is denoted as (v).

$$[\sigma] = \begin{bmatrix} \sigma_{xx} & \tau_{xy} \\ \tau_{yx} & \sigma_{yy} \end{bmatrix} \tag{2.6}$$

$$\begin{bmatrix} \sigma_{xx} \\ \sigma_{yy} \\ \tau_{xy} \end{bmatrix} = \frac{E}{(1+v)(1-2v)} \begin{bmatrix} 1-v & v & 0 \\ v & 1-v & 0 \\ 0 & 0 & 0.5-v \end{bmatrix} \begin{bmatrix} \varepsilon_x \\ \varepsilon_y \\ X_{xy} \end{bmatrix} \tag{2.7}$$

Several strain sensors are required to allow this tensor to be solved. Of most interest is the directions of the principal planes [4]. These orthogonal planes signify the directions of the maximum and minimum normal stresses and coincide with the orientation in which no net shear stresses are present. If the direction of these planes is known, then the maximum and minimum stresses experienced at that position can be directly measured using only two gauges. If these planes are not known before sensor deployment, the common approach is to use a three-gauge configuration (rosette), such as one of those seen in Figure 2.4. These configurations can be implemented in a single plane or implemented in a stack [4][7].
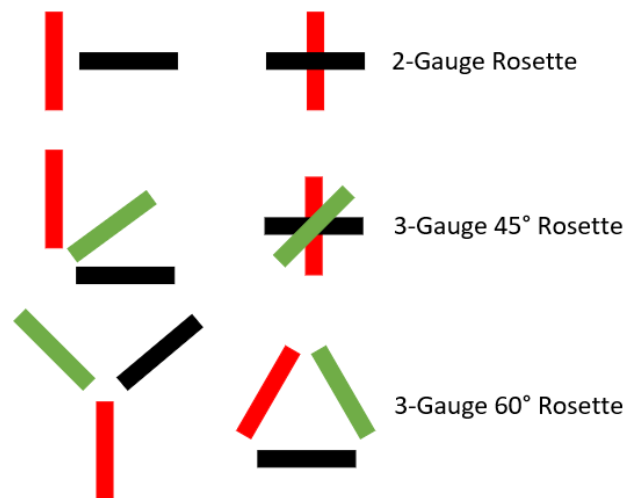
Figure 2.4: Various Conventional Strain Rosette Layouts

The exact angular location of the three gauges is not of critical importance as the three axial strain measurements will allow for the determination of the principal planes and from there, the stresses can be calculated. The diagram in Figure 2.5 depicts the configuration of a three-gauge rosette and based on the work found in [10], Equation 2.8 to Equation 2.10 are

9

presented here to describe how the measured strains ($\varepsilon_a, \varepsilon_b, \varepsilon_c$) can be related to the plane strain variables ($\varepsilon_1, \varepsilon_2$) mentioned earlier.
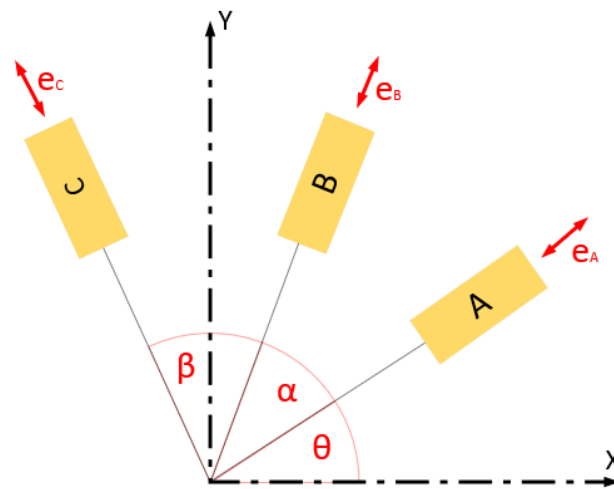
Figure 2.5: Labelled Diagram of 3-Gauge Rosette

$$\varepsilon_a = \frac{(\varepsilon_1 + \varepsilon_2)}{2} + \frac{(\varepsilon_1 - \varepsilon_2)}{2}\cos\theta \qquad (2.8)$$

$$\varepsilon_b = \frac{(\varepsilon_1 + \varepsilon_2)}{2} + \frac{(\varepsilon_1 - \varepsilon_2)}{2}\cos(\theta + \alpha) \qquad (2.9)$$

$$\varepsilon_c = \frac{(\varepsilon_1 + \varepsilon_2)}{2} + \frac{(\varepsilon_1 - \varepsilon_2)}{2}\cos(\theta + \alpha + \beta) \qquad (2.10)$$

Furthermore, for rosette angles of 45°, the magnitude and orientation of the principal strains relative to the co-ordinate frame of the rosette can be determined, as described in [10], using Equation 2.11 and Equation 2.12.

$$where\ \alpha = \beta = 45°: \qquad (2.11)$$

$$\varepsilon_1, \varepsilon_2 = \frac{(\varepsilon_a + \varepsilon_b)}{2} \pm \frac{1}{\sqrt{2}}\sqrt{(\varepsilon_a + \varepsilon_b)^2 + (\varepsilon_a - \varepsilon_b)^2}$$

$$tan2\theta = \frac{2\varepsilon_b - \varepsilon_a - \varepsilon_c}{\varepsilon_a - \varepsilon_c} \qquad (2.12)$$

2.3   Overview of Conventional Wired Temperature Sensors

This section sets out to give a basic introduction to the various wired temperature sensors that are currently used in electronic thermometry. This discussion is not an exhaustive discussion on the topic and avid readers are pointed to larger and more comprehensive discussions on the topic [11][12].

2.3.1   Resistance Temperature Detectors (RTDs)

As mentioned in the earlier discussion on strain gauges, various metals exhibit increasing resistance values with increasing temperature. This relationship can be and is non-linear for many different metals, but Platinum is one metal whose temperature coefficient of resistance is considered to be largely linear. Platinum is also highly resistant to the effects of oxidation/corrosion and has thus been used extensively as a temperature sensing material.

The operation of Platinum as a temperature sensing element has been long since explored and the Callendar -Van Dusen equations describe the temperature dependence of the resistance of this material. Equation 2.13 to Equation 2.15, found in [11], depict these relevant equations and coefficients.

$$R_t = R_0(1 + K_1T + K_2T^2 + K_3(t - 100)t^3), -200 \leq T < 0°C \qquad (2.13)$$

$$R_t = R_0(1 + K_1T + K_2T^2), 0 \leq T < 661°C \qquad (2.14)$$

$$K_1 = 3.90802x10^{-3}, K_2 = -5.802x10^{-7}, K_3 = -4.2735x10^{-12} \qquad (2.15)$$

Over a limited temperature range and with a limited level of accuracy, Platinum and other metals such as Copper, Nickel and Tungsten can be modelled as having a resistance which is linearly dependent on temperature (see Equation 2.16) [11][13]. Said materials can be used as RTDs up to temperatures ranging from 260°C to 1100°C. Platinum can support operation of up to 1000°C (±1.2% linear inaccuracy) but is usually operated below 650°C [13]. The standard commercial Platinum RTD has a resistance of 100Ω at 0°C (PT100 Series) and the resulting sensitivity is on the order of 0.36Ω/°C [11][13].

$$R \approx R_0(1 + a_1T) \qquad (2.16)$$

Several issues arise with the operation of these sensors. Similar to strain gauges, self-heating can occur, and the effects of lead wires also need to be considered, given the low sensitivity of the RTD. Wheatstone bridge circuits can also be used to alleviate these issues or other methods such as the 4-wire resistance measurement method. More on this topic can be found in Reference [9].

2.3.2 Thermistors

Conventional thermistors are semiconductor devices which have a significantly higher sensitivity than that found with RTDs [11]. These semiconducting materials are made from sintered oxides from the iron group of metals [11][13] and most commonly exhibit a Negative Temperature Coefficient (NTC) of resistance, that is to say, their resistance decreases with increasing temperature. Said sensitivity is a highly nonlinear function of temperature and the Resistance-Temperature response can be approximated as that seen in Equation 2.17, from [13]. That Equation can be recast into that seen in Equation 2.18 [13]. This beta (β) value is supplied by the device manufacturer, measured at a specific temperature. This overall measurement is based on just two datapoints and other approaches have been put forward to enhance accuracy.

$$R_t = R_0 e^{\beta\left(\frac{1}{T}-\frac{1}{T_0}\right)} \tag{2.17}$$

$$\beta = \frac{ln\left(R_t/R_0\right)}{\left(\frac{1}{T_0}-\frac{1}{T}\right)} \tag{2.18}$$

Equation 2.19, seen in [13], is a more popular mathematical description of the relationship between temperature and resistance for a thermistor. This latter equation is the Steinhart-Hart equation and includes three coefficients to be determined.

$$\frac{1}{T} = A + B\left(ln(R)\right) + C\left(ln(R)\right)^3 \tag{2.19}$$

As mentioned earlier, the sensitivity of these devices is usually quite high, but highly nonlinear. Example resistance output values would be 10kΩ at 0°C and just 200Ω at 100°C [9]. Operating ranges for basic thermistors are reported to be around -60°C to 150°C [9] but others may exist that surpass these figures.

2.3.3 Thermocouple Technology

Thermocouple devices make use of thermoelectric phenomena, namely the Seebeck effect, to give rise to an output voltage in response to a temperature difference across the device. These devices are commonly made out of two dissimilar metals which have different Seebeck (S) coefficients. Said coefficient is a measure of the voltage differential created by exposing the material to a temperature differential that has been applied across the material, and this value is usually given in the units of µV/K [12-14]. Figure 2.6 depicts the general configuration of a thermocouple and Equation 2.20 [14] depicts the output response of the device.
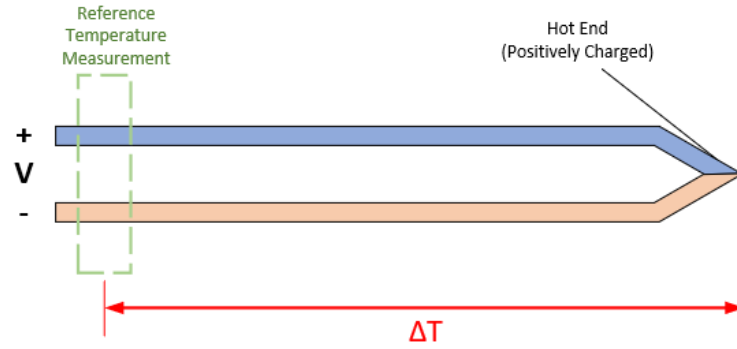
Figure 2.6: Thermocouple Sensor Diagram

$$V = (S_2 - S_1)\Delta T \qquad (2.20)$$

A valuable resource on the topic of thermocouple design and operation is that by Pollock [14], which arrives at mathematical definitions of the Seebeck coefficient through various theoretical models (thermodynamic-based, etc.). In each case arrive at an equation of the form seen in Equation 2.21 [14]. The constant of proportionality varies slightly depending on model assumptions [14] and the relevant parameters are summarised in Table 2.1 below.

$$S \propto \frac{\pi^2}{6}\left(\frac{k_B^2 T}{e E_f}\right) \qquad (2.21)$$

Table 2.1: Seebeck Equation Coefficient Table

Parameter	Name	Parameter	Name
S	Seebeck Coefficient	e	Electron Charge
k_B	Boltzmann's Constant	E_f	Fermi energy
T	Absolute Temperature	E_0	Reference Fermi Energy

As mentioned earlier, various explanations/theoretical models are presented in [14] to arrive at the above equation. A concise explanation/model is that a temperature difference across the conductor gives rise to a difference/gradient in the kinetic energy of the charge carriers in the conductor. This results in the net carrier diffusion from the hot end to the cold end, which results in a potential difference across the conductor [14]. The magnitude of this effect would be dependent on the conductor in question and thus dissimilar metals result in different potential difference between them at their cold ends. The above equation (Equation 2.21) is developed for normal metals (not semiconductors or transition metals) where the temperature variation in the fermi level of the material can be considered negligible [14]. If it is not negligible, the result can be expressed as having the form seen in Equation 2.22 [14].

$$S \propto \left(\frac{k_B^2 T}{e(E_0 - E_f)} \right) \qquad (2.22)$$

Thermocouple material pairs have been largely standardised and have been given specific lettering to define their materials and thus their range, sensitivities, and accuracies. Sensitivities of commercial thermocouples vary from 68μV/°C (Type E) to 10μV/°C (Type S) with inaccuracies of below ±0.75% whilst assuming statically defined Seebeck coefficients to be valid [13]. Operating ranges also vary with Type C thermocouples (Tungsten and Tungsten-Rhenium -based) devices supporting temperatures up to 2300°C [13].

These devices can be connected in series to form a thermopile and other circuit variants support averaging. These and other relevant circuitry for reference temperature compensation can be seen in Reference [9].

2.4 Overview of Optical Sensing Methods

Fiber Optic sensors of various designs have been used for the sensing of temperature and strain in a variety of aerospace applications. This section outlines some of the most prevalent sensors of this type, their underlying operation and their uses in documented aerospace settings.

2.4.1 Single-Ended Sensors

Optical pyrometers built with optical fibers are suitable for certain high temperature applications like turbine gas temperature monitoring but issues like soot build-up are a serious issue [8]. Other methods use tunable diode lasers to detect using spectroscopic techniques, turbine gas temperatures based on absorbance [15]. Examples of single-ended optical strain sensors include the Fabry-Perot interferometer. This device consists of an optical fiber along with a reflective surface at a distance from the cable end. Both optical signals (the reflected signal and continuously transmitted signal) will interfere constructively/destructively to form a net signal whose characteristics are highly dependent on the distance between the surface and the end of the fiber [8]. The work presented in Reference [8] by Edwards revealed 0.1με resolution and accuracies within 10με.

2.4.2 Distributed Sensors

Fiber Bragg Gratings (FBGs) are a commonly found type of optical sensors used in the aerospace Structural Health Monitoring (SHM) literature. This periodic arrangement of optical sections with alternating indices of refraction gives rise to sufficient constructive/destructive interference at a certain wavelength (Bragg wavelength) to block its transmission through the grating and to reflect it back to the source, as described graphically in Figure 2.7. In this Figure,

the application of the ultrawideband interrogation signal (P_i) to the input of the cable, results in a bandstop (notch) response observed at the output of the device (P_0). The reflected signal (P_r) from the grating to the input port has a bandpass response. Many good books on optical fiber systems, such as [16] will give further details on their design and operation, but a basic capsule summary is provided here [17];

- FBGs can be cascaded to form a distributed sensor network within a single fiber line
- Ultraviolet (UV) light can be used to alter the index of refraction in germanium doped optical fiber. But other mask-based approaches are also used
- Bundles of regular optical fibers can operate at temperatures up to 350°C
- Performance can be affected by ageing
- Bragg wavelength is also highly sensitive to temperature which enables use as a temperature sensor. This makes for a more versatile sensor but also means that temperature/strain compensation is required in relevant applications
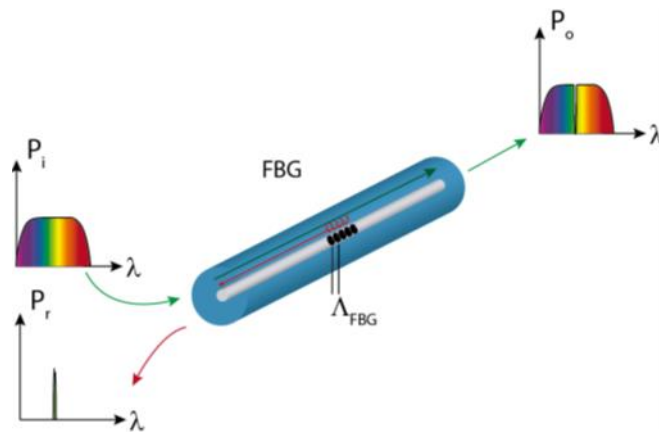
Figure 2.7: FBG Operation – from "Optical Fiber Sensors for Aircraft Structural Health Monitoring" by García et al., MDPI, CC BY 4.0 [17]

Several aerospace-related publications have made use of this sensor type, including that by Goossens et al. in Reference [18]. This work utilised FBGs as strain sensors at temperatures up to 120°C. This work showed that the FBGs used outperformed conventional metal foil strain gauges in endurance tests. The FBG sensors survived over 10^6 strain cycles whilst the strain gauges only survived $6.4 x 10^5$ cycles before effects such as creep and fatigue led to sensor failure. Other works, such as that by Shen et al. in Reference [19] used 64 FBGs mounted on a 10x10cm plate as a pressure sensing system. That specific work tested the sensors up to 1000με and also highlighted the need for compensation of transverse strains which greatly affected measurement accuracy. Other findings in this work is that the measurement error deemed sufficient is 4.52με. The total area of a single FBG and substrate was 36x12mm. The

research documented in Reference [18] utilises FBGs for strain levels up to 125με. The relevant operating temperature range for this sensor was 125°C as that was what was stipulated as the maximum operating temperature of a conventional optical fiber -based sensor. Operation of FBGs at temperatures over 1000°C has been documented by Wang in Reference [20]. That work made use of Sapphire-based optical fiber materials to achieve such a level of thermal robustness. Some FBG designs such as that found in the work of Sherman and Zappe in Reference [21], was tested up at temperatures up to 125°C and is designed to be printable and used polymer-based optical fibers. Note: the latter work describes the printable method to develop the FBG structure and not the polymer optical fiber itself.

2.5   Other Noteworthy Sensing Methods

The authors of Reference [22] developed a Zirconium Tin Titanate (ZST) resonator whose radio scattering characteristics are highly temperature sensitive and can operate at temperatures up to 700°C. Other sensing strategies of note include the piezocomposite sensors patented by the National Aeronautics and Space Administration (NASA) [23] and tested up to 2000με [24]. Ultrasonic-based equivalents of RFID tags have also been developed and tested at ranges up to 350mm in Reference [25] by Aftab. Ultrasonic approaches can be used directly for temperature sensing in gaseous environments, as discussed in Reference [15].

Other remote sensing approaches discussed in literature include the analysis of backscattered acoustic waves (Lamb waves) in aerospace structures/parts. Upon incidence of the Lamb wave with a defect or boundary, acoustic scattering occurs which can be detected and used to determine the change in structural characteristics of the element under test. Piezoelectric elements made of materials such as Lead Zirconate Titanate are used for sensing and actuation of the acoustic waves in the part/structure of interest [26]. The characteristics of the resulting scattered waves can be highly temperature and deformation dependent [27] and usually require significant signal processing to discern the physical change to the structure [28]. This subsequently requires an in-depth knowledge of the behaviour of Lamb waves in the part/structure of interest, to aid signal processing software development.

2.6   Challenges in the Aerospace Setting

The environment that aerospace sensors must operate in is quite harsh and includes temperature variations and extremes, radiation, vacuum and pressure extremes along with vibration and electromagnetic interference [15][29]. In order to reduce cabling (weight), the obvious choice is to make use of wireless sensor technologies. Existing wireless technologies such as WiFi and ZigBee and similar technologies require a power source to operate which brings about further complications. Chipped RFID tags and RFID tags that comprise small amounts of transistors use passive communication techniques such as load modulation [30] to communicate with the reader system. Existing chipped RFID tags support standardised communication protocols and has supporting layer 2 abilities as discussed by Dobkin in [30].

2.6.1   Sensing Requirements

The requirements for satellite SHM sensors include operating at temperatures up to 125°C [31]. Generic aerospace structures can experience temperatures from cryogenic levels (-150°C) up to temperatures above 1500°C [15][32][33]. Various materials such as metals/polymers exhibit variations in size [34][35], mechanical [34][36] and dielectric [37] properties variations with variations in temperature and/or humidity. The developed sensor system will need to survive and operate effectively under such environmental scenarios whilst supporting the general sensing requirements of the application.

Specific aerospace SHM applications, such as temperature sensing within gas turbines requires a robust SHM system, as excessive gas temperatures can degrade the life of a turbine blade by up to 50% [15]. Conventional sensors such as thermocouples can readily support these operating conditions [29], thus their prevalence as the standard measurement system in this industry [38]. One key issue with their use is that no previous work had demonstrated any way to successfully integrate them into chipless RFID technology. Furthermore, there are significant strain and temperature resolution requirements, as discussed in the previous sections on existing SHM sensor technologies.

Of further importance is the rate at which each sensor will need to be interrogated at. Real-time SHM sampling rates of at least 10Hz have been outlined in some aerospace applications [39] but other works have discussed sampling rates exceeding 1kHz [40][41]. With that being said, other aerospace applications would only require interrogation after several days have elapsed [42]. Requirements such as this could be very difficult to achieve as sensor counts suggested for certain aerospace SHM applications could be on the order of 10^3 [33][42].

2.6.2 Time Varying Stimuli

The topic of time varying stimuli is limited in this section to vibration as that was the main stimulus in which it has been most reported in the literature. This topic is brought up here as many of the reader architectures make use of interrogation signals whose duration can range from microseconds to seconds in some cases.

What is of importance here is the rate of change that can be present within the strain sensor response. Various aerospace-related publications, such as aircraft-related publications have reported vibration frequencies of up to and above 1kHz [43][44], whilst satellite-related publications have reported vibration at 2kHz [45].

2.6.3 Sensor Lifetime

This subsection discusses the impact that the aerospace environment can have on electronic devices, but mostly on their constituent materials. This does not include transient and potentially recoverable effects such as temperature or humidity, nor does it discuss other obvious long-term challenges such as fatigue or creep.

Radiation Effects

Radiation effects can take place due to transient radiation events and from the known radiation environment that surrounds the planet [46], the latter arising from the Van Allen belts [46][47] and the South Atlantic Anomaly [46]. Transient radiation effects include solar flares and cosmic rays [46][47].

Semiconductor Limitations

The main issue(s) that block the use of conventional, chipped passive wireless sensors in extreme environments are caused by the limitations of the semiconductor materials on which they are based. Above 125°C a silicon PN junction will begin to suffer significant leakage [29] and more complex/costly approaches must then be taken to reduce this effect. The semiconductor materials/technologies capable of operating above this temperature include Silicon on Insulator (SOI) and more recently, Silicon Carbide (SiC). A more in-depth discussion on the performances of these and other semiconductors, when exposed to high temperatures can be found in Reference [48] by Rodríguez-madrid et al. Another challenge that hampers the use of conventional semiconductor-based electronics in high temperature environments is the presence of ionising radiation. Ignorance of this challenge can lead to unpredictable failure/faults in complex semiconductor devices, such as those that execute programmable instructions as the flipping of a single bit can result in negligible or catastrophic system outcomes. A discussion on the formation of unwanted conduction paths and other radiation-

based semiconductor fault/failure mechanisms can be found in the work of Scheick et al. in Reference [49]. An example of a high temperature passive wireless pressure sensor based on SiC and SiCN semiconductor components can be found in Reference [50]. Such semi-conductive materials have a much wider bandgap and thus are more resilient to the effects of temperature and radiation. In the work presented in Reference [50] by Scardelletti et al., the device they developed was successfully operated at temperatures up to 300°C. One key issue with the use of more exotic semiconductor materials is that they have increasing fabrication complexity to the inkjet-printable semiconductor materials such as Indium Gallium Zinc Oxide (IGZO) [51].

Impact of Radiation on Other Materials

Generally speaking, the impact of radiation on metals is much less than that on either semiconductors or dielectrics [7][47]. Basically, lattice defects and other such events arise [47] and the resulting effect is usually just a small change in resistance [52].

Polymers are quite susceptible to UV exposure as the bonds contained in them can readily absorb radiation of these frequencies [52][53]. Other materials such as silicones, which are used as adhesives [53], exhibit mechanical hardening [7]. Of most interest here is that polyimides such as Kapton™ are highly resistant to UV exposure [7][53] and is used in aerospace settings for this reason.

Outgassing

This is an effect that takes place at high vacuums and temperatures which results in the desorption of components from within the outgassing material [54]. This is common in organic polymers that contain low weight additives [54]. This can result in contamination of nearby objects, and this is unwanted as it can damage/hinder the operation of other aerospace systems [54]. Reference [55] includes a thorough review of the outgassing effects observed in satellites and other space-related equipment. Silicones are prone to exhibit this effect [54] and it has also been demonstrated to be a significant issue in a variety of 3D printed dielectrics [56]. A common solution to this process is to "bake-out" the offending components (sometimes just moisture) through subsequent heat treatments [57][58].

Effects of Atomic Oxygen

Atomic oxygen (O_1) is formed by solar UV which breaks apart the O_2 molecules. The Low Earth Orbit (LEO) contents is 96% atomic oxygen, and this reacts with organic materials (can break C-C and C-O bonds) in this zone and slowly erodes the material [59]. This includes high performance polyimides and to combat these effects, inorganic coatings are used to protect

the devices [52][53]. Silicones are a notable class of materials that experience both cracking, shrinkage and significant variations in mechanical properties with increased exposure to AO [53].

Atomic Oxygen (AO) can cause non-volatile damage to metals and results in the formation of a self-limiting oxide layer on most metal [53]. Silver is heavily affected by AO as the oxidised layer does not remain intact but instead repeatedly exposes the next layer to oxidation [53][60][61].

Electrostatic Charge/Discharge

Electrostatic effects arise in spacecraft through the accumulation of charge from the space plasma, which has been formed by solar ionisation [62][46]. This can be found in both Low Earth and Geosynchronous orbits and results in conventional electronics suffering from logic upsets and other recoverable incidents [62]. Of interest to this discussion is the potential for internal charging of the craft which can result in large potentials between nearby objects/materials and the resulting effects can include arc discharges. Certain materials are poorer at distributing and passing charge (e.g. Kapton™ and Polytetrafluoroethylene (PTFE) [62]) and this exacerbates the potential for arcing and for dielectric breakdown [62][46]. These arcing effects can result in surface damage and ion sputtering effects [62]. Also of interest is that surface contamination can also occur as outgassed molecules/components can accumulate on charged surfaces [62]. These overall effects can alter the mechanical, thermal and electrical properties of the affected material surfaces [62][46]. The report presented by Leach and Alexander in [62] also gives details of over forty known catastrophic or non-catastrophic failures that are known to have occurred because of electrostatic effects. A side note to this discussion is the possibility that arc discharges could excite the chipless RFID devices discussed in the next section and hinder the overall sensor system operation. The work of Amin and Karmakar in [63] shows how electrostatic discharges can be used to trigger responses from chipless RFID tags.

2.7 Chipless RFID Technology

Chipless RFID technology makes use of the electromagnetic scattering or retransmission of an antenna and associated load circuit. The system includes a reader which transmits an interrogation signal and records the response. A more thorough introduction to chipless RFID has been developed by the author in [3].

Antennas are electromagnetic devices that are built to transmit and receive electromagnetic waves. A simple λ/2 dipole is a resonant antenna, whose electric and magnetic fields at frequency, $f = c/\lambda$ are described in [64] as that seen in Equation 2.23 to Equation 2.25 (assuming the dipole is sitting on the Y-axis). Note: In these equations, "r" denoted the radial distance from the origin, whilst "θ" and "ψ" denote the angle of the radial vector with respect to the XZ and YZ planes respectively.

$$E_r \propto \cos\theta \left(\frac{1}{\beta^2 r^2} - \frac{1}{\beta^3 r^3} \right) e^{-j\beta r} \tag{2.23}$$

$$E_\theta \propto \sin\theta \left(\frac{1}{\beta r} + \frac{1}{\beta^2 r^2} - \frac{1}{\beta^3 r^3} \right) e^{-j\beta r} \tag{2.24}$$

$$H_\theta \propto \sin\theta \left(\frac{1}{\beta r} + \frac{1}{\beta^2 r^2} \right) e^{-j\beta r} \tag{2.25}$$

As the distance from the antenna (r) increases, the radial component of the electric field disappears and only the angular components remain with a linear decrease in magnitude with increasing distance [64]. The electric and magnetic field components are in-phase [64] and propagate as a self-sustaining wave into a region known as the far field. Below this distance, the other terms in Equation 2.23 to Equation 2.25 are non-negligible and this zone is known as the near-field and reactive-based coupling can occur in this zone [64]. This zone is defined in [65] as being inside the maximum of the distances defined by Equation 2.26 and Equation 2.27 (Note: "D" represents the maximum dimension of the antenna). Other works suggest other values than that mentioned in Equation 2.27, some up to 3λ and above [64].

$$r > \frac{2D^2}{\lambda} \tag{2.26}$$

$$r > 2\lambda \tag{2.27}$$

2.7.1 Scattering Response of a Tag

The power loss of the resulting far-field wave obeys an inverse square law (Friis' equation) and the scattering of an isolated scatterer, as described in [65], should follow that seen in Equation

2.28. This equation contains the Radar Cross Section (RCS) of the antenna (σ) along with the gain of both antennas (G).

$$P_{RX} \propto \frac{\sigma\lambda^2}{r^4} G_t G_r P_{TX} \tag{2.28}$$

The actual RCS of an antenna is a special use-case and contains two separate parts. These are the structural component, which arises from scattering off a similar sized object and an antenna component. The latter component is absorbed/reflected from the antenna and its reflection is indicative of the loading of the device. This is described mathematically in [66], as that seen in Equation 2.29 and Equation 2.30. The antenna mode is related to the frequency response of the antenna, most of which are narrowband in nature.

$$\sigma = \left| \sqrt{\sigma_s} - (1 - \Gamma_A)\sqrt{\sigma_R} e^{j\varphi} \right|^2 \tag{2.29}$$

$$\Gamma_A = \frac{Z_{Antenna} - Z_{Load}}{Z_{Antenna} + Z_{Load}} \tag{2.30}$$

Equation 2.29 above includes a delay element (φ) between the structural and antenna modes, which is a key variable in the development of time-domain chipless RFID tags, as this variable can be altered within the antenna/load design. Also of importance is that the aforementioned equation is frequency dependent, and the tag design also make use of this variable to encode information. A distinction is made here that tags/sensors that make use of the delay and loading variables (ψ, Γ) as being considered to be time-domain tags. Designs that do not have a time domain encoding element are called frequency domain tags. Said tags rely on changing the location of the antenna mode within a wide interrogation frequency sweep. This is predominantly done through geometric alterations of the antenna/tag or dielectric loading of the device. It has to be mentioned at this point that the choice of one domain over the other has obvious knock-on effects for the design and development of the interrogation system.

Some tags make use of small numbers of transistors (usually $< 10^4$) to implement a makeshift IC to use load modulation [30][67] to alter the scattering signal. This is performed by switching a resistive or reactive element into the Z_{Load} variable seen in Equation 2.30 above. These designs have not been discussed further as part of this work, as their operation would appear to be more vulnerable to aerospace degradation (see Radiation section above). Furthermore, the direct printing of wide bandgap semiconductors seems to be a challenge too great to address within the scope of this overall project.

2.7.2   Harmonic-Based Tags

Some tag designs make use of nonlinear elements to return a harmonic response to the interrogation signals fundamental frequency. A thorough discussion on the design of such devices can be found in [68], but a basic discussion will be presented here. These designs comprise of several stages, as shown in Figure 2.8.
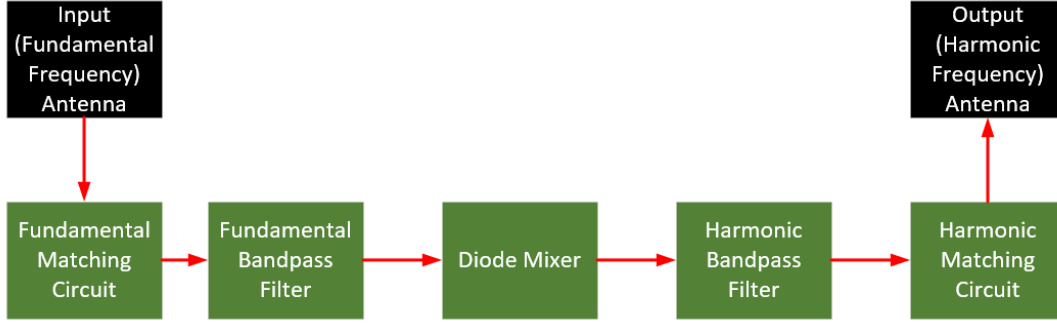
Figure 2.8: Harmonic Tag Stages in Block Diagram Form

The most commonly used nonlinear element is a (Schottky) diode whose current-voltage relationship is defined as that found in Equation 2.31 [65]. Series expansion of this expression along with a small-signal approximation results in Equation 2.32 [65] being formed.

$$I = I_s \left(e^{qV/nkT} - 1 \right) \tag{2.31}$$

$$I(V) = I_0 + v \frac{dI}{dV} + \frac{v^2}{2} \frac{d^2I}{dV^2} + \cdots \ldots \tag{2.32}$$

Finally, assuming a sinusoidal voltage is applied ($cos(\omega_0 t)$), the squared term now contains the square of a sinusoid which can be expanded to being expressed as $1 - sin^2(\omega_0 t)$. The full expansion of Equation 2.32 contains many harmonics of the fundamental frequency, but they decay off, meaning that the first harmonic is the strongest. Designs such as that found in [69] include a DC input to the anode side of the diode to force the mixing operation further towards a more nonlinear portion of the I-V curve, such as that found around the threshold voltage. This allows for an increase in the magnitude of the harmonic component(s) defined in Equation 2.32.

These tags are narrowband in nature as they rely on narrowband matching networks and said network is a critical part of the overall design. Other designs, such as that seen in Reference [70] make use of reversed bias varactor stages to allow for some degree of ad-hoc tuning of the matching network and also boasts a smaller footprint than its predecessor. Said designs tend to be somewhat large and have very sensitive matching networks that may suffer from

temperature/humidity and other such effects and would require the deposition of a high-quality diode. Given these reasons and the fact that the current chipless RFID reader literature is focussed on interrogating conventional chipless RFID tags, this approach was not explored further as part of this project.

2.7.3   Time Domain Tags

In order to encode information in the time domain, the antenna mode component (or equivalent response) needs to be delayed in some way. To add in such a delay, virtually all of the time domain tag designs make use of a relatively long transmission line between the antenna and the termination load. Transmission lines come in various forms, most commonly found in the chipless RFID literature are coplanar [63][71] and microstrip types [72][73]. The design and operation of these transmission lines and that of other types can be found most in available books on electromagnetics [74][65].

Generic Delay Line Tags

Basic time domain tag designs vary in their construction and operation. An example found in [75] by Chamarti and Varahramyan makes use of a two-transmission line system that allows for multiple taps between the lines to output multiple pulses in response to a single input pulse. More commonly found within the literature, the termination load was altered as a means to encode information, such as that seen in [76]. Magnitude and phase information can be encoded through the use of various reactive termination loads [77][78][79]. This is of importance as it means that a stimulus-sensitive dielectric loading, such as those discussed in Reference [3] could be used to turn these designs into chipless RFID sensors.

One limitation of this type of tag design is that they are quite large as a conventional transmission line, at the operating frequencies of interest, needs to be quite long to have a recognisable impact on the time-domain scattering of the tag. A more recent approach that has been used in a variety of chipless RFID tags is to make use of artificial transmission lines. These transmission lines can be fabricated from capacitances and inductances periodically configured in a circuit that is the dual of the conventional distributed transmission line model. This dual (left-handed (LH)) transmission Line unit cell circuit can be seen in Figure 2.9(a) below and the conventional model (right-handed (RH)) can be seen in Figure 2.9(b). Taking account of the conventional and now parasitic right-handed components that arise in this new transmission line circuit, the resulting transmission line (Composite-RLH) has the unit cell seen in Figure 2.9(c).
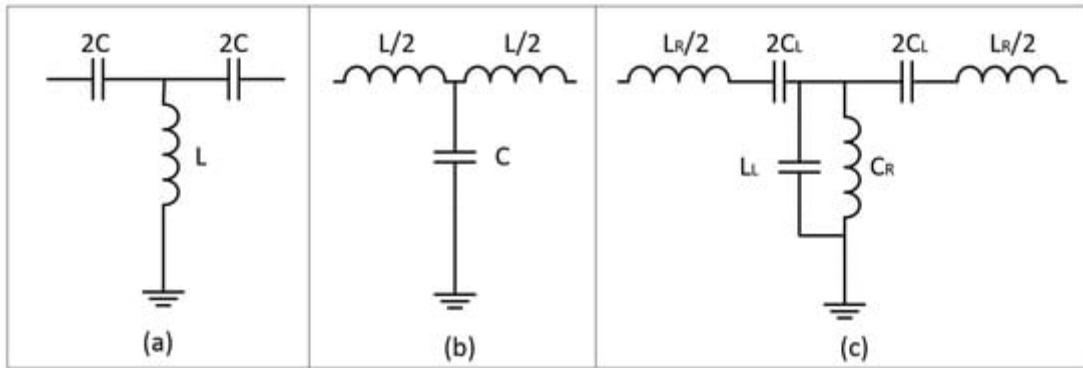
Figure 2.9: Transmission Line Unit Cells (a)-Left Handed, (b)-Right Handed, (c)-Composite Left Right Handed –from "A Review of Chipless Remote Sensing Solutions Based on RFID Technology" by McGee et al., MDPI, CC BY 4.0 [3]

The benefit of this new transmission line design is that the propagation characteristics of this design can be tailored. This means that a far more compact design (28% reduction [3]) can be developed as the guided wave propagates much more slowly through this transmission line than the conventional one. Example chipless RFID tags with implementations of CRLH transmission lines include those found in References [78][79][80].

Group Delay Line Tags

These designs differ slightly from the generic designs seen above. These designs make use of transmission line features that introduce frequency-dependent delays so that the incoming continuous wave or pulse would have certain frequency components that were delayed more than the rest response. This is implemented through the use of $\lambda/4$ sections that will act as open circuit elements at the appropriate frequency and capacitive coupling will be the only means through which that particular frequency will propagate forward through the circuit. Figure 2.10 depicts these transmission line $\lambda/4$ circuit inclusions.
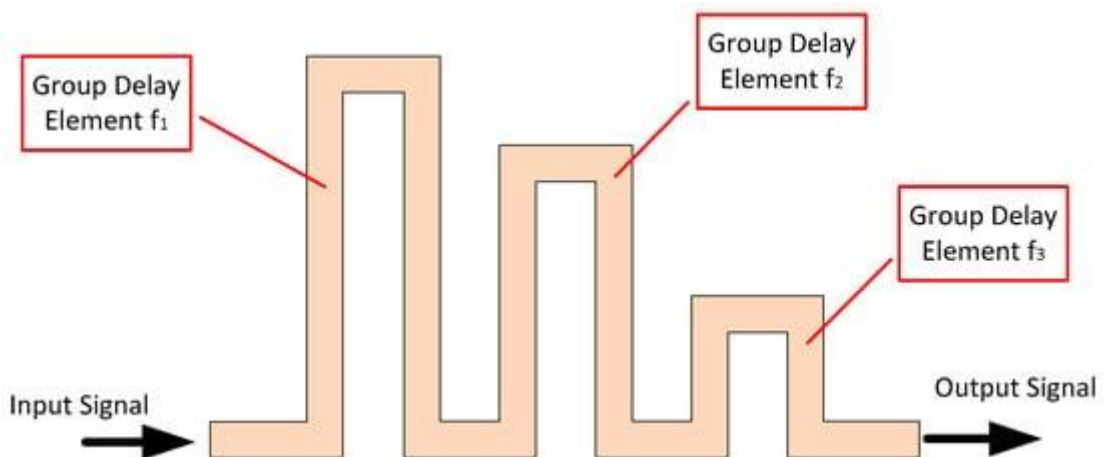
Figure 2.10: Group Delay Transmission Line Diagram – from "A Review of Chipless Remote Sensing Solutions Based on RFID Technology" by McGee et al., MDPI, CC BY 4.0 [3]

25

Surface Acoustic Wave Tags

This particular design approach is completely different than those discussed thus far in this chapter. Surface Acoustic Wave (SAW) devices work by inducing a surface acoustic wave into a piezoelectric substrate. This is done through a conductor pattern known as an Inter-Digital Tranducer (IDT) which is directly connected to the antenna. Metallic elements (reflectors) are placed at various distances from the IDT and the reflected signals induce a corresponding signal back into the IDT and the reflection then carries on back out from the antenna. This approach has been used in a variety of both tag and sensor applications as the propagation speed of the acoustic waves is extremely low compared to that of the signals found in a conventional transmission line. This allows much of the environmental echoes to occur before the tag response signal is received. Figure 2.11 depicts the basic layout of a SAW tag.
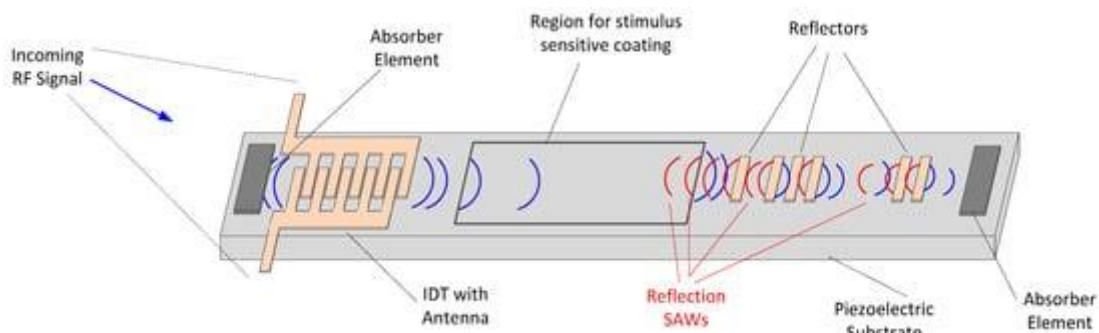
Figure 2.11: Surface Acoustic Wave Tag Diagram – from "A Review of Chipless Remote Sensing Solutions Based on RFID Technology" by McGee et al., MDPI, CC BY 4.0 [3]

Sensing can also be performed as certain piezoelectric materials have stimulus-dependent acoustic propagation rates [81][82]. In-situ fabrication of such devices has not been demonstrated as although many publications have managed to deposit the conductive patterns in-situ, deposition of a working piezoelectric material is a much more challenging undertaking [83]. For this reason, SAW devices have not been explored further, as part of this project.

2.7.4   Frequency Domain Tags

This type of design does not set out to separate the structural and antenna mode scattering but rather to rely on the changing the location of the narrowband frequency response of the narrowband antenna/resonator. These tags take two common forms: transmission line -based designs and sole resonators.

Resonator -Based Tags

These designs are simply unloaded antennas/resonators and a wide variety of examples can be seen in the current chipless RFID literature. Figure 2.12 depicts several popular resonator patterns seen in the current literature. Of importance here is that the resonant properties of antennas are dependent on the materials that the device is made of and/or coated in.
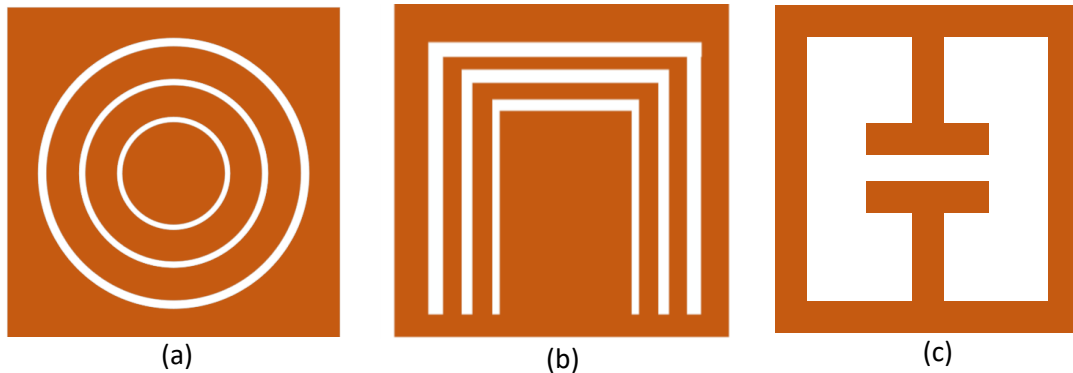
Figure 2.12: Resonator Designs (a) - Circular Ring Resonator, (b) - Slot Resonator, (c) - ELC Resonator

Many chipless RFID sensors have made use of this type of tag design [2][3]. The Electric LC (ELC) geometry similar to that depicted in Figure 2.12(c), has been used in [84] for temperature and humidity sensing. This device was developed through the coating of the resonators with an appropriate coating. The resonant response of the geometry seen in Figure 2.12(c) has been described in [85], can be seen in Equation 2.33 below.

$$f_r = \frac{1}{2\pi}\sqrt{\frac{2}{LC}}$$

(2.33)

Transmission Line -Based Tags

This design type is similar to the generic time-domain tags discussed above. Basically, they consist of an antenna, along with a transmission line and either a reflective termination or a separate re-transmission antenna. Frequency domain encoding is achieved through various types of frequency-dependent inclusions such as resonator loading [86][73] and conductor inclusions [71][73]. Commonly found types of inclusions are described graphically in Figure 2.13 below. The transmission line itself is also sensitive to magnetic and electric properties of the constituent materials [87].
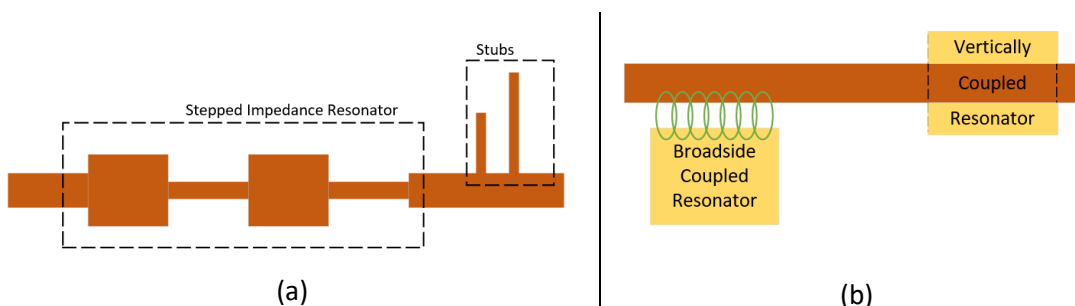
An example of such a tag is that used by Amin et al. in References [63][71]. This makes use of a Co-Planar Waveguide (CPW) with open-ended $\lambda/4$ Stepped Impedance Resonators (SIRs) to create a bandstop response in the output response of the CPW. This device works as $\lambda/4$ elements in a transmission line cause the opposite impedance to be observed at their entrance than that at their exit (half rotation around the Smith chart) so that it appears as a short circuit [74]. SIRs are commonly used for high-pass and low-pass planar circuits as the Richard's Transform and Kuroda Identities [65] explain how distributed elements such as these can be used in a similar way to conventional capacitors and inductors. Other works have also made use of $\lambda/4$ SIRs in the open circuit configuration for bandstop filter applications [88].

2.8   Chipless RFID Strain Sensing

The sensor performance required for aerospace strain sensing is a combination of both environmental stability criteria along with sensitivities/resolutions of around $10\mu\epsilon$ [8][39]. Stimulus range requirements will need to be at least $\pm0.3\%$ ($3000\mu\epsilon$) as that is what conventional foil gauges support [4]. Other materials such as certain carbon fiber blends, silicones or generic polymers appear to support significantly larger deformation ranges ($>1\%\epsilon$).

The basic operating principle of the existing chipless RFID strain sensor designs is to make use of geometric deformation of the resonator to give rise to changes in scattering response. These can be either magnitude [89] or frequency shift changes [90] or in some cases, both changes arise [91]. Table 2.2 compares the two most common deformation behaviours within the existing designs. Commonly found designs make use of the Meander Line Antenna (MLA) [89][92], patch antenna [90][93] or other resonator [91][94]. Not all of these designs can operate with metallic superstrates. The current limitations of these sensor designs are that their sensitivities are very low, i.e. on the order of kHz/$\mu\epsilon$ and significant fabrication challenges are present with the best of the existing designs [95][96]. From a further review of the existing designs, it can be seen that many of them rely on high-quality conductors and conductor-substrate bonds to achieve stable operation. This is a small remark but an important one as it remains to be seen if printed sensors can live up to these expectations, even with extensive pre and post -processing of the deposited conductive patterns.

Table 2.2: Existing Strain Sensor Deformation Behaviour Comparison

	Elastic Deformation	Bending
Examples	[90][91][93][94][95][96]	[89][92]
Benefits	More likely to give rise to frequency shift effects than bending designs	Bending forces are usually lower than conventional tensile/compressive deformation
Drawbacks	Device performance and longevity dependent largely on the quality of the conductor [91][92]	More complex deformation behaviour (potential wrinkling and stress concentrations). Designs are comparably harder to implement

2.9 Chipless RFID Temperature Sensing

The temperature sensing requirements outlined in a recent NASA roadmap document [39] suggest supporting resolvable temperature differences on the order of 0.1°C. Current chipless RFID temperature sensors that result in an alteration in the location of the frequency response of the tag exhibit sensitivities on the order of 1MHz/°C [3]. These chipless RFID designs are either dielectric constant -based or rely on mechanical deformation. A summary of the two approaches can be seen in Table 2.3 below. Of particular concern, is that the dielectric-based designs in some cases have significant cross sensitivity effects to other environmental stimuli, such as humidity [97].

In terms of stimulus range, many of the existing designs have not been shown to support the range of temperatures experienced by aerospace structures. This is particularly true of the polymer-based sensors but virtually all of the devices cannot support the temperature ranges boasted by conventional thermocouples.

Table 2.3: Chipless RFID Temperature Sensor Comparison with Conventional Approaches

	Chipless RFID - Dielectric Coating	Chipless RFID - Mechanical Behaviour	Conventional Sensors
Examples	Stanyl Polyamide [98], BST [99],	Bi-material strip [96][100], resonator swelling [101]	Thermoelectric/ thermoresistive effect
Benefits	Modular design, simpler fabrication (in some cases)	Simpler characterisation, very high sensitivity	Operating ranges of thermocouples exceed chipless RFID designs. Thermistors are far more sensitive to temperature than existing chipless designs

| Drawbacks | Range and (cross) sensitivity are mostly dominated by the coating performance | More complex resonator design, substrate design more important | More complex/ exotic materials used. Difficult to fabricate in-situ. None are wireless. |

2.10   Chipless RFID Sensor Fabrication

This subsection is a short overview of the fabrication challenges associated with trying to achieve an easily deployable chipless RFID sensor system. Different approaches could be taken here, each with their own benefits and drawbacks (see Table 2.4 below). These include the fabrication of the sensors offsite and dispensing/adhering them to the craft, which has been referred to as the "lick-and-stick" approach in this and in other works besides. Based on the application to tender put forward by the ESA [5], it can be seen that an in-situ fabricated sensor technology is currently preferred by members of the aerospace community.

Table 2.4: Comparison of Fabrication/Deployment Strategies

Approach	Applicable Technologies	Benefits	Drawbacks
Lick and Stick	All conventional fabrication methods	Can make use of high-quality bulk materials. Only the adhesive cure times contribute to the deployment time. Would allow for SAW or difficult materials to be used	The deployment process may have to be done manually (not automated). Only supports a fixed design (no ad-hoc changes)
In-situ Fabrication	Inkjet, Aerosol, FDM 3D Printing, in-situ moulding	In line with ESA trajectory [5] and its desire for deployment automation. Allows for ad-hoc reconfigurable design	Materials deposited are usually of poorer quality than that found in bulk. Deployment time could be extensive
Hybrid	Thermal transfer ribbon	In line with ESA trajectory [5] and its desire for deployment automation. Allows for reconfigurable design. Can make use of bulk materials	May not be capable of producing an arbitrary design (substrate/conductor thickness largely fixed) More reliant on adhesives that may not be aerospace compliant

2.10.1 Inkjet and Aerosol Technologies

Many of the publications in the area of printed electronics use inkjet technology as the deposition method as this technology is more readily available and more established than aerosol deposition. In any case, the same basic challenges arise in the realisation of a functional chipless RFID sensor using either technology. These fabrication approaches are considered whilst others are neglected, e.g. screen printing as this and other technologies do not easily support the ad-hoc modification of the sensor design which is necessary to ensure that each sensor has its own spectral address. This discussion will neglect the basic introduction to the two technologies as this has been exhaustively documented and discussed in various other works, such as [87] by Karmakar et al. and in many other works besides [102]. Instead, this section will focus on the fabrication steps required to fabricate the two main parts of basic RFID tag. Amongst other challenges involved with utilising such technologies neither of them can deposit thick layers in a single pass and both utilise small (usually nanoparticle sized) conductive particles to develop conductive depositions [103]. These particle colloids can be readily atomised (aerosol) and can be passed easily through a nozzle without clogging(inkjet) [103]. Some small variations between the two technologies include the fact aerosol deposition can be performed from a much further distance than possible with inkjet [103].

Sintering is then performed to remove now unwanted components from the deposited patterns so that the conductive nanoparticles can coalesce and form conduction paths. One exception to this is the Plasmajet® [104] technology, which removes the unwanted components as the material is being deposited. Said method can also deposit thick conductors and work with more complex conductive nanoparticles such as copper ones.

Dielectric Fabrication

Several works have deposited dielectric materials using direct write technologies. Examples include the work of Zhang et al. in [105] and in [106] which both use an inkjet printing approach. However, one issue with the potential use of Kapton and the subsequent deposition of conductive elements is that the surface is both highly inert and highly hydrophobic [107][108]. Solutions to this problem involve the use of strong acids or bases or other methods such as laser ablation or plasma etching [108]. Further discussion on plasma-based surface modification solutions to this problem can be found in [109]. A computer-controlled surface modification approach can be found in the work of Fang and Tentzeris in

[107]. Other issues that can arise in the use of Kapton as a substrate material is that although it is a highly inert material compared to other polymers, it can be thermally damaged during conventional sintering methods [110]. This is also a problem that will arise with many other substrates, including other polymers and glass [111]. There are also numerous examples of inkjet deposition on polyimide including the work of Wang et al. in [110]. More generally however, the various examples of printed electronics found in the literature make use of a substrate/dielectric layer made from normal bulk material, which was formed using conventional fabrication methods.

Conductor Fabrication

Many examples exist of the use of inkjet-printed silver nanoink -based RFID tags, including; References [91], [112] and [113] and also for the fabrication of microwave circuits, such as found in Reference [114] and [115]. A tabular comparison of the performances found in several published works can be seen in Table 2.5 below. Care should be taken when interpreting the results presented in Table 2.5 however, as different works emphasised differing performance goals or differing fabrication approaches. The work of Lee et al. in [115] was published in 2010 and successfully utilised inkjet-deposited copper nanoparticles and appropriate sintering strategies to achieve conductivities that were approximately on third of that found in bulk copper. The circuitry that was tested with signals up to 10GHz exhibited 0.32dB/mm losses, compared to the 0.02dB/mm expected from bulk copper. It is worth noting that commercial inks are also readily available and recent work by Larimore in [103] utilised the commercially available nScrypt 3Dn-300 printer and DuPont KA801 ink to achieve conductivities around 1.1×10^6 S/m. Other works that utilised more bespoke inks achieved further improvements in mechanical and electrical properties through the use of additional additives to the nanoparticle inks. Examples of such works include that by Wang et al. in [110]. In this work, additives such as Carbon Nanotubes (CNTs), graphene and Silicon Nanowires (SiNWs) were included in the ink to enhance the characteristics of the final depositions so far as achieving a conductivity of 9.091×10^6 S/m after sintering. Other works have made use of bimodal inks (2x same nanoparticle types but different size). An example of this can be seen in [116] where 10nm and 50nm silver nanoparticles were sintered at room temperatures to achieve a conductivity of 2.728×10^7 S/m. Similarly, Yu et al. used a bimodal copper ink in [117] and light sintering to achieve a conductivity of 17.61×10^6 S/m. Similar works with bimodal inks also revealed that enhancements in mechanical performance can also be achieved with the use of bimodal over unimodal inks [116].

Table 2.5: Comparison of Deposited Conductive Traces from Published Works

Reference	Year	Ink Material	Conductivity (10^7 S/m)
[103]	2019	Silver	0.110
[110]	2018	Silver NP + Flakes	0.909
[116]	2018	Bimodal silver	2.728
[114]	2017	Silver-based	≈1
[117]	2017	Bimodal copper	1.761
[115]	2010	Copper	≈1-2
Bulk Copper			5.8 [115]

2.10.2 Thermal Transfer Ribbon Technology

This technology differs significantly from the direct-write inkjet and aerosol systems in that it uses a heated printhead to selectively adhere portions of a metallic ribbon to a dielectric ribbon. This printhead contains many fine nibs/pins that are selectively used to heat portions of the metallic ribbon. These devices support spatial resolutions of around 300 Dots Per Inch (DPI) and can be reconfigured to transfer an arbitrary conductive shape onto the dielectric layer. A diagram of the system can be seen in Figure 2.14 below. The conductive ribbon contains the main conductive layer and a temperature-sensitive adhesive underneath it. The dielectric ribbon contains the main dielectric material along with a Pressure Sensitive Adhesive (PSA) layer, such as an acrylic-based adhesive on the bottom, and a topcoat (0.5-5µm [118]) which ensures adhesion between the thermal adhesive and the dielectric layer, without the need for pre-treatment of the dielectric top surface.
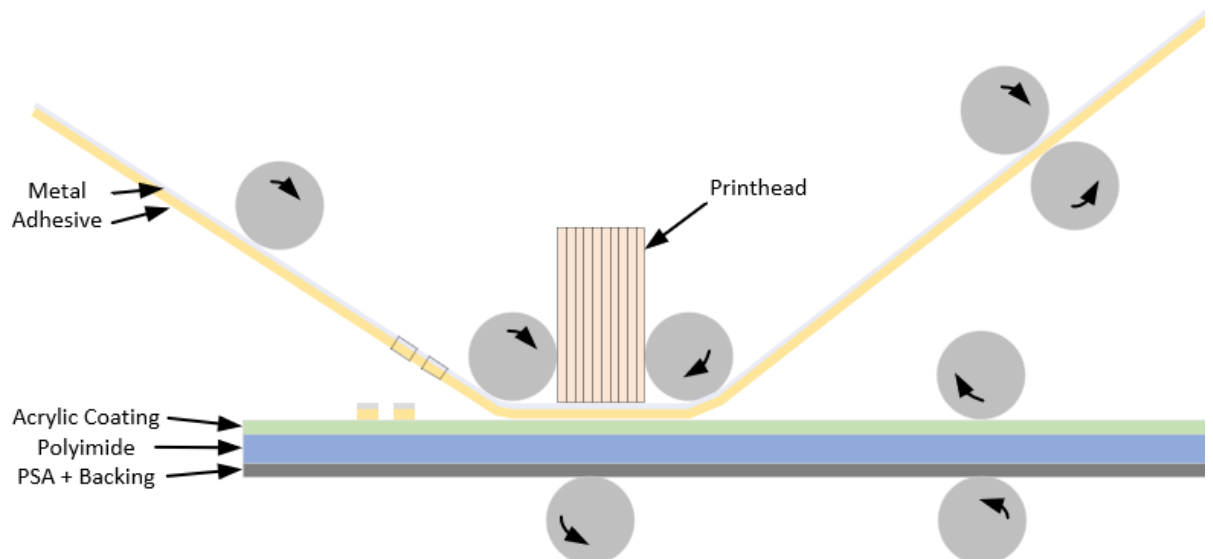
Figure 2.14: Thermal Transfer -Based Tag Fabrication Process

This approach has also been used/discovered by other researchers in the chipless RFID arena during the duration of this project [119][120]. These works have highlighted that there is no subsequent sintering steps required since the tag is made from bulk materials [119][120] and the electromagnetic response of the tags were found to be comparable if not exceed those developed through inkjet printing [120]. Potential issues related to the thin conductor layer of below 500nm were found to be non-existent for chipless RFID tag operations. Furthermore, Atomic Force Microscopy (AFM) analysis carried out in [120] revealed that the surface roughness was not considerable enough to warrant any further concern with the resulting tags. Not only that, said approach can support the in-situ placement/fabrication of previously difficult dielectrics such as polyimides.

Metallograph™[121], a provider of this particular service has suggested print speeds on the order of 50mm/s which is quite impressive. Yet to be demonstrated is the automation of the final step in the fabrication process, which is the adhesion of the tag/sensor to the desired surface.

2.11   Conclusions

This chapter has given a brief introduction to the general challenges posed by aerospace SHM and a review of the existing conventional technologies used within this space. A short discussion is also presented on the topic of chipless RFID tags/sensors, but the goal here has been to give a gentle overview to the topic here and more will be discussed in subsequent chapters. Finally, some useful review material has been presented on the topic of sensor fabrication.

What is important from the above discussion is that there is a great number of challenges associated with strain and temperature sensing for aerospace SHM. The existing technologies have clearly been very well-established and many of the cross-sensitivities have already been thoroughly explored. Also of importance is that the full in-situ fabrication and deployment of chipless RFID tags has not yet been demonstrated, although some technologies exist that may readily support it. Based on the discussion presented in this work and in a previously published work by the same authors [3], it can be concluded that the current state of chipless RFID sensor technology is somewhat behind the well-established and tested conventional strain and temperature sensing technologies.

2.12   References
[1]   A. Hashemi, A. H. Sarhaddi, and H. Emami, "A Review on Chipless RFID Tag Design," Majlesi J. Electr. Eng., vol. 7, no. 2, pp. 68–75, 2013.

[2]   C. Herrojo, F. Paredes, J. Mata-Contreras, and F. Martín, "Chipless-RFID: A Review and Recent Developments," Sensors, vol. 19, no. 15, p. 3385, Aug. 2019.

[3]   K. Mc Gee, P. Anandarajah, and D. Collins, "A Review of Chipless Remote Sensing Solutions Based on RFID Technology," Sensors, vol. 19, no. 19, p. 4829, 2019.

[4]   A. L. Window, Strain Gauge Technology, 2nd Edtn. London: Elsevier, 1992.

[5]   ESA, "ESA Open Invitation To Tender [FR] AO8922 - DIRECT PRINTING OF MECHANICAL AND THERMAL SENSORS ONTO SPACECRAFT HARDWARE." 2017.

[6]   W. M. Murray and W. R. Miller, The bonded electrical resistance strain gauge: An introduction, 1st Edtn. New York: Oxford University Press, 1992.

[7]   K. Hoffmann, An Introduction to Measurement Using Strain Gages. Hottinger Baldwin, 1989.

[8]   A. T. Edwards, "Comparison of Strain Gage and Fiber Optic Sensors On A Sting Balance In A Supersonic Wind Tunnel," Virginia Polytechnic Institute and State University, Blacksburg, 2000.

[9]   J. Turner and J. Watson, Automotive Sensors. Momentum Press, 2009.

[10]   B. J. MacDonald, Practical Stress Analysis with Finite Elements, 2nd Edtn. Dublin: Glasnevin Publishing, 2013.

[11]   S. P. Venkateshan, Mechanical Measurements. Ane Books, 2008.

[12]   A. S. Morris, Measurement and instrumentation : theory and application, Second edi. Amsterdam: Elsevier, 2016.

[13]   A. S. Morris and R. Langari, "Chapter 14 Temperature Measurement," in Measurement and Instrumentation: Theory and Application, Elsevier Science, 2015.

[14]   D. D. Pollock, Thermocouples: theory and properties, 1st Edtn. ASTM International, 1991.

[15]   A. Von Moll, A. R. Behbahani, G. C. Fralick, J. D. Wrbanek, and G. W. Hunter, "A Review of exhaust gas temperature sensing techniques for modern turbine engine controls," in 50th AIAA/ASME/SAE/ASEE Joint Propulsion Conference 2014, 2014.

[16]   S. O. Kasap, Optoelectronics and photonics: principles and practices, 2nd Edtn. Saskatatchewan: Pearson, 2013.

[17]   I. García, J. Zubia, G. Durana, G. Aldabaldetreku, M. Illarramendi, and J. Villatoro, "Optical Fiber Sensors for Aircraft Structural Health Monitoring," Sensors, vol. 15, no. 7, pp. 15494–15519, Jun. 2015.

[18]   S. Goossens et al., "Aerospace-grade surface mounted optical fibre strain sensor for structural health monitoring on composite structures evaluated against in-flight conditions," Smart Mater. Struct., vol. 28, no. 6, May 2019.

[19]   J. Shen, X. Zeng, Y. Luo, C. Cao, and T. Wang, "Research on strain measurements of core positions for the Chinese space station," Sensors (Switzerland), vol. 18, no. 6, Jun. 2018.

[20]   J. Wang, "Sapphire Fiber Based Sensing Technologies for High Temperature Applications," Virginia Polytechnic Institute and State University, 2011.

[21]   S. Sherman and H. Zappe, "Printable Bragg Gratings for Polymer-based Temperature Sensors," Procedia Technol., vol. 15, pp. 702–709, Jan. 2014.

[22]   J. M. Boccard, T. Aftab, J. Hoppe, A. Yousaf, R. Hutter, and L. M. Reindl, "Far-field passive temperature sensing up to 700°c using a dielectric resonator," in WiSEE 2014 - 2nd International IEEE Conference on Wireless for Space and Extreme Environments, 2014.

[23]   F. Ksica, Z. Hadas, and J. Hlinka, "Integration and test of piezocomposite sensors for structure health monitoring in aerospace," Meas. J. Int. Meas. Confed., vol. 147, p. 106861, Dec. 2019.

[24]   W. K. Wilkie, D. J. Inman, J. R. High, and R. B. Williams, "RECENT DEVELOPMENTS IN NASA PIEZOCOMPOSITE ACTUATOR TECHNOLOGY," 2004.

[25]   T. Aftab, T. Schaechtle, J. Hoppe, D. Shi, D. Schott, and L. Reindl, "Ultrasonic Coupled Passive Wireless Oscillating Sensor System," in Proceedings of Eurosensors 2017, 2017, vol. 1, no. 4, p. 574.

[26]   C. J. Keulen, B. Rocha, M. Yildiz, and A. Suleman, "Structural Health Monitoring Using Lamb Wave Based Piezoelectric Networks and Phased Array Solutions," in Noth Atlantic Treaty Organisation - Science and Technology Organisation, 2014, vol. 9, pp. 1–16.

[27]   F. Lanza di Scalea and S. Salamone, "Temperature effects in ultrasonic Lamb wave structural health monitoring systems," J. Acoust. Soc. Am., vol. 124, no. 1, pp. 161–174, Jul. 2008.

[28]   A. Muller, B. Robertson-Welsh, P. Gaydecki, M. Gresil, and C. Soutis, "Structural Health Monitoring Using Lamb Wave Reflections and Total Focusing Method for Image Reconstruction," Appl. Compos. Mater., vol. 24, no. 2, pp. 553–573, Apr. 2017.

[29]   P. French, G. Krijnen, and F. Roozeboom, "Precision in harsh environments," Microsystems and Nanoengineering, vol. 2, no. 1. Nature Publishing Group, pp. 1–12, 10-Oct-2016.

[30]   D. Dobkin, The RF in RFID: UHF RFID in Practice. Elsevier, 2012.

[31]   W. J. Thomes, Jr., R. F. Chuska, M. N. Ott, F. V. LaRocca, R. C. Switzer, and S. L. Macmurphy, "Fiber optic cable thermal preparation to ensure stable operation," in Optical Technologies for Arming, Safing, Fuzing, and Firing IV, 2008, vol. 7070, p. 70700B.

[32]   W. C. Wilson and P. D. Juarez, "Emerging needs for pervasive passive wireless sensor networks on aerospace vehicles," in Procedia Computer Science, 2014, vol. 37, pp. 101–108.

[33]   W. C. Wilson, D. F. Perey, G. M. Atkinson, and R. O. Barclay, "Passive wireless SAW sensors for IVHM," in 2008 IEEE International Frequency Control Symposium, FCS, 2008, pp. 273–277.

[34]   K. Sager, A. Schroth, A. Nakladal, and G. Gerlach, "Humidity-dependent mechanical properties of polyimide films and their use for IC-compatible humidity sensors," Sensors Actuators A Phys., vol. 53, no. 1–3, pp. 330–334, May 1996.

[35]   M. J. Adamson, "Thermal expansion and swelling of cured epoxy resin used in graphite/epoxy composite materials," J. Mater. Sci. 1980 157, vol. 15, no. 7, pp. 1736–1745, Jul. 1980.

[36]   E. J. Hughes and J. L. Rutherford, "DETERMINATION OF MECHANICAL PROPERTIES OF POLYMER FILM MATERIALS," 1975.

[37]   A. Blythe and D. Bloor, Electrical Properties of Polymers, 2nd Edtn. Cambridge: Cambridge University Press, 2005.

[38]   S. Manzari, S. Caizzone, C. Rubini, and G. Marrocco, "Feasibility of wireless temperature sensing by passive UHF-RFID tags in ground satellite test beds," in 2nd IEEE International Conference on Wireless for Space and Extreme Environments, WiSEE 2014, 2014.

[39]   "NASA Technology Roadmaps TA10: Nanotechnology." p. 99, 2015.

[40]   R. Di Sante, "Fibre optic sensors for structural health monitoring of aircraft composite structures: Recent advances and applications," Sensors (Switzerland), vol. 15, no. 8. MDPI AG, pp. 18666–18713, 30-Jul-2015.

[41]   D. L. Simon and K. J. Semega, "Sensor Needs for Control and Health Management of Intelligent Aircraft Engines," 2004.

[42]   T. Dong and N. H. Kim, "Cost-effectiveness of structural health monitoring in fuselage maintenance of the civil aviation industry," Aerospace, vol. 5, no. 3. MDPI Multidisciplinary Digital Publishing Institute, 01-Sep-2018.

[43]   E. F. Critchlow, "MEASUREMENT and PREDICTION of AIRCRAFT VIBRATION," SAE Trans., vol. 52, pp. 368–379, 1944.

[44]   S. Corda, R. J. Franz, J. N. Blanton, M. J. Vachon, and J. B. Deboer, "In-Flight Vibration Environment of the NASA F-15B Flight Test Fixture," Edwards, 2002.

[45]   A. Israr, "Vibration and modal analysis of low earth orbit satellite," Shock Vib., vol. 2014, 2014.

[46]   T. Mikaelian, "Spacecraft Charging and Hazards to Electronics in Space," Jun. 2009.

[47]   M. Yang, G. Hua, Y. Feng, and J. Gong, Fault-Tolerance Techniques for Spacecraft Control Computers. 2017.

[48]   J. G. Rodríguez-madrid, G. F. Iriarte, O. A. Williams, and F. Calle, "Sensors and Actuators A : Physical High precision pressure sensors based on SAW devices in the GHz range," Sensors Actuators A. Phys., vol. 189, pp. 364–369, 2013.

[49]   L. Scheick, A. Johnston, P. Adell, and S. Mcclure, "Total Ionizing Dose (TID) and Displacement Damage (DD) Effects in Integrated Circuits: Recent Results and the Implications for Emerging Technology," 2013.

[50]   M. C. Scardelletti, J. L. Jordan, G. E. Ponchak, and C. A. Zorman, "Wireless capacitive pressure sensor with directional RF chip antenna for high temperature environments," in IEEE International Conference on Wireless for Space and Extreme Environments, WiSEE 2015, 2016, pp. 1–6.

[51]   B. G. Streetman and S. K. Banerjee, Solid State Electronic Devices, 6th Edtn. New Jersey: Pearson, 2006.

[52] P. F. Mastro, Plastics Product Design. Wiley, 2016.

[53] K. K. de Groh, B. A. Banks, S. K. R. Miller, and J. A. Dever, "Chapter 28 - Degradation of Spacecraft Materials," in Handbook of Environmental Degradation of Materials (Third Edition), Third Edit., M. Kutz, Ed. William Andrew Publishing, 2018, pp. 601–645.

[54] L. A. Rogers et al., "Outgassing Environment of Spacecraft: An Overview," IOP Conf. Ser. Mater. Sci. Eng., vol. 611, no. 1, p. 012071, Oct. 2019.

[55] B. D. Green, "Satellite Contamination and Materials Outgassing Knowledgebase_ An Interactive Database Reference," Massachusetts, 2001.

[56] A. P. Povilus, C. J. Wurden, Z. Vendeiro, M. Baquero-Ruiz, and J. Fajans, "Vacuum compatibility of 3D-printed materials," J. Vac. Sci. Technol. A Vacuum, Surfaces, Film., vol. 32, no. 3, p. 033001, Apr. 2014.

[57] A. Riihimäki, "Outgassing Studies of Some Accelerator Materials," University of Helsinki, Helsinki, 2019.

[58] K. Battes, C. Day, and V. Hauer, "Outgassing behavior of different high-temperature resistant polymers," J. Vac. Sci. Technol. A Vacuum, Surfaces, Film., vol. 36, no. 2, p. 021602, Dec. 2017.

[59] T. Woods, "NASA - Out of Thin Air," 11-Feb-2011. .

[60] A. De Rooij, "The Oxidation of Silver by Atomic Oxygen," Noordwijk, 1989.

[61] A. De Rooij, "Exposure of Silver to Atomic Oxygen," Noordwijk, 2010.

[62] R. D. Leach and M. B. Alexander, "Failures and anomalies attributed to spacecraft charging," 1995.

[63] E. Amin, N. Karmakar, A. C. Rfid, and P. D. Sensor, "Partial Discharge Monitoring of High Voltage Equipment Using Chipless RFID Sensor," in Asia-Pacific Microwave Conference 2011, 2011, pp. 1522–1525.

[64] Y. Huang and K. Boyle, Antennas: From Theory to Practice. Sussex: Wiley, 2008.

[65] D. M. Pozar, Microwave Engineering, 4th ed. New York: Wiley, 2012.

[66] R. C. Hansen, "Relationships Between Antennas as Scatterers and as Radiators," Proc. IEEE, vol. 77, no. 5, pp. 659–662, 1989.

[67] K. Finkenzeller, RFID HANDBOOK: Fundamental sand Applications in Contactless Smart Cards and Identification, 2nd Edtn. Wiley, 2003.

[68] I. Nassar, "Long-Range, Passive Wireless Monitoring Using Energy-Efficient, Electrically-Small Sensor Nodes and Harmonic Radar Interrogator," University of South Florida, Tampa, 2013.

[69] I. T. Nassar, T. M. Weller, and J. L. Frolik, "A compact 3-D harmonic repeater for passive wireless sensing," IEEE Trans. Microw. Theory Tech., vol. 60, no. 10, pp. 3309–3316, 2012.

[70] S. M. Aguilar and T. M. Weller, "Tunable harmonic re-radiator for sensing applications," IEEE MTT-S Int. Microw. Symp. Dig., pp. 1565–1568, 2009.

[71]   E. M. Amin, R. Bhattacharyya, S. Sarma, and N. C. Karmakar, "Chipless RFID tag for light sensing," in 2014 IEEE Antennas and Propagation Society International Symposium (APSURSI), 2014, pp. 1308–1309.

[72]   A. K. M. Z. Hossain, S. M. A. Motakabber, and M. I. Ibrahimy, "Microstrip Spiral Resonator for the UWB Chipless RFID Tag," Adv. Intell. Syst. Comput., vol. 1089, pp. 355–358, 2015.

[73]   M. A. Ashraf et al., "Design and analysis of multi-resonators loaded broadband antipodal tapered slot antenna for chipless RFID applications," IEEE Access, vol. 5, pp. 25798–25807, Dec. 2017.

[74]   J. D. Kraus and D. A. Fleisch, Electromagnetics with Applications. Boston: McGraw-Hill, 1999.

[75]   A. Chamarti and K. Varahramyan, "Transmission Delay Line Based ID Generation Circuit for RFID Applications," IEEE Microw. Wirel. Components Lett., vol. 16, no. 11, pp. 588–590, Nov. 2006.

[76]   Linlin Zheng, S. Rodriguez, Lu Zhang, Botao Shao, and Li-Rong Zheng, "Design and implementation of a fully reconfigurable chipless RFID tag using Inkjet printing technology," in 2008 IEEE International Symposium on Circuits and Systems, 2008, pp. 1524–1527.

[77]   S. Majidifar, A. Ahmadi, O. Sadeghi-Fathabadi, and M. Ahmadi, "A novel phase coding method in chipless RFID systems," AEU - Int. J. Electron. Commun., vol. 69, no. 7, pp. 974–980, Jul. 2015.

[78]   C. Mandel, M. Schussler, M. Maasch, and R. Jakoby, "A novel passive phase modulator based on LH delay lines for chipless microwave RFID applications," in 2009 IEEE MTT-S International Microwave Workshop on Wireless Sensing, Local Positioning, and RFID, 2009, pp. 1–4.

[79]   K. T. Chandrasekaran et al., "A compact two-bit metamaterial inspired phase modulated chip-less RFID with temperature sensor," in 2017 IEEE MTT-S International Microwave Symposium (IMS), 2017, pp. 1571–1574.

[80]   M. Schussler, C. Damm, M. Maasch, and R. Jakoby, "Performance evaluation of left-handed delay lines for RFID backscatter applications," in 2008 IEEE MTT-S International Microwave Symposium Digest, 2008, pp. 177–180.

[81]   J. R. Humphries and D. C. Malocha, "Wireless SAW Strain Sensor Using Orthogonal Frequency Coding," IEEE Sens. J., vol. 15, no. 10, pp. 5527–5534, Oct. 2015.

[82]   W. Buff, S. Klctt, M. Rusko, J. Ehrenpfordt, and M. Goroll, "Passive remote sensing for temperature and pressure using SAW resonator devices," IEEE Trans. Ultrason. Ferroelectr. Freq. Control, vol. 45, no. 5, pp. 1388–1392, 1998.

[83]   E. R. Cholleti, "A Review on 3D printing of piezoelectric materials," in IOP Conference Series: Materials Science and Engineering, 2018, pp. 455–473.

[84]   E. M. Amin, N. C. Karmakar, and B. W. Jensen, "Fully printable chipless RFID multi-parameter sensor," Sensors Actuators A Phys., vol. 248, pp. 223–232, Sep. 2016.

[85]   D. Schurig, J. J. Mock, and D. R. Smith, "Electric-field-coupled resonators for negative permittivity metamaterials," Appl. Phys. Lett., vol. 88, no. 4, pp. 1–3, 2006.

[86]   W. M. Abdulkawi and A. F. A. Sheta, "Chipless RFID Sensors Based on Multistate Coupled Line Resonators," Sensors Actuators A Phys., vol. 309, p. 112025, Jul. 2020.

[87]   N. C. Karmakar, E. M. Amin, and J. K. Saha, Chipless RFID Sensors, 1st Edt. Wiley, 2016.

[88]   P. K. Singh, S. Basu, and Y. H. Wang, "Planar ultra-wideband bandpass filter using edge coupled microstrip lines and stepped impedance open stub," IEEE Microw. Wirel. Components Lett., vol. 17, no. 9, pp. 649–651, Sep. 2007.

[89]   C. Occhiuzzi, C. Paggi, and G. Marrocco, "Passive RFID strain-sensor based on meander-line antennas," IEEE Trans. Antennas Propag., vol. 59, no. 12, pp. 4836–4840, 2011.

[90]   G. Wan et al., "Separating strain sensor based on dual-resonant circular patch antenna with chipless RFID tag," Smart Mater. Struct., vol. 30, no. 1, p. 015007, Dec. 2020.

[91]   J. Kim, Z. Wang, and W. S. Kim, "Stretchable RFID for wireless strain sensing with silver nano ink," IEEE Sens. J., vol. 14, no. 12, pp. 4395–4401, 2014.

[92]   L. Teng, K. Pan, M. P. Nemitz, R. Song, Z. Hu, and A. A. Stokes, "Soft Radio-Frequency Identification Sensors: Wireless Long-Range Strain Sensors Using Radio-Frequency Identification," Soft Robot., vol. 6, no. 1, pp. 82–94, Feb. 2019.

[93]   A. Daliri, A. Galehdar, S. John, C. H. Wang, W. S. T. Rowe, and K. Ghorbani, "Wireless strain measurement using circular microstrip patch antennas," Sensors Actuators, A Phys., vol. 184, pp. 86–92, Sep. 2012.

[94]   R. Melik, E. Unal, N. K. Perkgoz, C. Puttlitz, and H. V. Demir, "Metamaterial-based wireless strain sensors," Appl. Phys. Lett., vol. 95, no. 1, 2009.

[95]   T. T. Thai, H. Aubert, P. Pons, G. Dejean, M. Mtentzeris, and R. Plana, "Novel design of a highly sensitive RF strain transducer for passive and remote sensing in two dimensions," IEEE Trans. Microw. Theory Tech., vol. 61, no. 3, pp. 1385–1396, 2013.

[96]   T. T. Thai et al., "A novel passive ultrasensitive RF temperature transducer for remote sensing and identification utilizing radar cross sections variability," in 2010 IEEE International Symposium on Antennas and Propagation and CNC-USNC/URSI Radio Science Meeting - Leading the Wave, AP-S/URSI 2010, 2010, pp. 1–4.

[97]   G. T. Pawlikowski, "Effects of Polymer Material Variations On High Frequency Dielectric Properties," MRS Online Proc. Libr. 2009 11561, vol. 1156, no. 1, pp. 1–7, Aug. 2009.

[98]   E. M. Amin and N. Karmakar, "Development of a chipless RFID temperature sensor using cascaded spiral resonators," in 2011 IEEE SENSORS Proceedings, 2011, pp. 554–557.

[99]   C. Mandel, H. Maune, M. Maasch, M. Sazegar, M. Schüßler, and R. Jakoby, "Passive wireless temperature sensing with BST-based chipless transponder," in 2011 German Microwave Conference, 2011.

[100]   X. Shi, F. Yang, S. Xu, and M. Li, "A Passive Temperature-Sensing Antenna Based on a Bimetal Strip Coil," Sensors 2017, Vol. 17, Page 665, vol. 17, no. 4, p. 665, Mar. 2017.

[101]   F. Requena et al., "Thermal Modeling of Resonant Scatterers and Reflectometry Approach for Remote Temperature Sensing," IEEE Trans. Microw. Theory Tech., vol. 69, no. 11, pp. 4720–4734, Nov. 2021.

[102] Z. Cui and E. Al, Printed Electronics: Materials, Technologies and Applications. Wiley, 2016.

[103] Z. J. Larimore, "Multi-material Additive Manufacture of RadioFrequency Devices and Systems," University of Delaware, 2019.

[104] R. P. Gandhiraman, V. Jayan, J. W. Han, B. Chen, J. E. Koehne, and M. Meyyappan, "Plasma jet printing of electronic materials on flexible and nonconformal objects," ACS Appl. Mater. Interfaces, vol. 6, no. 23, pp. 20860–20867, Dec. 2014.

[105] F. Zhang et al., "Reactive material jetting of polyimide insulators for complex circuit board design," Addit. Manuf., vol. 25, pp. 477–484, Jan. 2019.

[106] F. Zhang et al., "Inkjet printing of polyimide insulators for the 3D printing of dielectric materials for microelectronic applications," J. Appl. Polym. Sci., vol. 133, no. 18, May 2016.

[107] Y. Fang and M. M. Tentzeris, "Surface Modification of Polyimide Films for Inkjet-Printing of Flexible Electronic Devices," in Flexible Electronics, IntechOpen, 2018.

[108] Y. Fang, J. G. D. Hester, W. Su, J. H. Chow, S. K. Sitaraman, and M. M. Tentzeris, "A bio-enabled maximally mild layer-by-layer Kapton surface modification approach for the fabrication of all-inkjet-printed flexible electronic devices," Sci. Rep., vol. 6, Dec. 2016.

[109] N. Inagaki, S. Tasaka, and K. Hibi, "Surface modification of Kapton film by plasma treatments," J. Polym. Sci. Part A Polym. Chem., vol. 30, no. 7, pp. 1425–1431, Jun. 1992.

[110] X. Wang, W. Guo, Y. Zhu, X. Liang, F. Wang, and P. Peng, "Electrical and Mechanical Properties of Ink Printed Composite Electrodes on Plastic Substrates," Appl. Sci., vol. 8, no. 11, p. 2101, Nov. 2018.

[111] M. K. Kim, J. Y. Hwang, H. Kang, K. Kang, S. H. Lee, and S. J. Moon, "Laser sintering of the printed silver ink," in 2009 IEEE International Symposium on Assembly and Manufacturing, ISAM 2009, 2009, pp. 155–158.

[112] A. Vena, A. A. Babar, L. Sydanheimo, M. M. Tentzeris, and L. Ukkonen, "A Novel Near-Transparent ASK-Reconfigurable Inkjet-Printed Chipless RFID Tag," IEEE Antennas Wirel. Propag. Lett., vol. 12, pp. 753–756, 2013.

[113] A. Vena, L. Sydänheimo, L. Ukkonen, and M. M. Tentzeris, "A fully inkjet-printed chipless RFID gas and temperature sensor on paper," in 2014 IEEE RFID Technology and Applications Conference, RFID-TA 2014, 2014, vol. 2, pp. 115–120.

[114] G. McKerricher, M. Vaseem, and A. Shamim, "Fully inkjet-printed microwave passive electronics," Microsystems Nanoeng., vol. 3, no. 1, pp. 1–7, Jan. 2017.

[115] H.-J. Lee, S. Seo, K. Yun, J. W. Joung, and J.-G. Yook, "Loss characteristics of coplanar waveguide transmission lines fabricated with copper nanoparticles," Microw. Opt. Technol. Lett., vol. 52, no. 3, pp. 780–782, Mar. 2010.

[116] Z. Liu et al., "Enhanced Electrical and Mechanical Properties of a Printed Bimodal Silver Nanoparticle Ink for Flexible Electronics," Phys. status solidi, vol. 215, no. 14, p. 1800007, Jul. 2018.

[117] M.-H. Yu, S.-J. Joo, and H.-S. Kim, "Multi-pulse flash light sintering of bimodal Cu nanoparticle-ink for highly conductive printed Cu electrodes," Nanotechnology, vol. 28, no. 20, p. 205205, Apr. 2017.

[118]   Polyonics®, "Polyonics XF-552 POLYIMIDE LABEL," 2019. [Online]. Available: https://polyonics.com/TDs/XF-552.pdf. [Accessed: 27-May-2022].

[119]   J. M. Purushothama, S. Lopez-Soriano, A. Vena, B. Sorli, and E. Perret, "Application of Additive Manufacturing Based Thermal Printing Techniques for Realization of Electronically Rewritable Chipless RFID Tags on Flexible Substrates," 2021 34th Gen. Assem. Sci. Symp. Int. Union Radio Sci. URSI GASS 2021, Aug. 2021.

[120]   M. Kgwadi, M. Rizwan, A. Adhur Kutty, J. Virkki, L. Ukkonen, and T. D. Drysdale, "Performance comparison of inkjet and thermal transfer printed passive ultra-high-frequency radio-frequency identification tags," IET Microwaves, Antennas Propag., vol. 10, no. 14, pp. 1507–1514, Nov. 2016.

[121]   "Metallograph® Printed Electronics - SPF Inc - Specialty Papers & Films." [Online]. Available: https://spf-inc.com/metallograph. [Accessed: 04-Mar-2022].

Chapter 3 - Strain Sensor Development

3.1   Introduction

This chapter outlines the progress made towards developing a device capable of sensing mechanical strain in a passive and remote manner. As much as possible has been done to decouple the contents of the chapters from one another, but to save repetition, the reader will be at some stages pointed back or forward to a different chapter for further information on a particular topic.

This chapter contains a thorough discussion on chipless RFID strain sensors and three unique designs (Version 1 (V1), Version 2 (V2), Version (V3)) that boast various design features/enhancements have also been discussed. Several implementations of the V1 design have been implemented using simplified fabrication approaches and tested using a tensile testing machine. The concluding results are that a unique, highly sensitive design was developed and has been tested when fabricated using a variety of fabrication approaches.

3.1.1   Sensor Design Goals and Design Approach

The overall goal of this chapter is to develop and test a chipless RFID strain sensor with the following characteristics:

1. Exhibit a significantly higher sensitivity than previous works, in the hope that the detection of strains on the order of 10-100 microstrain ($\mu\varepsilon$) can be easily detected

2. Support a sufficient strain range that makes the device suitable for a variety of applications

3. Can be completely fabricated and/or deployed in-situ in an automated manner

4. Does not rely exclusively on conductor deformation as this would place a significant emphasis on the deposition of extremely high-quality conductive parts

5. Exhibit a small footprint

3.1.2   Sensor Development and Testing Goals

The additional goals alongside the development of a novel chipless RFID strain sensor is to develop a version of it that can be/is printed in-situ and to test it. On top of that, the impact of other variables such as environmental conditions should also be explored and considered within the overall design strategy. These variables would ideally include all kinds of effects that can take place in aerospace sensing but given the scope of the project, they will be limited to temperature and humidity. Other variables that can cause permanent alterations to the sensor and its response, such as radiation damage and/or mechanical creep and/or fatigue will not be considered at this time.

3.1.3   Chapter Methodology

The chapter makes use of both physical testing and simulation-based modelling to develop the desired strain sensor. The goal is to push towards a final version that can be fabricated in-situ, thus the designs are developed based on what is currently capable using the existing in-situ fabrication technologies. Where possible, physical testing is performed to determine the next step in the design process and simulations are used to model the more complex features of the developed designs. This was done as it makes the overall process less prone to error.

3.2   Overview of Existing Sensor Designs

From reviewing the existing chipless RFID strain sensor designs, it can be seen that their geometries undergo different effects as a result of mechanical strain. This work has categorised these effects as being one of three types; elastic deformation, bending or rigid body motion. Elastic deformation is defined here as behaviour where the conductor expands or contracts under deformation. Bending, as the name suggests defines occurrences where the conductor bends or buckles as a result of strain. Finally, rigid body motion defines occurrences where portions of the resonator move away from each other whilst not being deformed themselves.

Table 3.1 depicts the details of the previous publications in the area of chipless RFID strain sensing. The Gauge Factor (GF) calculation is a common metric used to define the sensing performance of various strain sensors and is calculated using Equation 3.1. One feature of interest in this table is that rigid body effects and elastic deformation are useful deformation mechanisms to make use of,to enhance strain sensitivity. Bending does not result in the same degree of sensitivity. One issue with the use of elastic deformation as the main deformation mechanism is that it will push a great deal of performance criteria onto the deposited conductors and onto their adhesion to the underlying substrate. This latter point has not been explored in the chipless RFID literature to any significant degree as little or no testing has been performed that assesses the number of strain cycles that the resulting sensors can survive. Furthermore, publications that make sole use of elastic deformation must rely on a flexible substrate to achieve strain ranges of over 1%. This is an important point as it means that the sensitivity and range of said designs are more dependent on the characteristics of the substrate. For the sensor developed in this work, it was decided that rigid body motion should be maximised so that a greater strain sensitivity can be achieved. Furthermore, the developed design should avoid elements such as cantilevers and other such elements so that the design is fully planar and thus can be fully printed in-situ using existing printing technologies.

$$Gauge\ Factor = GF = 100\ x\ \left(\frac{Sensitivity}{Initial\ Null\ Frequency}\right) \qquad (3.1)$$

Table 3.1: Comparison of Existing Chipless RFID Strain Sensors

Work	GF	Tested Range [%]	Superstrate	Substrate	Conductor	Deformation Mechanism(s)	Comments
[1]	0.9	25	Dielectric	Poly-dimethylsiloxane (PDMS)	MWCNT + Ag NP ink	Elastic, Rigid Body	Highly compact design
[2]	0.51	4	Dielectric	PDMS	Ag NP ink	Elastic, Rigid Body	Quality (Q) - factor variations present, may be environment-related
[3]	0.89	0.25	Dielectric/ Metallic	FR4, Carbon and Fiberglass Reinforced Polymer (CFRP, GFRP)	n/a	Elastic	Tested on metals and dielectrics
[4]	0.42	0.2	Dielectric	Silicon	Au film	Elastic, Rigid Body	Q-factor variations present
[5]	0.14	50	Dielectric	Ecoflex™ 00-50	Gallinstan	Bending	Gallinstan is a liquid metal that has a limited lower operating temperature
[6]	2.58	0.9	Dielectric	Kapton™ polyimide	Aluminium cantilever, n/a	Rigid Body, Bending	Uses a suspended cantilever to allow for

							rigid body motion

The simplest way to achieve a good deal of rigid body motion within the design is to make use of a resonator geometry that consists of several different parts. If the motion of these parts is in some way related to the resonant frequency of the resonator, then it should be possible to develop a highly sensitive sensor design. A multi-part resonator is not a fixed requirement, but single-part resonators will have to support/survive the effects of bending and/or elastic deformation so that the rigid body motion can occur.

So how can rigid body motion be promoted within the deformation behaviour of a multi-part resonator? The 2D diagram in Figure 3.1 depicts a substrate material that is experiencing an axial force and a resulting displacement. What is important to consider is the deformation of the top surface of the substrate, which is of course dependent on the impact that the two conductor elements have on the surface. Two scenarios of interest are; where the substrate is much stiffer than the conductors and where the conductor is far stiffer than the substrate. In the former scenario, a total substrate deformation of ΔX will result in ΔX_2 and ΔX_4 being zero and the value of ΔX_3 is as defined in Equation 3.2. In the latter scenario, ΔX_2 and ΔX_4 are non-zero and are at their maximum possible values. Equation 3.3 describes the deformation results found in this scenario. What is important to see here is that elastic deformation and rigid body motion occur in the second scenario whereas the first scenario results in a larger amount of rigid body motion and no elastic deformation of the conductor.
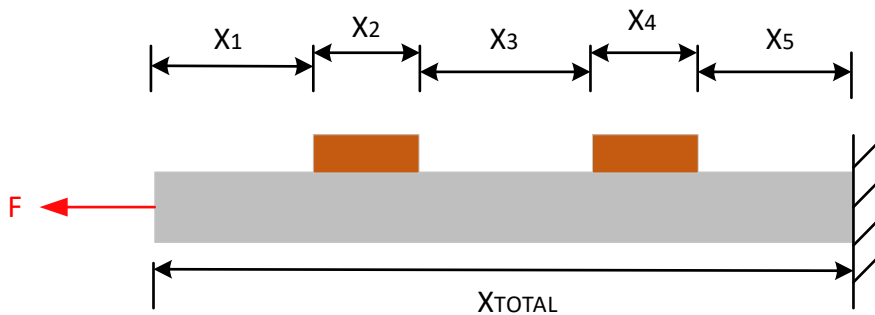
Figure 3.1: Theoretical Chipless RFID Strain Sensor Design

$$E_{SUBSTRATE} \ll E_{CONDUCTOR}, \; X_1 = X_3 = X_5 \; \therefore \; \Delta X_3 = \Delta X - \Delta X_1 - \Delta X_5 \qquad (3.2)$$
$$= \Delta X/3$$

$$E_{SUBSTRATE} \gg E_{CONDUCTOR}, \; X_1 = X_2 = X_3 = X_4 = X_5 \qquad (3.3)$$
$$\therefore \Delta X_3 = \Delta X - \Delta X_1 - \Delta X_2 - \Delta X_4 - \Delta X_5 = \Delta X/5$$

3.2.1   Simplified Exploration of Substrate-Resonator Behaviour

The use of rigid body motion as the prime or indeed as just a significant deformation effect within the sensor requires the chosen sensor materials to have certain mechanical properties. This section attempts to further explore the mechanical properties and geometric dependencies that are important to achieving this goal. For now, it will be assumed that the mechanical properties of each of the parts obeys an isotropic linear elastic model. Key assumptions made when choosing such a model are as follows:

- No viscoelastic behaviour occurs (i.e., creep)

- Low levels of strain are used within the simulation process (i.e., below yield strain)

- Elastic properties do not vary with orientation

Such models contain only two properties; Young's Modulus (E), which corresponds to stiffness and Poisson's ratio (v) which describes the amount of transverse strain that occurs as a result of an induced axial strain. Another property of interest that is derived from these two variables is the shear modulus of the material (G), which is described in Equation 3.4 [7]. The latter material property describes how strongly a shear strain that is being induced on the bottom surface of a material is transferred to the top surface. Armed with these material property definitions the exploration of the substrate-conductor behaviour can begin.

$$G = \frac{E}{2(1+v)} \tag{3.4}$$

An important note to make at this point is that this analysis negates the possibility of wrinkling and any other such effects that occur with extremely thin conductor or substrate layers. The topic of wrinkling is a very complex one and its effects in printed electronics is still under extensive research.

Elastic Deformation Mitigation

The use of a conductive element whose stiffness greatly exceeds that of the substrate will result in a stress concentration at its position on the substrate. Consider the diagram in Figure 3.2(a) which depicts the elevation view of a substrate with a conductive part on its top surface. If the stiffness of the conductor is infinite, the top surface of the substrate in contact with the conductor will exhibit no deformation under the applied force (F). Therefore, it could be assumed that the substrate behaves similarly to a large number of arrays of springs, as described in Figure 3.2(b). In this figure, the leftmost and rightmost columns of springs represent the behaviour of the substrate in the regions where it is not loaded with a

conductor and the central column of springs represents the impact of the conductor. Under the conditions where no conductor is present, all of these springs would have the same stiffness and their summation would be related to Young's Modulus (E). In the case where a stiff conductor is added, the stiffness values of the right and left columns remain the same but K_{10} becomes infinite and the stiffness values of K_{11}-K_{1N} decay away as the vertical distance from K_{10} increases. A similar effect can be expected in the other planes of the design, which brings up the possibility that the deformation of the substrate could concentrate around the conductor and not underneath it. The rate at which the stiffness values of K_{11}-K_{1N} decay away at will intuitively be related to the shear modulus (G).

(a)

(b)
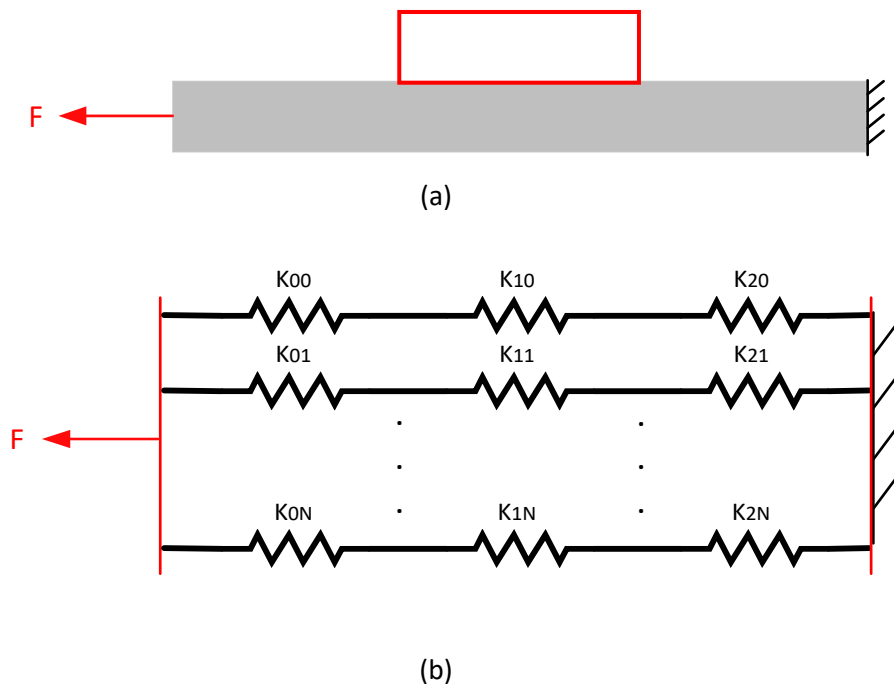
Figure 3.2: Substrate-Conductor Deformation Behaviour

If the mechanical properties of the conductor are relaxed, such that it exhibits a finite stiffness, the model in Figure 3.2 can be updated to look like that seen in Figure 3.3. In this model, the conductor can be modelled as a separate array of springs that are vertically coupled in relation to the shear modulus (G) and the springs K_{X0} and K_{10} are said to hold the same stiffness. The springs representing the conductor would all initially have a stiffness relating to the relevant Young's Modulus for that material.
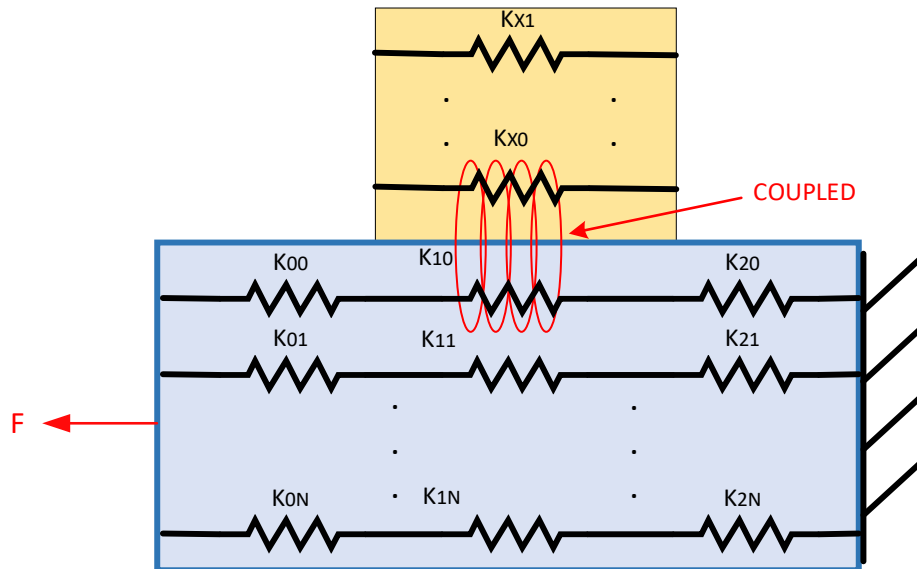
Figure 3.3: Substrate-Conductor Equivalent Model for a Weakened Conductor

The goal here is to explore what design parameters can be used to mitigate elastic deformation and thus promote rigid body motion. With that in mind, it would appear that based on the above discussion that the ratio of the stiffnesses of the conductor and substrate will dictate how much elastic deformation occurs. Therefore, the simplistic goal of maximising $E_{CONDUCTOR}/E_{SUBSTRATE}$ was identified. Note: This discussion is not yet concerned with stress concentrations and/or sensor lifetime and thus is solely focussed on sensitivity enhancement. Although that particular goal may seem like the best strategy to maximising sensitivity, there is a limit on its applicability. In the above discussion, it was mentioned that the substrate stiffness would decay away in the region under the conductor and that this would also occur in the plane of the top surface also. This raises the possibility that substrates with a low shear modulus (G) and/or a large thickness could exhibit strain effects that do not cause rigid body motion, but rather the induced strain "short-circuits" before/around the resonator. Figure 3.4(a) depicts the results of physical testing of the initial Ecoflex™ -based sensor which reveal this desensitising effect. Therefore, there will be a limit on how soft the substrate should be before sensor desensitising starts to occur. The diagram and Equations in Figure 3.4(b) try to explain this desensitising effect conceptually.

$$\Delta X1 = \Delta X3$$
$$\Delta X1 \gg \Delta X2$$
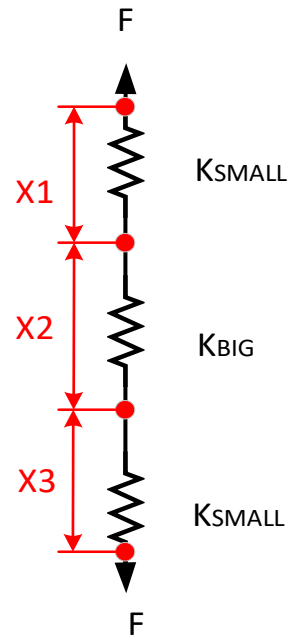
Figure 3.4: Short-Circuit/Necking Effects within Design

Bending Mitigation

The above discussion considered how elastic deformation could be avoided within the resonator design, through the use of a large stiffness ratio. One issue overlooked in that analysis is that even if that ratio is optimised, the resonator geometry may impact its own deformation in certain ways. Actual chipless RFID resonator designs are 3D objects with a width, length and thickness parameters. The above discussion largely neglects the fact that bending can occur in sections of the resonator that have an excessively small (bending result) or large (buckling result) planar aspect ratio in the direction of the strain vector. Figure 3.5 depicts a substrate and conductor part that is undergoing a compressive load. In this Figure, the conductor part is conceptually separated out into having two separate parts, an upper and a lower one. The edges of the upper part will have the proclivity to bend downwards because of the reaction force coming from the lower part of the conductor. Similarly, the lower part of the conductor may exhibit buckling (mid-point deformation/bulging in the transverse direction). The origin and magnitude of these effects will be heavily dependent on the planar aspect ratio and other parameters besides.
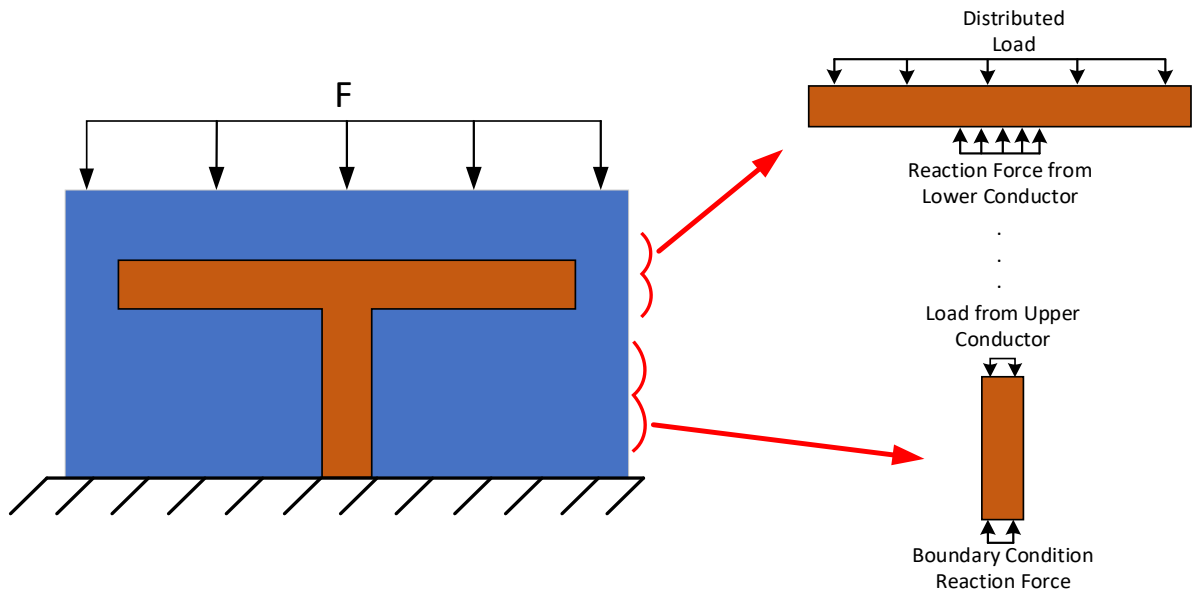
Figure 3.5: Bending and Buckling Effects in Theoretical Design

Both of these effects (cantilever bending under a distributed load and buckling) have long been understood and Equation 3.5 [7] and Equation 3.6 [7] describe the deflection and maximum force before buckling calculations that are commonly used to assess these effects.

$$\delta_{CANTILEVER} \propto \frac{FL^4}{EI_0} \tag{3.5}$$

$$F_{MAX-BUCKLING} = \frac{4\pi^2 EI_0}{L^2} \tag{3.6}$$

Key parameters other than details of the planar geometry are used in the above Equations. Of most interest is the presence of Young's Modulus (E) acting as a mitigating factor against these deformation effects. Similarly, another parameter of interest is I_o, which represents the Area Moment of Inertia and it too mitigates against buckling and bending. This is a measure of the conductor's cross section and how it is distributed around the bending/buckling axis. Further details on this topic can be found in any good Strength of Materials handbook, such as that by Singh in [7]. Given the fact that conductor cross sections are commonly rectangular as seen in Figure 3.6, this calculation can be simplified down as seen in Equation 3.7 [7]. Where the bending/buckling axis is different, the Parallel Axis Theorem adds for an additional term in Equation 3.7.

51
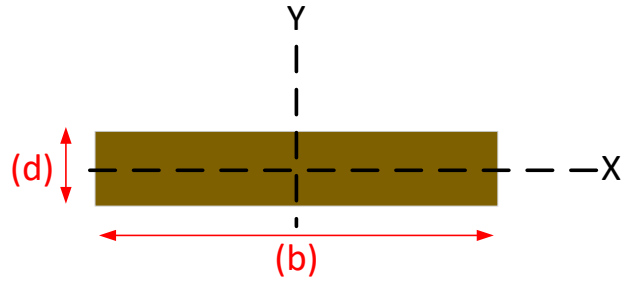
Figure 3.6: Example Conductor Cross-Section

$$I_X = \int y^2 dA \ \therefore \ I_X = \frac{bd^3}{12} \qquad\qquad (3.7)$$

The important points to take away from this subsequent discussion is that for a fixed resonator geometry, the conductor stiffness and height play a key role in mitigating bending and buckling effects.

3.2.2   Challenges of Differential Strain Sensing in Chipless RFID

This subsection outlines why a differential sensing approach was not pursued from the start of this research, as this approach may readily allow for sensitivity enhancement of the existing sensor designs. Interesting works focussed on the topic of differential sensing include that developed by Naqui et al. in [8] and that by Su et al. in [9]. The method used in these works involves the use of reference resonators and has been demonstrated to support the generation of a bandstop response whose null frequency location is related to the difference between the dielectric loading on the active and reference resonators. These designs are transmission-line based microwave circuits and have a significant footprint. It is also unclear, to what degree the stimulus sensitivity would be attenuated through the use of the "frequency splitting" approach used in these works.

The main concern here is the potential need to isolate the transmission line circuit from the effects of mechanical strain, whilst coupling to a resonator that is strain sensitive. This brings about the need for in-situ fabrication of several different materials with differing material properties. The most straightforward way to isolate the transmission line from the effects of strain is to make use of a material with a low shear modulus, such as a rubber, to isolate the transmission line from the resonator and superstrate (see Figure 3.7 below). The strain sensitive resonator and transmission line circuit will most likely make use of a stiffer dielectric material onto which the conductive traces are then deposited. Additional materials bring forth greater fabrication challenges, adhesion performance challenges and also brings forth the possibility of greater levels of cross-sensitivity.
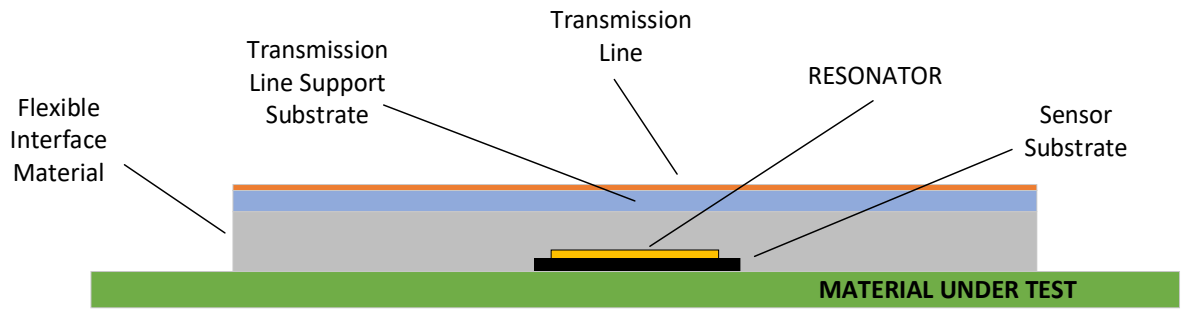
Figure 3.7: Proposed TL-Based Cross-Section

A more general critique on the use of transmission line -based chipless RFID tags is that the Ultrawideband (UWB) interrogation antennas will also need to be fabricated in-situ. This may not sound like a significant increase in complexity, but many planar UWB antenna designs require two metallization layers with a dielectric sandwiched in-between them. This lower metallisation layer is normally used as a ground plane for the antenna, but it does not usually reside completely under the main UWB antenna. It is therefore also unclear if such antennas would work on metallic surfaces. Furthermore, many of the high performance, compact UWB antenna designs such as Log Periodic Dipole Arrays (LDPAs) that support polarization discrimination or indeed enhanced directivity have not been demonstrated to work when located in a plane perpendicular to the interrogation beam. Phased array antennas or omnidirectional antennas could be used to achieve this goal [10][11], but such approaches would still significantly increase the overall footprint of the device and/or have very low gains.

In any case, the main feature of interest in these published designs is that transmission line -coupled resonator(s) can be configured to support differential sensing. Therefore, this chapter will focus on the development of a highly sensitive resonator design in the hope that it alone will provide the desired performance. If this is not achieved, the resulting resonator will still be of considerable use, as it can be implemented as part of a transmission line -based differential sensing strain sensor.

3.3   Geometric Design

The initial approach taken to developing a novel chipless RFID strain sensor design was to base it on an existing resonator design that had a highly sensitive capacitive region and was very compact. The ELC resonator discussed in References [12][13] was chosen as the ideal base resonator as it fulfilled both criteria. The desire for a sensitive capacitive region was that it would be an easy way in which rigid body motion could be utilised to make the device strain sensitive. In order to ensure that the design could operate over an arbitrary strain range, the resonator was split into four separate parts. These parts were two pairs of parts (see Figure 3.8); 1 pair were monopole-like side walls for the resonator and the other pair were a top and bottom section with a large capacitance between them. These parts are referred to as EL parts and EC parts respectively. Alternative configurations could have been implemented but this implementation was the most intuitive setup that would not result in significant shear strains between the parts during sensor operation. The manner in which the base resonator was split, was to ensure that the two planes of symmetry were still intact in the geometry. This was important as the time domain characteristics of the electromagnetic signals operating during the base resonance obey these symmetry relations [14]. Furthermore, the regions in which the resonator was split would have been stress concentration regions within the original design, if it had to be used in its current form as a strain sensor.
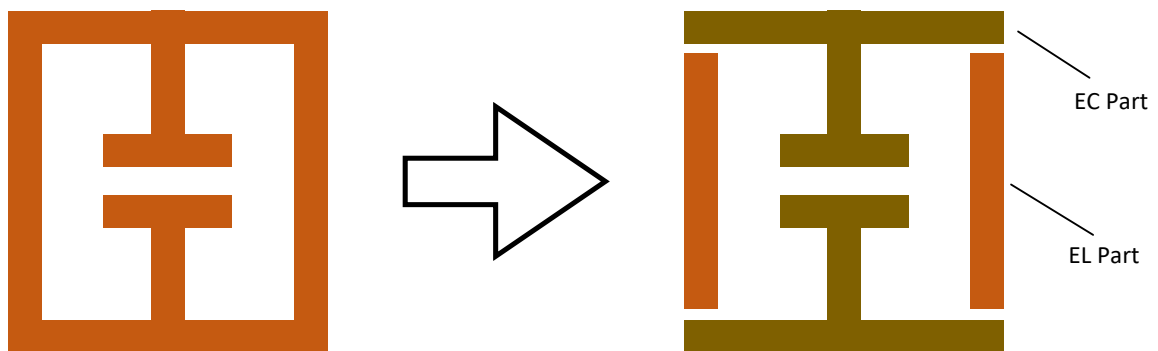
Figure 3.8: Initial Design Concept

3.3.1   Initial Design

An initial physical implementation was carried out to assess whether such a design exhibited the predicted resonance and once this was determined the next stages of sensor development could begin. The initial design explored is described in Figure 3.9 and its relevant dimensions can be found in Table 3.2. Said geometry was the initial design geometry and physical testing of this structure revealed it had an initial null frequency of approximately 2.8GHz.

Unfortunately, the "on-metal" resonances (discussed later) did not occur below the 3GHz limit of the available test equipment so the V1 design was developed soon afterwards.
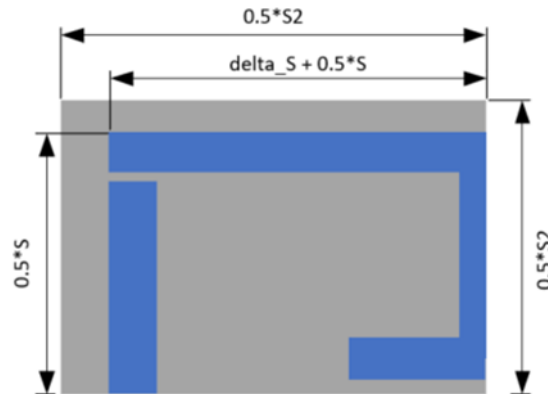
Figure 3.9: Quarter Symmetric Initial Sensor Diagram – from "Proof of Concept Novel Configurable Chipless RFID Strain Sensor" by McGee et al., MDPI, CC BY 4.0 [15]

Table 3.2: Initial Design Geometric Parameters – from "Proof of Concept Novel Configurable Chipless RFID Strain Sensor" by McGee et al., MDPI, CC BY 4.0 [15]

Design Parameters	S	S2	H	Mt
	24mm	40mm	0.5mm	0.05mm
Delta_S	Ws	Ws2	P	K
5mm	3mm	2mm	6mm	12mm

Theoretical Sensor Implementation

The theoretical sensor design proposed here consists of copper resonator parts that are bonded (in some way) to a polyimide substrate. It is assumed that the bonding between the copper and polyimide parts are the result of conductor deposition onto a treated polyimide surface. The reasons why these materials were chosen above all others are as follows:

- Polyimides are commonly used in aerospace settings [16][17]
- Polyimides such as Kapton® have high glass transition temperatures (above 350°C [18])
- Conductor deposition onto polyimide materials is a common goal of the printed electronics industry
- Silver conductors are oxidized by atomic oxygen and the resulting oxide layer can fall off and thus does not protect the underlying material from further oxidization [19]. It is unclear if copper nanoparticle -based depositions will suffer from the same behaviour

Exploratory Mechanical FEA

The next question to be answered is if rigid body motion can be achieved with the polyimide - based implementation or indeed any implementation of this sensor design. The Ansys Mechanical 2019R2 Finite Element Analysis (FEA) Simulation Package was used to characterise the deformation characteristics of this strain sensor. This analysis was performed with two different substrate materials; DuPont™ Kapton® Polyimide and EcoFlex 00-30 silicone rubber. The latter was chosen as it can be easily procured, formed and has been used in other RFID strain gauge designs such as that found in Reference [5] as a substrate material. A thorough discussion on the electrical characteristics of EcoFlex can be found in the work of Vaicekauskaite et al. in Reference [20]. Kapton® was modelled as a material with Isotropic Elasticity as it exhibits an elastic region and was deformed to no greater degree than that material model would allow. Since EcoFlex is a rubber, a hyperelastic material model was used as such a model allows for the necessary inflection points in the stress-strain curve. Hyperelastic material models of this type are alternatives to the commonly used linear elastic model, the latter of which assumes that a linear relationship exists between stress and strain. Hyperelastic material models are used to model materials whose stress strain curves that exhibit points of inflection, compressibility and other, more general nonlinear relationships [21]. These models are most commonly used to describe the behaviours of materials such as rubbers and biomaterials [21]. Said materials can support strains of over 500% [21] and certain hyperelastic models are more suited for certain materials and loading levels. The deformation levels seen in this work do not exceed 0.33% and thus a model that is accurate at that strain level is required. A third order Ogden hyperelastic material model was chosen as it is known to be relatively accurate for low levels of strain [21] and this material had already been used to model Ecoflex 00-30 in this way in works such as those found in References [22], [23] and using similar hyperelastic material models in References [24] and [20]. The conductor material is chosen as bulk copper as relevant tensile properties of inkjet/aerosol deposited conductors are heavily dependent on deposition protocol and the post-processing stages performed and thus cannot be easily determined. Appendix A gives further details on the FEA setup and the material models used within.

The axial deformation effects of axial strain of 0.33% (0.05mm displacement) on the sensor can be seen in Table 3.3. The various points of interest on the resonator are highlighted in Figure 3.10. This testing was done with the polyimide substrate as it is this material that is of most interest to the author. From these results, it can be seen that elastic deformation is occurring. This can be seen based on the fact that there is a difference in deformation

between the points; AC, BD, DF, EG, FH and the deformation of points I and J are also non-zero. Bending effects are also present, which can be seen in the results because there is a difference in deformation between points; AB, CD, EF, GH and IJ. Finally, there is a clear demonstration of rigid body motion also as no positions have deformation levels of zero.

Table 3.3: Initial Axial FEA Results – from "Proof of Concept Novel Configurable Chipless RFID Strain Sensor" by McGee et al., MDPI, CC BY 4.0 [15]

Setup	A	B	C	D	E	F	G	H	I	J
50µm Axial Def.	25	23	25	22	5.5	14	5.8	13	3.9	5.3
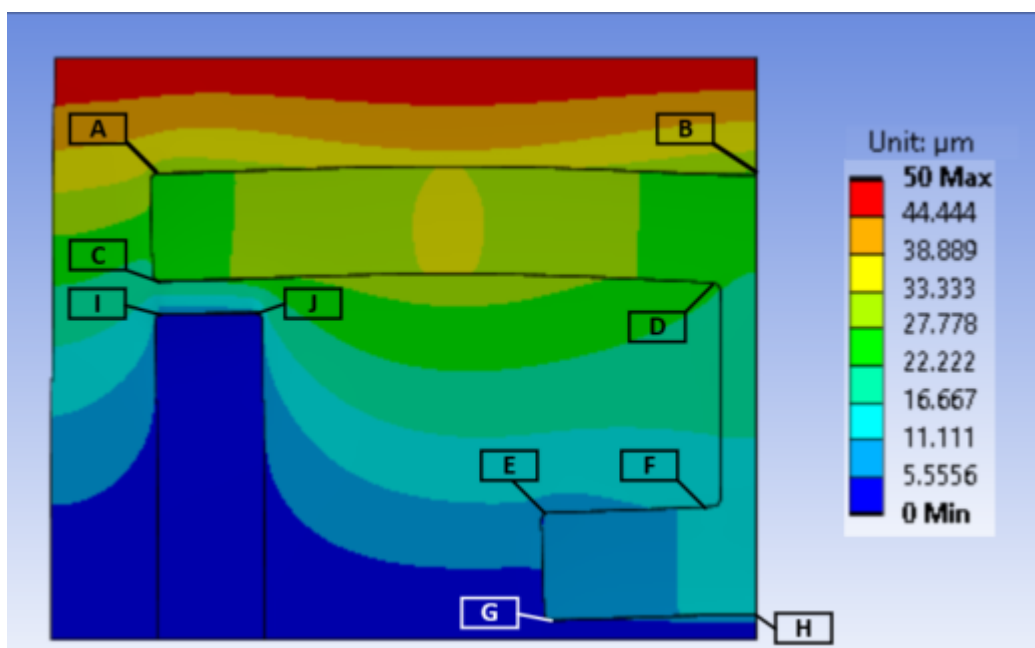
Figure 3.10: Sensor Axial Deformation Plot with Appropriately Labelled Positions - (Images Courtesy of ANSYS Inc)

From these results, it can be seen that the use of a polyimide substrate will result in a combination of deformation effects taking place. In any case, these results would suggest that basic testing which purely uses rigid body motion to emulate strain effects will potentially exaggerate the strain sensitivity that would be found with a polyimide substrate. Similar testing performed with an Ecoflex™ substrate can be found in Appendix A, which clearly demonstrates that a much greater degree of rigid body motion occurs, above the other two deformation effects.

Exploratory Electromagnetic FEA

The observed resonance from the device exhibits a sensitivity to the spacing between the resonator elements (sGap). Initial simulations performed in [15] resulted in the variation in

null frequency seen in Figure 3.11. Other results by the authors of [15] such as the sensitivity of the resonator to variations in the other geometric variables can be seen in Figure 3.12, where the variable "sGap" was kept constant.
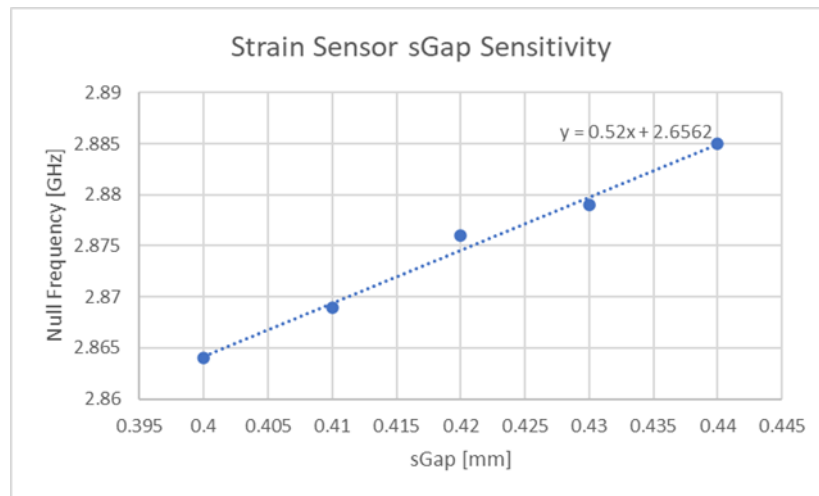
Figure 3.11: Exploratory Simulated Sensor Axial Sensitivity – from "Proof of Concept Novel Configurable Chipless RFID Strain Sensor" by McGee et al., MDPI, CC BY 4.0 [15]
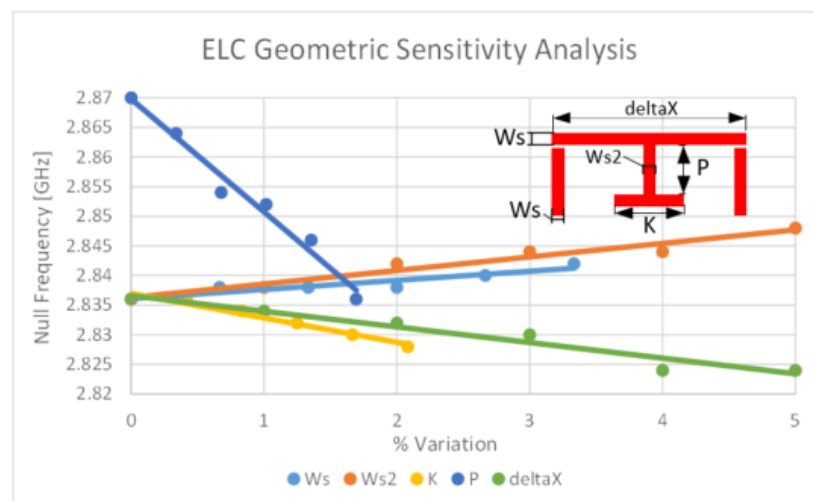
Figure 3.12: Simulated Geometric Sensitivity of Initial Design – Adapted from "Proof of Concept Novel Configurable Chipless RFID Strain Sensor" by McGee et al., MDPI, CC BY 4.0 [15]

What is of importance here is that rigid body motion results in a change in null frequency but so does variations in all of the other geometric variables. The results seen in Figure 3.12 also show that not all of the variables result in the null moving in the same direction. This will be of importance as it raises the possibility that a certain implementation of the sensor may result in having a strain sensitivity of zero. By the same token, other implementations may exhibit a sensitivity that is of the opposite sign to that of the sensor that exhibits purely rigid-body motion within the resonator.

3.3.2 Version 1 Design

The first version of this sensor has a slightly different geometry to that used in the exploratory analysis. Not discussed earlier is that the side walls of the geometry demonstrate the ability to support an additional/different resonance when the device was suspended above a metallic ground plane. As the test equipment available supported a maximum interrogation frequency of 3GHz, the geometry was modified so that both of these resonances occurred at different locations below 3GHz. This new geometry is depicted graphically in Figure 3.13 and the relevant dimensions are listed in Table 3.4.
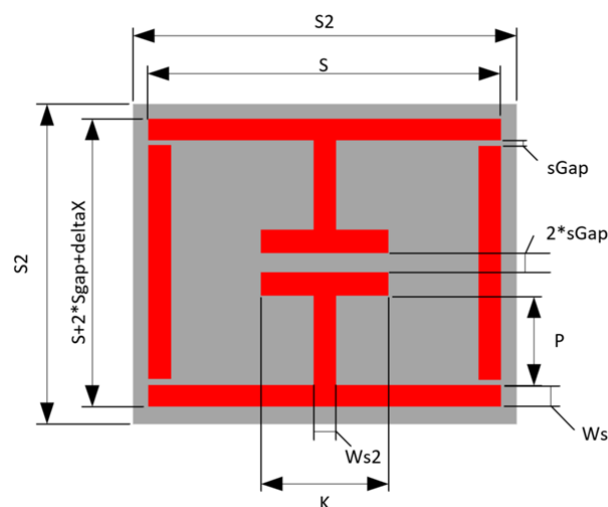
Figure 3.13: V1 Sensor Diagram – from "Proof of Concept Novel Configurable Chipless RFID Strain Sensor" by McGee et al., MDPI, CC BY 4.0 [15]

Table 3.4: V1 Sensor Geometric Parameters – from "Proof of Concept Novel Configurable Chipless RFID Strain Sensor" by McGee et al., MDPI, CC BY 4.0 [15]

Design Parameters	S	S2	H	Mt	sGap
	24	50, 76	3, 5	0.3, 0.1	1
deltaX	Ws	Ws2	P	K	
10	2	2	14	19	

The simulated sensor response of this device with a polyimide substrate has been presented in [15], and can be seen here in Figure 3.14. It demonstrates a dielectric resonance null at around 2.1GHz and two on-metal resonances at 1.96GHz and 2.45GHz respectively. The additional on-metal resonance (1.96GHz) arises due to the metallic ground plane and varies with its size.
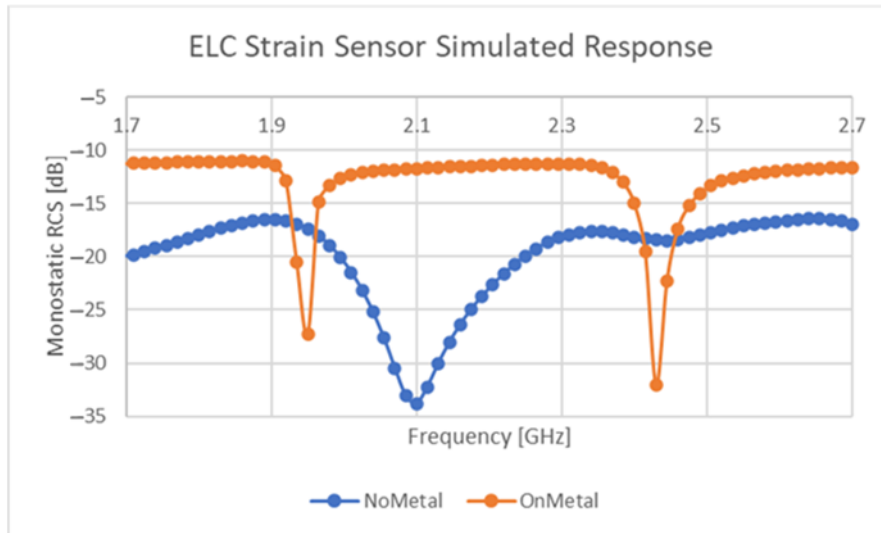
Figure 3.14: Simulated V1 Sensor RCS Response – from "Proof of Concept Novel Configurable Chipless RFID Strain Sensor" by McGee et al., MDPI, CC BY 4.0 [15]

Physical Implementations and Testing

Two different substrate materials were used during proof-of-concept testing, namely Ecoflex™ 00-30 silicone rubber and natural (latex) rubber. These materials could be easily procured and could also be easily deformed in a small/cheap bench press setup. Furthermore materials like this have also been used in already published chipless RFID strain sensor designs, such as that in Reference [5]. Before the discussion goes any further, it is worth noting that these materials exhibit notably different stiffnesses. Materials of this type (elastomers) are usually characterised using the Shore hardness scale [25]. This scale has various entries depending on the Shore hardness test performed, but the 00 series is for the softest materials and the A and D series are for harder materials. Ecoflex™ 00-30 falls in the "Extremely Soft" category [25] and natural rubber can have a Shore A hardness of between 20-90 placing it within the "Soft" to "Medium Hard" categories [26]. These Shore A categories correspond to a Shore 00 hardness of over 75 and thus are considerably harder than a Shore 00-30 material.

Test Setup

An anechoic environment and a HP8753D Vector Network Analyser (VNA) was used to perform the initial proof-of-concept strain sensor testing. A small bench press was used to carry out the strain tests and a bistatic antenna configuration was used with the press situated between the transmit and receive antennas. The interrogation antennas were both LDPA antennas (5-6dBi) with an operating range from 1.35-9.5GHz and they were both situated at distances ranging from 10-25cm from the press. These elements can be seen in Figure 3.15.
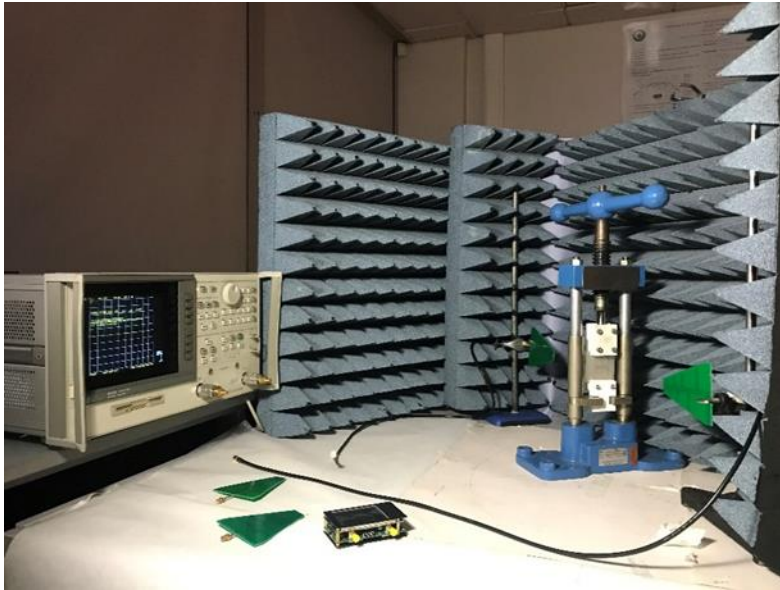
Figure 3.15: Strain Sensor Test Setup – from "Proof of Concept Novel Configurable Chipless RFID Strain Sensor" by McGee et al., MDPI, <u>CC BY 4.0</u> [15]

Ecoflex 00-30 Implementation

The initial implementations of the strain sensor used Ecoflex™ silicone rubber with a Shore hardness 00-30. This is a platinum cure silicone that consists of two parts that are mixed in equal proportions. Silicone rubber surfaces have a very low surface energy [27], which led to direct depositions of conductive inks with little or no surface adhesion. Other testing of the available conductive ink revealed that it exhibited extremely poor mechanical properties. To combat all of these issues, the desired conductive shapes were laser-cut out of Polymethyl methacrylate (PMMA) sheet and subsequently painted with the conductive paint. These new parts were then encapsulated in the Ecoflex™ substrate. To achieve this, the Ecoflex™ rubber was cured in a 3D printed mould (see Figure 3.16(a)) that included trenches for the PMMA parts. The PMMA parts were inserted in the cured silicone and a subsequent layer of silicone was used to seal the top surface of the sensor. The completed sensor can be seen in Figure 3.16(b). An alternative implementation used a screen-printing approach to add unsaturated polyester resin into the substrate trenches. Upon curing, the resonator design was painted on top of the resin. This particular implementation is mentioned here as said resin could be deposited in-situ.

<div align="center">(a)   (b)</div>
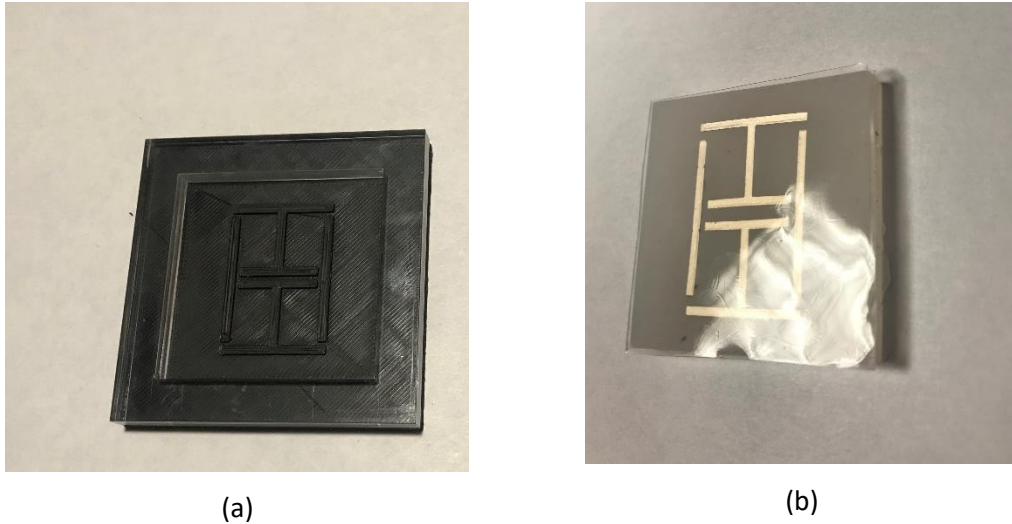
Figure 3.16: (a) - Ecoflex Mould and (b) - Resulting Sensor

Test results gathered with this sensor can be seen in Figure 3.17. These tests and all others in this subsection used the small bench press to deform the sensor.
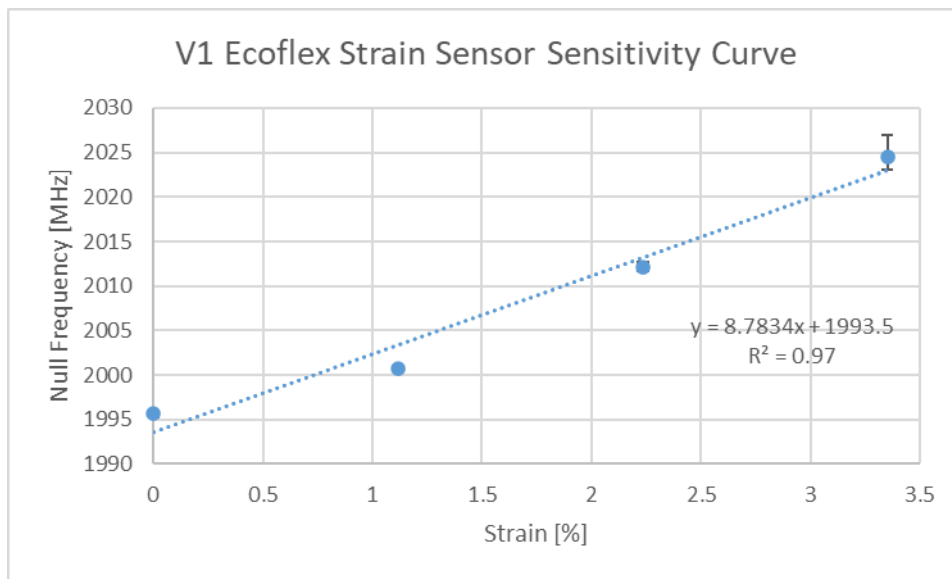
Figure 3.17: V1 Initial Strain Sensor Testing

These test results demonstrate a clear strain sensitivity within the sensor response. Interestingly, the deviation each of the datapoints exhibited from a straight line was largely consistent between repeated tests. This would suggest that the non-linearities are either inherent in the design or caused by the setup/environment.

Testing below 0.5% was quite difficult as the silicone substrate would expand in the axial direction upon clamping, which led to the device exhibiting a slightly different length, depending on clamping forces. Testing with initial pre-strain was required to ensure that the substrate was actually being strained by the 0-0.5% strain stimulus. Preliminary testing using

this approach resulted in the sensitivities comparable to that listed in Table 5 above (≈8.8MHz/%ε). This setup used a visual inspection to ensure that the initial press setting resulted in the clamping system imparting no compressive forces to the sensor.

Latex (natural) Rubber Implementation

Three observations were made during the development and testing of the Ecoflex -based strain sensor:

1. The axial deformation of the Ecoflex™ substrate appears to result in the substrate material surrounding the resonator to deform significantly whilst the deformation imparted onto the resonator was much less. This would suggest that the strain sensitivity of the Ecoflex™ implementation is lacking behind its optimal value.

2. Attempting to develop this design further so that it could be printed in-situ may be exceedingly difficult, due to the surface characteristics of the silicone

3. The resonant magnitude of these sensors was quite low. Perhaps the quality of the conductive ink and/or the dielectric properties of the PMMA or silicone are lacking

An alternative substrate material was the first step towards addressing the above limitations. Latex rubber was used as it can be moulded, is much stiffer and supported good levels of conductive paint adhesion. The reason why a stiffer substrate was acquired was that it would appear that it was the reaction forces from the resonator that resulted in the axial strain of the Ecoflex™ sensor to divert around that part of the substrate. Therefore, a stiffer substrate would, in theory, force a greater level of resonator deformation to occur. To combat the issue of resonant magnitude, it was postulated that the problem was that the conductive ink was of insufficient quality. Therefore, it was decided to fabricate the resonator parts out of bulk copper sheet. This 0.3mm thick copper sheet was cut using an Electro-discharge Machining (EDM) process. Cyanoacrylate glue was used to adhere the copper elements to the substrate. Initial testing with the use of latex substrates and painted conductive tracks were unsuccessful as the conductive tracks exhibited extremely poor mechanical strength. This resulted in the conductor remaining adhered to the substrate but exhibiting a significant number of physical cracks. This cracking arose consistently during sensor handling/movement. The geometric details of the implemented sensor can be seen in Table 3.5.

Table 3.5: Latex V1 Geometric Details – from "Proof of Concept Novel Configurable Chipless RFID Strain Sensor" by McGee et al., MDPI, [CC BY 4.0](link) [15]

Variable	Value [mm]	Variable	Value [mm]
S2	57,76	Ws	2
S	24	Ws2	2

sGap	1	K	19
H_substrate	3	P	14
H_resonator	0.3	deltaX	10

The resonant response of this device for various levels of strain can be seen in Figure 3.18. These responses are quite strong and exhibit a clear strain dependence. The location of the null frequencies in the initial test datasets are plotted against induced strain in Figure 3.19. This implementation clearly demonstrates a much higher sensitivity than that of the Ecoflex™ version. One issue once again observed during testing is the effects of substrate expansion during clamping.
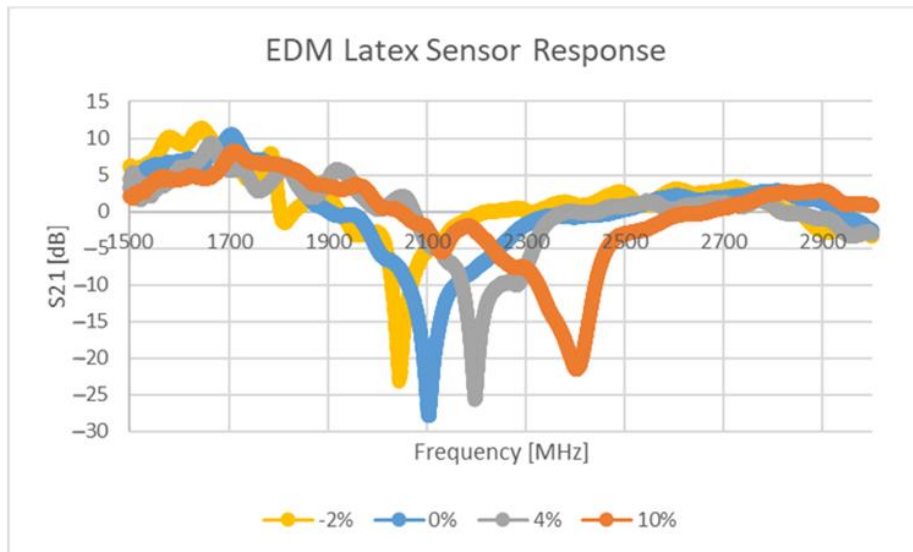
Figure 3.18: Latex Sensor Responses – from "Proof of Concept Novel Configurable Chipless RFID Strain Sensor" by McGee et al., MDPI, CC BY 4.0 [15]
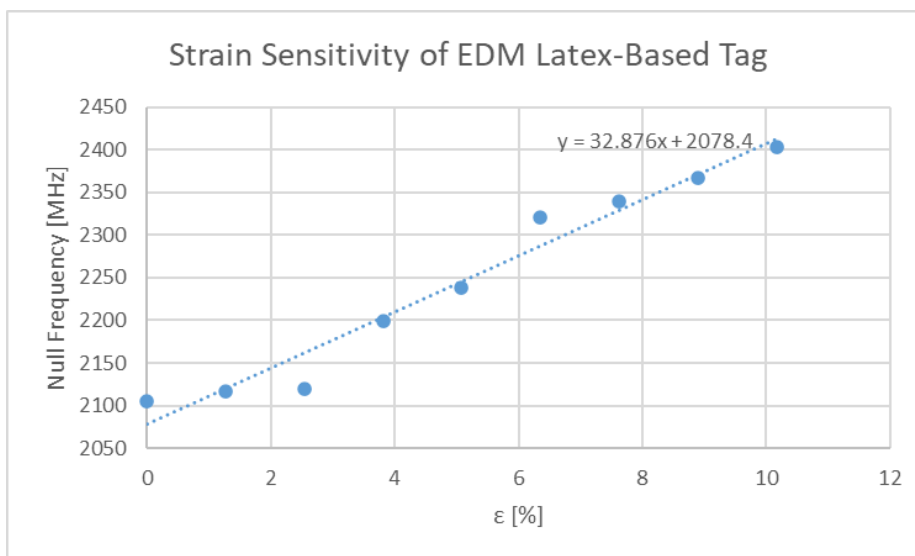
Figure 3.19: Latex Sensor Strain Sensitivity – from "Proof of Concept Novel Configurable Chipless RFID Strain Sensor" by McGee et al., MDPI, CC BY 4.0 [15]

65

Further testing was performed with another implementation of the same sensor and this testing focussed on the device performance below 2% strain, as Figure 3.19 demonstrates an apparent deadband below this strain level, which would be a detrimental outcome. It was initially believed, as stated earlier, that the press setup and clamping arrangement was the original source of this deadband. Figure 3.20 depicts sensitivity graph generated after three different test runs.
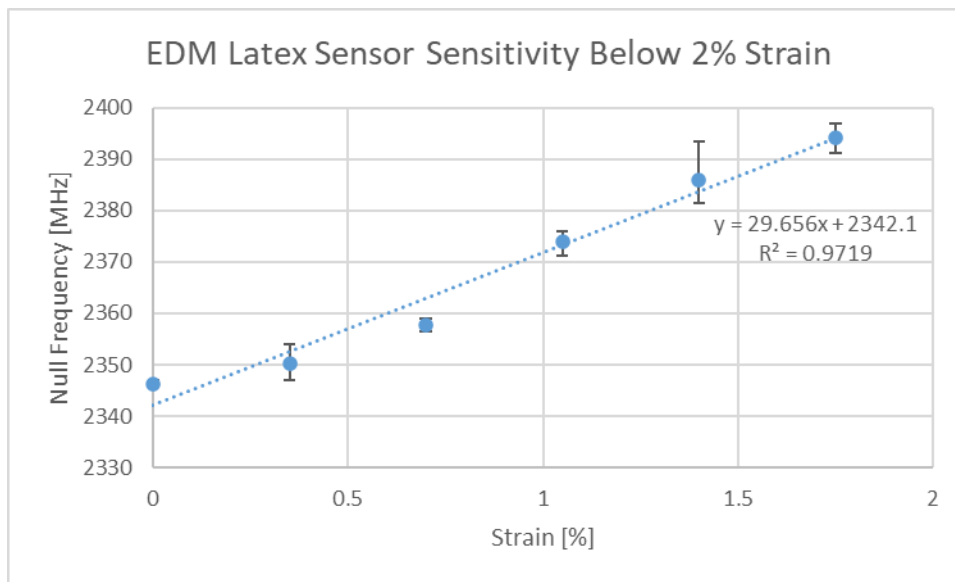
Figure 3.20: Repeated Latex Sensor Testing Below 2% – from "Use of Chipless RFID as a Passive, Printable Sensor Technology for Aerospace Strain and Temperature Monitoring" by McGee et al., MDPI, CC BY 4.0 [28]

Transmission Line -Based Testing

As this work may not eventually realise a sensor design that cannot avoid a differential sensing approach, it is useful to demonstrate that this device can indeed be successfully coupled to a transmission line. The developed resonator geometry supports coupling to a Co-Planar Waveguide (CPW) in two different polarizations. A CPW was milled into a copper clad FR4 Printed Circuit Board (PCB) with an approximate impedance of 50Ω. Details of the transmission line can be seen in Figure 3.21. Before any further analysis is performed, it must be noted that several other works including [29] have successfully coupled ELC-based resonators to transmission lines, prior to this work.
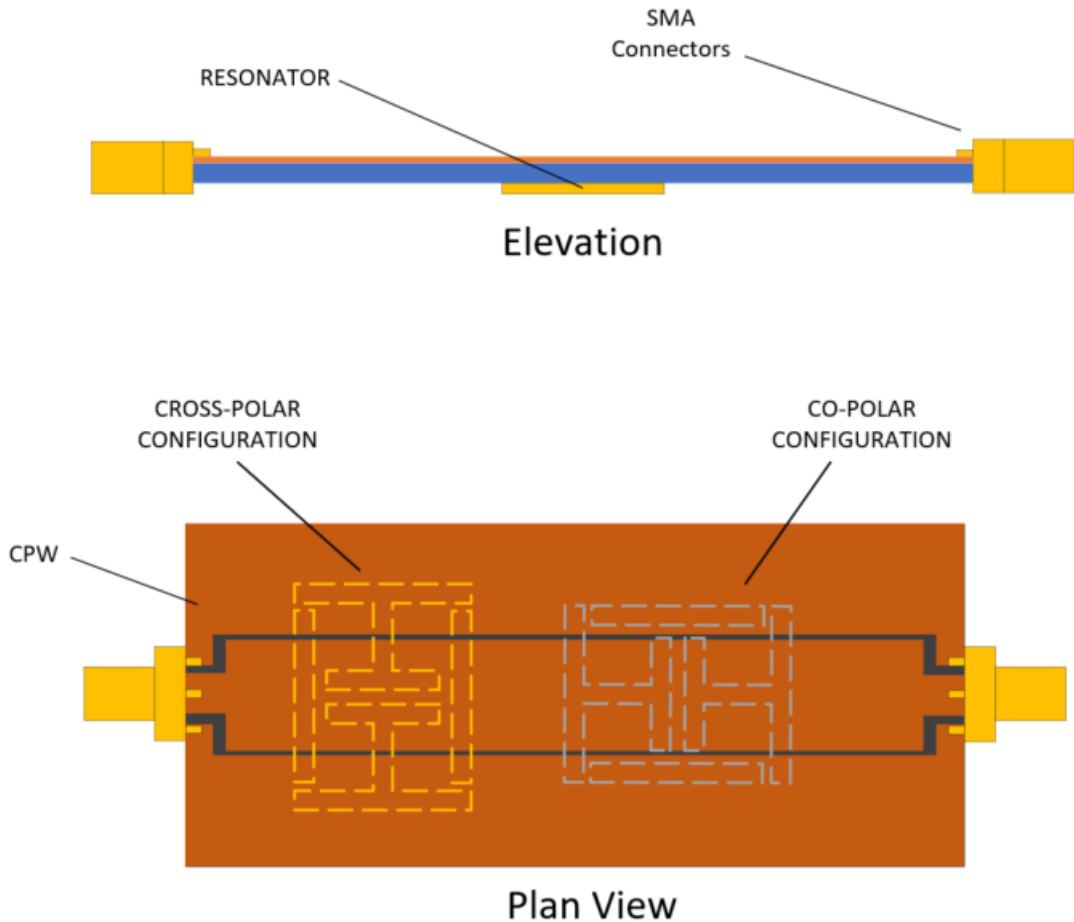
Figure 3.21: CPW Loading Strategy for V1 Sensors

The copper resonator elements were placed on the underside of the board, as seen in Figure 3.21 and were mechanically spaced out to simulate resonator deformation. This was performed for both orientations of resonator; Co-Polar (resonator in line with CPW) and Cross-Polar (resonator crossing CPW). The strain sensitivity of the Co-Polar resonance is depicted in Figure 3.22. Interestingly, this sensitivity is quite high, although there is no means by which a substrate can mitigate the sensitivity in this test configuration. Note: Error bars are present in Figure 3.22, but the errors are too small to be observed. The resonant magnitude was also explored for various resonator rotation angles. This is important to assess the stability of this resonance and therefore determine if a rosette can be supported using this resonance. Figure 3.23 depicts the magnitude of the resonance against several polarization angles, above which it was considered negligible.
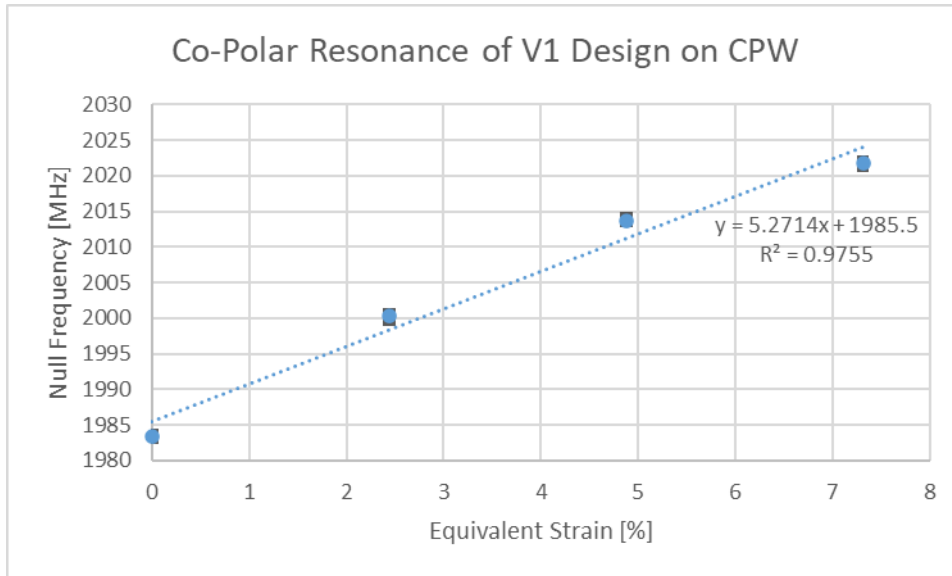
Figure 3.22: Co-Polar Sensitivity Curves for Axial Deformation of V1 Sensor On CPW
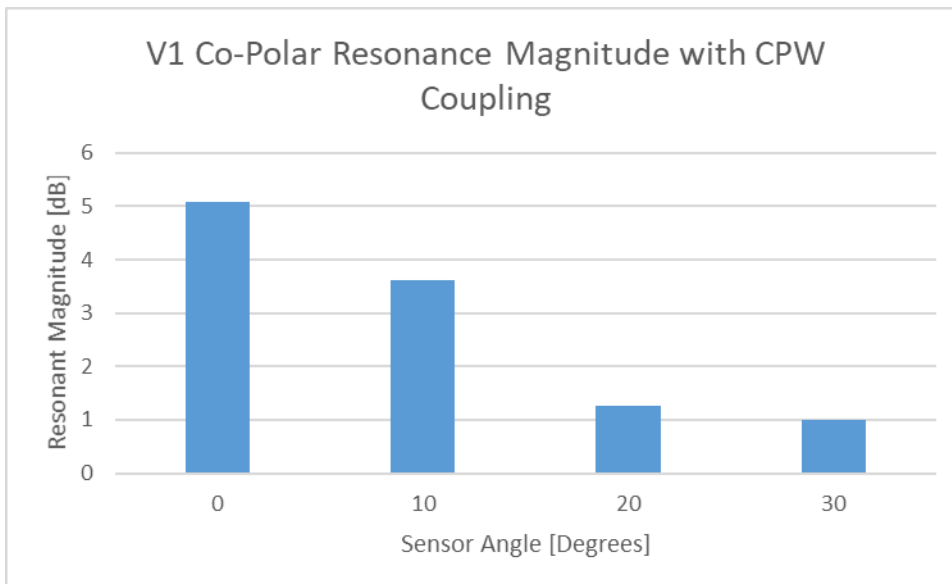
Figure 3.23: Effect of Polarization Mismatch on Co-Polar V1 Coupling to CPW

The cross-polar resonance was also explored to assess its strain sensitivity. These results can be seen in Figure 3.24. Similarly, the polarization sensitivity of this resonance can be seen in Figure 3.25. This resonance clearly demonstrates a weaker strain sensitivity but a much stronger resonant response both initially and with increasing polarization. The results in this Figure differ slightly from that in Figure 3.23 in that the resonant magnitude does not decay away at the same rate. However, the results in Figure 3.25 decay rapidly below the 30° angle, to approximately zero for each of the subsequent measurement angles. The rate of decay is lower however, at angles over 60°, suggesting some sort of asymptotic relationship. This behaviour is quite like that seen when the cosine of the change in angle is subtracted from

68

unity. Note: this statement is made as the angle values seen in Figure 3.25 are taken with respect to the co-planar polarization (see Figure 3.21 above). What this means is that the 90° angle in Figure 3.25 is the 0° angle for the cross-polar configuration. Furthermore, the transmission line polarization tests seen in [30] also exhibits similar behaviour to that seen in Figure 3.25. With all of that being said, it is noticeably different to that seen in Figure 3.23 and a future study is required to fully assess this behaviour. A further discussion on polarization is presented in Chapter 6 and includes results of a similar shape to that seen in Figure 3.25 below.
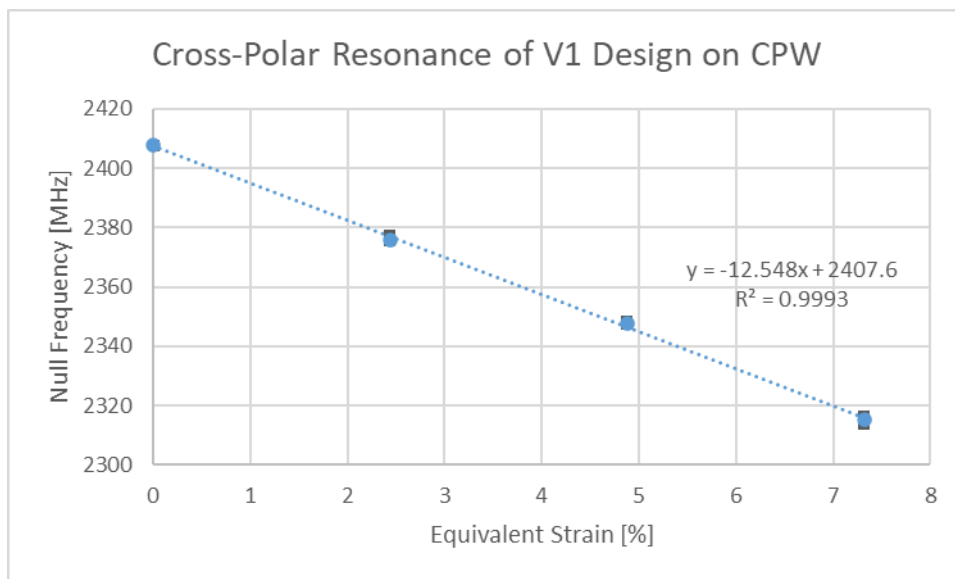
Figure 3.24: Cross-Polar Sensitivity Curves for Axial Deformation of V1 Sensor On CPW
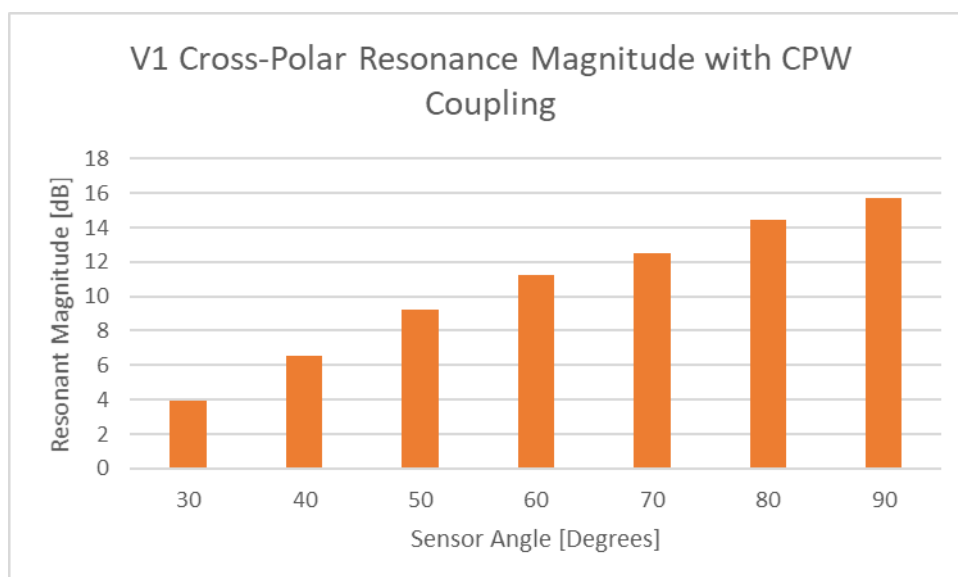
Figure 3.25: Effect of Polarization Mismatch on Cross-Polar V1 Coupling to CPW

The angular dependence of the two resonances is important because it demonstrates that it is possible to couple a resonator to the transmission line whose polarization is neither co- nor cross- polar. This result therefore demonstrates that a simple CPW transmission line could be used to support some form of a 3-gauge rosette.

On-Metal Testing

Testing of this sensor design was also performed with a metallic superstrate present (Layout depicted in Figure 3.26). Testing was performed with different implementations of the design that have different sGap values. Testing was also performed with a variety of different substrate thicknesses and superstrate sizes. Figure 3.27 reveals the response of a thermal transfer ribbon implementation of the V1 design depicted in the configuration seen in Figure 3.26. The background dataset utilised to generate the subtracted datasets in Figure 3.27 was performed with the metallic superstrate present. This is a more suitable approach as it may not be possible to remove the metallic superstrate from the background during background tests as it will most likely be an integral part of the structure of interest.
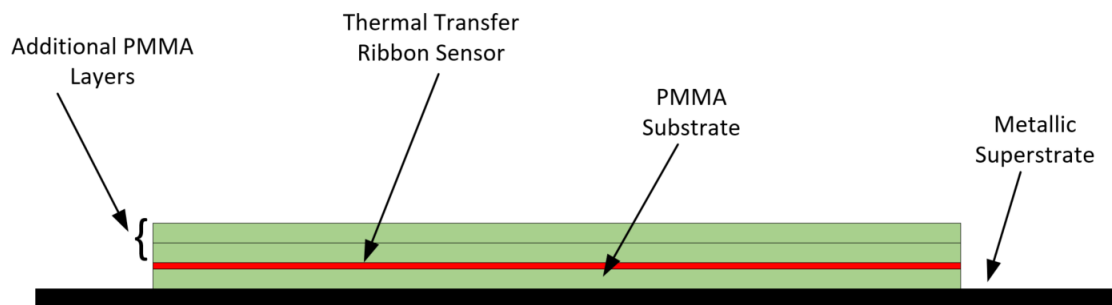
Figure 3.26: Cross Section of Test Setup
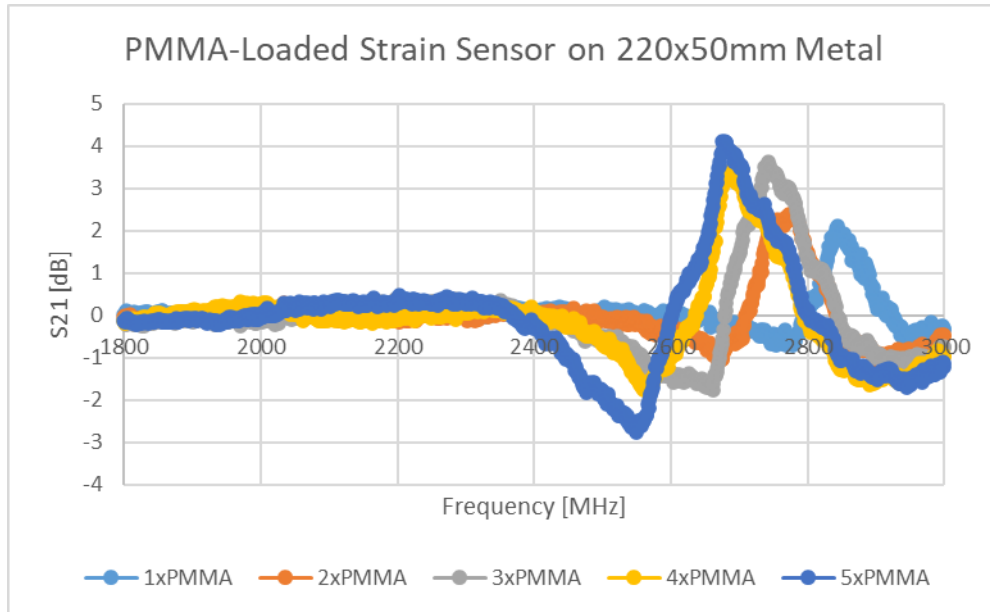
Figure 3.27: Impact of PMMA Loading of V1 on Metallic Superstrate

These test results in Figure 3.27 above demonstrate that similar to the dielectric implementation, this resonator is sensitive to dielectric constant variations. Further testing was also performed with other superstrate sizes and additional results were generated by fixing the resonator to the substrate with different sGap values. Figure 3.28 depicts one of the datasets generated by the EDM copper resonator placed onto a 2mm thick PMMA layer. The legend details in said figure represent the overall length of the resonator assembly. Two resonant regions arise during this testing; one after 2100MHz and another 2800MHz. Subsequent testing revealed that the presence of the former resonant region depends on the size of the metallic superstrate and disappears for larger superstrates. As the lateral dimensions (X,Y) of the plate increase, its scattering response differs and its presence could have a different impact on the resonant behaviour of the sensor, in a similar way to how ground plane size can alter other antenna responses. Note: All testing performed in this section used background datasets that contained the 0.3mm-thick metallic superstrate, and the interrogation range was in the ranges of 10-30cm.

71
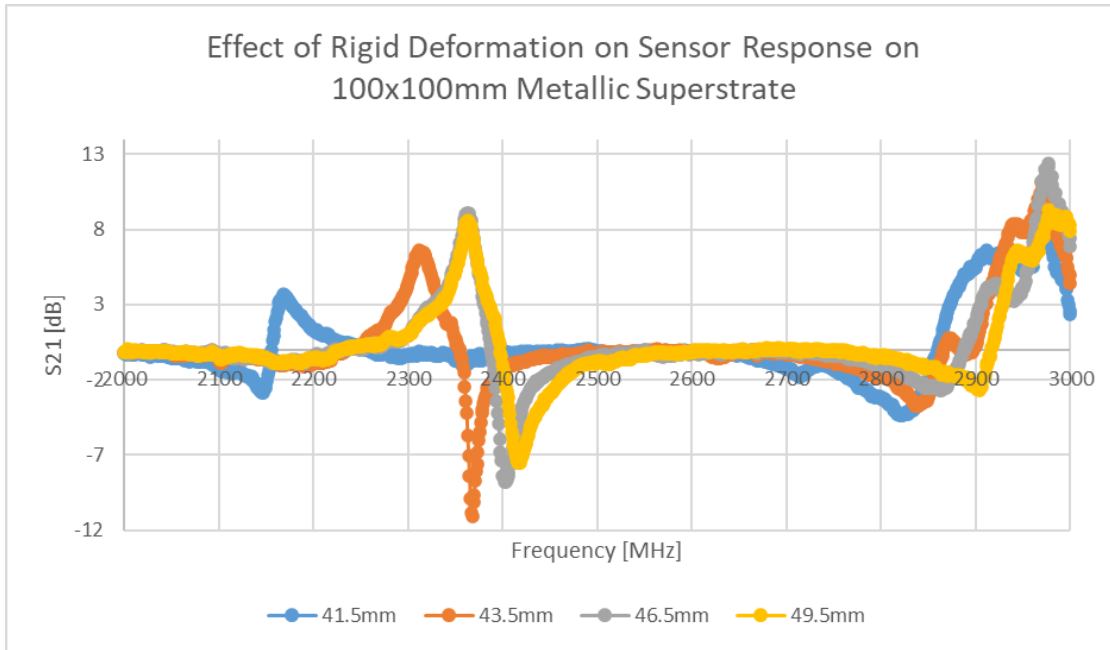
Figure 3.28: Impact of Axial Strain on V1 with Metallic Superstrate

The lower resonance in Figure 3.28 appears to be strain sensitive and the upper one similarly so. However, repeated testing that revealed repeatable results had to be performed at very small read ranges (<10cm).

The rest of this chapter will focus on the dielectric performance of this sensor as its sensitivity seems to be less sensitive to increased read range. Therefore, the V2 and V3 designs will not consider the topic of on-metal testing. Further study and testing are required to develop the "on-metal" performance of this sensor. The issue of environmental stability and noise in the context of chipless RFID strain sensing (on-metal) has been emphasised in other works such as [3] where the read range was limited to several centimetres or lower to combat this and other issues.

Transverse Sensitivity

The topic of transverse sensitivity is a complex one and will also depend heavily on the geometry and material choices made during sensor implementation. The following results are the result of transverse strain on sensor implementations that only support rigid-body motion. Other, future implementations will need to be appropriately tested to assess the degree to which key parts of the geometry will change under transverse strain.

Ecoflex™ Sensor Testing

Initial testing of the Ecoflex™ -based sensor revealed a negligible transverse strain sensitivity, with a sensitivity of zero in interrogations with a resolution of 0.9MHz. Further testing revealed that features of the environment (press orientation, temperature, etc.) dominated the features of the transverse sensitivity of the device. Repeated testing revealed no significant trend in the relationship between resonant frequency and strain, other than small variations in the amplitude of the response. Geometric measurements (0.1mm resolution) made during the deformation of this sensor during transverse strain (0-10%) revealed some interesting observations:

- The EC parts did not move in a compressive manner
- The EL parts moved up to 1mm under 6%ε

The reason why the weak transverse strain sensitivity arises is believed to be due to two phenomena; 1) The soft substrate is deforming around the resonator and not inducing deformation within the resonator (as seen in Figure 3.4). 2) The fact that the entire resonator is in contact with and submerged within the substrate, results in the EC parts being less free to move. This latter point is of interest and contains two statements. The fact that the resonator is fully bonded to the substrate results in the resonator geometry holding that surface of the substrate into having a fixed geometry, therefore transverse substrate expansion within the geometry is mitigated. Furthermore, the result of a thick layer encapsulating the resonator within the substrate results in the capacitive regions being filled with silicone, which will resist compressive deformation more than empty space. This is different than the latex -based implementation which has no filler material within the capacitive regions.

Latex Sensor Testing

The response of the latex-based sensor is considerably different to that found with the Ecoflex™ -based implementation. Figure 3.29 depicts the transverse strain sensitivity initially observed of this implementation which is considerably higher than that found with the silicone-based sensor. Furthermore, its magnitude is a far greater proportion of the axial strain sensitivity (approximately 20%), than that found with the silicone sensor. Further study is required to determine this sensitivity value with a greater level of certainty, but it is clearly a variable of concern.
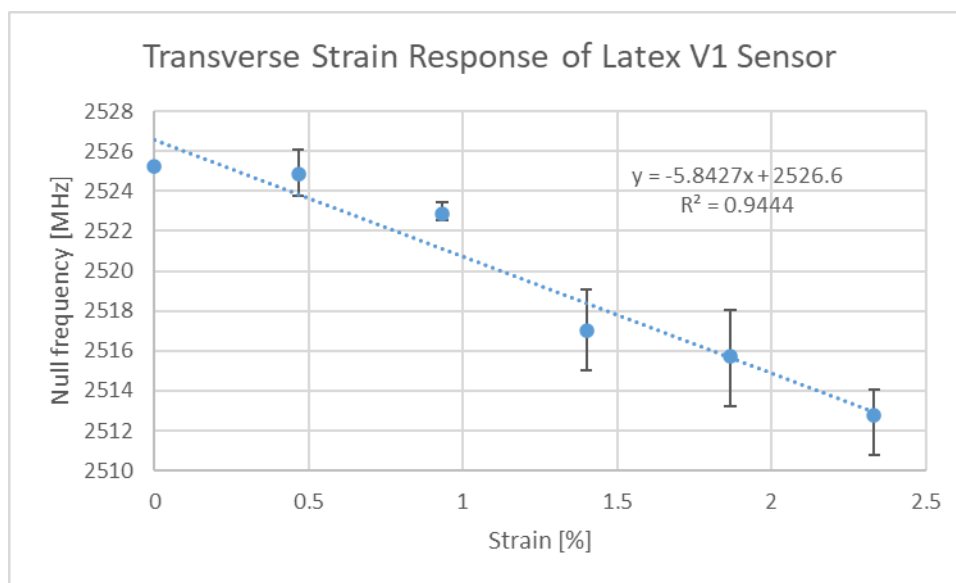
Figure 3.29: Transverse Strain Sensitivity of Latex-Based V1 Design – from "Use of Chipless RFID as a Passive, Printable Sensor Technology for Aerospace Strain and Temperature Monitoring" by McGee et al., MDPI, CC BY 4.0

[28]

The reason why this transverse sensitivity is so high, is because it is believed to be heavily dependent on the degree of adhesion between the resonator and the substrate and the lack of a coating material being present on top of the sensor. This conclusion is drawn from the observed transverse deformation behaviour of the resonator in the latex-based sensor. Simulation-based analysis on the topic of partial conductor adhesion is presented later on in this chapter and do in fact demonstrate that its effect is quite considerable on the axial and transverse deformation behaviour of the resonator.

Compensation Strategies

For now, this section will not consider the possibility that transverse deformation could alter the geometry in such a way that the axial sensitivity of the device could change, although this is considered in the V3 design. This is a slightly different effect to that caused by Poisson's

ratio and will need further study to investigate. With excessive levels of transverse strain, the EL parts may readily move outward under rigid body motion. If it is assumed that the strain sensor is operating below 1% strain, then perhaps this effect will be negligible. If this variable is not negligible in terms of the overall system performance, a compensation system will be required. What is important to note here is that this effect is separate to Poisson's effect, but they will both contribute to the net transverse strain sensitivity result.

It is not uncommon to find strain gauges in a rosette configuration, as described in Chapter 2 and the relevant strains ($\varepsilon_1, \varepsilon_2, \varepsilon_3$) can be calculated for in a 3-gauge delta rosette [31] using Equation 3.8 to Equation 3.13, found in [31], in which static transverse strain effects can be compensated for.

$$\varepsilon_1 = \frac{1 - vK_t}{1 - K_t^2}\left(\left(1 + \frac{K_t}{3}\right)\hat{\varepsilon}_1 - \frac{2}{3}K_t(\hat{\varepsilon}_2 + \hat{\varepsilon}_3)\right) \tag{3.8}$$

$$\varepsilon_2 = \frac{1 - vK_t}{1 - K_t^2}\left(\left(1 + \frac{K_t}{3}\right)\hat{\varepsilon}_2 - \frac{2}{3}K_t(\hat{\varepsilon}_1 + \hat{\varepsilon}_3)\right) \tag{3.9}$$

$$\varepsilon_3 = \frac{1 - vK_t}{1 - K_t^2}\left(\left(1 + \frac{K_t}{3}\right)\hat{\varepsilon}_3 - \frac{2}{3}K_t(\hat{\varepsilon}_1 + \hat{\varepsilon}_2)\right) \tag{3.10}$$

$$where\ K_t = \frac{Gauge\ Factor\ (Transverse)}{Gauge\ Factor\ (Axial)}, \tag{3.11}$$

$$v = Poisson's\ Ratio, \tag{3.12}$$

$$\hat{\varepsilon}_1, \hat{\varepsilon}_2, \hat{\varepsilon}_3 = Measured\ Strains\ from\ Gages\ 1,2,3 \tag{3.13}$$

Strengths and Weaknesses of Design

This initial geometric design does at least demonstrate that it is possible to develop a strain sensitive device whose sensitivity compares with and/or exceeds that of previously published works. A comparison of the V1 implementations and the other designs found in the literature can be found in Table 3.6. The developed sensor does indeed exhibit a high gauge factor, whilst supporting a large stimulus range and a "fully planar" design.

Table 3.6: Comparison of V1 Design with Already Published Designs – from "Proof of Concept Novel Configurable Chipless RFID Strain Sensor" by McGee et al., MDPI, CC BY 4.0 [15]

Publication	Sensitivity [MHz/%ε]	Base Null Frequency [MHz]	Tested Stimulus [%ε]	Gauge Factor
This work - Ecoflex™	8.783	1993	2.5	0.441
This work - Latex	32.876	2100	10	1.57
[1]	-14	1550	25	0.9

[2]	8.05	1610	4	0.5
[3]	-13.68	1530	0.05	0.89
[4]	51.48	12250	0.2	0.42
[5]	-1.2	860	50	0.14
[6]	85	3300	0.9	2.58
[32]	36.56	2900	1.65	1.26

There are, however, some performance weaknesses found with this design. These issues include the topic of transverse sensitivity, which was discussed earlier and is at least partially dependent on the nature of the implementation of the sensor design. Many other cross-sensitivities exist with this design and could also be assumed to affect other published chipless RFID strain sensors. These issues are discussed more thoroughly in Chapter 6.

3.3.3   Version 2 Design

Based on the strengths and weaknesses of the initial version of the sensor, a second version
was developed [33]. Two key points of interest were the issue of transverse strain sensitivity
and the impact of near-field (substrate, etc.) dielectric constant variations. A more thorough
discussion on these and other sensor cross-sensitivities can be found in Chapter 6. For now,
this section will focus on attempting to mitigate the effects of dielectric constant variations
and transverse strain. The most obvious approach to dealing with the issue of dielectric
constant variations is to include another resonator. How such a resonator could be
incorporated into the existing strain sensor is not immediately obvious, as it would be
beneficial if said resonator was not heavily impacted by axial strain. Similarly, the additional
resonator should not hinder the deformation characteristics of the axial strain resonator.
Although the contribution of Poisson's effect to transverse strain sensitivity cannot be easily
mitigated, observations made during transverse strain testing of the Ecoflex™ and latex
sensors was that rigid body motion occurred to the vertical monopole ("EL") parts. Therefore,
if these two parts could be connected in some way, then this effect would be lessened and the
only remaining deformation of the EL parts would be elastic deformation and bending. If this
connection is made using a conductive track, the resulting geometry actually exhibits a second
resonance as the device now has an alternate version of the ELC resonator in the opposite
polarization configuration to that of the original resonator. This new geometry is depicted
graphically in Figure 3.30. With regard to the original axial resonance, it was hoped that since
the signals flowing through the EL parts are symmetric during the base resonance [34], the
band would hopefully not alter the formation of the base resonance.
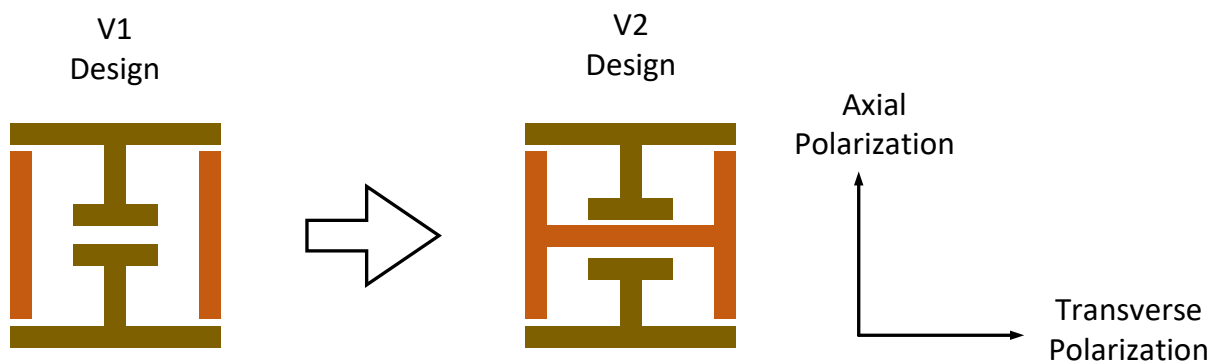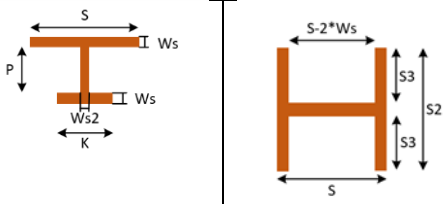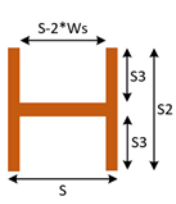
Figure 3.30: V2 Sensor Design

This new geometry consists of three separate parts and boasted the same footprint as the
original sensor. Table 3.7 gives details of the geometry implemented during proof-of-concept
testing. If the stiffness of the conductor is assumed to far exceed that of the substrate, the

transverse resonance will be unaffected by strain and the transverse strain in the axial resonance will simply be the contribution from Poisson's effect. This scenario is unlikely to occur with less forgiving substrates as substrates like polyimides exhibit modest stiffnesses and to assess the impact of a stiffer substrate on transverse deformation FEA was used. Figure 3.31 depicts the percentage reduction in transverse deformation caused by a transverse strain of 0.33%. These results were compiled by changing the original version of the resonator to include a metallic band joining the two monopole parts and performing the analysis on both geometries. Clearly, the addition of a metallic band does help mitigate the transverse deformation of many of the points of interest on the resonator, when a stiff polyimide substrate is used.

Table 3.7: V2 Geometric Details – © 2022 IEEE [33]

Geometry		Variable	Value [mm]	Variable	Value [mm]
		S	30	Ws2	2.5
		Ws	2.5	S2	38
		P	15	S3	17.5
		K	17	Element Vertical Spacing	1
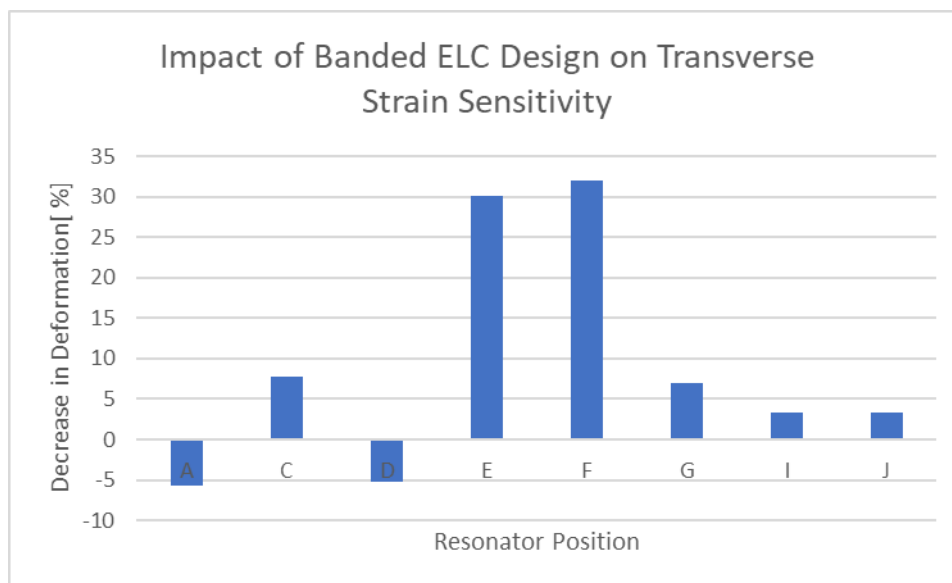
Figure 3.31: FEA Results of Banding EL Parts Together

Sensor Performance and Testing

The axial and transverse resonant responses can be seen in Figure 3.32(a) and Figure 3.32(b). Both of these resonances are clearly observable and were designed to be observed at distinctly different parts of the spectrum. During various different implementations of the design, it was found that the manner in which the device was clamped and the nature/quality of the gluing between the resonator and the substrate had a significant impact on the strain dependence of the device. With that being said, repeated testing for specific implementations of the sensor resulted in repeatable results. Details on the temperature-dependent properties of latex rubber can be found in the work of Hassan et al. in [35], which would suggest that said device is also temperature sensitive.

| (a) | (b) |
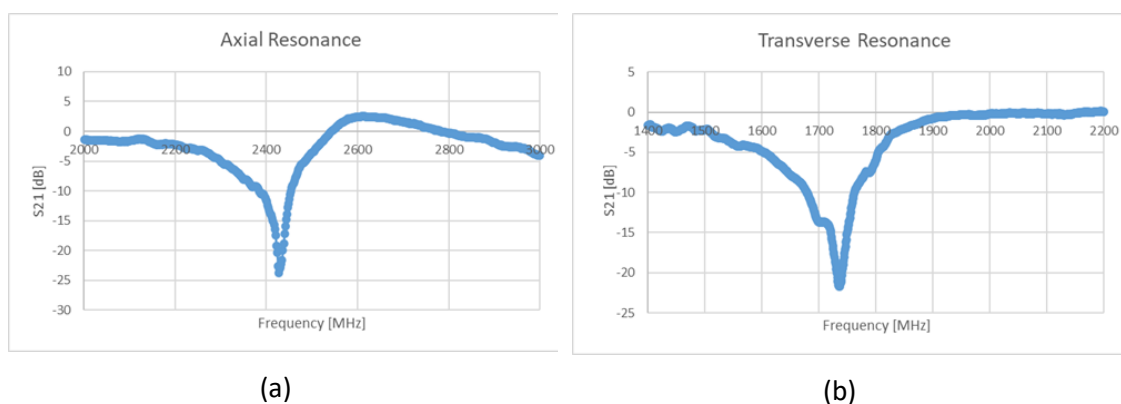
Figure 3.32: Axial (a) and Transverse (b) Resonant Responses of V2 Design – © 2022 IEEE [33]

A stable way to explore the dielectric sensitivity resonant effects is through the use of actual dielectric constant variations. This was done in this work by using 2mm thick layers of PMMA to load the uncovered side of the resonator. The results generated after doing this are seen in Figure 3.33(a) and Figure 3.33(b). The results displayed in these Figures clearly demonstrate that both resonances are sensitive to dielectric constant variations. These tests were performed so that a stable conclusion can be made regarding the dielectric sensitivity of the device.

(a)   (b)
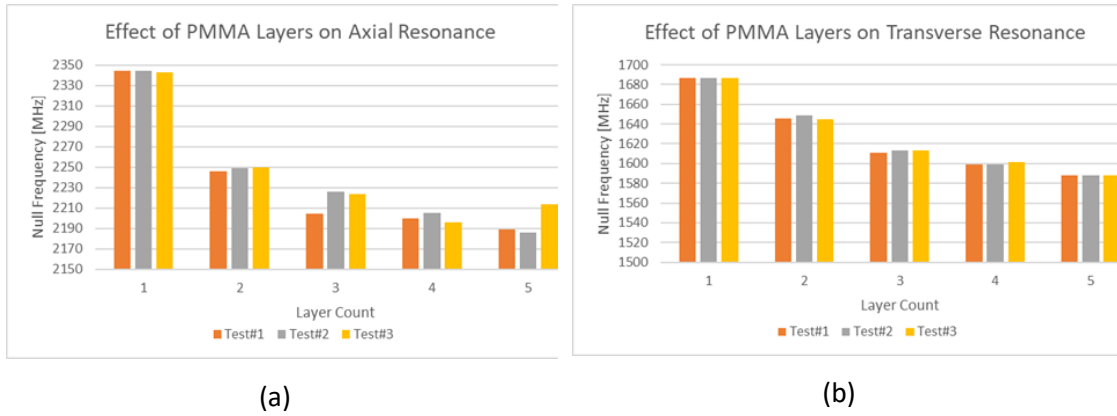
Figure 3.33: Effects of PMMA Loading on Axial (a) and Transverse (b) Null Frequencies – © 2022 IEEE [33]

Axial strain testing was also performed, and the null frequencies recorded have been plotted in Figure 3.34 below. The resulting strain sensitivity is considerably smaller than that found in the initial version of the sensor.
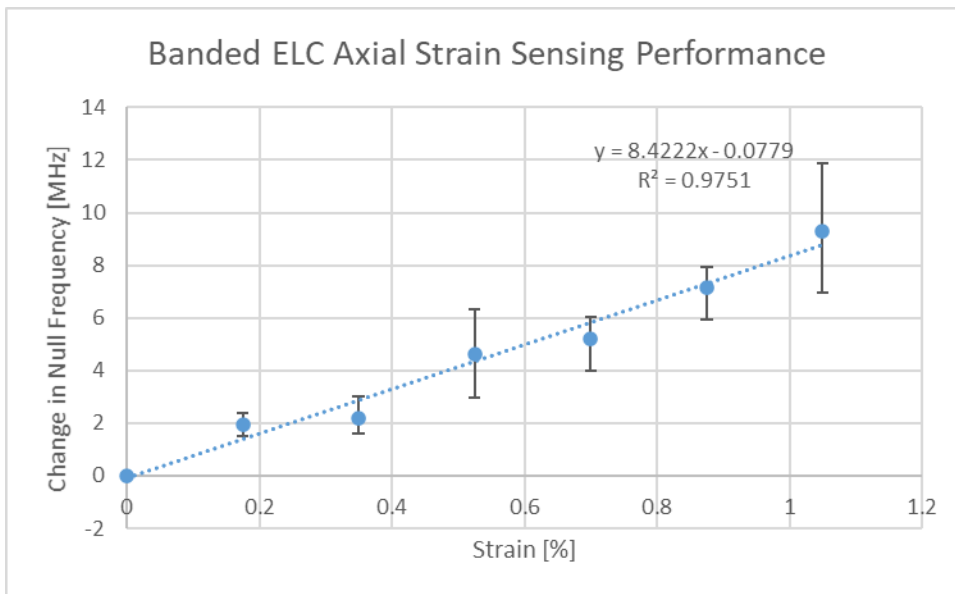
Figure 3.34: Axial Strain Performance of Latex-Based V2 Design

Transmission Line -Based Testing

The impact of loading the CPW circuit with this sensor, in the cross-polar configuration can be seen in Figure 3.35. Both resonances are present during this orientation and at slightly lower frequencies than that found during wireless testing. Testing was performed with multiple layers of 2mm thick PMMA over the resonator. This testing was performed with the latex sensor loaded on the top face of the CPW and the PMMA was placed on-top of the sensor.
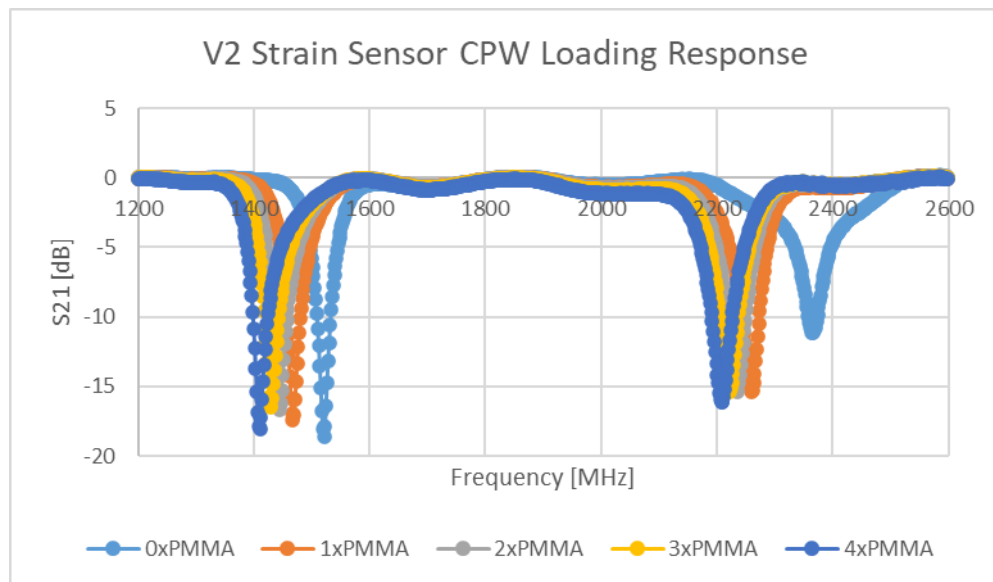
Figure 3.35: V2 PMMA Loading on CPW Responses

The variations in the null frequencies of the two resonances with increasing PMMA loading can be seen in Figure 3.36 and Figure 3.37. Of most importance, the results in Figure 3.36 and Figure 3.37 demonstrate that both resonators operate as viable dielectric sensors.
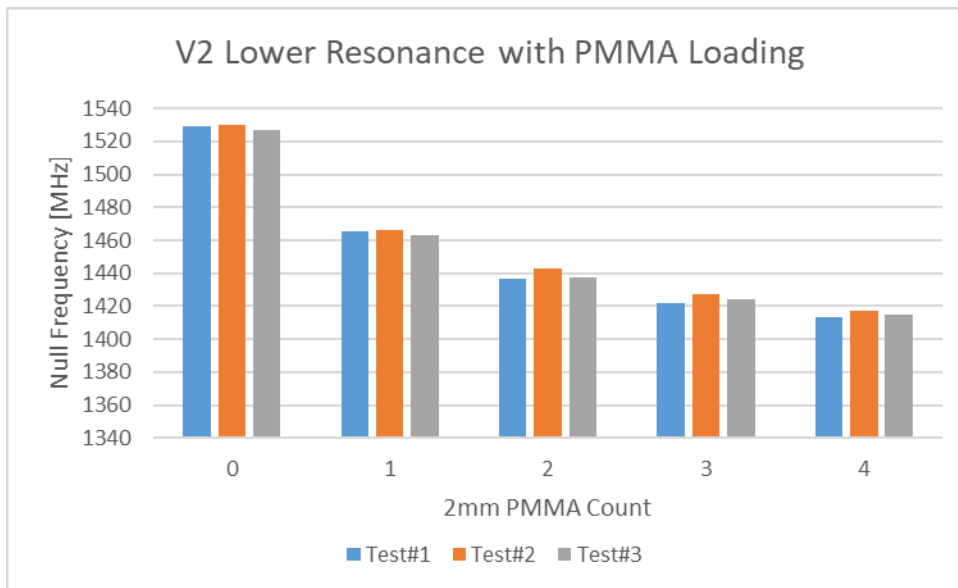
Figure 3.36: Effect of PMMA on V2 Transverse Resonance on CPW
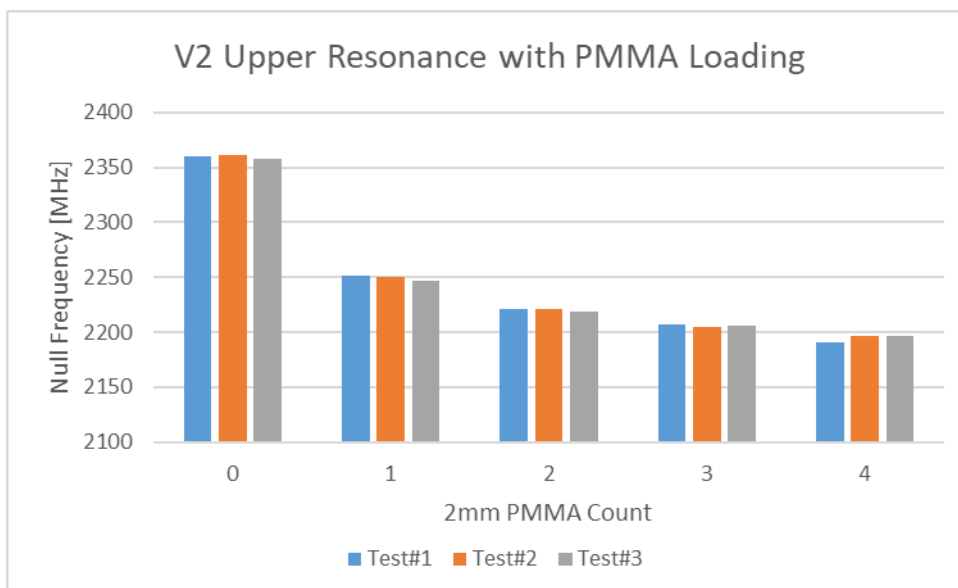
Figure 3.37: Effect of PMMA on V2 Axial Resonance on CPW

Strengths and Weaknesses of Design

This design allows for another measurement to be made that is relevant to the current state of the strain sensor. Characterising its dependencies on axial strain, transverse strain and dielectric constant are difficult as the fabrication/implementation method will undoubtably dictate these relationships. With that being said, another measurement variable adds significantly to the performance of the sensor. More generally however, two measurement variables may not be sufficient to compensate for the combined effects of axial strain, transverse strain and dielectric constant variations. Although this limits the direct use of the

82

V2 design to solve the various cross-sensitivity issues, the rosette-based transverse strain compensation method that is used with conventional strain gauges could allow for this sensor to allow for the sensing of axial strain whilst having the ability to compensate for both dielectric constant variation and transverse strain.

The sensor performance details of the implemented sensor can be found in Table 3.8. From this table, it is clear that this particular sensor design has a much lower sensitivity than that found with the latex based V1 geometry. A more subtle weakness of this design is that although it may be used for transverse deformation sensing (implementation dependent), the manner in which it does this will not be through the use of rigid body motion.

Table 3.8: Comparison of Latex-Based V1 and V2 Designs

Implementation	Sensitivity [MHz/%ε]	Base Null Frequency [MHz]	Gauge Factor
Latex (V2)	8.4222	2520	0.3342
Latex (V1)	29.6557	2343	1.2657

3.3.4 Version 3 Design

A third version of the sensor design was also considered, which builds upon the second version. If the Principal planes are known before sensor deployment, only two strain sensors are needed to fully determine the strain behaviour experienced by the superstrate (see Chapter 2 for more details). This design aims to incorporate further transverse strain sensitivity. Although the second version could be made to exhibit transverse strain sensitivity, it does not make use of rigid body motion to achieve this goal. This version of the design utilises rigid body motion in both the axial and transverse directions to achieve its strain sensitivity. A diagram of the geometry can be seen in Figure 3.38 and similar to Version 2, this is a dual resonant geometry that has separate axial and transverse resonances. A different design has also been published as a dual band planar antenna in [36]. That published design would also be suitable but differs from the one put forward here in that its central capacitor design would appear to be more likely to suffer from significantly larger stress gradients under combined axial and transverse strains, if that geometry was to be used as a chipless RFID strain sensor. It was also speculated that the referenced design would suffer to a greater degree from Poisson's effect given the small distances between multiple moving parts. Furthermore, the use of the V3 design seen in Figure 3.38 over that seen in [36] is also beneficial because the capacitance of the central capacitive region for both the axial and transverse resonance is less dependent on each other. This latter comment should reduce the cross sensitivity of the two resonances.
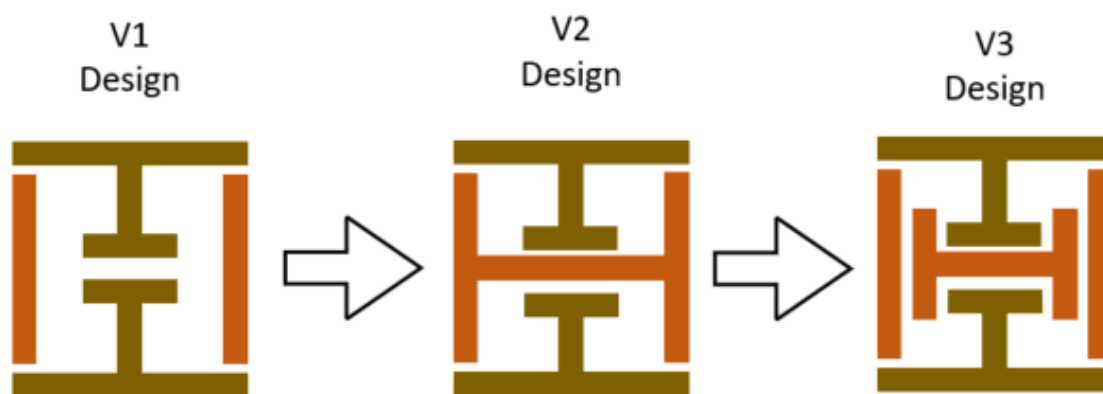
Figure 3.38: Potential V3 Design for 2D Strain Sensing

Initial Testing

Latex and Silicone based implementations were both developed for this sensor design. The response of the V3 design can be seen in Figure 3.39 and Figure 3.40. These initial tests revealed the expected resonances and should support strain sensing in both directions.
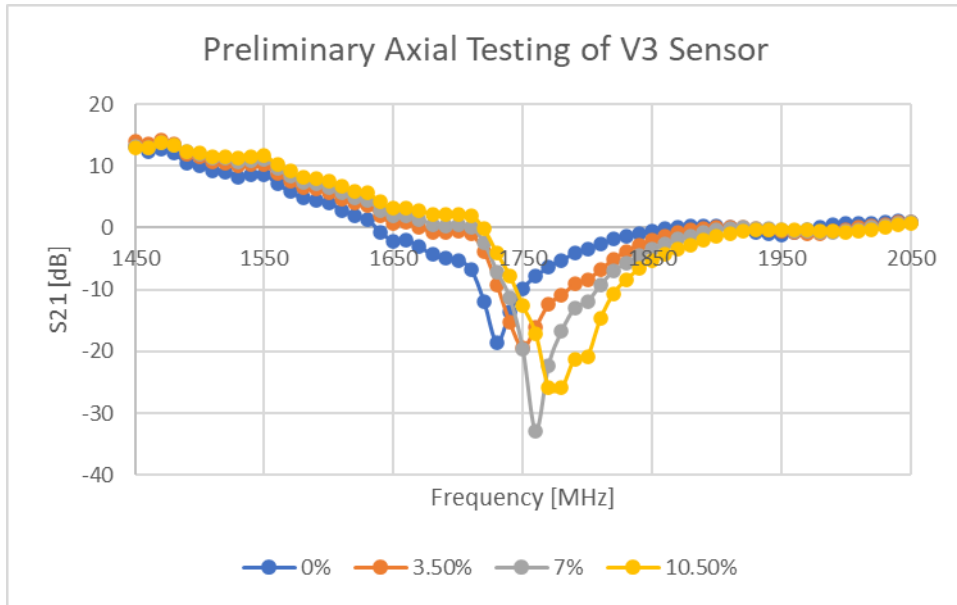
Figure 3.39: Axial Response of V3 Design
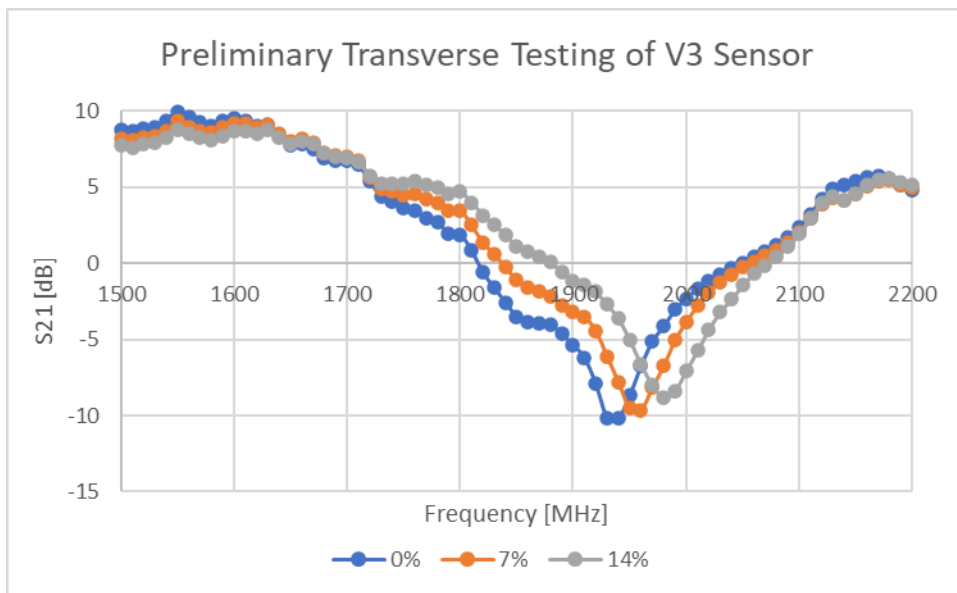
Figure 3.40: Transverse Response of V3 Design

Axial and Transverse Strain Decoupling

Interestingly, the sensitivity of the device remained consistent between substrate and conductor variations but did exhibit additional sensitivities. Of most concern is that the strain sensitivity of each resonance could depend on the current level of deformation of the other. The meaning of these dependencies on the measured strains, excluding Poisson's effect are depicted in Equation 3.14 and Equation 3.15. This is unsurprising as excessive resonator deformation (rigid body -based) will alter the electric field distribution in capacitive regions and therefore potentially alter the validity of the parallel-plate assumption.

$$\varepsilon_{AXIAL} = S_{AXIAL} \; x \; F_{AXIAL} , \qquad S_{AXIAL} = f(\varepsilon_{TRANSVERSE}) \qquad (3.14)$$

$$\varepsilon_{TRANSVERSE} = S_{TRANSVERSE} \; x \; F_{TRANSVERSE} , \qquad S_{TRANSVERSE} = f(\varepsilon_{AXIAL}) \qquad (3.15)$$

If the sensor has been appropriately characterised before deployment, then it is possible in some cases (see Chapter 2) to determine the true axial and transverse strains. This work has fabricated various implementations of the V3 design with different initial levels of rigid body displacement. This should allow for a compensation of the electromagnetic cross sensitivity of the sensor. The following Equations (3.16-3.22) describe the mathematics that can support the correction of both of the measured strains. These equations have assumed that the axial sensitivity consists of a term (M_{AX}) that describes its linear transverse dependence and a bias term (C_{AX}). It is also assumed that the transverse strain (ε_{TR}) also gives rise to a biasing effect in the measured axial strain (ε_{AX}) and its coefficient is defined as "α_{AX}", which given that it has been explored earlier on in this Chapter, will not be explored further here.

$$\begin{cases} \varepsilon_{AX} = (\varepsilon_{TR}(M_{AX}) + C_{AX})(F_{AX}) + \alpha_{AX}\varepsilon_{TR} \\ \varepsilon_{TR} = (\varepsilon_{AX}(M_{TR}) + C_{TR})(F_{TR}) + \alpha_{TR}\varepsilon_{AX} \end{cases} \qquad (3.16)$$

$$\therefore \begin{cases} \varepsilon_{AX} = \varepsilon_{TR}(\alpha_{AX} + M_{AX}F_{AX}) + C_{AX}F_{AX} \\ \varepsilon_{TR} = \varepsilon_{AX}(\alpha_{TR} + M_{TR}F_{TR}) + C_{TR}F_{TR} \end{cases} \qquad (3.17)$$

$$\therefore \varepsilon_{AX} = (\varepsilon_{AX}(\alpha_{TR} + M_{TR}F_{TR}) + C_{TR}F_{TR})(\alpha_{AX} + M_{AX}F_{AX}) + C_{AX}F_{AX} \qquad (3.18)$$

$$\therefore \frac{\varepsilon_{AX}}{\varepsilon_{AX}} = \left((\alpha_{TR} + M_{TR}F_{TR}) + \frac{C_{TR}F_{TR}}{\varepsilon_{AX}} \right)(\alpha_{AX} + M_{AX}F_{AX}) + \frac{C_{AX}F_{AX}}{\varepsilon_{AX}} \qquad (3.19)$$

$$= (\alpha_{TR} + M_{TR}F_{TR})(\alpha_{AX} + M_{AX}F_{AX})$$

$$+ \frac{1}{\varepsilon_{AX}}(C_{TR}F_{TR}(\alpha_{AX} + M_{AX}F_{AX}) + C_{AX}F_{AX})$$

$$\therefore \frac{1}{\varepsilon_{AX}} = \frac{1 - (\alpha_{TR} + M_{TR}F_{TR})(\alpha_{AX} + M_{AX}F_{AX})}{C_{TR}F_{TR}(\alpha_{AX} + M_{AX}F_{AX}) + C_{AX}F_{AX}} \qquad (3.20)$$

$$\therefore \varepsilon_{AX} = \frac{C_{TR}F_{TR}(\alpha_{AX} + M_{AX}F_{AX}) + C_{AX}F_{AX}}{1 - (\alpha_{TR} + M_{TR}F_{TR})(\alpha_{AX} + M_{AX}F_{AX})} \qquad (3.21)$$

$$and \; \varepsilon_{TR} = \frac{C_{AX}F_{AX}(\alpha_{TR} + M_{TR}F_{TR}) + C_{TR}F_{TR}}{1 - (\alpha_{AX} + M_{AX}F_{AX})(\alpha_{TR} + M_{TR}F_{TR})} \qquad (3.22)$$

Figure 3.41 depicts the axial strain sensitivity of the axial resonance. The device is clearly strain sensitive, as was expected from initial experimentation. The sensitivity is comparable with the Ecoflex V1 sensor.
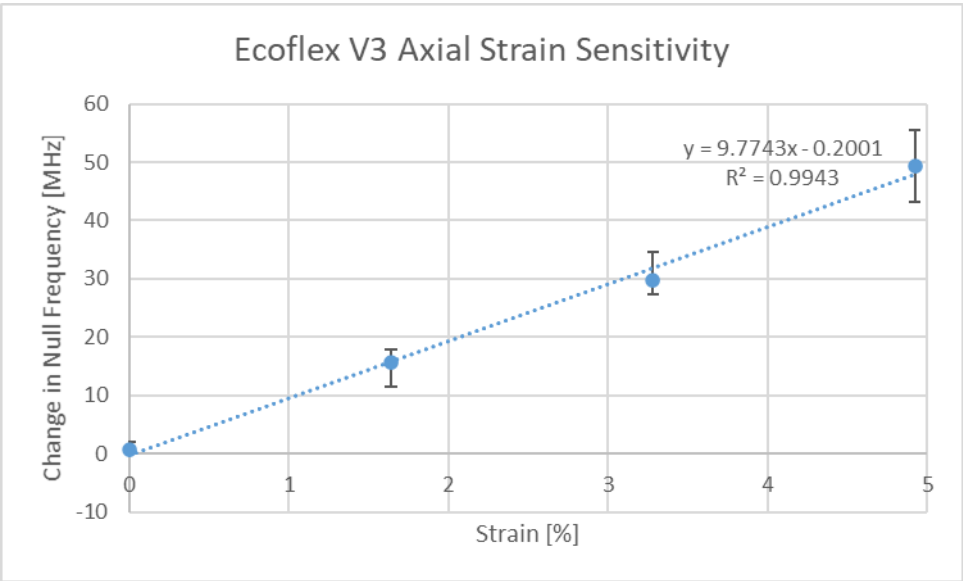
Figure 3.41: V3 Axial Strain Sensitivity – from "Use of Chipless RFID as a Passive, Printable Sensor Technology for Aerospace Strain and Temperature Monitoring" by McGee et al., MDPI, CC BY 4.0 [28]

The initial transverse strain response the senor is depicted in Figure 3.42 below, which also depicts a noticeable and consistent strain sensitivity.
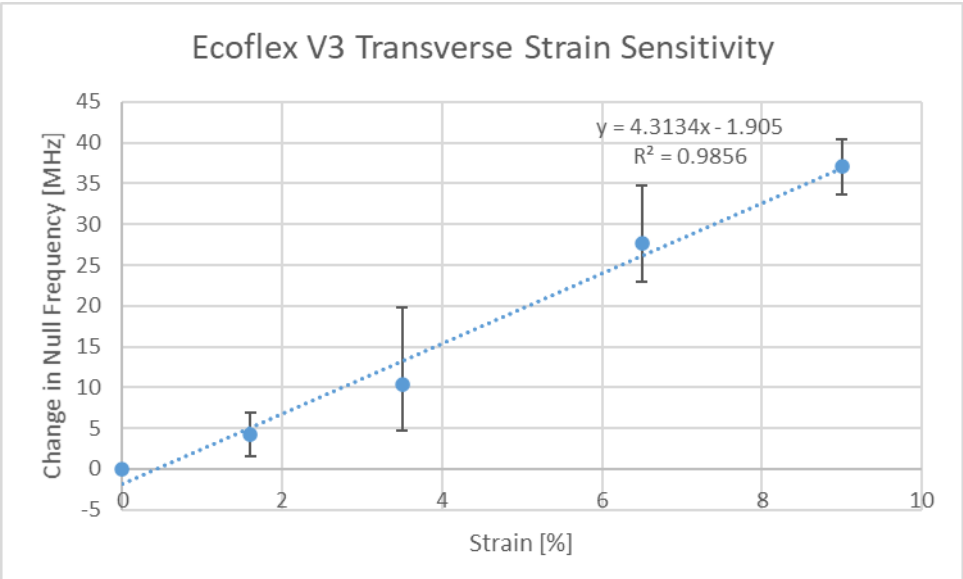
Figure 3.42: V3 Transverse Strain Sensitivity – from "Use of Chipless RFID as a Passive, Printable Sensor Technology for Aerospace Strain and Temperature Monitoring" by McGee et al., MDPI, CC BY 4.0 [28]

Testing was also performed with sensor implementations that included initial displacements of the movable parts so that the $M_{AX/TR}$ and $C_{AX/TR}$ terms in Equation 3.21 and Equation 3.22 can be determined. Note: This approach was taken as there was no testing machine available that could perform strain testing in two directions simultaneously and that would not bias the test results in some way. This analysis has ignored Poisson's effect as its impact was assumed to only be a biasing effect on the sensor response. This assumption is based on two observations made during testing of the silicone-based designs. The first observation is that rigid body motion is the only significant deformation mechanism in the silicone-based sensor implementations. The second observation is that the sensor frequency: strain (sensitivity) response is linear, and this is seen throughout the range of strains this device has been tested over. This work has also assumed that the relationships in Equation 3.21 and Equation 3.22 can be determined from just two datapoints. This relationship will undoubtably be different and more complex for even a slightly different sensor implementation or design and will need to be re-evaluated once the final sensor implementation has been defined. Equation 3.23 and Equation 3.24 depict the resulting terms taken from Figure 3.43.
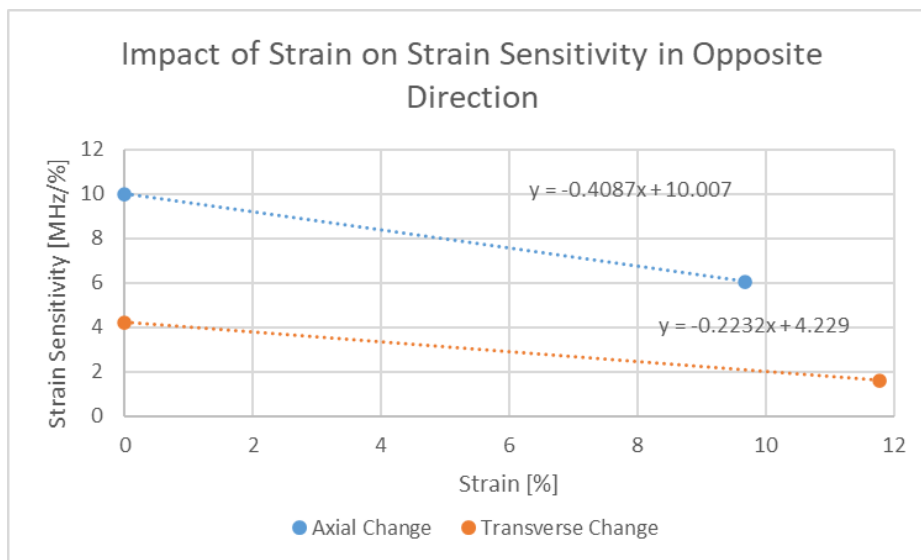
Figure 3.43: Variations in Sensitivity Caused by Strain in Alternate Direction

$$(M_{AX})(\varepsilon) + C_{AX} = -0.2232(\varepsilon) + 4.229 \qquad (3.23)$$

$$(M_{TR})(\varepsilon) + C_{TR} = -0.4087(\varepsilon) + 10.007 \qquad (3.24)$$

This section has attempted to demonstrate how the significant challenge of strain cross-sensitivity can be addressed within the design. Proper testing of the final sensor implementation will make use of a specialised tensile tester that is capable of stress testing in two directions at the same time and would apply shear loads instead of tensile loads to the sensor.

Transmission Line -Based Testing

Similar to the other resonator designs, this variation can be coupled to the CPW so that the relevant resonances can be determined. One point of note here is that the original design exhibits both resonances overlapping in the frequency domain and the other designs, referred to as "altTRGAP" and "altSGAP" in Figure 3.44 below do not initially have this behaviour.
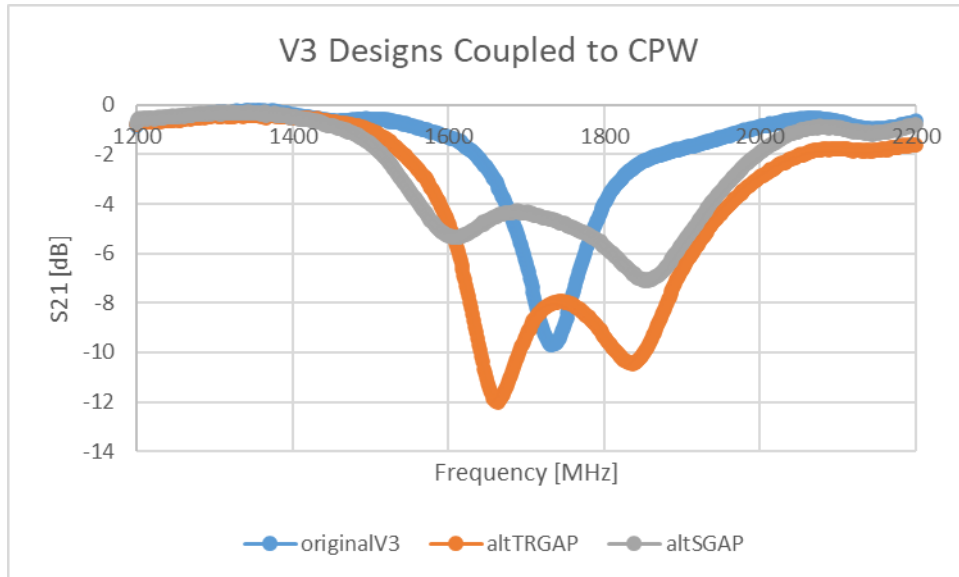
Figure 3.44: CPW Responses with Differing V3 Implementations

What is important here is that it is clear that both resonances are encoded in the CPW response, and a future work could and would strive to separate the two resonances sufficiently in the frequency domain.

Strengths and Weaknesses of Design

This alternate design boasts modest strain sensitivities in both polarizations but would still seem to be less sensitive than the V1 design. Table 3.9 gives a brief review of the sensor performance of this design. There is a clear difference in the sensitivity of the two resonances which is far from ideal, this may warrant the exploration of the geometry in [36] as an alternative or indeed the exploration of a completely new resonator design.

Table 3.9: Comparison of V1 and V3 Ecoflex-Based Designs

Implementation	Sensitivity [MHz/%ε]	Base Null Frequency [MHz]	Gauge Factor
Ecoflex™ (Axial)	10.007	1915.3	0.5226
Ecoflex™ (Transverse)	4.229	1880	0.2249

3.4 Fabrication and Performance Challenges for Published Strain Sensor

As described earlier, the relative stiffness of the conductor and substrate will dictate the behaviour of the resonator when the sensor assembly is subjected to mechanical strain. The initial design geometry (Version 1) and subsequent versions have been developed in a way to promote rigid body motion of the conductive parts whilst the parts themselves remain undeformed. With that being said, the sensitivity analysis results shown in Figure 3.12 above demonstrate that all of dimensions of the resonator geometry exhibits strain sensitivity. It can be seen that the variation of some of the geometric variables result in the resonant null moving in opposite directions. This means that it may be the case that under very specific conditions the total strain sensitivity may equate to zero. Other than this possibility, the geometry should exhibit strain sensitivity however this sensitivity will most likely be less than that found under the scenario where rigid-body motion is the dominant deformation mechanism.

3.4.1 Disadvantages of Highly Flexible Substrates

Thus far, proof-of-concept designs have relied on moulded, highly flexible substrates which allowed for device testing using small/cheap tensile testing equipment and the main deformation mechanism used in these implementations is rigid body motion. Although this does result in a viable strain sensor, there are several fabrication and performance challenges that arise with this approach. On the topic of sensitivity, the shear modulus of hyperelastic materials is quite low [37], meaning that in a realistic implementation of those sensors, the shear stress experienced by the bottom surface of the substrate will only be weakly/partially transferred to the top surface. Another performance issue is that such materials usually have high values of Poisson's ratio [38], leading to potentially large transverse sensitivities of the resonance that is used to encode the axial strain magnitude.

One of the main fabrication challenges are related to the fact that silicone and latex rubbers have significant cure times. Furthermore, silicone rubber has a low surface energy and requires significant post-treatment to allow for successful adhesion of an in-situ fabricated conductor to that surface. This issue was avoided in the earlier work by encapsulating the conductive element in the substrate. Such an approach may be suitable for proof-of-concept sensor implementation but unless the bonding between the encapsulated part and the substrate remains intact, separation of the parts could lead to increased wear. This type of wear is known as "fretting" and can lead to cracks, defects and other stress concentrations within the relevant parts [39]. Other issues with the use of silicones include the need for

90

specialised fabrication/deposition procedures to ensure outgassing is not a problem in the resulting deposition [40].

Further performance limitations of the flexible device are related to the dynamic response of the sensor and whether this material will more readily suffer from creep, than other polymeric materials. This latter limitation is of importance as it will induce a bias in the sensor response. The former limitation is related to the response of elastomer materials to vibration. Although further modelling is required to relate substrate Shore hardness to resonator deformation, the mechanical loss coefficient is much higher in elastomers than other material types [41]. High values of this parameter indicate that said material is suitable to be used in mechanical damping applications. A discussion on the dynamic characteristics of the tensile properties of elastomers can be found in [42]. In essence, the relationship between stress and strain becomes complex as there is now a loss factor present as the cyclic stress is partially dissipated as heat and the material response lags behind the applied stimulus [42]. It is unclear if this effect may lead to an attenuation of deformation transfer to the resonator, under vibrational loading. If this is indeed the case, attempts at both static and dynamic stimulus measurements could result in significant errors when the sensor is experiencing vibration.

3.4.2   Aerospace Sensor Fabrication and Deployment

This section outlines the refined implementations of the V1 strain sensor design, as the earlier implementations were merely initial proof-of-concept versions. The V1 design was chosen as the final design as the other implementations exhibited significantly lower strain sensitivities. These new V1 implementations have focused on the need for strain sensing below 1% and this time, testing was performed using a proper Instron™ tensile testing machine. On-Metal testing was also performed as part of this work, but the sensor range/sensitivity was far too low to be recognised.

This project has not focused exclusively on sensor fabrication, but rather on sensor design. Since this is the case, the approaches taken in this work have focussed on fabrication simplicity above sensor performance and sensor durability. It may be the case that other fabrication methods/technologies discussed earlier may have resulted in a better performing sensor, but this work will focus on methods/technologies that are within the author's grasp and would lead to a timely fabrication/deployment for each sensor. This is discussed more thoroughly in Appendix B.

Method #1: Laser Cut PMMA with Glued EDM Copper

The first fabrication method utilised, involved the gluing of a 0.3mm thick copper resonator design onto a 150x40x3mm PMMA substrate. Initial testing with this device in the tensile testing machine led to the sensor responses seen in Figure 3.45.
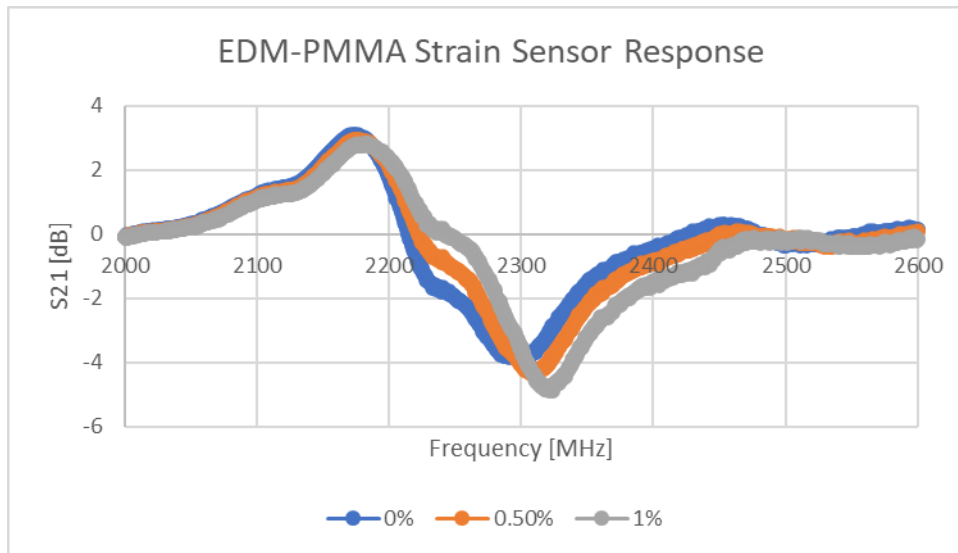
Figure 3.45: EDM-PMMA Sensor Responses

Initial testing revealed a sensitivity of over 20MHz/%ε but testing up to 1.5% strain resulted in the PMMA exhibiting a brittle failure. Additional testing was done with another implementation of the sensor, below 0.5% strain and the sensitivity results of this test can be seen in Figure 3.46. Variations in sensitivity between the two implementations has been put down to differences in the degree of adhesion between the resonator parts and the conductor.
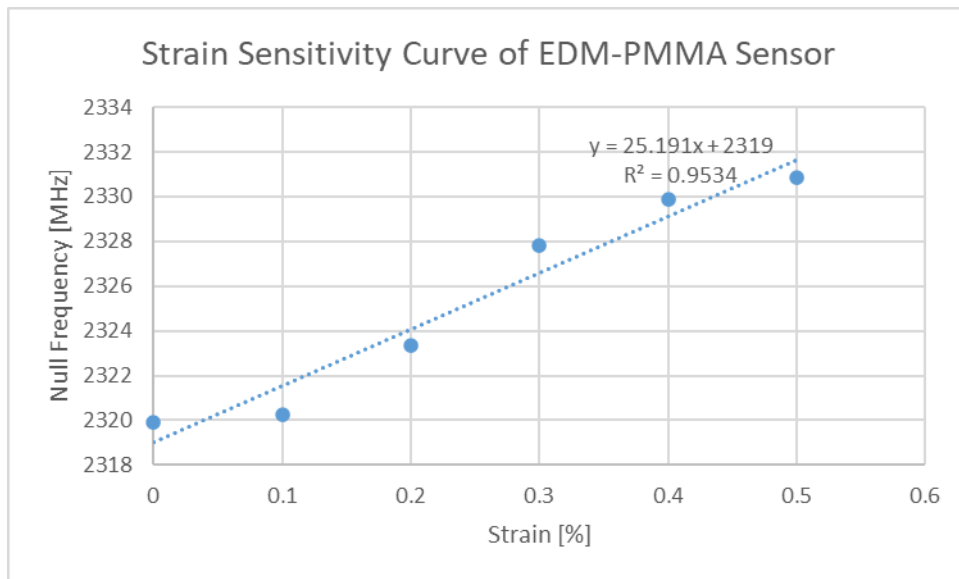
Figure 3.46: EDM-PMMA Sensor Sensitivity Curve

Method #2: Laser Cut PMMA with Conductive Paint

One critique of Method #1 is the need for the fabrication and adhesion of the 0.3mm thick copper resonator. An alternative method simply painted the resonator design onto the PMMA substrate, using a low-cost conductive paint. The sensor response of this device was somewhat lower, but curve fitting allowed for the minimum frequency of the bandstop response to be resolved. The sensitivity graph for this sensor can be seen in Figure 3.47.
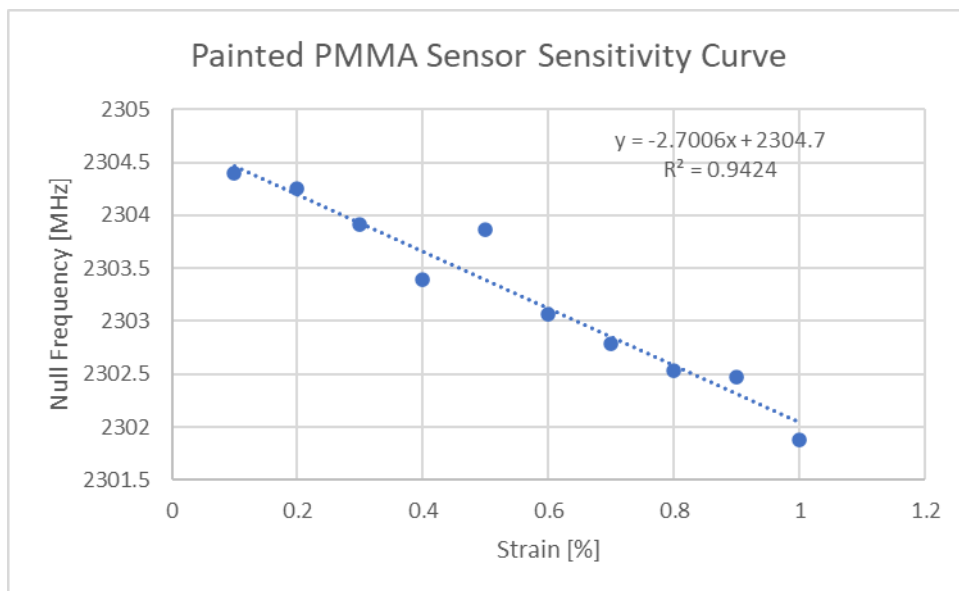
Figure 3.47: Painted PMMA Sensitivity Curve

93

Method #3: Metallograph Thermal Transfer Ribbon

The two methods explored above both have their benefits and drawbacks. One common drawback is that the deployment of such sensors is somewhat cumbersome. The thermal transfer ribbon approach would allow for deployment in the same manner as a sticker machine. The polyimide-based thermal transfer ribbon implementation was adhered to the PMMA substrate using the adhesive backing on the ribbon. This test differs slightly than the others as now the PMMA piece is no longer working as a substrate but is now acting as a superstrate. This test variation was important as it allows for an initial assessment on whether the adhesive backing is capable of transferring the strain to the resonator. The initial scattering response of this sensor can be seen in Figure 3.48. Note: Small setup variations around the tensile tester could considerably alter the magnitude of the resonant response observed during testing. Note: Initial testing up to 1% strain resulted in fractures in the resonator.
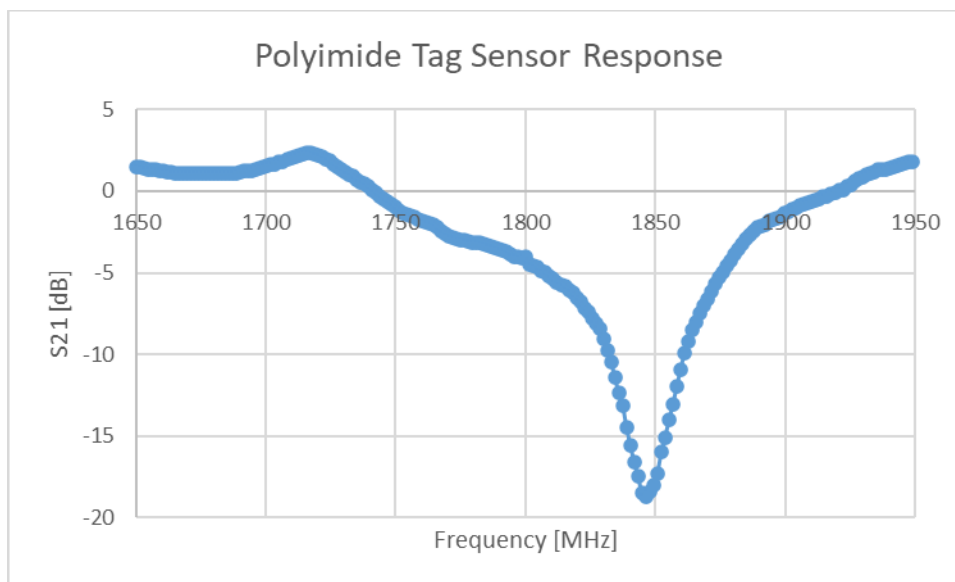
Figure 3.48: Thermal Transfer Ribbon Sensor Response

Using a curve fitting approach, the null frequencies were determined for several strain values below 0.3%. The sensitivity graph resulting from these datapoints can be seen in Figure 3.49.
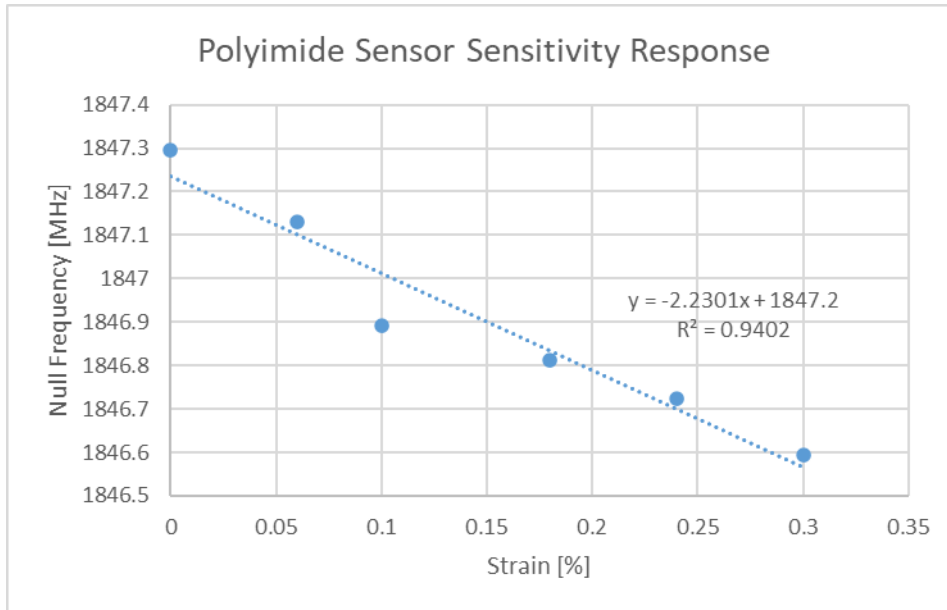
Figure 3.49: Sensitivity Curve of Thermal Transfer Ribbon Sensor

Comparative Performance of Implementations

Each of the above implementations has benefits and drawbacks associated with it. This is of course to be expected when a trade-off between performance and ease of fabrication/deployment arises. Table 3.10 compares the three implementations across several categories of interest.

95

Table 3.10: Comparison of Easily-Fabricated Strain Sensors – © 2022 IEEE [43]

Method	#1: Glued EDM Copper on PMMA	#2: Conductive Paint on PMMA	#3: Thermal Transfer Ribbon Sensor
Sensitivity [MHz/%ε]	25.191	-2.701	-2.230
Gauge Factor	1.086	0.1207	0.1172
In-Situ Resonator Reconfigurability	No – The resonator design is fixed	Yes – The resonator design could, in theory be deposited in a reconfigurable way	Yes – This process fully supports planar conductor variations
Operating Temperature Limit (without PMMA)	Cyanoacrylate is limited to continuous operation between -32°C -> +65°C [44]	N/A – unknown temperature range of conductive paint. Recommended upper sintering temperature is 148°C [45]	N/A - Ribbon operation for 100 hours at 150°C has been claimed by the manufacturers [46]
Possible Fabrication Enhancements	The use of an epoxy-based adhesive	Use of an enhanced fabrication protocol. Certain printed electronics have demonstrated operation at up to 850°C [47]	Further exploration into ribbon technology and how it could be tailored for high-temperature applications
Possible Design Enhancements	n/a	Use of slotting or multiple materials within the substrate (explored below)	n/a

3.6 Further Work

This section outlines the next steps to be taken to enhance the current sensor design so that it meets the aims of the project to a greater extent. Of most importance to this section is exploring how the in-situ fabricated strain sensor performance can be enhanced. This discussion focusses on how the requirement for a stiff (thick) conductor can be removed from the fabrication requirements and thus allow for more conventional printing technologies such as inkjet to be directly suitable.

3.6.1 Substrate Design Exploration

Other than selecting a substrate with the desired shear and tensile stiffnesses, this section sets out to explore the possible substrate-related design enhancements that could improve the overall performance of the sensor. As has been discussed earlier, this particular design performs better if the conductive parts are tall and not just thin film depositions. This poses significant fabrication challenges and this section explores various methods that could be used to promote rigid body motion with in the design, whilst reducing the need for thick conductive parts. Other performance enhancements/limitations resulting from these alternate substrate designs are also discussed.

Design Enhancement via Substrate Slotting

One possible method to mitigate the need for a highly stiff resonator is to force the substrate to deform around it. This can be done by weakening the substrate through the use of slotting and other such effects. Figure 3.50 depicts a diagram of a potential substrate design that should deform under axial strain in a way that will keep the resonator geometry undeformed during axial deformation of the substrate.
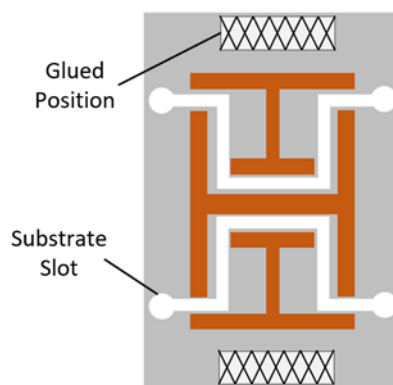
Figure 3.50: Example Substrate Slotting Design

An example substrate geometry was explored using FEA software, which included a partial slot (trench) that would hopefully force the sensor to support a greater degree of rigid body motion effects. This model used a 1mm thick stiff Kapton™ polyimide substrate and a thin copper resonator (500µm) with a substrate trench with a depth of 400µm. Figure 3.51 depicts the trench location used in this implementation. Test results seen in Figure 3.52 reveal a modest enhancement in rigid body motion and a mitigation of bending within the design.
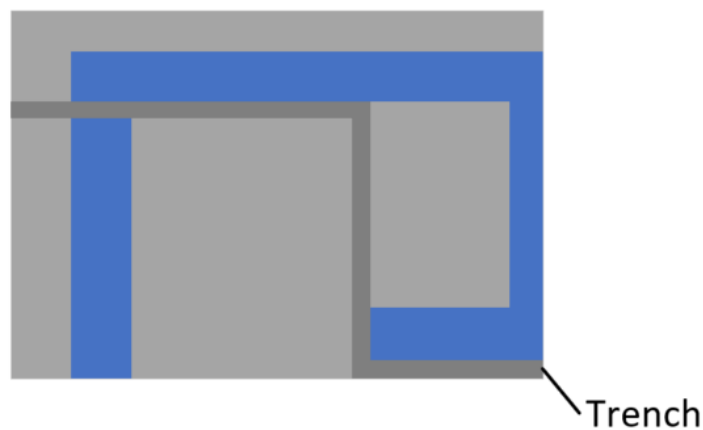
Figure 3.51: Trench Location Used in FE Analysis
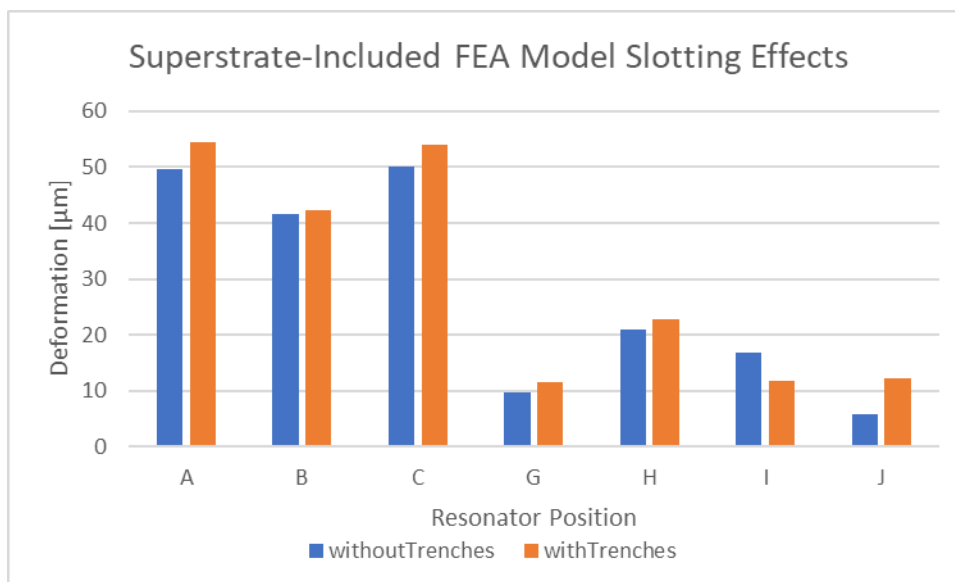
Figure 3.52: Impact of Partially Slotted Polyimide Substrate on Deformation Performance

Although a variety of geometric subtractions/slots could be added to the substrate design, their inclusion will inevitably result in a stress concentration factor. This is of particular importance as stress concentration factors can significantly reduce the fatigue

strength/lifetime of the substrate material. More details on the impact of stress concentrations on fatigue and creep can be found in any good Strength of Materials textbook.

The Use of Selective Substrate Adhesion

An alternative way to possibly avoid the need for excessively thick conductors is to adhere them only partially to the substrate. The contour lines in Figure 3.53 depict the adhesion regions on the basic design (Figure 3.53(a)) and an alternative configuration which only partially adheres the substrate and conductor (Figure 3.53(b)). The use of this partial adhesion at the conductor centroid stops the majority of the conductor being deformed and thus the conductor does not need to be as thick. Furthermore, this approach would also help enhance rigid body motion as the tendency of the resonator to bend or elastically deform will be severely mitigated. It is believed that this approach could in-part be responsible for the differences in sensitivity between the latex and silicone -based sensor implementations seen above.
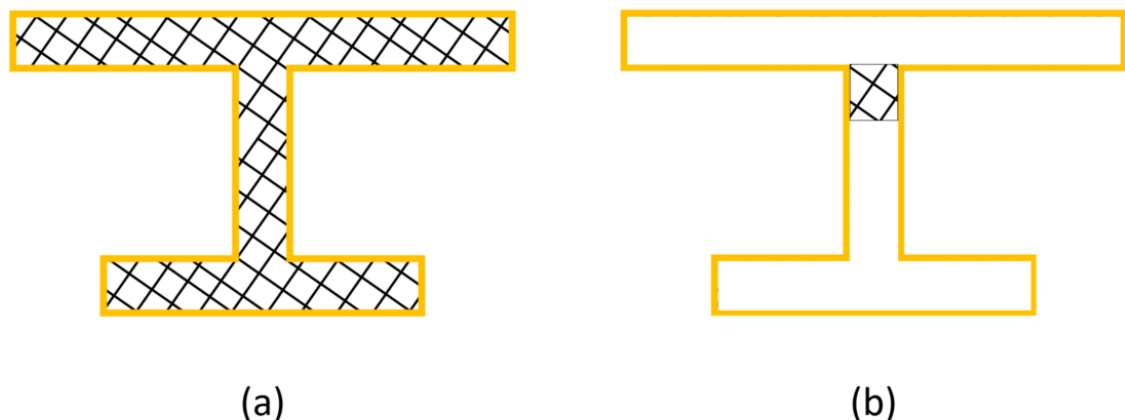
Figure 3.53: Potential Adhesion Variability (See Hatching). (a) – Fully Adhered, (b) – Partially Adhered

Methods to implement this depend heavily on the fabrication approach taken. The use of adhesives is the simplest method, but in-situ fabrication approaches could be also taken, such as those that support the deposition of a sacrificial layer. This sacrificial layer could be underneath the conductor or cantilever-style features could be added to the substrate and conductive ink/paint deposited on top of them. This cantilever system, whether it be implemented in the conductor, or the substrate would have a cross section similar to that depicted in Figure 3.54 below.
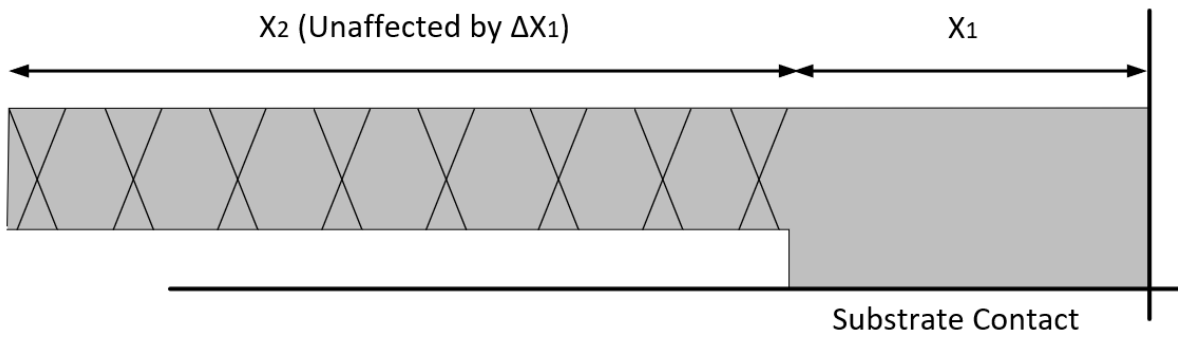
Figure 3.54: Partial Adhesion Impacts Diagram

Initial testing was performed using FEA software and used the conductor geometry seen in Figure 3.55 below, which raises the main conductor geometry by 0.2mm above the substrate. This design relies on a small fraction of the conductor being in contact with the substrate and it is by no means optimised yet. Figure 3.56 below reveals the impact that this design has on the resulting axial deformation.
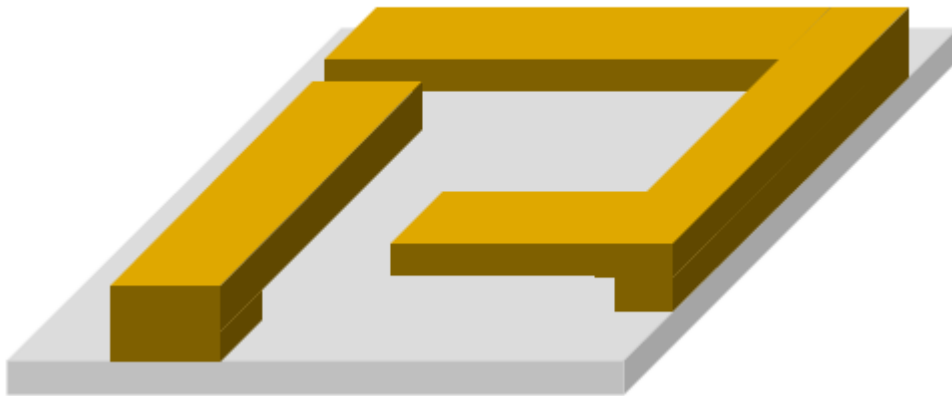
Figure 3.55: Diagram of Partial Adhesion FEA Model
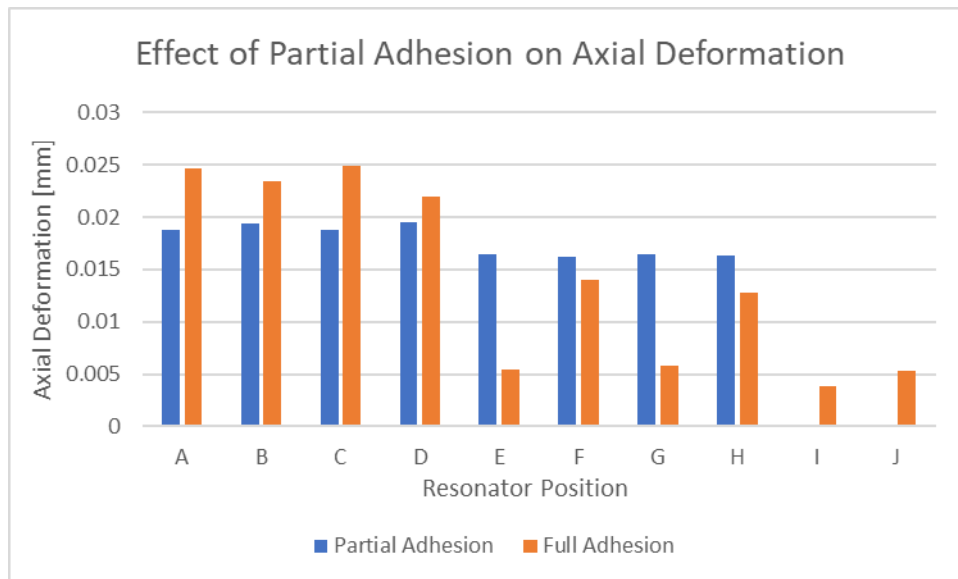
Figure 3.56: FEA Results with Partial Adhesion Design

The key point to be made about the results seen in Figure 3.56 is that the deformation of all of the relevant positions (A-H) are more similar than that found in the original simulation. This implies that a greater degree of rigid body motion has occurred, and conductor deformation has been significantly attenuated. The other two positions (I, J) display virtually no deformation in comparison to that of the original design, which further emphases the ability of this design approach to mitigating conductor elastic deformation.

Design Enhancement via Dual-Material Substrate

From the results generated using the existing FEA model it can be seen that unwanted effects such as bending and transverse deformation occur in the polyimide-based sensor. The same effects were not present to the same degree during equivalent testing with an Ecoflex™ substrate. Furthermore, it is becoming more important to explore potential methods to maximise rigid body motion within the design, without the use of stiff conductive elements.

This theoretical substrate design makes use of both substrate materials in its substrate so that the axial deformation of the resonator exhibits a greater degree of rigid body motion and less bending and/or elastic deformation. This approach has also been utilised to assess whether it can also be used for transverse strain mitigation. Figure 3.57 depicts the novel substrate design, which consists of a substrate whose features and dimensions are discussed in Table 3.11. The design could have been made more sophisticated than that seen in Figure 3.57, but the chosen design was selected to aid in the meshing process.
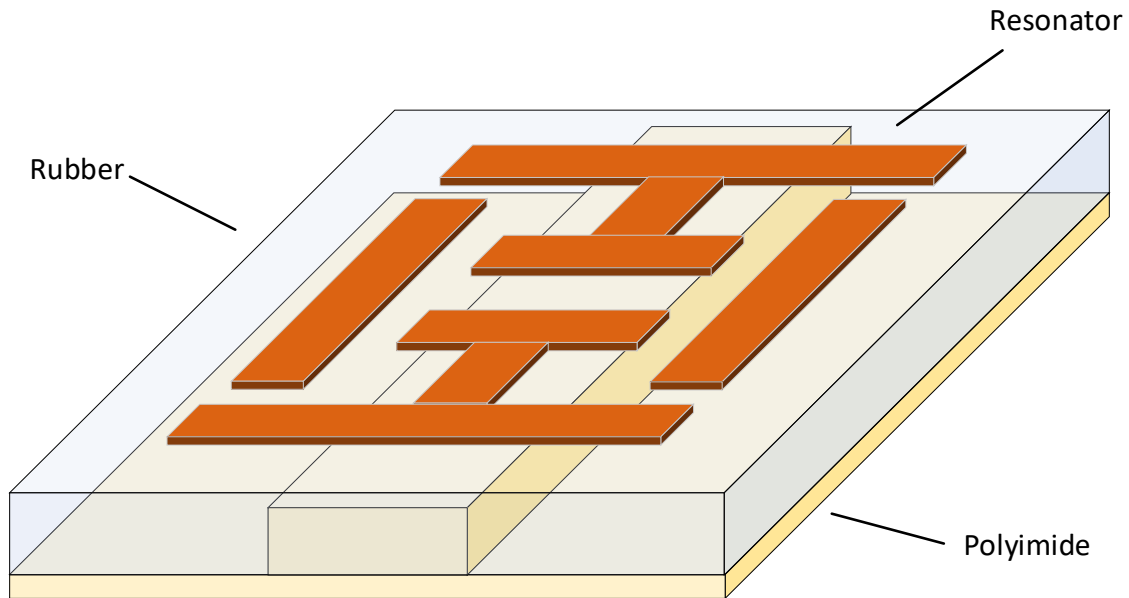
Figure 3.57: Example Dual-Material Substrate Design

Table 3.11: Dual-Material Substrate Details

Part	Material	Dimensions of importance
Lower Substrate	Polyimide	0.2mm thick
Upper Substrate	Ecoflex™ 00-30	0.8mm thick
Lower Substrate – Raised Section	Polyimide	0.5x5mm cross section

Axial and transverse loads were applied to the relevant external surfaces of the polyimide part of the substrate to better model the impact of the silicone layer above it. To ensure that the test results were not affected by the difference between this and the previous loading strategy, the initial fully-polyimide sensor was re-tested using the same loading as that described above. The axial deformation of the sensor with the regular and dual substrate design can be seen in Figure 3.58. From this Figure, it can be seen that the degree of bending that is present in the original design has been virtually completely removed and elastic deformation does not appear to occur.
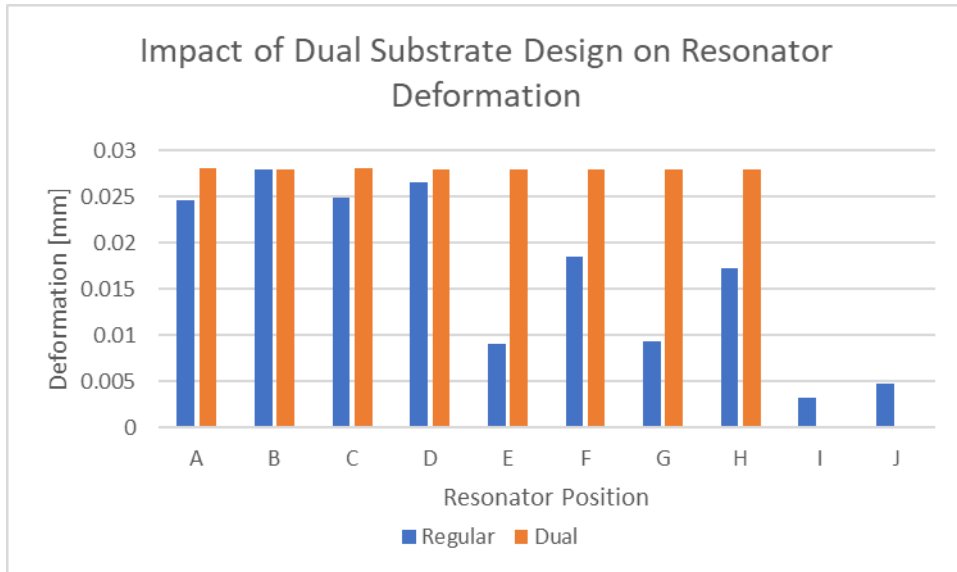
Figure 3.58: Impact of Dual-Material Substrate on Sensor Deformation

The transverse sensitivity of the design has also been significantly affected by the dual substrate approach (see Figure 3.59). This is certainly true of the positions A-G but the positions I and J exhibit greater degrees of transverse deformation. It would appear that these points, which correspond to the monopole ("EL") part, are demonstrating that this part is undergoing a rigid body motion effect from the introduction of the dual substrate.
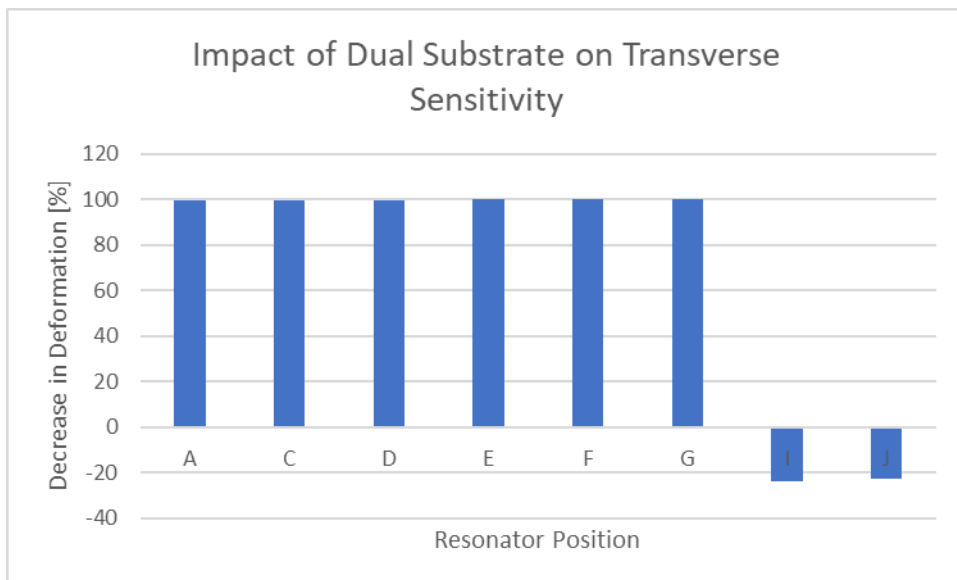
Figure 3.59: Reduction in Transverse Deformation with V2 Design on a Dual-Material Substrate

An unintended consequence of this substrate design being used with the V1 design is that it leaves the sensor far more exposed to thermal expansion issues. This is caused by the fact that CTE values are in many cases linked to the material stiffness ($CTE \propto E^{-1}$) [48]. This problem may not be as significant with the V2 design. Another potential issue is that the capacitive

regions (EC:EL and EC:EC) will experience the effects of different polymers in their near field. This could partially undermine the ability to use the V2 design to compensate for the substrate dielectric constant variations as the two materials will most likely exhibit different dynamic responses in the relationship between their dielectric constant and the environmental variables. Thermal expansion issues are discussed in more detail in Appendix C.

3.7   Conclusion

Overall, the work presented in this chapter has been successful in achieving the basic goals outlined in the overall project. With that being said, the design and subsequent implementations are far from being ready for an actual deployment. A subsequent project will most likely be needed that will focus on sensor fabrication and testing to bring this work up to the level needed, before it can be claimed to be ready for trial testing in the aerospace setting. Although that is the case, some key victories were achieved along the way, notably;

- A novel passive wireless strain sensor was designed and tested
- The device sensitivity is comparable with the best designs found in the current literature
- The sensor has been designed to support in-situ fabrication
- In-situ fabricated versions of the sensor have been developed and tested

3.8   References

[1]   S. H. Min et al., "Stretchable chipless RFID multi-strain sensors using direct printing of aerosolised nanocomposite," Sensors Actuators A Phys., vol. 313, p. 112224, Oct. 2020.

[2]   J. Kim, Z. Wang, and W. S. Kim, "Stretchable RFID for wireless strain sensing with silver nano ink," IEEE Sens. J., vol. 14, no. 12, pp. 4395–4401, 2014.

[3]   A. Daliri, A. Galehdar, S. John, C. H. Wang, W. S. T. Rowe, and K. Ghorbani, "Wireless strain measurement using circular microstrip patch antennas," Sensors Actuators, A Phys., vol. 184, pp. 86–92, Sep. 2012.

[4]   R. Melik, E. Unal, N. K. Perkgoz, C. Puttlitz, and H. V. Demir, "Metamaterial-based wireless strain sensors," Appl. Phys. Lett., vol. 95, no. 1, 2009.

[5]   L. Teng, K. Pan, M. P. Nemitz, R. Song, Z. Hu, and A. A. Stokes, "Soft Radio-Frequency Identification Sensors: Wireless Long-Range Strain Sensors Using Radio-Frequency Identification," Soft Robot., vol. 6, no. 1, pp. 82–94, Feb. 2019.

[6]   T. T. Thai, H. Aubert, P. Pons, G. Dejean, M. Mtentzeris, and R. Plana, "Novel design of a highly sensitive RF strain transducer for passive and remote sensing in two dimensions," IEEE Trans. Microw. Theory Tech., vol. 61, no. 3, pp. 1385–1396, 2013.

[7]   D. K. Singh, Strength of materials, Fourth edition. Cham, Switzerland: Springer, 2021.

[8]   J. Naqui et al., "Transmission Lines Loaded With Pairs of Stepped Impedance Resonators: Modeling and Application to Differential Permittivity Measurements," IEEE Trans. Microw. Theory Tech., vol. 64, no. 11, pp. 3864–3877, Nov. 2016.

[9]   L. Su, J. Mata-Contreras, P. Velez, and F. Martin, "Splitter/combiner microstrip sections loaded with pairs of Complementary Split Ring Resonators (CSRRs): Modeling and optimization for differential sensing applications," IEEE Trans. Microw. Theory Tech., vol. 64, no. 12, pp. 4362–4370, Dec. 2016.

[10]   W. M. Abdulkawi, N. Nizam-Uddin, A. F. A. Sheta, I. Elshafiey, and A. M. Al-Shaalan, "Towards an Efficient Chipless RFID System for Modern Applications in IoT Networks," Appl. Sci. 2021, Vol. 11, Page 8948, vol. 11, no. 19, p. 8948, Sep. 2021.

[11]   F. Babaeian and N. Karmakar, "A UWB Antenna for Chipless RFID Tag Detection," 2nd Int. Conf. Electr. Commun. Comput. Eng. ICECCE 2020, Jun. 2020.

[12]   W. Withayachumnankul, C. Fumeaux, and D. Abbott, "Compact electric-LC resonators for metamaterials," Opt. Express, vol. 18, no. 25, pp. 25912–25921, Dec. 2010.

[13]   A. Dhouibi, S. N. Burokur, A. de Lustrac, and A. Priou, "Study and analysis of an electric Z-shaped meta-atom," Adv. Electromagn., vol. 1, no. 2, pp. 64–70, Oct. 2012.

[14]   F. Martin, Artifical Transmission Lines for RF and Microwave Applications, 1st Edt. Wiley, 2015.

[15]   K. Mc Gee, P. Anandarajah, and D. Collins, "Proof of Concept Novel Configurable Chipless RFID Strain Sensor," Sensors, vol. 21, no. 18, p. 6224, Sep. 2021.

[16]   D. H. Berkebile and D. L. Stevenson, "The Use of 'Kapton' Polyimide Film in Aerospace Applications on JSTOR," SAE Trans., vol. 90, pp. 3562–3568, 1981.

[17]   V. Griseri, "Polyimide Used in Space Applications," Polyim. Electron. Electr. Eng. Appl., Sep. 2020.

[18]   DuPont TM, "DuPont TM Kapton® HN Polyimide Film."

[19]   A. De Rooij, "Exposure of Silver to Atomic Oxygen," Noordwijk, 2010.

[20]   J. Vaicekauskaite, P. Mazurek, S. Vudayagiri, and A. L. Skov, "Mapping the mechanical and electrical properties of commercial silicone elastomer formulations for stretchable transducers," J. Mater. Chem. C, vol. 8, no. 4, pp. 1273–1279, Jan. 2020.

[21]   B. J. MacDonald, Practical Stress Analysis with Finite Elements, 2nd Edtn. Dublin: Glasnevin Publishing, 2013.

[22]   D. Steck, J. Qu, S. B. Kordmahale, D. Tscharnuter, A. Muliana, and J. Kameoka, "Mechanical responses of Ecoflex silicone rubber: Compressible and incompressible behaviors," J. Appl. Polym. Sci., vol. 136, no. 5, p. 47025, Feb. 2019.

[23]   G. Agarwal, N. Besuchet, B. Audergon, and J. Paik, "Stretchable Materials for Robust Soft Actuators towards Assistive Wearable Devices," Sci. Rep., vol. 6, Sep. 2016.

[24]   P. Kulkarni, "Centrifugal forming and mechanical properties of silicone-based elastomers for soft robotic actuators," The State University of New Jersey, 2015.

[25]   "ISO - ISO 7619-1:2010 - Rubber, vulcanized or thermoplastic — Determination of indentation hardness — Part 1: Durometer method (Shore hardness)," ISO Standard. 2010.

[26]   J. M. Arguello and A. Santos, "Hardness and compression resistance of natural rubber and synthetic rubber mixtures," J. Phys. Conf. Ser., vol. 687, no. 1, p. 012088, Feb. 2016.

[27]   S. Cha and C. Kim, "Poly(dimethylsiloxane) Stamp Coated with a Low-Surface-Energy, Diffusion-Blocking, Covalently Bonded Perfluoropolyether Layer and Its Application to the Fabrication of Organic Electronic Devices by Layer Transfer," ACS Appl. Mater. Interfaces, vol. 10, no. 28, pp. 24003–24012, Jul. 2018.

[28]   K. McGee, P. Anandarajah, and D. Collins, "Use of Chipless RFID as a Passive, Printable Sensor Technology for Aerospace Strain and Temperature Monitoring,", Sensors, 2022, 22, 8681. https://doi.org/10.3390/s22228681

[29]   R. A. Alahnomi et al., "Review of Recent Microwave Planar Resonator-Based Sensors: Techniques of Complex Permittivity Extraction, Applications, Open Challenges and Future Research Directions," Sensors 2021, Vol. 21, Page 2267, vol. 21, no. 7, p. 2267, Mar. 2021.

[30]   J. Naqui, J. Coromina, A. Karami-Horestani, C. Fumeaux, and F. Martín, "Angular Displacement and Velocity Sensors Based on Coplanar Waveguides (CPWs) Loaded with S-Shaped Split Ring Resonators (S-SRR)," Sensors 2015, Vol. 15, Pages 9628-9650, vol. 15, no. 5, pp. 9628–9650, Apr. 2015.

[31]   Vishay Precision Group, "Strain Gages and Instruments: Errors Due to Transverse Sensitivity in Strain Gages," 2011.

[32]   T. T. Thai, H. Aubert, P. Pons, M. M. Tentzeris, and P. Robert, "Design of a highly sensitive wireless passive RF strain transducer," in 2011 IEEE MTT-S International Microwave Symposium, 2011.

[33]   K. Mc Gee, P. Anandarajah, and D. Collins, "Zero-Power Wireless Strain and Permittivity Sensor," 2022 33rd Irish Signals Syst. Conf., pp. 1–5, Jun. 2022.

[34]   F. Martín, Artificial Transmission Lines for RF and Microwave Applications, 1st Edt. Wiley, 2015.

[35]   J. Hassan, K. Khalid, and W. M. Daud Wn Yusoff, "Microwave Dielectric Properties of Hevea Rubber Latex in the Temperature Range of -30°C to 50°C," Pertanika J. Sci Technol., vol. 5, no. 2, pp. 179–190, 1997.

[36]   A. Gorai and R. Ghatak, "Multimode resonator-assisted dual band notch UWB antenna with additional bluetooth resonance characteristics," IET Microwaves, Antennas Propag., vol. 13, no. 11, pp. 1854–1859, Sep. 2019.

[37]   L. Otters, W. Olthuis, P. H. Veltink, and P. Bergveld, "The mechanical properties of the rubber elastic polymer polydimethylsiloxane for sensor applications," J. Micromech. Microeng, vol. 7, pp. 145–147, 1997.

[38]   A. Müller, M. C. Wapler, and U. Wallrabe, "A quick and accurate method to determine the Poisson's ratio and the coefficient of thermal expansion of PDMS," Soft Matter, vol. 15, no. 4, pp. 779–784, Jan. 2019.

[39]   J. A. Collins, Failure of Materials in Mechanical Design: Analysis, Prediction, Prevention, 2nd Edtn. New York: Wiley, 1993.

[40]   H. von Münchhausen and F. J. Schittko, "Investigation of the outgassing process of silicone rubber," Vacuum, vol. 13, no. 12, pp. 549–553, Dec. 1963.

[41]   M. Ashbey, Materials Selection in Mechanical Design, 2nd Edtn. Oxford: Butterworth-Heinemann, 1999.

[42]   A. S. Wineman and K. R. Rajagopal, Mechanical response of polymers : An Introduction. Cambridge University Press, 2000.

[43]   K. McGee, P. Anandarajah, and D. Collins, "Presentation - Zero-Power Wireless Strain and Permittivity Sensor." Cork, 2022.

[44]   W. M. Murray and W. R. Miller, The bonded electrical resistance strain gauge: An introduction, 1st Edtn. New York: Oxford University Press, 1992.

[45]   "RS PRO Conductive Paint, 5 g | RS Components," 2021. [Online]. Available: https://ie.rs-online.com/web/p/adhesives/1239911/. [Accessed: 28-Jul-2021].

[46]   Polyonics®, "Polyonics XF-552 POLYIMIDE LABEL," 2019. [Online]. Available: https://polyonics.com/TDs/XF-552.pdf. [Accessed: 27-May-2022].

[47]   M. Alhendi et al., "Printed electronics for extreme high temperature environments," Addit. Manuf., vol. 54, p. 102709, Jun. 2022.

[48]   E. Le Bourhis, "Appendix 3: Thermal Expansion and Elasticity," in Glass Mechanics and Technology, John Wiley & Sons, Ltd, 2007, pp. 271–274.

Chapter 4 - Temperature Sensor Development

4.1   Introduction

This chapter sets out to explore and implement ways of adding temperature sensing functionality to chipless RFID tags. The areas explored include both dielectric-based approaches and thermal expansion-based approaches and several novel designs and implementations have been conceived and tested. An initial attempt is also made here to integrate thermocouple technology into chipless RFID systems.

The purpose of this chapter is to explore the possible avenues that could be taken to implement a working chipless RFID temperature sensor. A great deal of emphasis is placed on key sensor characteristics such as; range, sensitivity, response time, ease of fabrication, and other metrics besides. This chapter has not focussed heavily on the more fundamental topic of heat transfer nor has it gone into great depth about potential fabrication methods. It is worth noting at this point that the fabrication section seen in Appendix B is of great relevance to this chapter also and perhaps should be read first.

4.1.1   Chapter Methodology
Given the time and resource constraints of this project, the temperature sensor development will rely on building upon existing chipless RFID tag designs and making use of a wired test configuration, so that the design process can be simplified. This approach has been used in other related works with great success. Where necessary, the existing materials science literature will be relied upon to provide the relevant materials characterisation information and this not only saves time, but also results in accurate and reliable datasets that were gathered by experts in the area.

4.2   Aims and Objectives

The purpose of this chapter is to explore and implement a variety of methods that could result in a chipless RFID tag response becoming temperature sensitive. Unlike the work seen in Chapter 3 where the chipless RFID resonator geometry is an integral part of the overall system, this chapter explores temperature sensing methods that can arguably be integrated into any chipless RFID resonator design. Resonator design is of course a key part but not the sole key part of this overall sensor design. This chapter will rely on the existing, highly sensitive resonator designs and attempt to add temperature sensing functionality to them. This deviation occurs in this chapter, because strain sensing is inherently related to geometric changes as no other means of encoding strain information into a chipless RFID tag response,

has been seen in the known literature. This is not the case for temperature sensing and a variety of different approaches (dielectric, swelling -based, etc.) have already been put forward in the chipless RFID sensing literature [1].

The general goal of this chapter is to demonstrate that temperature sensing capabilities can be integrated into chipless RFID technology. This testing has only been performed at temperatures between 20-90°C due to testing limitations but should demonstrate that temperature sensing is indeed possible. Testing of sensors above this range was limited by the adhesives used, glass transition temperatures of the constituent materials and test environment challenges. Attempts were made at using a hot plate and/or Peltier coolers to heat the developed sensors but their presence altered the sensor responses in undesirable ways. The concern with further use of these devices was that the sensor results gathered may only be valid if said heating devices were present. A hygrometer was used to monitor the humidity level in the air-conditioned environment and its value did not correlate with any of the results found during device testing. More often than not, testing was performed in batches and not spread over several days/weeks, which may have helped in the gathering of consistent sensor response results. Since this goal has already been performed in other works in the literature, this work also sets out to explore how thermal expansion may be exploited further to develop a new temperature sensor design which may boast additional performance enhancements over those found in the existing literature. Furthermore, these and other designs discussed in this work have also been developed with ease of fabrication as a key end requirement for the sensor design. A key point to be made here is that the effects of strain (axial or otherwise) has not been considered during the design or testing stages of the developed sensors. Further work will be required to explore this challenge.

Attempts are also to be made at integrating existing temperature sensors into chipless RFID tags, such as thermistors and thermocouples. The latter goal of thermocouple integration has never been seen in any other work and was considered a considerable challenge to undertake.

4.3   Existing Designs

There have been many works prior to this chapter that have focussed on giving chipless RFID tags the ability to sense temperature. This section discusses both the ways in which conventional temperature sensors have been added to chipless RFID tags and also discusses more novel approaches seen in the literature.

4.3.1 Conventional Sensor Integration

Conventional temperature sensors used in aerospace systems include thermocouples, thermistors and Resistance Temperature Detectors (RTDs) [2]. The latter two approaches are resistive based, and several works have already demonstrated how resistive-type elements can be integrated into chipless RFID designs. The result of which is usually a modulation of the magnitude of the resonant response. This modulation effect is largely ignored throughout this work as it is also heavily affected by read range and environmental conditions. The reason why this opinion has been formed is that a reduction in the resonant magnitude will reduce the range over which the sensor can be reliably interrogated. For the sake of completeness, a conventional thermistor has been integrated into a chipless RFID tag and tested in Appendix E.

As mentioned in a recent European Space Agency (ESA) application to tender [2], there is a need for in-situ fabricated thermocouples as well as thermistors and RTDs to perform adequate sensing on the aerospace structure of interest. Thermocouples are used in many high temperature aerospace applications and are used throughout the aerospace industry [2][3]. No publications found at the start of this project demonstrated thermocouple integration into chipless RFID technology. Subsequent searching revealed a design operating below 100MHz, that used a varactor diode to measure incoming DC voltages [4]. There are obvious concerns with taking this approach for thermocouple integration as the DC and AC circuits are not strongly isolated and the DC signals are comparatively small.

4.3.2 Frequency Shift Based Designs

A popular chipless RFID sensor design approach is to encode stimulus information in the spectral location of the resonant response of the tag. In the case of temperature sensing, this has been performed through the use of temperature-induced geometric alterations or temperature-induced dielectric variations. Table 4.1 highlights several of the key works found within the literature.

Table 4.1: Existing Sensor Design Comparison

Work	Maximum Tested Temperature [°C]	Sensitivity [MHz/°C]	Operating Frequency [GHz]	Normalised Sensitivity [%/°C]	Approach	Comment
[5]	+50	0.8	0.7	0.1143	Temperature sensitive	Sensitivity drops

					dielectric (Stanyl® TE200F6 polyamide [6])	considerably with decreasing humidity levels [6]
[7]	+250	6.8	22	0.0309	Bi-material strip (gold+silicon)	Clean room fabrication required [8]
[8]	+30	0.1	3	0.0033	Direct conductor expansion	Performance dominated by substrate
[9]	+50	4	0.85	0.4706	Commercial bi-metal strip (P675R [10])	3D design made from discrete parts – very difficult to fabricate in-situ
[11]	+40	-0.0077	0.035	0.0220	Dielectric-based: Graphene oxide	Temperature sensitivity is highly dependent on humidity. Device operation not proven in Ultrahigh frequency or Microwave frequency ranges
[12]	+60	2.5	4	0.0625	Bi-material strip (Aluminium + Polyethylene terephthalate (PET))	Only two temperatures tested. Did not use two metals in the strip,

						which may account for low sensitivity
[13]	+60	0.742	4.5	0.0164	Thin film polyamide	Little or no details on polyamide in question. Potential humidity-related issues may occur
[14]	+80	4.07	4.95	0.0822	Ethylene tetra-fluoroethylene (ETFE) based	ETFE thermal stability tested up to 400°C. Exhibits some humidity dependencies, as expected. Unclear if sensitivity is affected by other variables
[15]	+85	3.1	2.9	0.1069	Barium Strontium titanate (BST) based	Pre-made BST varactor was used

From the table presented above, it can be seen that there are a range of existing sensor designs with different levels of sensitivity and operating frequency ranges. Sensitivities found in Table 4.1 above vary significantly and most devices have not been tested above 60°C. At this point, it has to be mentioned that it is not clear if the sensitivities can be compared by normalising them against the base resonant frequency. This comment is made as the temperature sensitivity may not occur in an arbitrary device frequency range, this is particularly the case for temperature-sensitive polymer coatings [16]. However, the sensitivity levels have to be compared in some way, so this method was chosen and a further discussion

on its impact/relevance can be found in Appendix F. This normalised sensitivity with units of %/°C represent the percentage change in null frequency per degree Celsius change in temperature.

4.4 Temperature Sensor Development Overview

Before sensor development and testing is discussed any further, it is important to consider the context in which said sensors must operate. Unlike strain sensing, which is focussed solely on sensing deformation of the underlying structure, temperature sensors can be stimulated both from the underlying structure and from the open environment in which they are situated. This distinction need not be made in scenarios where the sensor is embedded within the structure, but one would imagine that it will be of relevance for an in-situ deposited sensor. Figure 4.1(a) and Figure 4.1(b) depict the two potential avenues of thermal excitation in the case of an externally mounted sensor on a structure of interest. This distinction is largely ignored in this work, but some testing is performed in relevant sections to highlight its importance, where it is deemed necessary. For now, it will be concluded that it is an important consideration that warrants careful attention for future sensor designers, as temperature differences between the environment and the underlying surface could give rise to different levels of sensor excitation.

(a) (b)
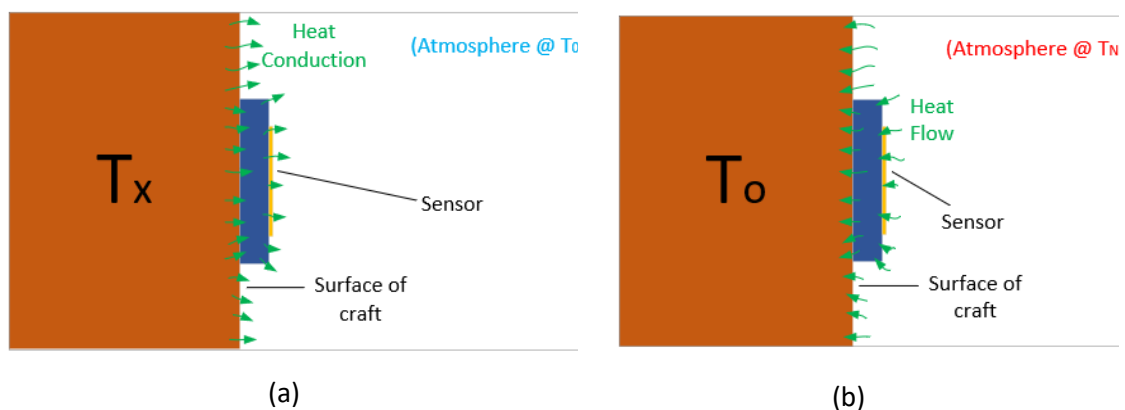
Figure 4.1: (a) - Heat Induced from Structure, (b) - Heat Induced from Environment– from "Use of Chipless RFID as a Passive, Printable Sensor Technology for Aerospace Strain and Temperature Monitoring" by McGee et al., MDPI, CC BY 4.0 [17]

Given the time and resource constraints associated with this project, a mixture of wired and wireless testing was used to explore the various sensing approaches that could be taken. This approach was inspired by that seen in [18] where Karmakar et al. make use of both wired Stepped Impedance Resonator (SIR)-based testing and wireless ELC-based testing. The use of the former approach in a wired configuration allowed this work to make use of a makeshift test environment and also removes the possibility of environment-induced challenges during sensor interrogation. Figure 4.2 depicts the basic $\lambda/4$ SIR geometry used in this chapter, which has been based on that found in the works of Karmakar in [18] and also in [19].
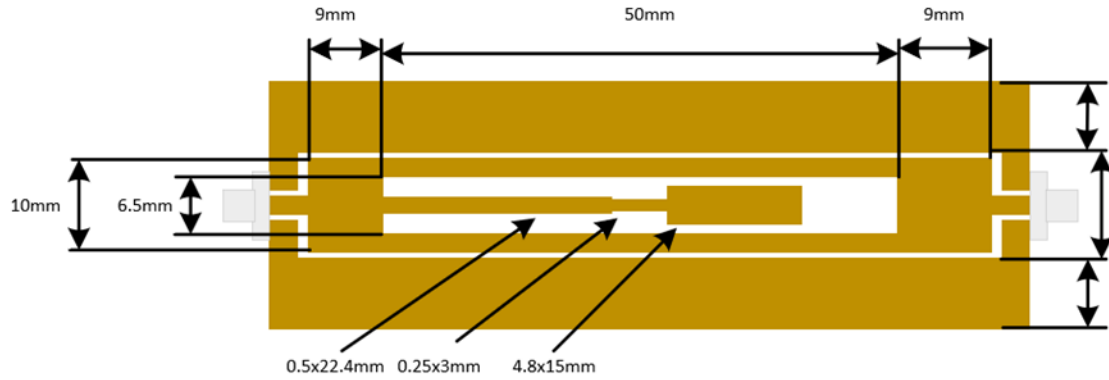
Figure 4.2: λ/4 SIR Circuit Integrated into Coplanar Waveguide (CPW) – from "Use of Chipless RFID as a Passive, Printable Sensor Technology for Aerospace Strain and Temperature Monitoring" by McGee et al., MDPI, CC BY 4.0

[17]

One further point to make in this subsection is that although there are numerous chipless RFID -based temperature sensors in the current literature [1], the approaches taken within those works could be and in most cases have been shown to be sensitive to other stimuli. One of the more common stimuli that impacts the various published sensor responses is humidity [8][11]. This chapter will not discuss strategies at mitigating this sensitivity in all sensor designs, nor will it involve the exploration of reference sensor design. This particular topic has been covered in more detail in Chapter 3 and Chapter 6.

As with other sensors developed during this overall project, a significant emphasis has been placed on ease of fabrication. More specifically, the designed sensors should in theory be capable of being printed in-situ. As demonstration of a working in-situ fabricated sensor system is realistically beyond the scope of this work, sensor implementations developed in this chapter will make use of simple, proof-of-concept fabrication approaches.

4.5 Thermocouple Integration into Chipless RFID

This section outlines the current progress made towards integrating thermocouple and chipless RFID technology to develop a thermocouple-based chipless RFID sensor. The basic operation of a thermocouple has already been covered in Chapter 2, so a simple overview is given here instead of reiteration of this and more dedicated works on the subject. A temperature differential along a piece of metal will result in the accumulation of a negative charge at the cold end and conversely a positive charge at the hotter end. Taking two dissimilar metals which have been joined together at one end, heating this end will result in dissimilar levels of charge accumulation at the free end of the respective metals [20].

To date, no published works have been found that discuss the integration of thermocouple and chipless RFID technology. Possible reasons as to why this is the case include the fact that thermocouples are effectively a DC source that AC signals can readily flow through. This is a significant problem for this application as unwanted current flow through a thermocouple leads to unwanted heating of the device itself. To overcome these challenges presented by the direct integration of thermocouple and chipless RFID technology, an alternative approach has been taken in this work. The resulting device is characterised with the inclusion of a K-Type thermocouple and also using a conventional signal generator.

Testing revealed significant thermal stability issues with the sensor which were then further explored, and a potential solution is then outlined. Finally, a simple proof-of-concept in-situ fabricated thermocouple is developed and tested to demonstrate that such a task can be readily achieved.

4.5.1 Explored Avenues of Research

As mentioned earlier in this chapter, a wide variety of chipless RFID temperature sensors have been developed. None of the chipless RFID -based implementations have demonstrated the ability to integrate with a thermocouple and/or have the ability to replace the need for such a device. In order to perform initial thermocouple integration into a chipless RFID tag, the overall design constraints that have been placed on other parts of the project have been relaxed. This was done because it is only reasonable to reduce importance of secondary design goals in order to achieve a more complex primary goal. Table 4.2 describes the way in which the overall goals were initially relaxed, so that a viable attempt at thermocouple integration can be performed.

Table 4.2: Thermocouple Sensor Design Criterion

Design Aspect	Desired Result	Acceptable Result
Sensitive to millivolt level bias voltages	• 1-5MHz/°C level of sensitivity with an in-situ fabricated thermocouple • Complete isolation between DC and RF circuits	• kHz/mV sensitivity or indeed any recognisable sensitivity • Thermocouple largely unaffected by RF/Microwave interrogation
Insensitive to other stimuli	• Integration method insensitive to heat, humidity, vibration, etc.	• Cross sensitivities less than a factor of 10-100 higher than mV sensitivity
Capable of operating in aerospace settings	• Integration method can operate in ±200°C • Integration method is robust to radiation, outgassing, etc.	• Device capable of operating in a controlled laboratory setting
Easily Fabricated In-situ	• Device can be fully printed in-situ using inkjet and/or aerosol technologies	• Device can be fabricated via any known means
Fully Wireless design	• Device has comparable wireless characteristics to other chipless RFID sensors	• Wired testing of the device is sufficient
Fully Passive design	• No battery required • Only one thermocouple required	• Multiple thermocouples allowed

This section highlights some promising methods that could be used to transform the DC output of the thermocouple into a measurable characteristic that a chipless RFID tag can detect. Before this discussion begins, the work of Dionne et al. in Reference [4] should be noted and discussed further. This work utilised a varactor diode to control the capacitance of

a resonant antenna and thus allow a DC signal to alter the resonant frequency of the tag. This tag has been tested at voltages up to 3V and had a sensitivity of 1.67MHz/V with a base frequency of 22.5MHz. Varactor diodes are diodes which usually have a specific junction profile and when operated in a reverse bias configuration, the junction capacitance of the device can be controlled by the reverse bias voltage level. Many other works discuss these classic semiconductor devices in far more detail and avid readers are pointed towards the books [21] and [22].

The work presented in this section avoids the need for semiconductor devices for the reasons outlined in Chapter 2 and because of the challenges that arise when attempting to deposit such a device in-situ. Furthermore, the use of this device does not allow for a complete isolation between the AC and DC circuits as the DC source is protected by a large resistance in the referenced design. Such a design, regardless of the limitations of semiconductor materials, may not be suitable for thermocouple interfacing as there is no protection against microwave signals from causing unwanted heating effects within the thermocouple. This chapter will focus on a finding an alternative stimulus sensitive material for this application as opposed to enhancing the aforementioned design as several alternative design approaches may be more suitable. Before a potential candidate material/approach is presented, it is worth mentioning that several other avenues were also considered but they were omitted from further analysis due to underlying shortcomings. These avenues include the use of shape memory alloys and ferrite materials, but both of these approaches were neglected given their large DC input power requirements. Three different approaches have been discussed in Appendix G, but the chosen approach is to make use of the ferroelectric material, Barium Strontium Titanate (BST).

4.5.2 BST-Based Sensor Development and Testing

Although BST was a promising material to use for the thermocouple-based sensor, there was no direct proof that it would not also have a relatively significant threshold voltage. From reviewing the literature on LCPs discussed above, it can be seen that the use of a seed layer alters the initial rotation angle of the inner dipoles. This does not change the large threshold voltage, but this behaviour is very different than how external materials/fields affect BST. In BST, the interfacial layers in the lattice are indeed affected by the underlying substrate material but their effect does not propagate through the entire material, as is found in LCPs. The proof of this is found in the way that said interfacial layers are modelled as "dead layers" when estimating the tangential dielectric properties of the material [23]. This would suggest that each dipole is coupled to its neighbours to a greater degree in the LCP materials than in BST. Based on the difference in interfacial modelling and the sub- one volt testing performed

by Kabir in [24], BST was chosen as a potential material to integrate chipless RFID and thermocouple technology.

As mentioned earlier and further discussed in Appendix G, there are significant fabrication challenges associated with the use of ferroelectric materials such as BST within chipless RFID sensor designs. Fortunately, ST Microelectronics has the STPTIC [25] range of BST-based varactors that can mitigate this challenge. The design in Figure 4.3 was implemented with the varactor and relevant traces placed on the opposite layer of the Printed Circuit Board (PCB) to that of the λ/4 SIR. Preliminary simulations were also performed to ensure that only one propagation mode occurred, to locate the new resonant regions and the estimated voltage sensitivity. This type of analysis can be performed, like the RCS simulations, with simulation packages such as Ansys HFSS (as used in Chapter 3) or using CST Microwave studio, as seen in [19]. Table 4.3 depicts the general specifications of the resulting circuit.
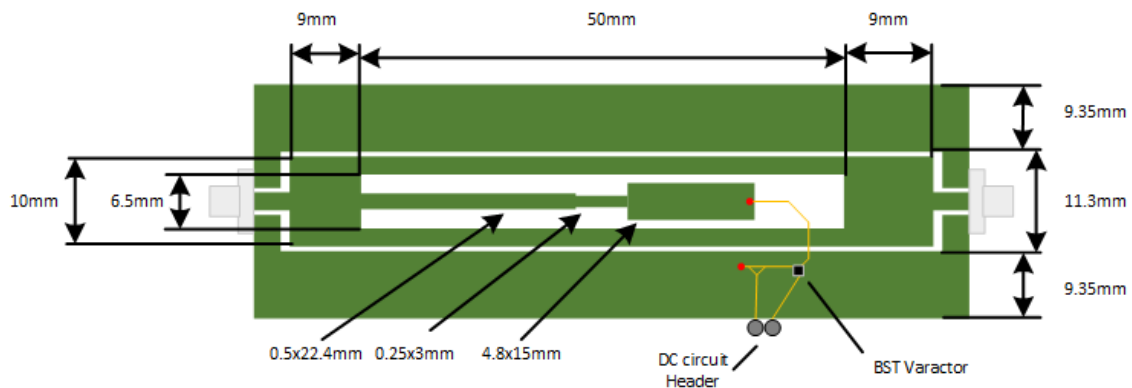
Figure 4.3: BST-Loaded SIR Circuit Diagram – from "Proof of Concept Novel Configurable Chipless RFID Strain Sensor." by McGee et al., MDPI, CC BY 4.0 [26]

Table 4.3: BST-Based Sensor Specifications – from "Proof of Concept Novel Configurable Chipless RFID Strain Sensor." by McGee et al., MDPI, CC BY 4.0 [26]

Specifications
Dimensions: 82 mm × 36 mm (excluding connectors)
PCB Material: Rodgers RO4003
Resonant Region(s): 235 MHz and 1090 MHz upwards
DC Voltage Range: 1–24 V [25]

The resulting device can be seen in Figure 4.4 below. The device is quite compact as the relevant antennas have been omitted from the design. This design choice was made because

the initial resonant region is at quite a low frequency, but since this is a proof-of-concept implementation, this is of negligible importance. A more pragmatic reason why the antennas were omitted was that it allows for wired testing of the sensor which removes the potential for wireless channel interference within the test results.

Figure 4.4: Resulting Wired Sensor – from "Proof of Concept Novel Configurable Chipless RFID Strain Sensor." by McGee et al., MDPI, CC BY 4.0 [26]

Effects of Large Bias Voltage

Initial testing was performed with an AimTTi signal generator to apply the relevant DC signals to the DC side of the Very High Frequency (VHF)/Ultra High Frequency (UHF) circuit. The NanoVNA V2 was used in conjunction with a laptop to record the scattering parameters whilst the DC bias voltage was changed. The STPTIC devices support a maximum voltage of 24 V but testing was only done here between 0-2.5 V as the device performance in this range was more relevant. Figure 4.5 depicts the test setup used during testing.
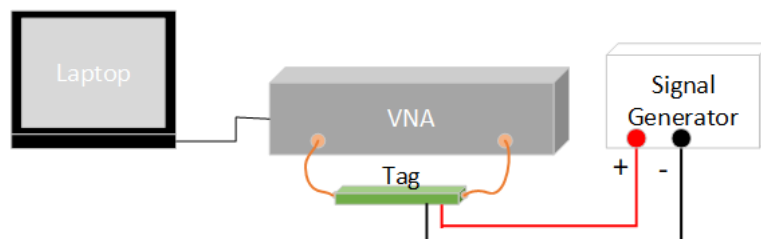
Figure 4.5: BST Circuit Test Setup Diagram – from "Proof of Concept Novel Configurable Chipless RFID Strain Sensor." by McGee et al., MDPI, CC BY 4.0 [26]

The DC voltage sensitivity of two different instances of the sensor design can be seen in Figure 4.6 below. From this Figure, it is clear that the device is clearly bias voltage sensitive, and the performance is repeatable across different sensor implementations. The results found in this

Figure have also been used in Chapter 5 which discusses the concept of a time-varying stimulus and the challenges it represents.
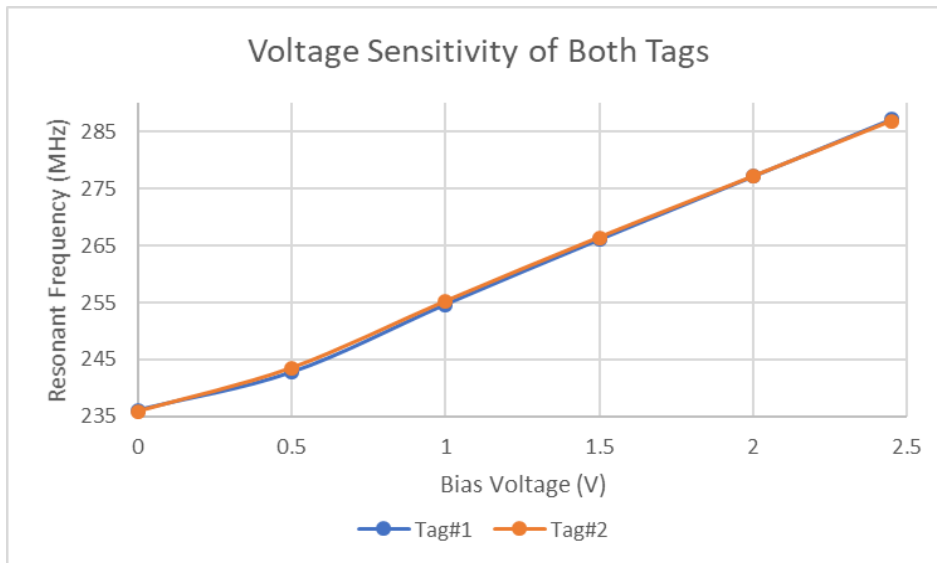
Figure 4.6: Voltage Sensitivity of Two Different Implementations – from "Proof of Concept Novel Configurable Chipless RFID Strain Sensor." by McGee et al., MDPI, CC BY 4.0 [26]

Thermocouple-Based Device Biasing

A low-cost K-Type thermocouple was sourced (RS:363-0250 [27]) which was initially tested using an oven and a Fluke multimeter to assess its thermoelectric response. Figure 4.7 depicts the response curve observed during device testing. Of importance to this discussion is that the DC voltage remains below 10mV which is far below the previous testing limits of the STPTIC varactors [24].
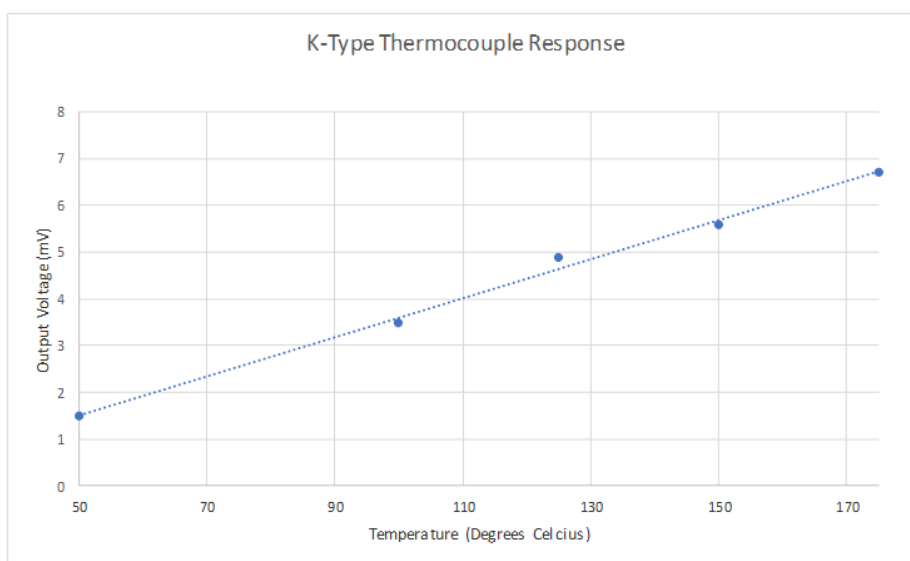
Figure 4.7: RS K-Type Thermocouple Response Curve – from "Proof of Concept Novel Configurable Chipless RFID Strain Sensor." by McGee et al., MDPI, CC BY 4.0 [26]

The next step was to add the thermocouple to the DC side of the BST-based sensor. To test the resulting device, the test setup seen in Figure 4.8 was used. This consisted of a temperature-controlled furnace/oven (MagaTherm MT1200) along with the Fluke multimeter and a fixed IR-based thermometer. The multimeter was used to ensure that a valid voltage output was coming from the thermocouple and the thermometer was used to monitor the temperature of the sensor at a fixed location. The same VNA and computer setup described earlier was used to perform the relevant VHF/UHF tests.
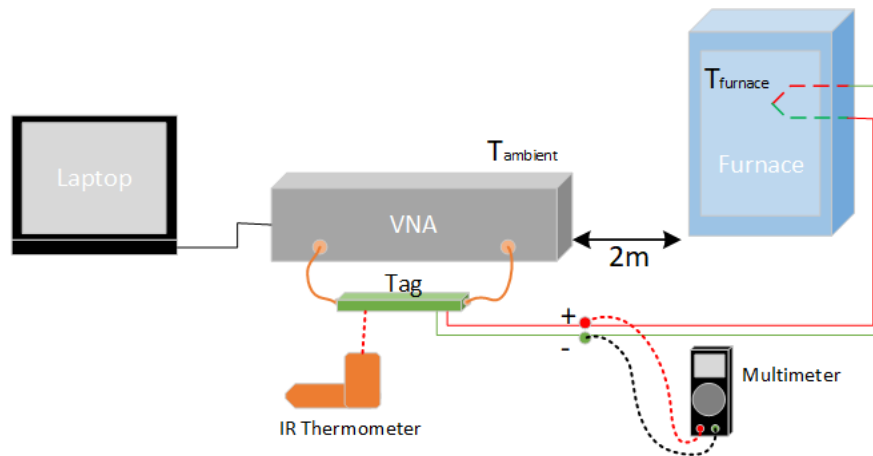
Figure 4.8: Thermocouple-Based Testing Setup for BST Tag– from "Proof of Concept Novel Configurable Chipless RFID Strain Sensor." McGee et al., MDPI, CC BY 4.0 [26]

Initial temperature testing revealed only slight changes in response curves so polynomial curve fitting was used to enhance the accuracy and stability of the results gathered. More details on accurate feature extraction of chipless RFID sensor responses can be found in Chapter 5. Table 4.4 depicts the quality of fit achieved for each of the datapoints presented in the graph in Figure 4.9. This figure reveals a rough sensitivity estimate on the order of 2.9kHz/°C.

Table 4.4: Curve Fitting Accuracies for Thermocouple-Induced Datasets – from "Proof of Concept Novel Configurable Chipless RFID Strain Sensor." by McGee et al., MDPI, CC BY 4.0 [26]

Temperature (°C)	Polynomial R^2 Value
50	0.9713
77	0.9425
100	0.9846
135	0.9784
155	0.9895

180	0.9969
200	0.9948
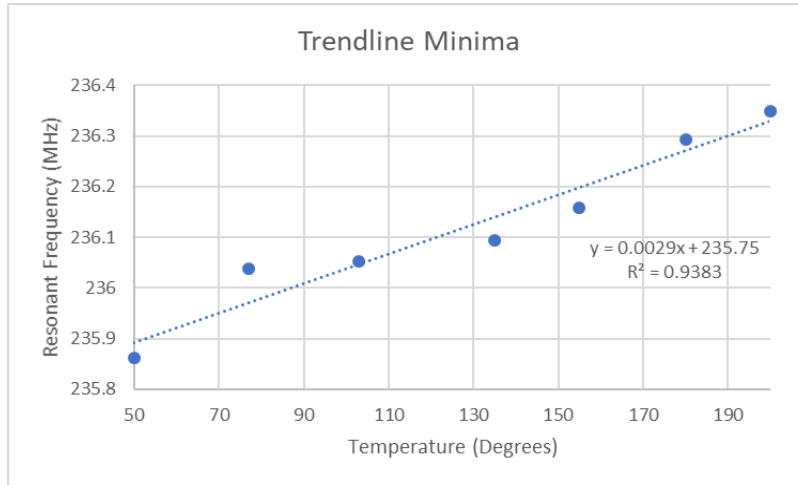
Figure 4.9: BST Tag with Integrated Thermocouple Response Curve – from "Proof of Concept Novel Configurable Chipless RFID Strain Sensor." by McGee et al., MDPI, CC BY 4.0 [26]

Additional testing revealed inconsistent results and further exploration suggested that these results were dependent on the ambient temperature of the sensor. Equation 4.1 to Equation 4.3, found in the work of McGee et al. [26], depict the sensitivity of the device to different ambient temperatures. Overall, this initial testing was largely unsuccessful at demonstrating a reliable sensor performance and the next section was compiled to explore stability issues associated with this device further. Regardless of the stability concerns associated with the above results, the sensitivities achieved with this setup are extremely low and it may therefore not be suitable for a realistic chipless RFID -based SHM system. With that being said, it is the only method in the known literature that achieves this task without the use of semiconductor materials.

$$19.7° \text{ C: MHz} = 0.0652(\text{mV}) + 236.11 \qquad (4.1)$$

$$19.8°\text{C: MHz} = 0.0378(\text{mV}) + 236.07 \qquad (4.2)$$

$$20.0°\text{C: MHz} = 0.0179(\text{mV}) + 235.99 \qquad (4.3)$$

Impact of Device Heating

In an earlier section, basic thermocouple integration into chipless RFID was attempted. There were some thermal stability concerns with the resulting device and more generally speaking, the resulting device had an inadequate sensitivity. One issue of concern was that variations in ambient temperature on the order of 0.1°C had a dominating effect on the response from the sensor. Observations during testing revealed that the grounded parts of the NanoVNA V2_2

124

Vector Network Analyser (VNA) heated up significantly during operation. This effect also was observed during normal device operation. To remove the effects causing significant levels of ambient temperature fluxuations, the thermocouple was replaced with a signal generator (Aim TTi) and the HP8753D VNA was used instead of the portable VNA. Testing was done in an air-conditioned room and subsequent testing was performed under these conditions. The null of the S21 curve for several different bias voltages can be seen in Figure 4.10 below. Repeated testing of greater resolution allowed for minimum values to be determined and the relationship between bias voltage and minimum frequency could be determined (as seen in Figure 4.11). These tests were performed with a descending bias voltage so that the effects of ambient fluctuations caused by the VNA would be maximised, if any occurred. This would be the case as the magnitude of heating effects in BST varactors are inversely related to the current bias voltage [28]. No significant effect of this nature occurred with this VNA and consistent, repeatable sensitivity values were achieved.
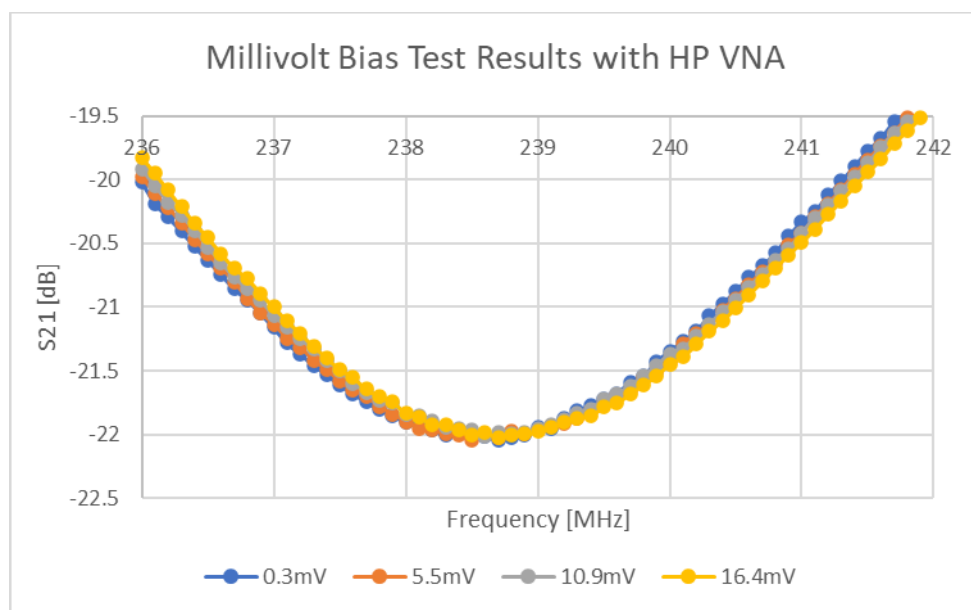
Figure 4.10: Millivolt Bias Effects on SIR Circuit
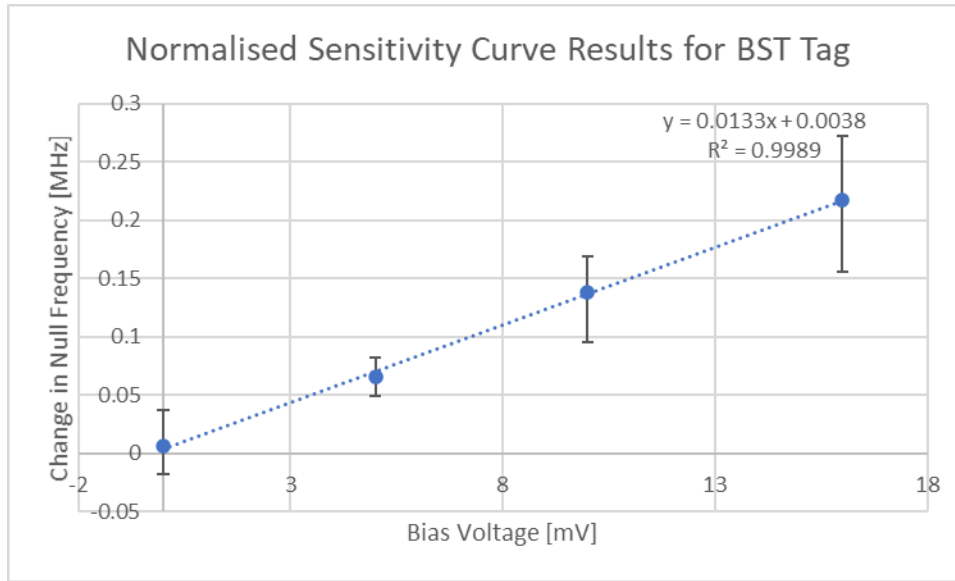
Figure 4.11: Millivolt Bias Effects on Null Frequency

The sensitivity found in this work, which was performed at an ambient temperature of 21.5°C was relatively consistent although perhaps lower than what was found in the earlier publications. Deviations are likely caused by the fact that furnace-based testing favours device testing at ascending thermocouple temperatures which would contribute to increasing the observed voltage sensitivity of the device. This is because increased temperature and bias voltage both lead to a decrease in BST permittivity [23][28].

Repeated testing was also performed with the NanoVNA but the VNA was operated before and after successive testing in the hope that the thermal characteristics of the VNA-sensor system would be in a repeatable, steady state configuration. Repeated testing of both VNAs at a 0mV bias voltage led to differences in the variation of the calculated minimum frequency. These results are displayed in Table 4.5. Variations in the mean null frequency are most likely caused by small differences in the cabling and tag orientation but there is a larger variation with the NanoVNA. However, sensitivities on the order of 13kHz/mV seen in Figure 4.11 far too low to allow for reliable millivolt-level resolution using either VNA but the issue is greater with the NanoVNA.

Table 4.5: Variation in VNA Test Results

VNA	Mean [MHz]	Sample Standard Deviation [kHz]
HP8753D	236.6373 (Tag#2)	7.1
NanoVNA	236.8648 (Tag#1)	11.5

Testing with the pre-heated NanoVNA between 0-100mV led to a stable parabolic sensitivity response where recognisable changes in null frequency do not occur until 40mV. Figure 4.12 depicts these results, where curve fitting has been used to determine the null frequencies, for added resolution.
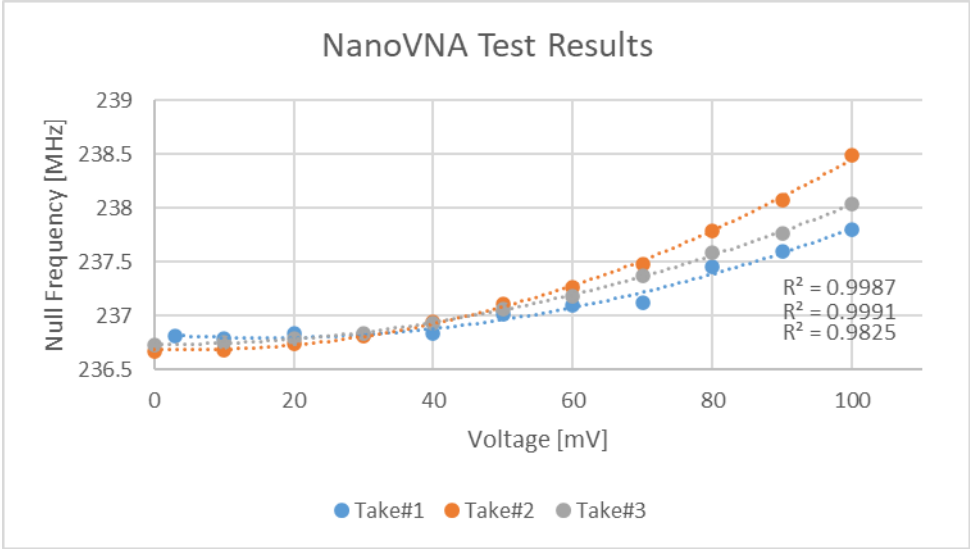
Figure 4.12: NanoVNA Millivolt Bias Results

An approach to mitigate both the effects of ambient temperature fluctuations and weak voltage sensitivity is to bias the device into a more electrically sensitive region of the BST Permittivity-Voltage curve which would also be away from the region where the ambient temperature sensitivity is a maximum [28]. More stable results were obtained with the NanoVNA when the BST varactor was pre-biased with 590mV. Testing of the device over a 35mV window resulted in the curves seen in Figure 4.13. These curves exhibit a much more noticeable change under the influence of millivolt level changes in bias voltage. The minimum of each of these curves is plotted against bias voltage in Figure 4.14.
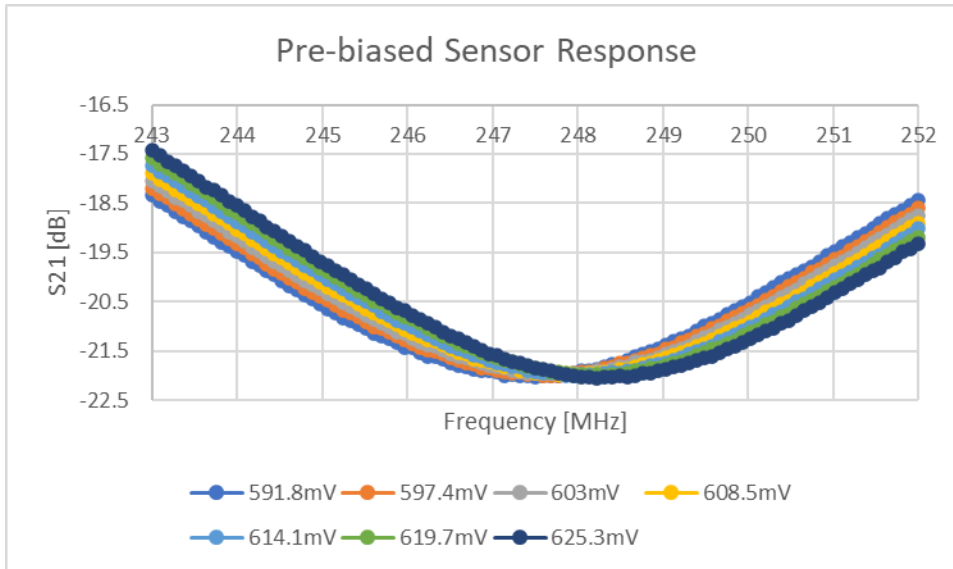
Figure 4.13: Null Curves with Pre-existing 590mV Bias
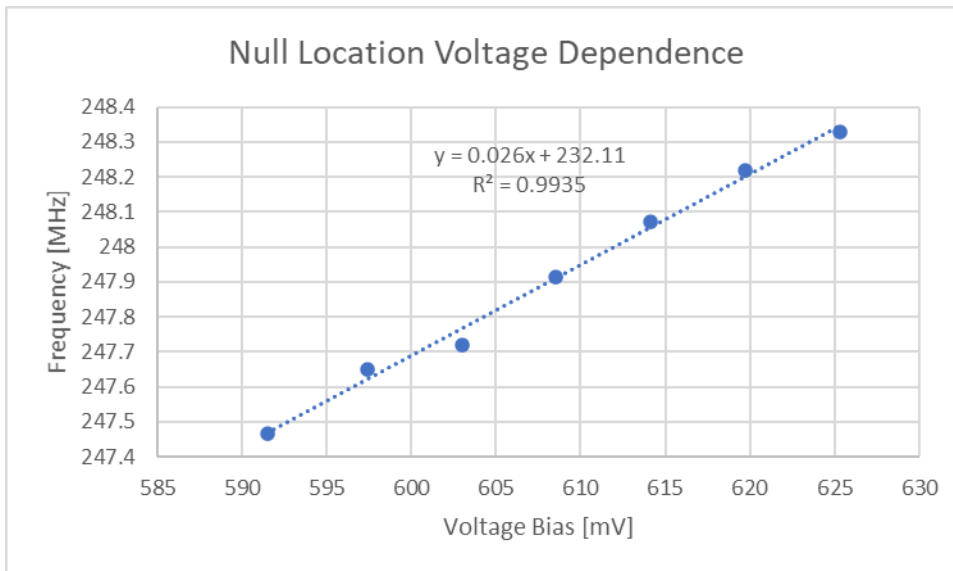
Figure 4.14: Null Millivolt Dependence with 590mV Bias

The results in Figure 4.14 support a claim of a 26kHz/mV sensitivity under the 590mV bias effect. This is approximately twice that found with the base millivolt input and the impact of any possible heating effects from the NanoVNA were not observed during repeated testing.

4.5.3   Example In-Situ Fabricated Thermocouple

Given the fact that this project is concerned with developing sensors that could potentially be printed in-situ, an initial attempt was made at in-situ fabrication of thermocouples onto a paper substrate. The standard thermocouples (J, K, T, etc.) exhibit sensitivities on the order of 40-50µV/°C. In situ fabricated thermocouples can exhibit lower sensitivities than that and thus integration with the BST-based tag discussed above will result a lower sensitivity than that

anticipated earlier. Testing of an in-situ graphite- silver paint -based thermocouple has been performed here with measured sensitivities on the order of 15-17µV/°C (see Table 4.6). The graphite track was formed using a 5B pencil, as characterised in other works [29][30][31] and a low-cost Silver Paint (RS:123-9911 [32]) that were deposited onto standard office paper. Temperature differentials from 0-80°C were achieved using the test setup discussed in subsequent sections. Other works such as those found in [33][34] have demonstrated temperature sensing over a much larger range and do not use graphite, but this work is merely focused on demonstrating proof-of-concept implementations.

Table 4.6: Trendline Results for In-Situ Thermocouples

Take	Sensitivity [mV/°C]	Bias [mV]	R-Squared
1	0.0173	0.0307	0.9803
2	0.0164	0.0383	0.9888
3	0.0150	0.0023	0.9695

4.5.4   Concluding Remarks on Thermocouple Integration Attempt

Perhaps a further work can figure out how to bias the tag up to 600mV, the effects of ambient temperature will need to be accounted for, as the ambient temperature can be expected to vary by much more than 0.1°C. If it is not possible to complete thermocouple integration into chipless RFID, an alternative temperature sensing strategy will be required. Therefore, there is a need to measure ambient temperature within a smaller but non-trivial range of temperatures.

4.6   Simplified Sensor Designs

This section outlines the performance of a basic dielectric-based sensor and alternate designs that make use of other sensing mechanisms. These designs are considered as simplified sensors as their design and construction has focussed on ease of fabrication as a key criterion throughout.

Wired testing was performed using a heat gun that was mounted above the sensor on a metallic stand. The tag was held in place using a separate clamp and a temperature probe was used in conjunction with a Fluke multimeter to measure temperature. This probe was positioned in a consistent position on the top surface of the sensor under test. The use of the heat gun allowed for convective heat transfer to occur onto the exposed top surface of the sensor and test results were gathered once the scattering parameter responses stabilised, which would consistently happen within 1-5 minutes. The presence and/or operation of the temperature probe and heat gun did not result in any noticeable change in the scattering responses. Figure 4.15 depicts the implemented test setup. An important point to make here is that the temperature probe seen in Figure 4.15 does not sit on the clamping device but rather it sits between the fingers of the clamp, and its tip sits on top of the ground plane of the CPW but separated from it by a thin dielectric barrier.
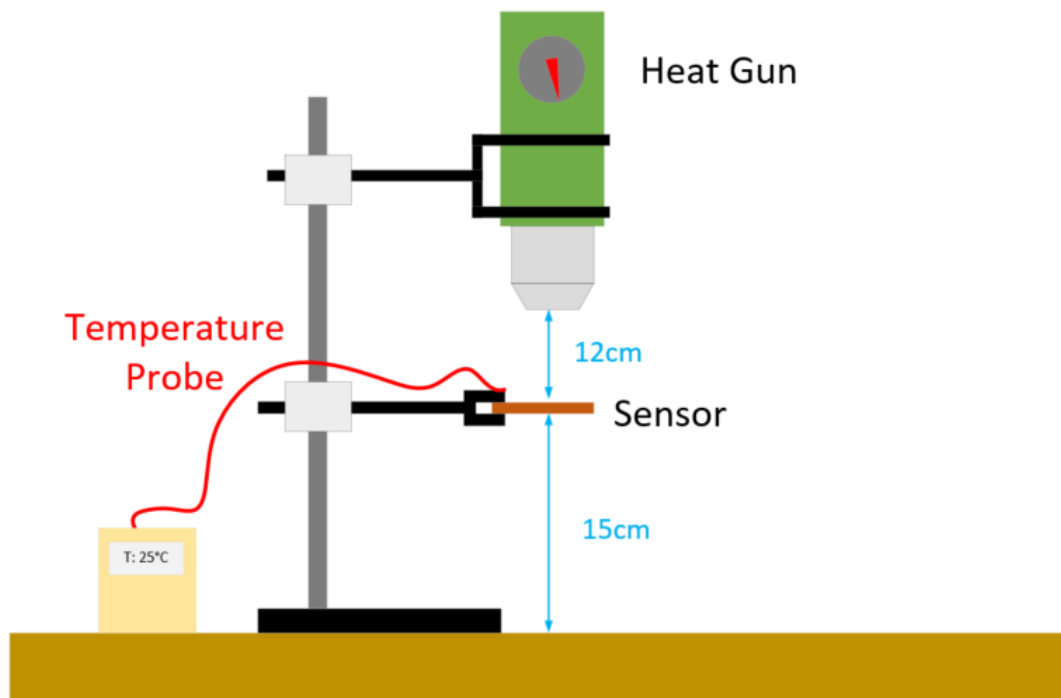
Figure 4.15: Wired UHF Sensor Temperature Testing– from "Use of Chipless RFID as a Passive, Printable Sensor Technology for Aerospace Strain and Temperature Monitoring" by McGee et al., MDPI, CC BY 4.0 [17]

A variety of methods for achieving temperature sensitivity within chipless RFID tag design are discussed below. The most basic approach makes use of temperature-dependent dielectric material properties and this approach is discussed first. This approach is most well-known and serves as a base line from which other approaches can be compared, therefore this sub-section is perhaps more thorough than the subsequent ones. The main alternative sensing method explored in this chapter is to make use of thermo-mechanical effects and several sensor design attempts have been made to improve upon the original dielectric sensors. Other avenues of exploration were also considered but were omitted due to performance inconsistencies. An example of this is the use of KEMET EFG2 [35] microwave absorbing sheets whose implementation resulted in a highly sensitive design but said design suffered from significant levels of thermal aging. Given that very little is known on this material, other than it is a polymer matrix containing magnetic powders of an unknown material, further exploration was abandoned.

4.6.1   Dielectric Constant Based Sensing

Many of the published chipless RFID sensor designs are built in a modular fashion, which consists of a substrate material, a conductive layer and a stimulus sensitive coating. This approach has been taken in the development of VOC sensing, humidity sensing and temperature sensing also [1]. Virtually all of these devices make use of the stimulus dependent dielectric properties of the coating or substrate material to enable the sensing of the desired stimulus. The materials used in other sensor designs include both polymers and other dielectrics such as perovskite materials like BST [36]. Various resonator designs are sensitive to dielectric constant variations and such behaviour can also be seen in Chapter 3 and Chapter 6. For now, this section will focus on the performance of dielectric materials that could be added to such resonator designs.

As mentioned earlier, polymers exhibit temperature dependent dielectric properties and have been used in works such as [5] and [37]. Key references on the topic of the dielectric properties of polymers include that by Blythe and Bloor in and that by Ahmad in [38]. When non-static fields are considered, relative permittivity is expressed as a complex number which includes both an in-phase component (ε'), which is representative of the energy stored per cycle [16] and a lossy (imaginary) component (ε''), which is representative of the energy dissipated per cycle [16]. This expression, found in [16], can be seen in Equation 4.4 and both of the components can vary significantly with excitation frequency.

$$\varepsilon^* = \ \varepsilon' - j\varepsilon'' \qquad\qquad (4.4)$$

Various mechanisms contribute to the total dielectric constant, these include; electron-level displacements, atomic-level displacements and in some cases dipole rotations [16][38]. The latter are likely to be present in some polar polymers as such polymers can have, i.e. side chains/groups branching off the main monomer backbone which may be free to rotate in the resulting polymer [16][38]. The magnitude of the resulting dipole moment depends on the net dipole charge and the degree to which it is free to partially rotate, which is known as steric hinderance. This dipole-based permittivity contribution is very important, as will be discussed later, but its contribution becomes increasingly lossy with excitation frequencies in the microwave range until its contribution disappears, usually below 10^{12} Hertz [16]. A classic model representing this behaviour is the Debye model [16], which assumes an exponential approach to equilibrium upon excitation with a static change in electric field. Said model is described mathematically in [16] and can be seen in Equation 4.5, where the permittivity terms $\varepsilon_0, \varepsilon_\infty$ and ε_s represent the absolute permittivity, along with the permittivity at an infinite and zero(static) excitation frequencies respectively. The other terms, "t" and "τ" represent the time variable and time constant of the model. This can be related back to Equation 4.4 through the expressions seen in Equation 4.6, that have been provided in [16].

$$\varepsilon = \varepsilon_0 \left(\varepsilon_\infty + (\varepsilon_s - \varepsilon_0)(1 - e^{-t/\tau}) \right) \qquad (4.5)$$

$$\varepsilon'(\omega) = \left(\varepsilon_\infty + \frac{\varepsilon_s - \varepsilon_\infty}{1 + \omega^2 \tau^2} \right), \qquad \varepsilon''(\omega) = \left(\varepsilon_\infty + \frac{(\varepsilon_s - \varepsilon_\infty)\omega\tau}{1 + \omega^2 \tau^2} \right) \qquad (4.6)$$

The distinction between polar and non-polar polymers is an important one in the context of temperature sensing as the steric hinderance of the dipolar contribution is highly temperature sensitive [16][38]. The relationship between complex permittivity and temperature is highly dependent on the selected polar polymer and the frequency range of interest [16]. In the case of the real part, the relationship can be highly nonlinear and exhibit regions of positive, negative and near-zero temperature sensitivities [39]. This is of concern to the sensor designer as changes in the sensitivity polarity or deadbands within the sensitivity will result in one sensor response corresponding to multiple possible temperatures. In other cases where a single sensitivity polarity occurs within the entire temperature response, the operating range will be limited by the melting temperature and/or the glass transition temperature, as these occurrences will result in a noticeable change in dielectric properties [16][40]. The dielectric losses can in many cases be highly temperature sensitive in polar polymers [16] and will thus impact the potential read range of the device. The work of Riddle et al. in [39] gives

experimental test results related to the temperature dependence of a wide variety of common polymers in the microwave region.

Fabrication of temperature sensitive polymers can easily be done off-site but this work has placed some degree of emphasis on fully printable sensors. A wide variety of polymers can be fabricated in-situ via FDM-based 3D printing, direct moulding and other such methods. A more pressing concern is that just because a polymer is polar, that does not mean it exhibits temperature-dependent dielectric properties in the microwave region. A classic example is the easily printed Polylactic Acid (PLA) polymer whose $T - \varepsilon_r$ relationship drops to near zero in the microwave region, despite its significance at lower frequencies [41].

This particular work has made extensive use of the commonly found PCB material, FR4. This material is a fiberglass-resin composite that like many other PCB materials has a temperature dependent dielectric constant. This dependency will most likely differ over a range of different FR4 suppliers but its behaviour is believed to be related to the temperature dependency of the dielectric constant of various epoxy resins [42][43]. Similar behaviour could in theory be expected from many aerospace-based composites that commonly rely on epoxies as a binding material [44]. Future implementations could make use of in-situ deposited epoxy layers but for now, the premade version will be used.

Other designs have relied on the impressive dielectric properties of perovskite materials such as BST [36] to form highly sensitive chipless RFID temperature sensors. As mentioned earlier in this chapter, materials which have a perovskite structure, such as Barium Titanate (BTO) [38], can under some conditions form an electric dipole within the unit cell. Said conditions, in the case of BTO involve the unit cell changing from a cubic one to a tetragonal one [38] with a resulting dipole forming in the centre of the cell. This cubic cell, seen in [45], is depicted graphically in Figure 4.16 below. Within a certain temperature range (5-120°C) [38], the aspect ratio of the unit cell changes, with the centrally based Titanium (Ti_{4+}) moving upward in the Y-direction whilst the Oxygen cations (O_{2-}) above and below it move downwards [38]. The four other oxygen cations also move down with respect to the centroid of the cell and the resultant is the formation of a considerable dipole within the unit cell. Sensors made using these materials have boasted large dielectric constants [38], modest temperature sensitivities and are mechanically robust to temperature extremes.
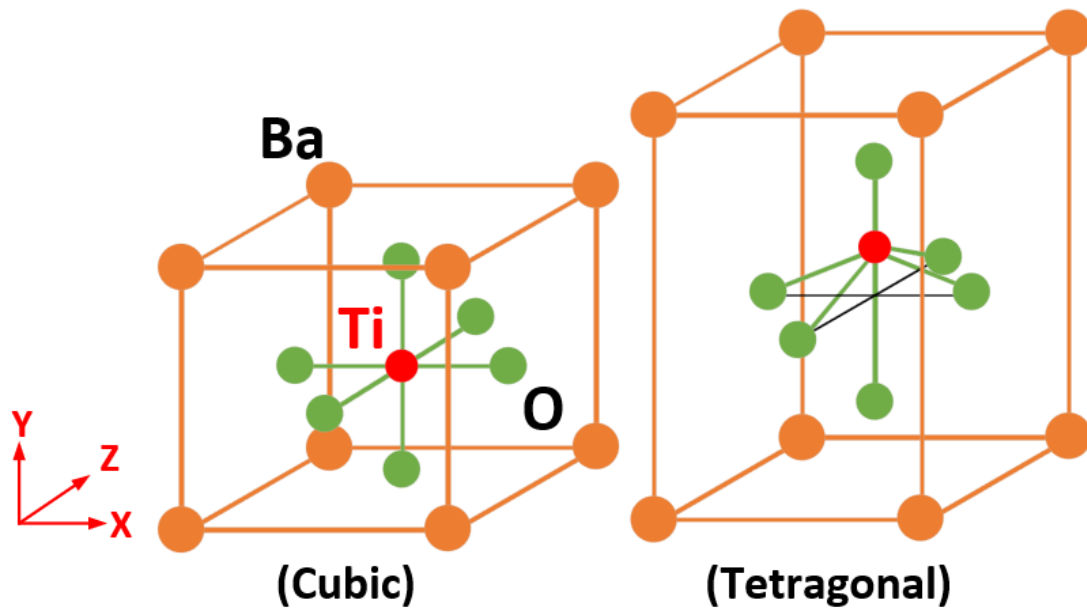
Figure 4.16: Wired Microwave Circuit Temperature Response – Adapted from "Recent Criterion on Stability Enhancement of Perovskite Solar Cells" by Hasan et al., MDPI, CC BY 4.0 [45]

Care is needed during fabrication to ensure that the depositions are operating within their paraelectric region (above the Curie temperature). This is a region in which the dielectric constant is temperature dependent and can be tuned in BST with additives and in BTO using similar methods. Operation of BST or other similar material below -40°C may not be possible [36] as this is the lower limit for the Curie Temperature for BST. The benefit of these ceramic materials is that they inherently boast higher operating temperatures than most/all polymers. These materials have not been explored as part of this work, due to the significant challenges that are present with their construction/implementation under normal conditions and with the enhanced difficulties in attempting to fabricate these materials in-situ. Appendix G discusses the fabrication challenges associated with these materials in a greater depth. Furthermore, although a sensor design could have made use of these materials, there are issues regarding sensitivity [46] and operating temperatures [38][46] that will require specialised effort to overcome.

Initial Designs

This section sets out to explore the most basic way to give temperature sensing capabilities to chipless RFID tags. This involves the use of a substrate whose dielectric properties are temperature sensitive. With this in mind, the λ/4 SIR tag design described in Figure 4.2 was etched out on an copper clad FR4 substrate, whose dielectric constant is known to be temperature and humidity [47] sensitive. Figure 4.17 reveals the scattering response of this wired tag for various temperatures.
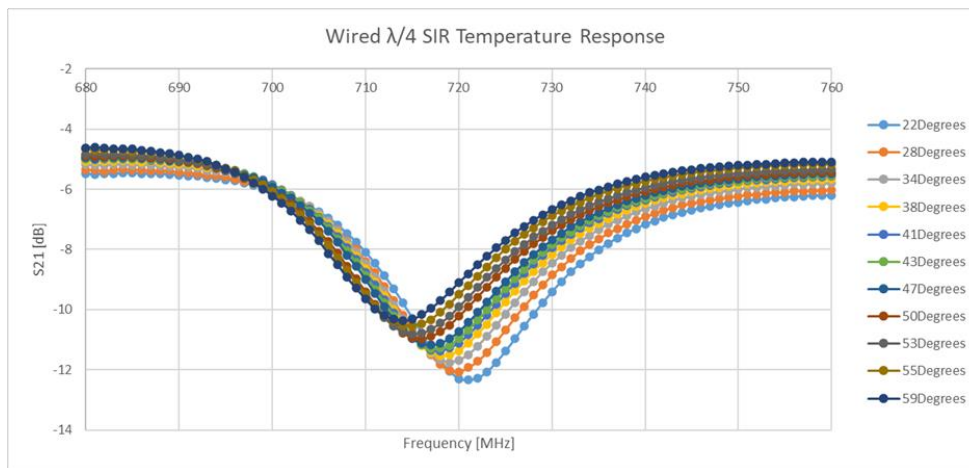
Figure 4.17: Wired Microwave Circuit Temperature Response

The resulting null frequencies recorded during testing are plotted against temperature in Figure 4.18. The results clearly demonstrate that this device is temperature sensitive, at least in the range of 20-60°C.
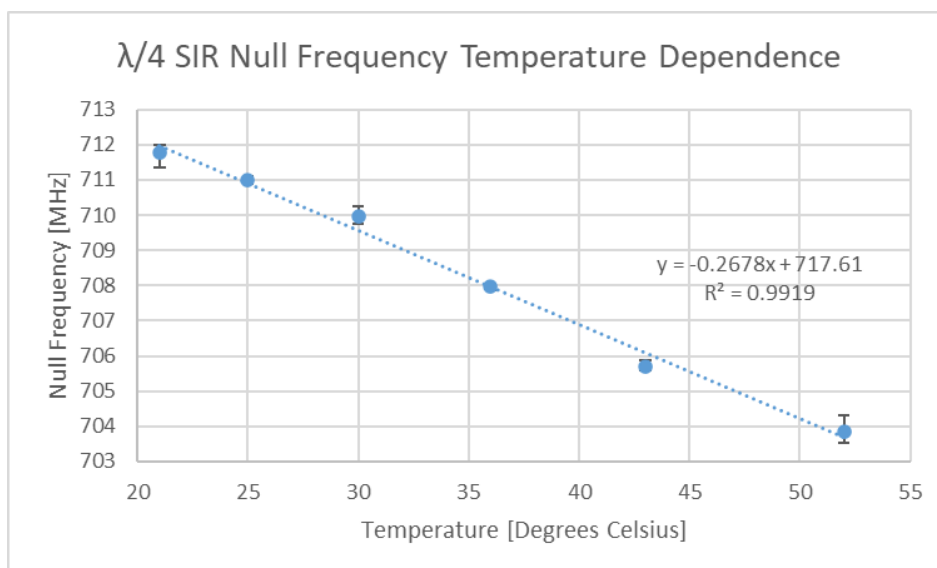
Figure 4.18: SIR Circuit Temperature Sensitivity– from "Use of Chipless RFID as a Passive, Printable Sensor Technology for Aerospace Strain and Temperature Monitoring" by McGee et al., MDPI, CC BY 4.0 [17]

Normalising these sensitivity results changed them from approximately 0.268MHz/°C to 0.0376%/°C and comparing these results with those found in Table 4.1, places this sensor design in fifth place out of nine.

FR4 SIR Time Domain Response

An important aspect of the performance of any sensor is the rate at which it can respond to a change in stimulus level. Although the test procedure used in this work is somewhat simplistic, it is in some way representative of a realistic scenario. Therefore, the aforementioned method was performed again but with a reference sensor located beside the RFID device. The reference sensor was a Negative Temperature Coefficient (NTC) thermistor (RS:210-4374 [48]) whose resistance was recorded in-tandem with the VNA test results. With the two datasets normalised as being a percentage of their final value, the data presented in Figure 4.18 was created. The curves seen in Figure 4.19 represent the time domain response of these devices to the incoming stimulus, both of which show a transient phase that appears to show a decaying exponential type of growth and a subsequent steady-state stage which remains constant. From this Figure 4.19, it is clear that the thermistor response is quicker but that the larger FR4 sensor is not as slow as initially expected. One final point to be made in relation to Figure 4.19 is that the final value is achieved (>97%) for both devices at times exceeding 400 seconds.
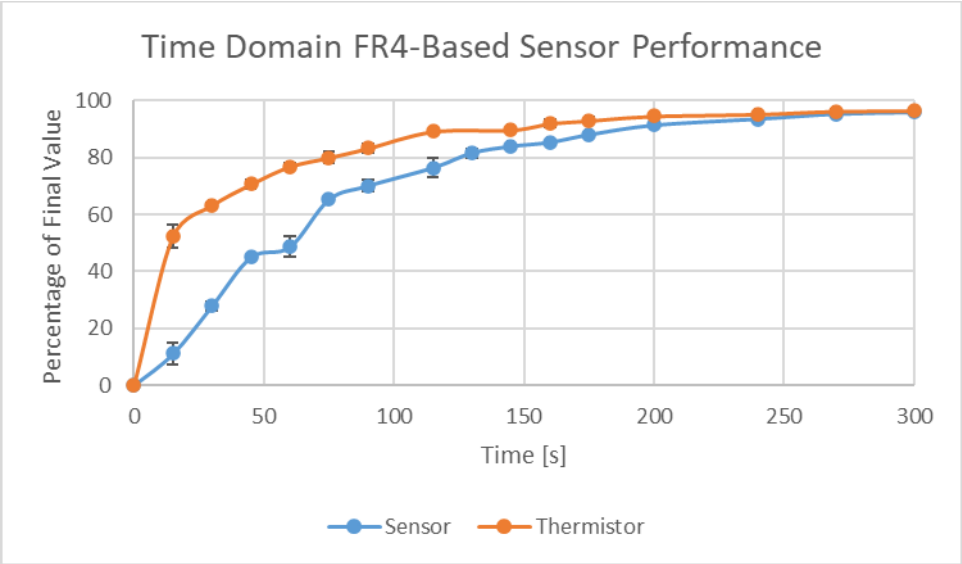
Figure 4.19: Time Domain Stimulus Response of SIR Circuit

The general heat equation [49] makes use of a material dependent coefficient referred to as Diffusivity. This coefficient (described in Equation 4.7) describes the time-dependent heat diffusion through a material, in terms of more basic material properties. All material

properties relevant to this discussion are described in Table 4.7. In the case of dielectric-based temperature sensors, the time needed for the temperature-sensitive dielectric to respond will be heavily related to this coefficient as the entire dielectric will need to reach its final temperature for the sensor output to become stable. Much of the subsequent discussion on sensor design will refer back to Equation 4.7 from [49] as a means of roughly estimating the time response characteristics of the developed designs. Relevant thermal properties of common material types can be found in Table 4.8.

$$Diffusivity = \ \alpha = \ \frac{k}{\rho c} \qquad (4.7)$$

Table 4.7: Description of Heat Transfer Properties [49][50]

Parameter	Name	Description
h	Heat Transfer Coefficient	A measure of how well heat energy is being transferred from the source to the system under test
V	Volume	Object volume
A	Area	Area exposed for heat transfer
k	Thermal Conductivity	A measure of how well a material can transfer heat
ρ	Density	Object density
c	Specific Heat Capacity	A measure of how much heat energy is required to raise the temperature of the material
T	Time	Time interval since system input change
T	Temperature	Temperature at this instant (Time = t)
T_0	Initial Temperature	Start temperature of the system
T_∞	Final Temperature	End temperature of the system

Table 4.8: Thermo-mechanical Properties of Common Materials

Material Type	C [J/kg.K]	k [W/m.K]	ρ [kg/m^3]
Metals	100-900 [49][50]	50-500 [49][50]	2000-20000 [49][50]
Polymers	1000-2000 [49][50]	0.1-0.3 [49][50]	1000-3000 [49][50]

A popular approach taken to characterise the time domain response of temperature sensors is to make use of a metric called time constant (τ). In essence, it is a measure of the time needed for the device to reach approximately 63% of its final value and is valid for exponential-type responses. This metric is valid for systems that can be characterised using the Lumped Capacitance Model [49] and it is sometimes listed in temperature sensor datasheets. Under the influence of convection-based heat transfer the validity of this model can be characterised using the Biot number [49] (see Equation 4.8 found in [49]), which should be less than 0.1 for the assumption to be valid. With that being said, comparative exponential curve fitting to the sensor response datasets revealed a strong exponential effect in the sensor response with average magnitude deviations below 0.87%, therefore the usage of time constant in this analysis is considered a valid one.

$$Biot\ Number = \frac{h(^V/_A)}{k} < 0.1 \tag{4.8}$$

The Lumped Capacitance Model equation described in [49] can be seen below in Equation 4.9 and allows for the calculation of the instantaneous device temperature based on the parameters outlined in Table 4.7 above. In this equation, the expression for the time constant is written in terms of its constituents but its isolated value can be calculated using Equation 4.10 [49].

$$\frac{T - T_\infty}{T_0 - T_\infty} = e^{-\left(\frac{hA}{\rho cV}\right)t} \tag{4.9}$$

$$\tau = \frac{c\rho V}{hA} \tag{4.10}$$

Repeated testing revealed sensor time constants of approximately 69 seconds the thermistor had a time constant of around 37 seconds. These results along with the information in Table 4.8 above allow for a basic characterisation of the response times of various temperature sensor implementations found in this chapter. Interpolation was used to enhance the accuracy of these results.

The basic SIR sensor is by no means optimised in order to achieve the minimum possible the time constant of the device, but this result is a good starting point towards estimating a future optimised implementation. For now, it will be assumed that the time constant can in some way be enhanced through alterations of the sensor geometry which can take the form of both geometric and material selection alterations. Software tools such as Ansys Mechanical are suitable for performing such an exploration.

Wireless FR4-Based Sensor

As this overall work is concerned with developing wireless passive sensors, a non-wired implementation of the above was implemented. This was developed and tested so as to show that the FR4-based approach taken above can be implemented into a highly compact and wireless sensor.

The ELC geometry described in Table 4.9 was used as the basis of an enhanced version of the FR4-based temperature sensor explored earlier. This design could be interrogated wirelessly as its resonant frequency was within that of the available Ultrawideband (UWB) interrogation antennas. Testing was performed using a bistatic radar configuration with the sensor located 10-20cm between the two antennas, which were separated by 20-40cm. Similar to the earlier tests, a heat gun was used to perform sensor heating. To shield the interrogation antennas from the heat source, the gun was located closer to the sensor than the nearby antenna and a physical shield was used to protect the other antenna from significant heat transfer. Under these test conditions, the background measurement varied by only insignificant amounts during device heating.

Table 4.9: FR4-Based ELC Sensor Details– from "Use of Chipless RFID as a Passive, Printable Sensor Technology for Aerospace Strain and Temperature Monitoring" by McGee et al., MDPI, CC-BY-4.0 [17]
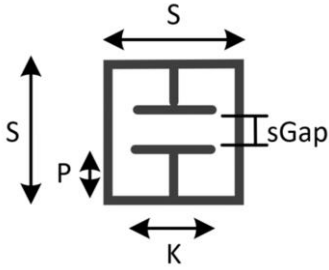
Geometry	Variable	Value [mm]
	S	20
	sGap	2
	P	6
	K	10
	Conductor Width	1.5
	Substrate Length	40
	Substrate Height	27
	Substrate Thickness	1.6
	Substrate Material	FR4

Figure 4.20 below depicts the initial null frequency temperature response of the ELC-based sensor. The device is clearly more sensitive than that of the SIR circuit, although the fact that the frequency range is considerably different may be playing a key role in this enhancement.
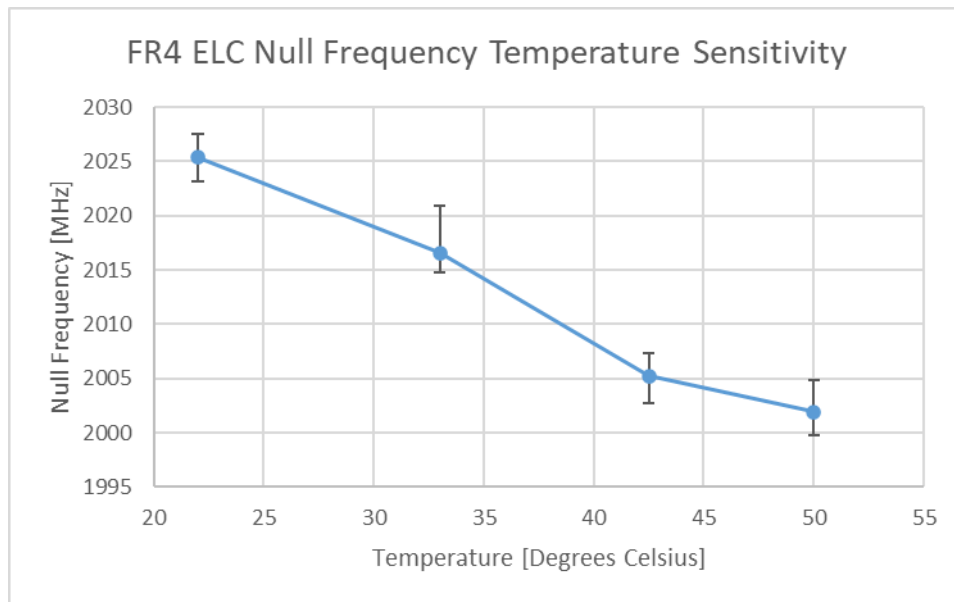
Figure 4.20: FR4 ELC Sensor Temperature Sensitivity Curve

Comparing the test results observed above to that seen in Table 4.1 was performed by normalising the sensitivity results from approximately 0.59MHz/°C (based on a linear trendline) to 0.032%/°C which puts this device in fifth place out of the nine sensors currently in the table. From the results seen in Figure 4.20, it can be seen that the lower temperature datapoints exhibit a high level of variance. Given the stability of the FR4 SIR temperature tests, it would seem to be the case that challenges within the wireless setting

4.6.2 Alternate Method: Thermal Expansion Based Sensing

An alternative approach to the use of dielectric constant variations is to make use of thermal expansion. This method has been used in a wide multitude of classical sensors including the classical mercury-based thermometer. Virtually all materials exhibit expansion when heated and a list of the thermal expansion coefficients of common material types can be found in Table 4.10. These values are usually temperature-dependent but unlike dielectric constant variations in polymers, thermal expansion is a more stable and predictable behaviour over a wide range of temperatures [39]. Furthermore, thermal expansion methods can in some cases be made out of humidity insensitive materials and unlike polymers, the temperature induced effects in thermal expansion systems are independent of the operating frequencies of the chipless RFID tag. An important point to be made here is that although a bimetallic strip may operate in a way that is humidity invariant, the environments dielectric constant may vary and still cause a significant sensor cross-sensitivity.

Table 4.10: Thermal Expansion Coefficients for Common Materials

Material Type	Coefficient of Thermal Expansion (CTE) (Linear) [10^{-6} °C^{-1}]
Metals	1-20 [50]
Polymers	80-300 [50]
Fiber- Reinforced Polymers	0.5-30 [50]

Although the aforementioned advantages may make thermal expansion a highly suitable for temperature sensing over a large stimulus range, a common shortcoming of this approach is that the thermal time constants are usually larger than that found with other approaches [51]. This subsection will design and test two different approaches to using this method as the basis of a chipless RFID temperature sensor.

Bi-material Expansion

A tried and tested way to measure temperature is through the use of a bimetallic strip [51]. This device comprises of two materials (usually metals) that are bonded together, which have different thermal expansion coefficients. Upon heating the device bends/deflects as the two constituent metals expand to differing degrees. A pre-existing implementation of a bi-material strip into chipless RFID can be seen in the work of Thai et al. in [52] and in various other works listed in Table 4.1. Figure 4.21 depict the manner in which it has been implemented in [52], where the bimetallic strip is used to alter one of the capacitances of the split ring resonator structure.

(a)   (b)
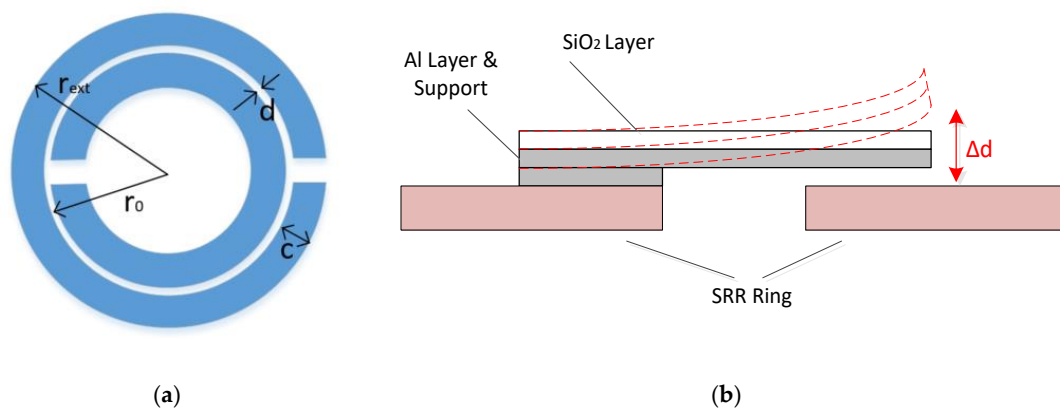
Figure 4.21: SRR(Split Ring Resonator) and Bi-material system – McGee et al., MDPI, CC BY 4.0 [1]

As mentioned earlier, a variety of chipless RFID temperature sensors have made use of bi-material strips and have achieved impressive sensitivity levels of up to 6.8MHz/°C [7]. Operating temperature ranges of the resulting devices depend very heavily on the fabrication method and on the selected materials.

Given the fact that this is a classical means of measuring temperature, the behaviour of this device has been long since characterised. Key references include that of Timoshenko [53] from which presents an equation to calculate the radius of curvature of a deformed bimetallic device (See Figure 4.22) as a function of geometric, mechanical and thermal variables. The goal of any such bi-material implementation is to minimise this variable so that the maximum level of deflection occurs within the design. This formula, presented in [53], can be seen in Equations 4.11 and 4.12, and the relevant parameters are described in Table 4.11. Interpretation of this formula is aided by the diagrams in Figure 4.22(a) and Figure 4.22(b) below.

(a)

(b)
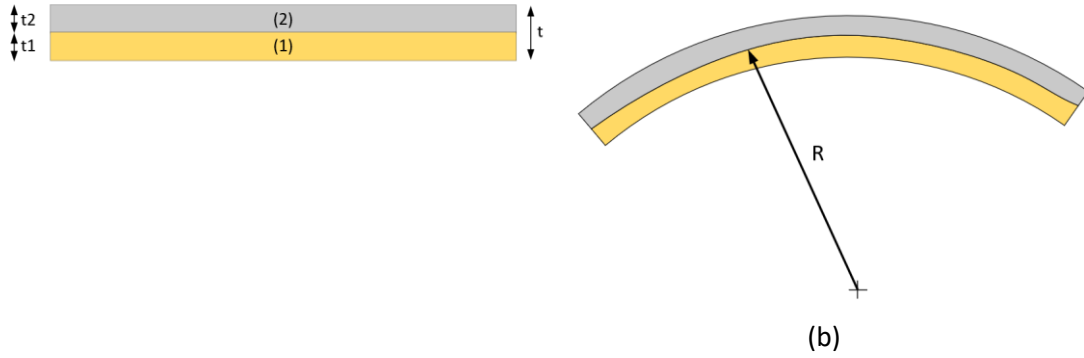
Figure 4.22: Bi-material System in Rest State (a) and in Heated State (b)

$$R = \frac{t\left(3(1+m)^2 + (1+m)\left(m^2 + \frac{1}{mn}\right)\right)}{6(\alpha_2 - \alpha_1)(T_{HIGH} - T_{LOW})(1+m)^2}$$
(4.11)

$$where \; m = \frac{t_2}{t_1}, n = \frac{E_2}{E_1}$$
(4.12)

Table 4.11: Relevant Thermal/Mechanical Properties

Parameter	Name	Parameter	Name
t	Thickness	E	Young's Modulus
α	Linear Thermal Expansion Coefficient	T	Temperature

Bi-material SIR Loading

Similar to the other designs seen in both literature [19][26] and throughout this work, a bi-material strip was added as a loading element to a resonator, in this case, to the end of a λ/4 SIR circuit. This implementation can be seen in Figure 4.23 and consists of a 10x3.5mm wide strip consisting of a 300μm copper layer with a cyanoacrylate adhered layer of 2x200μm Poly(methyl methacrylate) (PMMA). The strip was elevated with an additional block of 300μm copper and solder is added to the section of the CPW ground plane that the strip sits above. This is to ensure that the strip is more strongly coupled to the circuit ground as opposed to the central element of the CPW.

144
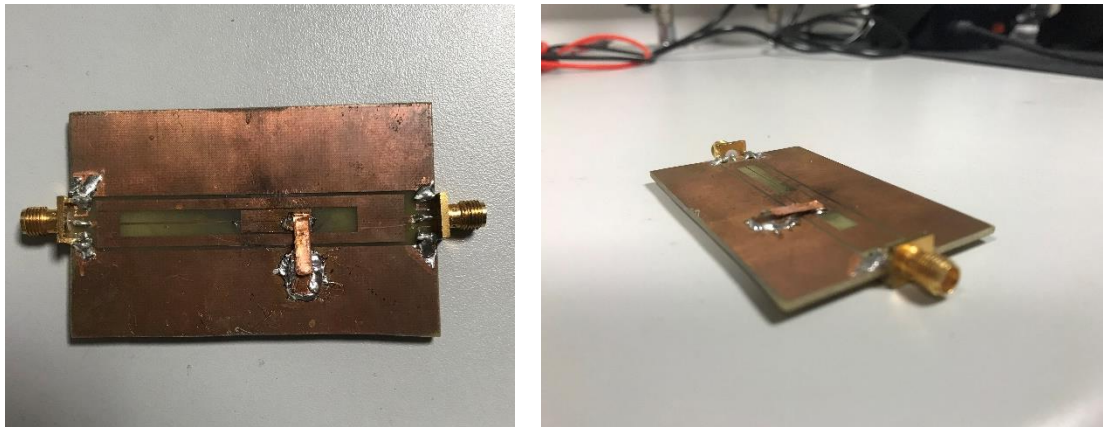
<center>(a)   (b)</center>

Figure 4.23: Images of Bi-material Loaded SIR Circuit

Initial testing of the original device involved heating the circuit from the bottom and measuring the gap between the bi-material strip and the ground plane using feeler gauges. The results of this test can be seen in Figure 4.24. Testing was initially performed with the heat source applied to the bottom of the sensor so as to ensure that the airflow was not the main factor contributing to the deformation of the strip.
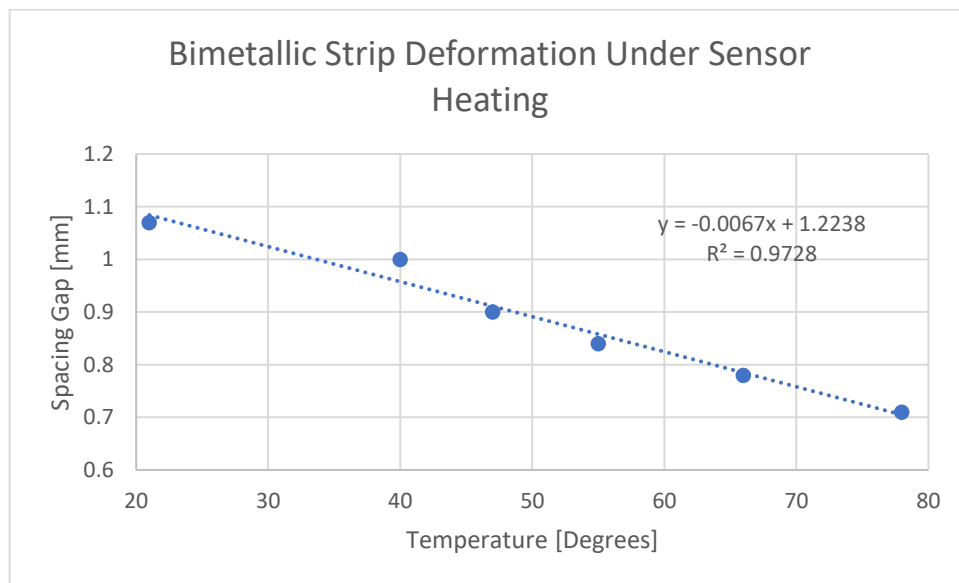
Figure 4.24: Deflection Measurement of Bi-Material System

The results of repeated testing of a subsequent bi-material implementation with an initial gap size of 0.4mm can be seen in Figure 4.25. Based on this figure, an estimate of 0.88MHz/°C was concluded as being the approximate sensitivity achievable with this particular sensor implementation. Normalising that sensitivity results in a value of 0.1375%/°C which puts it in third place in Table 4.1 in terms of sensitivity. This is behind another mechanical design, made with the commercial grade bimetallic strip which has a far more complicated fabrication

<center>145</center>

strategy associated with it. A subtle point to be made here is that the linearity of the response is expected to drift off after approximately 65°C as the operating limits of cyanoacrylate glue are expected to be exceeded beyond this temperature (see Appendix B for more details).
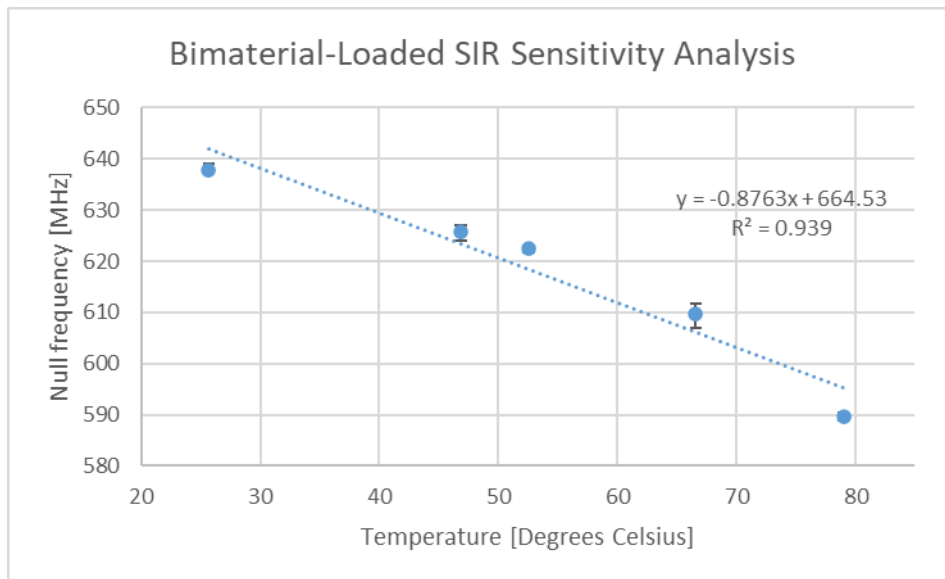
Unique Shortcoming of Bi-Material Inclusion

It must be noted at this point that the above test results were gathered with the incoming convective heat flow being directed at the top surface of the sensor (where the bi-material strip resides). Testing of the device with the same heat flow directed at the bottom of the sensor revealed repeatedly different results. This was an important test to carry out as it signifies the difference in sensor response to a heat source coming from the sensor substrate, as opposed to from the external environment. During these tests the device sensitivity changed from the earlier mentioned 0.88MHz/°C to approximately 0.4MHz/°C. During subsequent tests it was determined that the sensitivity of the gap size changed from 8.151μm/°C to 6.742μm/°C between testing with the heat source applied to the bottom and that performed with it applied to the top of the sensor. Similar testing was performed with the standard FR4-based λ/4 SIR where neither the time constant or temperature sensitivity varied to any significant degree (results were within the error bars seen in the conventional test results). Further study is needed on this issue, but it seems clear that the bi-material strip is not receiving the same level of heat transfer when the device is heated from the bottom. This is most likely caused by the fact that the strip element has a very small contact area with the rest of the device and that heat transfer is occurring between the rest of the heated

146

device to the environment in favour of the more thermally resistive path to the strip element. The degree to which this occurs will most likely be dependent on the underlying resonator design and size, and also be dependent on configuration/characteristics of the heat source.

Discussion on Bi-material Sensor Performance

Overall, the inclusion of a bi-metallic strip or other similar element significantly enhances the temperature sensitivity of the planar sensors. In this case, the sensitivity is enhanced, approximately, by a factor of four. There are some drawbacks to the inclusion of the bimetallic element including issues related to the direction from which the incoming heat flux is arriving and the more obvious fabrication challenges that arise with bimetallic strips. If this device is made completely of metals, its operation should be highly insensitive to variations in humidity and the performance of the bimetallic strip can be assumed constant, regardless of the interrogation frequency range. Both of these latter points do not apply with many of the temperature-sensitive polymer materials. The operating temperature range is limited for the proof-of-concept version of the bi-material strip as it contains a PMMA layer and cyanoacrylate glue.

Discussion on Bi-material Sensor Fabrication

Fabrication of the bi-material element clearly has more challenges than that of a sensor which uses a stimulus sensitive coating. This is compounded by the fact that the designs outlined above consist of a strip design that has a direct electrical connection to the underlying resonator circuit. The next stages of this design process would be to outline how such a device could be fabricated but one of the important points here is that the strip is suspended above the resonator circuit and thus a sacrificial layer will need to be deposited down first and subsequently removed at the appropriate time. Water-soluble Polyvinyl Alcohol (PVA) is used in Fused Deposition Modelling (FDM) 3D printing for a similar purpose and perhaps this approach could be taken to combat this issue. Furthermore, the thicknesses of the conductive elements (>100µm) may prove hard to implement using conventional inkjet processes. Technologies such as Plasma-jet [54] may provide a viable alternative that is capable of performing thick conductor depositions. As discussed earlier, material selection for the strip will limit the operating range and control the sensitivity of the device. In any case, the fabrication complexity of this device is considerably lower than that found in the sensor design in [9].

Direct Thermal Expansion

Alternate methods to make use of thermal expansion as the sensing mechanism have also been seen within the chipless RFID literature. A work of note is that of Glich et al. in [8] which relies on the thermal expansion of the actual resonator geometry to sense temperature. This particular approach was put forward in that work as it would potentially have a very large sensing range. Several challenges were reported in that work, most of which were related to the low thermal expansion coefficients that most conductive materials have, which would be on the order of 10^{-6} to 10^{-5}[50]. There were also issues with the impact of the rigidity of the substrate and other impacts it may have on the overall sensor performance. These issues tie in very heavily with the challenges of strain sensor design and a thorough discussion on this exact issue can be found in Chapter 3. That particular publication presented devices with simulated sensitivities on the order of 100kHz/°C, which are considerably lower than those observed with dielectric-based designs [5]. One critique of this design would be that the dielectric contribution of nearby polymers, such as epoxies, could dominate the total sensor response. Therefore, any use of those designs would need to make use of an accurately interrogated reference sensor. Liquid metals such as Gallinstan have expansion coefficients on the order of 10^{-4} which may provide a potential avenue towards sensitivity enhancement but said material has a melting point at -19°C [55], which would make it unsuitable for aerospace settings. The use of this material has been further discussed in [56].

Expansion Properties of Paraffin Wax

Instead of pursuing the same approach as that of Gilch et al. in [8], this work has set out to consider the potential of using thermal expansion as a means of building a sensor with a large temperature sensitivity. To do this, a brief review of candidate materials was explored and the material, paraffin wax was considered to be a good potential candidate. This material has a very high level of volumetric expansion (≈15%) upon melting and its expansion can be seen in other works to have a piecewise linear response with increasing temperature, even above the melting point. Expansion response curves can be seen in [57][58] for this material that demonstrates that the material expands continuously with increasing temperature, although the slope of the curve is sharpest just before the melting temperature. This material has been readily used in automobile thermostats as an actuation mechanism and this material has been well characterised before now [57]. Paraffins, or more generally, linear alkanes take the form C_NH_{2N+2} and the melting point can be altered by changing the number of carbon atoms in the main backbone [57][59]. This variability is asymptotic in nature but allows for a tuning of the melting temperature from -125°C to 100°C [57]. This is an important point to make as the use

of multiple grades of paraffin may allow for tuning of the final sensor response curve so that it is more linear and has a larger operating range. The final operating range of a sensor made using this material may fall short of the overall aerospace requirements defined in Chapter 2, but this research was continued as the resulting sensor may be capable of operation in a subset of aerospace applications.

As mentioned earlier, the thermal time constants associated with sensors of this type can be quite large. Similarly, the thermal properties of paraffin wax (thermal conductivity of 0.14 [50]) correspond to a device with a considerably larger time constant than even that of Galinstan, whose thermal properties have been presented in Table 4.12 below. With all of that being said, the use of this material will at least demonstrate the maximum possible static sensor performance that can be achieved through thermal expansion, as its expansive properties dwarfs that of all other considered materials.

Table 4.12: Thermal Properties of Paraffin and Galinstan

Material	*Specific Heat Capacity [J/kg.K]	*Thermal Conductivity [W/m.K]	CTE (Volumetric) [10^{-6} °C^{-1}]	Melting Temperature [°C]	Boiling Temperature [°C]
Paraffin Wax	≈2000 [59]	0.14 [60]	3250 (Interpolated 20-60°C) [58]	60 (variable)	>300 [61]
Galinstan	200 [62]	16.5 [62]	115 [56]	-19 [55]	>1300 [55]

*data recorded at room temperature

An initial exploration of the expansive properties of paraffin wax was performed using a 3D printed crucible that holds a volume of 10ml. This chamber was filled with molten paraffin wax and left to cool down. The region left in the container by the now cooled wax was filled with water and a pipette was used to estimate the volume of the added water. Although this test method is rudimentary, it did at least demonstrate that the acquired paraffin wax had the expansive properties suggested by the existing research literature. The test results showed more than a 20% decrease in volume between the molten and solid paraffin wax and this result is comparable with the other results seen in the literature [58]. Reasons why the estimated value exceeded that of the expected value include the fact that the actual temperature of the molten wax is unknown and thus expansion of over 15% could occur.

Planar Expansion using Paraffin Wax

The next point of discussion is how should such a material be used within a chipless RFID tag design to create a highly sensitive temperature sensor. This initial attempt made use of the V1 strain sensor design outlined in Chapter 3 as the base resonator for this sensor, since it has been designed to be highly sensitive to geometric deformation. This resonator design has also demonstrated the potential to operate on both dielectric and conducting superstrates which is an added reason to choose this as the basis of the temperature sensor design. Figure 4.26(a) depicts a modified V1 strain sensor design with a paraffin wax central element which was encapsulated within the Ecoflex™ substrate. The device was heated using a heat gun until the wax was fully melted (see Figure 4.26(b)). A visual check was used to assess whether the wax was melted as the wax changes from opaque to transparent upon melting.

<div align="center">(a)   (b)</div>
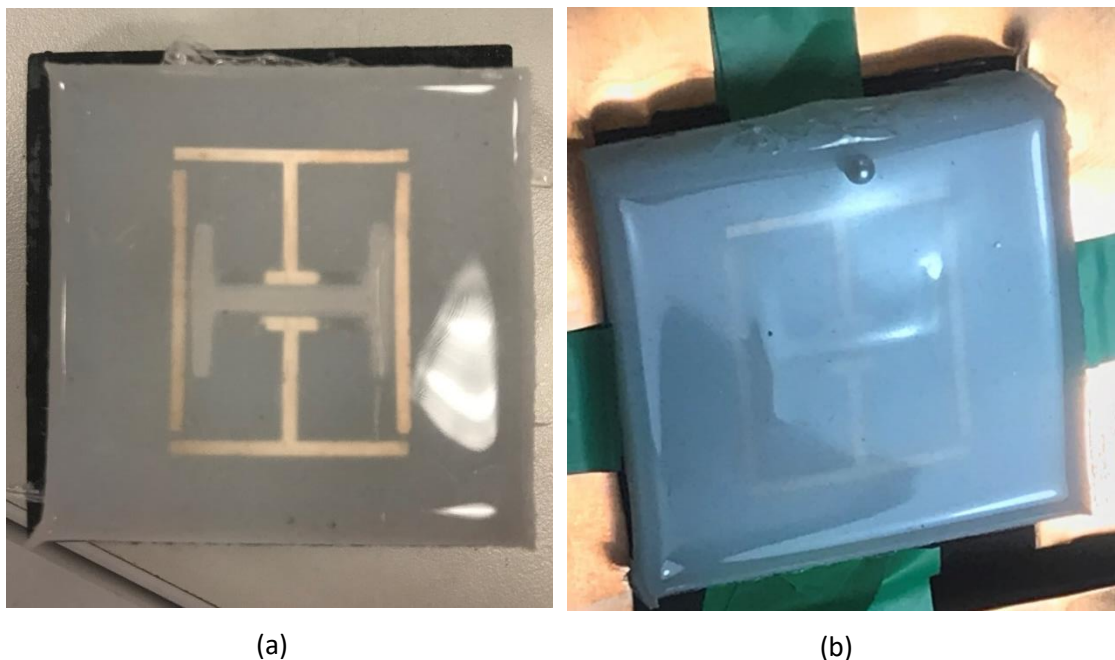
Figure 4.26: Strain Sensor with Paraffin Inclusion (a) Unheated and (b) Fully Melted

Testing with and without the paraffin wax present in the design revealed that the inclusion of the wax reduced the sensitivity of the device. The temperature dependence of silicone materials has been discussed in [63][64][65][66] and it is believed that the permittivity of the paraffin wax, which changes in the opposite direction to that of silicone had caused the desensitisation. Subsequent testing, along with physical measurements using a vernier calipers revealed that the melting of the paraffin wax did not result in any noticeable level of resonator deformation.

This particular design does not make use of a large amount of wax, and this is believed to be one of the main reasons why its presence in the sensor did not enhance the sensitivity of the

device. Along with the small amount of wax present in the sensor, temperature sensing using this device was largely fruitless as another key issue arose because of the use of a highly expansive molten material within a flexible substrate. This issue is that a molten material will just as readily expand vertically as in any other direction. Visible evidence of this vertical swelling can be seen above in Figure 4.26(b). This is not a problem within itself but chipless RFID sensors are planar in nature, and the desired motion is in a plane parallel to the underlying surface (horizontal) and not perpendicular to it (vertical). The only way to force the deformation to occur in the horizontal direction is to stop vertical deformation through the use of a rigid top layer of material that is mechanically connected to the substrate. This approach brings up significant fabrication challenges as many such materials are deposited at temperatures exceeding the melting temperature of the paraffin. Even if a stiff room-temperature deposition can be achieved (e.g. Polyester resin -based) there will still be significant shear forces occurring during device operation. This problem would also most likely occur with other highly expansive materials such as Gallinstan. It has therefore been concluded that to make use of a highly expansive material within a planar design, vertical expansion will need to be directly used, as it seems to be too difficult to mitigate in favour of horizontal expansion.

Vertical Expansion using Paraffin Wax

Despite the poor results achieved with using paraffin wax as a horizontal thermal expansion element, other works such as [67] have used paraffin wax to detect temperature as it also exhibits dielectric constant variations below its melting point. These variations may in part arise from vertical expansion of the material. Attempts at this approach in [67] were somewhat weak as the sensor response was dominated by the dielectric properties of the surrounding materials and not that of the paraffin. This arose because of the low dielectric constant of paraffin wax [67]. A similar result can be seen in the work of Gilch et al. in [8] where the behaviour of the substrate dominated the total response. In order to make better use of vertical deformation as a means of altering the resonant frequency of the sensor, an alternative approach has been taken here.

A potential way in which vertical expansion can be exploited within a chipless RFID tag is by using it to move a high dielectric material away from the main resonator, which would result in a change in resonant frequency. A theoretical sensor implementation would involve a moulded or a 3D printed flexible dielectric substrate that contains a region for the holding of paraffin wax. After the region is filled with paraffin wax and left to cool, a top layer is deposited down and a chipless RFID resonator is fabricated on the top surface. By making the dielectric constant of the substrate significantly higher than the other layers/elements, thermal expansion of the paraffin wax should result in a significant alteration in sensor null frequency. A simple proof-of-concept implementation has been implemented using latex rubber, a transparent polyester-based tag (MELINEX® ST506 Thermal Transfer Ribbon Tag) and a cyanoacrylate bonding glue (seen in Figure 4.27). Latex rubber was chosen as it should support the relevant level of deformation and it can easily be bonded with cyanoacrylate glue to a wide variety of other polymers. An approximate estimation for the dielectric constant of this material is 2.35 [67] and that of a similar grade of paraffin wax varies from 2.35 (30°C) to 3.1 (60°C), when heated below its melting temperature [67].

Figure 4.27: Proof of Concept Vertical Expansion Sensor

Initial test results can be seen in Figure 4.28 below where a wireless setup was used along with a heat gun to perform the relevant tests. The sensitivity of the device can be interpreted from Figure 4.28 below, but it is lower than that found in other temperature sensors documented in this chapter. If this curve was assumed to be linear, the results of repeated testing reveal a sensitivity of approximately 0.85MHz/°C, but more will have to be done to enhance this curve and the overall operating range of the device. Note: Testing done on the sensor without the inclusion of the paraffin wax revealed only a negligible/zero sensitivity. Furthermore, the test results are the result of both the latex rubber being moved away from the resonator and from variations in the dielectric constant of the paraffin. Interestingly, publications such as [67] have shown a dielectric sensitivity in the opposite direction to that seen in the combined sensor design seen here. This would suggest that the two effects may be working against each other in this current implementation.
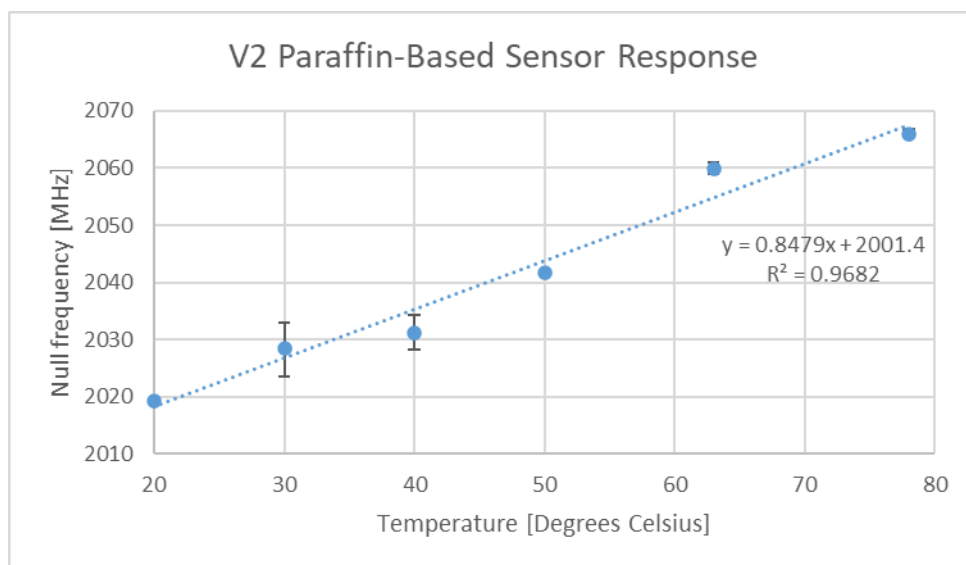
Figure 4.28: Vertical Expansion Sensor Sensitivity Curve

153

Discussion on Performance of Vertically Expanding Temperature Sensor

The proof-of-concept implementations seen in this work have made use of paraffin wax to achieve sensitives on the order of 0.85MHz/°C (normalised sensitivity in fifth place in Table 4.1) but the time constants involved in the sensor response are incredibly large. Specific Heat Capacity measurements performed in [59] reveal a large initial heat capacity of around 2000 but this value grows and peaks at a value of over 10000 at the phase change point in the material. Given that both of these values are both large (compared to most other materials) and different, the time constant will be long and vary greatly depending on the starting temperature of the device. Testing of the paraffin-based devices up to their melting point required heating times on the order of ten minutes (depending on quantity) to ensure the device was fully heated, which is much longer than the response time of the thermistor or RTD devices which were all below thirty seconds. Unlike the bimetallic strip approach, this approach has a fundamental temperature limit as the paraffin wax will begin to boil at temperatures exceeding 300°C [61]. Enhancing the linearity of the response curve can in theory be performed by adding in different grades of paraffin wax so that their expansion curves overlap in such a way that the total response is more linear, but this will result in an averaging of the curves which will most likely result in a more stable, but weaker level of overall sensor sensitivity. In terms of sensitivity enhancement, changing out the latex rubber for another material would seem appropriate, as increasing the permittivity of the backing material should result in a larger overall sensitivity.

Discussion on Fabrication of Vertically Expanding Temperature Sensor

Fabrication of devices that make use of direct thermal expansion have been reported in other works to be quite challenging, particularly with materials like Gallinstan [56]. As mentioned earlier, the main challenge will be controlling the expansive material during the process of inserting and sealing it within a chamber in the design. Further evidence is needed into the viability of this design before any further work is done regarding ease of fabrication, but it would seem that its design, like the bi-material design will be more difficult to fabricate in-situ than the dielectric-based sensors.

Conclusion on Expansion Based Sensors

These expansion-based designs do indeed boast some benefits over the conventional approaches, but these benefits come with considerable drawbacks. Of most concern is the significant increase in fabrication complexity and the performance issues such as sensor response time.

Based on the designs seen in this work, it would seem apparent that the use of direct thermal expansion is going to be very difficult to fabricate in-situ whilst working with materials that have large thermal expansion coefficients. Out of the two approaches taken in this section (bimetallic and paraffin based), the bimetallic element boasts a better level of performance as it greatly enhances device sensitivity and does not have the prohibitively large time constants associated with paraffin wax.

4.7   Future Work

As mentioned earlier, this chapter is not as thorough as that performed on the goal of strain sensing, but a good start has been made and several key avenues of further exploration have been identified. On the topic of thermocouple integration, alternative solutions will need to be found or the integration of a battery or supercapacitor will need to be considered. Furthermore, additional work is required to fully develop the sensor without the need for commercial components. This would involve the deposition of BST and design of the appropriate capacitive structure.

The temperature sensors outlined in this work are only proof-of-concept implementations and further work is needed to assess the performance of other approaches. These include the deposition of a material such as BST or BTO to be used as a temperature-sensitive dielectric.

The exact path forward will depend very heavily on how easily the temperature sensing approach (i.e. bimetallic strip) can be fabricated in-situ. Therefore, attempts at implementing the designs listed above and others using in-situ fabrication techniques should be performed. From there, a design decision should be made as to whether the benefits of mechanical deformation are enough to warrant the increase in fabrication complexity.

4.8   Conclusions

A good deal of progress was made in this chapter towards the overall goals of the project. These accomplishments include the following;

- A review of existing designs was completed
- A proof-of-concept thermocouple integration method was identified, implemented and successfully tested
- Several different simplified temperature sensor designs were developed, that boasted reasonable sensitivity levels

- The thermal expansion -based sensing approach has been explored here in more depth and several of the resulting designs boasted sensitives far exceeding other thermal expansion -based designs in the literature

A great deal of work and exploration still has to be performed in this particular area, most notably, the potential low-temperature use of BST or other such material. For now, it can be concluded that the use of direct thermal expansion is a difficult approach to use and that the use of bi-material strips is a much more suitable option. On this latter approach, further work is needed to fabricate such devices in-situ, as part of a chipless RFID resonator design. Finally, thermocouple integration was proven (at least partially) and further work is needed to mitigate the sensitivity of BST to ambient temperature and/or enhance the bias sensitivity of the device. Potential methods were tested above but more suitable methods will need to be explored/found. These and other approaches will likely require careful design and deposition of the BST material itself.

4.9   References

[1]   K. Mc Gee, P. Anandarajah, and D. Collins, "A Review of Chipless Remote Sensing Solutions Based on RFID Technology," Sensors, vol. 19, no. 19, p. 4829, 2019.

[2]   ESA, "ESA Open Invitation To Tender [FR] AO8922 - DIRECT PRINTING OF MECHANICAL AND THERMAL SENSORS ONTO SPACECRAFT HARDWARE." 2017. [Online]. Available: https://artes.esa.int/funding/direct-printing-mechanical-and-thermal-sensors-spacecraft-hardware-artes-4e073

[3]   W. C. Wilson and P. D. Juarez, "Emerging needs for pervasive passive wireless sensor networks on aerospace vehicles," in Procedia Computer Science, Jan. 2014, vol. 37, pp. 101–108. doi: 10.1016/j.procs.2014.08.018.

[4]   K. Dionne, H. El Matbouly, F. Domingue, and L. Boulon, "A chipless HF RFID tag with signature as a voltage sensor," in 2012 IEEE International Conference on Wireless Information Technology and Systems (ICWITS), 2012, pp. 1–4.

[5]   E. M. Amin and N. Karmakar, "Development of a chipless RFID temperature sensor using cascaded spiral resonators," in 2011 IEEE SENSORS Proceedings, Oct. 2011, pp. 554–557. doi: 10.1109/ICSENS.2011.6127344.

[6]   G. T. Pawlikowski, "Effects of Polymer Material Variations On High Frequency Dielectric Properties," MRS Online Proc. Libr. 2009 11561, vol. 1156, no. 1, pp. 1–7, Aug. 2009, doi: 10.1557/PROC-1156-D02-05.

[7]   T. T. Thai, F. Chebila, et al., "Design and development of a millimetre-wave novel passive ultrasensitive temperature transducer for remote sensing and identification," in The 40th European Microwave Conference, 2010, pp. 45–48. doi: 10.23919/EUMC.2010.5616282.

[8]   F. Requena, M. Gilch, et al., "Thermal Modeling of Resonant Scatterers and Reflectometry Approach for Remote Temperature Sensing," IEEE Trans. Microw.

Theory Tech., vol. 69, no. 11, pp. 4720–4734, Nov. 2021, doi: 10.1109/TMTT.2021.3096986.

[9]   X. Shi, F. Yang, S. Xu, and M. Li, "A Passive Temperature-Sensing Antenna Based on a Bimetal Strip Coil," Sensors 2017, Vol. 17, Page 665, vol. 17, no. 4, p. 665, Mar. 2017, doi: 10.3390/S17040665.

[10]   Engineered Materials Solutions - Wickeder Group, "Emsclad - P675R Specifications," Specification Document. https://www.emsclad.com/fileadmin/Data/Divisions/EMS/Download/P675R_Specs.pdf (accessed Jul. 05, 2022).

[11]   Q. Y. Ren, L. F. Wang, J. Q. Huang, C. Zhang, and Q. A. Huang, "Simultaneous Remote Sensing of Temperature and Humidity by LC-Type Passive Wireless Sensors," J. Microelectromechanical Syst., vol. 24, no. 4, pp. 1117–1123, Aug. 2015, doi: 10.1109/JMEMS.2014.2384591.

[12]   T. T. Thai, F. Chebila, et al., "A novel passive ultrasensitive RF temperature transducer for remote sensing and identification utilizing radar cross sections variability," in 2010 IEEE International Symposium on Antennas and Propagation and CNC-USNC/URSI Radio Science Meeting - Leading the Wave, AP-S/URSI 2010, 2010, pp. 1–4. doi: 10.1109/APS.2010.5562216.

[13]   W. M. Abdulkawi and A. F. A. Sheta, "Chipless RFID Sensors Based on Multistate Coupled Line Resonators," Sensors Actuators A Phys., vol. 309, p. 112025, Jul. 2020, doi: 10.1016/J.SNA.2020.112025.

[14]   G. Ayissi Eyebe, A. H. Rasolomboahanginjatovo, B. Bideau, and F. Domingue, "Investigation on temperature-dependent dielectric properties of ETFE fluoropolymer for microwave temperature sensing applications," Sensors Actuators A Phys., vol. 290, pp. 215–221, May 2019, doi: 10.1016/J.SNA.2019.01.025.

[15]   B. Kubina, C. Mandel, M. Schussler, M. Sazegar, and R. Jakoby, "A wireless chipless temperature sensor utilizing an orthogonal polarized backscatter scheme," Eur. Microw. Week 2012 "sp. Microwaves", EuMW 2012, Conf. Proc. - 42nd Eur. Microw. Conf. EuMC 2012, pp. 61–64, 2012, doi: 10.23919/EUMC.2012.6459267.

[16]   A. Blythe and D. Bloor, Electrical Properties of Polymers, 2nd Edtn. Cambridge: Cambridge University Press, 2005.

[17]   K. McGee, P. Anandarajah, and D. Collins, "Use of Chipless RFID as a Passive, Printable Sensor Technology for Aerospace Strain and Temperature Monitoring,", Sensors, 2022, 22, 8681. https://doi.org/10.3390/s22228681

[18]   N. C. Karmakar, E. M. Amin, and J. K. Saha, Chipless RFID Sensors, 1st Edt. Wiley, 2016.

[19]   E. M. Amin, R. Bhattacharyya, S. Sarma, and N. C. Karmakar, "Chipless RFID tag for light sensing," in 2014 IEEE Antennas and Propagation Society International Symposium (APSURSI), Jul. 2014, pp. 1308–1309. doi: 10.1109/APS.2014.6904980.

[20]   D. D. Pollock, Thermocouples: theory and properties, 1st Edtn. ASTM International, 1991.

[21]   B. G. Streetman and S. K. Banerjee, Solid State Electronic Devices, 6th Edtn. New Jersey: Pearson, 2006.

[22]   D. M. Pozar, Microwave Engineering, 4th ed. New York: Wiley, 2012.

[23]   X. Wang, "TUNABLE MICROWAVE FILTERS USING FERROELECTRIC THIN FILMS, PhD Thesis," University of Birmingham, 2009. [Online]. Available: https://core.ac.uk/download/pdf/75763.pdf

[24]   A. T. Kabir, "Voltage Controlled Oscillators Tuned with BST Ferroelectric Capacitors, Masters Thesis," University of Colorado Colorado Springs. Kraemer Family Library, Colorado, 2012. Accessed: Jul. 07, 2020. [Online]. Available: https://mountainscholar.org/handle/10976/251

[25]   S. Microelectronics, "Datasheet - ParascanTM tunable integrated capacitor," 2015. https://www.st.com/resource/en/datasheet/stptic-68g2.pdf

[26]   K. Mc Gee, P. Anandarajah, and D. Collins, "Current Progress towards the Integration of Thermocouple and Chipless RFID Technologies and the Sensing of a Dynamic Stimulus," Micromachines, vol. 11, no. 11, p. 1019, 2020, doi: 10.3390/mi11111019.

[27]   "RS Pro K Type Thermocouple 1/0.2mm diameter, -75°C → +250°C | RS Components." https://ie.rs-online.com/web/p/products/3630250/ (accessed Sep. 22, 2020).

[28]   T. Price, "Nonlinear properties of nanoscale barium strontium titanate microwave varactors," University of South Florida, 2012.

[29]   R. Mulla and C. W. Dunnill, "Single material thermocouples from graphite traces: Fabricating extremely simple and low cost thermal sensors," Carbon Trends, vol. 4, p. 100077, Jul. 2021, doi: 10.1016/J.CARTRE.2021.100077.

[30]   R. Mulla and C. W. Dunnill, "Sensors-on-paper: Fabrication of graphite thermal sensor arrays on cellulose paper for large area temperature mapping," HardwareX, vol. 11, p. e00252, Apr. 2022, doi: 10.1016/J.OHX.2021.E00252.

[31]   T. Dinh, H. P. Phan, D. V. Dao, P. Woodfield, A. Qamar, and N. T. Nguyen, "Graphite on paper as material for sensitive thermoresistive sensors," J. Mater. Chem. C, vol. 3, no. 34, pp. 8776–8779, Aug. 2015, doi: 10.1039/C5TC01650A.

[32]   "RS PRO Conductive Paint, 5 g | RS Components," 2021. https://ie.rs-online.com/web/p/adhesives/1239911/ (accessed Jul. 28, 2021).

[33]   C. Offenzeller, M. Knoll, B. Jakoby, and W. Hilber, "Fully Screen Printed Carbon Black-Only Thermocouple and the Corresponding Seebeck Coefficients," Proceedings, vol. 2, no. 13, p. 802, Nov. 2018, doi: 10.3390/proceedings2130802.

[34]   M. Knoll, C. Offenzeller, B. Mayrhofer, B. Jakoby, and W. Hilber, "A Screen Printed Thermocouple-Array on a Flexible Substrate for Condition Monitoring," in Proceedings of Eurosensors 2018, Nov. 2018, vol. 2, no. 13, p. 803. doi: 10.3390/proceedings2130803.

[35]   KEMET Electronics, "KEMET FLEX SUPPRESSOR ® Noise Suppression Sheet," Product Specifications/Overview, 2021. https://content.kemet.com/datasheets/KEM_FS8004_NSS.pdf (accessed Jul. 05, 2022).

[36]   C. Mandel, H. Maune, M. Maasch, M. Sazegar, M. Schüßler, and R. Jakoby, "Passive wireless temperature sensing with BST-based chipless transponder - IEEE Conference Publication," 2011. Accessed: Jul. 07, 2020. [Online]. Available: https://ieeexplore.ieee.org/document/5760714

[37]   E. M. Amin, N. C. Karmakar, and B. W. Jensen, "Fully printable chipless RFID multi-parameter sensor," Sensors Actuators A Phys., vol. 248, pp. 223–232, Sep. 2016, doi: 10.1016/J.SNA.2016.06.014.

[38]   Kao, K. C. Dielectric Phenomena in Solids, 1st Edt. Academic Press, 2004., pp. 41-105, 223-247

[39]   B. Riddle, J. Baker-Jarvis, and J. Krupka, "Complex permittivity measurements of common plastics over variable temperatures," IEEE Trans. Microw. Theory Tech., vol. 51, no. 3, pp. 727–733, Mar. 2003, doi: 10.1109/TMTT.2003.808730.

[40]   R. J. Young and P. A. Lovell, Introduction to Polymers, 3rd Edtn. Boca Raton: CRC Press, 2011.

[41]   C. Dichtl, P. Sippel, and S. Krohns, "Dielectric Properties of 3D Printed Polylactic Acid," Adv. Mater. Sci. Eng., vol. 2017, 2017, doi: 10.1155/2017/6913835.

[42]   G. Yang, J. Cui, Y. Ohki, D. Wang, Y. Li, and K. Tao, "Dielectric and relaxation properties of composites of epoxy resin and hyperbranched-polyester-treated nanosilica," RSC Adv., vol. 8, no. 54, pp. 30669–30677, Aug. 2018, doi: 10.1039/C8RA05846F.

[43]   W. A. Hussain, A. A. Hussein, J. M. Khalaf, A. H. Al-Mowali, and A. A. Sultan, "Dielectric Properties and a.c. Conductivity of Epoxy/Alumina Silicate NGK Composites," Adv. Chem. Eng. Sci., vol. 5, pp. 282–289, 2015, doi: 10.4236/aces.2015.53028.

[44]   F.-G. Yuan, Structural Health Monitoring (SHM) in Aerospace Structures. Elsevier, 2016.

[45]   Hasan, M. S.; Alom, J.; Asaduzzaman, M.; et al. Recent Criterion on Stability Enhancement of Perovskite Solar Cells, Processes, 2022, vol. 10, no. 7.

[46]   S. Devi and A. K. Jha, "Structural, Dielectric and Ferroelectric Studies of Tungsten Substituted Barium Strontium Titanate," Ferroelectrics, vol. 402, no. 1, pp. 168–174, 2010, doi: 10.1080/00150191003709347.

[47]   W. T. Beyene, N. Cheng, J. Feng, H. Shi, D. Oh, and C. Yuan, "Performance analysis of multi-gigahertz parallel bus with transmit pre-emphasis equalization," IEEE MTT-S Int. Microw. Symp. Dig., vol. 2005, pp. 1849–1852, 2005, doi: 10.1109/MWSYM.2005.1517089.

[48]   Amphenol Advanced Sensors, "Amphenol 10k NTC Thermistor," 2014. Accessed: Jul. 06, 2022. [Online]. Available: www.amphenol-sensors.com

[49]   J. P. Holmann, Heat Transfer, 7th Edtn. McGraw-Hill, 1990.

[50]   W. D. Callister, Materials science and engineering, 8th ed., S. Hoboken, N.J: John Wiley, 2011.

[51]   A. S. Morris, Measurement and instrumentation: theory and application, Second edi. Amsterdam: Elsevier, 2016.

[52]   T. T. Thai, F. Chebila, et al., "A novel passive ultrasensitive RF temperature transducer for remote sensing and identification utilizing radar cross sections variability," in 2010 IEEE International Symposium on Antennas and Propagation and CNC-USNC/URSI Radio Science Meeting - Leading the Wave, AP-S/URSI 2010, 2010, pp. 1–4. doi: 10.1109/APS.2010.5562216.

[53] S. Timoshenko, "Analysis of Bi-Metal Thermostats," JOSA, Vol. 11, Issue 3, pp. 233-255, vol. 11, no. 3, pp. 233–255, Sep. 1925, doi: 10.1364/JOSA.11.000233.

[54] R. P. Gandhiraman, V. Jayan, J. W. Han, B. Chen, J. E. Koehne, and M. Meyyappan, "Plasma jet printing of electronic materials on flexible and nonconformal objects," ACS Appl. Mater. Interfaces, vol. 6, no. 23, pp. 20860–20867, Dec. 2014, doi: 10.1021/AM505325Y/ASSET/IMAGES/MEDIUM/AM-2014-05325Y_0007.GIF.

[55] S. Liu, K. Sweatman, S. McDonald, and K. Nogita, "Ga-Based Alloys in Microelectronic Interconnects: A Review," Mater. 2018, Vol. 11, Page 1384, vol. 11, no. 8, p. 1384, Aug. 2018, doi: 10.3390/MA11081384.

[56] A. Traille, S. Bouaziz, et al., Eds., "A wireless passive RCS-based temperature sensor using liquid metal and microfluidics technologies | IEEE Conference Publication | IEEE Xplore," in 41st European Microwave Conference, Oct. 2011. Accessed: Jul. 06, 2022. [Online]. Available: https://ieeexplore-ieee-org.dcu.idm.oclc.org/document/6101891

[57] S. Ogden, L. Klintberg, G. Thornell, K. Hjort, and R. Bodén, "Review on miniaturized paraffin phase change actuators, valves, and pumps," Microfluid. Nanofluidics 2013 171, vol. 17, no. 1, pp. 53–71, Nov. 2013, doi: 10.1007/S10404-013-1289-3.

[58] A. Mann, C. M. Bürgel, and P. Groche, "A Modeling Strategy for Predicting the Properties of Paraffin Wax Actuators," Actuators 2018, Vol. 7, Page 81, vol. 7, no. 4, p. 81, Nov. 2018, doi: 10.3390/ACT7040081.

[59] "Thermal Analysis of Phase Change Materials-Three Organic Waxes using TGA, DSC, and Modulated DSC ®."

[60] W. H. McAdams, Heat transmission, 3d ed. Tokyo: McGraw-Hill Kogakusha, 1955.

[61] F. Creatini, G. M. Guidi, et al., "Pulsating Heat pipe Only for Space (PHOS): results of the REXUS 18 sounding rocket campaign," J. Phys. Conf. Ser., vol. 655, no. 1, p. 012042, Oct. 2015, doi: 10.1088/1742-6596/655/1/012042.

[62] T. Hao, H. Ma, and X. Ma, "Experimental Investigation of Oscillating Heat Pipe with Hybrid Fluids of Liquid Metal and Water," J. Heat Transfer, vol. 141, no. 7, Jul. 2019, doi: 10.1115/1.4043620/726959.

[63] C. Johansson and M. Robertsson, "Broadband Dielectric Characterization of a Silicone Elastomer," J. Electron. Mater. 2007 369, vol. 36, no. 9, pp. 1206–1210, Jul. 2007, doi: 10.1007/S11664-007-0124-6.

[64] P. Bertasius, S. Schaefer, et al., "Dielectric properties of polydimethylsiloxane composites filled with SrTiO3 nanoparticles," Polym. Compos., vol. 42, no. 6, pp. 2982–2988, Jun. 2021, doi: 10.1002/PC.26031.

[65] L. K. Namitha and M. T. Sebastian, "Microwave dielectric properties of flexible silicone rubber – Ba(Zn1/3Ta2/3)O3 composite substrates," Mater. Res. Bull., vol. 48, no. 11, pp. 4911–4916, Nov. 2013, doi: 10.1016/J.MATERRESBULL.2013.07.029.

[66] J. Belovickis, J. Macutkevic, et al., "Dielectric Spectroscopy of Polymer Based PDMS Nanocomposites with ZnO Nanoparticles," https://doi.org/10.1080/00150193.2015.1012016, vol. 479, no. 1, pp. 82–89, Apr. 2015, doi: 10.1080/00150193.2015.1012016.

[67]   S. P. Chakyar, T. A. Shanto, et al., "Measurement of dielectric constant of waxes at different temperatures using split ring resonator structure," 2016 IEEE MTTS Int. Microw. RF Conf. IMaRC 2016 - Proc., Jun. 2017, doi: 10.1109/IMARC.2016.7939638.

Chapter 5 - Sensor Response Analysis

5.1   Introduction

This chapter explores the steps needed to perform feature extraction from the incoming chipless RFID sensor response. Significant emphasis is placed on the accuracy and resolution of the extracted features as the strain sensors developed in Chapter 3 have a limited sensitivity. This chapter outlines the challenges associated with interrogating a chipless RFID sensor using the existing reader architectures and provides a calculation of the interrogation requirements required for the developed sensor(s). Attempts are then made at outlining the necessary software operations needed to ensure that a reliable and accurate stimulus measurement is performed. Further work is also performed in an attempt to decode time domain information resulting from a dynamic stimulus being applied to a sensor.

As one can imagine, the topic of chipless RFID reader system design is an ever-evolving one with continuous publications in this area. It must be noted at this point that much of this work was performed before publication of [1] in 2021 and even with that, the frequency resolution and general performance of Impulse Radio Ultrawideband (IR-UWB) readers for sensor interrogation is largely unknown (frequency resolution concerns raised in [2][3]). The former publication [1] differed from the IR-UWB reader architectures reviewed by Garbati et al. in [3] by using a less noisy method to enhance the resolution of the interrogation responses. This design is mentioned here as much of this chapter is concerned with interrogation times and frequency resolution and the frequency resolution of this design is unknown. Like with many of the publications in this area, the focus is on chipless RFID tags and not sensors and thus frequency resolution is not as important to the designers. With that being said, frequency resolution and interrogation time are not the only metrics of interest within the reader architecture. It is still unclear what reader architecture will be capable of supporting the successful interrogation of singular sensors in a multi-sensor setting. This topic is further discussed in Chapter 6 but for now, it will just be mentioned that the multi-sensor performance of Frequency Modulated Continuous Wave (FMCW) -based readers, which make use of "chirp" interrogation signals, have been simulated in 2016 [4] and simulated again in 2021 [5] but it was not until late 2020 that a similar sensor type was interrogated successfully, with the help of 3D radar imaging to isolate the response from nearby sensors [6]. This particular work made use of a FMCW-based reader, and it is yet to be seen if this is the only architecture that can readily support multi-sensor interrogation. This chapter will therefore

focus on addressing the stimulus extraction challenges for reader architectures of this type (continuous wave) and make reference to IR-UWB less frequently.

5.1.1 Methodology

This chapter attempts to make use of the existing signal processing literature to address the problem of sensor response analysis. This means that if at all possible, existing or indeed simplistic approaches will be taken to solve the upcoming problems and where necessary, readers are pointed to more advanced works on the topic. Similarly, the use of expensive software packages are also avoided, for the above reasons and also to keep the project within budget.

5.2 Interrogation Overview

The basic idea of chipless RFID -based sensing is that it is possible to make the scattering characteristics of antenna-based scatterers dependent on a variety of different stimuli. The exact methods used to encode stimulus information into the scattering response is not of critical importance here; what is important is that the changes in scattering characteristics from various sensor types can be categorised as either causing frequency shifts or Quality (Q) - factor variations to the resonant curve found in the magnitude of the scattering response. This work will ignore time-domain based encoding for now as it is not the focus of the design strategy taken in this project.

In many respects, the final interrogation system that should be capable of interrogating chipless RFID sensors in a challenging, realistic, multi-sensor environment and which successfully determines the stimuli levels of interest, has not yet been fully implemented. There are a variety of research groups that are focused on the development of such a system and this work does not wish to make comment on the impressive progress that this particular area of research continues to demonstrate. With that being said, it is important to highlight that many challenges still exist in the deployment of a real-world chipless RFID sensor Structural Health Monitoring (SHM) system which may result in the need for significant design variations (additional functionality requirements) in the interrogation system design. These challenges are mostly read-range and "single response isolation" -related and the following major design changes could be made to alleviate these issues:

- Cross polar transmission line -based sensor designs could help to halve the multipath/clutter interference
- Diode-based harmonic functionality could be used to encode the response signals in a different range of frequencies and to thus halve the multipath/clutter interference

- Different reader architectures (IR-UWB, FMCW, etc.) may alleviate read range limitations of the sensors

- Different reader architectures (FMCW) and software may be capable of isolating unique sensor responses in a multi-sensor environment and negate the need for configurable, directional interrogation antennas

For now, it is an assumption of this chapter that since this project is concerned with aerospace SHM, the target environment (satellite, aircraft, etc.) is being outfitted with these sensors during craft construction and the craft design budget and timeline allows for complete Electromagnetic (EM) modelling of the craft. This brings forth the possibility of extensive channel/environment modelling and possible environment design possibilities that can hopefully give rise to a final, fully functional passive wireless SHM system. A useful work that demonstrates the utility of environment modelling in the context of chipless RFID detection is that by Megahed in Reference [7].

Figure 5.1 gives a high-level abstract overview of the interrogation system for determining the stimulus being experienced by the sensor of interest. Given the variability in reader system/architecture, this work assumes that the retrieved Ultrawideband (UWB) responses can be transformed in some way, into the frequency domain (curve formation), in which the desired resonant curve can be found. From there, the curve needs to be interpreted and its features determined. Finally, with the measured features, the stimulus should be able to be determined using already known Stimulus (U)-Feature (Q, f_{null}, etc.) curves.

This chapter explores the challenge of feature extraction as the low sensitivity of many of the published strain and temperature chipless RFID sensors and rapid changes in stimulus levels brings forth difficulties in the determination of the desired features. Furthermore, several works including [7][8][9] and general testing performed by the authors of this work have found that the resonant curve can sometimes be comparatively weak to the contributions of the environment and it is possible that the frequency response dataset may not contain any noticeable resonant curve. The occurrence of this issue did not result in a flat frequency response, but instead consisted of a noise or clutter -dominated response. More favourable test setups and the removal of environmental clutter had significant effects on improving the magnitude of the contribution of the resonant scatterer, but the point here is that a visual check on the frequency response curves was required to ensure that a valid curve was being measured.

Sensor #1

Sensor #2

Sensor #N

Variations:
- The sensor/tag may make use of a harmonic response, so as to mitigate channel interference
- The sensor/tag may make use of cross polarization, so as to mitigate channel interference
- The sensor/tag may make use of both frequency and time-domain encoding

Antenna Array

Purpose:
- Support targeting of sensors (if necessary)
- Support the implementation of ranging, localisation being performed by the Reader System

Variations:
- The reader system may not need directive antennas
- The reader system may alternatively need beam steering abilities
- Polarization of various sorts/configurations may need to be supported

Tx Path
Rx Path
Array Control

Reader System

Curve Formation

Purpose:
- Generate the UWB interrogation signal(s)
- Decode the UWB response signals
- Perform frequency domain analysis on the response signals to form the bandpass/bandstop frequency datasets
- Perform background subtraction or similar operation to isolate effects of just the sensor

Possible Additional Purposes:
- Perform ranging/localisation -based isolation of singular sensor responses
- Channel/multipath compensation (enhanced range)

Variations:
- Reader architecture could be SFCW, FMCW, IR-UWB

$dB(Hz)$
$\phi(Hz)$

Feature Extraction

Purpose:
- To detect the presence of a sensor response
- To determine/extract the features of this response (Q-factor, ect.)

Requirements:
- Template resonant curve(s) which can be used for curve detection
- Time domain information pertaining to the interval between samples in the incoming dataset

$Q(t)$
$f_{null}(t)$
$f_{peak}(t)$

Stimulus Extraction

Purpose:
- Converts extracted features (Q, f_{null}, ect.) to a stimulus level

Requirements:
- The stimulus sensitivity curve(s) must be known
- The cross-sensitivity curve(s) must be known (this includes sensor orientation dependencies)
- The magnitude of the cross-sensitive stimulii must be known (this includes sensor orientation)

$U = \%\varepsilon, T, \%RH...U_x$

Legend
Software
Hardware

Figure 5.1: Stimulus Extraction Approach– from "Use of Chipless RFID as a Passive, Printable Sensor Technology for Aerospace Strain and Temperature Monitoring" by McGee et al., MDPI, CC BY 4.0 [10]

166

5.3 Static Stimulus Extraction

This section sets out to explore the detection of and feature extraction procedures that will be needed when analysing the sensor response signals. This first section will only consider these challenges in the face of a sensor response that is the result of a static (time-independent) stimulus. Key challenges include determining if a sensor has actually responded to the interrogation signal and what information did it return (Q, f_{null}). These challenges have been partially explored already in the work of Megahed in [7] but that focussed more specifically on chipless RFID tag detection and not sensor interrogation.

5.3.1 Reader System Overview

Spectrum Requirements

Before the topic of reader systems proceeds, it must first be established how much of the spectrum needs to be interrogated. Based on the V1 strain sensor design presented in Chapter 3, a basic estimate was made of the spectrum requirements needed for its operation in a generic aerospace setting. Details of this estimate can be seen in Table 5.1. This final value of 734MHz is quite significant as it will be assumed from here on that the interval between frequency datapoints is fixed. Consideration will be given later to the scenario where the entire resonant curve could be omitted from the sweep and all environmental variables ignored, but a strain sensitivity on the order of 33MHz/%ε only leads to a 33kHz change for a 10με stimulus. This is a modest lower limit on stimulus resolution and would require over 22200 datapoints to fully capture the entire spectrum to that level of resolution. This is of course only considering the impact of a single sensor; several works [11][12] have proposed the use of separate bands for some of or indeed each unique sensor. In any case, it will most likely not be possible to use separate frequencies bands for each unique sensor or sensor groups as the spectrum usage would be enormous for systems incorporating thousands of sensors. Therefore, it will be assumed that both for fabrication simplicity and efficient spectrum usage, most sensors will have the exact same response. A temperature sensor will most likely be present beside each strain gauge or set of gauges. Said device, based on the works reviewed and/or developed in Chapter 4 will have a sensitivity on the order of 1MHz/°C with resolution requirements of at least 0.1°C [13]. This resolution is not as difficult to achieve as that with the strain sensor system but the stimulus range is more considerable, as temperature sensing between -150°C to +250°C is a common requirement. The requirements for the operation of this sensor are also presented in Table 5.1 and the total usage of approximately 2100MHz with the total number of datapoints exceeding 32700.

Table 5.1: Spectrum Allocation Estimation– from "Use of Chipless RFID as a Passive, Printable Sensor Technology for Aerospace Strain and Temperature Monitoring" by McGee et al., MDPI, [10]

Performance Characteristic	Details	Required Spectrum [MHz]	Required Resolution
Strain range of ±0.25%	This range was taken as it exceeds the elastic range for metals but is below that found with many Carbon- and Glass-Reinforced Composites (CFRP and GFRP) [14]. Sensitivity of V1 design (Chapter 3) was approximately 30MHz/%ε [15]	15	Resolution/accuracy of at least 10με required and the location of the null could be anywhere within the total strain sensor spectrum allocation. At a sensitivity of 30MHz/%ε (3kHz/με), this resolution corresponds to 30kHz. Assuming that the true minimum sits within ±0.5 steps of the dataset minimum, the strain sensor requires an average of 715MHz (15+300+400) which means that the dataset will contain over 23800 data points
Strain gauge operating Temperature: -150°C to +250°C	This operating temperature range is not uncommon amongst some aerospace applications [16][13]. Some dielectrics can cause variations on the order of 0.5-1MHz/°C [17]	200-400	
Detect the total strain sensor Resonant Curve	Detecting the whole curve allows for robust checks to ensure a valid sensor response is present [7]. The total curve	300-500	

	ranged from 300-500MHz		
Temperature sensor range of -150°C to +250°C	Developed temperature sensors have sensitivities on the order of 0.88-1MHz/°C [17] but some are on the order of 4MHz/°C [18]	352	The dataset frequency resolution ranges from 100kHz (1MHz/°C designs) to 400kHz (4MHz/°C designs). The dataset required for the sensor characterised in Chapter 4 is thus 4570 data points in size with a frequency resolution of around 88kHz.
Detection of the entire temperature resonance curve	The total curve found in the SIR circuits seen above was less than 50MHz	50	
Conclusion	With 715MHz for the strain sensor and 402MHz (average) for the temperature sensor, leaves a total spectrum of 1117MHz	30kHz between datapoints required for strain sensing and 88kHz required for temperature sensing. Total number of datapoints should exceed 28350	

Reader Architectures

A number of different reader architectures have been used for the detection of chipless RFID tags, namely Stepped Frequency Continuous Wave (SFCW), Frequency Modulated Continuous Wave (FMCW) and Impulse Radio Ultrawideband (IR-UWB) architectures. Table 5.2 describes the characteristics of these architectures of most interest to this discussion, which is based on the thorough review performed by Garbati et al. in 2019 in Reference [3]. One key requirement laid out in Reference [13] was the need for 10Hz interrogation rates for that specific aerospace application and other works have discussed technologies/systems with interrogation rates far above 1kHz [19][20].

Table 5.2: Reader Architecture Comparison

Type	Description	Interrogation Time	Frequency Resolution
IR-UWB	This method uses an ultrawideband pulse (< 10ns) to interrogate the tag [3]. The resulting response contains a structural and antenna component, the latter of which contains the tag/sensor information. The short duration impulse signal can support significantly higher read ranges than other reader types as its duration allows for greater power transmission whilst maintaining compliance with UWB regulations [3]. Sampling is a difficult challenge and the Equivalent Time (ET) method [21] is commonly applied to combat this. Additional signal processing is required in this approach to isolate the tag response.	VERY GOOD - The impulse signals are on the order of nanoseconds and even if ET methods are used, the time is on the order of 10ms	N/A - Unknown resolution but reportedly very low for some implementations [2]. With that being said recent publications [1] have not used the ET method which would suggest that it may be comparable with other reader types.
SFCW	This reader type steps through each of the interrogation frequencies of interest and determines the amplitude/phase response that occurred at each frequency. This device utilises a continuous wave excitation of the tag, unlike what is found in IR-UWB approaches. Most conventional Vector Network Analysers (VNAs) use this approach.	POOR - Each frequency is stepped through and there is a considerable time spent on tuning and stabilisation of the Voltage Controlled Oscillator (VCO). Times are on the order of 100ms to 10s [3]	GOOD [3] - The IF bandwidth can be finely tuned to allow for very high-resolution interrogation sweeps
FMCW	This type is similar to SFCW except it ramps through the frequency range of interest. This method readily supports ranging and is a well-established RADAR architecture	POOR - Enhanced performance over the SFCW type but the chirped signal is usually of a similar duration (10-500ms) to that found in SFCW [3]	GOOD - Assumed similar to SFCW given its similar underlying architecture

As mentioned earlier, the research area of chipless RFID reader design is a flourishing area in which there has been a great deal of publications, since the start of this project. With that being said, the main concerns that were had with the use of IR-UWB architectures was that their frequency resolution was suggested to be inferior to that of the other reader types and there had been very little work done to demonstrate that it would support comparable

ranging abilities to that of FMCW. The latter architecture had previously demonstrated that it could support the isolation of the response of each individual chipless RFID tag amongst a group of tags that were being illuminated by the reader [6].

SFCW-Based System

The most readily available reader architecture was an SFCW -based one and at a low cost of below £200 (excl. shipping), the NanoVNA V2_2 came in considerably cheaper than the other SFCW and FMCW or IR-UWB implementations [3]. This device supported sample rates of 100 samples per second and allowed for interrogation signals between 50kHz and 3GHz. This device (seen in Figure 5.2) was very compact with dimensions of 9x6.5x3cm and the firmware source code can be found online as can details of the PCB layout (CC-BY-NC-SA Licensed). Similarly, the PC software to operate the device was also freely available. Although the dynamic range of the VNA would be a key limiting factor driving the maximum read range [3], other works [7][8] reveal that other variables are at play, that hinder tag/sensor detection even if the response magnitude is well above the noise floor. From References [8], it can be seen that the Radar Cross Section (RCS) magnitude of the tag/sensor and the impact of small environmental variations are more relevant. These environmental variations can include variations in clutter, coupling between the tag and the antennas and coupling/interaction between the tag and the environment [8].
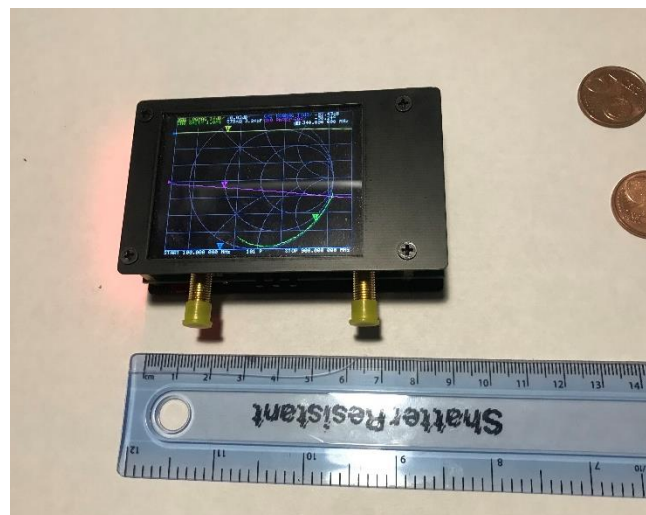
Figure 5.2: NanoVNA V2_2 Device

5.3.2 Response Types

From the continuous wave and impulse-based reader architectures, it can be seen that the resonant responses from a chipless RFID tag/sensor falls into one of two categories; bandpass or bandstop [22][23][24][25][26]. This behaviour originates from the nature of the loading present on the scattering resonator [27]. Fundamentally, the electromagnetic scattering off an antenna is a special use-case as it consists of both a structural component and an antenna component. The former component is the normal scattering effects that occurs upon radio waves interacting with an object of that shape and size, whereas the latter arises due to the fact that the antenna is a device built for absorbing and transmitting radiation (usually within a small band of frequencies). Upon reception of an incoming wave, this additional response from the antenna arises and is dependent on the antenna load matching characteristics, as described in [27] and seen in Equation 5.1. Key parameters within that equation are; the reflection coefficient (Γ_A), the impedance of the antenna ($Z_{Antenna}$) and the impedance of the attached load (Z_{Load}). Also as described by Hansen in [27], the Radar Cross Section (RCS) (Greek symbol "σ") of an antenna can be mathematically described as seen in Equation 5.2, where the first term (σ_s) represents the structural component (mode) and the rest of the equation represents the antenna mode (σ_R). Since some scenarios can result in a delayed antenna mode response, the exponential and "φ" delay terms are also included. It must also be mentioned at this point that no realistic loading is either perfectly short- or perfectly open-circuit and more generally, simulations are used to properly assess the nature of the RCS response of a chipless RFID tag [27]. Also, the exponential term in Equation 5.2 accounts for the possible phase delay between the two components, which is a characteristic that is more exclusively manipulated in time domain chipless RFID sensors/tags.

$$\Gamma_A = \frac{Z_{Antenna} - Z_{Load}}{Z_{Antenna} + Z_{Load}} \tag{5.1}$$

$$\sigma = \left| \sqrt{\sigma_s} - (1 - \Gamma_A)\sqrt{\sigma_R}e^{j\varphi} \right|^2 \tag{5.2}$$

The RCS response can exhibit orientation dependencies, as seen in [28] and also in several other works besides [15]. Interestingly, this behaviour cannot be purely assumed to be caused by orientation dependencies of the structural mode [28] as its effects are also present in the antenna mode too [23]. Further study is needed into the orientation dependencies of chipless RFID tag/sensor designs but for now, this issue will be ignored. Instead, this section will focus on the goal of extracting stimulus information from the bandstop responses found in earlier works by the authors.

5.3.3 Bandstop Response Discussion

The bandstop (notch) frequency response is a well-known frequency response and can be modelled in continuous time using the transfer function found in [29], and presented here in Equation 5.3. This formula describes the response of this type of system in the complex plane as having a magnitude that is the product of the distances from the current frequency to the location of the roots of the numerator (zeros), divided by that of the denominator. Similarly, the phase response of the system is the sum of the angles between the real axis and the vector between the current frequency and each of the roots of the denominator (poles), subtracted away from that of the zeros. In the aforementioned equation, magnitude gain is determined by H_0, the quality factor of the pole (peak) and zero (null) are represented by Q_p and Q_z respectively. Furthermore, the pole and zero frequencies are represented by ω_p and ω_z. The Laplace operator (s), has also been presented in Equation 5.3 as being the complex sum of a near-zero term (σ) and a frequency term (ω), where $j = \sqrt{1}$. One last point to be made in this section is that this project will focus on using/exploring the magnitude response data from the chipless RFID tag/sensor. Reasons as to why this was done include the following:

- Phase information may not be available or easily retrieved by a future reader architecture
- The phase information will need to be unwrapped appropriately

$$H(s) = \frac{H_0 \left(s^2 + \left(\omega_z / Q_z\right) s + \omega_z^2\right)}{s^2 + \left(\omega_p / Q_p\right) s + \omega_p^2}, \qquad s = \sigma + j\omega \qquad (5.3)$$

Standard Form

A standard bandstop (notch) filter can be constructed out of a series connection of a resistance (R), capacitance (C) and inductance (L) as described in Figure 5.3. The corresponding transfer function is one which the frequency of the zero is equal to that of the pole. This results in a symmetric-like magnitude response around the null point of the frequency response. Figure 5.4 depicts the frequency response of this type of filter. The other terms of Equation 5.4 describe the rate at which and magnitude of the effects of the poles and zeros on the system response.
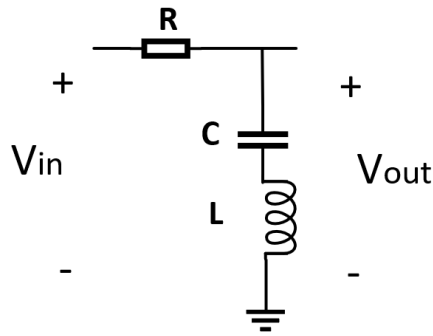
Figure 5.3: Example Bandstop Circuit

$$H(s) = \frac{V_{out}(s)}{V_{in}(s)} = \frac{\left(Ls^2 + {}^1\!/_C\right)}{Ls^2 + Rs + {}^1\!/_C} \qquad (5.4)$$
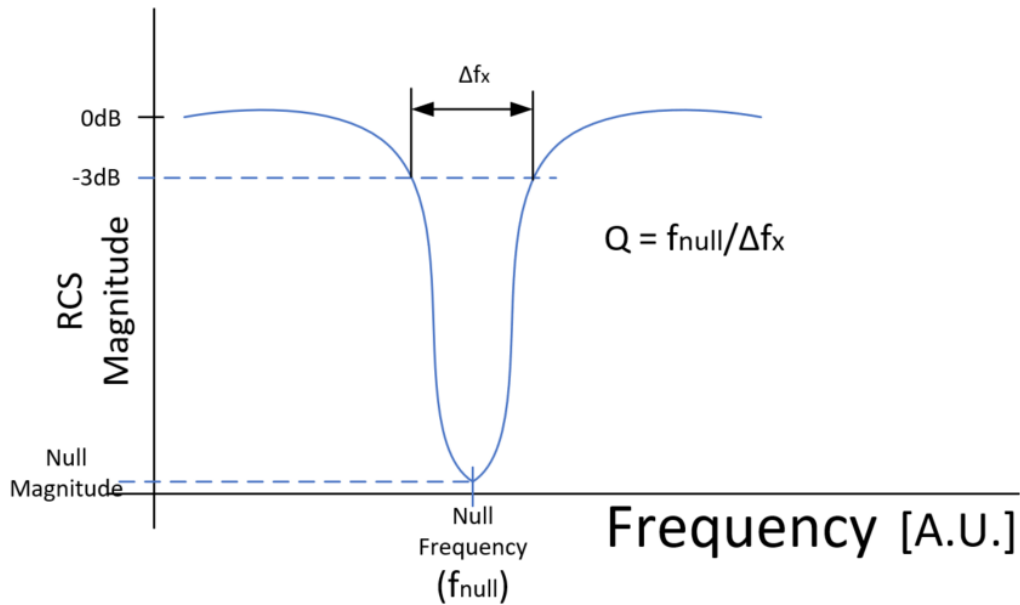
Figure 5.4: Bandstop Magnitude Response Diagram

Elliptical Form

The transfer function in Equation 5.3 above describes a different form of curve if the frequency location of the zero and pole are significantly different. These scenarios have been described as follows:

- $\omega_z > \omega_p$: Highpass bandstop or Elliptical Highpass filter [29][30][31][32]
- $\omega_z < \omega_p$: Lowpass bandstop or Elliptical Lowpass filter [29][30][31][32]

The frequency response of these two scenarios (1 & 2) is depicted in Figure 5.5 and Figure 5.6 respectively. The two Q-factor terms in this case define the magnitude and rate of change of

the response around the frequency of their respective pole/zero. Several manual fittings of the transfer function in Equation 5.3 to chipless RFID sensor responses can be seen in a later section of this report. These elliptical bandstop responses are mentioned here as many of the sensor responses detected both in Chapter 3, Chapter 4 and in other works besides [29][30][31][32], exhibit magnitude behaviour similar to these elliptical bandstop responses.
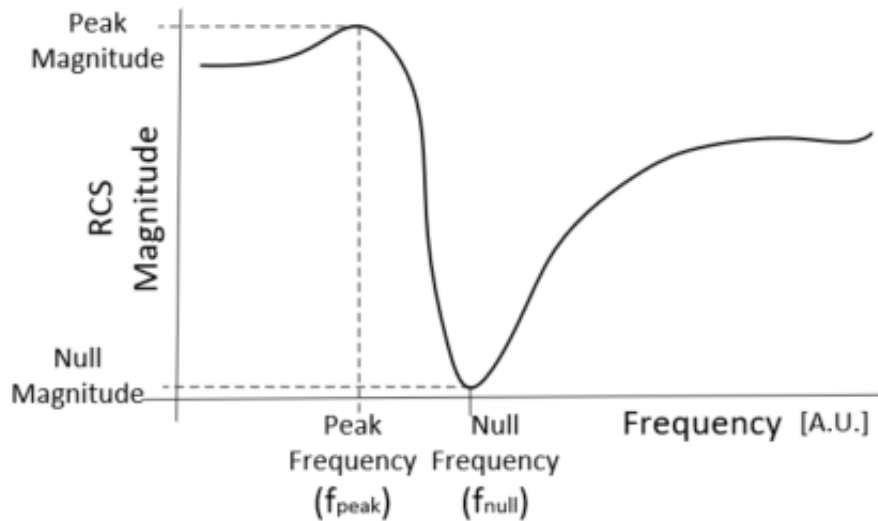
Figure 5.5: Lowpass Bandstop Response
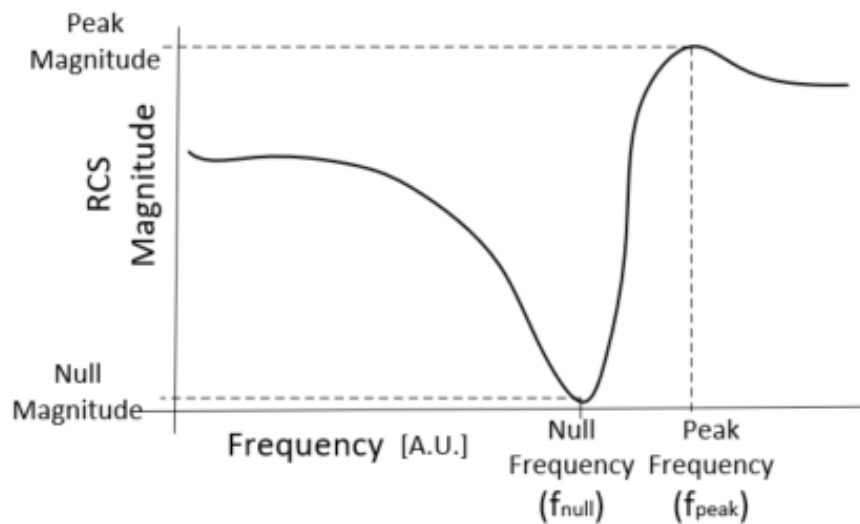
Figure 5.6: Highpass Bandstop Response

175

5.3.4 Features of Interest

The features of interest depend heavily on the approach taken within the sensor design. Basic bandstop responses have two features that can be used for stimulus encoding, as seen in Figure 5.4. These features are; null/zero frequency (f_{null}) and Quality (Q) factor. Similarly, the other two variations in bandstop response have these features along with another feature; the peak/pole frequency (f_{peak}), as seen in Figure 5.5. The strain sensor developed by the authors in an earlier work [15] does not exhibit stimulus-based variations in f_{peak} and thus this feature will not be considered as important from this point forward.

This particular work is focussed on the determination of the null frequency as this is the main characteristic that describes the strain level experienced by the strain gauge developed by the authors in an earlier work [15]. This feature (null frequency) is also a commonly used feature for stimulus encoding in the chipless RFID strain sensor literature and amongst other sensor types also. The preference towards the use of this feature for stimulus encoding, over Q-factor is that the latter is heavily affected by the environment and its wilful reduction/modulation will most likely lead to a reduced reading range of the sensor.

5.3.5 Limitations of Basic Feature Extraction Methods

Two main limitations exist in the basic approach taken to extract the stimulus information from the response curves. The basic approach is to assume that the minimum point in the retrieved dataset is at the null frequency of the resonant response. The limitations of interest are:

1. The minimum point in the dataset is assumed to be coincident with the null of the resonant curve
2. The resolution of the dataset dictates the resolution of the calculated stimulus levels

The majority of publications in the area of chipless RFID use visual checks to ensure that the RCS response observed can be successfully interpreted. It is the case however, that the channel and general system setup could give rise to RCS responses that contain little or no contribution from the sensor of interest [9]. These scenarios are detrimental to the simplistic approaches taken in proof-of-concept publications in the area of chipless RFID as the resonant response may not be present or may be dominated by noise (see Figure 5 in [9] for example). Both of these scenarios result in the basic null frequency detection method, which is to find the frequency corresponding to the lowest response magnitude, highly susceptible to catastrophic error. Although the authors have recorded a multitude of environment-based sensor responses where the resonant curve is not visually detected, a repeatable and

176

predictable way to test the effects of a reduced sensor response is through the use of polarization mismatches. This effect should and does cause the magnitude of the resonant response to reduce as it becomes a smaller part of the total response, as the linearly polarized sensor is rotated (see Chapter 6). As the curve becomes flatter, this leads to the possibility that the minimum point on the curve is the result of aspects of the system not captured by the simplistic background subtraction process and not the result of the current stimulus level [7][8]. Therefore, the assumption that the minimum point is coincident with the curve null becomes increasingly reliant on noise and other such effects, when the sensor response is becoming weaker. The work of Megahed in [7] demonstrated an increase of the successful probability of detection from a real-world chipless RFID tag deployment through the use of techniques other than assuming that a minimum value below a certain value is indicative of a true resonance. Said work contains resonant responses that are far below those predicted by basic electromagnetic simulation results. Random noise and other disturbances could also play a part in reducing sensor detection [7]. For most applications, it can be assumed that averaging should allow for the mitigation of the effects of ambient noise, but this may not be the case for other applications where a dynamic stimulus is present (i.e. vibration). Furthermore, the need for averaging could have a significant impact on the total interrogation time that each sensor requires. On the topic of disturbances, other features/artefacts may arise within the resonant response which could be the result of background variations or the result of multipath propagation. Spurious dips appear in the responses found in many other works including those referenced here [7][8][33]. These effects, which are going to be referred to as static noise from now on, could potentially ruin the ability of the system to accurately determine the stimulus, if the spurious contribution appeared at/around the null frequency.

The second issue with the use of the minimum point as being the measurement taken as being the true minimum is that the resolution of the dataset has a direct impact on the resolution of the determined null frequency. With strain sensitivities on the order of 30MHz/%ε in Chapter 3, a 1MHz frequency step corresponds to resolution of 333με. From the existing literature [3], it is clear that increasing the number of datapoints will either lead to significant increases in interrogation time and/or increasing hardware challenges. Given the fact that crack detection requirements set out by the National Aeronautics and Space Administration (NASA) in [13] and that demonstrated by existing SHM sensors, strain sensing below 10με is the required resolution and thus a significantly higher frequency resolution is required. The issue of environmental stability and noise in the context of chipless RFID strain sensing has also been

emphasised in other works such as [34][35] where the read range was limited to 3-10mm to combat this and other issues.

At this point, it is worth reviewing how frequency resolution is related to stimulus resolution. In the case of a response curve that is symmetric and convex about the null, the true null frequency can be said to sit within $\pm\frac{\Delta f}{2}$ of the frequency of the minimum value, where Δf is the fixed frequency interval between datapoints in the frequency response data. This is explained further in Figure 5.7(a) below, where three noise-free datapoints on such a curve are depicted graphically. The minimum measured point is the central datapoint (P2), and it can be concluded that the true minimum sits somewhere between the two outer data points (P1, P3). For a curve with X1 > X2, the true minimum must sit between P2 and P3 if the curve is symmetric. Similarly, if X1 < X2, the true minimum must sit between P1 and P2. The other type of scenario is where X1=X2 and this is depicted in Figure 5.7(b). In the case where the curve is symmetric about its true minimum, this true minimum will be found at the exact midpoint between P1 and P2. Further study of Figure 5.7 also reveals that the true minimum must sit within half a frequency step from the measured minimum, because if it were more than this, either X1 or X2 would become negative for a curve that is symmetric about its true minimum.

If curve convexity holds but symmetry cannot be assumed, as seen in Figure 5.7(c), then the true null can only be assumed to lie within a frequency band $\pm\Delta f$ around the frequency of the minimum value, because the scenario in Figure 5.7(b) above is no longer valid as two datapoints of equal magnitude on the asymmetric curve would not be at the same spacing from the true minimum. The importance of this finding will need to be considered later on in the sensor development process as it means that asymmetric responses will require dataset resolutions that are twice as large as those for symmetric ones.
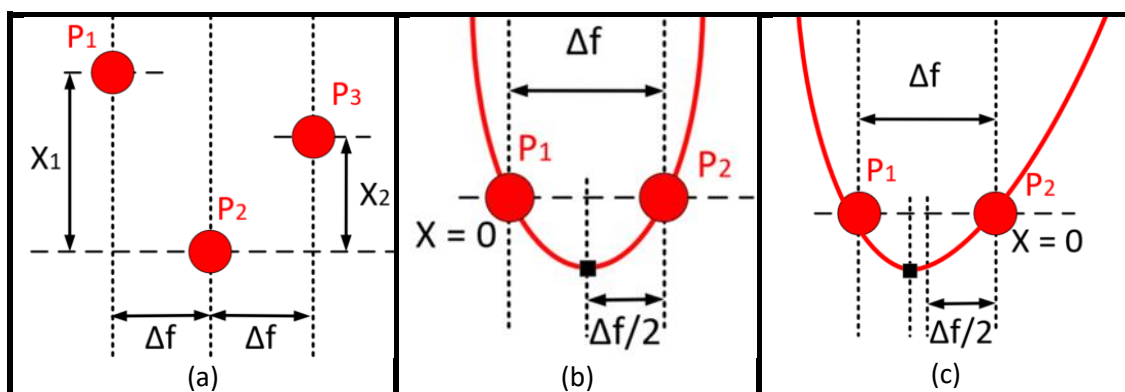
Figure 5.7: Response Curve Diagrams

The next part of this discussion is going to build upon the discussion above, as the feature extraction approach taken in proof-of-concept tag/sensor design publications is probably going to be insufficient in a real-world system implementation. The problems identified with the discussed simplistic approach are the following:

1. There is no computational test to check if a valid/recognisable resonant response has been observed in the dataset. Perhaps the channel losses have changed significantly, or the sensor is damaged, or it has fallen off its original placement

2. Relying on the resolution of the frequency response dataset to achieve accurate null frequency determination will have significant knock-on effects on interrogation times – some reader architectures may be more robust than others at combatting this problem but an SHM system consisting of thousands of sensors will need to consider the issue of interrogation time very carefully

5.3.6   Matched Filter Implementation

This section will explore the detection of the null frequency of the curves present in Figure 5.8, which are from a recent strain gauge publication [15]. It must be noted however, that many other publications [36] exhibit sensor responses with similar curves and have a similar need to determine null frequency, as that is how their stimulus of interested has been encoded into the sensor response. The two algorithms used are correlation and covariance, as they were the next step up in computational complexity to the minimum-point method. The analysis was performed using Scilab [37].
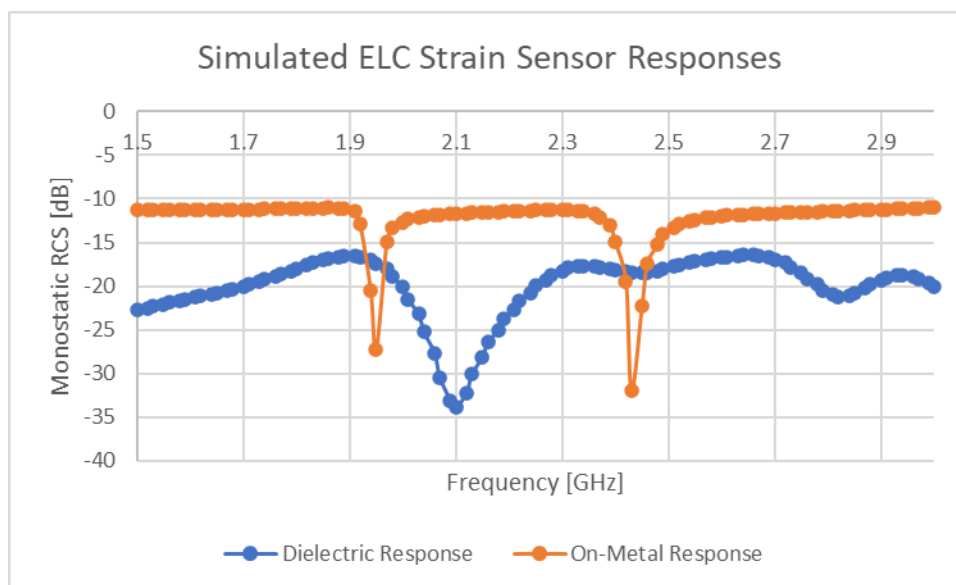
Figure 5.8: Simulated Strain Sensor Responses – from "Proof of Concept Novel Configurable Chipless RFID Strain Sensor." by McGee et al., MDPI, CC BY 4.0 [15]

Determining whether a specific characteristic is present in a dataset such as the ones in Figure 5.8 above is a challenge that has long being explored by other researchers. The next step in complexity above the rudimentary methods mentioned above, is to make use of a matched filter. Matched filters have been used in other works and despite their computational simplicity [7], are a useful tool for chipless RFID tag response detection [7]. Essentially this mathematical procedure involves the comparison of each position of the dataset with a smaller window function. Mathematically, this comparison (see Equation 5.5) is known as correlation, is performed by computing the sum of the products of the overlapping window (X_m) and dataset (Y_m) at each position in the dataset (k). The benefit of this approach is that there is now a measurement into the likelihood that the desired resonant curve is present or not, whereas before there, was no such measurement. This is also an improvement in the goal of successful null frequency determination as it now means that the estimated null frequency

180

is now dependent, to a greater extent, on the entire resonant curve. The resulting dataset can then be put through a thresholding process as described in [7] and the presence of the desired resonant curve can be confirmed or denied (and its location determined).

$$corr[k] = \sum_{m=1}^{M-k} (X_{m+k})(Y_m) \qquad (5.5)$$

This particular computation has a striking resemblance to the well-known discrete convolution operation. The only difference is that the window/kernel is mirrored in convolution for causality. Given the known relationship between convolution in the time domain and multiplication in the frequency domain, Equations 5.5 and 5.6 are usually computed using Fast Fourier Transform (FFT) algorithms [38]. The work in [7] made use of convolution to compute the matched filter results however, this approach is avoided in this work as some of the response signals in this work are not symmetric about the minimum point. Another important computation, called covariance, normalises the window and dataset before correlation, by subtracting away the respective averages (μ_X, μ_Y), as seen in Equation 5.6. This method may help to avoid unwanted effects in the results if they share distinctly different average values.

$$cov[k] = \sum_{m=1}^{M-k} (X_{m+k} - \mu_X)(Y_m - \mu_Y) \qquad (5.6)$$

Initial Testing

The window datasets used in the analysis of the "on-dielectric" and "on-metal" curves can be seen in Figure 5.9. Applying these windows with zero-padding to the datasets resulted in the correlation and covariance results seen in Figure 5.10 to Figure 5.12. Scilab was used to perform this analysis using the built-in "xcorr" [39] and "xcov" [40] functions.
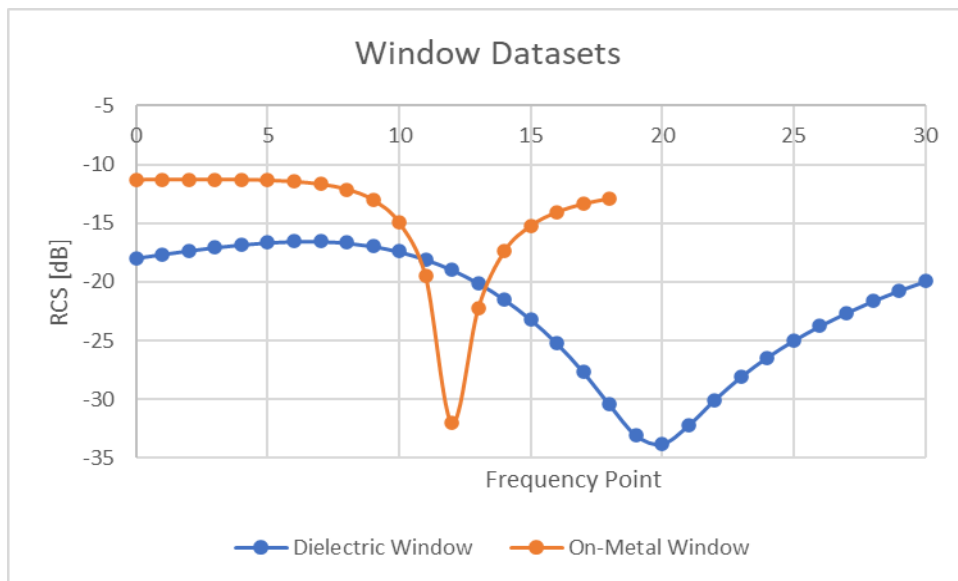
Figure 5.9: Window Datasets

181
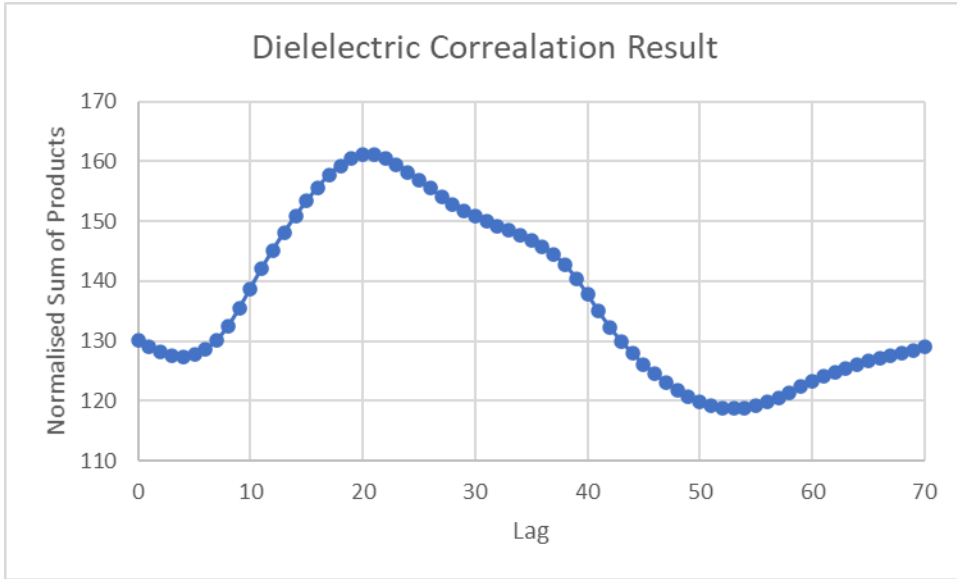
Figure 5.10: Dielectric Correlation Test Results
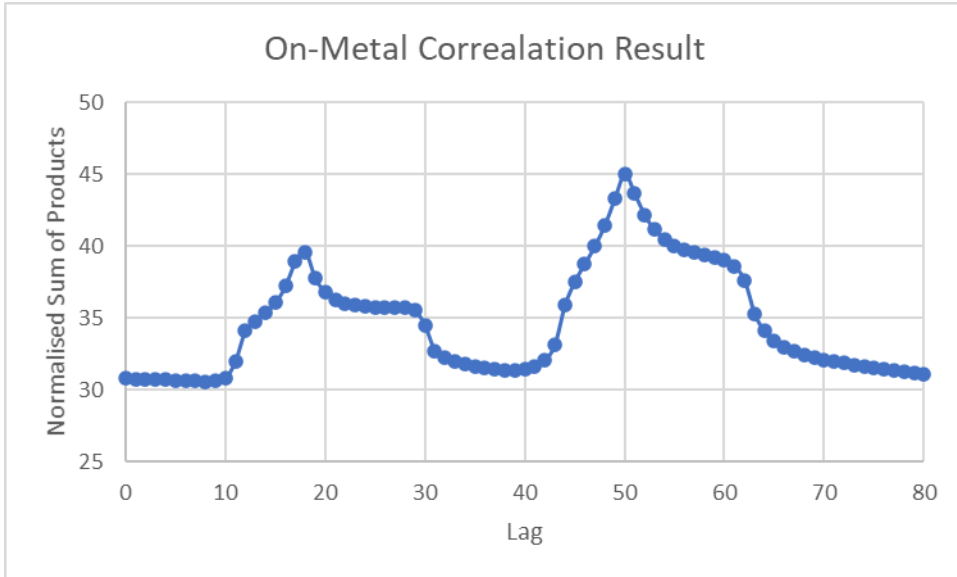
Figure 5.11: On-Metal Correlation Results
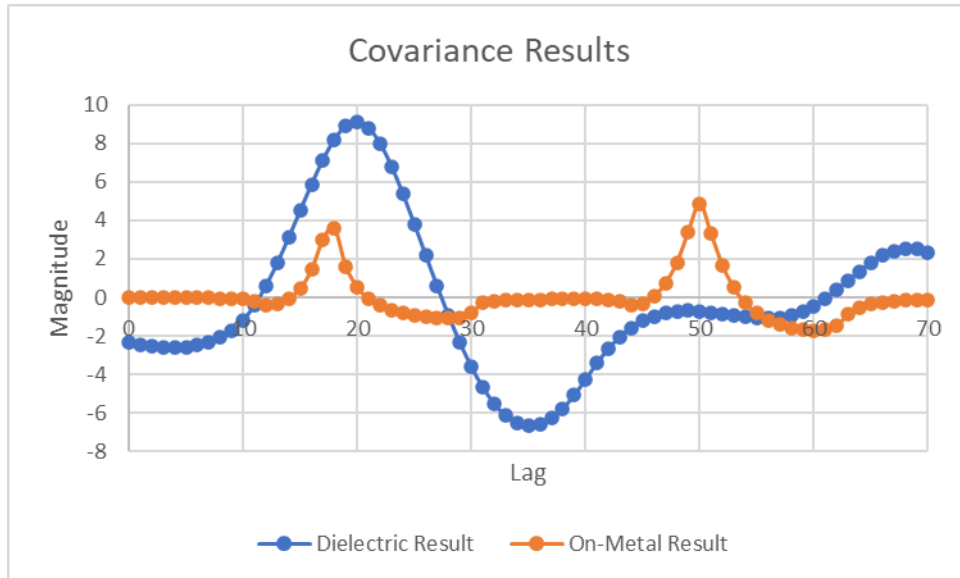
Figure 5.12: Covariance Test Results

From Figure 5.8, it was determined that the null frequency is located at the 42nd index which corresponds to 2100MHz. Looking at the window dataset depicted in Figure 5.9, the null frequency in that response is at the 22nd index. Taking the results from either the correlation or covariance graphs in Figure 5.10 and Figure 5.12, the maximum is found at the 20th index. Therefore, the predicted null frequency, according to the matched filter implementations, is also at the 42nd index in the main dataset. Similarly, the On-Metal results revealed peaks at lag values of 18 and 50. Since the offset in the window seen in Figure 5.9 above is 13, the predicted indices of interest in the interrogation dataset are indices 30 and 62. The same result was found by visually inspecting the on-metal interrogation dataset seen in Figure 5.8 above. Since the covariance results revealed more discernible peaks, this computation will be used for the remained of this section. The presence of sharper peaks was seen as a bonus because the threshold procedure that would be used in a fully automated system would probably perform better under those conditions, as wider peaks would more likely lead to the presence of noise affecting the result.

Since both static and random variations in the response curve can occur, the detected response curve could deviate from those seen in Figure 5.8 above. To mimic these potential effects, different levels of normally distributed noise was added to the base dataset. Since the variation between the null magnitude and its nearest neighbours was approximately 1dB, the first new dataset contained noise that had a mean of zero and a variance of one decibel. Additional datasets were also created that had variances up to five decibels. Figure 5.13

depicts a sample of these datasets, in which, it can be clearly seen that the curve experiences a significant amount of degradation.
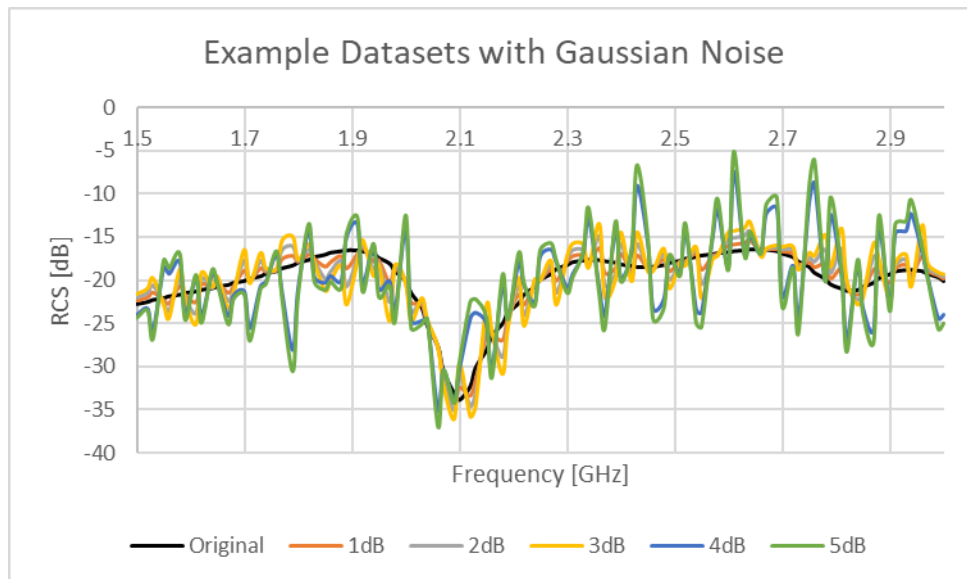
Figure 5.13: Dielectric Dataset with Varying Noise Levels

To assess the performance of the matched filter against the standard (minimum point) approach, 1000 different datasets were generated for each of the different noise levels and the null frequencies were calculated using the two methods: covariance and minimum point. From these results, the mean and standard deviation of the determined null frequency was determined, and the standard deviation results can be seen in Figure 5.14 below. Note: The frequency resolution of the input dataset was 15MHz steps.
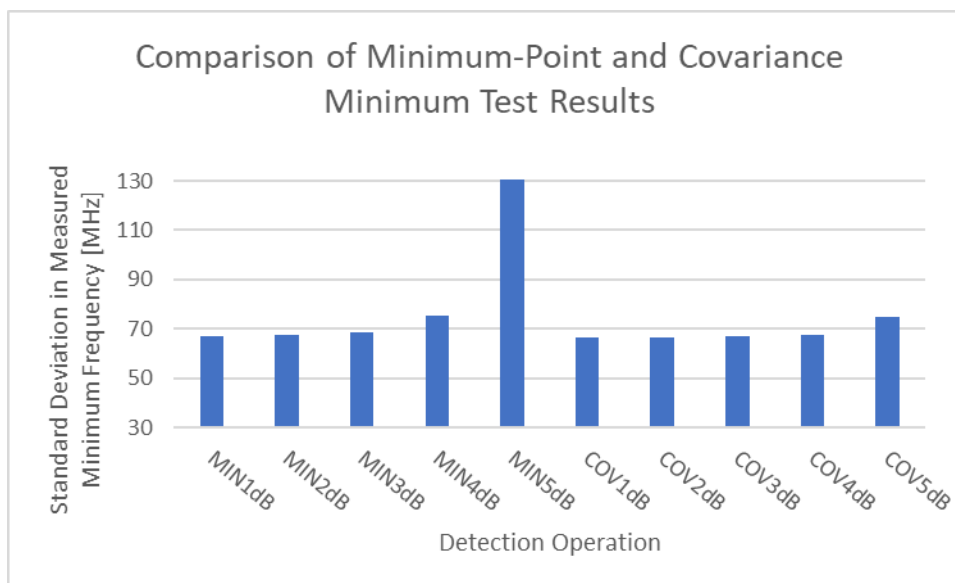
Figure 5.14: Impact of Covariance Method with Noisy Datasets

From the results presented in Figure 5.14 it is apparent that the use of the matched filter results in a far more stable null frequency detection than the minimum point method.

Resolution and Computation Considerations

Although the features of interest to different sensor designers may differ from the one emphasised in this work (null frequency), it is fair to say that frequency resolution will be of importance in the accurate determination of any such feature. This is predominantly the case in the strain sensor developed in an earlier work as the strain information is encoded in the position of the null frequency. Although the use of a matched filter does perhaps make the null frequency detection more reliable, both this method and the minimum point methods both have the same frequency resolution. Fundamentally, the computation can only be performed on the sampled data points which are discrete in nature. The most obvious way to enhance null frequency resolution is to enhance the frequency resolution of the response signals, which usually corresponds to an increase in interrogation time. It remains to be seen how much one can increase this resolution in a multi-sensor environment (1000+ sensors) before this approach becomes untenable.

An alternative approach could be taken where the need for initial curve detection could still be performed but with much less refined datasets and another step is then taken to go about the relevant feature extraction. This additional step could also make use of the result of the initial matched filter (i.e. rough location of null frequency) to perform a more resolved sweep in the appropriate part of the spectrum. This secondary sweep may utilise polynomial curve fitting or minimum value selection to determine the true null frequency. Said approach requires two separate interrogations for the strain variable and assumes that no significant variations in strain level occur between these sweeps. With regard to the need for two interrogations, it remains to be seen where the "bottle-neck" will appear in the stimulus extraction protocol, but it would be wise to consider the possibility that it may be found in the interrogation process, as the reader configuration and sweep times may indeed be the dominating factor in the total measurement time. Given the fact that the sweep time is the longest part in the sensor interrogation procedure currently, the use of two sweeps per sensor was abandoned. An alternative possible approach is to perform a single sweep of moderate resolution (Δf) and to have a high-resolution window dataset whose resolution is an integer multiple of that of the incoming dataset (($\Delta f/N$) $\in \mathbb{Z}$). This allows for decimation (down-sampling) of the window into several (N) separate windows that can then be separately applied, perhaps even in parallel, to the incoming dataset (covariance, etc.). Figure 5.15 depicts the formation of the windows used by this approach. This approach negates the need

for a secondary sweep and allows for an N-stage parallel processing of the high-resolution covariance measurement. One downside of this approach is that the stability of the determined minimum is dependent on 1/N times the number of datapoints in the window which would leave the result more vulnerable to error.
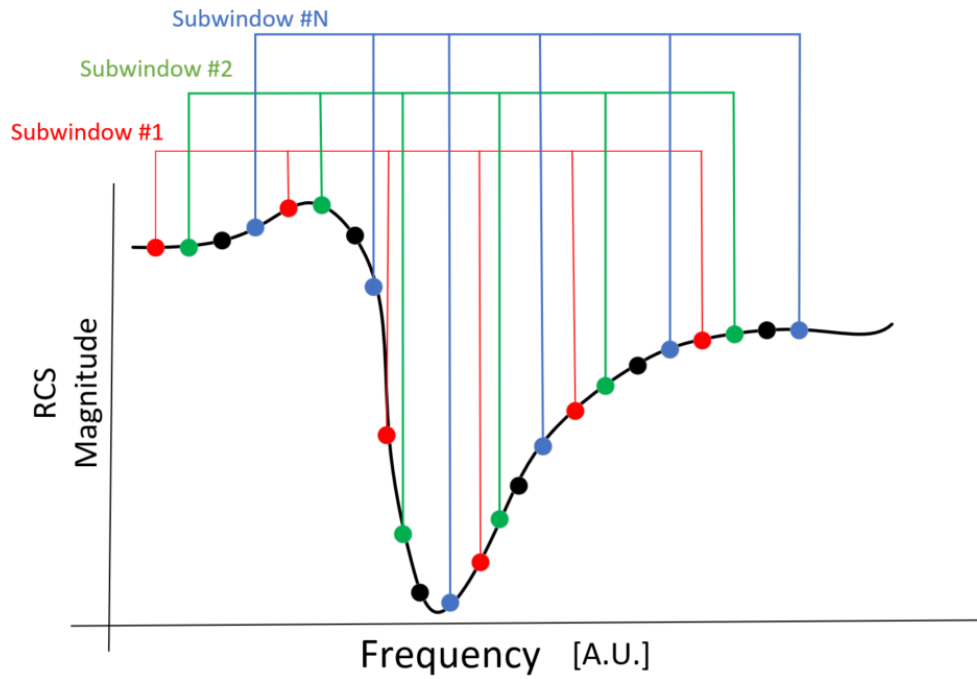
Figure 5.15: Sub- (Decimated) Window for Simplified Matched Filter Approach

Figure 5.16 depicts the standard deviation in the detected null frequency using the 2-part windowing process described above, along with the same results found by assuming that the minimum point coincides with the null point. Note: These 1000 datasets are the same as those used in the above tests except, they have been decimated (down-sampled) so that they only contain half the number of datapoints as the original datasets.
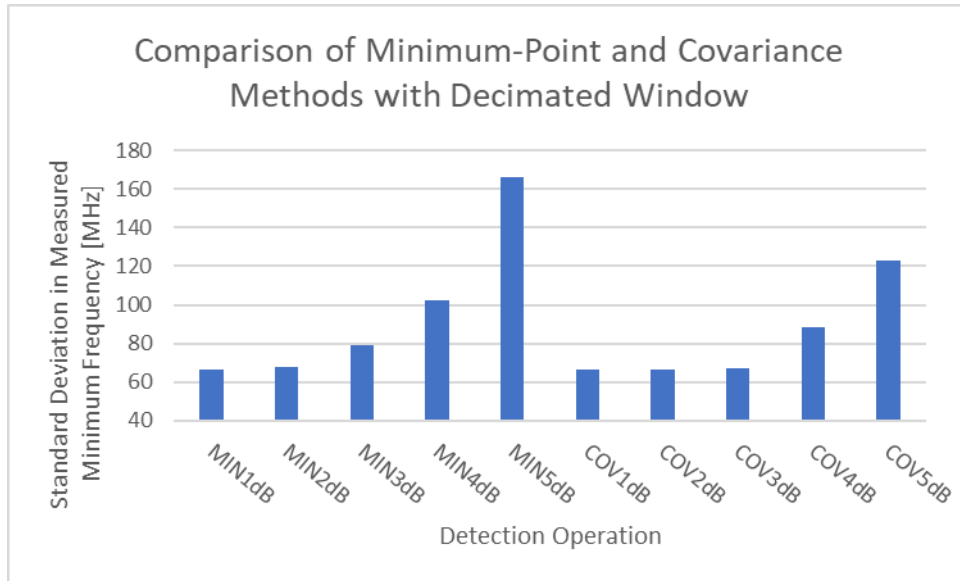
Figure 5.16: Results with 2-Part Matched Filter Window

Similar to the results found above, the use of the matched filter significantly reduces the noise-based variation in detected null frequency over the basic method. This is predominantly the case at increasing noise levels but comparing the results of Figure 5.14 and Figure 5.16 does show that the use of the two-part windowing process does not fully compensate for the effects of a reduced input dataset resolution. With that being said, it does boast a similar, albeit slightly weaker performance than that found with the minimum-point method used on the full input dataset.

Limitations of Basic Matched Filter

Other than the resolution limitations of the calculated null frequency, a more pertinent issue can occur when the resonant response of the sensor changes from that found in the window dataset. The standard bandstop response, given its symmetry, can only change its Q-factor but the result of which will be a less pronounced peak in the covariance results. From the resonant curves gathered during strain sensor interrogation in Chapter 3, it would appear that the peak (pole) frequency remained moderately stable over a range of strains whilst the null (zero) frequency moved considerably (see Figure 5.17). This is an interesting scenario because for a single window dataset, it leads to the possibility that the nulls in the window and incoming datasets no longer overlap at the position that their sum of products is a maximum. The magnitude of the error induced by this effect will depend on the characteristics of the window dataset. It has to be said that the strain ranges involved in the aforementioned datasets are quite extreme, but the sensitivity of these devices to dielectric constant

187

variations also brings forth the possibility that these conditions could potentially arise due to environmental variations also.
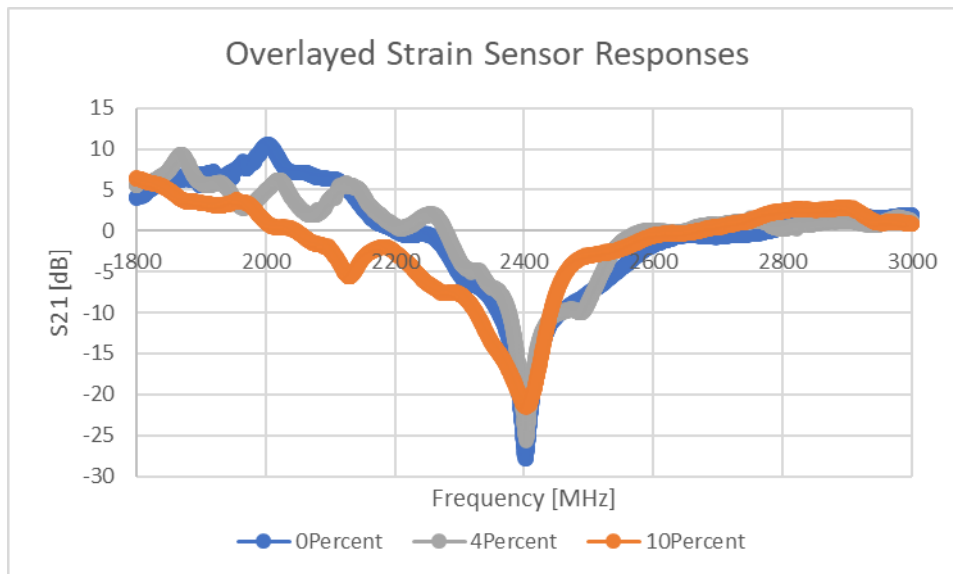
Figure 5.17: Overlayed Strain Sensor Responses – Adapted from "Proof of Concept Novel Configurable Chipless RFID Strain Sensor." by McGee et al., MDPI, CC BY 4.0 [15]

One approach to limiting the effect of this error involves altering the window dataset so that it only contains the portion of the resonant curve around the null frequency and does not contain the portion of the curve around the peak. Figure 5.18 depicts this alternate window alongside the conventional one, both of which are based on the resonant curve detected upon 0%ε.
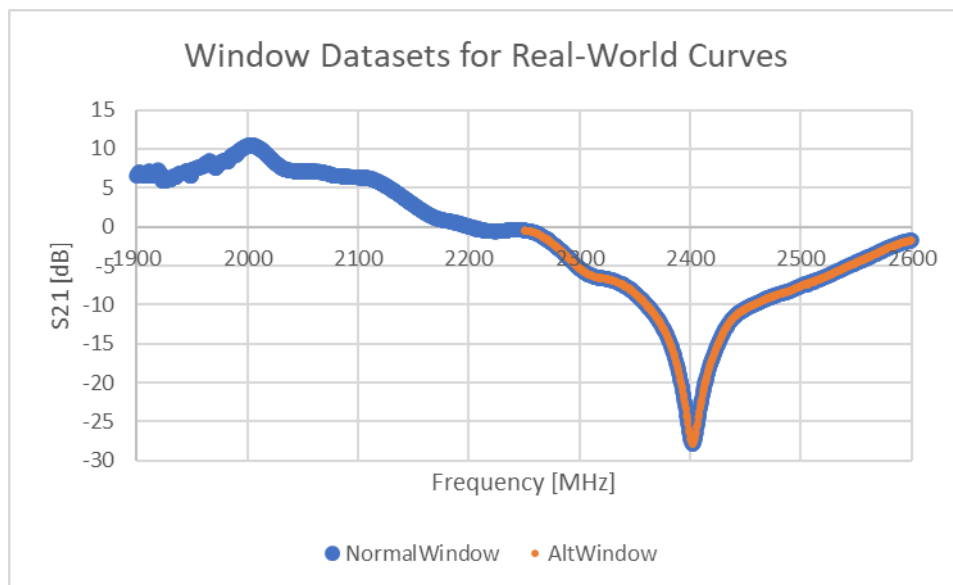
Figure 5.18: Original and Alternate Dielectric Window Datasets

188

The covariance results gathered for the strain datasets can be seen in Figure 5.19 and Figure 5.20. The former Figure 5.19 depicts the results of using the normal window and Figure 5.20 depicts the results gathered whilst using the alternate window.
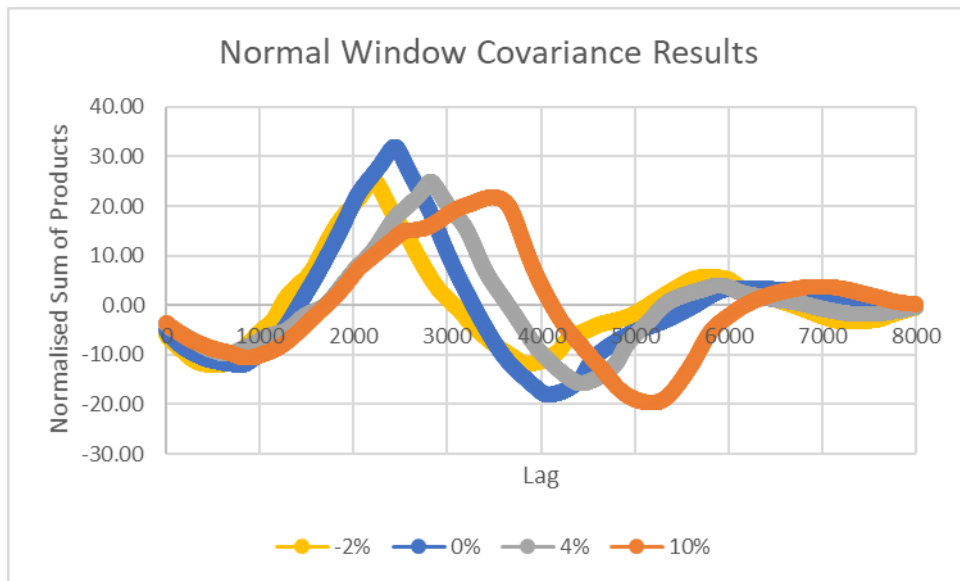
Figure 5.19: Original Window Covariance Results
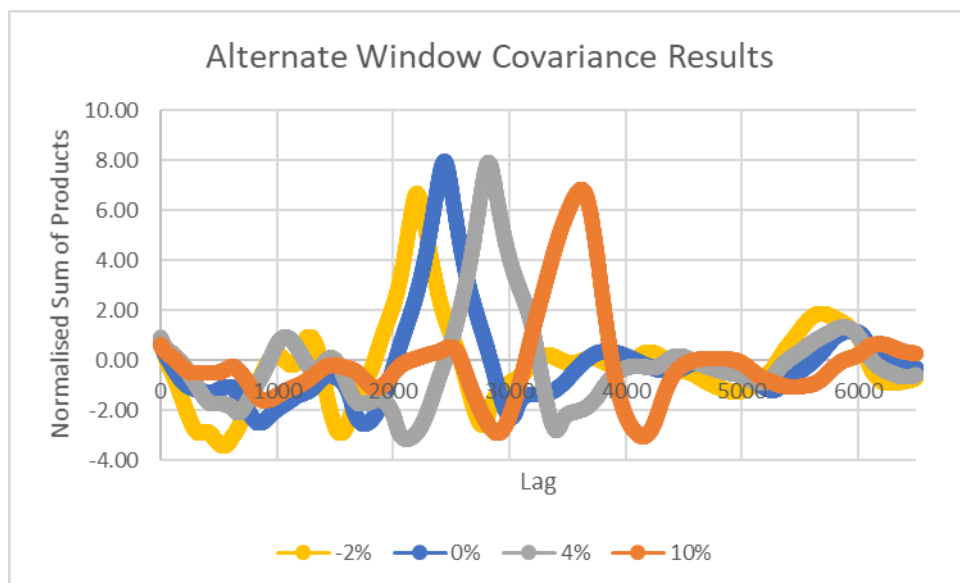
Figure 5.20: Alternate Window Covariance Results

The interesting result from the first Figure is that the width of the peak in the covariance result appears to increase for the larger strain datasets. The same cannot be said for the covariance results calculated with the alternate window. More importantly, the maximum of the covariance curves differs somewhat between the two tests. Table 5.3 depicts the final

calculated null frequency that has been calculated using the two windows and that found by searching for the minimum point in the dataset.

Table 5.3: Impact of Alternate Window on Determined Null Frequencies

	-2%ε	0%ε	4%ε	10%ε
Minimum Point	2045.881	2104.801	2197.638	2402.87
Normal Window	2045.881	2103.811	2198.381	2361.526
Alternate Window	2045.881	2104.306	2198.381	2395.881

From Table 5.3 above, it can be seen that the difference in results grows with increasing strain level and the normal window exhibits a results difference of approximately 40MHz at 10% strain. This is quite large and exceeds 1% strain for that particular sensor design. It must also be pointed out at this stage that the "Minimum Point" results found in Table 5.3 cannot be assumed to be free from the effects of noise, but their close relationship to the results found with the alternate window would suggest that they are somewhat accurate.

The results of using the alternate window therefore may help to more accurately determine the true null frequency for this response type, but there is still a significant divergence between the alternate window results and that of the minimum point method. As the error is not completely mitigated using this method, and exhibits an equivalent strain variation of 0.213%, the use of matched filter should probably be limited to assessing whether a resonant response of present in the incoming dataset. This is particularly the case where the null frequency needs to be accurately determined, as is the case in the sensing of strain. A more critical take on this issue would be to say that the current strain sensor designs are not sensitive enough, but the designs found in Chapter 3 do indeed compete well with the state-of-the-art designs in the literature.

Decoupling Stimulus Resolution from Dataset Resolution

A key limitation of both the matched filter and the minimum-point method is that the resulting stimulus resolution is tied to the frequency resolution of the dataset. The decimated window approach described in Figure 5.15 also suffers from this limitation, albeit to a smaller degree.

One approach to enhancing the resolution of the detected stimulus is to fit continuous curves to the discrete datapoints, which would allow for interpolation between datapoints and the determination of the actual stimulus level to a greater resolution. The authors have already used this approach in an earlier work [41] where the symmetric nature of the sensor response allowed for second order polynomial curve fitting to the dataset and the true response null

frequency was determined by finding the minimum point on the continuous curve. Other works such as that by Aliasgari and Karamakar [26] have attempted to fit bandpass/bandstop response curves to the sensor responses. Their results showed that there were some discrepancies between the template curves and the actual datasets and this finding was also made by the authors in Appendix H. Essentially, this area of work sets out to make greater use of software to overcome the limitations of the reader hardware and the limitations of the sensor performance.

From Appendix H, it can be concluded that bandstop transfer function fitting does not fit perfectly to either simulation or physically generated datasets, for certain sensor responses. Attempts were made during the development of Appendix H at both manual and automated curve fitting but the main strain sensor responses presented by the authors in Reference [15] proved difficult to work with. Other sensor responses, some of which are presented by the authors in References [15][41] proved far more suitable for performing curve fitting on.

5.4   Dynamic Stimulus Extraction

This section is focussed on dealing with behaviour seen in the response curve when the stimulus has changed significantly during its collection. This may not arise for many environmental stimuli such as temperature or humidity, but vibration and other such effects could result in response curves that differ significantly than those found under static stimulus conditions. On the topic of vibration, studies on aerospace systems such as [42], [43] and [44] have reported normal operating vibration levels with frequencies on the order of 1kHz. This section sets out to see how software can deal with the challenges presented by a dynamic stimulus.

There are two main questions of interest to this discussion:

1. Is it possible to still retrieve a static stimulus measurement when the sensor is experiencing a time-varying stimulus?

2. Is it possible to retrieve the time-dependent characteristics of the stimulus that the sensor is responding to?

5.4.1   Stimulus Gradient Detection

An example of a simple time varying stimulus is a linear gradient. To explore its effects on a chipless RFID sensor, the chipless RFID DC voltage sensor discussed by the authors in Chapter 4 was used, along with an Aim TTi signal generator. Initial tests were performed with the sensor connected to the VNA in a wired configuration. Figure 5.21 depicts the normalised sensor response found under a variety of stimulus gradients.
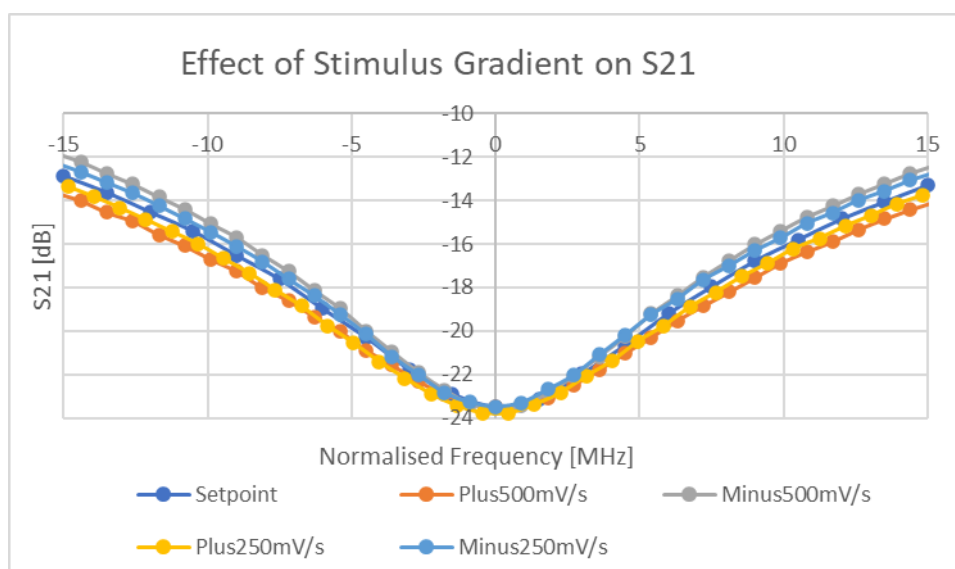
Figure 5.21: Effect of Stimulus Gradient on Sensor Response – from "Current Progress towards the Integration of Thermocouple and Chipless RFID Technologies and the Sensing of a Dynamic Stimulus" by McGee et al., MDPI, CC BY 4.0 [41]

192

The variation in the resonant response under the influence of a dynamic stimulus appears to be a growth or reduction of the width of the resonant response. Clearly the minimum value has not changed and the magnitude of the gradient could in theory be calculated through assessing the area under the resonant response curve. Figure 5.22 depicts this value for several different voltage gradients. Nonlinear features seen in Figure 5.22 are most likely caused by the non-linear response characteristics of the varactors within the sensor.
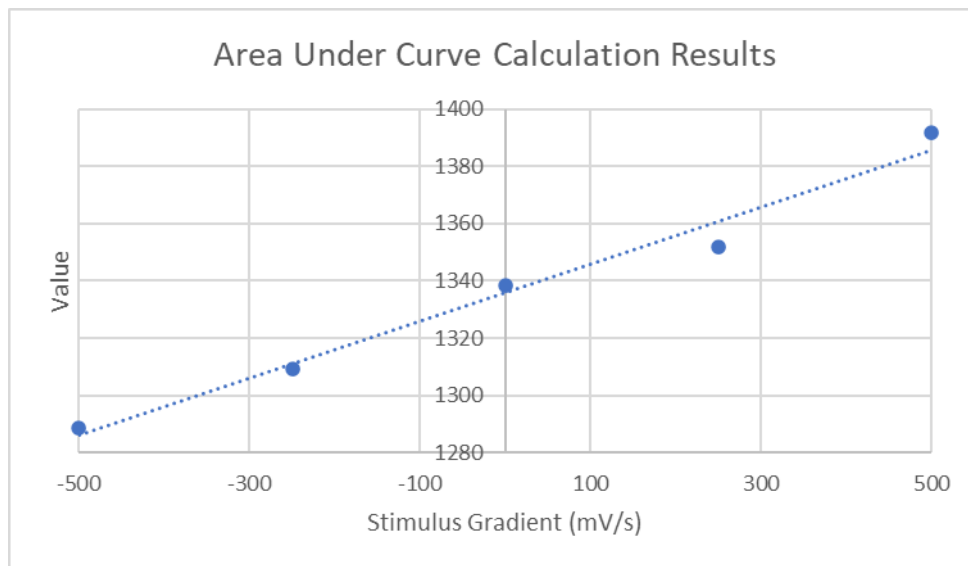
Figure 5.22: Area Under the Curve Calculations for Gradient Responses – from "Current Progress towards the Integration of Thermocouple and Chipless RFID Technologies and the Sensing of a Dynamic Stimulus" by McGee et al., MDPI, CC BY 4.0 [41]

The stimulus gradients used in the above testing are quite simplistic and were chosen because it was known that their effects could be easily interpreted from the resulting sensor response. More generally however, the effects of a stimulus gradient on the observed sensor response depend on other variables such as those listed in Table 5.4. Two key scenarios can arise when attempting to interrogate a sensor experiencing a stimulus gradient. If the gradient moves in the opposite direction to the frequency sweep, then both the static and dynamic effect can be detected. If the gradient is in the same direction as the frequency sweep, the dynamic effect may not be detected as the stimulus could outrun the frequency sweep. If the sensor response is however, bounded to a known frequency range, then some sensor response will be picked up during the sweep.

Table 5.4: Variables of Importance in Dynamic Stimulus Extraction

Variable	Comment
Sampling Rate [Hz]	This relates the frequency measurements to a specific point in the duration of the sweep
Frequency Step Size [Hz]	More frequency datapoints that capture a position on the instantaneous resonant curve will allow for a more accurate determination of the stimulus characteristics
Resonator Bandwidth [Hz]	A wider resonance will be easier to detect than a thin one which may not be picked up as there may be no intersection between the discrete sampling timesteps and the instantaneous stimulus level
Frequency Sweep Range [Hz]	The sweep range may impact whether the sweep can catch up with a slower moving stimulus gradient effect
Frequency Sweep Direction	This will dictate which side of the resonant curve is detected first during the sweep

The next question to be asked is whether the stimulus gradient information can be extracted directly from the response signals. To do this, the setpoint resonant curve dataset will be used as a lookup table. The bandstop response seen in Figure 5.23 below contains both magnitude and phase information and from the magnitude and phase information retrieved during sensor interrogation it is possible to recreate the dynamic stimulus information. The main problem is to figure out which side of the resonant curve that the frequency sweep encounters first (LHS or RHS), assuming that the reader sweep may not have started outside the operating frequency band of the device. This can be determined from the phase response and once this is done, each magnitude in the sensor response dataset can be mapped to the null frequency at that exact instance in time, through the use of the setpoint lookup curve. The resulting dataset contains the null frequency values that the stimulus had at each of the points in the interrogation sweep. For a fixed time interval between frequency samples, the timestamp of each of the entries in the dataset can be determined. Finally, the sensitivity curve can be used to convert the null frequency values to their equivalent stimulus levels. Figure 5.24 depicts the voltages that were experienced by the sensor during each point in the frequency sweep.
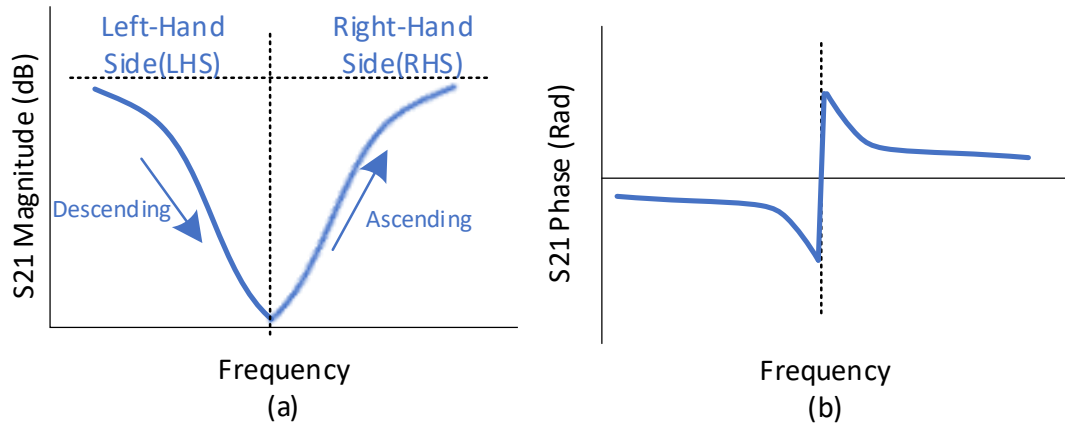
Figure 5.23: Bandstop Response Features – from "Current Progress towards the Integration of Thermocouple and Chipless RFID Technologies and the Sensing of a Dynamic Stimulus" by McGee et al., MDPI, CC BY 4.0 [41]
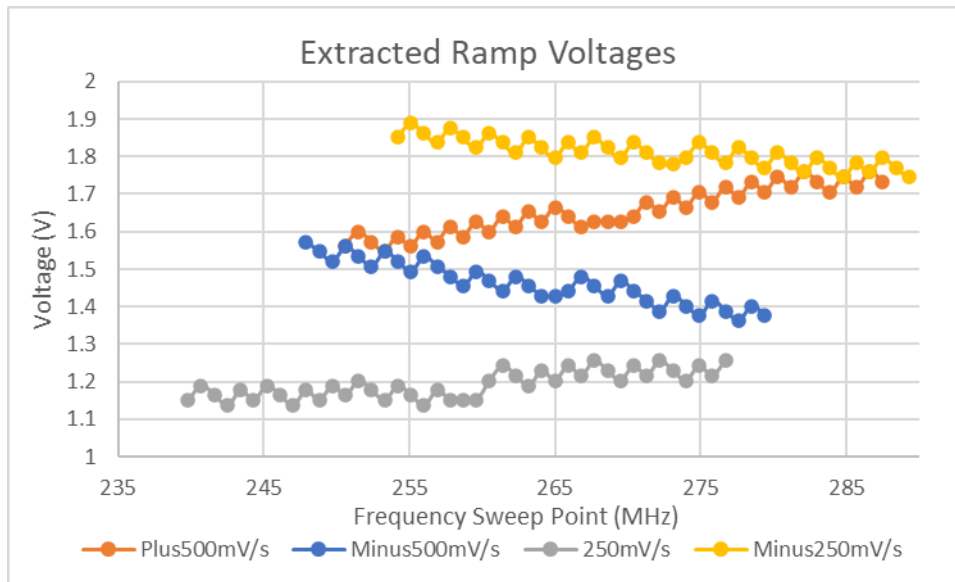
Figure 5.24: Extracted Ramp Stimulus Signals – from "Current Progress towards the Integration of Thermocouple and Chipless RFID Technologies and the Sensing of a Dynamic Stimulus" by McGee et al., MDPI, CC BY 4.0 [41]

Applying linear trendlines to the datasets found in Figure 5.24 above resulted in the following Equations, which were found in the work of McGee et al. [41]. The sensitivities found in the trendlines below (0.0052, -0.0056, 0.0025, -0.0029) can be interpreted as meaning that the voltage changes by that value with each passing sample. Therefore, since the sample rate of the NanoVNA V2_2 is 100 samples per second, the final time-dependent characteristics of the gradients can be determined as being; 520mV/s, -560mV/s, 250mV/s and -290mV/s respectively.

$$500 \text{ mV/s Trendline: } V = 0.0052(f) + 0.2635 \qquad (5.7)$$

$$-500 \text{ mV/s Trendline: } V = -0.0056(f) + 2.9452 \qquad (5.8)$$

$$250 \text{ mV/s Trendline}: V = 0.0025(f) + 0.5504 \qquad (5.9)$$

$$-250 \text{ mV/s Trendline}: V = -0.0029(f) + 2.5876 \qquad (5.10)$$

The approach taken in this section is far from ideal but does result in some interesting outcomes. Several issues exist with this approach, including;

- No interpolation or other form of smoothing was carried out after using the lookup curve, which would help account for the sharp transitions in the curves seen in Figure 5.24
- This work has ignored the possibility that the Q-factor of the resonant response could change with stimulus/frequency assumed that a single lookup curve is indicative of what will be observed at all stimulus levels
- The lookup curve and sensor datasets have poor frequency resolutions of 0.9MHz/step, this has also contributed to the presence of sharp transitions in the graphs seen in Figure 5.24

5.4.2   Sinusoidal Stimulus Detection

Since the topic of dynamic stimulus extraction has been arrived at from a concern about vibration, the effect of a sinusoidal stimulus is also of great interest. This subsection contains results from both wired and wireless testing setups, but the initial test results seen below in Figure 5.25 depict the impact of a 5Hz sinusoid with an amplitude from 1.8-2.2v being applied to the wired sensor.
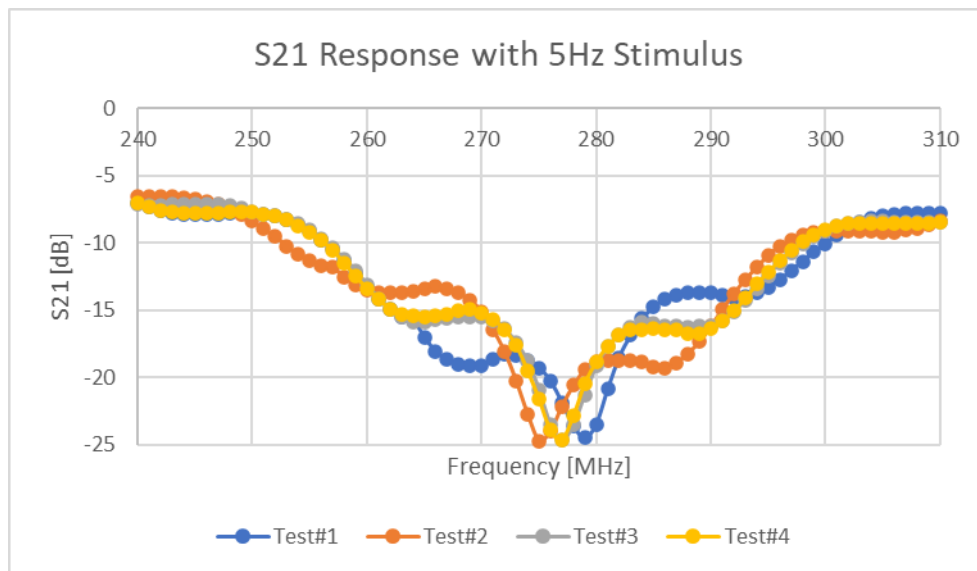
Figure 5.25: Stimulus Response with 1.8-2.2v 5Hz Sinusoid

Using the same approach as that used for the gradient detection, the potential sinusoids were formed as seen in Figure 5.26. Note: This figure contains two solutions to the lookup, one which clearly is not a standard sinusoid. Being able to discern which of the two possible solutions is the valid one, based on other information, can remove the need for phase information as part of the stimulus extraction requirements.
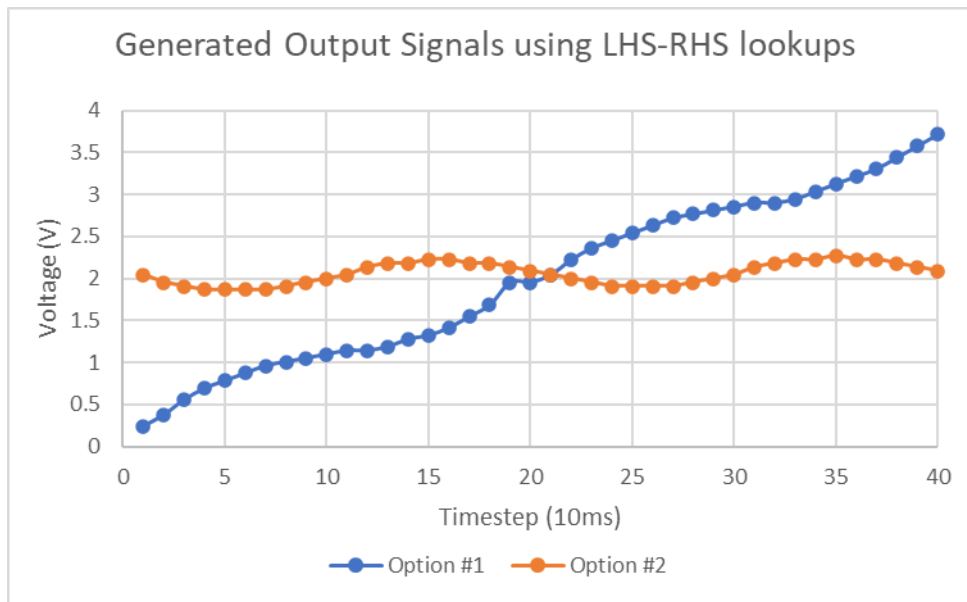
Figure 5.26: Extracted Stimulus Sinusoids – from "Current Progress towards the Integration of Thermocouple and Chipless RFID Technologies and the Sensing of a Dynamic Stimulus" by McGee et al., MDPI, CC BY 4.0 [41]

The results of running this procedure on other 5Hz datasets can be seen in Figure 5.27. To confirm that there is a noticeable 5Hz component, it is possible to interpret the curves visually, but a more suitable approach is to use the Discrete Fourier Transform (DFT) or more suitably the Fast Fourier Transform (FFT). These (FFT [38]) results can be seen in Figure 5.28 and although they are somewhat low, there is a pronounced peak around 5Hz. It is assumed that windowing would help enhance these results further but given the proof-of-concept nature of this work, that particular task has been omitted. Repeated 5Hz testing at a larger voltage resulted in the FFT results seen in Figure 5.29. Again, these results show a strong, clear peak around the 5Hz frequency bin.
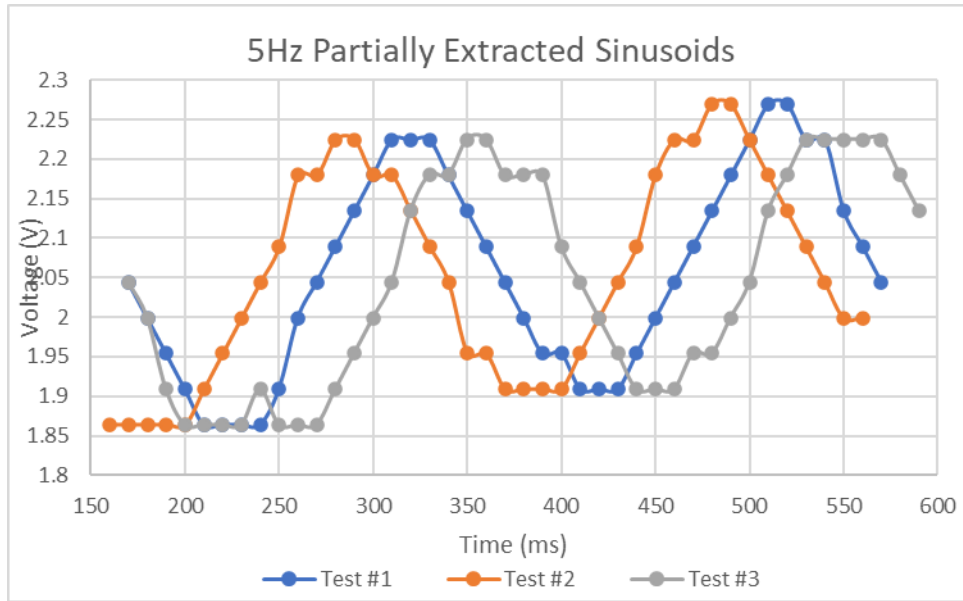
Figure 5.27: Extracted 5Hz Sinusoids – from "Current Progress towards the Integration of Thermocouple and Chipless RFID Technologies and the Sensing of a Dynamic Stimulus" by McGee et al., MDPI, CC BY 4.0 [41]
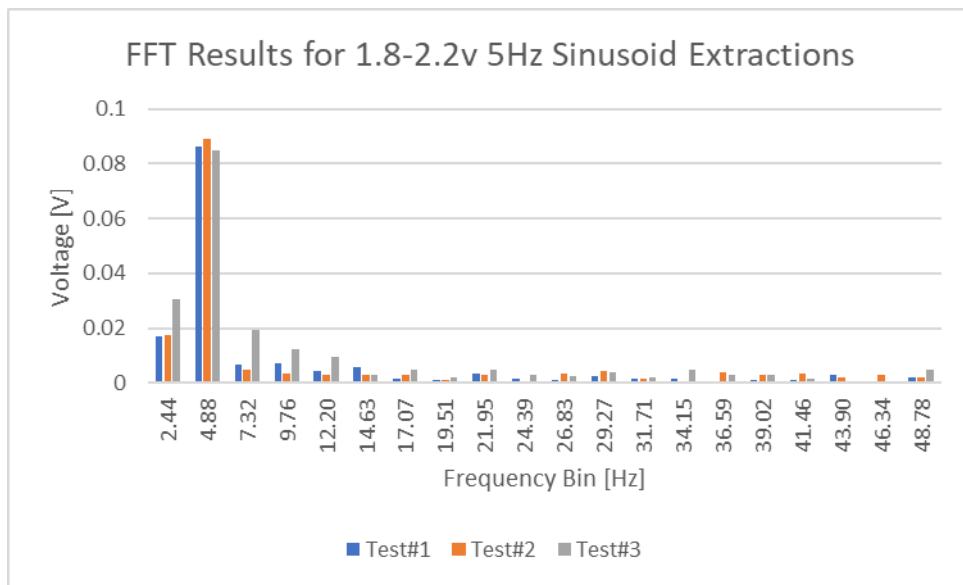
Figure 5.28: FFT Results of 400mV PTP 5Hz Sinusoids

199
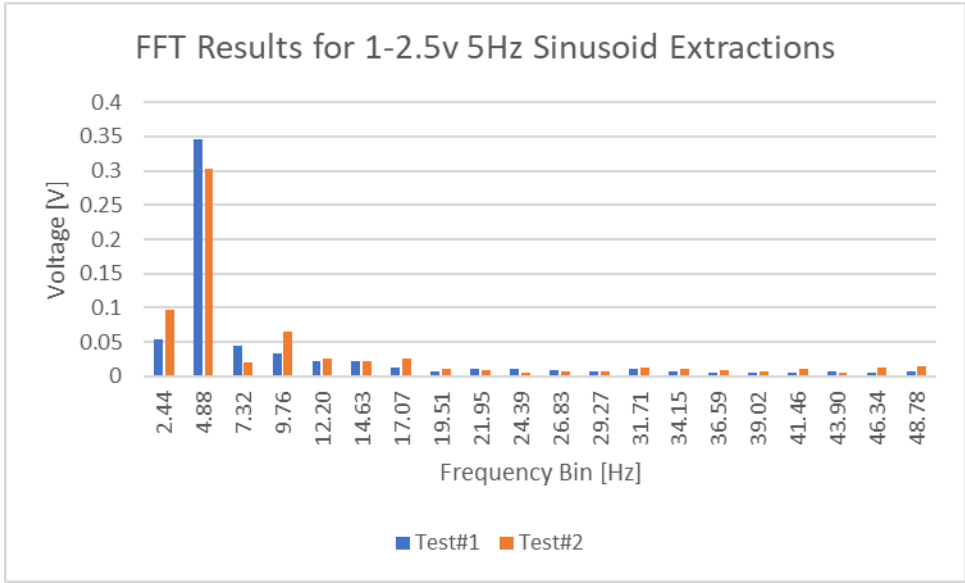
Figure 5.29: 1500mV PTP 5Hz FFT Results

Testing was also performed at both 10Hz and 3Hz and the 1.8-2.2v 10Hz sensor response can be seen in Figure 5.30. Extracting the stimulus resulted in the curves seen in Figure 5.31 and the FFT results of those curves can be seen in Figure 5.32. Similar testing was also performed on a larger 10Hz stimulus input and the results of that can be seen in Figure 5.33.
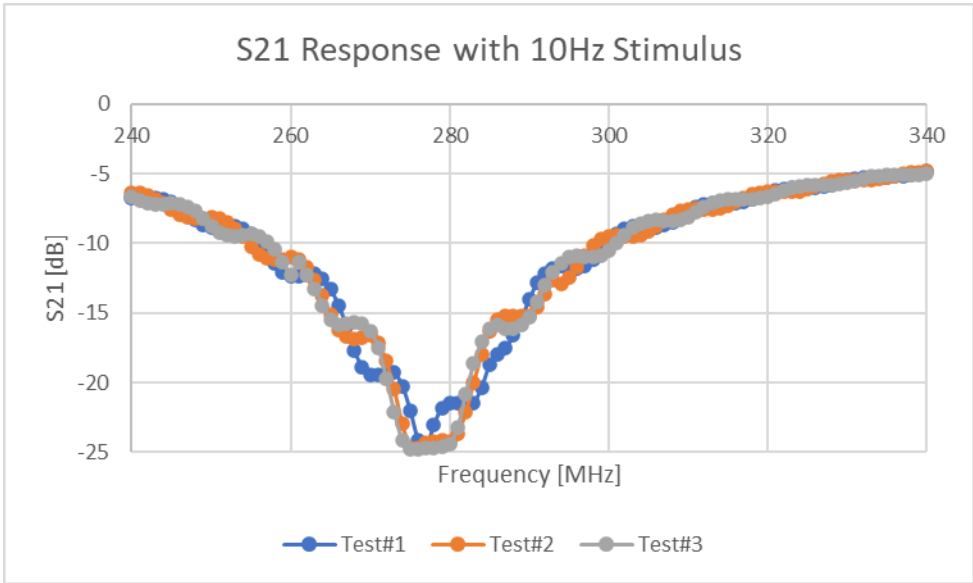
Figure 5.30: 10Hz 400mV PTP Sinusoid Sensor Response
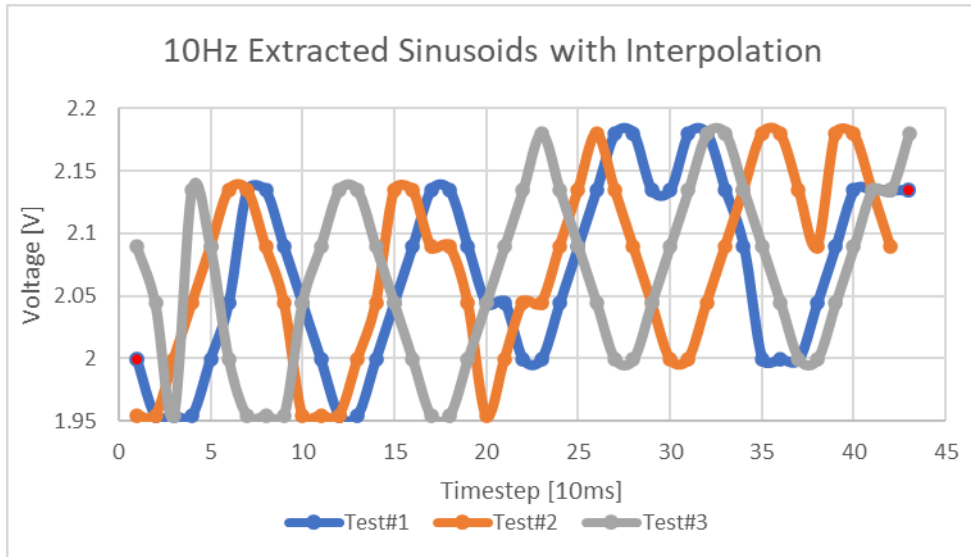
Figure 5.31: 10Hz 400mV PTP Extracted Stimulus Curves
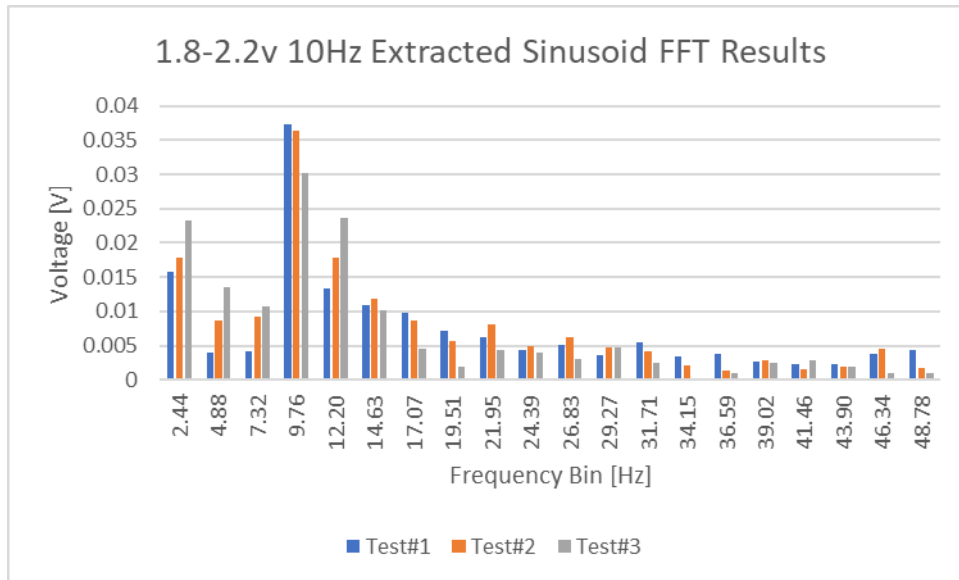
Figure 5.32: 10Hz 400mV PTP FFT Results
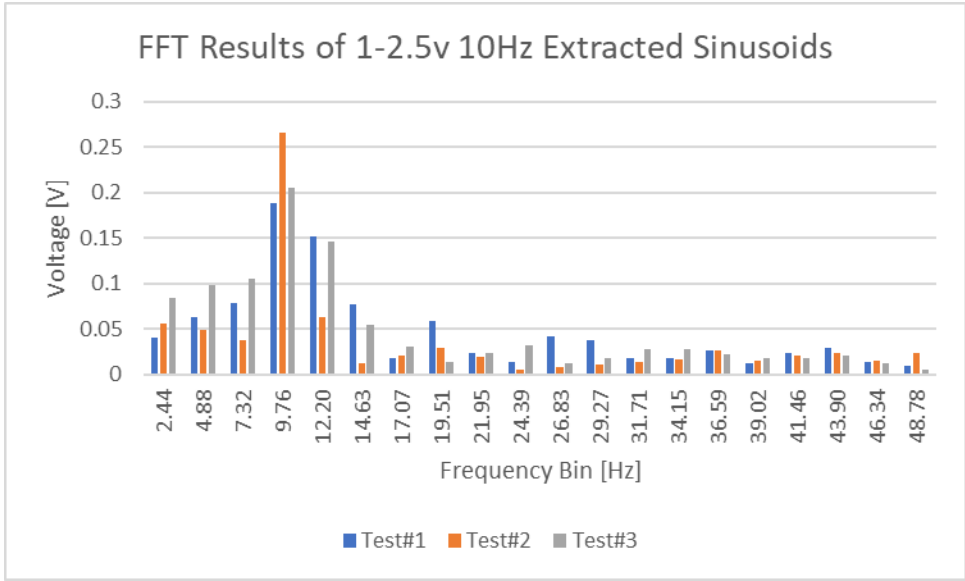
Figure 5.33: 10Hz 1500mV PTP FFT Results

Testing at 3Hz was also performed but it revealed that for reasonable sinusoids to be extracted, interpolation was needed along with the lookup curve. This is believed to be the case as the resolution of the lookup curve is somewhat low and the 3Hz sinusoid is slow moving. Figure 5.34 reveals the FFT results gathered during these tests.
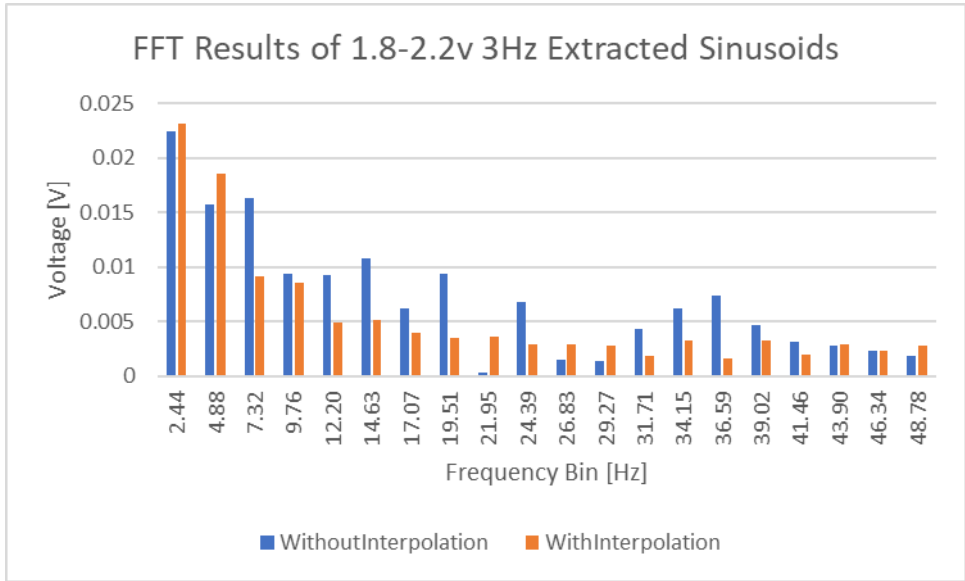
Figure 5.34: 3Hz FFT Results

Wireless testing was also performed and made use of a resonant region of the sensor at 1400MHz, which was suitable to be interrogated wirelessly using the 1.35-9.5GHz Log Periodic Dipole Array (LPDA) antennas. A cross-polar testing approach was used to enhance the magnitude of the sensor response. The response of the device to various DC voltages can be

seen in Figure 5.35. Note: These responses were compiled with the help of background subtraction.
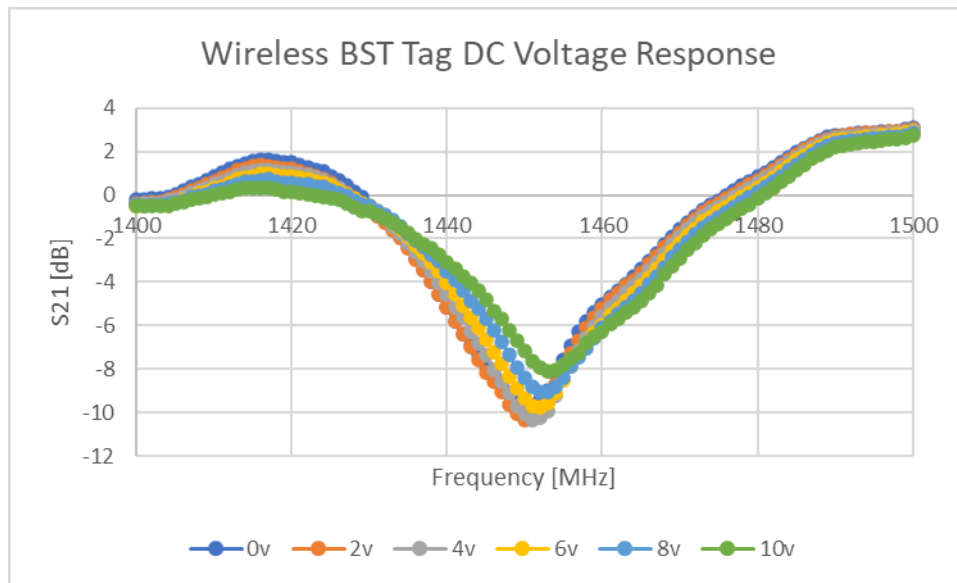
Figure 5.35: Wireless DC Voltage Sensor Response Curves

As this resonant behaviour contains a significant level of Q-factor variations and only a minor level of null frequency variations, it was decided that a different approach would be taken to determine the instantaneous stimulus level. To determine the stimulus level, each amplitude in the response dataset was converted to a stimulus level by relating the amplitude at that frequency to the curve that it would sit on. This was performed with the help of linear interpolation and this method does not require phase information, but it is more suited to situations where amplitude changes are the predominant dynamic effect. The extracted 3Hz sinusoids can be seen in Figure 5.36 and there FFT results can be seen in Figure 5.37.
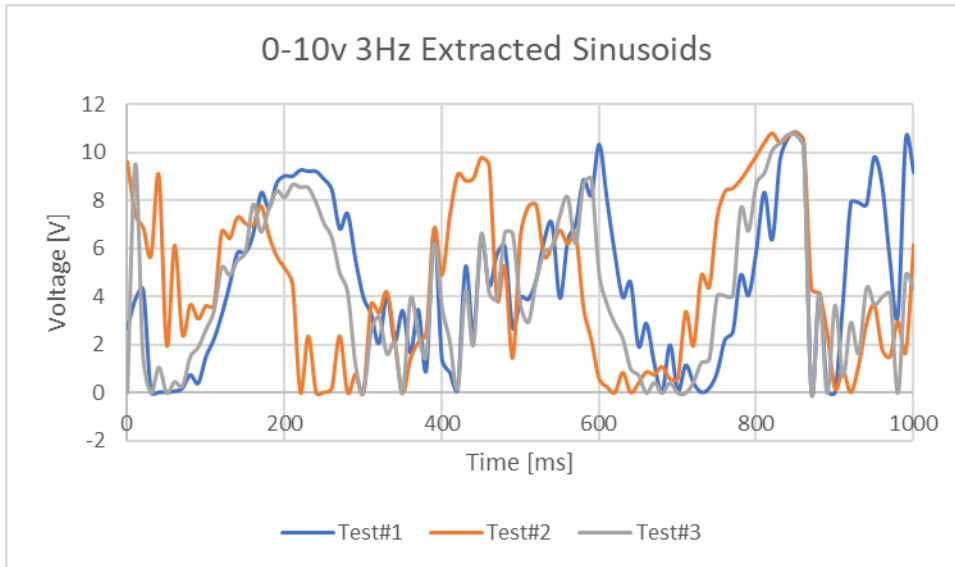
Figure 5.36: Wireless 3Hz Extracted Sinusoids
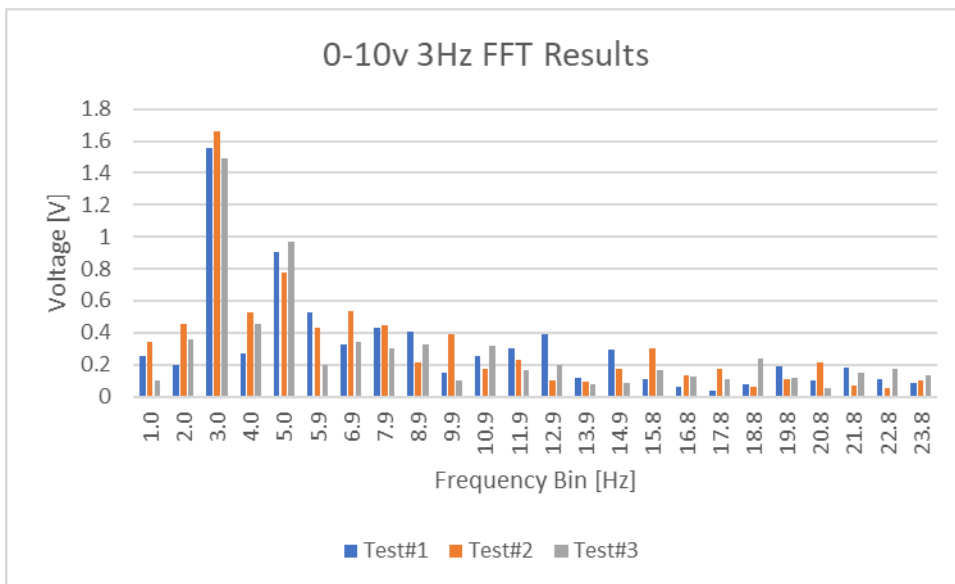
Figure 5.37: Wireless 3Hz FFT Test results

Similarly, testing at 5Hz resulted in the stimulus curves seen in Figure 5.38 being extracted. FFT results of these curves can be seen in Figure 5.39. What is important in both of these cases is that there are distinct peaks at the frequencies of interest in the FFT results. It must also be noted that windowing was performed with a 10th order uniform window to help enhance the test results before FFT processing of all of the wireless sinusoid test results.
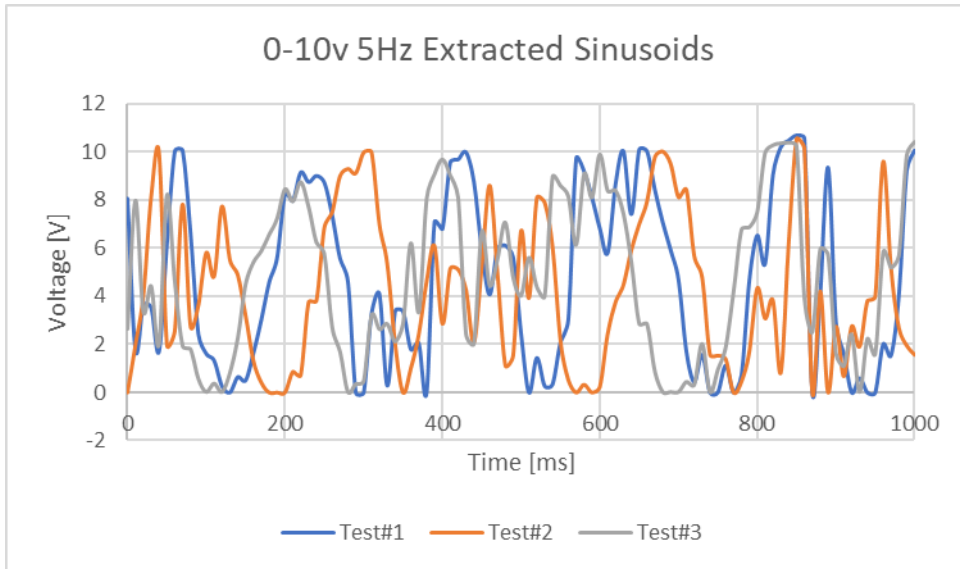
Figure 5.38: Wireless 5Hz Extracted Sinusoids
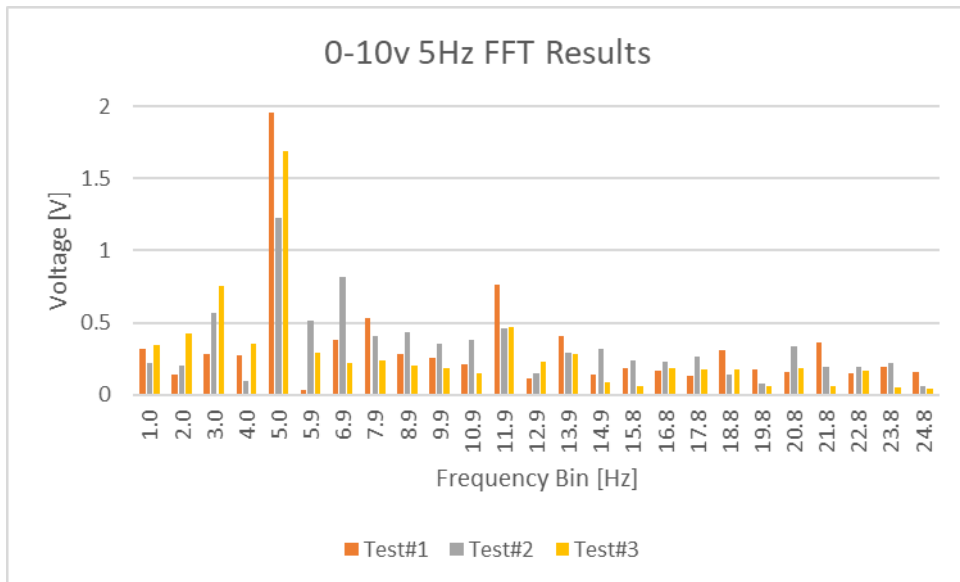
Figure 5.39: Wireless 5Hz FFT Test Results

5.4.3   Dynamic Stimulus Extraction Results

Clearly the response is affected by the occurrence of a dynamic stimulus. In most of the cases outlined above, the response still resembles a bandstop response. For the sake of completeness, the wired sensor response measured for a 1-2.5v 10Hz stimulus input can be seen in Figure 5.40. This figure, more so than the others, clearly highlights how destructive a dynamic stimulus can be to the anticipated sensor response.
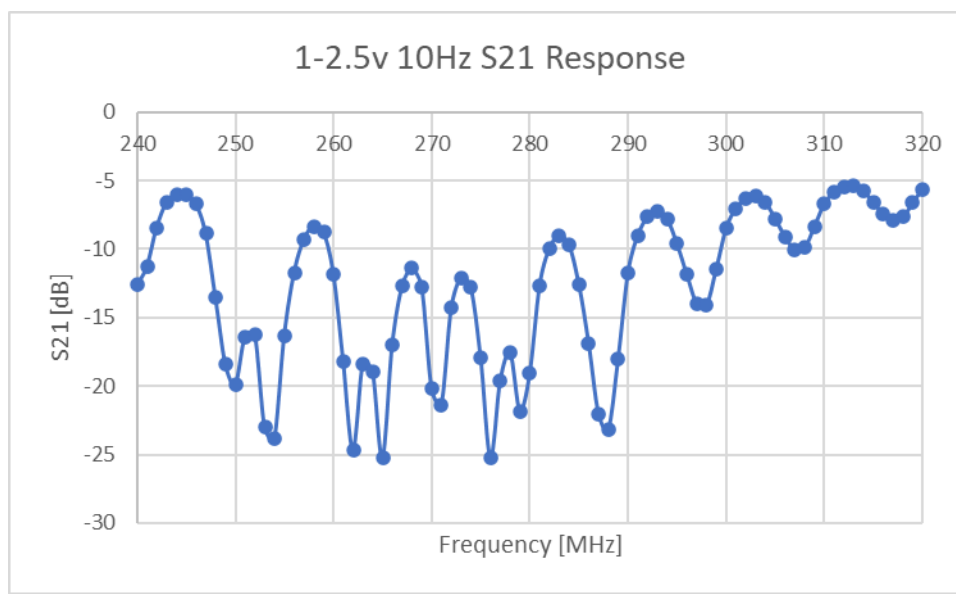
Figure 5.40: Example Impact of 10Hz Stimulus on Sensor Response Curves

Where a more recognisable bandstop response is observed, the minimum of the curve is still the main feature of interest as its value represents the null of the instantaneous resonant curve. Therefore, depending on the magnitude and frequency of the stimulus, the static feature extraction methods could be used.

From the above analysis, it is clear that it is possible to extract both the gradient and sinusoid information from the datasets although it must be admitted that the only safe way to ensure that the extractions are not merely the result of overfitting of noise within the dataset is to perform the analysis and interpret the FFT results appropriately.

5.5   Future Work

Overall this work has been a successful endeavour but is by no means the final discussion on the topic. Further work would focus on two main goals;

1. Develop an algorithm that will fit a more valid curve to the strain sensor responses observed in Chapter 3

2. Enhance the dynamic stimulus work so that the results are more accurate (i.e. have a higher amplitude) than that calculated in this work

As the chipless RFID technology literature advances, the reader systems will undoubtably improve and by proven successful at interrogating sensors with a high degree of resolution. Future work may alternatively focus on developing reader systems for this technology that have been designed with chipless RFID sensor interrogation in mind, as opposed to the conventional ones which have largely focussed on tag detection.

On the topic of the curve fitting seen in Appendix H, one thing that this research area is lacking is a database of response curves and accurately determined features. To make use of machine learning or indeed to implement any other type of smart feature extraction algorithm, a training set is needed. It is unclear what the best way to develop that training set is, although one option would be to manually fit transfer function curves to the data. This approach is somewhat dangerous as it can be seen in the earlier discussion that noticeable discrepancies can arise between the transfer function curve and the incoming dataset.

5.6   Conclusions

This chapter has explored the challenges and steps involved in feature detection and extraction from a chipless RFID sensor response. As the chipless RFID reader literature continues to evolve and is still in a state of flux, this work has primarily focussed on a "worst case" scenario where the reader system will require a significant amount of time to interrogate each sensor (i.e. SFCW, FMCW) and phase information may not be available (i.e. Spectrum analyser and tracking oscillator -based reader).

The feature extraction steps included the use of a matched filter to combat the effects of both static and statistical disturbances in the sensor response. Along with that, curve fitting methods were also evaluated to enable the determination of features, such as the null frequency, so that the resulting value has a value that is not directly tied to the resolution of the dataset. This latter point will be very important as many of the existing chipless RFID strain sensors exhibit very low strain sensitivities. The results of curve fitting have demonstrated that it is possible in many cases to greatly enhance the stability and accuracy of the determined null frequency, although issues exist with transfer function curve fitting and more generally with asymmetric bandstop responses.

Finally, the effects of a dynamic stimulus were also explored because stimuli such as vibration could readily have a detrimental impact on the interrogation response if the stimulus frequency was large, relative to the interrogation rate. The results of this demonstrated that it

is possible, in some cases, to approximately extract information such as stimulus ramp rate, stimulus frequency, stimulus amplitude and stimulus phase.

5.7   References

[1]   Aliasgari, J. et al. IR-UWB Chipless RFID Reader Based on Frequency Translation Technique for Decoding Frequency-Coded Tags, IEEE Trans. Instrum. Meas., 2021, vol. 70.

[2]   Marindra, A. M. J. Chipless RFID sensor systems for structural health monitoring, Newcastle University, Newcastle, 2020.

[3]   Garbati, M. et al. Ultrawideband Chipless RFID: Reader Technology from SFCW to IR-UWB, IEEE Microw. Mag., 2019, vol. 20, no. 6, pp. 74–88.

[4]   Karmakar, N. C. FMCW RADAR-BASED MULTI-TAG IDENTIFICATION, in Chipless Radio Frequency Identification Reader Signal Processing, New Jersey: Wiley, 2016, pp. 183–213.

[5]   Zhang, Q. et al. Chipless tag detection and recognition based on frequency modulated continuous wave, in International Conference on Internet of Things and Smart City (IoTSC 2021), 2021.

[6]   Henry, D. et al. Identification of Chipless Sensors in Cluttered Environments from 3D Radar Imagery and Polarimetry, 2020 33rd Gen. Assem. Sci. Symp. Int. Union Radio Sci. URSI GASS 2020, 2020.

[7]   Fawky Megahed, A. Realistic Chipless RFID: Identification and Localization, University of Duisburg-Essen, 2016.

[8]   Barbot, N. et al. Classical RFID Versus Chipless RFID Read Range: Is Linearity a Friend or a Foe?, IEEE Trans. Microw. Theory Tech., 2021, vol. 69, no. 9, pp. 4199–4208.

[9]   Fawky, A. et al. UWB chipless RFID system performance based on real world 3D-deterministic channel model and ZF equalization, 8th Eur. Conf. Antennas Propagation, EuCAP 2014, 2014, pp. 1765–1768.

[10]   McGee, K. et al. Use of Chipless RFID as a Passive, Printable Sensor Technology for Aerospace Strain and Temperature Monitoring. Sensors, 2022, 22, 8681. https://doi.org/10.3390/s22228681

[11]   Min, S. H. et al. Stretchable chipless RFID multi-strain sensors using direct printing of aerosolised nanocomposite, Sensors Actuators A Phys., 2020, vol. 313, p. 112224.

[12]   Amin, E. M. et al. Fully printable chipless RFID multi-parameter sensor, Sensors Actuators A Phys., 2016, vol. 248, pp. 223–232.

[13]   NASA Technology Roadmaps TA10: Nanotechnology. p. 99, 2015.

[14]   Stanciu, M. D. et al. Mechanical Properties of GFRPs Exposed to Tensile, Compression and Tensile-Tensile Cyclic Tests, Polymers (Basel)., 2021, vol. 13, no. 6.

[15]   Mc Gee, K. et al. Proof of Concept Novel Configurable Chipless RFID Strain Sensor, Sensors, 2021, vol. 21, no. 18, p. 6224.

[16]   Thomes, Jr., W. J. et al. Fiber optic cable thermal preparation to ensure stable operation, in Optical Technologies for Arming, Safing, Fuzing, and Firing IV, 2008, vol. 7070, p. 70700B.

[17] Amin, E. M.; Karmakar, N. Development of a chipless RFID temperature sensor using cascaded spiral resonators, in 2011 IEEE SENSORS Proceedings, 2011, pp. 554–557.

[18] Ayissi Eyebe, G. et al. Investigation on temperature-dependent dielectric properties of ETFE fluoropolymer for microwave temperature sensing applications, Sensors Actuators A Phys., 2019, vol. 290, pp. 215–221.

[19] Di Sante, R. Fibre optic sensors for structural health monitoring of aircraft composite structures: Recent advances and applications, Sensors (Switzerland), vol. 15, no. 8. MDPI AG, pp. 18666–18713, 30-Jul-2015.

[20] Simon, D. L.; Semega, K. J. Sensor Needs for Control and Health Management of Intelligent Aircraft Engines, 2004.

[21] Garbati, M. et al. High performance chipless RFID reader based on IR-UWB technology, in 2015 9th European Conference on Antennas and Propagation (EuCAP), 2015.

[22] Garbati, M. et al. Impact of an IR-UWB Reading Approach on Chipless RFID Tag, IEEE Microw. Wirel. Components Lett., 2017, vol. 27, no. 7, pp. 678–680.

[23] Kalansuriya, P. et al. On the detection of frequency-spectra-based chipless RFID using UWB impulsed interrogation, IEEE Trans. Microw. Theory Tech., 2012, vol. 60, no. 12, pp. 4187–4197.

[24] Rance, O. et al. RCS Synthesis for Chipless RFID: Theory and Design, 1st Edtn. Elsevier, 2017.

[25] Svanda, M. et al. Polarisation independent chipless RFID tag based on circular arrangement of dual-spiral capacitively-loaded dipoles with robust RCS response, IET Microwaves, Antennas Propag., 2018, vol. 12, no. 14, pp. 2167–2171.

[26] Aliasgari, J.; Karmakar, N. C. Mathematical model of chipless rfid tags for detection improvement, IEEE Trans. Microw. Theory Tech., 2020, vol. 68, no. 10, pp. 4103–4115.

[27] Hansen, R. C. Relationships Between Antennas as Scatterers and as Radiators, Proc. IEEE, 1989, vol. 77, no. 5, pp. 659–662.

[28] Knott, E. F. et al. Radar Cross Section, 2nd Edtn. Raleigh: Scitech Publishing, 2004.

[29] Devices, A. Analog Filters. [Online]. Available: https://www.analog.com/media/en/training-seminars/design-handbooks/Basic-Linear-Design/Chapter8.pdf.

[30] Manara, G. et al. EMERGENT project: ChiplEss multisensor RFID for green networks, 2019 IEEE Int. Conf. RFID Technol. Appl. RFID-TA 2019, 2019, pp. 187–191.

[31] Jalil, M. E. B. et al. High Capacity and Miniaturized Flexible Chipless RFID Tag Using Modified Complementary Split Ring Resonator, IEEE Access, 2021, vol. 9, pp. 33929–33943.

[32] Majidifar, S. et al. A novel phase coding method in chipless RFID systems, AEU - Int. J. Electron. Commun., 2015, vol. 69, no. 7, pp. 974–980.

[33] Costa, F. et al. A chipless RFID based on multiresonant high-impedance surfaces, IEEE Trans. Microw. Theory Tech., 2013, vol. 61, no. 1, pp. 146–153.

[34]   Wan, G. et al. Separating strain sensor based on dual-resonant circular patch antenna with chipless RFID tag, Smart Mater. Struct., 2020, vol. 30, no. 1, p. 015007.

[35]   Daliri, A. et al. Wireless strain measurement using circular microstrip patch antennas, Sensors Actuators, A Phys., 2012, vol. 184, pp. 86–92.

[36]   Karmakar, N. C. et al. Chipless RFID Sensors, 1st Edt. Wiley, 2016.

[37]   Scilab, 2022. [Online]. Available: https://www.scilab.org/about/scilab-open-source-software. [Accessed: 05-Oct-2022].

[38]   Scilab fft - Fast Fourier transform, Scilab Documentation, 2019. [Online]. Available: https://help.scilab.org/docs/6.0.2/ru_RU/fft.html. [Accessed: 26-May-2022].

[39]   Scilab xcorr - Computes discrete auto or cross correlation, Scilab Documentation, 2015. [Online]. Available: https://help.scilab.org/doc/5.5.2/en_US/xcorr.html. [Accessed: 26-May-2022].

[40]   Scilab xcov - Computes discrete auto or cross covariance, Scilab Documentation, 2019. [Online]. Available: https://help.scilab.org/docs/6.0.2/ru_RU/xcov.html. [Accessed: 26-May-2022].

[41]   Mc Gee, K. et al. Current Progress towards the Integration of Thermocouple and Chipless RFID Technologies and the Sensing of a Dynamic Stimulus, Micromachines, 2020, vol. 11, no. 11, p. 1019.

[42]   Israr, A. Vibration and modal analysis of low earth orbit satellite, Shock Vib., 2014, vol. 2014.

[43]   Critchlow, E. F. MEASUREMENT and PREDICTION of AIRCRAFT VIBRATION, SAE Trans., 1944, vol. 52, pp. 368–379.

[44]   Corda, S. et al. In-Flight Vibration Environment of the NASA F-15B Flight Test Fixture, Edwards, 2002.

Chapter 6: Sensor Deployment Challenges

6.1   Introduction

The purpose of this chapter is to highlight some of the issues with the deployment/interrogation of chipless RFID sensors in the target application environment and to discuss both published and novel solutions to the arising challenges.

6.1.1   Sensor Interrogation Problem Outline

This chapter also compliments the works seen in Chapter 5 where the diagram seen in Figure 6.1 is also present. Chapter 5 focussed on aspects of the overall sensor system coloured in orange whereas this Chapter explores the parts of the overall sensor system seen in blue. This is comprised of the reader system, the reader antennas and the features of the sensors that are relevant to the overall reader system. The reader system technology (SFCW, IR-UWB, etc.) is discussed in more detail in Appendix I and the rest of this chapter focusses on the interrogation antennas and sensor design, with an emphasis on key challenges such as polarization mismatch and multi-sensor support.
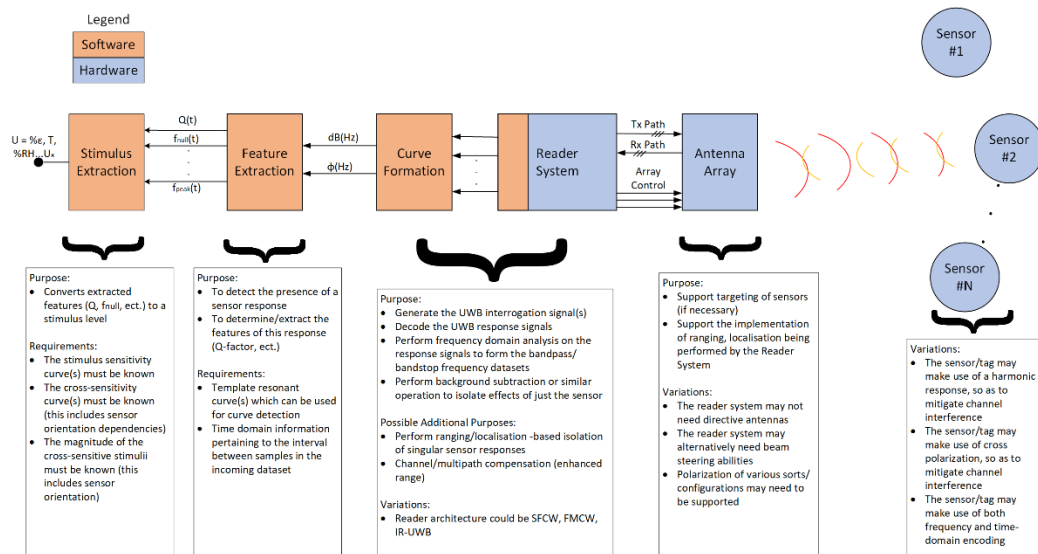
Figure 6.1: Sensor System Overview – from "Use of Chipless RFID as a Passive, Printable Sensor Technology for Aerospace Strain and Temperature Monitoring" by McGee et al., MDPI, CC BY 4.0 [1]

Existing wireless sensor technologies, such as those based on IEEE802.15.4 (e.g. ZigBee) and IEEE802.11 (WiFi) include a unique address that is used for identification purposes. Along with the ability to uniquely identify different sensors, the unique address is also used as a means to control messaging within the network. This functionality is implemented in hardware where incoming messages that are not destined for a particular sensor node, are not responded to

by said node. In the context of generic wireless sensing, the need for node addressing and more importantly Media Access and Control (MAC) is as follows:

- Identification: To give each sensor a unique identifier, so that the sensor response(s) retrieved from a particular interrogation can be attributed to a known sensor
- Localisation: To allow for the measured stimulus to be attributed to a specific part of the structure under observation
- Discrimination: To allow for the responses of multiple sensors to be discriminated from each other

With regard to the known chipless RFID sensor literature, several approaches have been taken to tackle the needs outlined above. These methods are reviewed in the subsections below. This particular work has focussed on analysing the issue of tag/sensor identification and discrimination with a focus on sensor design. Much of the existing literature appears to be increasingly relying on advanced reader types and complex signal processing to combat these issues. Although this may be a popular way to potentially combat these issues, very few proposed approaches have been demonstrated in realistic multi-sensor settings.

This work has largely ignored the phase component of the sensor/tag responses. This has been done for several reasons, including simplicity and the fact that not all potential reader architectures have reported the collection of phase information (i.e. Scalar Network Analysers).

6.1.2 Sensor Cross Sensitivity Challenges

Upon the fabrication of the desired sensors in the appropriate positions on the structure of interest and setup of the interrogation system, the resulting sensors are going to be affected by a wide number of static and dynamic environment variables. Since the strain sensor designs in Chapter 3 have reached a greater level of readiness than the temperature sensors in Chapter 4, this exploration will focus on exploring the impact that environmental variables will have on that sensor. Also, since the strain sensor has more stringent sensing requirements, this sensor is the more suitable one to perform this analysis on anyway. This section of the chapter reviews the other variables that will impact the response of the sensor using a mixture of physical testing and FEA simulations, with a key emphasis on the effects of temperature and humidity. More details on the FEA setup can be found in Appendix A.

6.1.3 Chapter Methodology

This chapter makes extensive use of physical testing to assess the deployment challenges associated with chipless RFID sensor systems. This method was chosen as it is more likely to reveal flaws in the realistic implementation of a chipless RFID sensor deployment. In terms of cross-sensitivity analysis, a mixture of simulation-based and physical testing is performed to both show real-world challenges and to explore those challenges in more depth.

6.2 Sensor Identification and Detection

This subsection explores the existing approaches used in the literature to identify and detect individual chipless RFID sensors. These two approaches are to either design each sensor to have a unique portion of the spectrum or to give each sensor an addressing scheme. This subsection considers this topic initially without the possibility that other sensors could also be illuminated by the interrogation wave. That particular issue is more thoroughly discussed later on in this chapter.

6.2.1 The Use of Unique Sensor Responses

The simplest approach to solving the aforementioned issue is to give each possible sensor a unique region to operate, within the total available spectrum. Figure 6.2 depicts this spectral layout, which has been used in a number of chipless RFID sensor publications including that by Min et al. in [2]. There are a few problems associated with this approach, most importantly is the high spectral usage of such an approach. This is a problem as the reader architecture needs to operate over a large band of frequencies which is associated with greater interrogation challenges. Furthermore, it may not be possible to find a large enough part of the spectrum within which one can fit all of the sensor responses. The frequency band required for each sensor needs to be larger than the resonant region associated with the sensor as it moves between the maximum and minimum sensor stimulus limits. This particular requirement brings up a performance conflict within the sensor design strategy as it may not be prudent to maximise sensor sensitivity if the spectrum bandwidth required for each sensor is now too large. As well as this basic spectrum allocation, there will need to be guard bands around this initial band so that other (dielectric) variations do not cause the responses from different sensors to overlap. A more pressing concern with this approach is that significant material or geometric variations are required to achieve the appropriate spacing in the spectral response. These variations could be very difficult to fabricate in-situ and/or may cause unwanted variations in the sensitivity curve of the device. This latter point is of critical concern in applications where high-resolution sensing is required and these small but significant variations could lead to noticeable measurement errors.
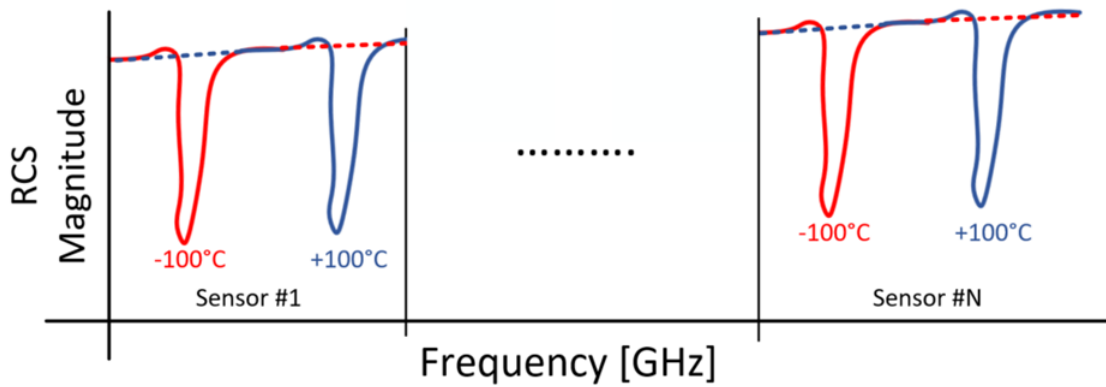
Figure 6.2: Unique Spectral Allocation Diagram

This particular approach will be considered in this work as a last resort, but other approaches will be considered first. A more pragmatic reason as to why this approach will be considered last is that it could prove to be a considerable hindrance to the feasible deployment of these sensors in large quantities, in complex environments. It will most likely be the case that a sensor design that is capable of meeting a reasonable level of sensing performance, will use a small but significant portion of the available spectrum. In multi-sensor settings where sensor counts above 10^3, the approach taken will most likely require multiple reuses of sensor spectrum allocations. This approach will only work if sensors are grouped in such a way that the spectrum can be reused, knowing that no other identical sensor is in radio range. Such an approach could make the "lick and stick" fabrication of Structural Health Monitoring (SHM) sensors, documented in Appendix B very difficult as details of the environment and of nearby existing sensors would need to be known before each new sensor is added.

6.2.2 The Use of an Addressing Tag

The research area of chipless RFID tag design has numerous examples [3][4][5] of densely encoded tag designs that have uniquely identifiable response characteristics. Several chipless RFID sensor designs [4][6] have included chipless RFID tag elements in their overall design, to give each sensor a unique response. This spectral layout is depicted in Figure 6.3. Although this approach may possibly make a particular sensor uniquely identifiable, these inclusions will not stop several nearby sensors from returning a combined response as the sensors share a common region in the spectrum. Furthermore, the response of several nearby sensors with unique addresses could combine into a composite response that could hinder the identification of any specific sensor.
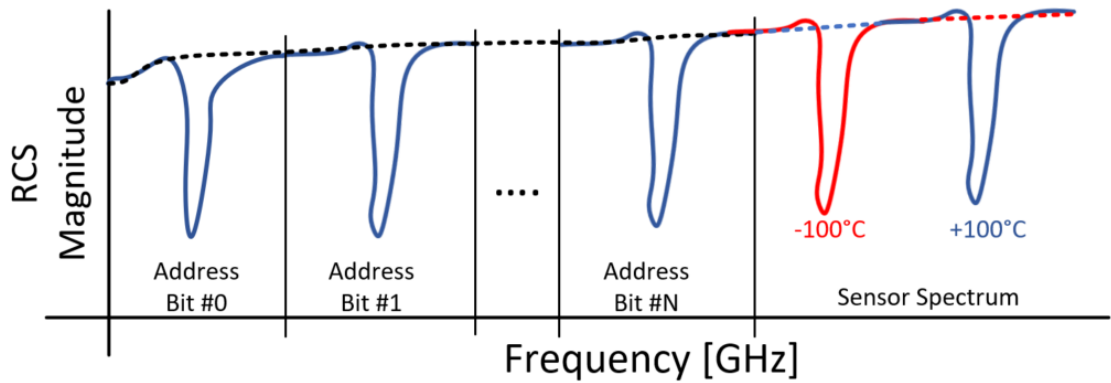
Figure 6.3: Address Tag and Fixed Sensor Spectral Allocation Diagram

Example Addressing Schemes

This subsection presents commonly found chipless RFID tag designs, which could be placed alongside the sensor, to allow the sensor to be uniquely identified. This section is not focussed on developing the optimal RFID tag but rather demonstrates how an example tag can be used to uniquely identify a particular sensor. The development of the optimal tag is something that the wider chipless RFID research community is focussed on and avid readers are pointed towards recent review papers for more details on these and other tag designs [7][8].

There are a wide variety of possible designs that can implement the approach described in Figure 6.3. Two simple examples are described graphically in Figure 6.4 and Figure 6.5. Both of these approaches make use of the resonant properties of slots in a conductive plate/layer. These designs can also be interrogated with any polarization [3][9][10](see Polarization section below).

Figure 6.4: Circular Slot Ring Resonator – Design adapted from [3]

Figure 6.5: Square Slot Ring Resonator – Design adapted from [10]

Test results of a 3-bit addressing Circular Ring Resonator (CRR) from Figure 6.4, are displayed in Figure 6.6 below. These datasets were gathered from physical testing of an FR4-based implementation of the design, details of which can be found in Table 6.1. This tag was tested using the same test setup as that used for strain sensor testing (see Chapter 3). The three resonant regions (960-1100MHz, 1200-1360MHz, 1430-1735MHz) are present when three unique slot rings are present in the structure. The presence or lack thereof of said slots allow for 2^3 possible addresses. This tag was designed to make use of the spectrum between 1GHz and 2GHz which would allow 2-3GHz to be left free for sensing using the previously published strain sensor design seen in Chapter 3. The leftmost bit in Figure 6.6 is somewhat weak and that is because the VSWR of the interrogation antennas increases significantly at frequencies below 1.2GHz. Table 6.1 gives details of the implementation of this physical device.
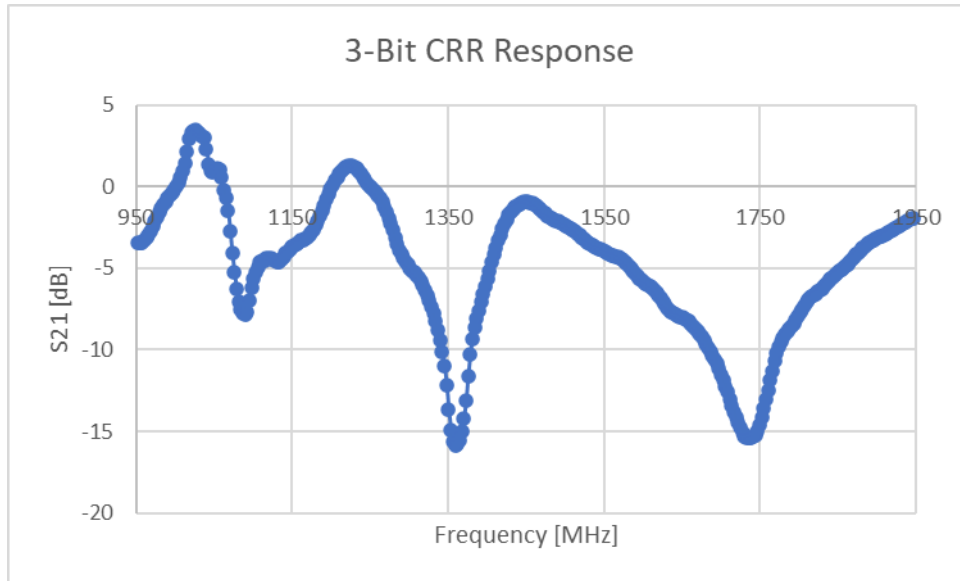
Figure 6.6: 3-Bit CRR S21 Response

Table 6.1: CRR Design Variables

Property	Value	Property	Value
Substrate	1.6mm FR4	Ring 1 Diameter	39.25mm
Outer Diameter	> 65mm	Ring 2 Diameter	47.25mm
Slot Width	2mm	Ring 3 Diameter	56.25mm

Similarly, the Square Slot Ring resonator (SqRR) seen in Figure 6.5, exhibits a similar response.
A single slot version of this resonator was tested as was an unslotted version of the design.
The physical details of this device can be found in Table 6.2. The inclusion of the slot can be
seen to result in a resonant dip, such as that seen in Figure 6.7.
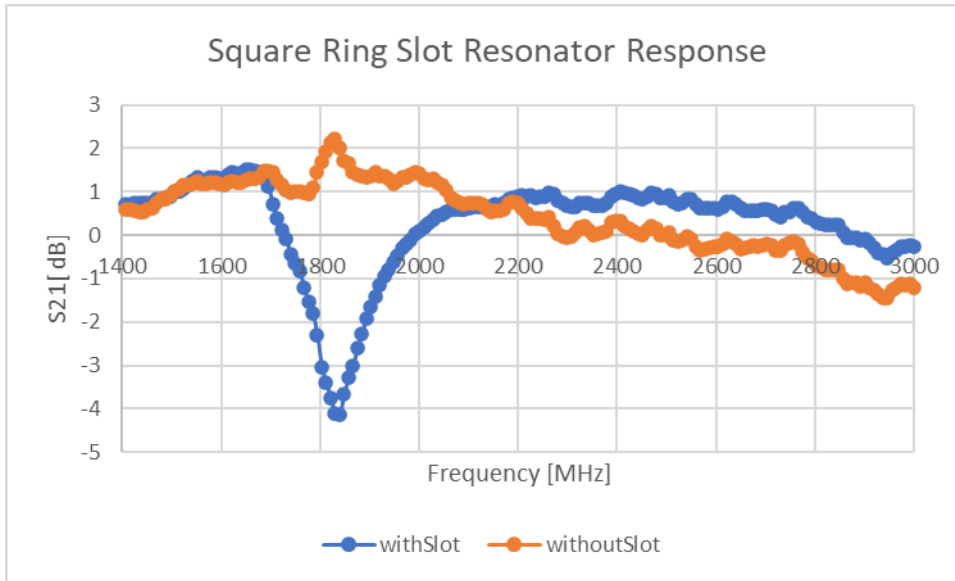
Figure 6.7: Resonant Response of Square Ring Resonator

Table 6.2: Square Ring Resonator Design Details

Property	Value
Overall Size	50x50mm
Slot Width	2mm
Slot Length (single side)	29.5mm
Substrate	1.6mm FR4

Shortcomings of Address Tags

As mentioned earlier, the sensor count found in aerospace SHM systems can be on the order of several thousand, which makes the use of unique addressing a very difficult challenge. The designs explored in this work are not necessarily the most compact but to support addressing levels on the order of 10^3, it has to be concluded that the address tag will be considerably larger than the designs described in Table 6.1 and Table 6.2. Said designs have already doubled the footprint of the overall sensor and it can therefore be assumed that address tags supporting 10^4 addresses will take up a significant amount of real estate. This will most likely result in a significant increase in conductor/substrate fabrication time and there may not be enough room between nearby sensors to put in such tag. Other issues related to cross-sensitivity also have to be considered if this approach is to be used. Works such as [6] made use of an additional substrate layer that could flex enough to isolate the address tag from the operation of the strain gauge below it.

The use of an address tag will be overlooked for now as it would appear that ranging will be a more viable method to identify/isolate the response of each sensor. This topic is discussed in further detail, later in this chapter.

6.3　Strain/Temperature Sensor Polarization Challenges

Polarization is an important factor to consider in the deployment of chipless RFID tags/sensors. Transverse Electromagnetic (TEM) waves that propagate from a linearly polarized reader antenna consist of a time varying electric field, an orthogonal time varying magnetic field that both sit in fixed, orthogonal orientations to that of the propagation vector [11]. The propagation of this wave is sustained through the temporal characteristics of these fields and the wave couples with/excite an antenna via the interaction of the electric (E) and magnetic (H) fields with the relevant parts of the antenna. Linearly polarized antennas theoretically are not excited at all by TEM waves with electric/magnetic fields not sitting in the appropriate plane, but usually some small amount of power is induced in real-world antennas. In any case, the magnitude of the response of a linearly polarized chipless RFID design to an incoming signal with a polarization mismatch, will be diminished.

One critique of many of the known chipless RFID tag and sensor designs such as the ELC (Electric LC resonator) tag seen in Figure 6.8 is that they support linear polarization. Several designs, such as those referenced here [3][9][10][12] support optimal excitation at any polarization but they are a minority of the total number of designs. This particular issue will arise with the implementation of many of the published strain sensor designs as their angular orientation could be at an arbitrary angle with respect to that of the interrogation antennas. Furthermore, it is commonplace to see strain sensors configured in a rosette configuration which commonly makes use of several sensors at different orientation angles between 0-90 degrees. Further details on rosettes can be found in Chapter 2. The problem is that the magnitude of the resonant response of a linearly polarized chipless RFID tag to an incoming linearly polarized interrogation signal falls off with increasing polarization mismatch. A small subset of strain sensor designs do support arbitrary polarizations but the direction of the measured strain is indicative of the polarization of the interrogation signal [6][12].

Figure 6.8: ELC Resonator at Various Polarization Angles

The V1 strain sensor proposed in Chapter 3 has been analysed in this section. These tests included polarization testing of different implementations of the device. The bistatic linearly polarized antennas were kept in a fixed configuration and the sensor was rotated about its central point. The effects of sensor rotation on the magnitude of minimum of the resonant dip of a polyimide-based implementation of the sensor can be seen in Figure 6.9 (The separation between antennas was 24cm). What is important to see here is that the responses are heavily

attenuated and that for adequate strain sensing, sensors with multiple different polarizations will be required.
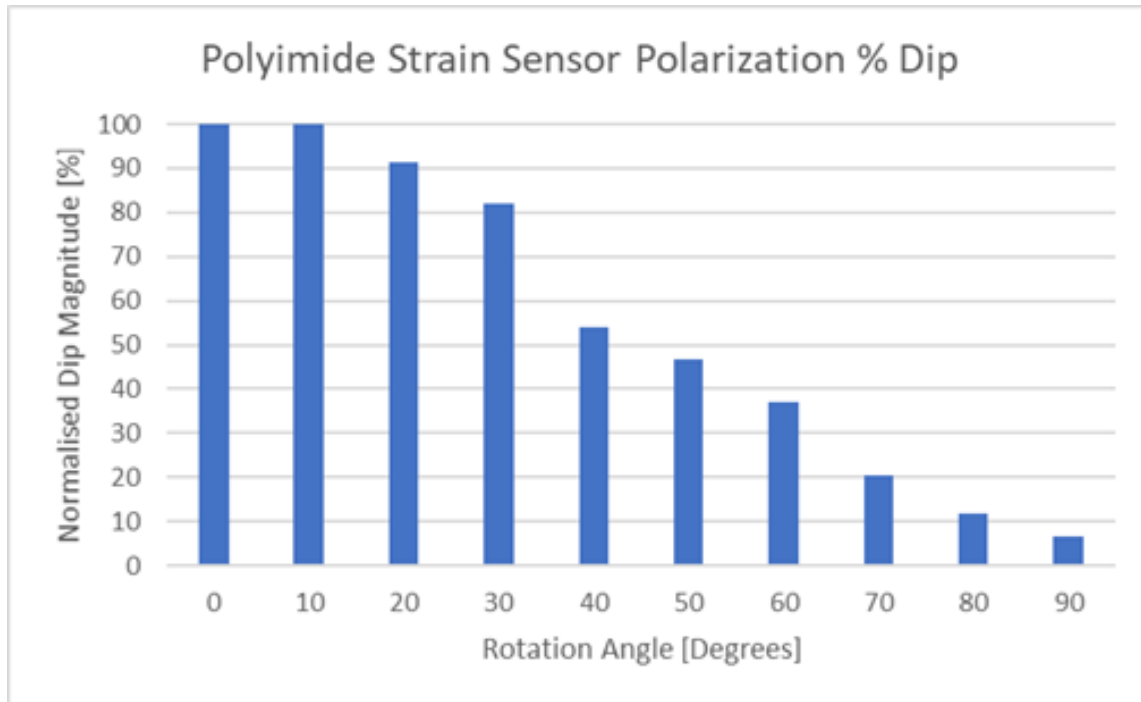
Figure 6.9: Effects of Polarization Mismatch on Polyimide Strain Sensor Response

6.3.1   Potential Sensor-Based Solutions

A possible way to achieve a single polarization throughout the sensor system deployment is through the use of parasitic elements that force part of the EM signal to flow in an opposite orientation to that found in the base sensor resonator, such as those discussed in [13] and [14] which cause elliptically polarized responses to emanate from a linearly polarized antenna. This approach could possibly be utilised alongside a chipless RFID resonator to perform the same duty. One drawback of this approach is that mechanical strain could slightly alter the resonant properties of the antenna, which would skew the sensor response in an unwanted way.

This approach was abandoned as it has only a weak effect on changing the polarization and since it works on coupling, the resulting performance would be sensitive to stimuli such as strain [13]. Further issues with this approach include the challenge of using it with a working sensor as its operation is based on the coupling of several narrowband resonant elements. The sensors developed in this document are designed to alter their resonant frequency in

accordance with a specific stimulus, which could result in degraded polarization correction performance with increasing stimulus level.

6.3.2   Potential Reader Antenna -Based Solutions

A more well-known approach to mitigate against the effects of polarization mismatch is to use an interrogation signal that exhibits circular or elliptical polarization. This wave consists of orthogonal electric and magnetic fields, but the wave is generated with the electric/magnetic field being generated in a rotational pattern. This would mean that a single, global polarization would not need to be adhered to. This result has both positive and negative consequences. As mentioned earlier, this work has considered the use of identical sensors throughout the sensor deployment strategy. This will significantly simplify both fabrication and interrogation system requirements (as discussed in Chapter 3 and Chapter 5). Before the use of circularly polarized interrogation antennas was considered/recommended, the author had considered the use of linearly polarized Tx/Rx antennas as a means of isolating the responses from identical sensors within a multi-sensor rosette. For the sake of brevity, the results of this exploration are not included, and this idea was abandoned because even if near-field coupling can be avoided, i.e. through increasing the operating frequency or through the use of 2-sensor rosettes with opposite polarizations, the more common 3-gauge rosette cannot be interrogated in this way. Potential issues may arise in this case because no polarization exists where only one sensor is excited and only one is observed, furthermore near-field coupling is expected based on the analysis presented in References [15][16]. The conclusion from this work, although not ideal, is to make use of different parts of the spectrum for each sensor in a strain gauge rosette. This approach has also been put forward by Min et al. in [2]. Therefore, the approach recommended by the author on the topic of polarization is to make use of circularly polarized interrogation antenna(s) and for the scenario of rosette implementation, to use different parts of the spectrum for each sensor in the rosette.

6.4   General Multi-Sensor Considerations

Ignoring the potential scenarios where nearby sensors may be coupling together, there is a need to isolate the response from other nearby sensors. A recent publication by Shen et al. in Reference [17] about SHM on the Chinese Space Station was using strain sensor rosettes with a spacing of just 20cm which is approximately 1.3 wavelengths with the sensors operating at 2GHz. Appendix I reviews the commonly found reader architectures and gives some commonly known details about their spatial selectivity (ranging) capabilities. From the analysis found in Appendix J, it is apparent that the illumination of more than one sensor in this layout [17] will cause potential errors in the detected stimulus level. The use of addressing tags may not however help mitigate this problem as unlike other technologies, these sensor nodes do not have the ability to make the intelligent decision to selectively respond to the interrogator. The following subsection considers some novel ideas that can help to solve the issue of multi-sensor interrogation.

6.4.1   Opportunities in Sensor Design and Reader Configuration

From the review of reader antenna characteristics above and the subsequent overview of reader architectures in Appendix I, it is clear that there are several promising routes that could lead to a fully functional chipless RFID multi-sensor implementation. With that being said, many of the known approaches push greater levels of functionality contribution onto the reader design. This route, which leads to significant increases in hardware and software complexity may reach a point where one of several outcomes may occur:

- It is not currently possible to integrate all of the required functionality into the reader, because of fundamental limitations of the software/hardware system
- The reader system is prohibitively expensive for most realistic real-world applications
- The associated hardware/software is simply too computationally intensive and results in stimulus detection times that are too long for most SHM applications

Therefore, this subsection will focus on what can be done in the area of sensor design and configuration that could help alleviate these concerns. Earlier on in the literature related to chipless RFID read range, the use of Vector Network Analysers (VNAs) as viable reader architectures was dismissed because they are usually quite expensive and their architecture does not readily support UWB regulations in a manner that makes them viable [18]. The latter point was made based on a classical interpretation of the path loss, which was assumed to be indicative of the ranged behaviour of a chipless RFID system [18]. Other publications [19][20] have revealed that environmental effects can result in undetectable tags/sensors at distances

224

below the maximum predicted read range of the respective readers, thus the argument against the use of VNAs based on cost is no longer strictly valid. Further study is needed into whether regulations can also be adhered to with a cheap VNA but compared to the price of novel chipless RFID reader systems [18], a low-cost VNA appears to be a favourable approach. One such VNA, discussed in Chapter 5, is the NanoVNA V2_2 [21], which can be purchased for €200 (excl. shipping) and has a very compact size of 90x65x30mm. Perhaps other cheap non-SFCW VNAs exist but SFCW is the most primitive reader architecture of those reviewed earlier and any such sensor design modifications should focus on being supportive of this reader type. The final reader architecture and design that will support multi-sensor chipless RFID sensing may not exist yet, but this work will attempt to briefly explore simplistic sensor-based solutions to the known problems.

As the literature on sensor identification is equivalent to that for chipless RFID tag design, the general issue of sensor identification is neglected in this section. Readers are pointed towards the results presented in earlier sections on Addressing Schemes for a possible solution. Instead, this section will focus on ways to discriminate between nearby sensors with a Stepped Frequency Continuous Wave (SFCW) -based reader architecture.

6.4.2   Spatial Dependencies of Sensor Response

To explore the problem posed by the multi-sensor setting, the first thing to be explored was how the sensor response changes as the VNA interrogation beam is focussed away from the device. To do this, two antennas were placed in the configuration seen in Figure 6.10 below and the chipless RFID sensor/tag was then interrogated with increasing levels of displacement in the (Y-) vertical direction. This displacement could alternatively be performed in the X-direction as it is assumed that the power distributions overlap perfectly during these tests.
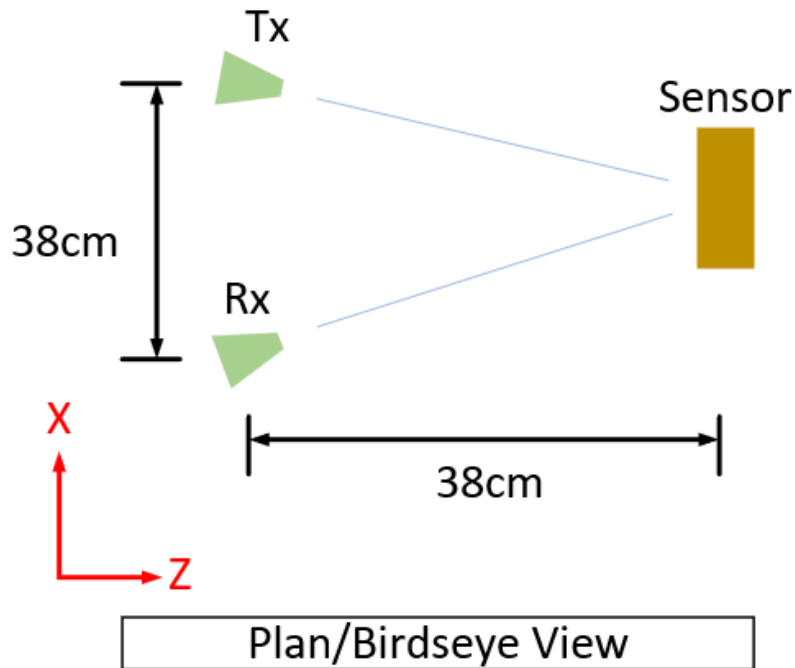
Figure 6.10: Multi-Sensor Test Configuration Layout – from "Use of Chipless RFID as a Passive, Printable Sensor Technology for Aerospace Strain and Temperature Monitoring" by McGee et al., MDPI, CC BY 4.0 [1]

These tests made use of the same Log Periodic Dipole Array (LDPA) antennas used throughout this work and the results were initially shown to be dependent on interrogation distance, as one would expect. This is because the power distribution coming from the transmission antenna will grow in accordance with Friis' Transmission Equation. Initial test results with the square ring resonator tag can be seen in Figure 6.11 below.
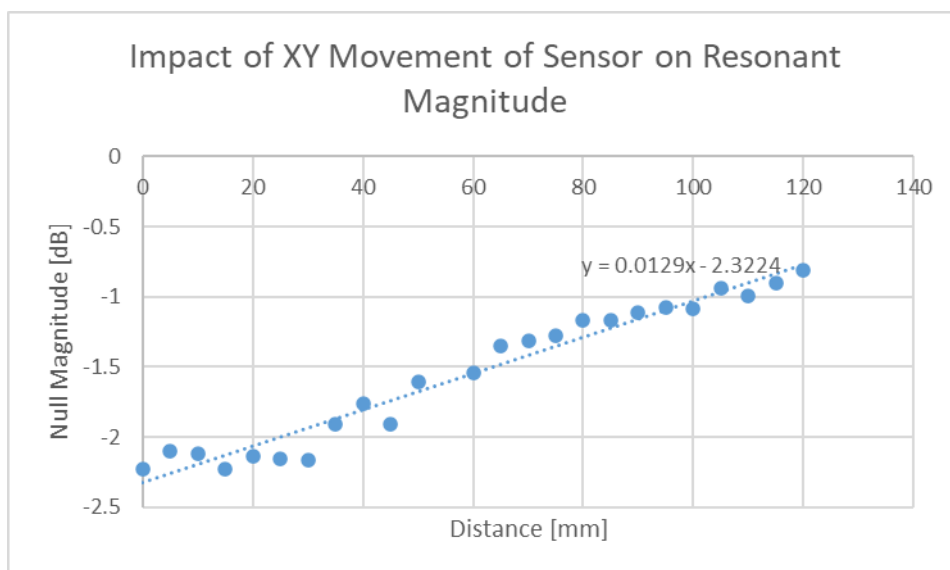
Figure 6.11: Impact of Vertical (In-Plane) Displacement on Detected Sensor Response Magnitude

226

Subsequent testing was normalised as small variations occurred through the reassembly/ reconfiguration of the test environment, and these test results can be seen in Figure 6.12 below. Applying a linear trendline to that dataset results in an R-squared value of 0.9517 and a sensitivity of -0.3254%/mm. Therefore, assuming that the linearity of the trendline holds beyond the region tested in Figure 6.12, it can be approximated that the sensor separation will need to exceed 300mm before the contribution of the nearby sensor is approximately zero, at this particular read range.
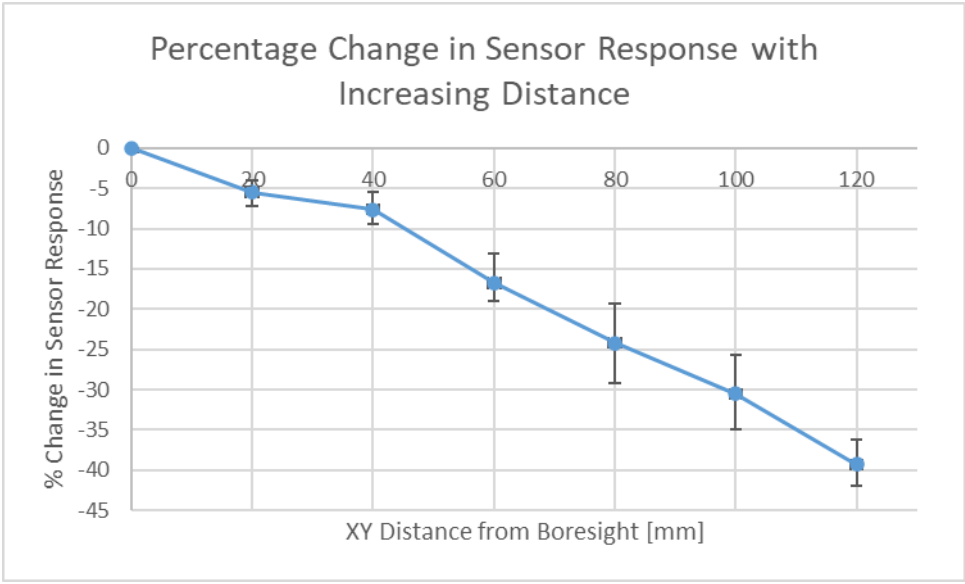
Figure 6.12: Impact of Sensor Displacement on Response Magnitude with Fully Overlapped Distributions – from "Use of Chipless RFID as a Passive, Printable Sensor Technology for Aerospace Strain and Temperature Monitoring" by McGee et al., MDPI, CC BY 4.0 [1]

From these results, it can be seen that the contribution of the sensor to the total interrogation response weakens with increasing displacement from the interrogation antenna(s) line of sight. With that being said, the contribution is not completely diminished, even at distances of over 10cm. It has to be repeated here that these results are distance dependent and larger read ranges will result in the transmission and reception Tx/Rx power distributions growing larger and thus encompassing a larger area. This will cause the rate of change of the sensor response magnitude to fall off even more slowly with displacement.

6.4.3 Partially Overlapped Power Distributions

The above analysis used transmission and reception antennas that were orientated so that their line of sight was directly on the centroid of the tag. A potentially useful alternative is to only partially overlap the transmit and receive power distributions so that the spatial selectivity of the reader system is enhanced. This is done however, at the expense of transmission and reception power.

As mentioned earlier, the above analysis assumed that the power distributions of the transmit and receive antennas perfectly overlap (see Figure 6.13(a) where the different distributions are coloured in red and black). An alternative approach would be to only overlap the power distributions over the sensor of interest. This approach, outlined in Figure 6.13(b) is similar to that of a Venn diagram and the above analysis was repeated with this novel approach. Testing in this work implemented this approach by changing the line of sight of both the transmit and receive antennas in Figure 6.10 above so that they are parallel to each other and both normal to the planar sensor. It was subsequently discovered that this approach was depicted in Reference [22] by Barahona et al. but no justification for its use was further discussed in that work. Thus, this section aims to explore how effective this alternate antenna configuration is at enhancing spatial selectivity. Further detail on the assumptions made regarding the shape of the power distributions seen in Figure 6.13 can be seen in Appendix J. Regardless of the shape of the resulting power distributions however, the use of partial overlaps will still have a significant potential to greatly enhance the spatial selectivity of the interrogation system.
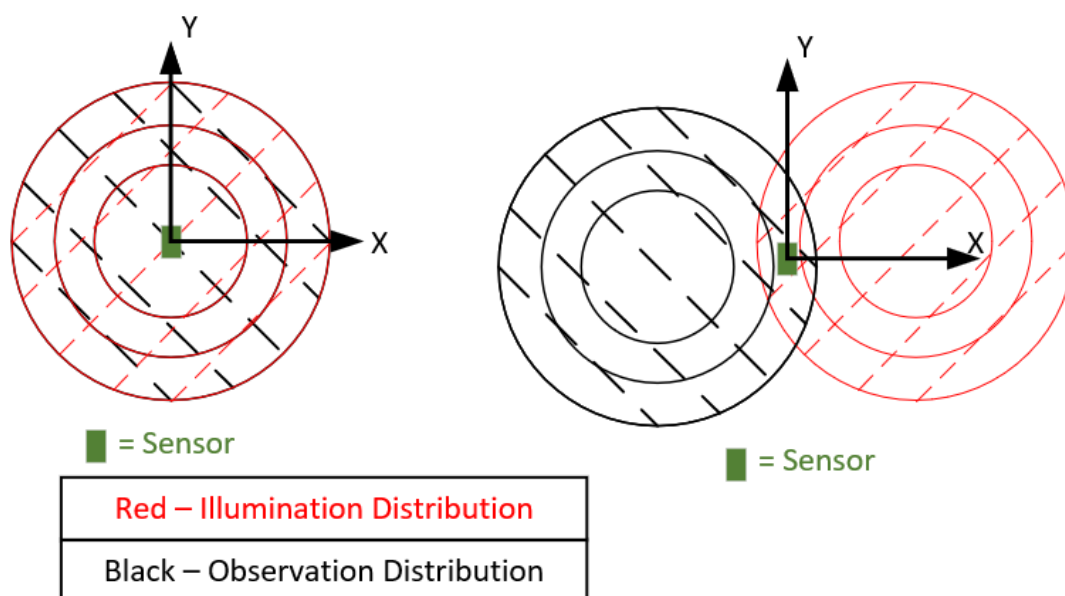
Figure 6.13: Conventional and Partially Overlapped Observation and Illumination Distributions – from "Use of Chipless RFID as a Passive, Printable Sensor Technology for Aerospace Strain and Temperature Monitoring" by McGee et al., MDPI, CC BY 4.0 [1]

228

Initial test results can be seen in Figure 6.14 below where the change in the magnitude of the null of the sensor response is plotted against displacement distance. Curve fitting of those test results resulted in a trendline with a slope of approximately 0.55dB/mm. From these initial tests, it is quite apparent that the partial overlap results show a far sharper fall off in the sensor response caused by vertical (Y-direction) displacement. Displacement in this direction was tested as movement in the horizontal plane would most likely have steeper power gradients in it because many directive antennas have sharper changes in power closer to the first null than the boresight position. With the configuration seen in Figure 6.13 above, the overlap of these two circles is an ellipse and the vertical direction is and always will be its major axis, regardless of how far separated the two power distributions are, thus the vertical direction would most likely be the direction in which its spatial selectivity is worst.
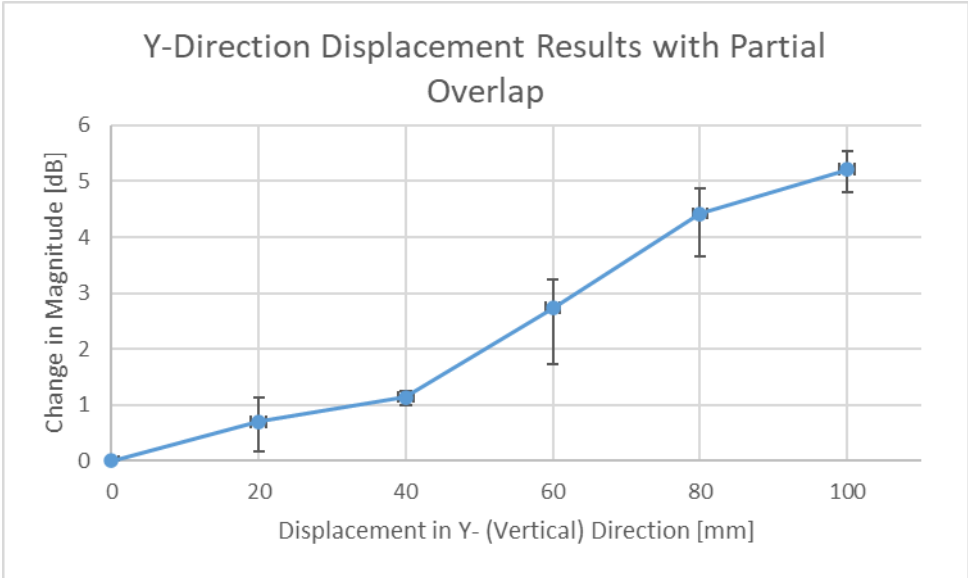
Figure 6.14: Test Results found With Partial Interrogation Overlap

Normalising these results has been performed and the results of this can be seen in Figure 6.15 and Table 6.3. From the results in Table 6.3, it is apparent that a greater degree of spatial selectivity is possible with the use of partially overlapped distributions.
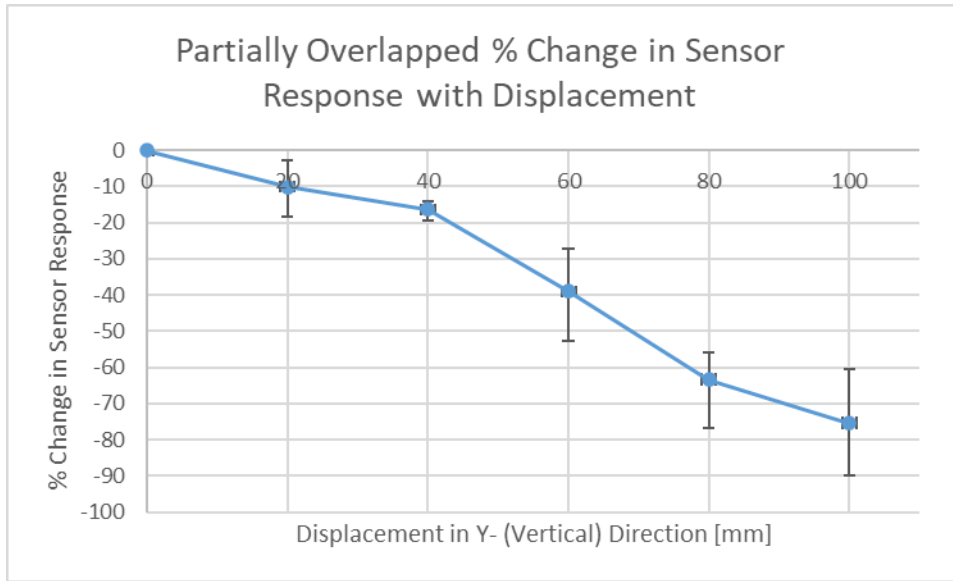
Figure 6.15: Effect of Sensor Displacement on Response Magnitude with Partial Distribution Overlap – from "Use of Chipless RFID as a Passive, Printable Sensor Technology for Aerospace Strain and Temperature Monitoring" by McGee et al., MDPI, CC BY 4.0 [1]

Table 6.3: Percentage-Based Trendline Results from Partial Overlap Testing

	Sensitivity [%/mm]	R-Squared
Partial Overlap	-0.80	0.9412
Full Overlap	-0.325	0.9517

Initially the impact of illuminating and observing empty regions of the environment was overlooked. This may work for an anechoic-like environment, but this overall approach may be more susceptible to clutter-based interferences in a realistic setting. The 5-node analysis seen in Appendix J also includes analysis with the partial overlap configuration. These results demonstrate similar effects to that seen above, but a finding of concern is that the modelling results suggest that this approach can be more sensitive to multipath effects. This result does not occur for the same test configuration performed with the regular overlap setup seen in Appendix J.

This novel approach has been explored here in this work but the approach has some key limitations. These limitations include;

- The overall idea is based on a single-ray line of sight propagation model for the environment and may struggle to isolate certain sensors in more complex propagation environments

- A significant amount of power is directed towards a region of the environment that does not include the sensor, and this may partially limit the maximum interrogation range of the system
- From repeated testing, it can be seen that a high degree of beam steering control accuracy and resolution will be required

6.4.4 Unique Stimulus Discrimination Approach

A design cost associated with the use of highly directive antennas in SHM applications is that there is a need to perform beam steering.This usually involves a significant increase in both design complexity and antenna footprint. An alternative approach has been outlined below that does not rely on highly directive antennas to perform sensor isolation. This alternative approach outlined below, similar to the previous idea, cannot be said to counter any potential near-field coupling between nearby sensors.

This proposed approach sets out to excite a selected sensor using an additional stimulus to allow for an operation to be performed within the sensor, akin to intelligent decision making. Ideally, all sensors would be made identical as this would not only be the most spectrally efficient method but would also reduce the need for in-situ design choices/alterations. To support sensor response discrimination, two possible approaches are outlined:

1. Push the resonant region of the selected sensor sufficiently beyond that of the unselected sensor so that it can be uniquely measured (see Figure 6.16(a))
2. Destroy or mitigate the response of the selected sensor. This approach allows for a dynamic background subtraction measurement to be made as the response now only contains contributions from N-1 sensors. The measurement can then be repeated without selecting any sensor and the subtraction of these two measurements is the response of the previously selected sensor (see Figure 6.16(b))

(a)

(b)
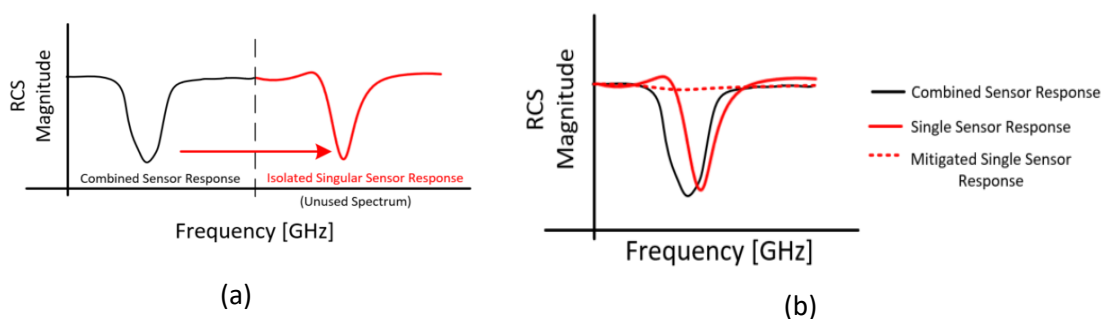
Figure 6.16: Unique Stimulus Desired Spectrum Response Alterations - (a) Frequency Shift, (b) Amplitude Shift

The next question is how to give the sensor such functionality and how can the additional stimulus be more spatially selective than the existing interrogation signals. From the earlier

discussion, it can be seen that the power distribution from conventional directive antennas can become very large. However, the spatial focus of a laser beam is significantly greater and could serve as a possible way to apply a highly spatially selective stimulus to the sensor of interest. Light Dependent Resistors (LDRs) are example devices that could be excited using a laser and so this section focussed on this possible method to achieve unique discrimination of a sensor stimulus. Compensating for ambient lighting effects may require colour filters and/or the use of other semiconductive Light Dependent Resistor (LDR) materials.

A common material that LDRs are made from is Cadium Sulphide (CdS). The work of Amin et al. in Reference [23] has previously characterised the impedance (Z=R+j*X) of such a device between 0.6-0.7GHz. These results demonstrated both a significant increase in resistance and a change in reactance from capacitive to inductive [23]. Impedance spectroscopy performed with the VNA from 0.5-3GHz also revealed similar values and trends for several luminosity levels. Said reference has also integrated this device into a chipless RFID tag to create a chipless RFID light sensor.

Such a device could be highly suitable therefore to destroy or at least mitigate the response from the selected sensor if the LDR is sufficiently illuminated. Figure 6.17 outlines two ways to integrate this device into compact chipless RFID sensor designs. A similar approach to that found in [23] was implemented in this work, where a wired λ/4 SIR circuit was shorted with a CdS LDR. The results of its illumination can be seen in Figure 6.18.
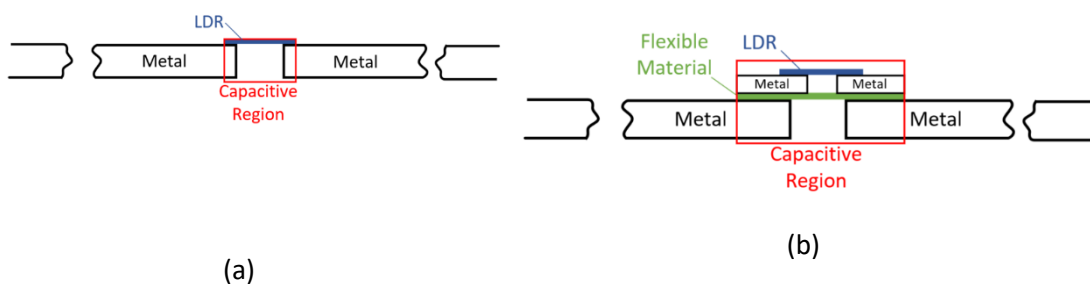
Figure 6.17: Methods to Integrate LDR into Conventional ELC (a) and Published Strain Sensor (b)
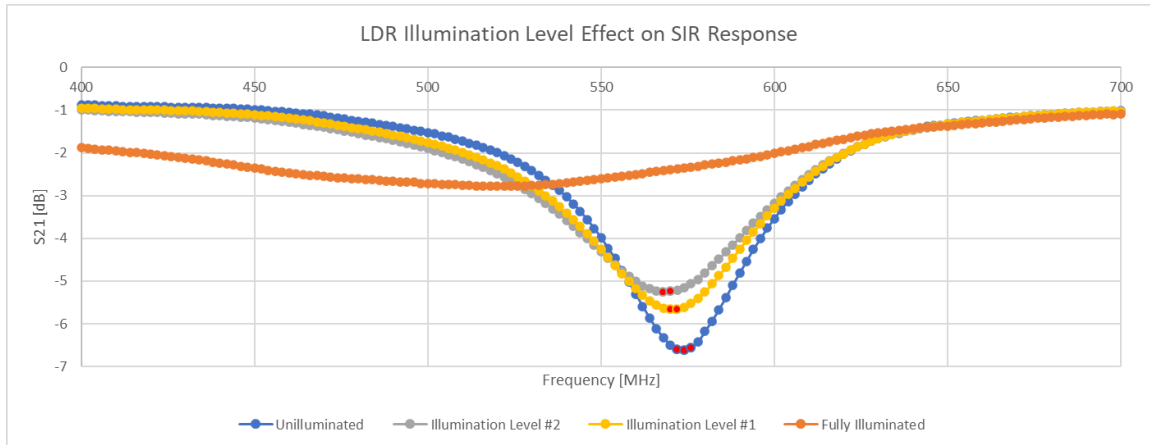
Figure 6.18: Impact of Illumination on LDR-Loaded SIR Response

The results in Figure 6.18 and those found in Reference [23] show that the resonant dip is significantly attenuated, and the location of its minimum value also moves with changes in illumination level. This last point is an unwanted effect as it would be better if only one of the two approaches outlined in Figure 6.17 above was implemented. Since the effect in Figure 6.17(b) is the dominant one of the two effects, the results of effect in Figure 6.17(a) will need to be compensated for. This will be the case for sensors whose stimulus is encoded in the location of the minimum as the effect of the illuminated and the unilluminated LDR on the location of this minimum will need to be known. If known, the contribution of the sensor stimulus and the LDR could be separated from each other, and the stimulus level determined.

The effects of adding an LDR between the central capacitance (as described in Figure 6.17(a)) of an ELC-based tag can be seen in Figure 6.19. The results of subtracting the unilluminated signal from the illuminated one (≈1000LUX) can be seen in Figure 6.20. Clearly the illumination-based change in impedance is not significant enough to completely mitigate the resonant response but the subtraction signal does consist of a detectable resonant effect.
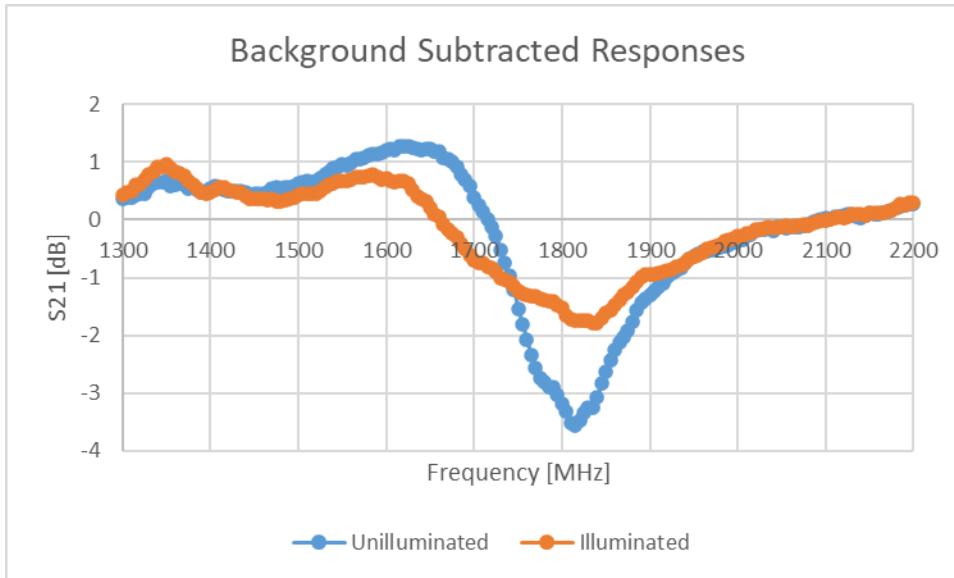
Figure 6.19: Result of Illumination on LDR-Loaded ELC Tag – from "Use of Chipless RFID as a Passive, Printable Sensor Technology for Aerospace Strain and Temperature Monitoring" by McGee et al., MDPI, CC BY 4.0 [1]
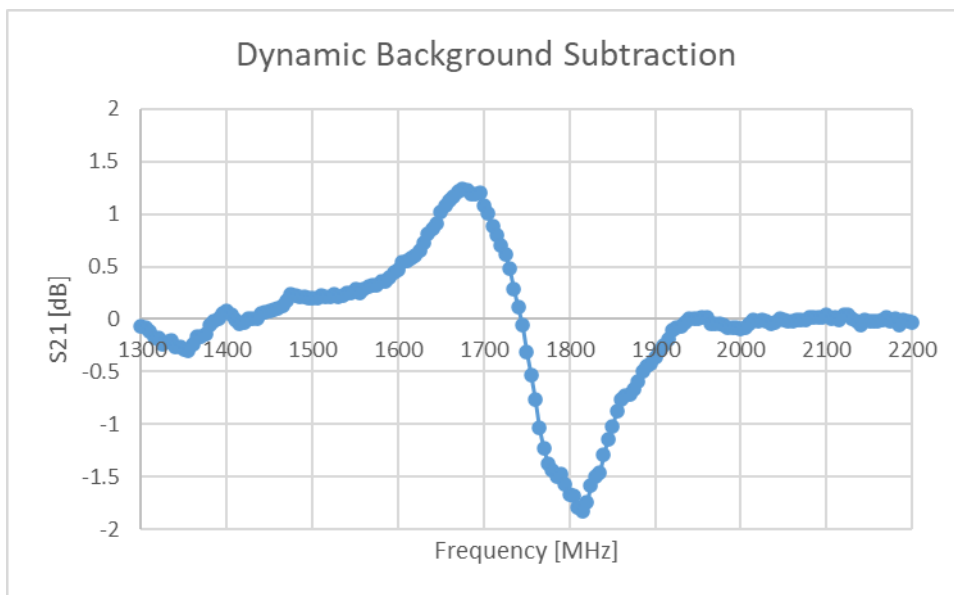
Figure 6.20: Subtraction Result of Illuminated and Unilluminated ELC Tag Responses – from "Use of Chipless RFID as a Passive, Printable Sensor Technology for Aerospace Strain and Temperature Monitoring" by McGee et al., MDPI, CC BY 4.0 [1]

The effects of adding an LDR between the central capacitance (as described in Figure 6.17(b)) of an ELC-based tag can also be seen in Figure 6.21. Similarly, the results of subtracting the unilluminated signal from the illuminated one can be seen in Figure 6.22.
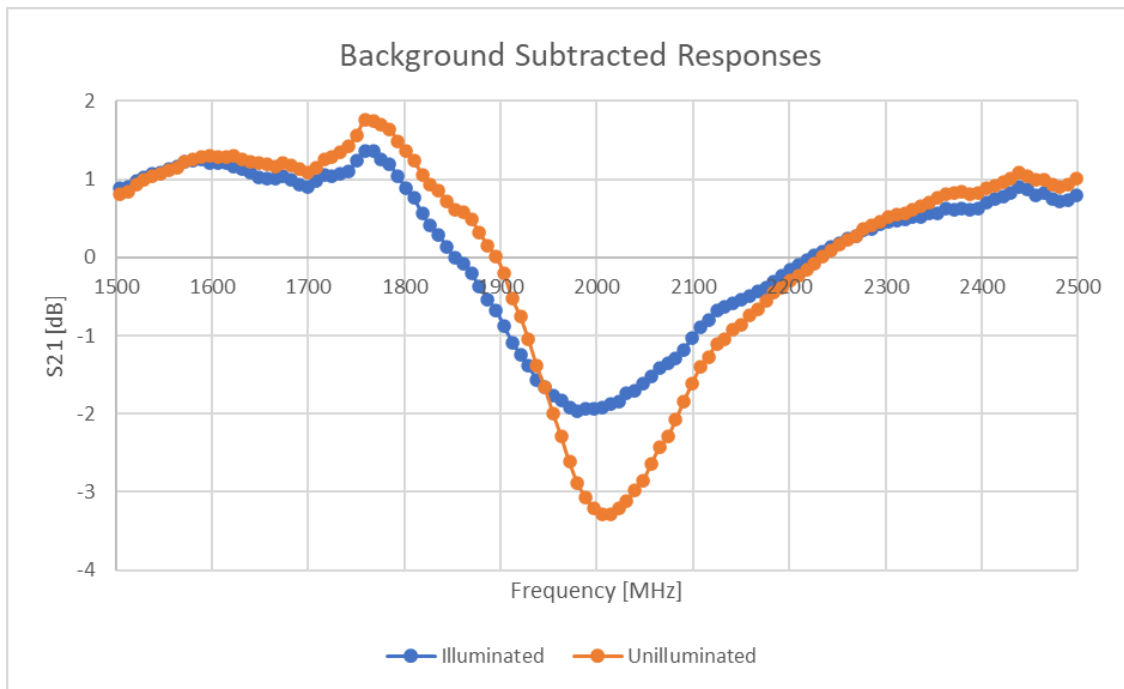
Figure 6.21: Result of Illumination on Capacitively Loaded LDR Strain Sensor
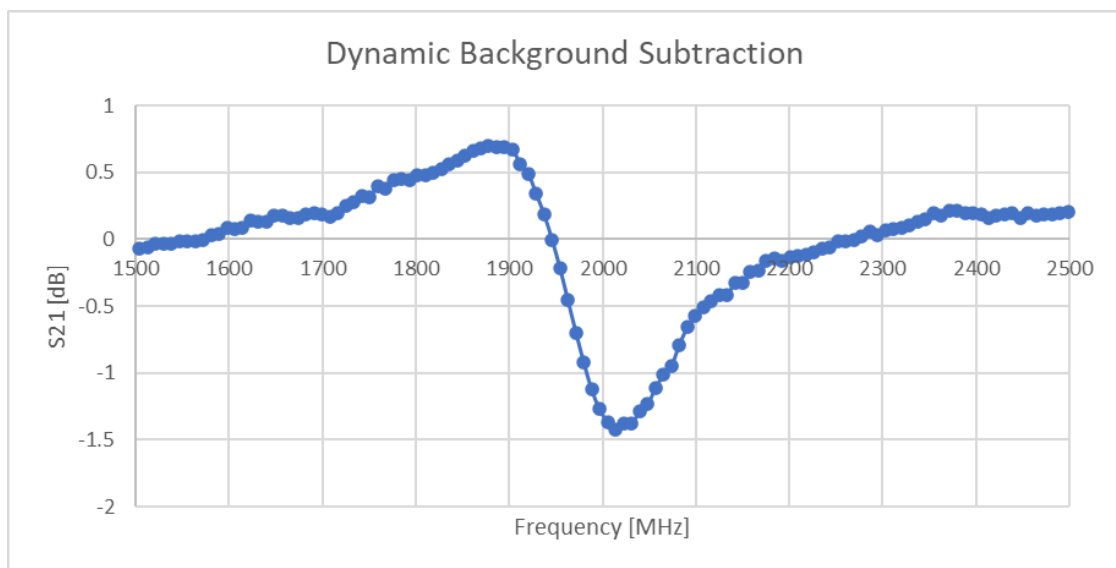
Figure 6.22: Subtraction Result of Illuminated and Unilluminated LDR-Loaded Strain Sensor

Further study into LDR-loaded chipless RFID tags was suspended as although this approach has some impressive benefits to bring to reducing the complexity of the reader system, it is not without several key faults. Attempts at illuminating these tags with a low-grade laser pointer was insufficient to replicate the results seen in the figures above. Therefore, a more complex and higher power laser system will be needed, and it will need to support raster-like scanning of the environment to illuminate each of the sensors. More pressing concerns with this approach are that LDRs are themselves temperature sensitive as their operation is based on

235

the excitation of electrons from the valence to the conduction band by the incoming EM wave. Excitation of said carriers can happen with increasing ambient temperature [24] and would thus result in the device no longer being one with a unique stimulus. This is a key issue that will hamper tag detection in aerospace settings, where a wide range of temperatures can be experienced by the device.

6.5   Sensor Cross Sensitivity Issues

A key problem with the developed strain sensors and also with those found in the literature, is that there are many variables other than axial strain that can contribute to the sensor response. This will not only be the case in aerospace settings but also in more conventional environments also.

In essence, this section is interested in the other variables that could affect the response of the sensor. This analysis will focus predominantly on effects that are independent of each other, but some explorations of more complicated effects are also performed. Although a full characterisation of the developed sensors is perhaps unwarranted for now, until the final application, materials and fabrication approach have been chosen, it is important to at least consider how this may be done. This section of the document focusses on dielectric constant variations and variations induced by swelling but other effects are to be expected. With a full characterisation of the final sensor performed, it is hoped that response modelling equations such as those discussed below can allow for each of the stimuli of interest to be determined. Solving all of the subsequent equations is beyond the scope of this work, but they serve as a basis from which this challenge can begin. Some assumptions have been made in the development of the equations below, namely that the (cross-)sensitivities exhibit linear relationships. Equation 6.1 describes the relationship between the stimulus of interest (U_N) and the variables that impact the sensor response (X_1, X_2...Xn). The sensitivity matrix (S) for a three variable system is described in Equation 6.2 where S_{NN} is the sensitivity of U to the variable X_{NN} and solving of Equation 6.2 with S_0 in place of S would allow for the modelling of only independent effects on the sensor performance. These effects can by definition be added together so that their impact is merely a sum of their singular effects. There is, however, the chance that the magnitudes of certain variables could alter the sensitivity that U has to another variable. A classic example of this is temperature, as its effects can include dielectric constant variations (independent effect) and changes in mechanical properties of the materials, the latter of which will undoubtably affect the base strain sensitivity of the strain sensor device (dependent effect). Matrix P is described in Equation 6.3 for a three variable system where the variable P_{IJ} represents the sensitivity of sensitivity "I" to the variable "j".

236

Note: The non-diagonal coefficients in P can be a function of the diagonal ones in S_0 to allow for both summative and proportional dependencies to be represented. The subsequent Equations, Equation 6.4 and Equation 6.5 gives the total calculation for the stimulus of interest, U for a three-variable system.

$$U = [S][X], \qquad [X] = [X_1 \quad X_2 \quad \cdots \quad X_n]^T \tag{6.1}$$

$$[S] = [S_0][P], \qquad [S_0] = [S_{11} \quad S_{22} \quad S_{33}] \tag{6.2}$$

$$[S] = [S_0][P], \qquad [P] = \begin{bmatrix} 1 & P_{12} & P_{13} \\ P_{21} & 1 & P_{23} \\ P_{31} & P_{32} & 1 \end{bmatrix} \therefore \tag{6.3}$$

$$U = [S_1 + P_{21}S_2 + P_{31}S_3 \quad S_2 + P_{12}S_1 + P_{32}S_3 \quad S_3 + P_{23}S_2 + P_{13}S_1] \begin{bmatrix} X_1 \\ X_2 \\ X_3 \end{bmatrix} \therefore \tag{6.4}$$

$$U = S_1(X_1 + P_{12}X_2 + P_{13}X_3) + S_2(P_{21}X_1 + X_2 + P_{23}X_3) + S_3(P_{31}X_1 + P_{32}X_2 + X_3) \tag{6.5}$$

It is important to note here that there will be a significant variation in environmental sensitivity of the sensor, depending on the materials it is made from. Therefore, the following discussion will where possible, limit the analysis to the use of a polyimide substrate and a copper conductor.

Table 6.4 depicts the stimuli that can affect the designed strain sensor. The effects of many, if not all of these variables on chipless RFID sensors can be assessed by reviewing the existing materials science literature. There are some however, such as material expansion and material model variations, that require proper sensor modelling in order to assess their effects.

Table 6.4: Variables that can impact the strain sensor response – from "Use of Chipless RFID as a Passive, Printable Sensor Technology for Aerospace Strain and Temperature Monitoring" by McGee et al., MDPI, CC BY 4.0 [25]

Variable Name	Known Dependencies	Comment
Axial Strain	Axial deformation, Transverse strain (due to Poisson's effect), material models	This variable is designed to be the dominant contributing variable to the sensor response. Where this is not possible, compensation will be required
Transverse Strain	Transverse deformation, substrate transverse expansion, conductor transverse expansion, material models	This variable should be mitigated against within the design or through compensation within the overall sensor implementation, as seen in Reference [2]
Substrate Expansion/ Contraction	Thermal expansion, humidity-based swelling	Polyimides and other substrate materials of interest suffer from significant levels of humidity and/or thermal -based expansion [26][27]

Conductor Expansion/ Contraction/ Material Loss	Thermal expansion, corrosion, material models	This parameter is perhaps one of the more difficult variables to mitigate against. This variable can be reversable or irreversible as corrosion and creep can cause permanent expansion/ contraction.
Conductor Resistance	Temperature, corrosion	Conductor resistance influences the Q-factor of chipless RFID tags. Certain resonant elements will also exhibit changes in null frequency. Corrosion could result in a complex change in resistance, caused by material loss and by surface oxidation
Structural material Models	Temperature, pressure, humidity	These models vary from simple isotropic elasticity models to more complex models that include effects such as creep. Most if not all these models contain properties that are sensitive to temperature [28][29][30] and other environmental parameters [31]
Dielectric/ Magnetic Material Model	Temperature, humidity, pressure	Properties described by this model consist of dielectric constant(permittivity) and loss tangent. These parameters can be highly sensitive to environmental effects within a variety of dielectric materials [32][33]

Many of these variables have already been thoroughly explored within either the existing chipless RFID or materials science research literature. The only variables which have a short-term/rapid impact on the operation of the designed sensor are conductor/substrate expansion and material model variations, as the others are more related to device aging, thus these are the key variables that should be mitigated against in the first instance. The effect of conductor resistance is important when discussing the topic of resonant magnitude present in the scattering response but should not considerably affect the resonant frequency of the resonator. This claim is made as the effects of temperature on the developed wireless sensors did not result in a significant degradation of the resonant magnitude. Furthermore, it has been noted in many previous works on the topic that resistance changes are used in chipless RFID designs for their ability to alter the magnitude of the response and not its frequency location [8]. As this section is only concerned with the variables that could affect the location of the resonant location frequency, the effects of electrical resistance variations and dielectric loss will also be ignored here. Of interest to the author is the design-dependent cross sensitivities, which will be explored below using FEA software and/or physical testing.

6.5.1 Dielectric Constant Variations

As mentioned in Chapter 3 and Chapter 4, the impact of dielectric constant variations in chipless RFID sensor performances is a well-known effect. In terms of its relevance to the developed chipless RFID sensor, these effects will arise under some commonly found scenarios. These scenarios include the following:

- The initial dielectric constant of the superstrate is unknown
- The thickness of the superstrate is unknown
- Atmospheric dielectric constant is unknown
- Environmental dependence of atmospheric dielectric constant may potentially arise
- Environmental dependence of superstrate and substrate dielectric constant may arise

The first three scenarios listed above result in a static change in the resonant response of the device that can be dealt with using a single-point calibration procedure. The other two scenarios are more complicated and require direct compensation for the variation in dielectric constant.

The thermal transfer based V1 strain sensor has been tested with various layers of 2mm thick PMMA behind the sensor. Figure 6.23 reveals the magnitude of these emulated superstrate thickness variations with the null frequency changing by more than 62MHz. With strain sensitivities on the order of 30MHz/%ε (3kHz/με), strain sensing in the microstrain range will definitely require that this variation is accounted for, most likely through the use of a single-point calibration measurement. An interesting result seen in Figure 6.23 below is that the variation in null frequency changes with PMMA thickness in a non-linear way. This observation is of interest because it suggests that the dielectric layers closest to the resonator will be of the most importance and subsequent layers are less so. This is believed to be the case as the strength of the fringe fields arising from the planar capacitive region(s) of the design will decay rapidly with distance, and thus make the design more sensitive to dielectric variations that are located closer to the surface of the sensor.
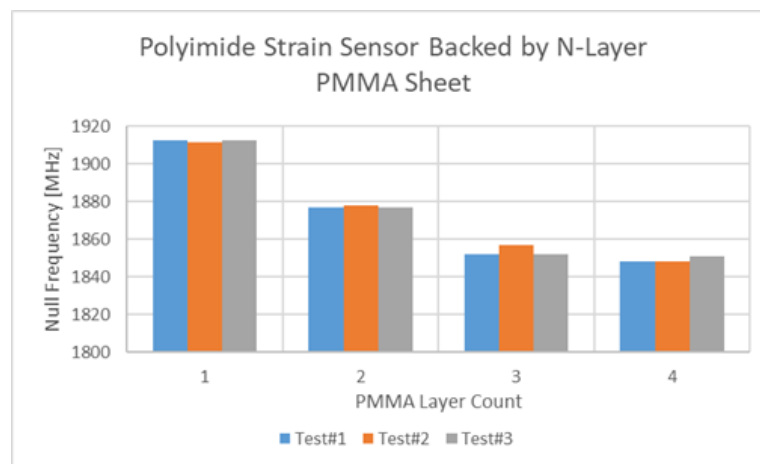
Figure 6.23: Impact of 2mm-thick PMMA layers on Sensor Response – © 2022 IEEE. [34]

Environment-Based Variations

Environmental effects can also cause significant variations in the dielectric constant of the nearby materials. The testing in this section has focussed on temperature-based variations instead of humidity-based variations as the former is easier to explore. It must be noted that materials such as polymers can exhibit temperature-dependent mechanical and dielectric properties [33]. These effects have been discussed more thoroughly in Chapter 2 and Chapter 4.

The second and third version of the sensor geometry (V2, V3) seen in Chapter 3 allow for an additional resonance to be detected. This would, in theory allow for the detection of the total dielectric constant being experienced by the sensor, if the only variables within the system are axial strain and dielectric constant. One assumption made during this approach is that the

reference resonance must exhibit an environmental dependence similar to that of the axial resonance. Table 6.5 depicts the average test results found during temperature testing of an FR4 covered latex based V2 strain sensor.

Table 6.5: Example Temperature Dependence of V2 Strain Sensor Response

Test (20-70°C)	Sensitivity [MHz/°C]	R-Squared
Axial	0.4273	0.9916
Transverse	0.2723	0.9569

The fact that the two resonances have a different level of dielectric constant sensitivity is not of critical importance here, but one key problem with these sensor designs is that the above sensitivities must consistently have the same proportionality between them if they are to allow for uncalibrated temperature compensation. If the ratio between the two sensitivities (0.4273:0.2723) alters when a different dielectric is introduced, then a multi-point temperature calibration procedure will be required to re-evaluate the relationship between the two sensitivities. At this point, the main question is; How could such a variation occur? As part of the design of the V2 and V3 strain sensors, both resonators share the same centroid, have a small aspect ratio and occupy an area that is assumed to be small, relative to any potential stimulus (temperature, humidity, etc.) gradient that the structure may experience, so that should not be the source of a potential change in relative dielectric constant sensitivity. Unfortunately, however, because these designs make use of two slightly different resonator designs within them, the sensitivity of the two resonances to changes in dielectric loading appears to be different. From Figure 6.24 below, it can be seen that the resonant frequency of the two resonances of the V2 design depend to differing degrees on increasing dielectric loading, as the addition of additional PMMA layers (3-4) to the sensor have a bigger impact on the transverse resonance. This implies that if the dielectrics within the sensor design are not excessively thick, that said designs will have two resonances that depend to differing degrees on the dielectric properties of the underlying material (superstrate). Therefore, a temperature dependency in the dielectric properties of the substrate will affect the net temperature sensitivity of the two resonators disproportionally and alter the original ratio between their sensitivities. Therefore, to avoid this potential issue, it is the recommendation of this work that any/all reference sensors have the same base resonator design as that of the original (strain) sensor.
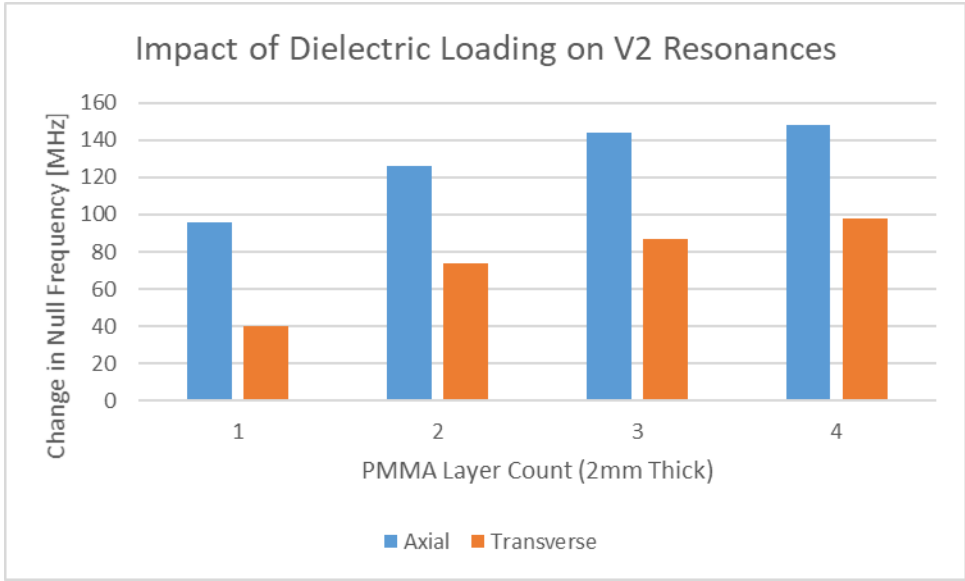
Figure 6.24: Nonlinear Dependency of V2 Strain Sensor Resonances on Dielectric Loading

6.5.2 Geometry Expansion

As mentioned earlier in this section and in Chapter 2, geometric variations can be expected to occur with both the substrate (polyimide) and conductor (copper) parts, due to material swelling. This can arise from at least two key environmental phenomena; temperature variations and humidity variations. This subsection explores these two effects using FEA software and reviews potential mitigation methods. This particular section is isolated from the humidity and temperature effects on dielectric constant as the effect of swelling is geometry specific and need to be explored in the context of the proposed design.

Thermal Swelling

The thermal effects arising within the sensor have the potential to result in a dielectric constant variation along with swelling effects. The latter effect arises naturally and occurs in virtually all known polymer materials to some degree. It can itself vary with temperature variations in many materials but will be assumed constant in this work. The relevant material properties that describe thermomechanical effects for the polyimide sensor can be found in Table 6.6.

Table 6.6: Thermo-mechanical Properties of Sensor Materials – from "Proof of Concept Novel Configurable Chipless RFID Strain Sensor" by McGee et al., MDPI, CC BY 4.0 [25]

Material	Young's Modulus [GPa]	Poisson's Ratio	Coefficient of Thermal Expansion (CTE) [C_{-1}]	Thermal Conductivity [$Wm_{-1}C_{-1}$]
Polyimide [35][36]	2.5	0.34	$1x10^{-4}$	0.12
Copper	125	0.345	$16.8x10^{-6}$	385

Initial FEA testing was performed with the sensor being unconstrained by the superstrate for the axial tests and a constraining superstrate for the thermal expansion tests at 350°C, the total deformation results of from these tests can be found in Table 6.7, Figure 6.25 and Figure 6.26 also. The earlier developed results for the sensor experiencing a 0.33% axial strain are also included in Table 6.7 to allow for a relevant comparison. From these results, it can be seen that thermal expansion of the unconstrained sensor will rival, if not exceed that found with axial strains of 0.33%. This is a key finding as this value is the equivalent of 3333µε and conventional strain sensing systems for SHM have demonstrated resolutions on the order of 10µε.

Setup	A	B	C	D	E	F	G	H	I	J
Axial Def. [µm]	24.6	23.4	24.9	22	5.5	14	5.8	12.8	3.9	5.3
350 °C Thermal Def. [µm]	74	72.8	57.6	55	20	23	32	48.1	51.5	49.8
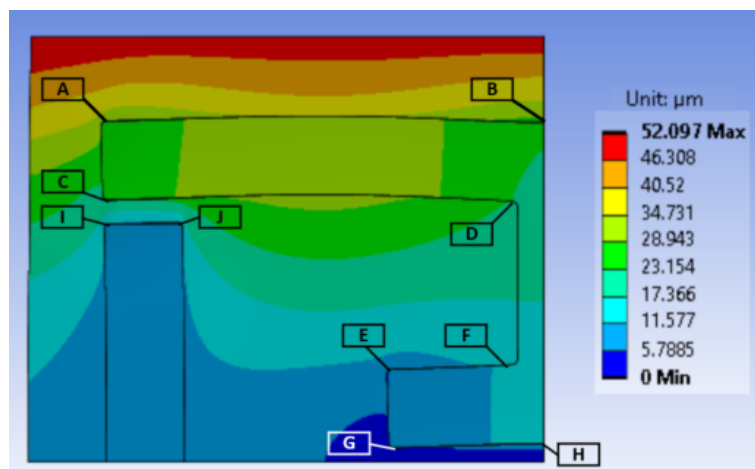
Figure 6.25: Effects of Axial Deformation on Total Deformation Result - (Images Courtesy of ANSYS Inc)
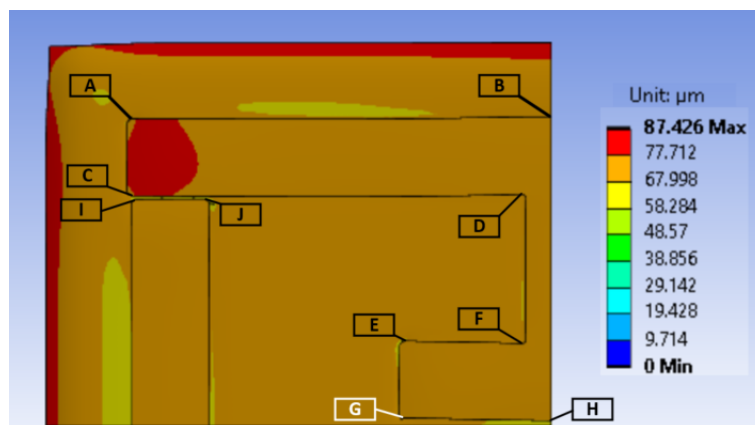
Figure 6.26: Effects of Thermal Swelling on Total Deformation Result - (Images Courtesy of ANSYS Inc)

One key critique of the above results is that they are not directive measurements and their magnitudes may be dominated by vertical swelling and not planar deformation. Therefore, Figure 6.27 shows the temperature dependency of the axial deformation of the sensor under these boundary conditions and Figure 6.28 depicts the thermal expansion of the sensor under these conditions at 350°C in both the axial and transverse directions.

244
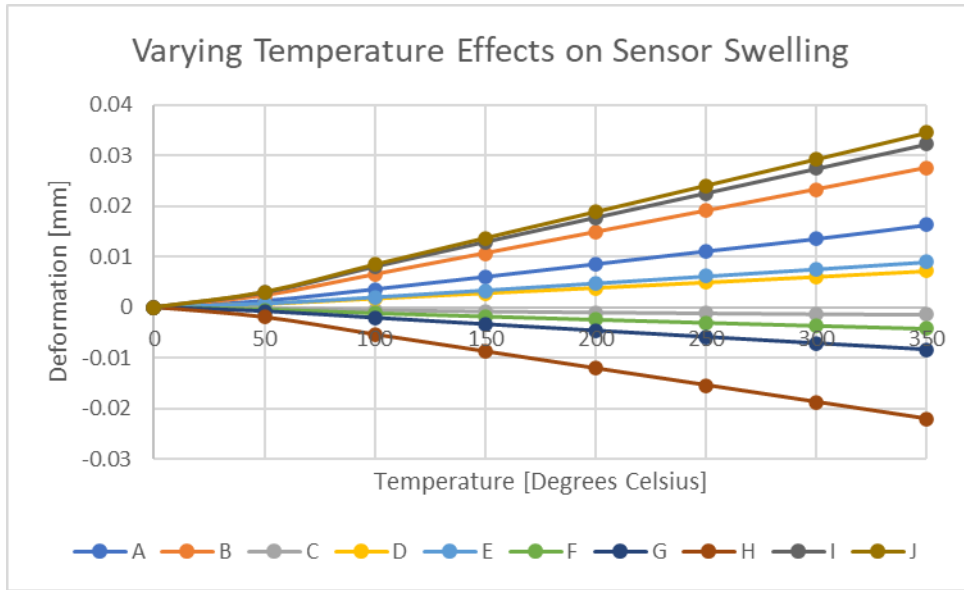
Figure 6.27: FEA-Based Swelling Results with Increasing Temperature

Figure 6.28: Thermal Swelling Effects with a Fixed Superstrate – from "Proof of Concept Novel Configurable Chipless RFID Strain Sensor" by McGee et al., MDPI, <u>CC BY 4.0</u> [25]

The deformation behaviour seen in Figure 6.28 above would appear to demonstrate a different behaviour than that seen during regular axial deformation. Positive values of axial deformation in positions I, J, A and B demonstrate a capacitive variation that appears to be similar to that found under compressive loading. Similarly, the negative axial values at positions F, G, and H would also signify a compressive effect taking place at the central capacitance. All of the transverse deformation was in the expansive direction. Of most interest is the deformation results found in Figure 6.28, are on the same order of magnitude as those found during axial strains of 0.33% (see Table 6.7 above).

To assess where the majority of the deformation was arising from, the subsequent test involved thermal deformation of the conductive elements. This test was performed with the substrate acting as a rigid body and thus the results in Figure 6.29 represent the response of the sensor under the conditions where the substrate experiences no thermal deformation. Comparing the results in Figure 6.28 and Figure 6.29 would suggest that the deformation of the constrained conductive elements is not the main cause of, or main contributor to the total deformation of the resonator.
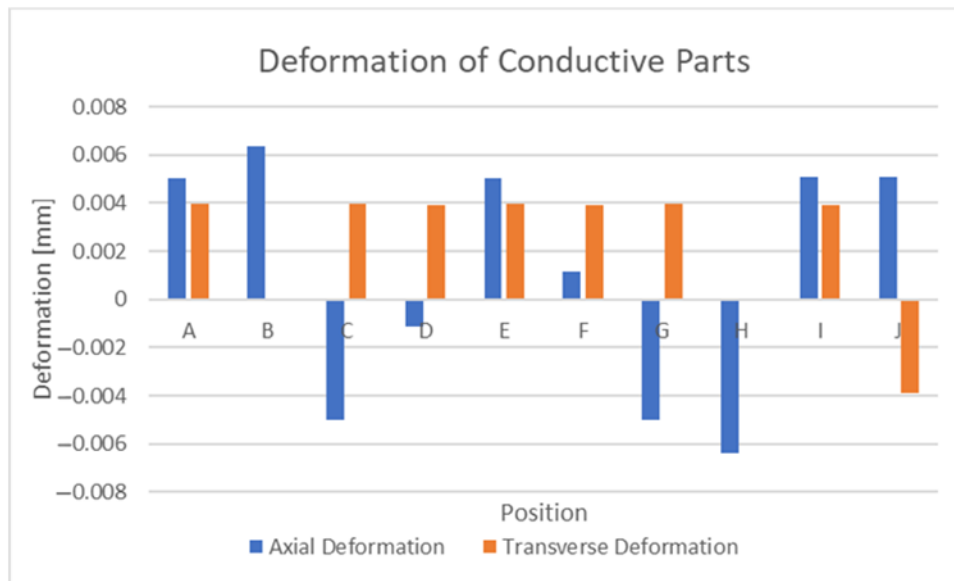
Figure 6.29: Contribution of Conductor Swelling to Total Deformation – from "Proof of Concept Novel Configurable Chipless RFID Strain Sensor" by McGee et al., MDPI, CC BY 4.0 [25]

At this point it is evident that thermal expansion is an issue of importance and will result in a static thermal deformation that will be considerable, in comparison to that which arises under axial strains of below 0.33%. The next question to be considered is if/how could this particular issue be dealt with within the sensor design? Several design modifications were made to address this issue, but these methods did not result in significant enough results for this problem to be considered fixed. The proposed various design modifications are thoroughly discussed in Appendix C.

Humidity-Based Swelling
Similar to the thermally induced swelling, humidity variations can also result in geometry expansion as a wide variety of polymer materials readily absorb moisture. Similar to thermal expansion, several works have developed a metric called the Coefficient of Humidity Expansion (CHE). Values of this for polyimides are on the order of 60-90ppm [26][31] and the value of 90ppm is considered in this work during FE-based testing. It is important to note that

the conductor expansion cannot be expected under the influence of humidity variations. This is important as this environmental variable will give rise to a dielectric constant variation, similar to temperature variations. Of most importance is that the deformation behaviour does not correlate with the same geometric effect as the conductor does not expand. FEA results gathered from the effects of 100%RH on the sensor can be seen in Figure 6.30.
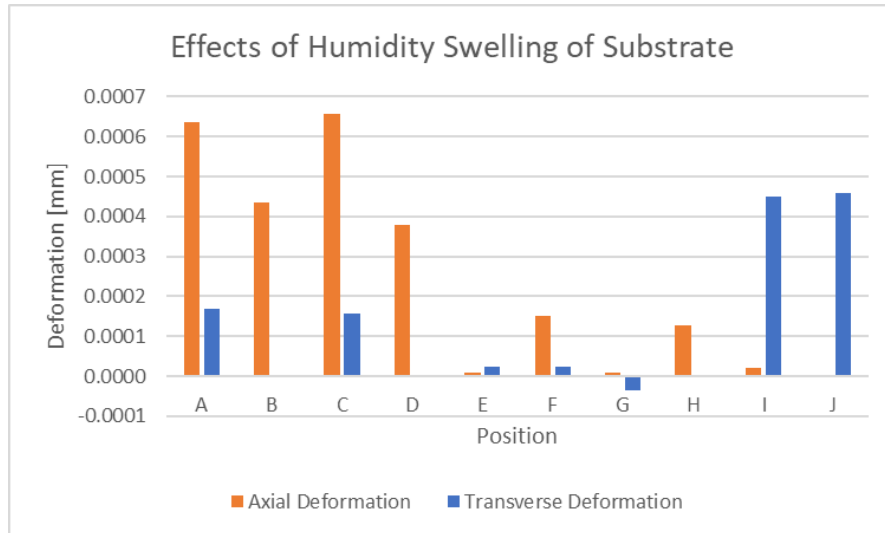
Figure 6.30: Impact of Humidity-Based Swelling on Sensor Design – from "Proof of Concept Novel Configurable Chipless RFID Strain Sensor" by McGee et al., MDPI, CC BY 4.0 [25]

Comparing the results in Figure 6.28 to those found in Figure 6.30 above clearly demonstrate that the humidity-based variations result in geometric changes that are considerably smaller, approximately a factor of ten smaller than those found under thermal-based swelling. The results in Figure 6.30 can be converted into equivalent strain values and this dataset can be seen in Table 6.8. The results seen in Table 6.8 clearly demonstrate that this effect still needs to be accounted for.

Table 6.8: Equivalent Strains Resulting from Humidity-Based Swelling – from "Proof of Concept Novel Configurable Chipless RFID Strain Sensor" by McGee et al., MDPI, CC BY 4.0 [25]

Position	A	B	C	D	E	F	G	H	I	J
Axial Strain [$\mu\varepsilon$]	18.5	12.7	20.3	11.7	3.4	63.3	20.3	316.7	0.535	0.084
Transverse Strain [$\mu\varepsilon$]	4.9	n/a	4.9	-0.03	9.8	9.55	-89	n/a	11.8	12.0

A system design choice is available here where the effects of humidity could be somehow negated within the design as opposed to compensated for using another measurement.

Unfortunately, since the dielectric and expansive effects of temperature and humidity differ and cannot be summed, it may not be possible to compensate for their combined effects (static and dynamic) using a single reference resonator. This opens up a more fundamental issue; should each relevant environment variable be measured at each sensor position or where possible, should their effects be mitigated within the sensor design. As this project is focussed on sensor design, the latter approach is considered first. Inert coatings that are hydrophobic in nature, such as Silicone (PDMS) are largely resistant to moisture [37] and their dielectric properties can vary only slightly as a result [38]. Epoxies as well as polyimides on the other hand, readily absorb moisture and thus would not be suitable as a protective coating. What is required is a material that will not support the diffusion of moisture through it and is not in any way affected by water. This latter point can be refined down into two smaller requirements, namely, the material is dimensionally stable in the presence of moisture and its dielectric properties are also stable. A good starting material is PFTE which is considered to be highly dimensionally stable in the presence of moisture as it has incredibly low moisture absorption [39] and low diffusion characteristics [40][41]. PTFE is also a commonly used material in the aerospace industry as it boasts low outgassing characteristics and also has a wide operating temperature range on the order of ±200°C [41]. This material has a lower stiffness than that of polyimide, which will mean that its presence should not significantly mitigate the deformation of the resonator [41]. Further study is required into the efficacy of such a coating, mainly, to what degree will it shield the sensor from the effects of both a static moisture level and a changing one. For now, the main concluding points of this subsection is that a single reference sensor will not be capable of providing response information that will allow for compensation of the effects of both temperature and humidity.

6.5.3 Material Model Variations

As mentioned in Chapter 2 conventional strain gauges exhibit changes in gauge factor when the mechanical material models vary, usually brought about by temperature variations. FEA was used to assess how material model variations would affect the sensor. This has been limited to assessing the effect that temperature would have on a Kapton H substrate structural material model. The effects of thermal swelling have been omitted from this analysis so that both effects can be discussed in isolation because swelling induces a static variation in the foil gauge response [42] whilst a material model variation results in a sensitivity change [42] . A report by Hughes and Rutherford [30] shows with Kapton H, a temperature variation between -195°C and +200°C, results in Poisson's ratio changes from 0.28 to 0.49 and Young's Modulus variations from 5.215GPa to 1.218GPa. Applying a 0.33% strain to the sensor model using this material model data resulted in the data seen in Figure 6.31 below. The results have been expressed as a percentage change of that found at 25°C.
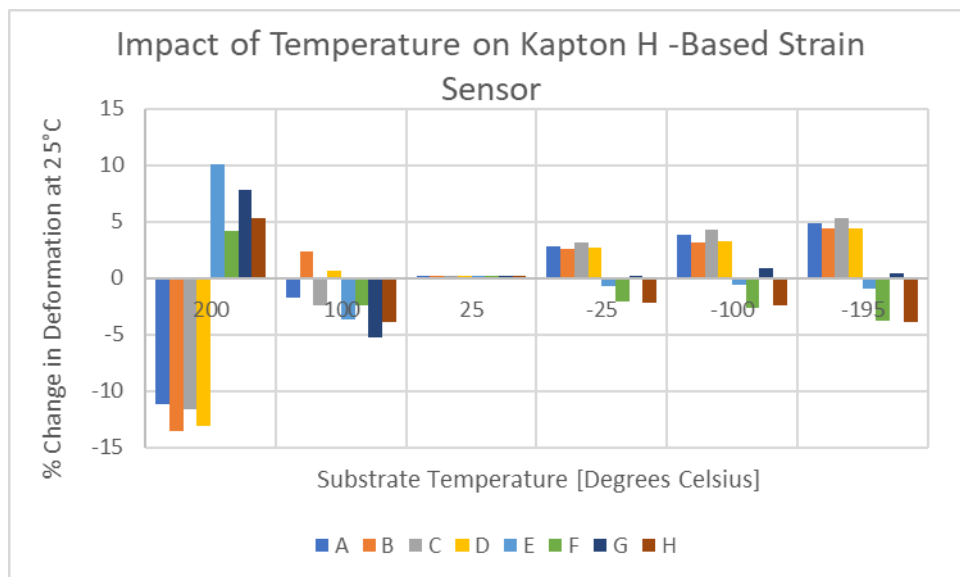
Figure 6.31: Effect of Substrate Material Model Temperature Dependencies on Sensor Response

Figure 6.31 demonstrates that all of the positions of interest on the resonator deform to a different extent than that found at 25°C. Also of importance is that the results at each position (A-H) do not scale linearly with temperature, therefore the levels of bending/elastic deformation appear to be temperature dependent. It is unclear what way this particular cross-sensitivity can be mitigated for within the sensor design. Because of this, the author has conceded that like some of the other challenges presented in this section, a reference measurement will be needed to determine the temperature of the device.

6.5.4 Implications of the Compiled Results

The above analysis has several key findings of key importance to the use of chipless RFID strain sensors in SHM applications. Most important of which is that the effects of nearby dielectric materials on the sensor response will need to be compensated for with a reference measurement. In the case where such nearby dielectrics could vary, a reference sensor will be needed. The reference sensor should have the same dielectric dependencies as that of the main sensor, or a multi-point temperature calibration may be needed in certain scenarios to re-evaluate the relationship between the dielectric sensitives of the two sensors.

Of further importance is that a single reference sensor cannot be used to allow for compensation of environmental variables such as temperature and humidity levels. Variables such as temperature can be expected to induce both static offsets in the measured strain level and alterations in the stimulus sensitivity curve. This brings up the need for a considerable amount of laboratory testing of the sensor, so that the reference temperature measurement can be used to compensate for this effect.

6.6   Future Work

This chapter serves as an introductory exploration of the other parts of the overall sensor system, not already described in Chapter 5. In general, a reader system that can operate successfully in a multi-sensor setting needs to be developed, similar to that outlined by Henry et Al. in [43], which was not used for interrogating chipless RFID sensors. Said system needs to be capable of performing interrogation ideally over several metres but support at least a range of one metre. Finally, the resulting device would ideally be capable of providing a sensor response dataset with the resolution requirements and providing the interrogation time requirements set out in Chapter 5.

6.6.1   Sensor Orientation Challenges

Additional work also needs to be performed such as an exploration of topics such as the implementation of static or dynamic beam steering methods (i.e. Van Atta array method [44]) at the sensor node to enhance the orientation challenges presented by sensors that are not orientated normal to the incoming interrogation wave. A variety of works have reported variations in the response of a chipless RFID tag when interrogated at various orientations [9][10][20][45][46]. These variations include both magnitude changes but also slight changes in resonant location. This is an important development to the overall picture presented in this thesis because it is most likely going to be the case that many of the deployed sensors will be interrogated at angles perhaps even exceeding 45° from the boresight direction of the tag. A

variety of testing was performed with a background and sensor clamping system that exhibited a consistent response throughout testing. These tests were performed at distances exceeding 2λ [47] between the interrogation antennas and the tag. The tests were carried out in a monostatic-like configuration where both antennas were facing the same side of the tag. Figure 6.32 depicts the initial resulting change in null magnitude of the square ring resonator described in Table 6.2 above, with increasing tag rotation.
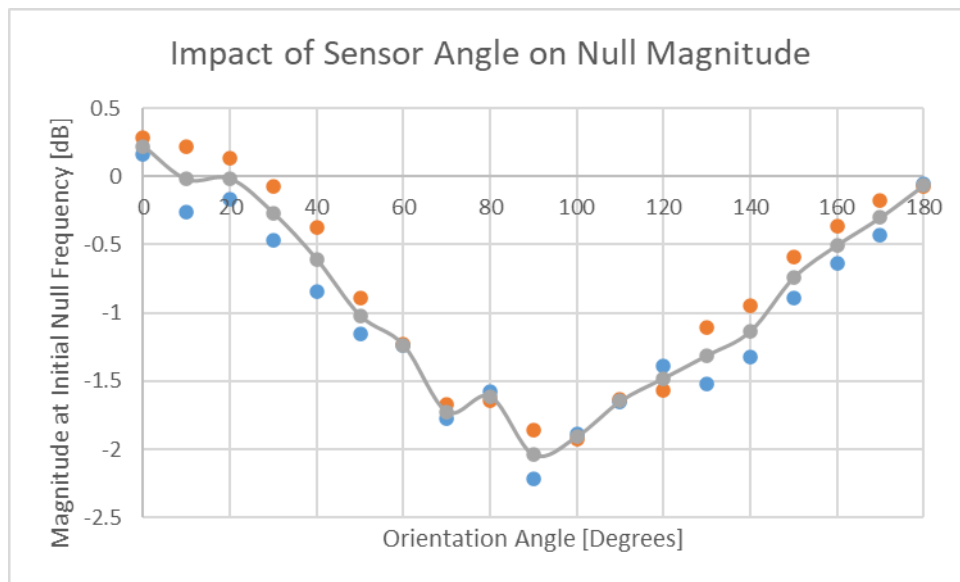
Figure 6.32: Impact of Orientation Angle on Sensor Response Null Magnitude

Although some changes of the null frequency were also observed, these results showed levels of variability that could not be definitively said to be the result of resonator behaviour, as it is unclear what part the orientation of the substrate material plays in this observed change. Simulation-based testing can be seen in [20] and [25] which clearly show similar results to that in Figure 6.32 above as the peak and null radiation patterns in said works are not scaled versions of each other. These variations in radiation patterns prove that the magnitude of the change of scattering power between the peak and null of the various tag responses will be dependent on the orientation in which they are interrogated. This is yet another reason why encoding information in the resonant magnitude/ Q-factor is a dangerous thing to do. Other simulation and test results presented in [46] show variability in the null frequency but no explanation is given for its origin. Testing in this work revealed that increasing the change in orientation angle left the resonant response more vulnerable to small variations in the background, as the contribution of the sensor to the total response became increasingly diminished. An interesting discussion on the electromagnetic scattering off antennas can be found in the work of Knott et al. in [48] which shows that the structural mode component of

the scattering has an orientation-dependent characteristic. More details on the structural mode can be found in Appendix I. This is perhaps what is the contributory factor leading to the simulation and test results referenced above but it would seem that the environmental variables such as interrogation range may also play a key role. For now, it will be concluded that this particular issue will need to be explored further as part of a future work and that in general, interrogation of these sensors at angles off from the normal-to vector will result in diminished sensor responses.

6.6.2   Enhancing Sensor Detection Range

In terms of enhancing sensor detection, several approaches are seen in the literature, including environmental modelling as seen in [20]. Other, more simplified methods include the use of time-domain style of chipless RFID tags which allow for the separation of the clutter and structural mode scattering responses to be isolated from the stimulus-dependent antenna mode (see Appendix I for more details). Such sensors/tags make use of transmission lines with metamaterial elements or other delay elements along with transmission line loading using conventional resonators [49][50]. Time domain tags have been shown to be capable of being interrogated at ranges of over one metre [18] but have a larger footprint than their frequency domain alternatives [7]. It remains to be seen if the more popular frequency domain tags can be interrogated at similar ranges, although it seems like said challenge could be very difficult [19]. It therefore may be required that the sensor designs seen in Chapter 3 and Chapter 4 may need to be added to a transmission line so that a time-domain reader system can be used. The testing in Chapter 3 includes a demonstration of successful transmission line coupling for the developed strain sensors.

Other approaches have also been shown to be successful to enhance sensor detection including the use of bistatic interrogation with a ninety-degree polarization difference between the antennas [18]. This approach is used to interrogate a tag/sensor at an angle of forty-five degrees and the principle is that the clutter response is mitigated because the initial environmental echo will not be detected by the reception antenna. Similarly, it is commonplace for transmission line -based chipless RFID tags to make explicit use of cross polar transmission-line based tags to ensure that the response from the tag/sensor is in a completely orthogonal orientation to that of the interrogation wave, and this is also done to enhance tag detection [7].

It is currently unclear what flavour of chipless RFID tag design will be most suitable for aerospace SHM but it seems from the current literature that time-domain based designs have

a clear read range advantage. The designs proposed in this document have been proven theoretically to be capable of being integrated into such a design, if such a requirement is needed.

6.7 Conclusions

This chapter has given a comprehensive review and exploration into the sensor interrogation challenges that are present with chipless RFID sensor technology. This includes an exploration of challenges in several key areas including;

- Sensor polarization variation
- Interrogation antenna configuration
- Multi-sensor environment challenges
- Sensor cross-sensitivities

Throughout this chapter, novel solutions have been put forward/implemented on several of the topics listed above and a great emphasis has been placed on finding straightforward solutions to the problems at hand. Other challenges which have not been explored to the same degree also exist, but where possible, realistic solutions to these problems have been outlined based on potential solutions seen in the existing literature.

This chapter serves as an initial attempt at addressing the problems associated with deploying this technology in aerospace SHM applications. As mentioned above, the next steps are to begin developing a reader architecture capable of addressing all of the challenges explored in this work and test it in an appropriate setting.

6.7 References

[1]   McGee, K. et al. Use of Chipless RFID as a Passive, Printable Sensor Technology for Aerospace Strain and Temperature Monitoring, Sensors, 2022, 22, 8681. https://doi.org/10.3390/s22228681

[2]   Min, S. H. et al. Stretchable chipless RFID multi-strain sensors using direct printing of aerosolised nanocomposite, Sensors Actuators A Phys., 2020, vol. 313, p. 112224.

[3]   Islam, M. A. et al. Orientation independent compact chipless RFID tag, in 2012 IEEE International Conference on RFID-Technologies and Applications, RFID-TA 2012, 2012, pp. 137–141.

[4]   Amin, E. M. et al. Fully printable chipless RFID multi-parameter sensor, Sensors Actuators A Phys., 2016, vol. 248, pp. 223–232.

[5]   Jalil, M. E. B. et al. High Capacity and Miniaturized Flexible Chipless RFID Tag Using Modified Complementary Split Ring Resonator, IEEE Access, 2021, vol. 9, pp. 33929–33943.

[6]   Wan, G. et al. Separating strain sensor based on dual-resonant circular patch antenna with chipless RFID tag, Smart Mater. Struct., 2020, vol. 30, no. 1, p. 015007.

[7]   Herrojo, C. et al. Chipless-RFID: A Review and Recent Developments, Sensors, 2019, vol. 19, no. 15, p. 3385.

[8]   Mc Gee, K. et al. A Review of Chipless Remote Sensing Solutions Based on RFID Technology, Sensors, 2019, vol. 19, no. 19, p. 4829.

[9]   Ma, Z.; Jiang, Y. High-Density 3D Printable Chipless RFID Tag with Structure of Passive Slot Rings, Sensors 2019, Vol. 19, Page 2535, 2019, vol. 19, no. 11, p. 2535.

[10]   Costa, F. et al. A chipless RFID based on multiresonant high-impedance surfaces, IEEE Trans. Microw. Theory Tech., 2013, vol. 61, no. 1, pp. 146–153.

[11]   Huang, Y.; Boyle, K. Antennas: From Theory to Practice. Sussex: Wiley, 2008.

[12]   Daliri, A. et al. Wireless strain measurement using circular microstrip patch antennas, Sensors Actuators, A Phys., 2012, vol. 184, pp. 86–92.

[13]   Byun, G.; Choo, H. Antenna polarisation adjustment for microstrip patch antennas using parasitic elements, Electron. Lett., 2015, vol. 51, no. 14, pp. 1046–1048.

[14]   Yoo, S. et al. Design of microstrip patch antennas with parasitic elements for minimized polarization mismatch, 2016 URSI Asia-Pacific Radio Sci. Conf. URSI AP-RASC 2016, 2016, pp. 1845–1846.

[15]   Martin, F. Artifical Transmission Lines for RF and Microwave Applications, 1st Edt. Wiley, 2015.

[16]   Naqui, J. et al. Symmetry-Related Electromagnetic Properties of Resonator-Loaded Transmission Lines and Applications, Appl. Sci. 2015, Vol. 5, Pages 88-113, 2015, vol. 5, no. 2, pp. 88–113.

[17]   Shen, J. et al. Research on strain measurements of core positions for the Chinese space station, Sensors (Switzerland), 2018, vol. 18, no. 6.

[18]   Garbati, M. et al. Ultrawideband Chipless RFID: Reader Technology from SFCW to IR-UWB, IEEE Microw. Mag., 2019, vol. 20, no. 6, pp. 74–88.

[19]   Barbot, N. et al. Classical RFID Versus Chipless RFID Read Range: Is Linearity a Friend or a Foe?, IEEE Trans. Microw. Theory Tech., 2021, vol. 69, no. 9, pp. 4199–4208.

[20]   Fawky Megahed, A. Realistic Chipless RFID: Identification and Localization, University of Duisburg-Essen, 2016.

[21]   NanoVNA V2 Official Site. [Online]. Available: https://nanorfe.com/nanovna-v2.html. [Accessed: 22-Sep-2020].

[22]   Barahona, M. et al. Automatic IR UWB chipless RFID system for short range applications, 2017 IEEE-APS Top. Conf. Antennas Propag. Wirel. Commun. APWC 2017, 2017, vol. 2017-January, pp. 274–279.

[23]   Amin, E. M. et al. Chipless RFID tag for light sensing, in 2014 IEEE Antennas and Propagation Society International Symposium (APSURSI), 2014, pp. 1308–1309.

[24]   Román-Raya, J. et al. Light-Dependent Resistors as Dosimetric Sensors in Radiotherapy, Sensors 2020, Vol. 20, Page 1568, 2020, vol. 20, no. 6, p. 1568.

[25]   Mc Gee, K. et al. Proof of Concept Novel Configurable Chipless RFID Strain Sensor, Sensors, 2021, vol. 21, no. 18, p. 6224.

[26]   Sager, K. et al. Humidity-Induced Volume-Expansion of Polyimide Films:, http://dx.doi.org/10.1177/1045389X9600700304, 2016, vol. 7, no. 3, pp. 264–266.

[27]   Adamson, M. J. Thermal expansion and swelling of cured epoxy resin used in graphite/epoxy composite materials, J. Mater. Sci. 1980 157, 1980, vol. 15, no. 7, pp. 1736–1745.

[28]   Sahputra, I. H. et al. Temperature dependence of the Young's modulus of polymers calculated using a hybrid molecular mechanics–molecular dynamics method, J. Phys. Condens. Matter, 2018, vol. 30, no. 35, p. 355901.

[29]   Huang, P.-Y. et al. General Model of Temperature-dependent Modulus and Yield Strength of Thermoplastic Polymers, Chinese J. Polym. Sci. 2019 384, 2019, vol. 38, no. 4, pp. 382–393.

[30]   Hughes, E. J.; Rutherford, J. L. DETERMINATION OF MECHANICAL PROPERTIES OF POLYMER FILM MATERIALS, 1975.

[31]   Sager, K. et al. Humidity-dependent mechanical properties of polyimide films and their use for IC-compatible humidity sensors, Sensors Actuators A Phys., 1996, vol. 53, no. 1–3, pp. 330–334.

[32]   Riddle, B. et al. Complex permittivity measurements of common plastics over variable temperatures, IEEE Trans. Microw. Theory Tech., 2003, vol. 51, no. 3, pp. 727–733.

[33]   Ree, M. et al. Anisotropic properties of high-temperature polyimide thin films: Dielectric and thermal-expansion behaviors, J. Appl. Phys., 1998, vol. 72, no. 5, p. 2014.

[34]   Mc Gee, K. et al. Zero-Power Wireless Strain and Permittivity Sensor, 2022 33rd Irish Signals Syst. Conf., 2022, pp. 1–5.

[35]   Polyimide films | DuPont. [Online]. Available: https://www.dupont.com/electronic-materials/polyimide-films.html/general/H-38479-4.pdf. [Accessed: 28-Jul-2021].

[36]   Elsner, G. et al. Anisotropy of thermal expansion of thin polyimide films, Thin Solid Films, 1990, vol. 185, no. 1, pp. 189–197.

[37]   Bian, P. et al. Rediscovering Silicones: The Anomalous Water Permeability of "Hydrophobic" PDMS Suggests Nanostructure and Applications in Water Purification and Anti-Icing, Macromol. Rapid Commun., 2021, vol. 42, no. 5, p. 2000682.

[38]   Gong, B. et al. Moisture absorption characteristics of silicone rubber and its effect on dielectric properties, Annu. Rep. - Conf. Electr. Insul. Dielectr. Phenomena, CEIDP, 2013, pp. 430–433.

[39]   Alhaji, I. A. et al. Effects of Particle Size on the Dielectric, Mechanical, and Thermal Properties of Recycled Borosilicate Glass-Filled PTFE Microwave Substrates, Polymers (Basel)., 2021, vol. 13, no. 15.

[40]   Hansen, C. M. Water transport and condensation in fluoropolymer films, Prog. Org. Coatings, 2001, vol. 42, no. 3–4, pp. 167–178.

[41]   The Chemours Company FC, L. TeflonTM FEP Information Bulletin, 2017.

[42]   Window, A. L. Strain Gauge Technology, 2nd Edtn. London: Elsevier, 1992.

[43]   Henry, D. et al. Identification of Chipless Sensors in Cluttered Environments from 3D Radar Imagery and Polarimetry, 2020 33rd Gen. Assem. Sci. Symp. Int. Union Radio Sci. URSI GASS 2020, 2020.

[44]   Mulloni, V.; Donelli, M. Chipless RFID sensors for the internet of things: Challenges and opportunities, Sensors (Switzerland), vol. 20, no. 7. MDPI AG, 01-Apr-2020.

[45]   Vena, A. et al. A Novel Near-Transparent ASK-Reconfigurable Inkjet-Printed Chipless RFID Tag, IEEE Antennas Wirel. Propag. Lett., 2013, vol. 12, pp. 753–756.

[46]   Kalansuriya, P. et al. On the detection of frequency-spectra-based chipless RFID using UWB impulsed interrogation, IEEE Trans. Microw. Theory Tech., 2012, vol. 60, no. 12, pp. 4187–4197.

[47]   Pozar, D. M. Microwave Engineering, 4th ed. New York: Wiley, 2012.

[48]   Knott, E. F. et al. Radar Cross Section, 2nd Edtn. Raleigh: Scitech Publishing, 2004.

[49]   Mandel, C. et al. Passive wireless temperature sensing with BST-based chipless transponder - IEEE Conference Publication, in 2011 German Microwave Conference, 2011.

[50]   Alahnomi, R. A. et al. Review of Recent Microwave Planar Resonator-Based Sensors: Techniques of Complex Permittivity Extraction, Applications, Open Challenges and Future Research Directions, Sensors 2021, Vol. 21, Page 2267, 2021, vol. 21, no. 7, p. 2267.

Chapter 7 - Conclusion

7.1   Project Overview

Overall, a good deal of progress was made towards the development of chipless RFID sensors for aerospace Structural Health Monitoring (SHM). Having a look at each of the chapters, it can be seen that this technology and the designs put forward within this document still have a number of outstanding concerns that will need to be addressed within a future work. This chapter attempts to take a high-level overview of the results and concluding remarks found in each of the other chapters. The progress of this work is compared against the idealised sensor technology that chipless RFID may one day become, however it must be noted that this was not the main goal of this project and something that it could only strive for.

7.2   Literature Review Conclusions

Chapter 2 presents a thorough literature review that discusses the topic of strain and temperature sensing, along with the challenges/requirements put forward by the aerospace setting. A brief introduction to chipless RFID tags and sensors is also performed in this chapter and an initial discussion on sensor fabrication is also presented.

7.3   Strain Sensor Development Conclusions

This chapter outlines the results and findings drawn from the strain sensor development work performed as part of this project. This includes the development and testing of novel strain sensor designs, a deep exploration of the cross sensitivity that these devices would exhibit is presented in Chapter 6. As well as that, in-situ fabrication was also explored, and various fabrication methods were tested and implemented. Figure 7.1 below depicts the progress/aspects of strain sensor development that can be seen in Chapter 3. It is worth mentioning that the diagram seen in Figure 7.1 above is related to the design flow of a fully-functional aerospace sensor and not that of a proof-of-concept implementation.
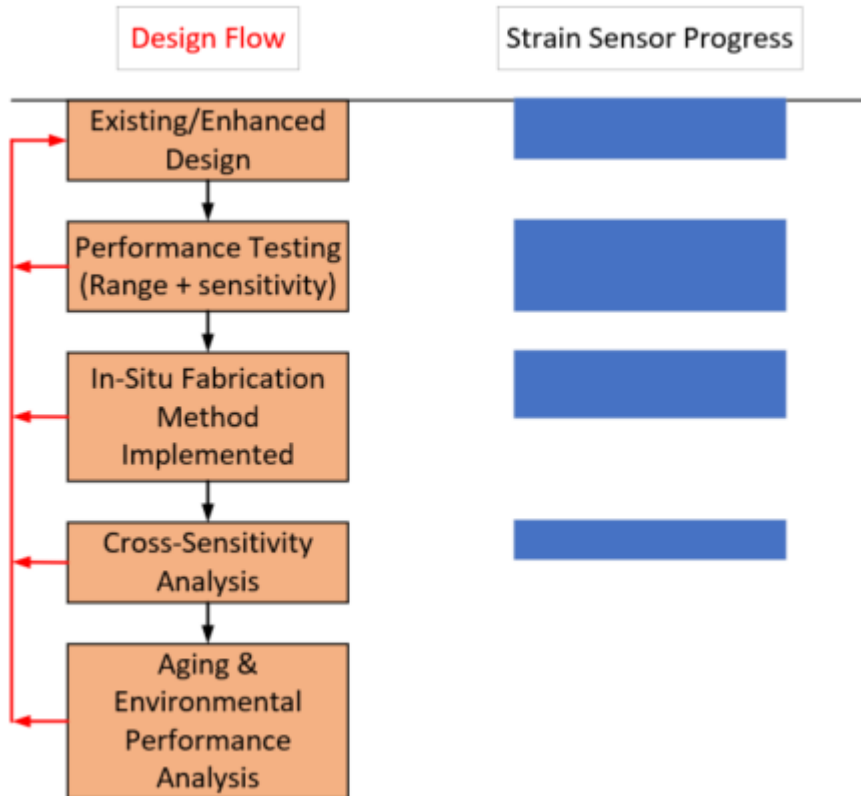
Figure 7.1: Strain Sensor Development Progress

7.4   Temperature Sensor Development Conclusions

As discussed in Chapter 2, thermocouple devices are used in extreme high temperature applications, including those at temperatures above the melting points of most metals. Thermocouple integration into chipless RFID technology is attempted, with moderate levels of success. Figure 7.2 depicts the level of sensor development progress made in this chapter.
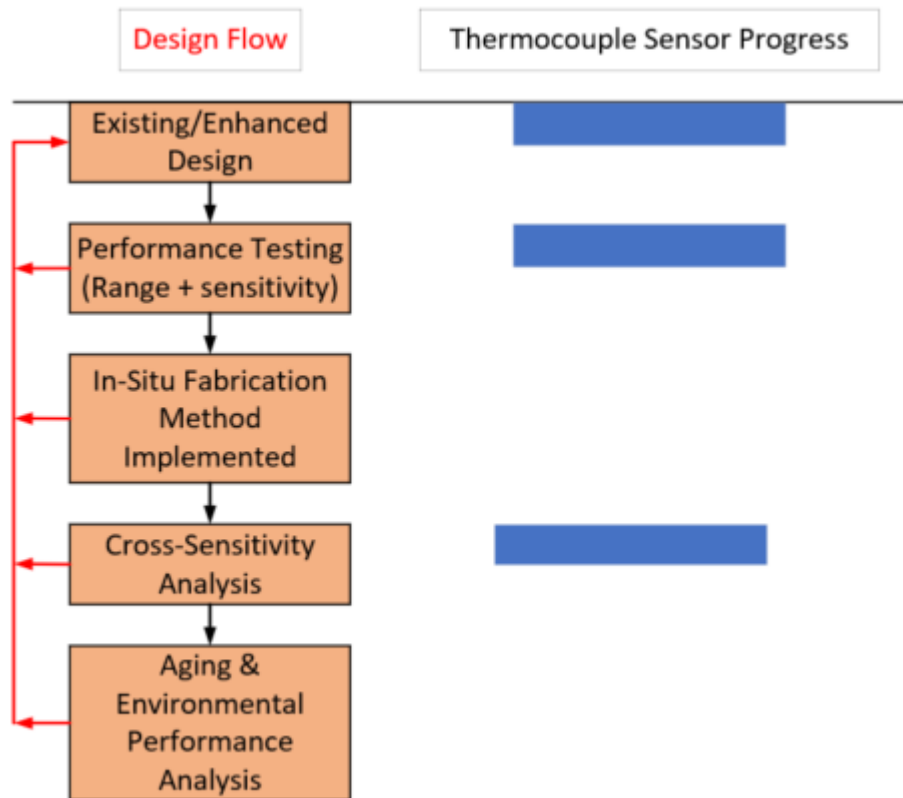
Figure 7.2: Thermocouple-Based Chipless RFID Sensor Development Progress

Thermocouple devices require an ambient temperature sensor to determine the temperature of the reference side of the thermocouple. Similarly, not all temperature sensor applications require extreme sensing ranges. A variety of different ambient temperature sensors were developed in Chapter 4 and their performances explored but less emphasis was placed on in-situ fabrication. Figure 7.3 describes the progress towards the development of an aerospace grade ambient temperature sensor.
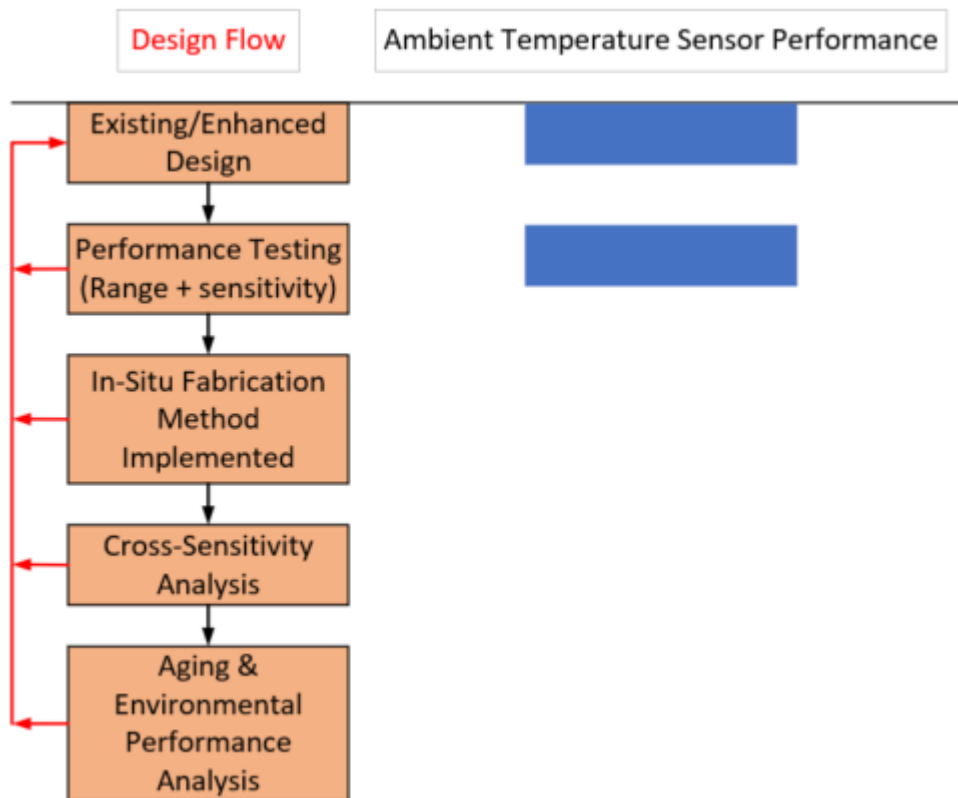
Figure 7.3: Ambient Temperature Chipless RFID Sensor Development Progress

7.5   Sensor Response Analysis Conclusions

This chapter explores the challenges of extracting the desired information from the incoming sensor response datasets. From this work, it can be seen that achieving the desired stimulus resolution is going to be very difficult as it will have significant knock-on effects on the sensor interrogation requirements. Similarly, the stability of such measurements is also explored and combatted through the use of matched filter algorithms.

Transfer function fitting was also explored here and in Appendix H, as a means of decoupling the stimulus resolution requirements from the knock-on interrogation requirements. The results of which were poor as the response curves did not align well with known transfer function responses.

Finally, the effects of a dynamic stimulus on the sensor response datasets are also explored. From the resulting analysis, methods to extract the time-domain information from the response datasets were presented and tested with moderate-to-high degrees of success.

7.6 Sensor System Deployment Conclusions

The final research chapter focusses on the interrogation challenges associated with chipless RFID technology. The first half of the chapter is concerned with sensor addressing and polarization, amongst other aspects related to aerospace SHM. The findings of this section indicate that sensor rosettes cannot make use of identical sensors, due to coupling effects. Furthermore, tag/sensor orientation and polarization challenges are indeed going to be difficult to combat and will impact the final sensor system configuration. Also, read ranges demonstrated in this work will need to be enhanced if this technology is going to be used in aerospace SHM.

Addressing/isolation of each sensor is also explored in this chapter. The findings of this are that this challenge is going to become very significant and little or no works within the known literature have demonstrated achieving this goal in a physical implementation. Attempts are also made in this chapter to explore alternative/additional reader and/or sensor designs that can aid the future development of a working chipless RFID SHM system.

7.7 Future Project Planning

In terms of future planning, there are three main avenues of research to explore. Two of these avenues; sensor performance and sensor fabrication are related to enhancing the work put forward in Chapter 3 and Chapter 4. The other avenue, which is reader system design, is related to building upon the work seen in Chapter 5 and Chapter 6. In terms of further sensor design goals, Table 7.1 depicts the next steps to be taken within the scope of achieving aerospace SHM using chipless RFID technology.

Table 7.1: Future Sensor Development Goals

Goal	Current State	Potential/ Viable Approach	Result of Future Failure
Enhanced thermocouple integration	Barium Strontium Titanate (BST) - based sensor has poor sensitivity and high cross sensitivity.	n/a	Significant fabrication and cross- sensitivities arising with BST
Enhanced low temperature (<350°C) sensing device	Existing designs are difficult to fabricate. Some other avenues were not explored	Several previously unknown polymers and nanomaterials may prove useful	Need to fabricate metallic cantilevers in-situ
Device miniaturisation	Major dimensions of designs are between 2-8cm	Move the current designs into the X- band of the spectrum or above	n/a

Full device (cross-) sensitivity exploration	Cross sensitivities need to be redone when final fabrication method is developed	Environmental chambers and 2D strain testing equipment could be used	Devices will most likely not be suitable to meet aerospace requirements

Similar to the sensor performance steps outlined in Table 7.1 above, Table 7.2 below depicts the next steps within the context of sensor fabrication. As discussed earlier, this work has focussed on the fabrication of the strain sensor above that of the incomplete temperature sensor design. In either case further work is needed to enhance this aspect of the project.

Table 7.2: Future Development Goals for Senor Fabrication

Goal	Current State	Potential/ Viable Approach	Result of Future Failure
Ferroelectric in-situ deposition	Extreme temperatures required to sinter/fire BST depositions	n/a	Fully in-situ sensor goal not possible
Enhanced fully-printable strain sensor performance	Thermal transfer approach has low sensitivity	Use of substrate slotting and thick conductors. This could be supported by plasmaJet technology and Fused Deposition Modelling (FDM) printing	Resulting strain sensors will be easy to fabricate/deploy but have low sensitivities
Fully printable temperature sensor(s)	Existing designs are only proof-of-concept	Thermal transfer and/or inkjet/FDM could be applied to the final design	Without the printable aspect of chipless RFID, ceramic resonators would be a more suitable approach

Finally, Chapter 5 and Chapter 6 have focused on the reader system required to support the interrogation and stimulus extraction requirements set out by the application. This system has yet to be fully developed and tested as it has not been seen in any of the known literature. These goals are seen in Table 7.3 and are expected to be by far the most important and most difficult to achieve within a future work.

Table 7.3: Future Interrogation System Development Goals

Goal	Current State	Potential/ Viable Approach	Result of Future Failure
Enhanced stable & reliable feature extraction	Minimum-point and polynomial curves are most stable	n/a	Serious interrogation challenges

			associated with SHM applications
Demonstrate read ranges exceeding one metre	Interrogation distances below 40cm used in testing	n/a	Need to try and use Impulse Radio Ultrawideband (IR-UWB) reader and integrate existing designs into compliant tag designs
Perform isolated sensor interrogation in multi-sensor settings	Simulated Frequency Modulated Continuous Wave (FMCW) -based solutions can support this but not demonstrated in reality	FMCW or IR-UWB - based readers could potentially support this requirement	Either a breakthrough addressing scheme is developed or each sensor needs to have its own spectrum allocation

Appendix A: Mechanical Finite Element Analysis Setup

Structural Finite Element Analysis (FEA) is a software approach that uses the minimum potential energy method to solve the material model equations and determine the displacements within a supplied geometric model [1]. This total potential energy term is the sum of the strain energy in the model and the external work applied to the model [1].

A.1   Material Modelling

Ecoflex™ 00-30 silicone rubber was one of the substrate materials of interest to this work and is considered to be a hyperplastic material. Equation A.1 is the strain energy density function used in Ansys to represent the Ogden hyperelastic material model. Equation A.1 found in [1][2], and Table A.1 gives details of the EcoFlex hyperelastic material model, relevant material parameters and their sources. Nonlinear material models are given in the form of a strain energy density equation (W) which can be related to stress (σ), as stated in [1], through Equation A.2.

$$W = \sum_{i=1}^{N} \frac{\mu_i}{\alpha_i}\left(\lambda_1^{\alpha i} + \lambda_2^{\alpha i} + \lambda_3^{\alpha i} - 3\right) + \sum_{k=1}^{N} \frac{1}{d_k}(J-1)^2 \qquad \text{(A.1)}$$

$$Incompressibility\ Parameters: d_1 = \frac{2}{G}, d_2 = d_3 = 0\ where\ G = Bulk\ Modulus$$

$$\lambda_i^{\alpha i} = Deviatoric\ Principle\ Stretches\ "i"$$

$$\frac{\partial W}{\partial \varepsilon} = \sigma \qquad \text{(A.2)}$$

Table A.1: Ogden Model Ecoflex Material Parameters [2]

Ogden Model Parameters	
$\lambda = 375$ [2], E = 0.1 MPa [3][4][5] => $d_1 = 0.005967$ [6]$, d_2 = d_3 = 0$ [7]	
$\mu_1 = 22\ kPa$	$\alpha_1 = 1.3$
$\mu_2 = 0.4\ kPa$	$\alpha_2 = 5$
$\mu_3 = -2\ kPa$	$\alpha_3 = -2$

The polyimide material (Kapton®) was modelled as having linear elastic isotropic stress-strain properties. This choice was made based on the behaviour this material and its variants exhibited under tensile testing presented in Reference [8], Reference [9] and this approach was also used in the FEA performed in Reference [10]. This linear elastic isotropic material model equation described in [1], can be seen in Equation A.3 where just two material properties are required; Young's Modulus (E) and Poisson's Ratio (ν).

$$
\begin{bmatrix} \sigma_x \\ \sigma_y \\ \sigma_z \\ \tau_{xy} \\ \tau_{yz} \\ \tau_{zx} \end{bmatrix}
$$

(A.3)

$$
= \frac{E}{(1+v)(1-2v)}
\begin{bmatrix}
1-v & v & v & 0 & 0 & 0 \\
v & 1-v & v & 0 & 0 & 0 \\
v & v & 1-v & 0 & 0 & 0 \\
0 & 0 & 0 & (1-2v)/2 & 0 & 0 \\
0 & 0 & 0 & 0 & (1-2v)/2 & 0 \\
0 & 0 & 0 & 0 & 0 & (1-2v)/2
\end{bmatrix}
\begin{bmatrix} \varepsilon_x \\ \varepsilon_y \\ \varepsilon_z \\ \gamma_{xy} \\ \gamma_{yz} \\ \gamma_{zx} \end{bmatrix}
$$

As there is some variation between grades of Kapton®, the approach taken in this work was to source the material properties from DuPont™. The necessary material properties, found in [11], are listed in Equation A.4 below.

$$E = 2.5GPa, v = 0.34$$
(A.4)

Similarly, copper is used as the conductor material and its material model is a linear elastic isotropic one, with E=125GPa and v=0.345. Those values were already present in the software material libraries.

A.2 Symmetry and Boundary Conditions

The strain sensors designed in this work exhibits two planes of symmetry and thus only one quarter of the model needs to be simulated, which greatly increases the maximum mesh density of the simulations. Figure A.1 highlights the position labels on the sensor that are used in Table A.2 to denote the results of the axial strain response. Also seen in Figure A.1 is an example deformation contour plot obtained during thermal swelling of the device.

The following loads and boundary conditions were placed on the model:

- The bottom face of the superstrate was constrained in the Z-direction using a frictionless constraint
- All bodies in contact with the South and East faces of the sensor was constrained using frictionless constraints (mimics symmetry and reduces computation time)
- The West face of the superstrate in was set as a symmetry region to stop the superstrate's small width from unduly causing stresses in the X-direction as the superstrate in real life would be a large object
- Bonded contact regions were added between the resonator and the substrate and separately between the substrate and superstrate

- A relevant displacement load was applied to the north face of the superstrate in both models. The reason why a superstrate was included was to capture the behaviour of the substrate when it experiences a shear strain as opposed to a tensile one

Table A.2 also includes the results of a simplified model that applies the tensile load to the north face of the substrate and does not include a superstrate. This results in the substrate experiencing axial-induced deformation instead of shear-induced deformation.

(a)   (b)
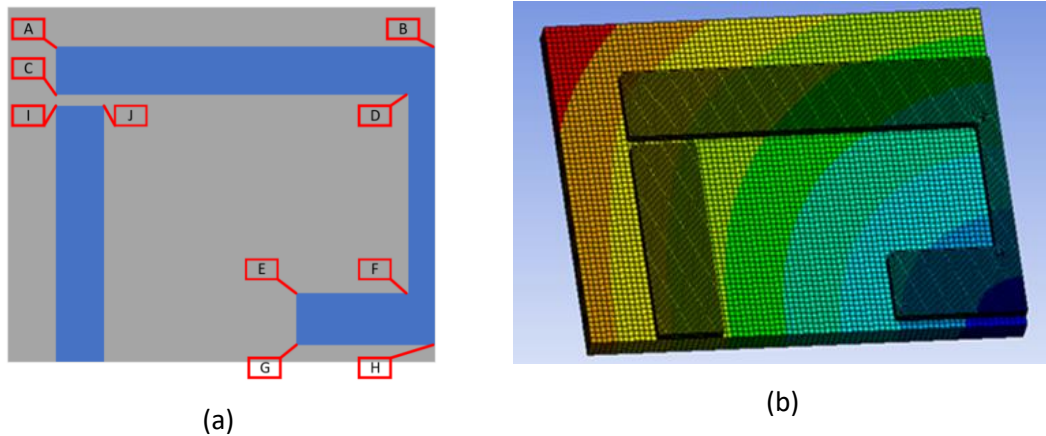
Figure A.1: (a)-Strain Sensor Position Legend, (b)-Total Deformation Contour Plot. – from "Proof of Concept Novel Configurable Chipless RFID Strain Sensor" by McGee et al., MDPI, CC BY 4.0 [12]

Table A.2: FEA Results with/without Superstrate

ELC Sensor		Position									
Regular Design		A	B	C	D	E	F	G	H	I	J
Eco-Flex	Displacement (mm)	1.2	1.2	1.2	1.2	1.2	1.2	1.2	1.2	1.4 e-4	1.4 e-4
Kapton® (0.1mm)	Displacement (µm)	47.9	41.3	48.6	39.3	8	39	8.4	19.4	14.1	14.8
Simplified Design		A	B	C	D	E	F	G	H	I	J
Kapton® (0.1mm)	Displacement (µm)	48.8	46.7	49.8	46.4	11.2	26	11.7	25.7	7.6	10.5
Kapton® (0.05mm)	Displacement (µm)	24.6	23.4	24.9	22	5.5	14	5.8	12.8	3.9	5.3

A.3   Mesh Convergence

The results of the regular and simplified material models would suggest that the behaviour of the simplified model is largely indicative of the regular one. Details of the sensor mesh convergence can be seen in Figure A.2 below. Said Figure shows the convergence curves for the deformation of the positions of interest against total element count. The meshing of each part of the sensor assembly needed to be meshed with increasing resolution but these operations could not be done independently of each other, therefore the total element count is used as the X-axis in Figure A.2 below. The final mesh details were as follows; 0.25mm quadrilateral meshing with 0.25mm elements on the conductive parts and the fillets (radius=0.2mm) present on the conductors had three mesh divisions. This result is important as its solution time is considerably quicker than the regular model as it does not contain a superstrate and additional contact region. The FEA results presented throughout this thesis will use the simplified sensor model as its basis.
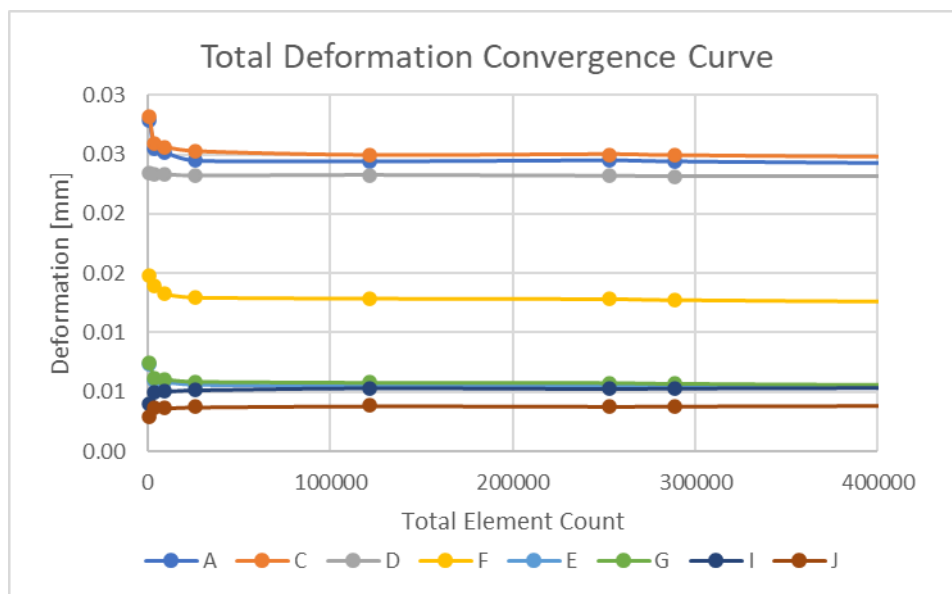
Figure A.2: Simplified Model Mesh Convergence Curve

A.4   References

[1]   MacDonald, B. J. Practical Stress Analysis with Finite Elements, 2nd Edtn. Dublin: Glasnevin Publishing, 2013.

[2]   Steck, D. et al. Mechanical responses of Ecoflex silicone rubber: Compressible and incompressible behaviors, J. Appl. Polym. Sci., 2019, vol. 136, no. 5, p. 47025.

[3]   Vaicekauskaite, J. et al. Mapping the mechanical and electrical properties of commercial silicone elastomer formulations for stretchable transducers, J. Mater. Chem. C, 2020, vol. 8, no. 4, pp. 1273–1279.

[4]   Moser, R. et al. From Playroom to Lab: Tough Stretchable Electronics Analyzed with a Tabletop Tensile Tester Made from Toy-Bricks, Adv. Sci., 2016, vol. 3, no. 4, p. 1500396.

[5]   Shintake, J. et al. Soft pneumatic gelatin actuator for edible robotics, in IEEE International Conference on Intelligent Robots and Systems, 2017, vol. 2017-September, pp. 6221–6226.

[6]   Vaicekauskaite, J. et al. Mapping the mechanical and electrical properties of commercial silicone elastomer formulations for stretchable transducers, vol. 8, no. 4. Royal Society of Chemistry, p. 1273–1279.

[7]   Agarwal, G. et al. Stretchable Materials for Robust Soft Actuators towards Assistive Wearable Devices, Sci. Rep., 2016, vol. 6.

[8]   Kattamis, N. T. et al. Finite element analysis of blister formation in laser-induced forward transfer, J. Mater. Res., 2011, vol. 26, no. 18, pp. 2438–2449.

[9]   Yu, D. Y. W.; Spaepen, F. The yield strength of thin copper films on Kapton, J. Appl. Phys., 2004, vol. 95, no. 6, pp. 2991–2997.

[10]   Choi, W.-C. Polymer Micromachined Flexible Tactile Sensor for Three-Axial Loads Detection, Trans. Electr. Electron. Mater., 2010, vol. 11, no. 3, pp. 130–133.

[11]   MIT Material Property Database: Polyimide. [Online]. Available: http://www.mit.edu/~6.777/matprops/polyimide.htm. [Accessed: 09-Jul-2020].

[12]   Mc Gee, K. et al. Proof of Concept Novel Configurable Chipless RFID Strain Sensor, Sensors, 2021, vol. 21, no. 18, p. 6224.

Appendix B - Fabrication and Deployment Review

The aim of this overall project is to develop a passive remote sensor technology that can be printed in-situ. This is in line with the goals outlined in a recent European Space Agency (ESA) Application to Tender [1] which is focussed on Technology Readiness Level (TRL) -5 implementations of printed strain gauges, thermocouples, thermistors and RTDs. The fabrication methods of interest in this document range from screen printing to inkjet and aerosol technologies. The desired sensors in the ESA document are to be wired back to a control unit and thus the aims in that document deviate slightly from the goals of this project. This project has focussed on in-situ fabrication as being the most suitable approach and all other approaches as alternatives. The reason behind this particular focus is that the some of the known chipless RFID interrogation challenges are addressed through the use of geometric resonator variations between nearby sensors/tags.

The fabrication requirements of chipless RFID tags for operation on both metals and dielectrics includes the need to fabricate/deposit both a substrate part and conductive resonator part(s). Although the need for substrate fabrication can be avoided for sensor operation on dielectric materials, this work will include substrate fabrication as the specific substrate design and material is an integral part of virtually all of the strain sensor designs discussed in Chapter 3.

The underlying objective within the sensor design is to design it in such a way that an automated machine can fabricate and/or deploy the sensors onto the structure of interest. Before this discussion proceeds, the author would like to define the term "implementation time" as being the summation of the "fabrication time" and the "deployment time". Essentially, there are two possible avenues available through which sensor implementation can be achieved. The first approach is to fabricate the part(s) remotely and to then adhere the resulting devices to the structure of interest. It should be possible, in theory, to do so using a robotic arm, coupled with an adhesive deposition system. This approach, commonly referred to as the "lick and stick" approach has the major limitation that part variations cannot be fully supported. With that being said, the ability to (largely) fabricate the sensors prior to deployment effectively renders the implementation time to be equal to the deployment time. The second avenue consists of the "in-situ" fabrication of the part(s) using a deposition process(es) that can hopefully be attached to a robotic manipulator. This alternative approach may allow greater design flexibility, but it comes at a cost as it forces greater delays into the critical path of the fabrication and deployment process.

B.1   Substrate Fabrication

A variety of fabrication technologies were explored to assess their ability to support the fabrication/deployment requirements. Table B.1 summarises the various technologies under review.

Table B.1: Substrate Fabrication Technologies

Method	Design Variability	Fabrication Time	System Simplicity	Quality	In-Situ Performance
In-situ Moulding	Bad – Conventional moulds generally support the moulding of a fixed geometry, but other types have also been reported [2]	Moderate – The cure time of polymer materials will most likely exceed the deployment time of pre-fabricated polymer or conductive parts. Moulding is usually faster than FDM approaches [3][4]	Moderate – Depending on the flow properties of the molten material, careful sealing will be required between the superstrate and the mould. This could make automating the process difficult	Good – Material characteristics can be assumed to be consistent with other moulded parts	Moderate – Sealing between the mould and the superstrate would be a main concern here, as is the challenges posed by curved/rough superstrates
Thermal Transfer	Bad – No demonstration of configurable substrate. Height variability could be achieved through successive layers but the resultant substrate is a sandwiched system consisting of adhesive and substrate layers [5]	Good – Development and application is similar to conventional labelling equipment (t<5s) [6]. Furthermore, the ribbon is pre-coated with an acrylic layer to negate the need for post-treatment of the polyimide layer [7]	Good – Metallograph ™ printing devices have already demonstrated fast fabrication time and the use of a pre-treated ribbon negates the need for a post-treatment stage	Good – The technology supports a highly repeatable process and makes use of bulk-quality materials [7]	Good – The material rolls already come with an adhesive backing [7]
Fused Deposition	Good – Full 3D geometric	Bad – Times can be considerable	Moderate – The superstrate	Moderate – Thermal warping and	Moderate – Unknown issues may

272

Modelling (FDM)	variability is possible	but can also be easily sped up through the use of reduced infill, which reduces material usage whilst attempting to maintain mechanical stability [8][3]	may need to be heated to allow successful adhesion and to avoid part warping [8]	overall resolution issues can lead to consistent errors in the resulting substrate [5]. FDM prints usually exhibit weaker characteristics than their bulk counterparts [5]	arise as a result of an unheated or poorly heated superstrate. Most important of all of these issues is adhesion [8]
Laser/ Waterjet	Moderate – Arbitrary geometries can be cut out, but little or no options are available to allow for height variation	Good – Planar cutting using these methods is a very quick process	Moderate – Fabrication using this method is straightforward, but the challenge will arise in the deployment/ adhesion of this part onto the superstrate	Good - The technology supports a highly repeatable process and makes use of bulk-quality materials	Bad – The resulting substrate will need to be adhered in-place

B.2   Substrate Pre-/Post-processing

B.2.1   Surface Treatment

In order to facilitate further in-situ deposition or adhesion, several materials require surface treatments. The nature of the surface treatments can be quite varied but of most importance to this discussion is the issue presented by a material with low surface energy. Common materials that exhibit this behaviour include silicone rubbers and polyimides. These materials will exhibit low wettability and adhesion which will hinder the deposition and performance of a subsequent deposition. Of course, the nature of the subsequent deposition plays a role in the wettability and adhesion performance [9] but most importantly, nanomaterial-based depositions usually require polyimide and other such substrates to undergo a surface treatment operation before deposition. A common way to assess surface energy is through the use of water contact angle measurements or contact angles with other solutions. The first method involves depositing a drop of water onto a prepared surface and observing the angle made between the edge of the droplet and the surface, at the contact point (see Figure B.1). Angles below 90° are considered to be indicative of a hydrophilic surface and above 90° are

considered indicative of a hydrophobic surface [10][9]. Measures of adhesion can be carried out by monitoring the change in contact angle after droplet volume reduction (Sessile Droplet Method), or by using the tilting method [10]. The latter method involves tilting the surface until the droplet "depins" from the surface and slides away. By monitoring the contact angles just before depinning, a metric called the "Retentive Force" can then be calculated [10].
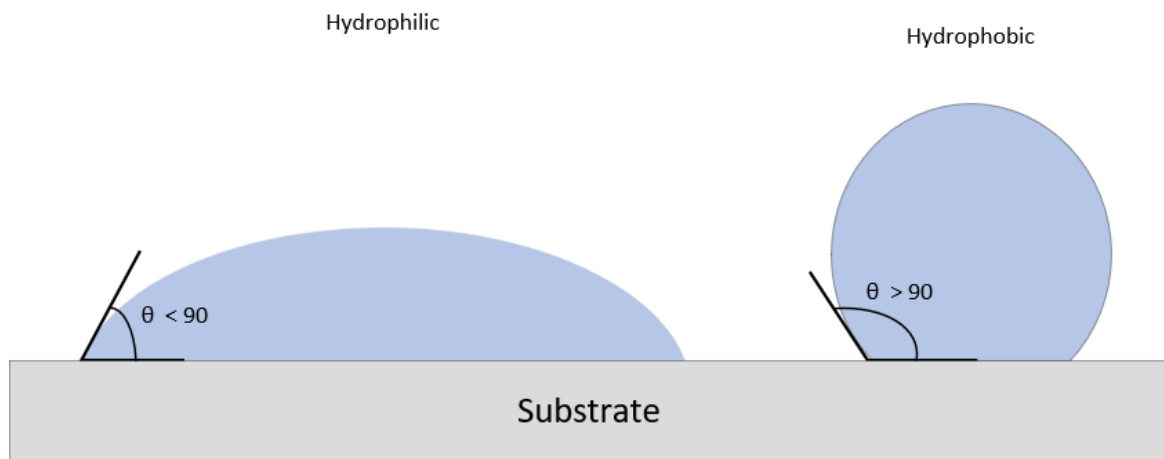
Figure B.1: Water Contact Angle Interpretation

B.2.2   Bonding

Substrate-Superstrate bonding can take place though the use of an intermediate material (an adhesive) or arises after in-situ deposition of the substrate onto the superstrate. This subsection will only consider the approach that makes use of adhesives to achieve this goal as the use of adhesives is a distinct additional step in the overall fabrication process, whereas in-situ adhesion occurs alongside material deposition. The underlying mechanics of adhesion are not well-understood [10][11] and are said to arise due to a combination of, or distinct mechanical and/or chemical phenomena. More information on the topic of adhesion mechanisms can be found in [10] and [11].

The process of bonding the substrate to the superstrate through the use of an adhesive, consists of several steps:

• Application of appropriate adhesive

• Placement of the substrate

A more in-depth study into appropriate adhesives is required but it is clear that adhesives such as epoxy resins are suitable for a wide variety of aerospace applications, as they are already used in Glass/Carbon Fiber reinforced Composites (GFRP/CFRPs) that are suitable for

those settings. Much of the sensor development performed in this work has made use of cyanoacrylate and/or unsaturated polyester resins as they are easier to work with and/or cheaper. Below is a discussion of these three adhesives and their strengths and weaknesses, i.e. cure time, environmental stability, etc. Note: Curing time is defined here as the time needed to support the assembly after gluing. Full curing of most adhesives takes hours, but the time needed to provide a stable assembly is the time that will most likely dominate the total fabrication/deployment time of the (thousands of) sensors onto the structure. Table B.2 provides a brief comparison between these adhesives and their suitability for the end application space of the strain sensors. The important point to take away from Table B.2 is that cyanoacrylate may be easier to work with, it does not boast the performance or stability provided by the more specialised adhesives [11]. Note: Drying time is defined here as the time required until the adhesive is touch dry.

Table B.2: Adhesives Comparison Table

Adhesive	Curing Details of Interest	Operating Temperature Range (Continuous)	Stability Comments
Cyanoacrylate	1-Part adhesive that cures during exposure to small amounts of moisture [11]. Rapid curing adhesive that achieves a modest level of curing in one minute	-32°C -> +65°C [12]	Becomes brittle with age [12]. It is also soluble in polar solvents [11]. Considered less robust to radiation than Epoxy and Polyester -based resins
Polyester Resin	Is on the order of hours, based on experiences of the author	-40°C -> +200°C [13]	Good chemical resistance [14]
Epoxy Resin	Is on the order of hours [11]. 1-Part epoxies can be cured in 20 mins at elevated temperatures [11]. Further details can be found in [15]	Static operation: -150°C -> +260°C [12][11] Dynamic range supported: -60°C -> 200°C [11]	Used throughout the aerospace industry

B.3   Conductor Fabrication

The next step in the sensor fabrication process is the fabrication/addition of the conductive parts. It is worth noting at this point that many chipless RFID tag/sensor implementations make use of conductor geometry variations to allow the tag/sensor responses to be unique. Therefore, the ability to support geometric variations within the conductor fabrication process is a useful feature for the finalised fabrication system to have. Table B.3 summarises the various conductor fabrication methods that could be used. Vapor deposition technologies have not been included in this table because of the complexity associated with their

use/optimisation and the need for a high vacuum may make an in-situ form of the technology, very difficult to develop. With that being said, a more thorough exploration on the potential use of this technology type will be required in a future work, particularly in light of ongoing projects such as that document in Reference [16].

Table B.3: Conductor Fabrication Technologies

Method	Design Variability	Fabrication Time	System Simplicity	Quality	In-Situ Performance
Inkjet or Aerosol [17][18] [19]	Moderate – Full in-plane geometry variability. Limited demonstrations of its ability to deposit thick layers	Moderate – Single layer should be similar to that of conventional printing	Moderate – Substrate preparation will most likely be needed	Moderate – At time of review, considerable time/ complexity is involved with achieving properties that are similar to that of the bulk material	Good – Broad range of literature on aerosol/ inkjet deposition onto various substrate materials
Electro-Discharge Machining (EDM) / Laser/ Waterjet	Bad - Arbitrary geometries can be cut out, but no/limited options are available to allow for height variation. Not viable to develop sensors with unique responses remotely	Good - Planar cutting using these methods is a very quick process	Good - Fabrication using this method is straightforward, but the challenge will arise in the deployment/ adhesion of this part onto the substrate	Good - The technology supports a highly repeatable process and makes use of bulk-quality materials	Bad - The resulting conductors will need to be adhered in-place
Thermal Transfer [6]	Moderate – Full in-situ, in-plane geometry variations possible. Limited/No conductor thickness	Good – Ribbon is already fabricated thus fabrication and deployment time is similar to that of a labelling machine	Good – No additional postprocessing steps required [7] and high-speed deployment is possible	Good – Transfer ribbon is made from bulk materials	Good – High speed fabrication [6] and deployment

	variation support [5].				
Screen/ Offset/ Gravure	Moderate – Limited/No in-plane geometry variations possible. Potential conductor thickness variation support [20].	Good – Details supplied in [21] would suggest that the conventional implementations of this technology are rapid	Moderate – A variety of steps are required for these processes, but this area of research has been extensively explored	Good – High quality conductive layers anticipated as this technology has been well-established	Bad – Miniaturizing of these technologies could be difficult and their performance is unknown
Plasmajet [22]	Good – Full variability of Aerosol with possibility of thicknesses of over 1mm boasted	Moderate – Single layer should be similar to that of conventional printing	n/a (Limited Information) – Sintering already performed within the deposition process	n/a (Limited Information) – Technology is aimed towards aerospace applications [23] and thus is assumed to be of high quality	Good - Broad range of literature on aerosol deposition onto various substrate materials. It is assumed that this result is similar for this method

B.4 Conductor Postprocessing

Additional processing steps may not be required with all of the possible fabrication methods listed above, but most of the in-situ fabricated chipless RFID tags use nanoparticle-based conductive inks, which usually require postprocessing. Other conductor fabrication approaches which fabricate the conductive elements out of bulk material will require an adhesion step to complete the sensor. Both of these steps are discussed below.

B.4.1 Bonding of Prefabricated Parts

The process of bonding conductive elements consists of several steps:

- Application of appropriate adhesive
- Placement of conductive parts

Placement of conductive parts requires either a "pick and place" robotic system or some form of automated part dispensing system. The geometry of the developed strain sensor consists of multiple conductive parts and may also require other conductive parts to allow for the sensing of interfering stimuli. The multiple parts comprising the designed strain sensor will require accurate placement as the sensitivity of the geometry to relative displacement is very high. If

this sort of method is to be considered as the final sensor fabrication strategy, the placement accuracy will most likely be the critical factor within the system design as the various capacitive regions within the design are sensitive to displacement.

B.4.2   Sintering of In-situ Deposited Inks

Sintering is performed on nanoparticle-based depositions to remove now unwanted components from the deposited patterns so that the conductive nanoparticles can coalesce and form conduction paths [18]. The temperatures involved are much lower than the melting point of the bulk conductive material due to the thermodynamic size effect [24]. Further details on the topic of sintering can be found in Reference [18].

Several strategies have been proven to be very successful to perform this task and these need to be considered to investigate how viable it is to fabricate a working sensor as conventional sintering methods are very time consuming. Table B.4 summarises the sintering methods that have been demonstrated in the printed electronics literature.

Table B.4: Sintering Methods Comparison

Method	Description	Challenges/ Limitations
Conventional Sintering	The basic sintering method involves exposing the deposited conductors to high temperatures using a furnace or oven. This approach can also include the use of a variety of inert or other such environmental conditions to enhance the process. The time required to achieve adequate sintering is usually on the order of hours [25]	This requires high ambient temperatures (350-400°C) and is done in an enclosed environment. The sintering time is quite significant
Laser Sintering	One issue with the use of conventional sintering methods is that there is a great chance that significant thermal damage can be inflicted in the substrate [26]. Laser sintering allows for more selective heat transfer to the deposition and can achieve spatial resolutions down to one cm^2. An example of a laser setup to perform sintering can be found in the work of Theodorakos et al. in Reference [27]. The time required to perform this sintering approach is significantly less than conventional sintering methods	Can cause localised extreme heating and thus possible damage to the substrate
Intense Pulsed Light (IPL) -based	Intense Pulsed Light (IPL) sintering uses a Xenon lamp with emission between UV and IR regions of the spectrum. The light is pulsed with a duration shorter than the thermal equilibrium time of the nanoparticle(s) to ensure that the nanoparticles begin to coalescence. Sintering times are lower than those achieved with laser sintering	One issue with the use of this sintering approach is that given the inverse square law power loss, the degree of sintering varies throughout the depth of the deposition [25]. Another issue with this approach is that although it is quite fast [25][28], cracking of the conductor is more likely to occur than if other sintering methods were used
Reactive Sintering	Several works have made use of reactive sintering techniques where an additional agent is deposited to promote the increase of deposition conductivity. A recent example of this can be found in the work of Wang et al. in Reference [29]	Subsequent heat treatment was used in some of the known implementations. Some works [30] used reaction times of 15-60 minutes
Ohmic Sintering	The electrical sintering method works by sending currents through the depositions until the current flow is maximized. An Example implementation of this approach can	Some publications suggest that this sintering approach can lead to distinct regions within the conductor where sintering was unsuccessful [25]. Another issue

	be found in the work of Allen et al. in Reference [31]. Sintering times in the referenced work were in the order of microseconds.	with this approach is that in many cases there will be a need for a pre-sintering step such as an initial heating step to allow for initial conductive paths to form [25]. If this initial step is not performed, the final conductivity after sintering is said to be a function of the degree to which pre-sintering was not performed

B.5   References

[1]   ESA ESA Open Invitation To Tender [FR] AO8922 - DIRECT PRINTING OF MECHANICAL AND THERMAL SENSORS ONTO SPACECRAFT HARDWARE, 2017. [Online]. Available: http://emits.sso.esa.int/emits/owa/emits_online.showao?typ1=7345&user=Anonymous. [Accessed: 10-Oct-2017].

[2]   Kirby, A.; Stauffer, L. A. Analysis of pin characteristics for a variable geometry mold, Int. J. Adv. Manuf. Technol. 2006 327, 2006, vol. 32, no. 7, pp. 698–704.

[3]   Oelsch, E. et al. Comparative investigation on the mechanical behavior of injection molded and 3D-printed thermoplastic polyurethane, J. Rubber Res. 2021 242, 2021, vol. 24, no. 2, pp. 249–256.

[4]   Khan, W. Comparison on Performance of Injection Moulding and 3D Printed Parts, Edinburgh Napier University, Edinburgh, 2020.

[5]   Wickramasinghe, S. et al. FDM-Based 3D Printing of Polymer and Associated Composite: A Review on Mechanical Properties, Defects and Treatments, Polymers (Basel)., 2020, vol. 12, no. 7, pp. 1–42.

[6]   Metallograph® Printed Electronics - SPF Inc - Specialty Papers & Films. [Online]. Available: https://spf-inc.com/metallograph. [Accessed: 04-Mar-2022].

[7]   Polyonics® Polyonics XF-552 POLYIMIDE LABEL, 2019. [Online]. Available: https://polyonics.com/TDs/XF-552.pdf. [Accessed: 27-May-2022].

[8]   Horvath, J. Mastering 3D Printing, 1st ed. Berkley: Apress, 2014.

[9]   Rios, P. F. et al. The effect of polymer surface on the wetting and adhesion of liquid systems, http://dx.doi.org/10.1163/156856107780684567, 2012, vol. 21, no. 3–4, pp. 227–241.

[10]   Mittal, K. L. Progress in Adhesion and Adhesives, Volume 2. Wiley, 2017.

[11]   Ebnesajjad, S.; Landrock, A. H. Adhesives technology handbook, 3rd Edtn. Elsevier, 2015.

[12]   Murray, W. M.; Miller, W. R. The bonded electrical resistance strain gauge: An introduction, 1st Edtn. New York: Oxford University Press, 1992.

[13]   Fetouhi, L. et al. Mechanical, dielectric, and physicochemical properties of impregnating resin based on unsaturated polyesterimides, Eur. Phys. J. Appl. Phys., 2017, vol. 80, no. 1, p. 10901.

[14]   Mastro, P. F. Overview of Plastics Materials, in Plastics Product Design, Wiley, 2016, pp. 31–64.

[15]   Ellis, B. Chemistry and Technology of Epoxy Resins, 1st Edtn. Dordrecht: Springer
        Netherlands, 1993.

[16]   NASA TechPort - Laser-Directed CVD 3D Printing System Refractory Metal Propulsion
        Hardware. [Online]. Available: https://techport.nasa.gov/view/33864. [Accessed: 02-
        Sep-2022].

[17]   Larimore, Z. J. Multi-material Additive Manufacture of RadioFrequency Devices and
        Systems, University of Delaware, 2019.

[18]   Beedasy, V.; Smith, P. J. Printed electronics as prepared by inkjet printing, Materials,
        vol. 13, no. 3. MDPI AG, 01-Feb-2020.

[19]   Cui, Z.; Al, E. Printed Electronics: Materials, Technologies and Applications. Wiley,
        2016.

[20]   Leppävuori, S. et al. A novel thick-film technique, gravure offset printing, for the
        realization of fine-line sensor structures, Sensors Actuators A Phys., 1994, vol. 42, no.
        1–3, pp. 593–596.

[21]   Wiklund, J. et al. A Review on Printed Electronics: Fabrication Methods, Inks,
        Substrates, Applications and Environmental Impacts, J. Manuf. Mater. Process. 2021,
        Vol. 5, Page 89, 2021, vol. 5, no. 3, p. 89.

[22]   Gandhiraman, R. P. et al. Plasma jet printing of electronic materials on flexible and
        nonconformal objects, ACS Appl. Mater. Interfaces, 2014, vol. 6, no. 23, pp. 20860–
        20867.

[23]   Space Foundry. [Online]. Available: http://www.spacefoundry.us/about.html.
        [Accessed: 23-Sep-2022].

[24]   Garrigos, R. et al. Melting for lead particles of very small sizes; influence of surface
        phenomena, Small Part. Inorg. Clust., 1989, pp. 497–500.

[25]   Roshanghias, A. et al. Sintering strategies for inkjet printed metallic traces in 3D
        printed electronics, Flex. Print. Electron., 2017, vol. 2, no. 4.

[26]   Wang, X. et al. Electrical and Mechanical Properties of Ink Printed Composite
        Electrodes on Plastic Substrates, Appl. Sci., 2018, vol. 8, no. 11, p. 2101.

[27]   Theodorakos, I. et al. Selective laser sintering of Ag nanoparticles ink for applications
        in flexible electronics, in Applied Surface Science, 2015, vol. 336, pp. 157–162.

[28]   Niittynen, J. et al. Comparison of laser and intense pulsed light sintering (IPL) for
        inkjet-printed copper nanoparticle layers, Sci. Rep., 2015, vol. 5, no. 1, pp. 1–10.

[29]   Wang, Y. et al. Reactive Conductive Ink Capable of In Situ and Rapid Synthesis of -
        Conductive Patterns Suitable for Inkjet Printing, MDPI Mol., 2019, vol. 24, no. 3458.

[30]   Kheawhom, S.; Foithong, K. Comparison of reactive inkjet printing and reactive
        sintering to fabricate metal conductive patterns, Jpn. J. Appl. Phys., 2013, vol. 52, no.
        5 PART 2, p. 05DB14.

[31]   Allen, M. L. et al. Electrical Sintering of Nanoparticle Structures, Nanotechnology,
        2008, vol. 19, no. 17.

Appendix C - Thermal Expansion Mitigation Techniques

This appendix discusses the different design approaches taken to mitigate the deformation of the resonator caused by thermal swelling of the sensor's constituent materials. Issues can arise in the operation of a device, over a large temperature range, due to thermal expansion. Regarding the strain sensor outlined in this work, it needs to be assessed if thermal expansion leads to several unwanted outcomes, including:

- Deformation sufficient to alter the measured strain levels

This analysis can be performed in many ways but a simple way to do so is through the use of Finite Element Method (FEM) software. Alternative methods include physical testing, which would involve the use of sensor interrogation and High Definition (HD) photography. This alternative method requires measurement inside a region with a tightly controlled temperature and challenges may arise with thermal sensitivities of test equipment. Furthermore, resource limitations may result in the analysis being only indicative of the straightforward fabrication approaches used to develop the Device Under Test (DUT).

The first aspect of this work is to assess the thermal deformation of the sensor design. Ansys Mechanical 2019R2 was once again used to perform this analysis and the analysis is constrained to steady-state thermal modelling of the system. This approach was taken as it is the simplest approach to modelling the behaviour of the sensor. The thermal loading applied to the geometric model is quite simplistic and does not include thermal gradients of any kind across the model. Instead, each part in the model was defined as having the same internal temperature and the generated results thus describe the response of the device under idealised thermal loading. This idealised loading consists of the temperature being a constant everywhere in the device and the calculated deformation levels have reached a steady-state value. No Electromagnetic (EM) modelling was performed in this section as this issue was originally considered to be a purely geometric one and there were concerns that using only the single datapoint EM results to drive the design revisions may be risky as the design process would become more opaque.

Structural loading of the model consisted of both fixed and frictionless constraints representing the behaviour of the superstrate surface. The fixed loading strategy allows for the investigation of the thermal warpage of the sensor, assuming that the superstrate has not being strained either mechanically or thermally. This type of investigation is important as it represents the situation where the superstrate has not been deformed, thus in an ideal case,

no deformation should take place in the sensor. There are also some other assumptions in this analysis that are worth noting:

- The use of this constraint assumes that the stiffness of the substrate is much lower than the superstrate, thus no deformation is induced in the superstrate due to sensor deformation. The lack of induced deformation in the superstrate will result in greater levels of stress and strain in the sensor model

- This constraint ignores thermally induced deformation in the superstrate either by design or due to the superstrate having an assumed thermal expansion coefficient significantly smaller than that of the substrate. The reasoning behind such an assumption is that thermally induced strains should be considered to be valid, in that they should result in the appropriate deformation of the sensor

- Thermal Expansion of Aerosol printed conductive traces has been experimentally analysed in [1] by Aga et al. and although such deformation was due to an electrically induced thermal effect, permanent deformation was experienced by the conductor. This effect and the resulting internal void formation is not observed in vacuum evaporated silver depositions [1]. The importance of this finding is that it highlights that differing thermal behaviour may be present under the use of different fabrication methodologies

The alternative constraint which allows for frictionless movement of the sensor is used to merely investigate the behaviour of the sensor structure under unconstrained thermal expansion. Further information of interest to this conversation is that all material parameters are assumed to be constant across the temperature range and the chosen substrate material is Kapton polyimide. This material was chosen as it has been earmarked as the final substrate material. Several key effects have been removed from this analysis including all forms of material anisotropy and the conductive material chosen is cast copper, as opposed to a material more closely related to that deposited in-situ using printing processes. Also of note is the fact that the conductor: substrate bonds are assumed to be sufficiently strong to ensure total adherence during all simulation tests. There are some challenges in procuring in-situ related material models to use in this analysis, as several unaccounted effects cannot be easily characterised. These effects include the following:

- The Coefficient of Thermal Expansion (CTE) of many common conductive materials is already known but it is unclear how valid this is in characterising generically deposited

conductors. The reason for this is due to the fact that sintering has a large effect on the final constituents of the deposited layer and its porosity [2]

- The effects of the CTE mismatch between the conductor and substrate materials can often result in wrinkling, cracking and internal stresses arising in the conductors during sintering [2][3].

Although limitations exist on the utility of this thermal analysis, it does however highlight some of the issues that are experienced by a sensor design of this type, when exposed to temperature extremes. The relevant material properties are documented in Table C.1 below. Note: The choice of conductor used in this analysis is somewhat arbitrary as the thermal conductivity is irrelevant in this analysis and thermal expansion coefficient of other conductive materials, such as silver is of a similar magnitude [2] compared to that of the polyimide. Further of interest to this discussion is the temperature range used to assess the behaviour of the sensor. Upper temperature limits of 350°C and lower temperature limits of -100°C were used. A linear elastic material model has been used to model the polyimide material as this model allows for timely solving of the simulations and this model can be seen to be a relevant depiction of the behaviour of this material under low levels of loading [4][5].

Table C.1: Thermo-mechanical Material Properties – from "Proof of Concept Novel Configurable Chipless RFID Strain Sensor" by McGee et al., MDPI, *CC BY 4.0* [6]

Material	Young's Modulus	Poisson's Ratio	Coefficient of Thermal Expansion	Thermal Conductivity
Kapton Polyimide [7][8]	2.5GPa	0.34	0.0001 C^{-1}	0.12 $Wm^{-1}C^{-1}$
Copper	125GPa	0.345	0.0000168 C^{-1}	385 $Wm^{-1}C^{-1}$

The deformation of the sensor has been recorded at several key points in the structure (see Figure C.1), as a means of assessing how the electrical properties of the device would correspondingly change. The selection of these points on the resonator were constrained to the top surface, as it is assumed that due to the skin effect, this region of the resonator would hold the greatest influence on the sensor performance. Initial testing of the sensor with a frictionless support and axial loading has already been presented in the preceding sections. As the levels of thermally induced deformation were of the same magnitude as those found in the axial deformation simulations, the converged mesh from the previous simulations was used as the mesh on which to perform the thermal analysis. Further mesh refinements were performed at higher levels of mesh resolution, of similar design of those found in the plateau region of the axial deformation convergence curve. Since the variations in deformation had a

285

mean value of below 0.2% and a standard deviation of just over 0.6%, it was concluded that the chosen mesh had indeed achieved convergence.
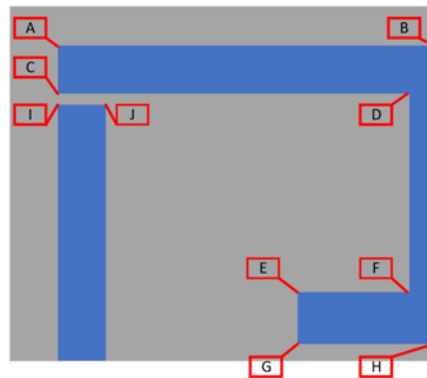
Figure C.1: FEA Model Position Labelling Diagram – from "Proof of Concept Novel Configurable Chipless RFID Strain Sensor" by McGee et al., MDPI, CC BY 4.0 [6]

C.1 Mitigation Attempt #1: Guard Ring on Top Surface

From the preceding section, it is clear that thermal deformation is an issue that needs to be addressed and that such a task could be extremely difficult. Although it has been mentioned that simplistic methods that may act to restrict thermal deformation of the sensor may inherently reduce the functionality of the sensor, simplistic methods are worth investigating, nonetheless. The reasoning behind this was that if the key features of working, simplistic designs could be extracted, a better design could be developed that would not hinder sensor operation to the same degree. These simplistic methods consist of the use of guard rings of various designs, designed to constrain various part(s) of the substrate's deformation. Cross sectional views of the various guard ring designs can be seen in Figure C.2(a) and Figure C.2(b) below. For clarity's sake, it must be mentioned at this point that these rings surround the entire resonator and were modelled as being made of copper, as it was assumed that such rings would be deposited in-situ during deposition of the resonator parts. Furthermore, the distance between the resonator and guard rings was fixed at 3.1mm and the thickness of the substrate was 1mm.

Figure C.2: Example Guard Ring Designs

The first attempt at constraining thermal deformation of the sensor involved the addition of a planar guard ring on the top surface of the substrate. Since earlier analysis revealed that the majority of the resonator deformation could be attributed to substrate expansion, it was hoped that constraining the top surface of the substrate would help to mitigate resonator motion in the axial and transverse directions. Although such a successful design may promote vertical expansion of the sensor, it was hoped that given the large aspect ratio of the substrate, that this trade-off would be for the greater good. Such an assumption was made at this point so as to allow for some basic attempts at thermal deformation mitigation.

To evaluate the performance of the guard ring addition, the deformation results have been compared against that of the sensor without the guard ring. Furthermore, the second iteration of the design (V2) includes a ring which is partially suspended above the idealised superstrate. This design feature is present as although the real-life design would have a thin substrate extension to support the ring, such an inclusion in the simulation model forces meshing complexities in the design and thus this feature was removed.

The initial simulation test procedure for these sensor assemblies used a fixed support on the bottom surface of the substrate and used a temperature of 350°C as the body temperature of each part of the assembly. Table C.2 reveals the reduction levels of deformation achieved by the inclusion of ring designs V1 and V2 respectively. Note: The values are given as a percentage of the original deformation level and negative values indicate a worsening of the measured deformation levels.

Table C.2: Reduction in Deformation Caused by Guard Rings

Position	Design V1		Design V2	
	Transverse (%)	Axial (%)	Transverse (%)	Axial (%)
A	-0.9044	2.51	-2.445	-10.8849
B	n/a	-0.6225	n/a	-9.732
C	-0.5935	-6.998	-0.386	38.205
D	-1.777	-1.302	-1.217	-32.516
E	-0.4462	0.7148	-0.8414	0.1759
F	0.073	-1.082	-0.1844	12.22
G	-0.5886	-0.4736	0.2579	-0.5576
H	n/a	-0.3541	n/a	2.183
I	16.344	-0.9889	0.3758	-1.156
J	-138.511	-0.4397	0.8009	-0.1319

From Table C.2, it can be seen that the results from these ring designs are combination of both improvements and impairments of the sensor behaviour. Overall conclusions on the results are that the current guard ring designs do not significantly mitigate against thermal

deformation. If anything, their inclusion supports further axial deformation in the resonator along the lines of ¼ symmetry as this region is where the ring bulges under thermal loading. Further work could be performed to assess the reduction in strain sensitivity caused by the inclusion of the guard ring elements; however, this was left out as it bares little relevance to the current goals As discussed in earlier sections of this document, the superstrate is neglected from the model and axial loads are applied directly onto the substrate. Therefore, the inclusion of a guard ring may result in an overemphasis of the strain sensitivity loss caused by its inclusion. It does stand to reason however that a sensor whose operation relies on deformation of the top surface of the substrate will inherently suffer if further parts are added to its assembly that actively act to mitigate deformation of said top surface.

C.2   Mitigation Attempt #2: Symmetric Substrate Design

Additional exploration of the deformation behaviour of simplistic geometries suggests that the thermally induced motion of the conductive parts of the sensor could be mitigated if the substrate was modified such that these low-deformation bands exist under all of the conductive parts. More general implementations of this idea include that depicted in Figure C.3 below. In this Figure, the neutral line describes the plane in the model in which no net deformation is experienced. In such a scenario, the top part of the assembly will not exhibit lateral rigid body motion as the symmetry of the geometry inherently stops this occurring. Furthermore, in designs that have differing values of X_1 and X_2, net motion will occur as the assembly is heated up. One issue with using this approach is that it will inevitably lead to the difference in coefficients of thermal expansion of the two parts becoming a more present contributor to the magnitudes of the required conductor:substrate bond strength.
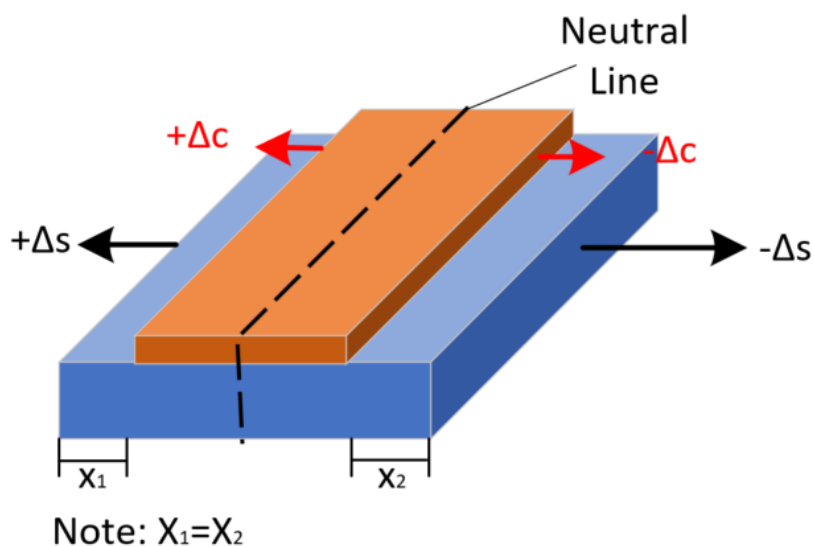

Figure C.3: Symmetry Properties of Deforming Objects

Based on the results presented in above, it would appear that the inclusion of greater degrees of substrate symmetry around the conductor: substrate bonding regions would help reduce resonator deformation significantly. With this idea in mind, the substrate design depicted in Figure C.4 was developed. In this Figure, there are two symmetry regions (not planes) that are there to target the following goals;

- The symmetry region (EL Part) is added such that the I,J positions do not significantly deform significantly in the transverse direction
- The EC symmetry region has been designed to allow the A,B,C,D positions deform in equal and opposite magnitudes such that the net motion of the top half of this part
- Also included in this EC symmetry region is the part of the substrate that does not support the resonator. This has been added to help mitigate the unequal E,F deformation and help to generally mitigate net resonator motion

Figure C.4: Symmetry-Inspired Substrate Design – from "Proof of Concept Novel Configurable Chipless RFID Strain Sensor" by McGee et al., MDPI, CC BY 4.0 [6]

The deformation experienced by the same 350°C thermal stimulus was analysed, and the results are depicted in Figure C.5 and Figure C.6. The results are compared in these Figures to

the original sensor and although certain positions (A,C,E,H) have had improvements on their thermal behaviour, other positions(B,D,F,G) have behaved more poorly.
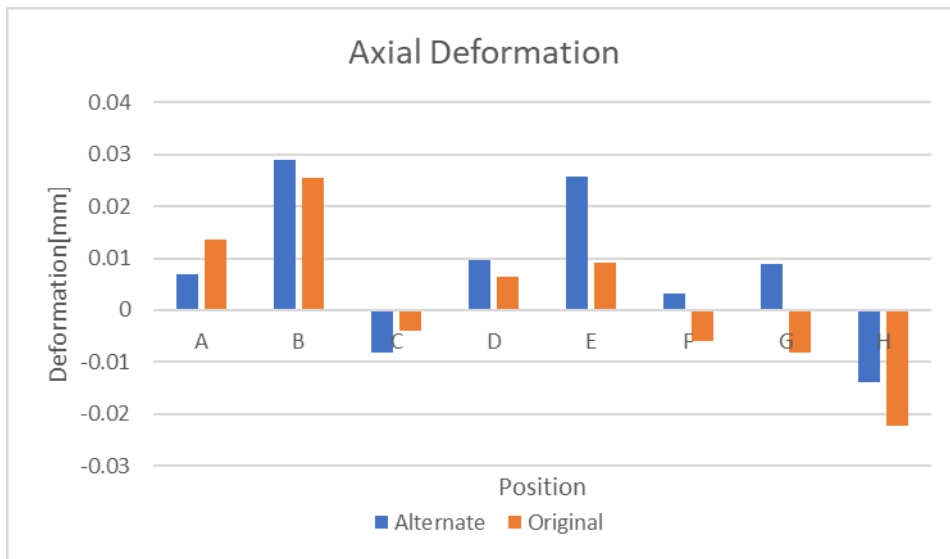
Figure C.5: Axial Deformation of Modified Sensor – from "Proof of Concept Novel Configurable Chipless RFID Strain Sensor" by McGee et al., MDPI, CC BY 4.0 [6]
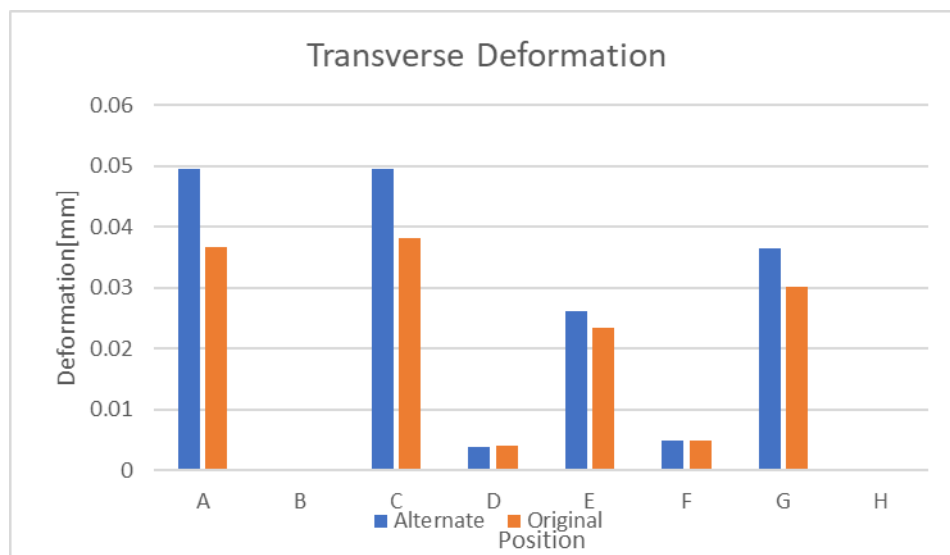
Figure C.6: Transverse Deformation of Modified Sensor – from "Proof of Concept Novel Configurable Chipless RFID Strain Sensor" by McGee et al., MDPI, CC BY 4.0 [6]

To understand the thermal stability of this substrate design, the sensor was tested at various temperatures between 0°C(Ambient) and 350°C. The results of this analysis are shown in Figure C.7 and it can be seen that by comparing these results to the original results in Chapter 6, it can be seen that the deformation of some of the positions have been reduced, not only at 350°C but also throughout the temperature range. Another interesting feature in Figure C.7 is

that the deformation remains comparatively stable below 25°C, which is a feature not seen in the thermal response of the original design.
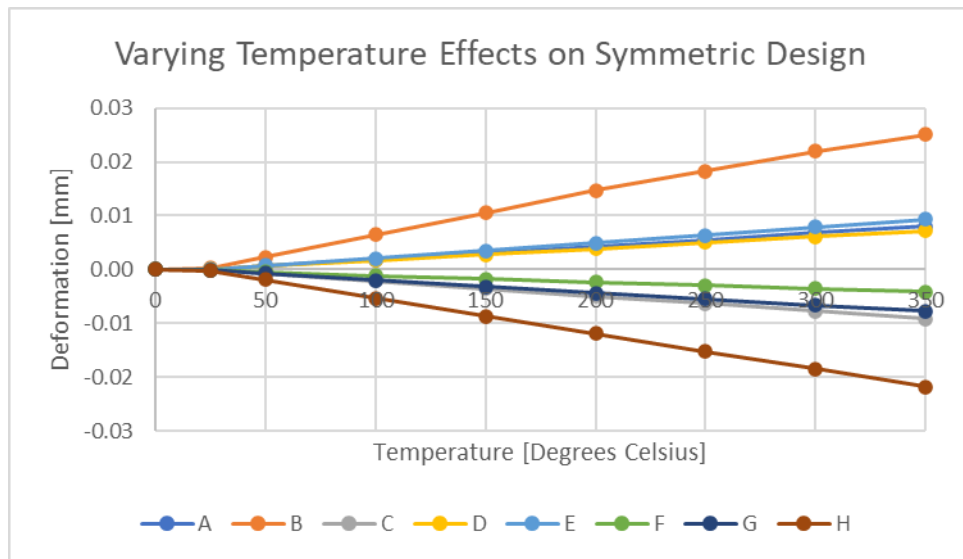
Figure C.7: Deformation of Modified Sensor wrt. Temperature

The attempts made in this subsection to mitigate thermal deformation have shown promise but there is inevitable thermally induced deformation and rigid body motion of the resonator, as interpreted from the results in Figure C.5 and Figure C.6 above. Therefore, the use of purely symmetrical substrate characteristics would appear to not be capable of reducing thermal deformation. Although some reduction in deformation was achieved, the resulting deformation at 350°C was of the same magnitude as that of the original design.

C.3   Mitigation Attempt #3: Iterative Substrate Design

Analysing the known deformation of the sensor discussed earlier, it can be concluded that the positions on the central part are overall, deforming more than in the original design. Also, there appears to be thermally induced bending in the central capacitance of the sensor which should also be mitigated. Figure C.8 gives a diagrammatic description of the suggested sensor design which includes various tuneable parameters (A,B,C, α) that can be used to achieve the desired change in resonator deformation.
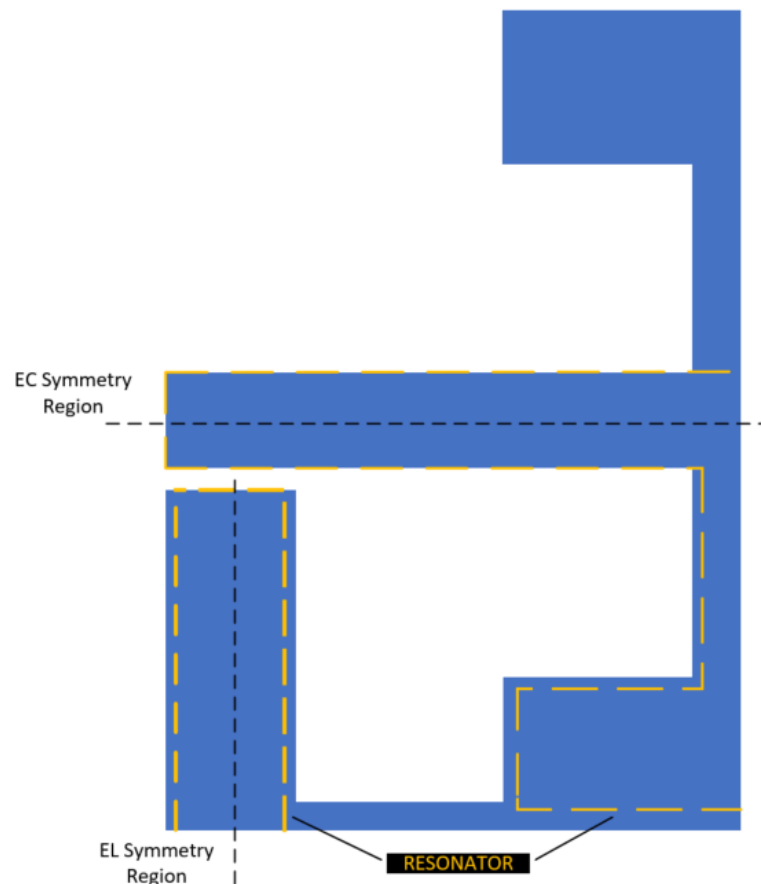
Figure C.8: Alternate Substrate Design Approach – from "Proof of Concept Novel Configurable Chipless RFID Strain Sensor" by McGee et al., MDPI, <u>CC BY 4.0</u> [6]

Initial testing of a modified substrate with arbitrarily chosen tuneable parameters resulted in modest levels of success in altering the deformation of the sensor. These results included a complete reversal of the deformation behaviour of position "A" and significant reductions in other measured deformation levels. Unfortunately, several positions experienced significant increases in deformation levels. These results can be seen in Table C.3.
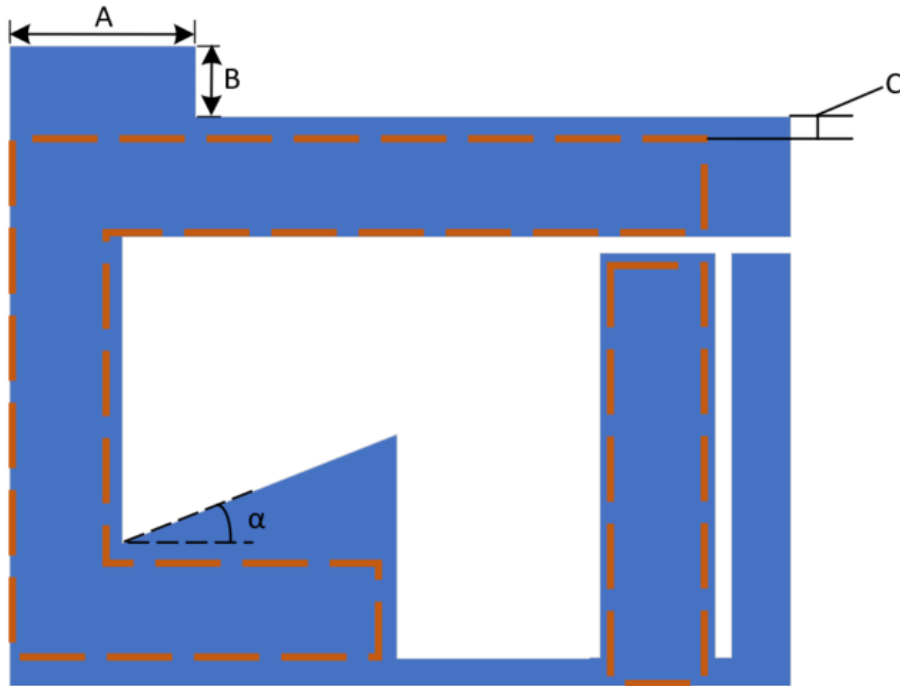
Table C.3: Sensor Deformation Level Changes [%] with Alternate Substrate Design

	A[%]	B[%]	C[%]	D[%]	E[%]	F[%]	G[%]	H[%]	I[%]	J[%]
Axial	186.24	18.54	-600	53.39	-2.85	-17.22	3.214	-3.688	-35.97	-23.7
Trans.	-6.09	n/a	-7.64	4.847	0.582	0.284	-1.369	n/a	49.27	-385.5

Although the results presented in Table C.3 reveal that the deformation of certain regions of the sensor are mutually dependent on eachother. This issue arises from characteristics of the geometry and from CTE mismatches between the conductive and substrate parts. Given the fact that the electrical sensitivity of this device is predominantly dependent on the capacitive regions, further steps were taken to tune the various dimensions outlined in Figure C.8 to force the resonator to keep those dimensions constant. The results of this tuning procedure that focused on reducing the deformation of position "C" and thermal loading at 350°C

resulted in a deformation of $-1.677x10^{-5}$mm at this position, instead of the magnitude of $3.81x10^{-2}$mm found in testing with the original substrate design. This is a significant reduction in deformation of this position, which would suggest that at least some of the resonator positions can be held at a constant position, regardless of the sensor temperature. To investigate this further, the modified substrate design was tested at various temperature levels. It was assumed that since the levels of deformation at temperatures of lower than 350°C would result in lower average levels of deformation and thus the current mesh was assumed to be converged for these lower temperature levels. The results of this thermal analysis can be seen here in Figure C.9. Of most interest here is the nonlinear variation in deformation between 0°C and 350°C and that it does not remain at zero but the maximum deformation had a magnitude of $3x10^{-4}$mm. Further analysis of these results also showed that the thermally induced bending in the central capacitor was also reduced by this substrate design.
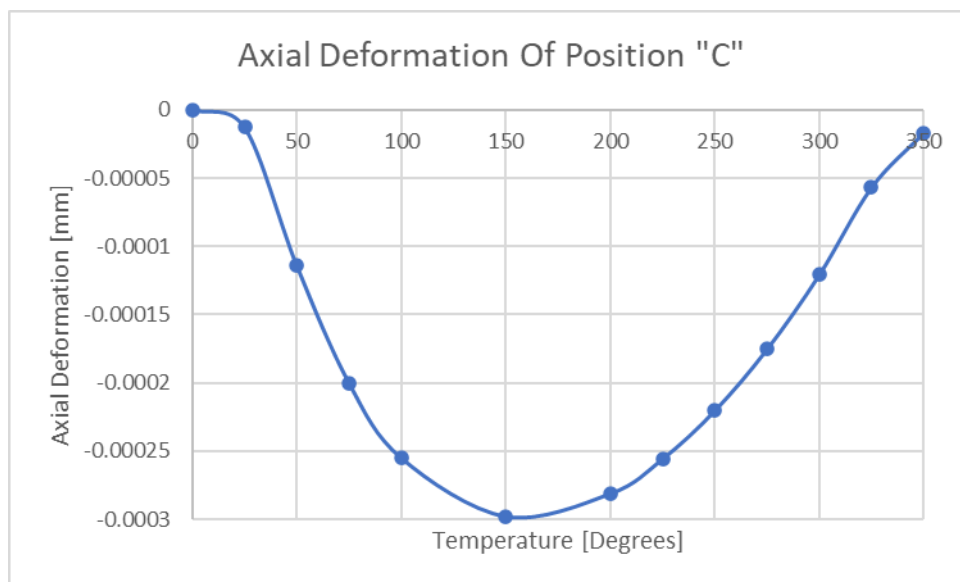
Figure C.9: Temperature Stability of Tuned Substrate Design

C.4   Concluding Remarks on Thermal Expansion

Up until this point, the thermally induced deformation in the conductive elements has been largely overlooked in the sensor design process. Although such deformation is significant, it stands to reason that this deformation cannot be as easily constrained or mitigated against. This postulation was put forward based on the following observations:

1. These parts are very small (slender) and cannot be overly modified to the degree that the substrate part can be, as there simply is not the same amount of room within the

      boundaries of the parts that can be removed/modified such that specific deformation

      behaviour can occur

2. The overall geometry of these parts is critical for sensor interrogation and thus there

      is not the same flexibility to arbitrarily modify the outline of these parts

3. Pocketing or other operations carried out on the internal region of these parts may

      heavily mitigate conductor:substrate bonding strength or promote other issues

      relating to buckling or mechanical fatigue of these parts

The question now turns to; how could the thermal deformation of the sensor be mitigated against? It seems evident that changes in conductor geometry is inevitable, but the strain sensitivity of this device is mostly dependent on the major capacitive features of the tag. In theory, the capacitances could be controlled in such a way that transverse and axial changes in the geometry would result in zero net change in capacitance. This may be possible, given the geometric dependence of a parallel plate capacitor and the additional fringe field. Equation C.1, found in [9], describes the idealised relationship between capacitance (C), transverse dimension (x) and axial dimension (d) for an idealised parallel plate capacitor configuration with a plate of length (l), width (w) and separation (d). With an unaltered substrate design, the expansion in the two directions will undoubtably be related to a variety of parameters including the aspect ratio of the observed part. It would seem to be a huge undertaking to follow such a line of enquiry and would appear to require a significant deal of automated simulations and iterative geometric alterations that would also need to be automated.

$$C = \varepsilon_0 \varepsilon_r \left(\frac{l.w}{d}\right) + \varepsilon_0 \varepsilon_r \left(\left(\frac{w}{2\pi}\right) ln \left(\frac{2\pi l}{d}\right)\right) \hspace{2cm} \text{(C.1)}$$

Although this discussion on the thermal behaviour of the sensor is based on a multitude of idealised assumptions, it does however outline that even with such ideal materials and general system behaviour that thermally induced deformation of the sensor cannot be easily mitigated against. Therefore, the conclusion of this thermal modelling section is that a second sensor is needed to sense the ambient temperature of the strain gauge. It was hoped that this would not be the case as this brings up further issues regarding secondary sensor location as spatial temperature gradients of various sorts may arise in real-life settings. Furthermore, this conclusion complicates the lookup needed to convert the measured resonant frequency to an equivalent level of axial strain. Testing of the finalised strain sensor will thus also need to be rigorously performed with both ambient temperature and strain level as independent variables.

C.5   References

[1]   Aga, R. S. et al. In situ study of current-induced thermal expansion in printed conductors using stylus profilometry, Flex. Print. Electron., 2016, vol. 1, no. 1, p. 012001.

[2]   Lee, D. J.; Oh, J. H. Inkjet printing of conductive Ag lines and their electrical and mechanical characterization, Thin Solid Films, 2010, vol. 518, no. 22, pp. 6352–6356.

[3]   Mikkonen, R. et al. Inkjet Printable Polydimethylsiloxane for All-Inkjet-Printed Multilayered Soft Electrical Applications, ACS Appl. Mater. Interfaces, 2020, vol. 12, no. 10, pp. 11990–11997.

[4]   Qu, C. et al. Morphology and Mechanical Properties of Polyimide Films: The Effects of UV Irradiation on Microscale Surface, Materials (Basel)., 2017, vol. 10, no. 11.

[5]   Chang, W. Y. et al. Physical characteristics of polyimide films for flexible sensors, Appl. Phys. A 2008 923, 2008, vol. 92, no. 3, pp. 693–701.

[6]   Mc Gee, K. et al. Proof of Concept Novel Configurable Chipless RFID Strain Sensor, Sensors, 2021, vol. 21, no. 18, p. 6224.

[7]   Polyimide films | DuPont. [Online]. Available: https://www.dupont.com/electronic-materials/polyimide-films.html/general/H-38479-4.pdf. [Accessed: 28-Jul-2021].

[8]   Elsner, G. et al. Anisotropy of thermal expansion of thin polyimide films, Thin Solid Films, 1990, vol. 185, no. 1, pp. 189–197.

[9]   Chen, X. et al. Fringing Effect Analysis of Parallel Plate Capacitors for Capacitive Power Transfer Application, 2019 IEEE 4th Int. Futur. Energy Electron. Conf. IFEEC 2019, 2019.

Appendix D - IEEE Content Permission Reuse Form

Appendix E - Thermistor Temperature Sensors for Chipless RFID Integration

This appendix briefly discusses the challenge of thermistor integration into chipless RFID sensor design. This work has been performed in other chipless RFID sensor designs such as those found in [1]. In-situ fabrication of thermistors has been performed in numerous works including [2] and [3], the latter of which has also been replicated as part of this work. One key point to be made here is that the thermistor construction and connection design will probably be of considerable importance and will impact the sensor response.

E.1 Thermistor Integration in RFID Tag

A cheap 10kΩ thermistor (RS:210-4374 [4]) was soldered into the λ/4 Stepped Impedance Resonator (SIR) circuit used in the testing seen in the Chapter 4. This approach was inspired by the work of Amin et al. in [5] which performed the same implementation but with a Light Dependent Resistor (LDR). Direct temperature testing of the device resulted in the response curves seen in Figure E.1. This figure clearly shows that both a considerable amplitude and frequency variation occurs with variations in temperature. Note: These tests were performed by applying a hot airflow to the back surface of the sensor, as opposed to the top surface where the thermistor is found.
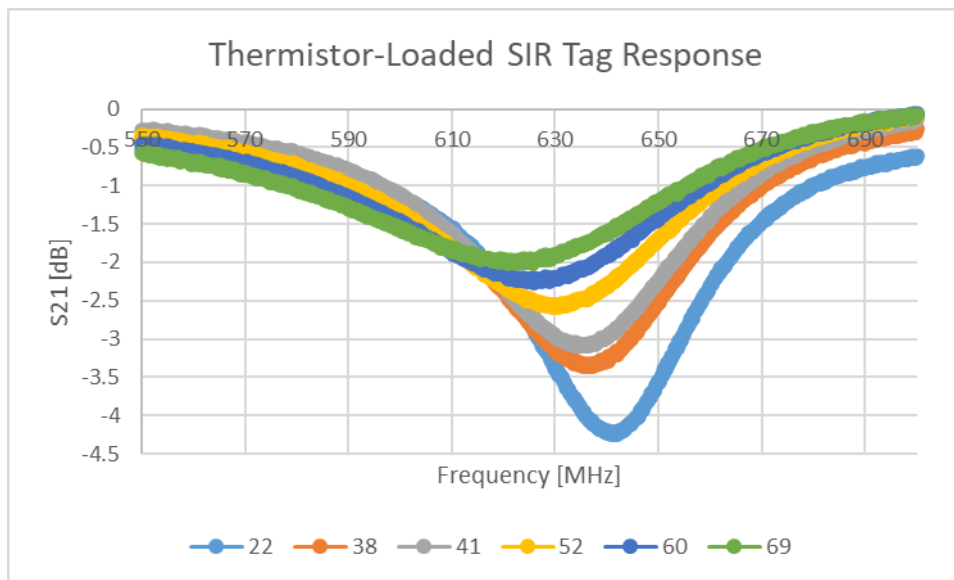
Figure E.1: Scattering Response of Thermistor Loaded SIR Circuit

The null frequency sensitivity of this resulting sensor is plotted against temperature in Figure E.2. Repeated test results documented in Table E.1 clearly demonstrate a temperature sensitivity of approximately 0.38MHz/°C. This sensitivity is higher than that found with the

non-loaded tag (≈0.26MHz/°C) and the works seen in [6][7][8] demonstrate that Negative Temperature Coefficient (NTC) thermistors do indeed exhibit both real and imaginary parts of their impedances that are temperature sensitive. A key point to be made here is that given the nature of the package of the thermistor and the way in which it is attached to the SIR, it is expected that the overall sensor will perform differently, depending on the direction of heating.
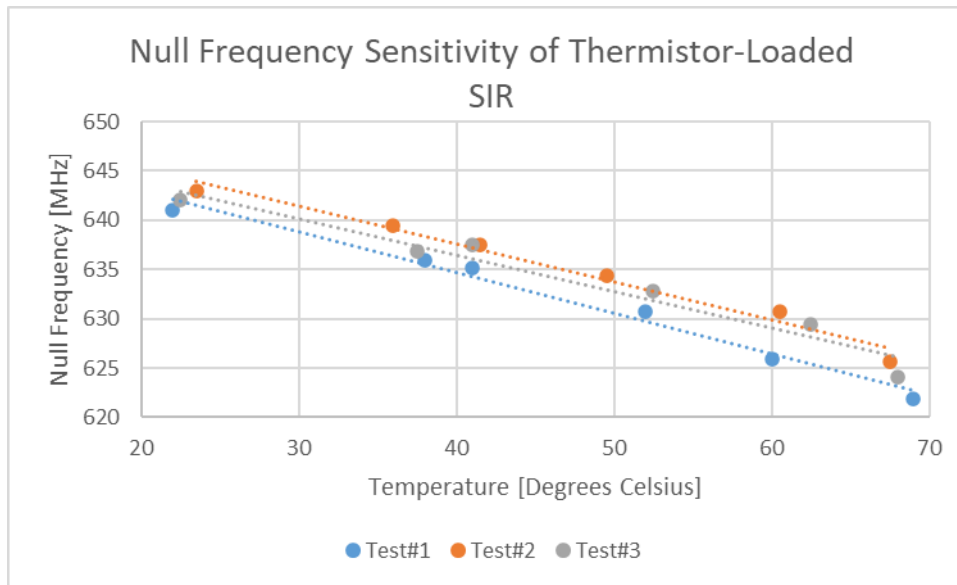
Figure E.2: Null Frequency Sensitivity Curve for Thermistor Loaded SIR Circuit

Table E.1: Sensitivity Trendline Results Obtained with Thermistor-Loaded SIR

Test	Sensitivity [MHz/°C]	R-Squared Value
1	-0.4131	0.9836
2	-0.3829	0.9780
3	-0.3699	0.9512

Simplistic AC impedance spectroscopy was performed using a Vector Network Analyser on these thermistors from 500-3000MHz. Testing was performed with both 1-port and 2-port test configurations [9] and all of the results demonstrated that the reactance changed with ambient temperature, but its effect was largest at 500MHz and less noticeable with increasing frequency. These results tie in with those found in [6][7][8] which at lower frequencies have identified the same trend. This would suggest that the use of conventional thermistors in chipless RFID sensor designs will limit their behaviour to amplitude modulation if the final sensor system is to operate high up in the microwave range.

298

Further study is required on the topic of the impedance response of these devices in the Ultrahigh-Frequency/Microwave range and their material dependencies, but their use will not be further explored as part of this work, given their fabrication complexities.

E.2 References

[1]   Girbau, D. et al. Passive wireless temperature sensor based on time-coded UWB chipless RFID tags, IEEE Trans. Microw. Theory Tech., 2012, vol. 60, no. 11, pp. 3623–3632.

[2]   Kong, D. et al. Temperature-dependent electrical properties of graphene inkjet-printed on flexible materials, Langmuir, 2012, vol. 28, no. 37, pp. 13467–13472.

[3]   Dinh, T. et al. Graphite on paper as material for sensitive thermoresistive sensors, J. Mater. Chem. C, 2015, vol. 3, no. 34, pp. 8776–8779.

[4]   Amphenol Advanced Sensors Amphenol 10k NTC Thermistor, 2014.

[5]   Amin, E. M. et al. Chipless RFID tag for light sensing, in 2014 IEEE Antennas and Propagation Society International Symposium (APSURSI), 2014, pp. 1308–1309.

[6]   Schmidt, R.; Brinkman, A. W. ac hopping admittance in spinel manganate negative temperature coefficient thermistor electroceramics, J. Appl. Phys., 2008, vol. 103, no. 11, p. 113710.

[7]   He, L.; Ling, Z. Y. Electrical conduction of intrinsic grain and grain boundary in Mn-Co-Ni-O thin film thermistors: Grain size influence, J. Appl. Phys., 2011, vol. 110, no. 9, p. 093708.

[8]   Schmidt, R.; Brinkman, A. W. Studies of the Temperature and Frequency Dependent Impedance of an Electroceramic Functional Oxide NTC Thermistor, Adv. Funct. Mater., 2007, vol. 17, no. 16, pp. 3170–3174.

[9]   Walker, B. Make Accurate Impedance Measurements Using a VNA, Copper Mountain Technologies, [Available at: https://www.clarke.com.au/pdf/CMT_Accurate_Measurements_VNA.pdf]

Appendix F - Justification of Normalised Sensitivity Measurement for Sensor Comparison

This appendix discusses the thought process and subsequent validity of using frequency normalised sensitivity values to compare the different temperature sensors reviewed in Chapter 4. The general idea behind chipless RFID sensor design is that the device sensitivity to the desired stimulus is created by the product of two separate sensitivities; the sensitivity of some feature (X) of the resonator design to the target stimulus (T) and the sensitivity of the resonators resonant frequency (f) to change in that feature (see Equation F.1).

$$\frac{\partial f}{\partial T} = \frac{\partial f}{\partial X}\left(\frac{\partial X}{\partial T}\right) \tag{F.1}$$

What was needed was a way to compare the sensitivity of sensors in a way that was unrelated to the initial resonant frequency of the device. The next question is, assuming that the same resonator design is used, will the sensor sensitivity actually scale with operating frequency? Different resonator designs achieve different levels of resonant frequency for a fixed footprint size, with a lower resonant frequency normally being desired. Equation F.2 below describes the resonant frequency equations found in a variety of chipless RFID tags/antennas and the relevant parameters have been summarised in Table F.1. The constant of proportionality will differ between designs, such as those seen in [1][2][3], but assuming that the permittivity is greater than unity, Equation F.2 could be approximated by that seen in Equation F.3, although the constant of proportionality will differ slightly between resonators.

Table F.1: Resonant Equation Parameters List

Parameter/Variable	Description	Variable Type
f	Resonant frequency of resonator	n/a
L	Geometric length of a feature of that specific resonator	Geometric variable
c	Speed of light	Constant
n	Integer number (to account for harmonic behaviour)	Constant
r	Geometric length (radius) of a feature of that specific resonator	Geometric variable
π	Ratio of circumference to diameter of circle	Constant
ε	Permittivity/Dielectric constant of surrounding material	Electric variable

$$f_1 \propto \frac{c}{2L\sqrt{\varepsilon}}, \qquad f_2 \propto \frac{c}{2L}\sqrt{\frac{2}{1+\varepsilon}}, \qquad f_3 \propto \frac{nc}{\pi r\sqrt{\varepsilon}} \tag{F.2}$$

$$f \propto \frac{c}{2L\sqrt{\varepsilon}} \tag{F.3}$$

The derivative of Equation F.3 with respect to permittivity can be seen in Equation F.4 and from this expression, it can be seen that the resonator sensitivity is a product of the device operating frequency and an expression including only one variable, the electrical permittivity. The inclusion of the "2" term in the final expression in Equation F.4 also shows that the relevant constants of proportionality in Equation F.3 will carry through to the final device sensitivity. What all of this this means is that the sensitivity will in-fact grow in proportion to the resonator operating frequency, so frequency-based normalisation of the measured sensitivity is a reasonable way to compare designs with dissimilar operating frequencies. By multiplying the final expression in Equation F.4 by a change in permittivity ($\Delta\varepsilon$), the result is a change in resonant frequency which is proportional to the proportional change in dielectric constant. Thus, the impact of differing initial permittivity's across different coatings does not impact the sensor performance, rather it is how large its proportional change is to the desired stimulus that defines the final part of the design sensitivity.

$$\frac{\partial f}{\partial \varepsilon} = \left(\frac{-cL(\varepsilon)^{-1/2}}{4L^2\varepsilon}\right) = \frac{-c(\varepsilon)^{-1/2}}{4L\varepsilon} = \frac{-1}{2\varepsilon}\left(\frac{c}{2L\sqrt{\varepsilon}}\right) = \frac{-1}{2\varepsilon}(f) \tag{F.4}$$

In the case of designs that make use of mechanical swelling/deformation, the sensitivity can be expressed as that seen in Equation F.5. Similar to that found above, Equation F.5 below now includes a geometric term, which will mean that multiplication by a change in geometry (ΔL) will result in the change in resonant frequency being proportional to the proportional change in geometry. It is, however, unclear if certain elements such as bi-metallic strips will impact the design in a proportional manner with proportional geometric changes. With all of this being said however, this metric seems like the most appropriate one, currently available to compare dissimilar designs.

$$\frac{\partial f}{\partial L} = \left(\frac{-c\sqrt{\varepsilon}}{2L^2\varepsilon}\right) = \frac{-\sqrt{\varepsilon}}{L\sqrt{\varepsilon}}\left(\frac{c}{2L\sqrt{\varepsilon}}\right) = \frac{-1}{L}(f) \tag{F.5}$$

Further study is however, required to investigate the resonant frequency equations for other resonators not referenced above. Such analysis could be done from further literature review and/or by inferences of simulation-based parametric sweeps.

F.1   References

[1]   Singh, R.; Kumar, G. Broadband Planar Monopole Antennas, Bombay, 2003.

[2]   Karmakar, N. C. et al. Chipless RFID Sensors, 1st Edt. Wiley, 2016.

[3]   Mc Gee, K. et al. A Review of Chipless Remote Sensing Solutions Based on RFID Technology, Sensors, 2019, vol. 19, no. 19, p. 4829.

Appendix G - Ferroelectric Material In-Situ Fabrication Overview

This appendix presents further details about the materials that were considered when developing the thermocouple-based chipless RFID sensor. For the sake of brevity, this material has been placed into an appendix, so that the main body of the text can be more succinct.

G.1   Liquid Crystal Polymers (LCPs)

Liquid Crystal Displays make use of compartmentalised liquid crystals that are used as voltage-controlled polarization rotators [1]. Initial research into liquid crystals and their electronically controlled properties revealed that their electrical permittivity is also altered by the presence of an external electric field [2]. These materials have also been used in microwave applications to achieve effects other than polarization modification. The main use of these materials in this field is that their electrical permittivity in one direction can be altered, by applying an electric field across the piece in an orthogonal direction. The mechanism by which the permittivity changes within this material is owed to their dielectric anisotropy [3][4]. As described in other publications, such as [2], the maximum change in permittivity is given as that described in Equation G.1.

$$\Delta\varepsilon_r = \ \varepsilon_{r\parallel} - \ \varepsilon_{r\perp} \qquad\qquad (G.1)$$

With the ability to electrically configure the permittivity, this material is well-suited for varactor and tuneable antenna applications, as implemented in Reference [4] and Reference [5]. The biasing of such a material with the output of a thermocouple brings about some challenges. One of the main challenges presented is that the input impedance of the DC circuit needs to be high, so that excessive current is not drawn from the thermocouple and result in an alteration of the measured voltage and temperature. Other unwanted effects include current leakage from the microwave to the DC circuit which would also be detrimental.

Although the permittivity of this material is bias voltage dependent, there are several issues associated with its voltage dependence. The main issue with using this material with a low bias voltage is that there is a significant threshold voltage to be exceeded, before the relationship between permittivity and bias voltage are proportional. The mechanisms by which this high threshold voltage exists, originates from the elastic effects within the material whilst transitioning from the parallel to the perpendicular permittivity [6]. Conservative estimates for this threshold voltage, such as those found in Reference [5] can exceed one volt. Possible ways to mitigate this problem may involve the addition of a battery of some sort to help bias the material into the region of interest. Also of interest to this discussion, some of

the literature on these materials exposes the possibility of a frequency-dependent threshold voltage [6].

Other than a variation in loss tangent with frequency, as seen in the 5GHz antenna design in Reference [5] which severely affects radiation efficiency, this material is not very sensitive. This issue of sensitivity cannot be easily mitigated as the full tunability of any LCP device is usually quite low as the difference between the perpendicular and parallel dielectric constant is usually much less than 32% in most cases [2]. Example antenna-based implementations of this material include the work of Liu and Langley in [5] where a 7.826% change in resonant frequency was achieved with a 10V bias voltage. Similarly, the work outlined in Reference [7] by Fritzsch et al., achieved a 10% change in resonant frequency with a bias voltage of 90V. More promisingly, the results of Reference [4] show that for certain LCPs, 80% of the tunability can be utilised with bias voltages below 4V. These voltages and others quoted in similar publications are quite large for a thermocouple interface circuit as thermocouples exhibit μV/K sensitivities [8][9][10][11]. The capacitor design also plays a key role in this sensitivity value but achieving a low threshold voltage and a high sensitivity are mutually exclusive parameters. The reduction of threshold voltage requires a concentrated electric field which favours a small parallel-plate capacitor design and not an interdigital design [12]. However, a high sensitivity can only be achieved by biasing a larger area of LCPs which thus favours a large parallel-plate capacitor design [12]. Other performance issues that arise in the use of this material in varactor applications includes a frequency-dependent dielectric anisotropy, as discussed in Reference [4]. Other issues with the use of this material include the fact that it is also sensitive to stimuli other than electric fields. Examples of its use in other applications are beyond the scope of this work. Instead, details on the use of LCPs in the detection of Volatile Organic Compounds (VOCs) can be found in Reference [13] and the temperature sensing capabilities of these materials are described in Reference [14].

Further challenges also arise when attempting to deposit this material in-situ. Although it has been shown that Chemical Vapor Deposition (CVD) can be used to deposit this material, as seen in Reference [15], the deposited layer(s) also need to be orientated/initialised properly. This is usually dictated by the characteristics of the substrate material and/or other, subsequently deposited layers. Many parameters need to be tuned appropriately to ensure that the threshold voltage, capacitance, leakage losses and other characteristics are set accordingly. These parameters include:

- Layer thickness

- Initialisation layer selection such as Polyvinyl Alcohol (PVA), as described in [4]

- Specific LCP selection

- Deposition method

- Underlying capacitor design

G.2   Electrostatic Actuators

This section explores the possibility of using electrostatic actuators to vary the capacitive element of a microwave resonator. These devices are usually only found in Micro Electro-Mechanical Systems (MEMS) sensors, particularly gyroscopes. Although they are widely discussed and operated in a digital fashion, below the "pull-in" voltage, the relationship between applied voltage and displacement is analogue in nature. A simplified diagram and equations relating to an idealistic parallel plate actuator are given below. With regard to integration of these actuators with chipless RFID technology, the sensor outlined in Reference [16] uses a bi-metallic strip temperature sensor as part of the capacitor on a split ring resonator structure. A similar approach to that could be taken, in order to integrate this technology into chipless RFID tags. As described in Reference [17], a simplified model of an electrostatic actuator consists of a rigid beam and a cantilever beam separated by a distance (d), with the cantilever system imparting a spring stiffness (k) to the system. A potential is placed across the two beams a capacitive field occurs between the two nearby surfaces (of cross-section "A") of the beams. The upward and downward forces are expressed as follows [17]:

$$F_{down} = -\frac{1}{2}\frac{\varepsilon_r \varepsilon_0 A V^2}{(d)^2} \; from \; Coulomb's \; law \; with \; parallel \; capacitor \qquad \text{(G.2)}$$

$$F_{up} = k(d_0 - d) \; from \; hooke's \; law \qquad \text{(G.3)}$$

Interestingly at the deflection distance (d) of d = d_0/3 [18], the displacement behaviour changes from analogue to discrete as the spring force, which is proportional to displacement cannot balance the electrostatic force, which is proportional to displacement[2] [18]. The voltage needed to reach this pull-in point is called the pull-in voltage. This voltage is expressed as [18]:

$$V_{pi} = \sqrt{\frac{8kd^3}{27\varepsilon_0 \varepsilon_r A}} \qquad \text{(G.4)}$$

In any case, there is an issue with using this type of approach and that is that many of these structures have sub-µm tolerances and still exhibit pull-in voltages exceeding several volts, as

discussed in References [19], [20] and [21], the latter of which required an 8v pull-in voltage. As this voltage is quite large for thermocouple integration, it can be concluded that the sensitivity of this device in the analogue region may be quite poor. The issues with operating this device in the larger discrete region via external biasing include;

- Hysteresis exists upon recovery
- Displacements are very small(sub-mm)
- Overall size and general manufacturing tolerances are quite small. Scaling upwards to alleviate this issue is foolhardy as volumes increase with size^3 but areas increase with size^2
- The system would need to have several actuators of different geometries(sensitivities) to allow for a flash ADC style of voltage sensor

G.3 Ferroelectric Materials (BST - $Ba_xSr_{1-x}TiO_3$)

Several ferroelectric materials exist that exhibit effects of interest for this application. One of the most widely characterised and utilised material of this type is the ceramic, Barium Strontium Titanate (BST). Most materials of this type, such as $BaTiO_3$ and $SrTiO_3$ have a perovskite structure. Alone and to greater degree when combined together ($Ba_xSr_{1-x}TiO_3$), they support the formation of electric dipoles within the unit cells of the resulting lattice. The effect of an external electric field reduces the permittivity in the opposite plane, regardless of polarity. A diagram of this relationship with BST in the paraelectric phase can be seen in Figure G.1 below. A further discussion on the atomic modelling and characterisation of the ferroelectric behaviour of BST can be found in Reference [22] by Wexler et al. For the sake of completeness, it will be mentioned here that generic perovskite structures ($^{XII}A^{2+VI}B^{4+}C^{2-}O_3$) can support B^{4+} and O^{2-} ions shifting to form a dipole when exposed to an electric field [12].
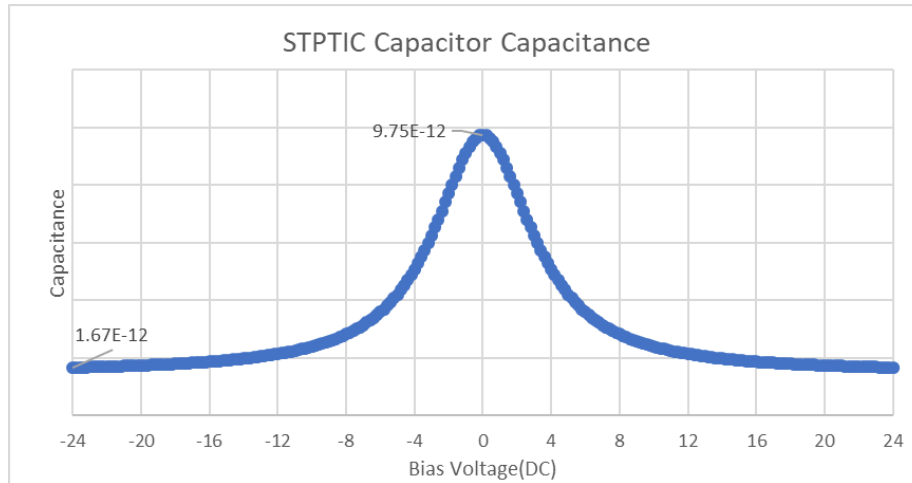
Figure G.1: BST Permittivity Bias Voltage Dependence Curve - Adapted from Equations and Data in References [22][23]

Within a given temperature range, this material exhibits ferroelectric behaviour with hysteretic electrical polarizability which makes BST a useful material for Ferroelectric Random Access Memory (FRAM) [24]. Above the Curie temperature, this hysteretic behaviour disappears, in what is known as the paraelectric phase. Operation in this phase also exhibits temperature dependent variations in permittivity [25][26]. Around this transition temperature, the maximum permittivity is also found [25][27]. This temperature can be tuned between -40°C and 385°C by altering the Barium:Strontium (x) concentration [12]. However, care is needed in controlling this ratio as the microwave loss tangent of this material increases with increasing Barium concentration [28]. Doping with materials such as Potassium, Bismuth, Magnesium or Iron can also result in significant alterations in many of the key properties of BST thin films [29][30]. Example alterations that can be achieved through doping include a reduction in the levels of oxygen vacancies which in turn leads to a reduction in loss tangent [29][30], along with a reduced dielectric constant and a reduced dielectric dispersion [29]. Also, the dopants utilised by Khalfallaoui et al. in Reference [29] revealed that the tunability of the films can also be significantly altered, with a maximum increase from 23.5% to 36% by doping with Potassium.

This material is most commonly operated in the paraelectric phase as opposed to the ferroelectric phase as the latter results in high losses in the microwave range [28] and also exhibits significant levels of hysteresis in the permittivity-voltage curve [12]. However, there is some debate as to the shortcomings of the ferroelectric phase, in the work of Nadaud et al. in Reference [26]. This work revealed negligible hysteresis in the ferroelectric phase and thus also exhibited permittivity characteristics that could not be significantly altered by temperature variations, as long as the material remained in this phase. This temperature

stability of 2% permittivity variation was achieved between -80°C and 20°C and tunability within 10% of maximum was recorded from -70°C to 100°C. Operating this material in the paraelectric phase, millivolt bias voltages have been successfully used to result in a measurable change in permittivity by Kabir in Reference [31] and by Done et al. in Reference [32]. The work presented in Reference [32] involves the use of STPTIC capacitors from ST Microelectronics which is reported to be a doped version of BST. Most importantly, these and other works do not exhibit the explicit threshold voltage present in LCPs. This material is however, quite temperature sensitive in the paraelectric phase and has found direct use in temperature sensitive chipless RFID tags already, as can be seen in Reference [33]. However, the degree to which this temperature dependence arises is highly dependent on homogeneity/quality of the deposited BST film and is usually much less than that found in bulk BST [34]. Furthermore, more advanced fabrication operations such as varying the curie temperature between layers throughout the final film [34] or the addition of various doping strategies [35][36] can alleviate the temperature dependence.

Although a great deal of research has been performed on thick/thin film realisations of this material, there are significant challenges in ensuring that the deposited film performs as intended. Prepared forms of BST suitable for inkjet deposition include sol-gel preparation [29][24] and nanoparticle-based inks [37]. Differences in bulk and film loss tangent and other properties can vary massively, even up to a five-fold increase in loss tangent for the thin film implementation [30]. Likewise, the work of Shaw et al. in Reference [38] revealed a significant difference in temperature sensitivity between bulk BST and the developed BST thin film deposition. Furthermore, the Quality factor of the films, particularly around low bias voltages is heavily affected by deposition environment and temperature [39]. Similarly, the thickness of the film also has a significant effect on the resulting Curie temperature, as described in Reference [40]. Careful sintering of the resulting film is also required as the sintering temperature and time affect the resulting dielectric constant, as discussed by Loachim et al. in Reference [28]. The sintering requirements of this material can also be reduced/relaxed with the addition of certain dopants [28].

At this point it is worth mentioning that the use of ferroelectric materials, like the use of LCPs or Electrostatic Actuators brings about significant fabrication challenges. The main challenge with the use of BST and other ferroelectric ceramics is that they require very large firing/sintering temperatures of up to 1200°C [41][42] and durations on the order of hours [43]. Temperatures on the scale of 1200°C exceed the melting temperatures of most polymers [44] and popular aerospace materials such as aluminium [45]. Rapid sintering methods have

been outlined in publications such as [46] but it remains unclear if surrounding (substrate) materials will be able to survive this sintering method either. With regard to in-situ deposition of BST, sol-gel derived BST along with an appropriate solvent was deposited via inkjet technology in [43] which was then sintered at 1150°C for one hour.

Low temperature processing of BST has also been performed in publications such as [47] where BST particles were added to a PMMA (Polymethyl methacrylate) and then deposited via inkjet using a solvent based ink. Sintering temperatures in these cases were on the order of 150°C. Although this is a more promising result, it is inevitable that such a deposition will have weaker ferroelectric properties than its bulk counterpart.

G.4   References

[1]   A. Safrani and I. Abdulhalim, "Liquid-crystal polarization rotator and a tunable polarizer," Opt. Lett., vol. 34, no. 12, p. 1801, Jun. 2009.

[2]   P. Yaghmaee, O. H. Karabey, B. Bates, C. Fumeaux, and R. Jakoby, "Electrically Tuned Microwave Devices Using Liquid Crystal Technology," Int. J. Antennas Propag., vol. 24, no. 25, Nov. 2013.

[3]   S.-W. Oh, J.-H. Park, and T.-H. Yoon, "Near-zero pretilt alignment of liquid crystals using polyimide films doped with UV-curable polymer," Opt. Express, vol. 23, no. 2, p. 1044, Jan. 2015.

[4]   N. Martin, P. Laurent, C. Person, P. Gelin, and F. Huret, "Patch antenna adjustable in frequency using liquid crystal," in Conference Proceedings - 33rd European Microwave Conference, EuMC 2003, 2003, vol. 2, pp. 699–702.

[5]   L. Liu and R. J. Langley, "Liquid crystal tunable microstrip patch antenna," Electron. Lett., vol. 44, no. 20, pp. 1179–1181, 2008.

[6]   M. Schadt, "LIQUID CRYSTAL MATERIALS AND LIQUID CRYSTAL DISPLAYS," in Annual Review of Material Science, 1997, pp. 305–379.

[7]   C. Fritzsch, S. Bildik, and R. Jakoby, "Ka-band frequency tunable patch antenna," in IEEE Antennas and Propagation Society, AP-S International Symposium (Digest), 2012, pp. 1–2.

[8]   S. Duby, B. Ramsey, D. Harrison, and G. Hay, "Printed thermocouple devices," in Proceedings of IEEE Sensors, 2004, vol. 3, pp. 1098–1101.

[9]   C. Offenzeller, M. Knoll, B. Jakoby, and W. Hilber, "Fully Screen Printed Carbon Black-Only Thermocouple and the Corresponding Seebeck Coefficients," Proceedings, vol. 2, no. 13, p. 802, Nov. 2018.

[10]   J. Kita et al., "Screen-printable type S thermocouple for thick-film technology," in Procedia Engineering, 2015, vol. 120, pp. 828–831.

[11]   M. Knoll, C. Offenzeller, B. Mayrhofer, B. Jakoby, and W. Hilber, "A Screen Printed Thermocouple-Array on a Flexible Substrate for Condition Monitoring," in Proceedings of Eurosensors 2018, 2018, vol. 2, no. 13, p. 803.

[12]   X. Wang, "TUNABLE MICROWAVE FILTERS USING FERROELECTRIC THIN FILMS, PhD Thesis," University of Birmingham, 2009.

[13]   P. V. Shibaev, M. Wenzlilck, J. Murray, A. Tantillo, and J. Howard-Jennings, "Rebirth of Liquid Crystals for Sensoric Applications: Environmental and Gas Sensors," Adv. Condens. Matter Phys., vol. 2015, 2015.

[14]   J. Torres, B. García-Cámara, I. Pérez, V. Urruchi, and J. Sánchez-Pena, "Wireless Temperature Sensor Based on a Nematic Liquid Crystal Cell as Variable Capacitance," Sensors, vol. 18, no. 10, p. 3436, Oct. 2018.

[15]   T. Itadani and K. Saito, "Controlling the molecular orientation of liquid crystalline polymer films deposited by polarized-laser chemical vapor deposition," Nucl. Instruments Methods Phys. Res. Sect. B Beam Interact. with Mater. Atoms, vol. 121, no. 1–4, pp. 415–418, Jan. 1997.

[16]   T. T. Thai et al., "A novel passive ultrasensitive RF temperature transducer for remote sensing and identification utilizing radar cross sections variability," in 2010 IEEE International Symposium on Antennas and Propagation and CNC-USNC/URSI Radio Science Meeting - Leading the Wave, AP-S/URSI 2010, 2010, pp. 1–4.

[17]   T.-R. Hsu, MEMS and microsystems: design, manufacture, and nanoscale engineering, 2nd Edtn. Hoboken: Wiley, 2008, pp.55-59, 233.

[18]   C. Liu, Foundations of MEMS, 1st Edtn. New Jersey: Pearson, pp.127-140.

[19]   P. D. Hanasi, B. G. Sheeparamatti, and B. B. Kirankumar, "Study of pull-in voltage in MEMS actuators," in 2014 IEEE International Conference on "Smart Structures and Systems", ICSSS 2014, 2015, pp. 108–111.

[20]   O. Pertin and Kurmendra, "Pull-in-voltage and RF analysis of MEMS based high performance capacitive shunt switch," Microelectronics J., vol. 77, pp. 5–15, Jul. 2018.

[21]   S. Kumar, N. Chattoraj, M. K. Sinha, and N. Danu, "Investigation of electrostatic actuation scheme for low voltage MEMS switch," in Proceedings of the International Conference on Nano-electronics, Circuits & Communication Systems, 2017, vol. 403, pp. 167–176.

[22]   R. B. Wexler, Y. Qi, and A. M. Rappe, "Sr-induced dipole scatter in $BaxSr_{1-x}TiO_3$: Insights from a transferable-bond valence-based interatomic potential," Phys. Rev. B, vol. 100, no. 17, p. 174109, Nov. 2019.

[23]   S. Microelectronics, "Datasheet - ParascanTM tunable integrated capacitor," 2015. [Online]. Available: https://www.st.com/resource/en/datasheet/stptic-68g2.pdf.

[24]   eddin A. Saif, Z. A. Z Jamal, and P. Poopalan, "Effect of the chemical composition at the memory behavior of $Al/BST/SiO_2/Si$-gate-FET structure," Appl. Nanosci., vol. 1, pp. 157–162, 2011.

[25]   J. H. Jeon, "Effect of $SrTiO_3$ concentration and sintering temperature on microstructure and dielectric constant of $Ba_{1-x}Sr_xTiO_3$," J. Eur. Ceram. Soc., vol. 24, no. 6, pp. 1045–1048, 2004.

[26]   K. Nadaud, C. Borderon, R. Gillard, E. Fourn, R. Renoud, and H. W. Gundel, "Temperature stable $BaSrTiO_3$ thin films suitable for microwave applications," Thin Solid Films, vol. 591, pp. 90–96, Sep. 2015.

[27]   O. G. Vendik and S. P. Zubko, "Ferroelectric phase transition and maximum dielectric permittivity of displacement type ferroelectrics ($BaxSr_{1-x}TiO_3$)," J. Appl. Phys., vol. 88, no. 9, pp. 5343–5350, Nov. 2000.

[28]   A. Ioachim et al., "Transitions of barium strontium titanate ferroelectric ceramics for different strontium content," Thin Solid Films, vol. 515, no. 16 SPEC. ISS., pp. 6289–6293, Jun. 2007.

[29]   A. Khalfallaoui, G. Vélu, L. Burgnies, and J. C. Carru, "Characterization of doped BST thin films deposited by sol-gel for tunable microwave devices," in 2009 IEEE International Frequency Control Symposium Joint with the 22nd European Frequency and Time Forum, 2009, pp. 295–298.

[30]   A. Vorobiev, P. Rundqvist, K. Khamchane, and S. Gevorgian, "Microwave loss mechanisms in Ba0.25Sr0.75TiO 3 thin film varactors," J. Appl. Phys., vol. 96, no. 8, pp. 4642–4649, Oct. 2004.

[31]   A. T. Kabir, "Voltage Controlled Oscillators Tuned with BST Ferroelectric Capacitors, Masters Thesis," University of Colorado Colorado Springs. Kraemer Family Library, Colorado, 2012.

[32]   A. Done, A. M. Căilean, and A. Graur, "Active frequency stabilization method for sensitive applications operating in variable temperature environments," Adv. Electr. Comput. Eng., vol. 18, no. 1, pp. 21–26, 2018.

[33]   C. Mandel, H. Maune, M. Maasch, M. Sazegar, M. Schüßler, and R. Jakoby, "Passive wireless temperature sensing with BST-based chipless transponder," in 2011 German Microwave Conference, 2011.

[34]   M. W. Cole, E. Ngo, S. Hirsch, J. D. Demaree, S. Zhong, and S. P. Alpay, "The fabrication and material properties of compositionally multilayered Ba1-x Srx Ti O3 thin films for realization of temperature insensitive tunable phase shifter devices," J. Appl. Phys., vol. 102, no. 3, p. 034104, Aug. 2007.

[35]   T. Schneller, S. B. Majumder, and R. Waser, "Ceramic Thin Films," in Ceramics Science and Technology: Volume 1, Wiley-VCH Verlag, 2005, pp. 449, 483–488.

[36]   M. Jain, S. B. Majumder, R. S. Katiyar, F. A. Miranda, and F. W. Van Keuls, "Improvement in electrical characteristics of graded manganese doped barium strontium titanate thin films," Appl. Phys. Lett., vol. 82, no. 12, pp. 1911–1913, Mar. 2003.

[37]   A. Friederich et al., "Preparation of integrated passive microwave devices through inkjet printing," in 9th International Conference and Exhibition on Ceramic Interconnect and Ceramic Microsystems Technologies (CICMT 2013), 2013.

[38]   T. M. Shaw, Z. Suo, M. Huang, E. Liniger, R. B. Laibowitz, and J. D. Baniecki, "The effect of stress on the dielectric properties of barium strontium titanate thin films," Appl. Phys. Lett., vol. 75, no. 14, pp. 2129–2131, Oct. 1999.

[39]   N. K. Pervez, P. J. Hansen, and R. A. York, "High tunability barium strontium titanate thin films for rf circuit applications," in Applied Physics Letters, 2004, vol. 85, no. 19, pp. 4451–4453.

[40]   I. S. Golovina et al., "Controlling the phase transition in nanocrystalline ferroelectric thin films: Via cation ratio," Nanoscale, vol. 10, no. 46, pp. 21798–21808, Dec. 2018.

[41]   M. Nikfalazar et al., "Compact tunable phase shifter based on inkjet printed BST thick-films for phased-array application," in 2013 European Microwave Conference, 2013, pp. 432–435.

[42]   Y. Sakai, T. Futakuchi, T. Iijima, and M. Adachi, "Preparation of (Ba,Sr)TiO3 thick film on ZrO2 substrates by Inkjet printing," Japanese J. Appl. Physics, Part 1 Regul. Pap. Short Notes Rev. Pap., vol. 45, no. 2 A, pp. 846–849, Feb. 2006.

[43]   M. Nikfalazar et al., "Inkjet printed BST thick-films for X-band phase shifter and phased array applications," 2013 Int. Work. Antenna Technol. iWAT 2013, pp. 121–124, 2013.

[44]   W. D. Callister, Materials science and engineering, 8th ed., S. Hoboken, N.J: John Wiley, 2011.

[45]   S. Shekhawat et al., "A Clustering Classification of Spare Parts for Improving Inventory Policies," IOP Conf. Ser. Mater. Sci. Eng., vol. 114, no. 1, p. 012075, Feb. 2016.

[46]   L. R. Devi, O. P. Thakur, and C. Prakash, "Conventional and microwave sintering of BST for tunable devices," https://doi.org/10.1117/12.514527, vol. 5062, pp. 373–377, Oct. 2003.

[47]   M. Mikolajek et al., "Direct Inkjet Printing of Dielectric Ceramic/Polymer Composite Thick Films," Adv. Eng. Mater., vol. 17, no. 9, pp. 1294–1301, Sep. 2015.

Appendix H - Simplistic Sensor Response Curve Fitting

This appendix presents the attempts made at curve fitting of the sensor response datasets seen in Chapter 3 and Chapter 4.

H.1   Localised Second Order Polynomial Curves

The benefits of curve fitting, such as second order polynomial fitting to the null region of the response have been utilised by the authors in [1] and other in works besides. It can allow for a reduction in averaging needed (assuming normally distributed noise) and also allows for null frequency determination at resolutions beyond the limitations of the sampling interval of the dataset. One concern is that the use of simplistic polynomial curve fitting is highly situational and ideally a more appropriate basis curve should be used. Although the idealised bandstop magnitude is not a polynomial function, the authors have had success with curve fitting using second order polynomial curves within a small band of frequencies around the null frequency. Example tests carried out on the sensor published in [1] revealed the response curves seen in Figure H.1. Polynomial curve fitting on these curves resulted in R-squared values ranging from 0.9822 to 0.9882 and more impressive results were also achieved when curve fitting was performed on a smaller region of the dip. Taking the derivative of the polynomial curve is a trivial undertaking and the resolution of the determined minimum point is now determined by the precision of the data types used in the polynomial curve calculation.
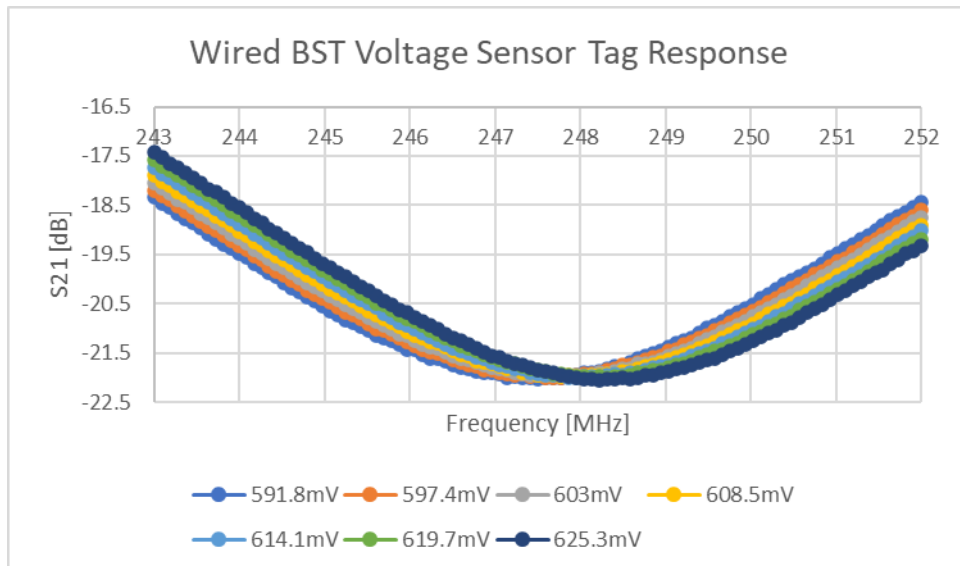

Figure H.1: BST-based DC Voltage Sensor Response Curves

The use of second order polynomial curve fitting is a simple least-squares-regression calculation that can be directly solved (quick, non-iterative based solution) and allows for the

estimation of the null frequency (null of the polynomial curve) at a resolution exceeding that of the resolution of the frequency response dataset. Its use has been mainly employed because the Q-factors of the response curves are sufficiently small that the sharp transitions in magnitude around the null are not present. If, however, the dataset curve is not symmetric about the null, the symmetry of the polynomial curve will result in fitting errors which would lead to an error in the estimation of the true null frequency. Furthermore, high-Q responses will lead to the polynomial curve fitting being reliant on a very small number of datapoints. The use of polynomial curve fitting was of great benefit when sensing below 100µε but there are limits to its use, as mentioned earlier. Figure H.2 depicts the results of a fixed 20-datapoint polynomial curve fitting approach taken with the strain datasets presented in Reference [2]. The asymmetries around the minimum point are the result of noise and the general asymmetry of the null regions. The quality of the polynomial fits is reasonable for most of the datasets except the 10% dataset where the flatness of the region around the null makes the curve fitting unreliable.
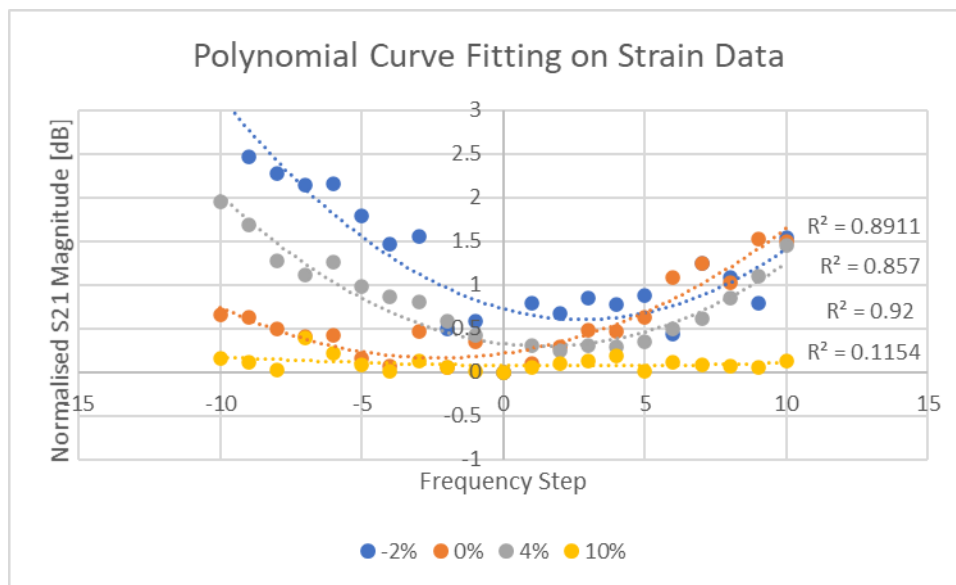

Figure H.2: Polynomial Curve Fitting on Strain Datasets

With enhanced curve fitting on the 10% dataset (not based on a fixed number of datapoints around the null), the polynomial curve null points were determined and the results of this are compared to the minimum point method results, in Table H.1. Note: The original datasets had a resolution of 250kHz steps. It can only be assumed that if the polynomial curve fitting had a good R-squared value, that the minimum value is quite accurate, that is to say, if the asymmetry of the chosen dataset is not considered significant.

Table H.1: Impact of Polynomial Curve Fitting on Null Frequency Determination

%ε	-2	0	4	10
Minimum Point	2045.881	2104.801	2197.638	2402.870
Polynomial Curve	2045.085	2104.230	2198.001	2403.545

H.2   Transfer Function Fitting

As discussed in other works referenced earlier, it is believed that the response of the sensor takes the form of a bandstop filter. As the strain sensor datasets and the popular ELC resonator exhibit a peak region before the dip in their Radar Cross Section (RCS) responses, the first step was to attempt to manually fit the bandstop transfer function magnitude curve to that of those sensor responses. This curve fitting focussed on fitting the Transfer Function (TF) curve around the peak and null region, at the expense of the other regions of the total response. Figure H.3 depicts the attempted curve fitting for the simulated strain dataset presented in Chapter 3. Similarly, the dataset gathered from physical testing of the sensor published by the authors in [2] also had a TF curve fitting procedure performed on it. The results of this can be seen in Figure H.4.
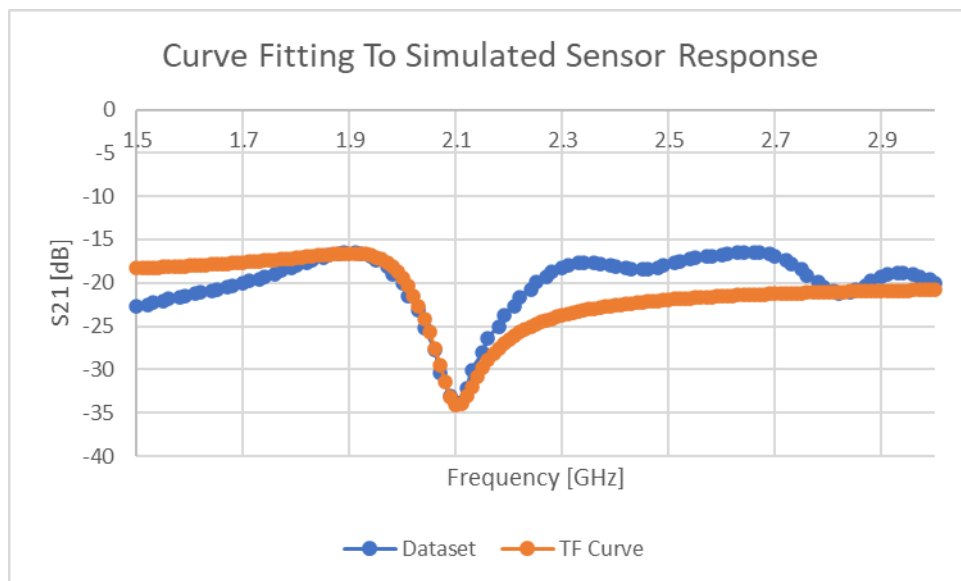

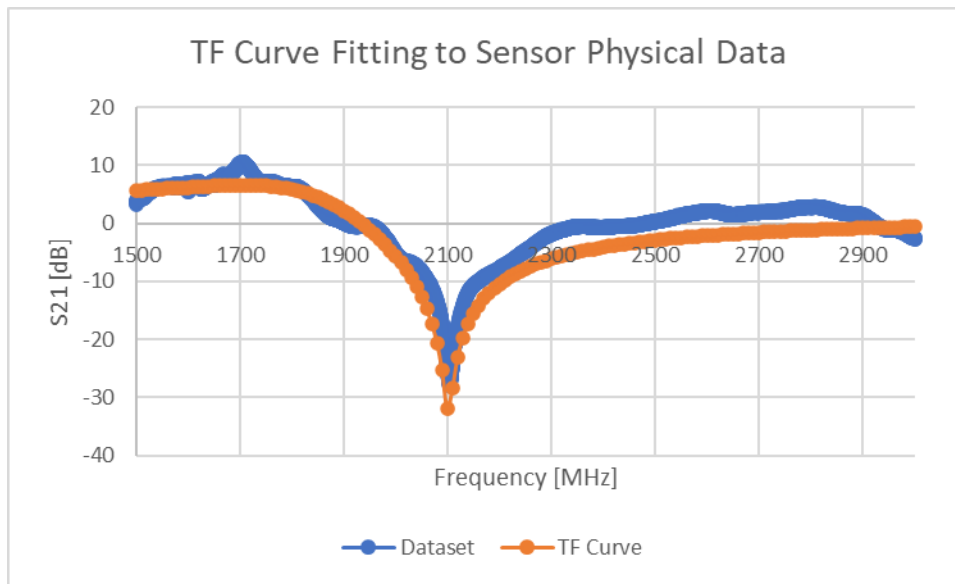*Figure H.3: Manual Curve Fitting to Simulated Sensor Response*

Figure H.4: Manual Curve Fitting to Physical Sensor Response

Both of the TF curves seen in the above figures were manually fitted, and no amount of further tuning would alleviate the variations between the TF curve and the actual datasets. It was then speculated that the reason why the elliptical bandstop responses would not perfectly fit either of these datasets was because of some unique characteristic of this sensor design. To test this theory out, physical test results from a standard ELC-based chipless RFID tag were used as the basis of a subsequent transfer function fitting attempt. The results of this research revealed that the elliptical bandstop response would only provide a quality fit to the dataset in the region between the zero (dip) and the pole (peak) frequencies. This result is a disappointing one and would bring into question if it is indeed possible or not to make use of transfer function -based curve fitting as a means of enhanced null frequency determination. Simply put, if the function onto which it is assumed that the dataset mimics cannot provide a good fit around the region of interest (null region), it could then be speculated that its use would not allow for enhanced characterisation of said region.

The next step was to explore the use of automated methods for transfer function curve fitting. Transfer function calculation from frequency and/or time domain data is a task that has been explored in many works and continues to be a thriving area of research. This work has attempted to make use of existing Scilab functions such as "frfit", "mrfit" and "frep2tf" to attempt to derive the transfer function that most accurately corresponds to the RCS response. These operations were performed without phase unwrapping and the results in all cases were poorer than the results from assuming the minimum data point is the true curve minimum. Simplistic phase unwrapping yields far more suitable results but further work is needed into

taking the state-of-the-art systems identification software and applying it to chipless RFID response characterisation. With phase unwrapping and the addition of phase shift poles/zeros to the standard transfer function, the use of "frep2tf" resulted in curves that are considerably visually different than that found in the dataset, but these differences were smaller than in the wrapped case. One disadvantage that these curve fitting algorithms possess is that the incoming dataset can be assumed to has a bandstop-like response and the pole (peak), zero (null) frequencies and Q-factors can already be roughly estimated from the dataset. In an attempt to make use of this information, a simplistic transfer function curve fitting code was developed. This approach made use of the popular Gradient Descent (GD) method [3] to iteratively tune the coefficients of the transfer function to what is assumed is a nearby minimum in the loss function. The results of this did not significantly improve the ability to accurately determine the null frequency of the curve as the TF curve overfit to this region at the expense of accuracy at the null frequencies. One option at this point would be to use the location and slope of the line between the peak and null as an alternate feature which would be indicative of the stimulus level. This approach was dismissed as the slope would have Q-factor dependencies and the location of the centroid of the slope would be sensitive to the tuning quality achieved around the peak and null frequencies. Since the performance of this curve fitting approach is based on a poor fit around the null frequency, this alternate metric was therefore fully dismissed.

The other type of resonant response that has been observed in this project and indeed throughout the chipless RFID literature is that of a more symmetric bandstop response. Manual and automated curve fitting of these datasets revealed far more promising results than that found with the alternate bandstop responses. Figure H.5 depicts the result of manual TF curve fitting to the simulated dataset presented by the strain sensor when placed on a small metallic superstrate. Additional testing was performed with other datasets and similar/better quality fits were achieved for this bandstop response type.
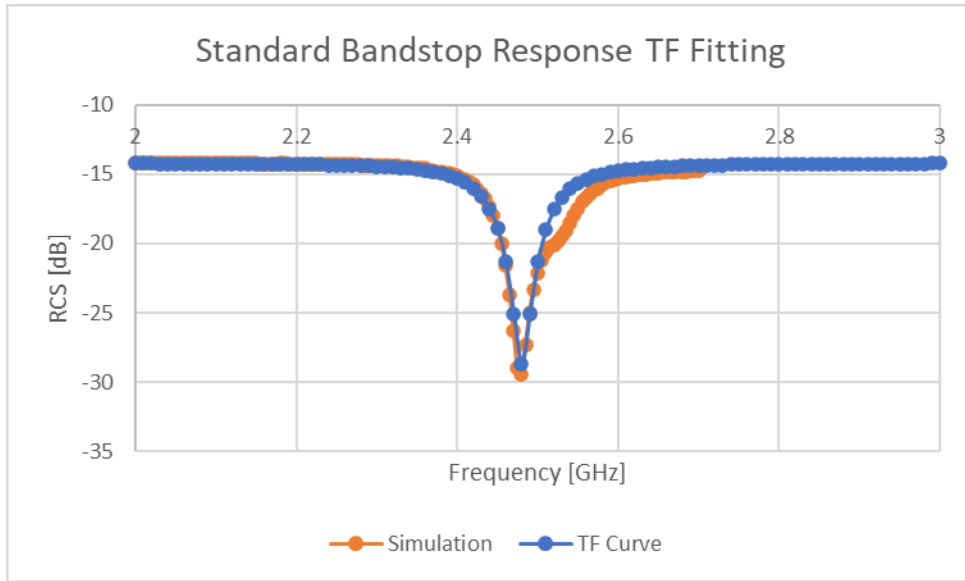
Figure H.5: Metallic Strain Sensor Response with TF Curve Fitting

From the above exploration, it is apparent that the symmetric bandstop responses can be easily accommodated for, either with polynomial curve fitting or transfer function curve fitting. Bandstop responses that are not symmetric are a greater challenge and attempts at transfer function curve fitting have been somewhat unsuccessful. The solution put forward by the author is to make use of polynomial curve fitting with these sensor responses and although that basis function is not exactly valid for this application, the resulting mismatch will be proportional to the asymmetry and that mismatch should be consistent. This effect will appear as an apparent reduction or enhancement of the sensitivity, depending on the direction of the asymmetry. In the case of the published strain sensor, the use of a polynomial curve will result in a greater underestimation of the null frequency with increasing stimulus. Figure H.6 describes this change in device sensitivity that is caused by polynomial curve fitting on an asymmetric dataset.
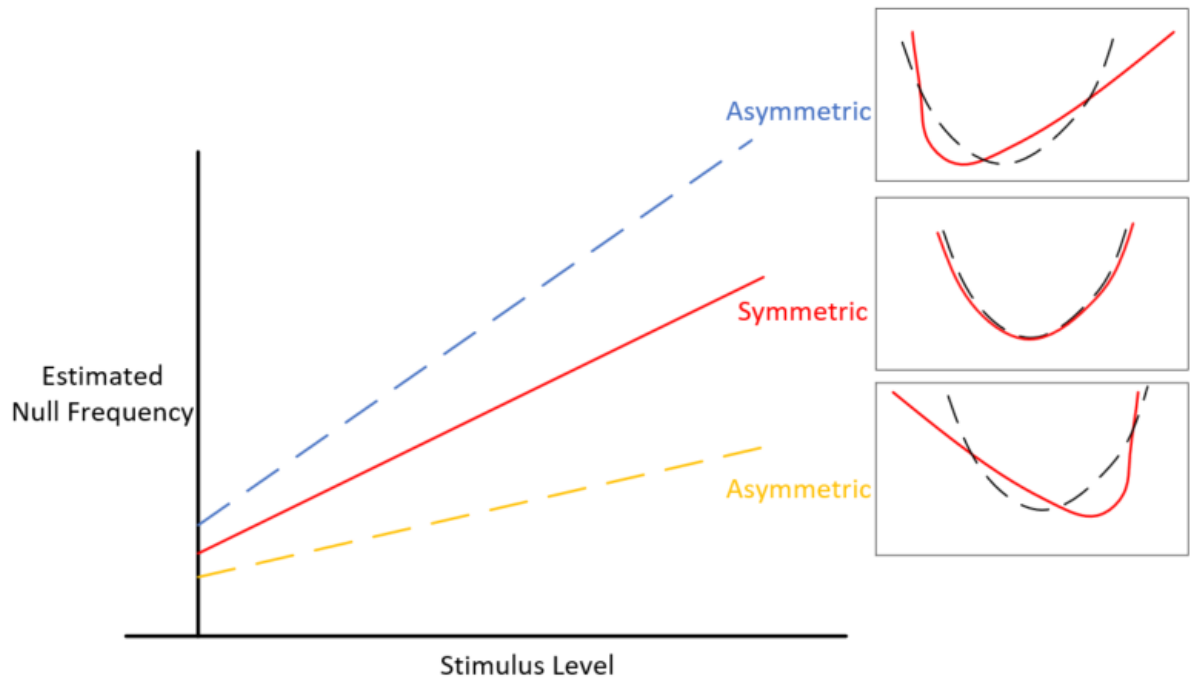
Figure H.6: Effect of polynomial curve fitting on Sensor Sensitivity with Asymmetric Bandstop Response

H.3 References

[1] Mc Gee, K. et al. Current Progress towards the Integration of Thermocouple and Chipless RFID Technologies and the Sensing of a Dynamic Stimulus, Micromachines, 2020, vol. 11, no. 11, p. 1019.

[2] Mc Gee, K. et al. Proof of Concept Novel Configurable Chipless RFID Strain Sensor, Sensors, 2021, vol. 21, no. 18, p. 6224.

[3] IBM Cloud Education What is Gradient Descent? | IBM, Oct-2020. [Online]. Available: https://www.ibm.com/cloud/learn/gradient-descent. [Accessed: 26-May-2022].

Appendix I - Reader Architecture Overview

This subsection reviews the currently published/used reader architectures for chipless RFID tags and sensors. Three main types are discussed here; Stepped Frequency Continuous Wave (SFCW), Frequency Modulated Continuous Wave (FMCW) and Impulse Radio Ultrawideband (IR-UWB) architectures.

I.1   Stepped Frequency Continuous Wave (SFCW) Architecture

This first type of architecture comprises of an oscillator system which is stepped through the frequency range of interest, as described in Figure I.1 below. At each step, the response signal is mixed with the continuously outgoing transmitted signal (of a constant frequency) for down conversion and then the signal is sampled/demodulated, before being analysed by a computer. Additional bandpass/bandstop filters and mixer stages also exist within such a setup. The final mixer stage at the receiver usually contains a bandpass filter at the Intermediate Frequency (IF) whose bandwidth can be varied such that the step resolution can be increased to comparatively high levels. This has made this reader architecture capable of performing high degrees of frequency resolution [1].
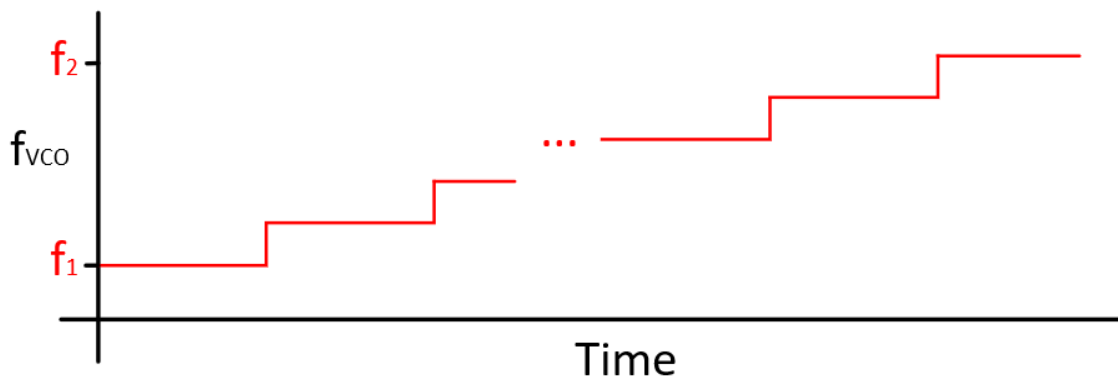

Figure I.1: SFCW Interrogation Signal Frequency Details

Most commonly found Vector Network Analysers (VNAs) are based on this architecture [1]. The difference between the simplified architecture described above and that of a common VNA is that the testing is performed to compute the 2-port scattering response of the Device Under Test (DUT) [2][1]. The computed response contains two sets of equal values, which can be summarised as S11 and S21. These two parameters are similar to the monostatic (S11) and bistatic (S21) radar responses. Care is needed when interpreting these results as their units differ than those of RCS and a reference RCS measurement is needed to convert the S-

parameters to their RCS equivalent [3]. More details on VNAs can be found in the works of Zhang in [4] and Argudo in [5].

I.2 Frequency Modulated Continuous Wave (FMCW) Architecture

An alternative approach which uses a similar hardware implementation to that of SFCW is FMCW. This approach uses a continuously ramped oscillator instead of a stepped one, this new signal can be seen in Figure I.2. This approach readily allows for device ranging (R) as the Round-Trip Time (RTT) of the signal results in a frequency difference between the incoming signal and the outgoing one. Mixing of these signals results in an IF signal whose frequency domain information is related to the RTT of the various components of the incoming signal. The mathematical relationships describing this relationship are described in [6], and can be seen in Equation I.1 to Equation I.3.
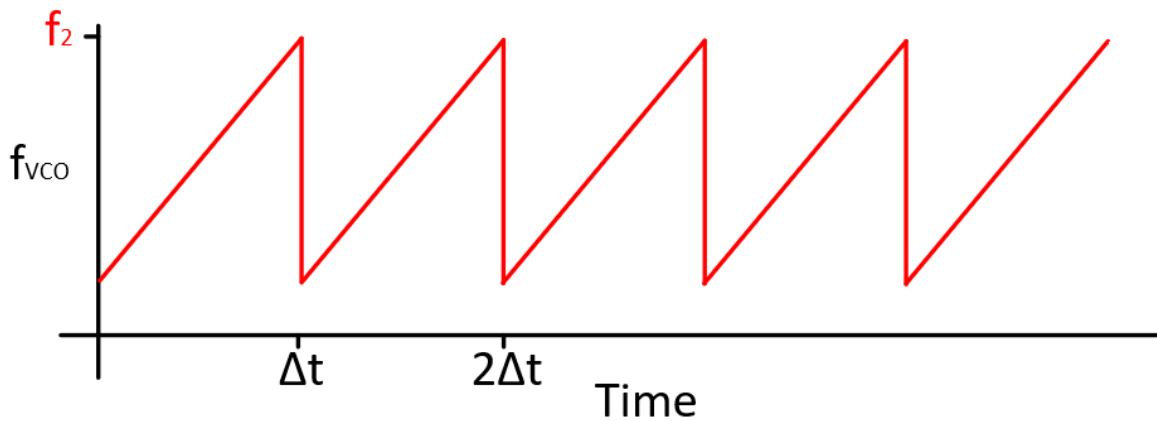

Figure I.2: FMCW Interrogation Signal

$$RTT = \frac{2\ x\ R}{c} \tag{I.1}$$

$$f_{IF} = \frac{RTT\ x\ (f_2 - f_1)}{\Delta t} \tag{I.2}$$

$$\therefore\ R = \frac{c\ x\ \Delta t}{2\ x\ (f_2 - f_1)}\ x\ f_{IF} \tag{I.3}$$

This approach allows for spatial selectivity of the tag response signals based on Euclidean distance because the tag responses are encoded at different intermediate frequencies in accordance with their RTT from the reader. Essentially, the frequency response determined through SFCW is encoded in the time domain response of the IF signal [6]. Several works have described the use of this approach in chipless RFID applications, such as the 2016 publication by Karmakar [6] but has also been discussed again in 2021 by Zhang et Al. [7]. With that being

said, the multi-tag tests performed in these works have been simulation-based. Based on the review of the known literature, it remains to be seen if this approach is suitable for a realistic setting and/or if multipath effects are a greater concern to the detection of the sensor responses. Furthermore, although several sensors/tags may share the same Euclidean distance from the reader, perhaps the use of antenna diversity can help combat this possible issue. Frequency resolution is relatively high as its architecture is similar to that of SFCW-based systems.

What is important to note is that for a set range value, a beat frequency is generated with the time domain amplitude characteristics the same as those found during the frequency domain result found with the SFCW architecture. This means that the sensor response dataset is sampled over the interval "Δt" which normally would be minimised to enhance the spatial resolution of the ranging. This would suggest that there could be a trade-off between sensor dataset resolution and spatial resolution, the impact of which is currently unknown.

I.3   Impulse Radio Ultrawideband (IR-UWB) Architecture

This reader architecture differs significantly from the aforementioned continuous wave types. This approach involves transmitting a discrete UWB pulse out to the tag and the response signal is sampled using high speed Analog to Digital Converters (ADCs). The response of a frequency domain chipless RFID tag is slightly different to the response found in the continuous wave cases. The interrogation signal is a frequency domain gaussian pulse, that can be generated using Step Recovery Diode (SRD) circuits [8]. The transmitted pulse exhibits a favourable Power Spectral Density (PSD) in that high powers can be used whilst maintaining regulation compliance [1], because the pulse is usually shorter than 2-5ns [9]. The hardware design consists of the pulse generation hardware and an associated power amplifier that is connected to the transmit antenna. The receiver hardware consists of obviously an antenna, followed by a sampling system (ADC).

The response signal from an isolated tag contains several key components, including a coupling signal originating from the scattering environment and from leakage between the antennas in a bistatic configuration. Said component ideally arrives first and has the largest magnitude of all of the response components [9]. The next significant component, which may not be easily separable from the third component, is called the structural mode. This mode arises from the normal scattering response of the tag geometry and has a significantly smaller magnitude than the coupling component. The final component is the antenna mode, which arises from the loading characteristics of the antenna/tag which gives rise to an encodable

scattering signal. Figure I.3 depicts the characteristics of the response, note; the time labels have been arbitrarily assigned based on the results found in [9] but other publications have similar time labels.
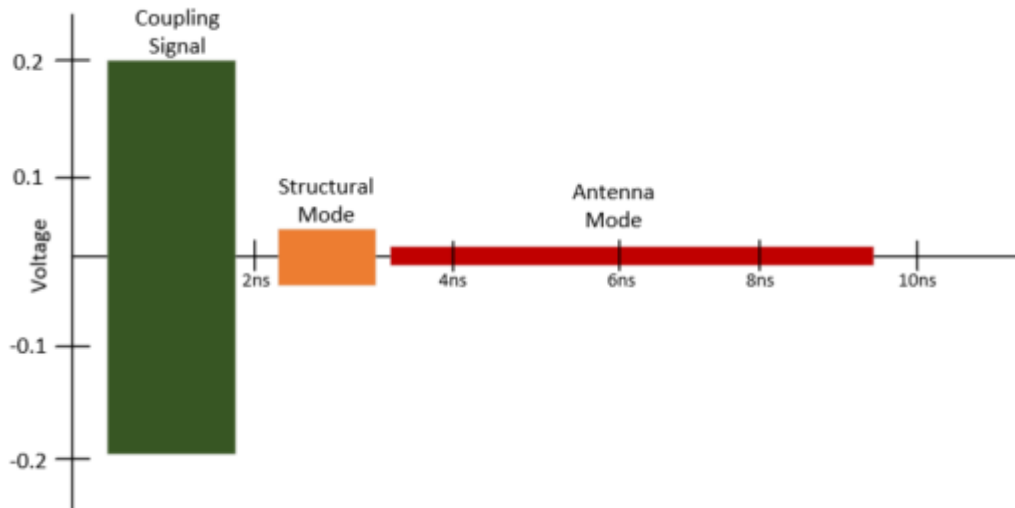

Figure I.3: Impulse-Induced Chipless RFID Tag/Sensor Response – Based on information found in Reference [9]

The sampling of such a short signal containing high frequency content is a difficult task that can lead to prohibitively high costing sampling and processing hardware. Basic hardware limitations thus limit the possible frequency resolution of the response and thus an iterative interrogation approach, called the Equivalent Time (ET) approach [10][11] is used to circumvent this. This approach uses a configurable delay to offset the triggering of the sampling stages such that successive response signals can be sampled at positions in the antenna mode that are separated by smaller timesteps than those possible when sampling a single response signal.

An alternate implementation of the IR-UWB reader architecture was developed by Aliasgari et Al. in [12] which used a down-conversion stage to remove the need for the ET system. This architecture may be capable of high-resolution frequency domain sweeps, but similar to most of the literature on chipless RFID reader systems, the emphasis during device testing is on detecting tags and not sensors. For this reason, further work is needed on the dataset resolution performance of this and the other reader architectures as much of the literature is not focussed on chipless RFID sensor interrogation.

I.4   References

[1]   Garbati, M. et al. Ultrawideband Chipless RFID: Reader Technology from SFCW to IR-UWB, IEEE Microw. Mag., 2019, vol. 20, no. 6, pp. 74–88.

[2]   Huang, Y.; Boyle, K. Antennas: From Theory to Practice. Sussex: Wiley, 2008.

[3]   Marindra, A. M. J.; Tian, G. Y. Chipless RFID Sensor Tag for Metal Crack Detection and Characterization, IEEE Trans. Microw. Theory Tech., 2018, vol. 66, no. 5, pp. 2452–2462.

[4]   Zhang, H. High speed digital design : design of high speed interconnects and signaling, First edit. Waltham, MA: Elsevier.

[5]   Argudo, M. M. Design and implementation of a compact Vector Network Analyzer, University of Wisconsin-Madison, 2014.

[6]   Karmakar, N. C. FMCW RADAR-BASED MULTI-TAG IDENTIFICATION, in Chipless Radio Frequency Identification Reader Signal Processing, New Jersey: Wiley, 2016, pp. 183–213.

[7]   Zhang, Q. et al. Chipless tag detection and recognition based on frequency modulated continuous wave, in International Conference on Internet of Things and Smart City (IoTSC 2021), 2021.

[8]   Malajner, M. et al. Design of a Low-Cost Ultra-Wide-Band Radar Platform, Sensors 2020, Vol. 20, Page 2867, 2020, vol. 20, no. 10, p. 2867.

[9]   Kalansuriya, P. et al. On the detection of frequency-spectra-based chipless RFID using UWB impulsed interrogation, IEEE Trans. Microw. Theory Tech., 2012, vol. 60, no. 12, pp. 4187–4197.

[10]   Garbati, M. et al. High performance chipless RFID reader based on IR-UWB technology, in 2015 9th European Conference on Antennas and Propagation (EuCAP), 2015.

[11]   Garbati, M. et al. Impact of an IR-UWB Reading Approach on Chipless RFID Tag, IEEE Microw. Wirel. Components Lett., 2017, vol. 27, no. 7, pp. 678–680.

[12]   Aliasgari, J. et al. IR-UWB Chipless RFID Reader Based on Frequency Translation Technique for Decoding Frequency-Coded Tags, IEEE Trans. Instrum. Meas., 2021, vol. 70.

Appendix J - Numerical Exploration of Power Distribution Effects

A simplistic exploration of the effects of multiple sensors in a single interrogation zone is performed here. Fundamentally, the power distribution on a flat plate at a distance from the transmitting antenna will supply power to the tags/sensors on that plate in some accordance with their location in the power distribution. Similarly, the response of the antenna mode part of the tag/sensor will depend on the power delivered to the device. Finally, the total response of the environment, including the sensors is summated at the receiver antenna in accordance with its radiation pattern. As the response of one of the sensors is mitigated, due to reduced power transmission and reception at that location, its part in the total response is less dominant. When this total response is interpreted in decibel form, the magnitude resonant effect appears to have been reduced, as can be seen in earlier polarization tests.

J.1   Basic Antenna Configuration

If a setup where two or more sensors are being illuminated by the interrogation beam occurs, several scenarios may occur in the total response. These scenarios, (excluding phase-based effects) include;

- All of the sensor responses overlap in the spectrum exactly and sum together to give a stronger resonant response. This scenario needs no further interpretation as all of the sensors exhibit one specific stimulus level

- All of the responses do not significantly overlap as their stimulus levels are considerably different and all sensors contribute a distinct (isolated) resonant peak/dip and these can be detected

- The responses overlap but result in fewer non-isolated peaks/dips than the number of sensors being interrogated. The challenge now is to somehow discern the contribution from each sensor

The designs developed in this work and associated interrogation antennas are based on those that rely on E(Electric) -field excitation when operated in the near-field [1][2]. This section has assumed that the sensors are now in the far-field and the classic radiation pattern(s) associated with the interrogation antennas can be assumed to be in operation.

The following analysis has considered the far-field behaviour of these sensors and has made the assumption that approximately speaking, the main lobe of the interrogation radiation pattern/front has two planes of symmetry in it or more ideally, has radial symmetry about the boresight direction. Observations made on radiation patterns listed in various books on

antennas show such assumptions are roughly valid for a number of highly directive antennas [3][4][5]. The resulting power distributions can be thus assumed to be of an elliptical or circular shape, which simplifies the analysis and said assumption has also been made in other works such as [6] and both simulation and physical testing of power distributions performed in [7] would also back up such an assumption. This analysis will consider the final scenario in isolation and will use the datasets found in [8] which correspond to that of an ELC-based chipless RFID tag. The five datasets can be seen in Figure 1 below and are offset versions of each other. The test setup has been inspired by the physical layout seen on a recent publication regarding SHM on the Chinese Space Station [9] and consists of several supposed strain sensors sitting at a distance of 20cm from each other. The layout can be seen in Figure J.2 below and the supposed stimulus applied to the sensors is a linear gradient whose response matches the five responses shown in Figure J.1. It is also assumed that the sensors are not coupled in any way to each other during operation.
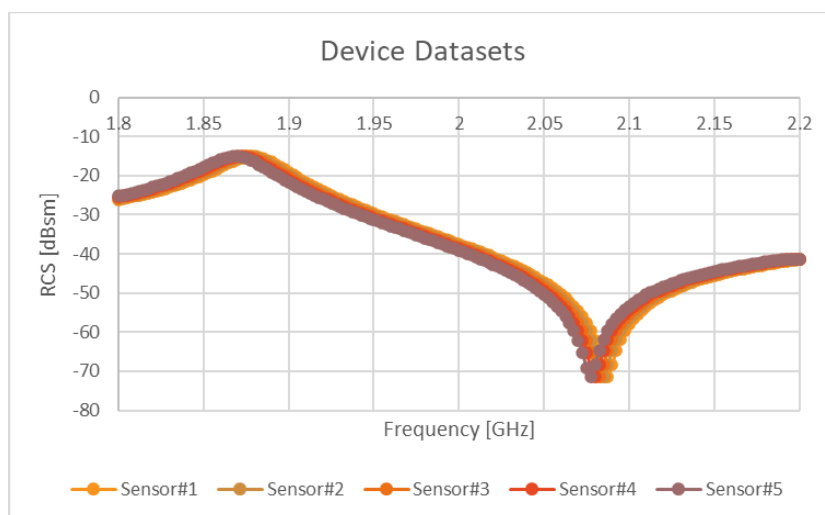

Figure J.1: Example ELC Resonator Response Datasets – Adapted from "Proof of Concept Novel Configurable Chipless RFID Strain Sensor" by McGee et al., MDPI, CC BY 4.0 [1]
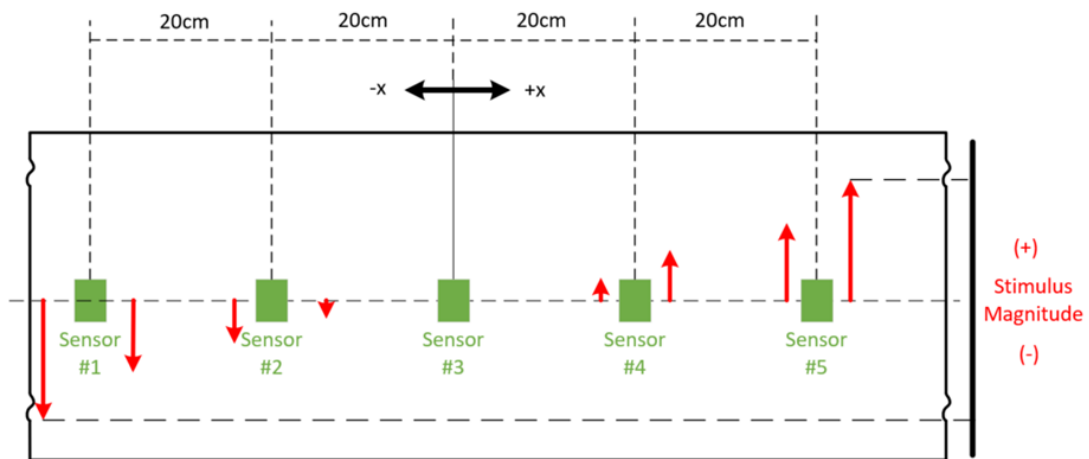
Figure J.2: Theoretical Sensor Layout and Stimulus Details

The mathematical approach taken in this work is to add the relevant magnitude gains to each of the sensor responses, depending on their location in the transmission and reception power distributions. The effects of path loss, phase-based destructive interference, and possible orientation-based variations are ignored in this analysis, for the sake of simplicity. Each of the newly computed sensor responses is converted out of decibel form and summed together before being reconverted into decibel form. The exact accuracy of simply adding gains to the sensor response in accordance with their position in the power distribution may not be ideal but what is important is how the shape of the combined response changes with increasing sensor count in the interrogation zone.

An example, highly directive Ultrawideband (UWB) chipless RFID reader antenna design has been developed by Khaliel et Al. in Reference [10]. The properties of this antenna have been summarised in Table J.1. A radiation pattern dataset was formed that was inspired by the antenna found in [10], and this dataset was used to perform the subsequent system analysis. Although this antenna has not been designed to operate at the frequencies of interest to the sensor responses found in Figure J.1 above and the radiation pattern will exhibit frequency-based variations, these minor details have been ignored so that the current exploration can proceed. As the far-field criterion effectively describe the point at which the spherical wavefront can be considered to be a plane wavefront, it stands to reason that the power distribution at a specific position on a distant plate can be considered proportional to the tangent of the angle of that position to the boresight of the interrogation beam. The interrogation antenna radiation pattern is assumed to only contain a main lobe and all other angles on the pattern have the same gain as that of the null positions on the main lobe.

Furthermore, linear interpolation is used to compute the power distribution at regions between known data points in the radiation pattern.

Table J.1: Directive Chipless RFID Reader Antenna #1 - Details found in [10]

Parameter	Value (At 6GHz)
Half Power Beam Width (HPBW)	9.9°
First Null Beam Width	22.125°
Approximate Null Gain	-20dB (normalised)
Main Lobe Gain	0dB (normalised)

The impact that increasing read range has on the detected response at the first sensor can be seen in Figure J.3. Subsequently, Figure J.4 describes the null frequency of the total computed response of the sensors when the interrogation/reception beam is focussed on each of the five sensors. This work will focus on how the minimum of the resonant curve moves throughout the analysis. This result has been plotted for several different interrogation distances as the radiation pattern is distributed over a larger area and thus contains stronger contributions from nearby sensors with increasing interrogation distance.
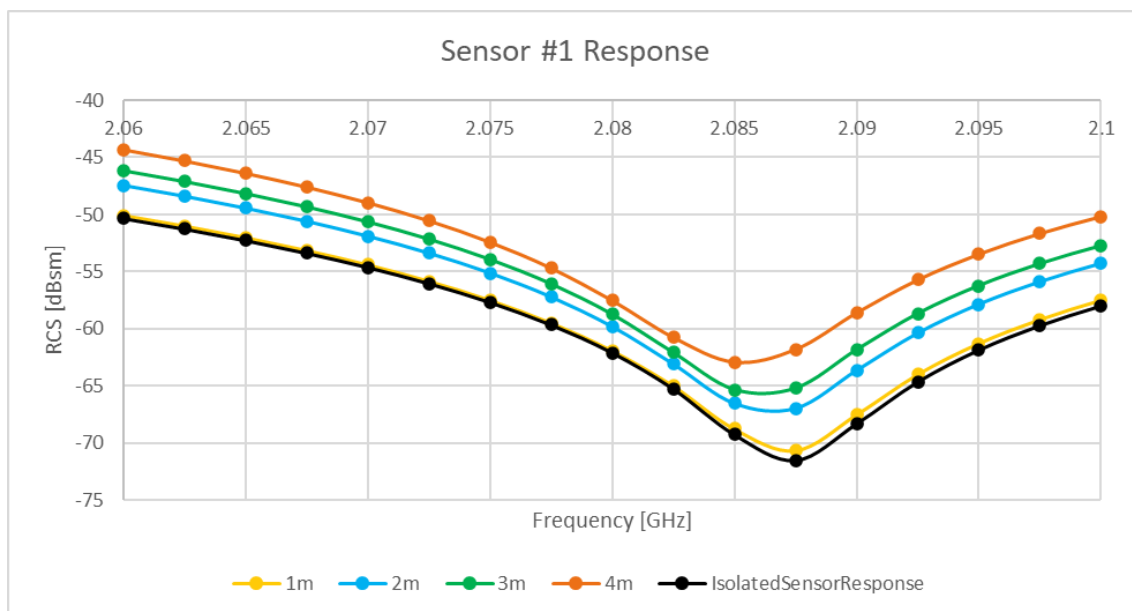

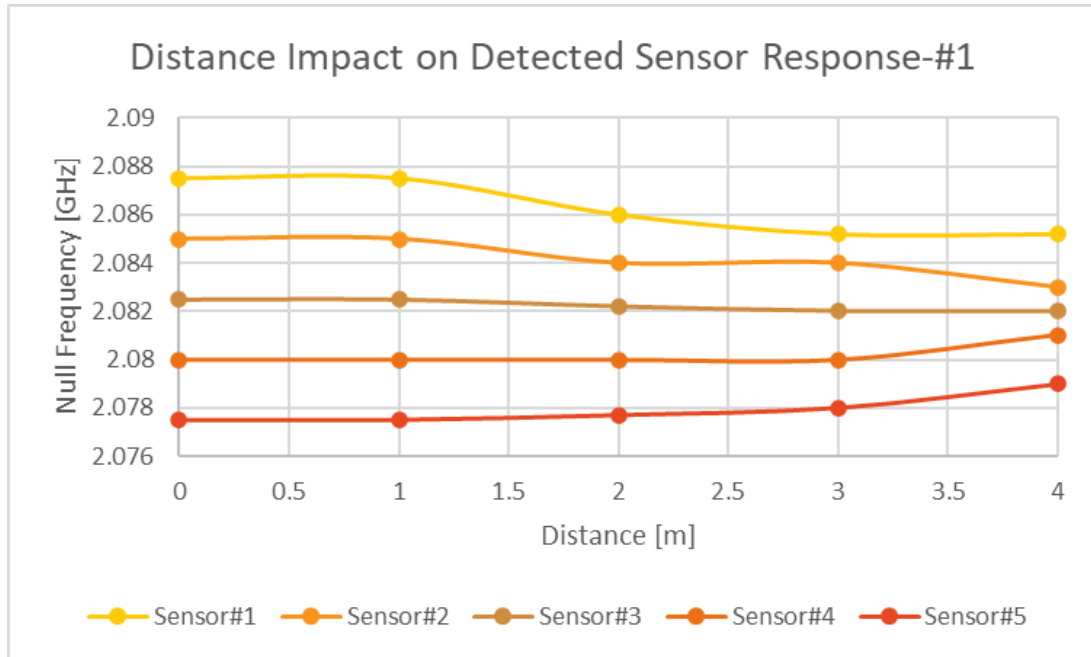*Figure J.3: Antenna #1 Read Range Impact on Sensor #1 Response*

Figure J.4: Impact of Read Range on Sensor Responses with Antenna #1

From the results in Figure J.4 found above, it is clear that the total sensor response can in certain cases deviate significantly from the isolated response. This effect differs between the five sensors with the induced change in dip location being greatest in the outermost sensors and least in the central sensor response. Reasons why this is the case is most likely caused by the fact that the stimulus gradient results in the combined effects surrounding the central sensor may cancel each other out.

A similar analysis is performed with the reader antenna inspired by the design by Babaeian and Karmakar in [11]. The relevant characteristics of this antenna and associated main lobe radiation pattern can be found in Table J.2.

Table J.2: Directive Chipless RFID Reader Antenna #2 - Details found in [11]

Parameter	Value (At 7GHz)
Half Power Beam Width (HPBW)	20.7°
First Null Beam Width	57.791°
Approximate Null Gain	-10dB
Main Lobe Gain	14.3dB

The response of the first sensor to the use of this antenna in transmission and reception configurations can be seen in Figure J.5. Similar to the results found with the other reader antenna design, these results show significant variations in dip location, caused by increasing contributions by nearby sensors. Figure J.6 depicts how the detected null frequency varies with increasing read range, for each of the five sensors.
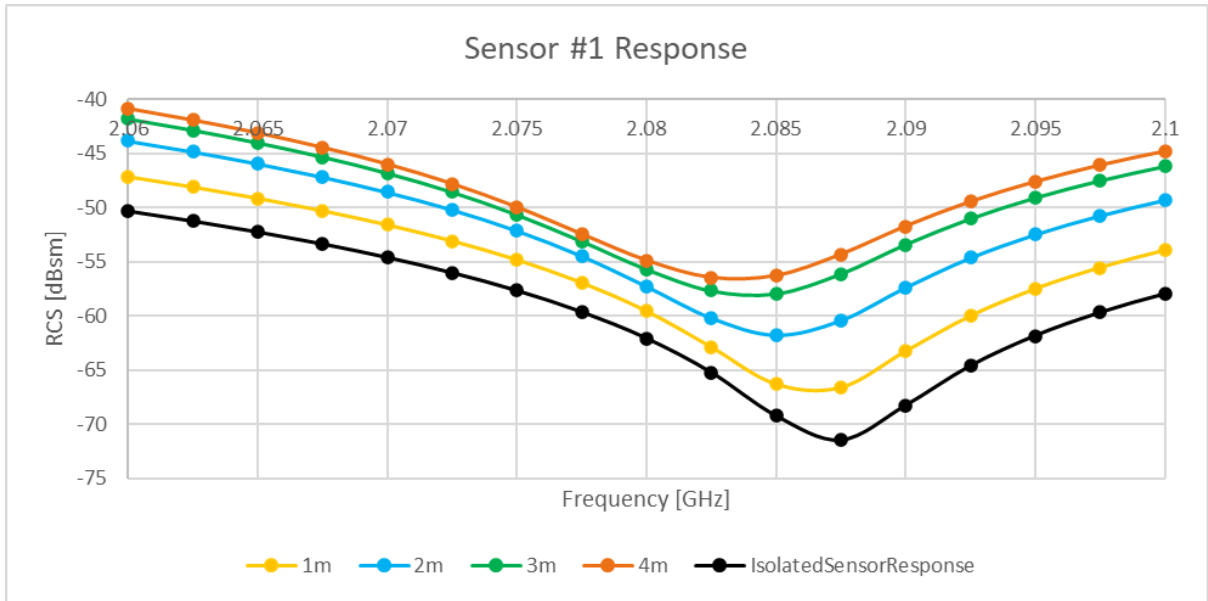
331

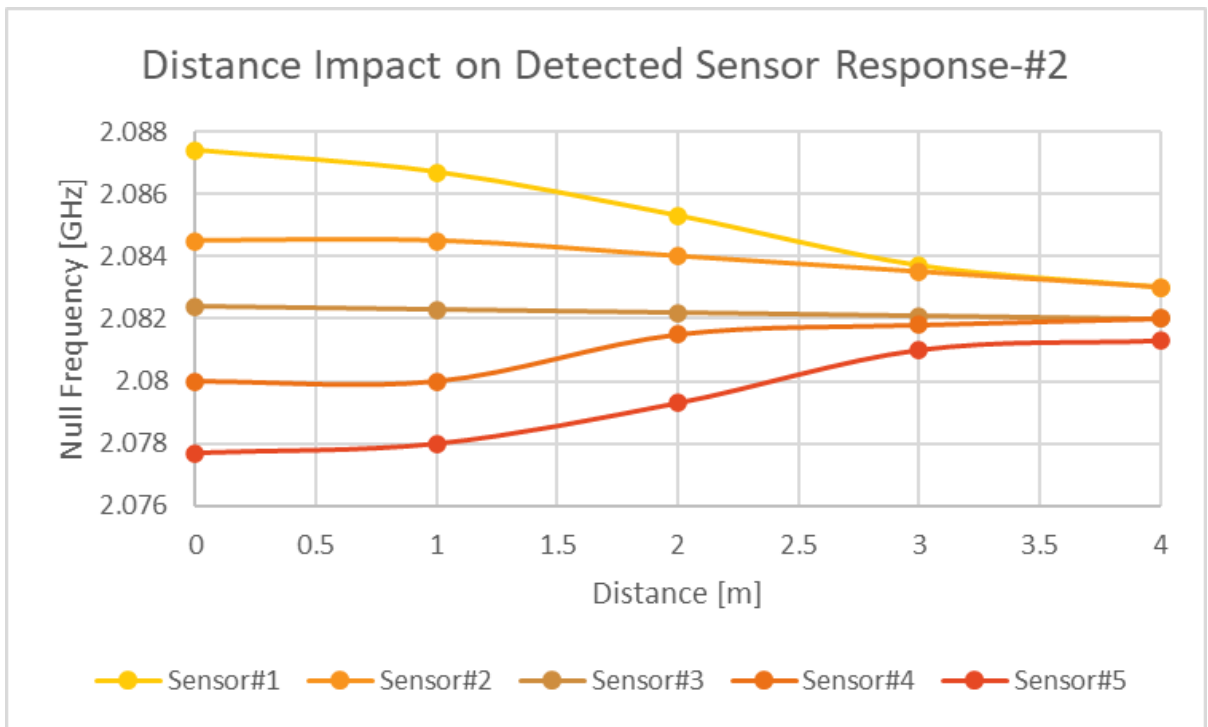Figure J.5: Antenna #2 Read Range Impact on Sensor #1 Response

Figure J.6: Impact of Read Range on Sensor Responses with Antenna #2

The effect appears to be far greater with the second reader antenna design, which would result in some general conclusions about the desirable characteristics of the main lobe of the reader antennas (narrow lobe with a sharp reduction in power with increasing distance from the boresight). However, this work is not focussed on trying to compare these antennas as both will experience this issue at some level of read range. What is important is how the magnitude and shape of the response curves change and how the stimulus levels could give

332

rise to scenarios where these effects cancel each other out. The stimulus levels in this work could be described as: {Sensor#1=1, Sensor #2=2, Sensor#3=3, Sensor#4=4, Sensor#5=5}. The location of the minimum in the response of Sensor#3 was not significantly affected with increasing contributions from the other sensors but that would not be the case in other stimulus levels such as {1,2,3,2,1}. In such a case, the combined effects would not cancel each other out, but rather reinforce each other. What is important here is whether it will be possible at all to discern each of the isolated sensor responses from this idealised response. Initial impressions suggest that the use of spatial sweeps to form sets of simultaneous equations will be computationally intensive and may require at least one interrogation where only one sensor response is present. Furthermore, these results show clear examples of situations in which transfer function curve fitting, such as that described in Chapter 3 will not be appropriate, as the curves are no longer comprised of a single sensor response.

J.2   Partially Overlapped Power Distribution Challenges

Further testing was also performed with partially overlapping power distributions, as described in Chapter 6. The first null power of the receive antennas was varied from the value specified in the respective paper down to significantly lower values. This value is important as it attempts to describe the sensitivity of the setup to multipath/environmental effects. This parameter was investigated as the drawback of using partially overlapped power distributions is that the majority of the transmitted power is sent into a region that the does not contain the sensor of interest and the receive antenna is still observing a large sensor-less region of the environment. A similar comment can also be made regarding the receptivity of the receiver antenna. The origin of these effects is described graphically in Figure J.7.
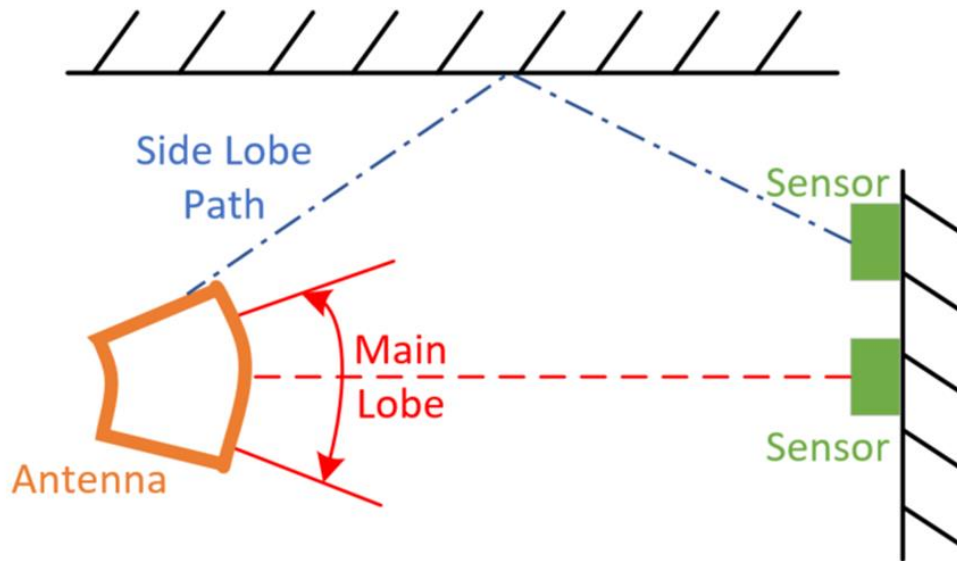
Figure J.7: Diagram of Potential Limitation of Partial Overlap Approach

Testing was performed upon Sensor #1 for both antennas at a distance of one metre. It stands to reason that longer read ranges can be achieved using this approach through beam steering such that the two main lobe power distributions only overlap over a single sensor. From the results in Figure J.8 and Figure J.9 it can be seen that the dip locations are still affected by the presence of other sensors that are not within the power distribution overlap. The effects of varying the background (main lobe null power) differed for the two reader antenna types. However, it stands to reason that the dip variation in Figure J.9 will still take place with the use of the antenna described in [10] at greater read ranges. These results show a significant degree of variability in the isolated sensor responses to that of the other curves seen in the Figures below.
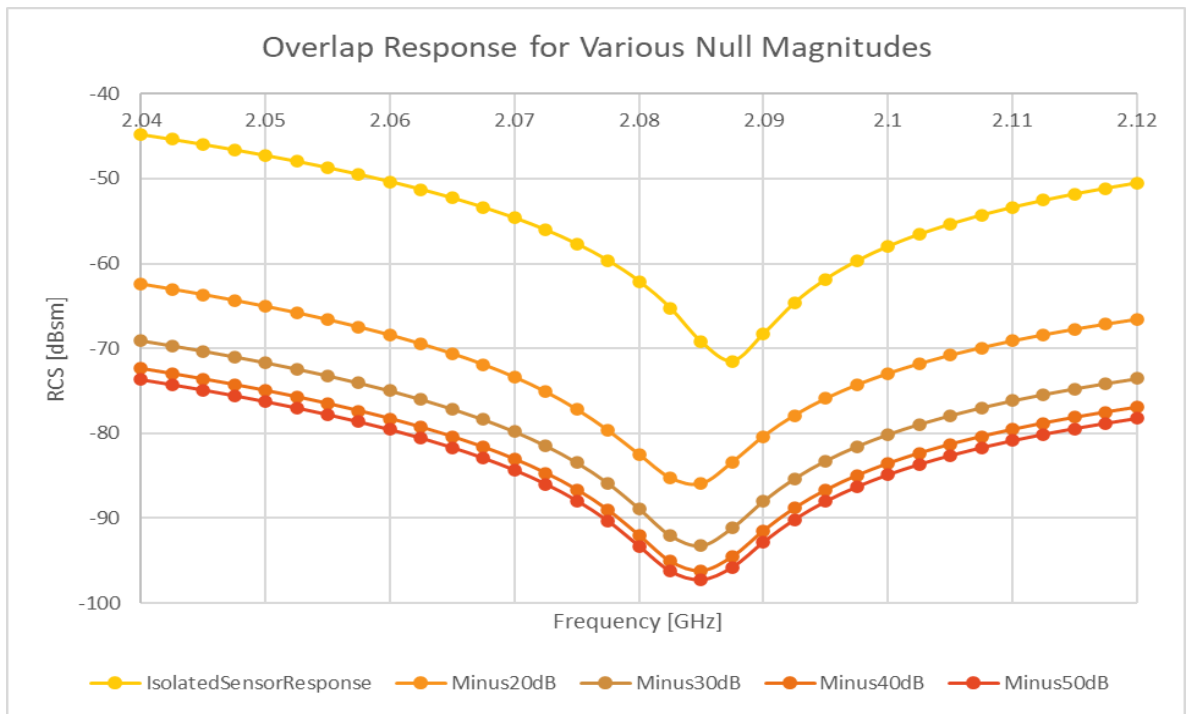
Figure J.8: Antenna #1 [10] *Response*
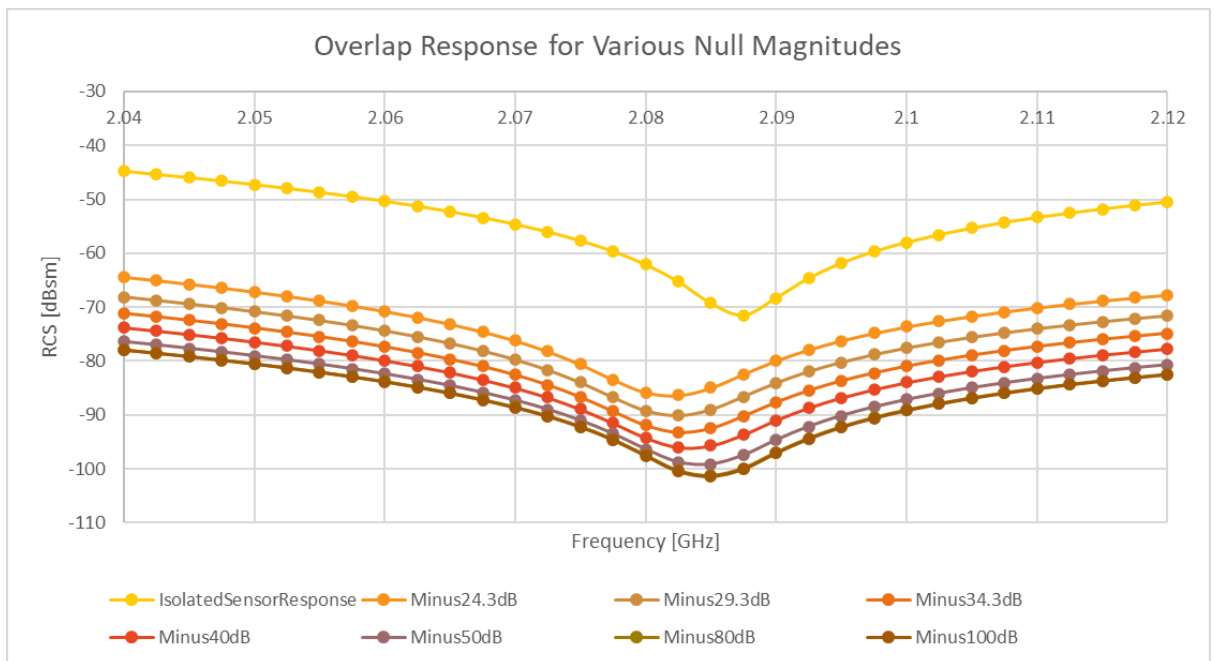

Figure J.9: Antenna #2 [11] *Response*

J.3   References

[1]   Schurig, D.; Mock, J. J.; Smith, D. R. Electric-field-coupled resonators for negative permittivity metamaterials, Appl. Phys. Lett., 2006, vol. 88, no. 4, pp. 1–3.

[2]   Pendry, J. B.; Holden, A. J.; Robbins, D. J.; et al. Magnetism from conductors and enhanced nonlinear phenomena, IEEE Trans. Microw. Theory Tech., 1999, vol. 47, no. 11, pp. 2075–2084.

[3]   Huang, Y.; Boyle, K. Antennas: From Theory to Practice. Sussex: Wiley, 2008, pp. 80-220

[4]   Kraus, J. D. Antennas, 2nd Edtn. McGraw-Hill, 1988, pp. 22-652

[5]   Blake, L. V Antennas. Wiley, 1966, pp. 190-194

[6]   Barahona, M.; Betancourt, D.; Ellinger, F.; et al. Automatic IR UWB chipless RFID system for short range applications, 2017 IEEE-APS Top. Conf. Antennas Propag. Wirel. Commun. APWC 2017, 2017, vol. 2017-Janua, pp. 274–279.

[7]   Hayashi, R.; Kanaura, R.; Yagitani, S.; et al. Radio-frequency power distribution measurement system using thin metamaterial absorber, 2016 Int. Work. Antenna Technol. iWAT 2016, 2016, pp. 157–160.

[8]   Mc Gee, K. et al. Proof of Concept Novel Configurable Chipless RFID Strain Sensor, Sensors, 2021, vol. 21, no. 18, p. 6224.

[9]   Shen, J. et al. Research on strain measurements of core positions for the Chinese space station, Sensors (Switzerland), 2018, vol. 18, no. 6.

[10]   Khaliel, M. et al. Long reading range chipless RFID system based on reflectarray antennas, 2017 11th Eur. Conf. Antennas Propagation, EUCAP 2017, 2017, pp. 3384–3388.

[11]   Babaeian, F.; Karmakar, N. A UWB Antenna for Chipless RFID Tag Detection, 2nd Int. Conf. Electr. Commun. Comput. Eng. ICECCE 2020, 2020.